Finite Element Error Estimation and Adaptivity for Problems of Elasticity

A thesis submitted for the degree of Doctor of Philosophy

by

Marcus John Ludwig

Department of Mathematics and Statistics, Brunel University

September 1998

Abstract

A posteriori error estimation employing both a recovery based error estimator derived from the work of Zienkiewicz and Zhu, [69], [70], and a residual based estimator derived from the work of Johnson and Hansbo, [27], is discussed in the context of two-dimensional linear elasticity and, more importantly, Reissner-Mindlin type plates modelled using the first-order shear deformation theory of Reddy, [40].

The extension of the *recovery based* estimator for use with plates involves firstly the search for high accuracy or superconvergent sampling points on all elements, including the transition element family of elements which have irregular midside nodes. This leads to the development of an original algorithm for choosing patches of elements for the recovery process at each node and which will be applicable to meshes containing the aforementioned transition elements and irregular nodes.

The main area of interest in this work, and one which is believed to be also original, lies in the extension and application of the *residual based* estimator to the plate problem and used in conjunction with transition elements. The characteristic difficulty of additional computation of interpolation error constants is also addressed for a variety of problems and ultimately leads to the presentation of a general technique for computing such constants. Values for the constants are provided in both the linear elasticity and plate contexts as well as over triangular, quadrilateral and transition elements. In this way an additional contribution to the field is made in the form of a catalogue of results for the interpolation error constants for error estimator use. This enables the estimator to be extended in order to be applied again over meshes containing transition elements.

Numerical results for selected test problems in both linear elasticity and plate theory are presented for the estimators. In addition, numerical comparisons with results from a physical plate test problem are presented along with estimator performance. This physical test has been performed on a sample of particle board commonly used as a flooring material and subjected to a transverse concentrated load. The model is also enhanced to consider the layers or laminates of the plate, which exist in the physical particle board sample, and again the estimator performance discussed.

Brunel University, Uxbridge
Department of Mathematics and Statistics

Marcus John Ludwig
Ph.D. thesis, 1998

Finite Element Error Estimation and Adaptivity for Problems of Elasticity

Abstract

A posteriori error estimation employing both a recovery based error estimator derived from the work of Zienkiewicz and Zhu, [69], [70], and a residual based estimator derived from the work of Johnson and Hansbo, [27], is discussed in the context of two-dimensional linear elasticity and, more importantly, Reissner-Mindlin type plates modelled using the first-order shear deformation theory of Reddy, [40].

The extension of the *recovery based* estimator for use with plates involves firstly the search for high accuracy or superconvergent sampling points on all elements, including the transition element family of elements which have irregular midside nodes. This leads to the development of an original algorithm for choosing patches of elements for the recovery process at each node and which will be applicable to meshes containing the aforementioned transition elements and irregular nodes.

The main area of interest in this work, and one which is believed to be also original, lies in the extension and application of the *residual based* estimator to the plate problem and used in conjunction with transition elements. The characteristic difficulty of additional computation of interpolation error constants is also addressed for a variety of problems and ultimately leads to the presentation of a general technique for computing such constants. Values for the constants are provided in both the linear elasticity and plate contexts as well as over triangular, quadrilateral and transition elements. In this way an additional contribution to the field is made in the form of a catalogue of results for the interpolation error constants for error estimator use. This enables the estimator to be extended in order to be applied again over meshes containing transition elements.

Numerical results for selected test problems in both linear elasticity and plate theory are presented for the estimators. In addition, numerical comparisons with results from a physical plate test problem are presented along with estimator performance. This physical test has been performed on a sample of particle board commonly used as a flooring material and subjected to a transverse concentrated load. The model is also enhanced to consider the layers or laminates of the plate, which exist in the physical particle board sample, and again the estimator performance discussed.

Contents

List of Tables

List of Figures

Acknowledgements

I would like to thank Professor J.R. Whiteman for his excellent guidance, supervision and encouragement during this work. Special thanks also go to Dr. S. Shaw for his thoughts and comments, particularly towards the final stages of the work and to Dr. M.K. Warby for his additional help and technical aid. In addition, I would like to thank all the other members of BICOM both past and present for their help and useful discussions along the way, the staff in the Mathematics and Statistics Department here at Brunel and friends both in academia and elsewhere for providing continual support and enjoyment throughout my research time. I would like to take this opportunity to also thank Professor J.N. Reddy for donating a version of his plate code as a base tool upon which to build and also Professor P. Hansbo for his helpful and informative thoughts and observations and also for allowing the inclusion of our communications in this work.

My sincere thanks also go to my family who have been not only supportive but also encouraging and understanding at all times, this could not have been done without you.

Finally, I would like to thank the EPSRC for their financial support.

To Mum, Dad and Nicholas.

Chapter 1

Introduction

Physical problems such as those encountered in the field of Engineering can manifest themselves in many different ways. Whether the problem at hand is to determine the heat flow in a body or the structural integrity of a building the first step towards obtaining the corresponding solution is to decide upon how the problem is to be described or modelled. The resulting model will usually be of a mathematical form and may itself contain assumptions and a degree of error in a bid to completely describe the underlying problem. This error is called the modelling error and although important will not be of concern here. Once the mathematical model has been established the task becomes that of solving it in order to obtain the required unknowns of the initial problem and which shall be denoted here as $\mathbf{u}$. At this point $\mathbf{u}$ can be thought of as a vector of unknowns, each of which may be in turn thought of as being position dependent in the problem domain Ω so that $\mathbf{u} \equiv \mathbf{u}(\mathbf{x})$ for $\mathbf{x} \in \Omega$. For many problems, particularly those encountered in industry, it is usually not possible to find the analytic form of $\mathbf{u}$ and in such cases an option open to the modeller is to resort to approximating the mathematical model numerically. The resulting numerical model will yield a corresponding numerical solution $\mathbf{u}_h$ which is itself an approximation to the solution $\mathbf{u}$ of the mathematical model. This approximation $\mathbf{u}_h$ will usually consist of a number of discrete points or nodal values located over a mesh which are characterised over Ω by the discretisation parameter h and interpolated using polynomial terms of order p. In this way it is thus possible to evaluate $\mathbf{u}_h \equiv \mathbf{u}_h(\mathbf{x})$ for $\mathbf{x} \in \Omega$ and express the error involved between the solutions as $\mathbf{e}(\mathbf{x}) = \mathbf{u}(\mathbf{x}) - \mathbf{u}_h(\mathbf{x})$. Unfortunately this error quantity is not directly computable due to the unknown $\mathbf{u}$ involved. The task of assessing the quality of the numerical solution thus becomes a critical one and is the impetus behind the work presented in this thesis.

Following the inception of the finite element method in the 1960's as detailed by Zienkiewicz, [65], it has become increasingly used to solve problems arising in industry ranging from the automobile and aerospace sectors to those as diverse as mining. Soon after the method had been established as a powerful numerical problem solving tool, researchers began to look at ways of measuring the error in the resulting numerical solutions. As mentioned in Oden, Demkowicz, Rachowicz and Westermann, [38], a basic question raised with increasing frequency in modern computational mechanics is, "What is the accuracy of the solution?" or equivalently, "How good are the answers?". To the modeller, the answers to questions of this kind are of paramount importance and must be provided in order to guarantee the method reliability and robustness as noted by Zienkiewicz and Zhu, [68], where it is also observed that in addition the these two requirements of the method it is also necessary for the modeller to be able to apply reasoning to the problem at hand and to the results obtained.

Attempts to answer such questions on solution quality have led to the development of error estimators. Of particular interest in this work are *a posteriori* error estimators, so called because they employ the finite element solution itself to extract information on the error present in the numerical solution. In addition to providing a global error estimate over the whole problem domain, these error estimators can also provide the modeller with elemental *error indicator* values which, for a given finite element discretisation or mesh may be used in conjunction with an adaptive strategy to highlight areas of the mesh where the numerical solution could be improved. In this way the mesh can be tailored or adapted to suit problem characteristics resulting in an *optimal* mesh which, as first described by Zienkiewicz and Zhu, [66], can be thought of as one in which the elemental contributions to the global error are equilibrated over all elements in the mesh.

It is thus clear that by employing an error estimator the quality of the numerical solution, which previously would have been estimated by the intuition of the modeller alone, can be measured by using justified and non-biased mathematical techniques. In addition, the mesh can be adapted in order to give a final numerical result for which the estimated global error is less than or equal to a desired tolerance supplied by the modeller. This is obviously a desirable capability in both industry and academia alike.

As also stated by Oden, Demkowicz, Rachowicz and Westermann, [38], the construction of an a posteriori error estimate is made with the following conditions in mind.

- The error estimator should be computable from existing data and the approximating finite element solution itself.
- The global error estimate should behave like the global error in some suitable norm. Thus if we consider the global estimate to be E then we have that,

$$C_1 E \leq ||\mathbf{e}|| \leq C_2 E, \tag{1.1}$$

  where $\mathbf{e}$ is the true error taken here in the vector context, $||\cdot||$ is some norm and C_1 and C_2 are constants which can be established asymptotically for sufficiently small meshsize h and or large order of approximant p.

The bounds given in Equation (1.1) ensure that the actual error and estimated error decrease or increase at the same rate as the mesh is adapted or as the order of approximation p is altered. Further, if such an adaptive step is implemented which can be shown to decrease E, then $||\mathbf{e}||$ will also be decreased and at the same rate as E. In order to measure the quality of an error estimator, an *effectivity index* is often employed. This quantity is expressed as,

$$\theta = \frac{E}{||\mathbf{e}||}, \tag{1.2}$$

which, it is hoped, will be close to unity and will approach unity as the adaptive process proceeds and $h \rightarrow 0$. If an error estimator is such that the effectivity index does tends to unity in this way then it is termed *asymptotically exact*. The effectivity index is viewed by many authors as an invaluable tool for assessing the quality of an error estimator. However, it has been noted by Johnson and Hansbo, [27], that the acceptable bounds on the effectivity index are by no means clearly defined. It has been shown therein that, for certain types of error estimator, it is possible to obtain values of θ ranging from 1-3 in some cases. Indeed, it is stated in [27] that the magnitude of θ depends upon the difficulty of the problem and how much effort is spent in calculating possible constants from the ancillary difficulties which may appear in the derivation of the error estimator itself. Further, it is claimed in [27] that it is not considered essential for θ to be close to unity and that estimator generality be traded for larger values of θ. If an error estimator yields a value $\theta \neq 1$, however, it is desirable for the estimation to be pessimistic with $\theta > 1$ rather than optimistic where $\theta < 1$ which would lead the modeller into thinking that the situation is better than it in fact is. Interestingly it is also claimed in [27] that efficiency has no clear connection with the effectivity index being close to unity. It is argued that, even if the error is accurately estimated so that $\theta \approx 1$, the underlying mesh may be far from an optimal mesh and there is no way this can be detected by simply looking at the effectivity index.

This work is concerned with the investigation of two types of error estimator which differ fundamentally in their approach. These estimators belong to two main groups of estimator types which are those of the recovery (or post-processed) estimators and the residual estimators. It will be shown that each type has both characteristic and ancillary problems which must be addressed. Such implementational difficulties will be compounded further in this work particularly by the use of transition elements and the subsequent presence of irregular nodes in the mesh.

The recovery based estimators have been pioneered by the work of Zienkiewicz and Zhu. In their work an estimate of the error is obtained by comparing a post-processed version of the approximate solution with the approximate solution itself as will be detailed in Section (4.2). Interest in this area grew initially from Zienkiewicz and Zhu, [66], in which a simple error estimator and adaptive procedure was proposed. This estimator was subsequently analysed by Ainsworth, Zhu, Craig and Zienkiewicz, [3], where it was shown to not be asymptotically exact but at the same time found to be efficient. This was also shown to be the case by Babuška and Rodríguez, [8], in the one-dimensional setting. The initial estimator of [66] was followed by Zhu and Zienkiewicz, [64], in which the authors proposed the idea of superconvergent recovery for use in recovery type error estimators in one dimension. The extension of the idea to two dimensions was proposed by Zienkiewicz and Zhu, [69], which outlined a new recovery technique performed over element patches constructed around nodes, and [70], which detailed the use of the recovered solution in an error estimate. It was claimed that the error estimator resulting from this latest superconvergent patch recovery technique would be asymptotically exact. These two publications subsequently attracted much attention from fellow researchers mainly with recommendations on how to improve the recovery procedure. One of the first of these contributions involved the two main authors themselves in Zienkiewicz, Zhu and Wu, [72], which detailed an improvement to be made in order to obtain superconvergent results for problems involving higher order finite element shape functions. At approximately the same time Wiberg and Abdulwahab, [56], proposed a recovery procedure which was an extension of that in [69]. In this technique a residual term is included in the functional to be minimized over each patch of elements. In this way it is claimed that the equilibrium equations are coupled in the recovery technique which leads to a higher accuracy particularly at the domain boundary. This observed improvement on the boundary led to a presentation being given at the MAFELAP 1993 conference and subsequently publication by Wiberg, Abdulwahab and Ziukas, [57]. This period saw many implementations and analyses of the Zienkiewicz-Zhu type (Z-Z) estimators, the reason for this being probably due to the estimator's ease of implementation which made it attractive to researchers. Rodríguez, [45], showed asymptotic exactness of the original estimator proposed in [66] for certain 'parallel' meshes with the name parallel being given if the union of any two triangles in the mesh sharing an edge form a parallelogram. It was also shown however, that the asymptotic exactness property did not hold for general meshes, an observation also made in [8] at approximately the same time. In addition Zhang and Victory, [62], were also able to verify the superconvergence claim of the recovery technique presented in [69] for uniform rectangular meshes and provided some theoretical justification for the estimator success.

Elsewhere in the field researchers were continuing to provide enhancements to the original estimator and recovery technique. Tabbara, Blacker and Belytschko, [54], for example, proposed a new recovery technique where it was claimed that no knowledge of the superconvergent points required in that of [69] was required whilst Li and Wiberg, [30], proposed a change in the patch selection itself. This modified patch is defined as an element patch and is formed by the union of all elements surrounding the element of interest. This differs from the node patch proposed in [69] which is defined as the patch of elements surrounding the node at which recovery is required. This idea was taken one step further by Wiberg, Abdulwahab and Ziukas, [58], where weights were introduced to the recovery procedure. Due to implementational difficulties encountered by Labbé and Garon, [28] detailed improvements to be made for the implementation of the recovery procedure given in [69]. These difficulties included the task of recovery for a node patch consisting of only one or two elements, a feature also observed by Ludwig, [32]. The solution to this problem proposed in [28] was to modify the number of sampling points in the patch whereas in [32] the solution found was to modify the patches in such problem cases. In Zienkiewicz and Zhu, [71], it was shown that superconvergent stresses or gradient values would be obtained providing that the sampling points used in the patches possessed superconvergent properties. This observation leads on to the related field of superconvergence and the existence of superconvergent points in the finite element approximation.

From early in the life of the finite element method, modellers particularly within the engineering field have postprocessed the finite element approximation in order to obtain improved derivative values and correspondingly improved strain and stress values. Such procedures usually rely on the fact that there exist superconvergent points in the finite element approximation which can be used in the postprocessing stages of the analysis. One of the first publications in this area was that of Barlow, [14], in which a method for determining the locations of 'optimal stress points' is detailed. This is done by comparing the displacement field which can be exactly represented by the chosen finite element approximation over an element with that desired. By equating the two it is possible to determine where the agreement will be high in accuracy as discussed further in Section (4.3.1). The work of Barlow led to the identification of Barlow points as discussed by Reddy, [41], where it is also noted that these points coincide with Gauss points. A similar finding was also proposed by Zlámal, [73], who was able to show superconvergence of the finite element gradient at Gauss points on regular meshes of quadrilateral elements. A different technique to that of Barlow for predicting the locations of such points was proposed by Mackinnon and Carey, [33], in which an analysis based on Taylor series was proposed. By differentiating the finite element interpolant or approximation certain points can be identified which give an approximation to the true derivative which has a higher convergence rate. This property is called superconvergence and such points are the sought after superconvergent points. This analysis will be applied along with that of Barlow in Section (4.3.1). More recently Babuška, Strouboulis, Upadhyay and Gangaraj, [9] and [10] have provided a computer based proof of the locations of superconvergent points. In [9], the notion of η%-superconvergence is introduced, this quantity measures the quality or degree of superconvergence measured at a point. The percentage measure can be thought of as a percentage error tolerance upon the degree of superconvergence at a point. Thus for a general mesh, all points in each element will be 100%-superconvergence points and the classical superconvergence points may be considered 0%-superconvergence points. In this way it is thus possible to establish areas of varying degrees of superconvergence and, coupled with the computer based approach, illustrate these areas upon nonuniform meshes. In [9] this technique is also applied to meshes of quadrilateral elements containing irregular midside nodes. Although these midside nodes are constrained and thus not 'active' in the finite element model the results bear a strong similarity to those presented in Section (4.3.1) in this work where the irregular nodes are active.

The residual type estimators have a more theoretical background. Indeed such estimators are usually born from the bilinear form of the parent problem and adapted in such a way as to be evaluated on the elements. Ordinarily such estimators involve a residual to be integrated over the interior of each of the elements and also the presence of gradient or stress jumps which must be integrated along the interelement edges. A global error estimate may then be obtained by summing over all the element contributions. Residual based estimators may be largely attributed to the work of Babuška and his co-workers with one of the initial publications appearing as early as 1978 by Babuška and Rheinboldt [7] which involved the solution of local Dirichlet problems surrounding each node in the finite element mesh. Bank and Weiser, [13], later proposed three new a posteriori error estimators, these involved the solution of local Neumann problems defined on each element. The ideas behind the estimator of [7] were used again in Babuška and Miller, [6], where an estimator was described for meshes of quadrilateral elements and meshes again containing constrained midside irregular nodes. The residual based estimator of Johnson and Hansbo, [27], is computed in a different way. In their work the elemental indicator contributions to the global error estimate are obtained as previously described by computing the norm of the local residual and also the jump in normal derivative of the computed solution at interelement boundaries and will be discussed further in Section (4.4). This estimator also relies upon the computation of interpolation error constants for error estimates in the energy norm and this task will be detailed in Chapters 5 and 6. At approximately the same time as that of [27] a similar estimator by Brenner and Sung, [16], was also proposed. In addition, proofs for the existence of the interpolation error constants are given therein.

More recently the Johnson-Hansbo error estimation technique has attracted interest from researchers wishing to employ it in a variety of problems. Stewart and Hughes, [51], proposed an application to the Helmholtz equation. Due to the characteristics of this equation it is found that the estimator is required to be computed in a norm which in turn requires the computation of stability constants in addition to the aforementioned interpolation error constants. A method for doing this is detailed in [51] and although the computation of such stability constants will not be required in this work a reference to the method proposed in [51] is included here for completeness. A feature of the Johnson-Hansbo error estimator is that it can be used to treat non-steady state problems involving space and time. The initial work of Shaw and Whiteman, [48], investigates the application of a 'Johnson type' a posteriori error estimator to a prototype history integral quasistatic viscoelastic model. Although it is found possible to obtain a computable error bound, no means is found for selecting the time step in order to control the error and consequently a heuristic adaptive criterion is developed. This initial model is enhanced in Shaw and Whiteman, [49], where a full viscoelastic problem is modelled by an elliptic partial differential equation along with a Volterra (memory) term. By again applying the Johnson 'machinery' and allowing only nested refinement of the space meshes - due to the viscoelastic memory term memorizing the jumps over all element edges in all previous space meshes - the a posteriori bound is found to contain two principal terms. The first of these terms can be used to control the spatial meshes whilst the second term contains the 'time error'. It is stated in [49] however, that the 'time error' term is not robust although it is possible to improve the situation by measuring it in a different norm. This is explained in more detail in Shaw and Whiteman, [50], where the original model of [48] is again modelled and the error measured in a weaker negative norm which enables a time step selection criterion to be established. A similar negative norm approach is adopted by Süli and Houston in

[53] for the Johnson type error estimator approach applied to first order hyperbolic systems and unsteady scalar hyperbolic problems and which is discussed in greater detail in Süli, [52]. As a final note on the general applicability of the Johnson type residual estimator, the work of Jackson and Süli, [25], details the application to the one-dimensional Black-Scholes financial model. Mathematical finance is currently a fast growing area of research and such applications have immediate value to the finance industry where there seems to be little error estimation currently performed.

Work here will be particularly concerned with the estimator of Johnson and Hansbo, [27], which generally requires the investigation of two constants, a stability constant and an interpolation error constant. For the case where the estimator is required in the energy norm, however, the stability constant is included in the interpolation error constant definition which in turn contains a dependence on the energy norm as will be seen in Chapter 4. The error estimator in this work will thus require the investigation of subsidiary interpolation error problems and the subsequent calculation of interpolation error constants. A strong reliance is placed upon the accuracy of the calculated interpolation error constants and it is thought that in addition to providing a general technique for computing them this work will also detail them, for the first time to the best of our knowledge, for the case of transition elements. A recent publication by Handscomb, [23], analyses the interpolation error in both one dimension and two dimensions over a triangle in terms of both L_2 and L_∞ bounds. Although these results will not be used in this work it is interesting to see that for the two-dimensional cases Handscomb resorts to numerical solutions of the problems via the solution of generalized eigenvalue problems. This mirrors the techniques developed independently in this work and presented in Chapters 5 and 6 along with interpolation error constant results.

In addition to the many publications concerning a posteriori error estimation, there have been a number of publications which provide an overview of the estimator scene. Such publications include [2], [11] and [38].

Another aim of this work is to extend novel error estimation techniques to problems of Reissner-Mindlin plate theory modelled using the first-order shear deformation theory (FSDT) used by Averill and Reddy, [5] and detailed in Ochoa and Reddy, [37], Reddy, [40] and Reddy and Miravete [41]. In many cases the methods will initially be described in the context of two and three dimensional linear elasticity and then modified to the plate context. The error estimators will be built on the previous estimators of Zinekiewicz and Zhu, [69],[70] and Johnson and Hansbo, [27], and will be extended firstly for use in the plate problem and secondly to cope with the presence of transition elements in the mesh and the associated difficulties these elements introduce.

Chapter 2 of this thesis introduces the mathematical models to be used. This begins with a description of a three dimensional linear elasticity model and also the construction and content of material property matrices. The plate models are then introduced in the form of both classical plate theory and plates of Reissner-Mindlin type, [35], [42], modelled using FSDT. The inclusion of the classical theory, however, is merely for completeness and it is the FSDT which will be persued further in this work.

Chapter 3 begins with the derivation of the weak formulations of the models. This is followed by descriptions of the finite element formulations to be used for both the linear elasticity and plate models. For the case of the plate finite element formulation a numerical tool known as reduced integration is discussed which increases the capability of the model to cope with thin plates. This is done by eradicating the 'locking' phenomenon often observed in which the deflections are underpredicted as the thickness of the plate decreases. The chapter concludes with an introduction to the transition element family and the modifications required for their quadrature schemes.

Chapter 4 is concerned with the error estimators proposed by Zienkiewicz and Zhu (Z-Z), [69] and [70] and Johnson and Hansbo (J-H), [27], and their subsequent adaptation and extension to the problems of interest in this work. The difficulty of identifying the locations of optimal sample points for the implementation of the Z-Z estimator is addressed, it is believed that this is the first time this has been illustrated in the case of the transition element family. An algorithm resulting from these findings will then be proposed for the patch selection to be used in the estimator. Following an illustration of the J-H estimator applied to a problem of two dimensional linear elasticity, an extension to cope with transition elements is proposed. This is followed by a new implementation of the estimator to the plate problem and also the corresponding extension for transition elements. As previously noted, this estimator relies upon the accurate computation of interpolation error constants and this task will be addressed in the two following chapters.

Chapter 5 details the computation of the interpolation error constants for scalar valued problems. This chapter begins by taking a problem in one dimension for which the interpolation error constant value is obtained analytically and then verified computationally. In two dimensions results are then presented for both triangular and square elements. The technique is then refined to present results for the transition element family.

Chapter 6 details the computation of the interpolation error constants for vector valued problems. More specifically, results are presented for problems in the linear elasticity and plate contexts and results are again presented for both triangular and square elements. The plate results are compared with those for elasticity where it is shown the plate thickness has a strong effect upon the resulting interpolation error constant value. The chapter concludes with a verification of the results and, it is believed, their justification as improvements over those given in [27].

Chapter 7 presents the numerical results for the error estimators. This begins by considering test problems in linear elasticity and shows the effectiveness of both the modified Z-Z and J-H estimators from Chapter 4 when used adaptively in conjunction with the transition elements. Results for test problems applied to plates are then presented and again the estimators are demonstrated to perform well. Comparisons are then made between results from a physical experiment conducted at the Forest Products Research Centre located at Buckinghamshire College in High Wycombe and those obtained from the model. It is shown that good agreement is observed illustrating an immediate application of the work presented.

Chapter 8 concludes the thesis by providing conclusions and thoughts about the work presented as well as possible future enhancements and recommendations.

Chapter 2

Model Formulations and Background

The aim of this chapter is to provide an overview of the types of problems modelled in this work. Such problems may be grouped into two main areas of application. The first of these is linear elasticity in both two and three dimensions and the second is that of plate theory. In addition to posing the problems involved, an attempt will also be made to discuss the assumptions and approximations made in the modelling of the problems and also to describe the details upon which the models are based.

2.1 Linear Elasticity

The behaviour of most elastic solids conforms well to a linear elastic model under the following three restrictions:

- At each point the stress, and hence the strain, is sufficiently small.
- Time dependent effects are negligible.
- The material satisfies Hooke's law which linearly relates the stress to strain in the material.

Consider the deformation of a solid body, defined in the region $\Omega \subset \mathbb{R}^3$ with boundary $\partial\Omega$ and under the action of external forces. Let the displacement at any point $\mathbf{x} \equiv (x_1, x_2, x_3)^T$ of Ω be denoted by $\mathbf{u} \equiv (u_1, u_2, u_3)^T$ and also let the stress and strain tensor components be denoted respectively by σ_{ij} and ε_{ij}, $1 \leq i, j \leq 3$. These components make up the symmetric stress and strain tensors $\boldsymbol{\sigma}$ and $\boldsymbol{\varepsilon}$ which have the forms $(\sigma_{ij})_{i,j=1}^3$ and $(\varepsilon_{ij})_{i,j=1}^3$ respectively.

In order to establish the governing equations for linear elasticity, we begin by using laws of Physics. Based on the law of conservation of momentum for the steady state case (when there is no acceleration) the stress experienced by a body under the action of an external force $\mathbf{f} \equiv (f_1, f_2, f_3)^T$ satisfies the *equilibrium equation* system,

$$\sum_{j=1}^{3} \frac{\partial \sigma_{ij}(\mathbf{x})}{\partial x_j} + f_i(\mathbf{x}) = 0, \quad \text{for } \mathbf{x} \in \Omega \text{ and } i = 1, 2, 3. \tag{2.1}$$

This may be written alternatively as,

$$-\mathrm{div}\boldsymbol{\sigma} = \mathbf{f}, \quad \text{for } \mathbf{x} \in \Omega,$$

where we define,

$$\mathrm{div}\boldsymbol{\sigma} := \left(\sum_{j=1}^{3} \frac{\partial \sigma_{ij}}{\partial x_j} \right)_{i=1}^{3}, \quad \text{and where} \quad \boldsymbol{\sigma} = (\sigma_{ij})_{ij=1}^{3} \equiv \begin{bmatrix} \sigma_{11} & \sigma_{12} & \sigma_{13} \\ \sigma_{21} & \sigma_{22} & \sigma_{23} \\ \sigma_{31} & \sigma_{32} & \sigma_{33} \end{bmatrix},$$

is the previously introduced stress tensor with components given by Hooke's law in terms of the material properties and strain which will be defined in the following section. In modelling a physical body which is being acted upon by such a force it is also necessary to consider the possible rigid body motions. These are those which would ordinarily occur if there were no physical supports restraining the orientation and position of the body. Thus a rigid body motion can be thought of as a displacement of the body which yields zero strain or stress in the body. Alternatively the body can be thought of as moving without changing shape and with the distance between any two particles remaining constant throughout the body translation. In practice a body will be normally restrained by static supports as in the case of floor boarding or shelving. These supports act on the perimeter or the boundary of the body under consideration and thus need to be built into the mathematical model. This is done using boundary conditions which may be of Dirichlet, Neumann or mixed type. Typically Dirichlet boundary conditions have the form,

$$\mathbf{u}(\mathbf{x}) = \mathbf{0}, \quad \text{for } \mathbf{x} \in \partial\Omega_C, \tag{2.2}$$

where the behaviour of the displacement on a portion or all of the boundary is prescribed and is commonly set to zero. Neumann boundary conditions prescribe derivative terms and for elasticity problems have the form,

$$\sum_{j=1}^{3} \sigma_{ij}\, n_j = g_i(\mathbf{x}), \quad \text{for } \mathbf{x} \in \partial\Omega_T \text{ and } i = 1, 2, 3, \tag{2.3}$$

where $\partial\Omega \equiv \partial\Omega_C \cup \partial\Omega_T$ is a partition of the boundary $\partial\Omega$, and $\mathbf{n}$ is the unit outward normal vector to $\partial\Omega$. All problems in this work will be modelled using boundary conditions of Dirichlet type. To give some idea of the measure of stress and strain, the following section derives the relationship between strain and displacement.

2.1.1 The Strain-Displacement Relation

In order to measure how a body deforms under an applied force it is necessary to define what is meant by the strain. This quantity measures the relative movement between particles in a deformable body. Consider the position vector $\mathbf{X}$ of a point in an undeformed body. On application of an external force, this point will move to a new position $\mathbf{x} = \mathbf{X} + \mathbf{u}$, where $\mathbf{u}$ denotes the displacement vector. By considering another point on the undeformed body at the point $\mathbf{X} + \Delta\mathbf{X}$, a line segment dS may be defined between the two, as shown in Figure (2.1). On application of the

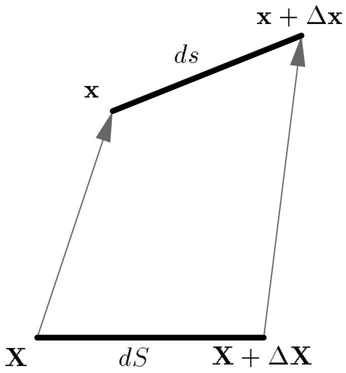

Figure 2.1: Illustration of possible line segment orientations.

force this new point will move to a new position $\mathbf{x} + \Delta\mathbf{x}$. Thus, we may redefine the line segment in the deformed body as ds. In order to have a measure of the deformation, we shall consider the change in length squared of the line segment from the undeformed or reference position to the deformed body configuration given by $(ds)^2 - (dS)^2$. Firstly the length $(ds)^2$ may be defined as,

$$(ds)^2 := \|d\mathbf{x}\|^2 = d\mathbf{x}^T.d\mathbf{x},$$

where,

$$d\mathbf{x} = \begin{bmatrix} dx_1 \\ dx_2 \\ dx_3 \end{bmatrix} = \begin{bmatrix} \frac{\partial x_1}{\partial X_1}dX_1 + \frac{\partial x_1}{\partial X_2}dX_2 + \frac{\partial x_1}{\partial X_3}dX_3 \\ \frac{\partial x_2}{\partial X_1}dX_1 + \frac{\partial x_2}{\partial X_2}dX_2 + \frac{\partial x_2}{\partial X_3}dX_3 \\ \frac{\partial x_3}{\partial X_1}dX_1 + \frac{\partial x_3}{\partial X_2}dX_2 + \frac{\partial x_3}{\partial X_3}dX_3 \end{bmatrix}.$$

Thus it is possible to express,

$$d\mathbf{x} = \begin{bmatrix} \frac{\partial x_1}{\partial X_1} & \frac{\partial x_1}{\partial X_2} & \frac{\partial x_1}{\partial X_3} \\ \frac{\partial x_2}{\partial X_1} & \frac{\partial x_2}{\partial X_2} & \frac{\partial x_2}{\partial X_3} \\ \frac{\partial x_3}{\partial X_1} & \frac{\partial x_3}{\partial X_2} & \frac{\partial x_3}{\partial X_3} \end{bmatrix} \begin{bmatrix} dX_1 \\ dX_2 \\ dX_3 \end{bmatrix} \equiv \mathbf{F}d\mathbf{X}.$$

The line segment length squared of ds may thus be expressed as,

$$\begin{aligned} (ds)^2 = \|d\mathbf{x}\|^2 = d\mathbf{x}^T.d\mathbf{x} &= (\mathbf{F}d\mathbf{X})^T\,\mathbf{F}d\mathbf{X} \\ &= d\mathbf{X}^T\mathbf{F}^T\mathbf{F}d\mathbf{X}. \end{aligned}$$

Also, dS may similarly be expressed as,

$$(dS)^2 = \|d\mathbf{X}\|^2 = d\mathbf{X}^T.d\mathbf{X}.$$

The difference in line segment length squared may thus now be written,

$$\begin{aligned}(ds)^2 - (dS)^2 &= d\mathbf{X}^T\mathbf{F}^T\mathbf{F}d\mathbf{X} - d\mathbf{X}^T.d\mathbf{X}\\ &= d\mathbf{X}^T\left[\mathbf{F}^T\mathbf{F} - \mathbf{I}\right]d\mathbf{X}\\ &= 2\left(d\mathbf{X}\right)^T\mathbf{E}d\mathbf{X},\end{aligned}$$

where,

$$\mathbf{E} \equiv \frac{1}{2}\left[\mathbf{F}^T\mathbf{F} - \mathbf{I}\right]. \tag{2.4}$$

Since we know that,

$$\mathbf{F} = \begin{bmatrix} \frac{\partial x_1}{\partial X_1} & \frac{\partial x_1}{\partial X_2} & \frac{\partial x_1}{\partial X_3}\\ \frac{\partial x_2}{\partial X_1} & \frac{\partial x_2}{\partial X_2} & \frac{\partial x_2}{\partial X_3}\\ \frac{\partial x_3}{\partial X_1} & \frac{\partial x_3}{\partial X_2} & \frac{\partial x_3}{\partial X_3}\end{bmatrix} \qquad \text{and} \qquad \begin{aligned} x_1 &= X_1 + u_1,\\ x_2 &= X_2 + u_2,\\ x_3 &= X_3 + u_3,\end{aligned}$$

then $\mathbf{F}$ may be rewritten as,

$$\mathbf{F} = \begin{bmatrix} 1 + \frac{\partial u_1}{\partial X_1} & 0 + \frac{\partial u_1}{\partial X_2} & 0 + \frac{\partial u_1}{\partial X_3}\\ 0 + \frac{\partial u_2}{\partial X_1} & 1 + \frac{\partial u_2}{\partial X_2} & 0 + \frac{\partial u_2}{\partial X_3}\\ 0 + \frac{\partial u_3}{\partial X_1} & 0 + \frac{\partial u_3}{\partial X_2} & 1 + \frac{\partial u_3}{\partial X_3}\end{bmatrix}.$$

Also, by defining

$$\nabla\mathbf{u} := \begin{bmatrix} \frac{\partial u_1}{\partial X_1} & \frac{\partial u_1}{\partial X_2} & \frac{\partial u_1}{\partial X_3}\\ \frac{\partial u_2}{\partial X_1} & \frac{\partial u_2}{\partial X_2} & \frac{\partial u_2}{\partial X_3}\\ \frac{\partial u_3}{\partial X_1} & \frac{\partial u_3}{\partial X_2} & \frac{\partial u_3}{\partial X_3}\end{bmatrix},$$

then $\mathbf{F}$ may be expressed as,

$$\mathbf{F} = \left(\mathbf{I} + \nabla\mathbf{u}\right).$$

Thus, substituting this new form of $\mathbf{F}$ into (2.4),

$$\begin{aligned}\mathbf{E} &= \frac{1}{2}\left[\left(\mathbf{I} + \nabla\mathbf{u}\right)^T\left(\mathbf{I} + \nabla\mathbf{u}\right) - \mathbf{I}\right]\\ &= \frac{1}{2}\left[\nabla\mathbf{u} + \left(\nabla\mathbf{u}\right)^T + \left(\nabla\mathbf{u}\right)^T\left(\nabla\mathbf{u}\right)\right]\\ &= \frac{1}{2}\left[\nabla\mathbf{u} + \left(\nabla\mathbf{u}\right)^T\right] + \frac{1}{2}\left[\left(\nabla\mathbf{u}\right)^T\left(\nabla\mathbf{u}\right)\right].\end{aligned} \tag{2.5}$$

Assuming small strain theory and hence small displacements, the second order term in Equation (2.5) may be neglected. The term $\mathbf{E}$ then denotes the strain matrix, given by,

$$\mathbf{E} = \frac{1}{2}\left(\begin{bmatrix} \frac{\partial u_1}{\partial X_1} & \frac{\partial u_1}{\partial X_2} & \frac{\partial u_1}{\partial X_3} \\ \frac{\partial u_2}{\partial X_1} & \frac{\partial u_2}{\partial X_2} & \frac{\partial u_2}{\partial X_3} \\ \frac{\partial u_3}{\partial X_1} & \frac{\partial u_3}{\partial X_2} & \frac{\partial u_3}{\partial X_3} \end{bmatrix} + \begin{bmatrix} \frac{\partial u_1}{\partial X_1} & \frac{\partial u_2}{\partial X_1} & \frac{\partial u_3}{\partial X_1} \\ \frac{\partial u_1}{\partial X_2} & \frac{\partial u_2}{\partial X_2} & \frac{\partial u_3}{\partial X_2} \\ \frac{\partial u_1}{\partial X_3} & \frac{\partial u_2}{\partial X_3} & \frac{\partial u_3}{\partial X_3} \end{bmatrix}\right).$$

Thus we may express,

$$\mathbf{E} = \begin{bmatrix} E_{11} & E_{12} & E_{13} \\ E_{21} & E_{22} & E_{23} \\ E_{31} & E_{32} & E_{33} \end{bmatrix} = \begin{bmatrix} \frac{\partial u_1}{\partial X_1} & \frac{1}{2}\left(\frac{\partial u_1}{\partial X_2} + \frac{\partial u_2}{\partial X_1}\right) & \frac{1}{2}\left(\frac{\partial u_1}{\partial X_3} + \frac{\partial u_3}{\partial X_1}\right) \\ \frac{1}{2}\left(\frac{\partial u_2}{\partial X_1} + \frac{\partial u_1}{\partial X_2}\right) & \frac{\partial u_2}{\partial X_2} & \frac{1}{2}\left(\frac{\partial u_2}{\partial X_3} + \frac{\partial u_3}{\partial X_2}\right) \\ \frac{1}{2}\left(\frac{\partial u_3}{\partial X_1} + \frac{\partial u_1}{\partial X_3}\right) & \frac{1}{2}\left(\frac{\partial u_3}{\partial X_2} + \frac{\partial u_2}{\partial X_3}\right) & \frac{\partial u_3}{\partial X_3} \end{bmatrix}.$$

The components of strain matrix $\mathbf{E}$ are the strain components and which, from this point on, shall be denoted by tensor notation ε_{ij}. Assuming small displacements the strain tensor can thus be expressed as,

$$\varepsilon_{ij} = \frac{1}{2}\left(\frac{\partial u_i}{\partial x_j} + \frac{\partial u_j}{\partial x_i}\right), \tag{2.6}$$

where $i,j = 1,2,3$ for three-dimensional cases and simplifies to $i,j = 1,2$ for two dimensions. The components of strain in three dimensions may be visualised as depicted in Figure (2.2). The

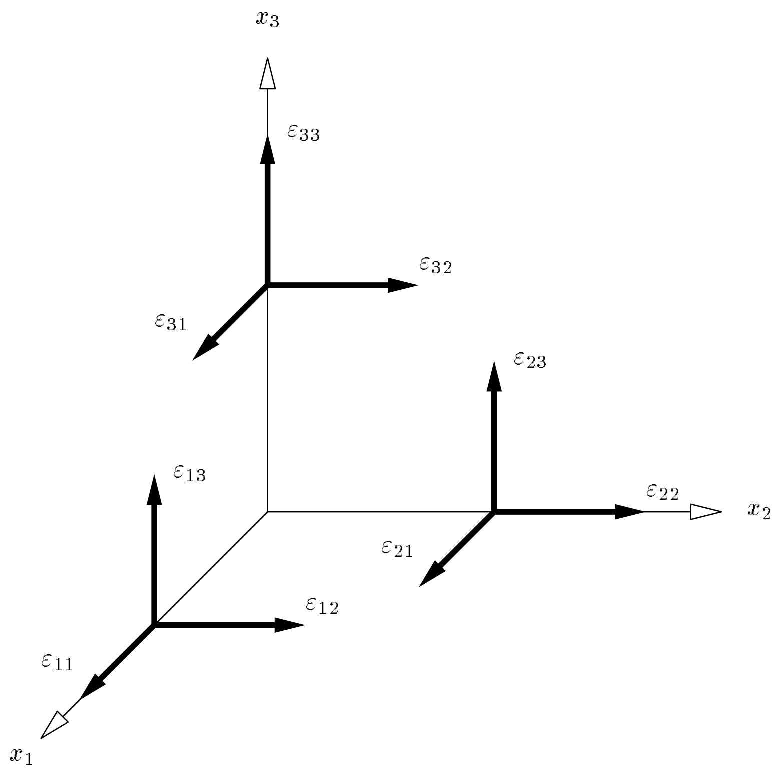

Figure 2.2: Components of strain in three dimensions.

symmetric strain tensor $\boldsymbol{\varepsilon}$ may thus be defined for three dimensions using Equation (2.6) as,

$$\boldsymbol{\varepsilon} = \begin{bmatrix} \varepsilon_{11} & \varepsilon_{12} & \varepsilon_{13} \\ \varepsilon_{21} & \varepsilon_{22} & \varepsilon_{23} \\ \varepsilon_{31} & \varepsilon_{32} & \varepsilon_{33} \end{bmatrix} .$$

Alternatively the symmetric strain and stress tensors may be considered in vector form as,

$$\boldsymbol{\varepsilon} = [\varepsilon_{11}, \varepsilon_{22}, \varepsilon_{33}, 2\varepsilon_{12}, 2\varepsilon_{13}, 2\varepsilon_{23}]^T \equiv [\varepsilon_1, \varepsilon_2, \varepsilon_3, \varepsilon_4, \varepsilon_5, \varepsilon_6]^T , \tag{2.7}$$

and,

$$\boldsymbol{\sigma} = [\sigma_{11}, \sigma_{22}, \sigma_{33}, \sigma_{12}, \sigma_{13}, \sigma_{23}]^T \equiv [\sigma_1, \sigma_2, \sigma_3, \sigma_4, \sigma_5, \sigma_6]^T , \tag{2.8}$$

with the right-hand sides in what is known as contracted notation. These forms will be used in the next section to define the constitutive relationships for differing material properties.

2.1.2 Orthotropic and Isotropic Elasticity

Having investigated the strain tensor in the previous section, we now look at stress, strain and the relationship between them. The law relating stress to strain is a special case of a general class of equations known as *constitutive equations*. The fact that most materials possess some internal organisation helps to simplify the stress-strain equations. If a material has directional properties but exhibits no symmetry it is classified as an *anisotropic* substance. Materials which have symmetry about three mutually perpendicular planes are termed *orthotropic*. A good example of an orthotropic material is wood which has distinctively different properties in the x_1, x_2 and x_3 directions as illustrated in Figure (2.3). A material is termed *isotropic* when it exhibits no specific

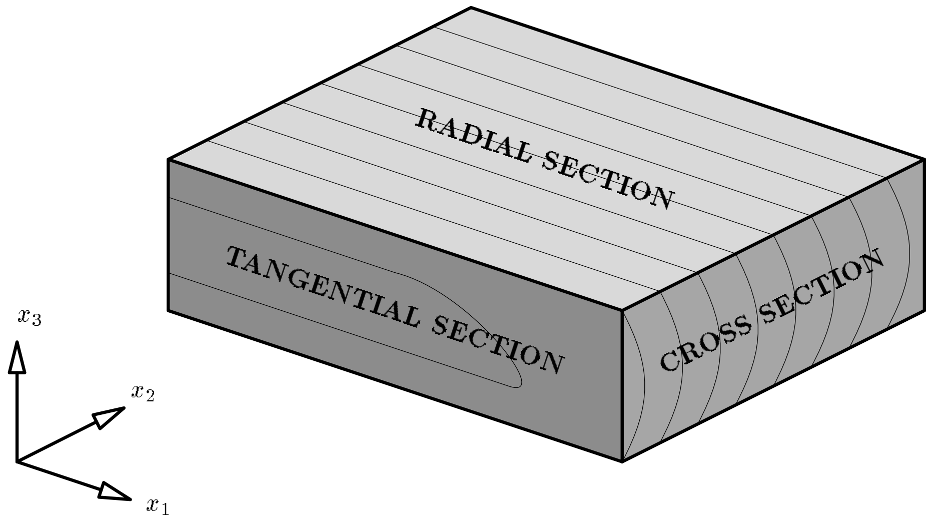

Figure 2.3: Typical block of wood with grain orientation shown.

internal symmetry and hence no preferred directional properties. Such a material has, in fact, an infinite number of symmetry planes of arbitrary orientation. A material termed *plane isotropic* is one which possesses an infinite number of symmetry planes, all orientated in a direction normal to the plane of the sheet of material in question.

The constitutive relations may be written in two forms, either the stress-strain relationship, which is of the form,

$$\boldsymbol{\sigma} = \mathbf{C}\boldsymbol{\varepsilon},$$

where $\mathbf{C}$ is termed the *stiffness* matrix and which is defined by Hooke's law for linear elastic materials, or the strain-stress relationship,

$$\boldsymbol{\varepsilon} = \mathbf{S}\boldsymbol{\sigma},$$

in which $\mathbf{S}$ is known as the *compliance* matrix. Here the vector forms of $\boldsymbol{\varepsilon}$ and $\boldsymbol{\sigma}$ have been used and it is clear that the stiffness matrix is the inverse of the compliance matrix. In order to determine the form of the matrices $\mathbf{S}$ and $\mathbf{C}$, which in three dimensions both consist of six rows and six columns, we shall first consider the behaviour of an orthotropic material as this is the most general case. The resulting system of equations will then be simplified to that of an isotropic material before further simplification to two dimensions with the introduction of plane systems. Such systems can be cast in either plane strain or plane stress configurations and will be employed in the forthcoming problems of linear elasticity in two dimensions and problems of plate theory.

Orthotropic Behaviour

One technique which may be used to determine the form of the compliance matrix of an orthotropic material is to consider the effect of applying single stress components to a typical volume element of the material. Alternatively a similar approach may be attempted by applying strains but, due to the fact that application of a single normal strain induces both orthogonal normal strains - a phenomenon known as the Poisson effect - this is not easy. As described in Bodig and Jayne, [15], application of σ_{11} alone produces all three normal strains $\varepsilon_{11}, \varepsilon_{22}$ and ε_{33}, with ε_{22} and ε_{33} resulting from the Poisson effect. We may thus write these strains in terms of the stress σ_{11} as,

$$\varepsilon_{11} = S_{11}\sigma_{11}, \quad \varepsilon_{22} = S_{21}\sigma_{11}, \quad \text{and} \quad \varepsilon_{33} = S_{31}\sigma_{11}. \tag{2.9}$$

Application of normal stress σ_{22} alone, produces again the three orthogonal normal strains given by,

$$\varepsilon_{11} = S_{12}\sigma_{22}, \quad \varepsilon_{22} = S_{22}\sigma_{22}, \quad \text{and} \quad \varepsilon_{33} = S_{32}\sigma_{22}, \tag{2.10}$$

which differ in their magnitudes to those when σ_{11} was applied. Finally when σ_{33} is applied alone, the strains,

$$\varepsilon_{11} = S_{13}\sigma_{33}, \quad \varepsilon_{22} = S_{23}\sigma_{33}, \quad \text{and} \quad \varepsilon_{33} = S_{33}\sigma_{33}, \tag{2.11}$$

result. Considering the total strain resulting from application of all the stress components, we have,

$$\varepsilon_{11} = S_{11}\sigma_{11} + S_{12}\sigma_{22} + S_{13}\sigma_{33},$$

$$\begin{aligned}\varepsilon_{22} &= S_{21}\sigma_{11} + S_{22}\sigma_{22} + S_{23}\sigma_{33}, \\ \varepsilon_{33} &= S_{31}\sigma_{11} + S_{32}\sigma_{22} + S_{33}\sigma_{33}.\end{aligned} \tag{2.12}$$

As described in [15], the application of shear stress σ_{12} alone will produce only shear strain ε_{12}. The same effect is observed for the remaining shear stresses and we may write,

$$2\varepsilon_{12} = S_{44}\sigma_{12} \quad 2\varepsilon_{13} = S_{55}\sigma_{13} \quad \text{and} \quad 2\varepsilon_{23} = S_{66}\sigma_{23}. \tag{2.13}$$

By combining (2.12) and (2.13) we may write the compliance form of the orthotropic material as,

$$\begin{bmatrix} \varepsilon_{11} \\ \varepsilon_{22} \\ \varepsilon_{33} \\ 2\varepsilon_{12} \\ 2\varepsilon_{13} \\ 2\varepsilon_{23} \end{bmatrix} = \begin{bmatrix} S_{11} & S_{12} & S_{13} & 0 & 0 & 0 \\ S_{21} & S_{22} & S_{23} & 0 & 0 & 0 \\ S_{31} & S_{32} & S_{33} & 0 & 0 & 0 \\ 0 & 0 & 0 & S_{44} & 0 & 0 \\ 0 & 0 & 0 & 0 & S_{55} & 0 \\ 0 & 0 & 0 & 0 & 0 & S_{66} \end{bmatrix} \begin{bmatrix} \sigma_{11} \\ \sigma_{22} \\ \sigma_{33} \\ \sigma_{12} \\ \sigma_{13} \\ \sigma_{23} \end{bmatrix} \tag{2.14}$$

From Equation (2.14), it can be seen that normal stresses do not produce shear strains and shear stresses do not produce normal strains. In fact, shear stresses will produce shear strains only in the same plane. It is important to note that this relationship holds only when the material symmetry and geometric axes are coincident. A further property of the above compliance matrix is that $S_{ij} = S_{ji}$. This can be verified by calculating the strain energy involved in applying normal stress components again. By applying these in order to a volume element and then again in reverse order, it can be shown that the strain energy or work done per unit volume in both cases remains unchanged. This technique is illustrated in greater detail in [15].

The parameters which identify one material as being different from another are known as the *elastic moduli* which are determined experimentally. These are the parameters upon which the unidentified terms in the compliance matrix depend on. For an orthotropic material, in which there are three orthogonal planes of symmetry, there are six elastic moduli. Three of these values are the ratios of a normal stress to the normal strain in the principal directions, and the remaining three are ratios of shear stress to shear strain in the orthotropic planes. Thus, we have the elastic moduli $E_1, E_2, E_3, G_{12}, G_{13}$ and G_{23}, given by,

$$\begin{aligned} E_1 &= \frac{\sigma_{11}}{\varepsilon_{11}}, \quad E_2 = \frac{\sigma_{22}}{\varepsilon_{22}}, \quad E_3 = \frac{\sigma_{33}}{\varepsilon_{33}}, \\ G_{12} &= \frac{\sigma_{12}}{2\varepsilon_{12}}, \; G_{13} = \frac{\sigma_{13}}{2\varepsilon_{13}}, \; G_{23} = \frac{\sigma_{23}}{2\varepsilon_{23}}, \end{aligned} \tag{2.15}$$

where E_1, E_2 and E_3 are known as the *moduli of elasticity* or *Youngs moduli*, and G_{12}, G_{13} and G_{23} are known as the *moduli of rigidity* or *shear moduli*. Comparison of Equation (2.15) with Equations (2.9)-(2.11) and (2.13) enables the diagonal terms of the compliance matrix to be determined in terms of the elastic moduli. In order to determine the off-diagonal elements in the compliance matrix in terms of the elastic moduli, one must consider a further parameter which is known as the Poisson's ratio. The deformation in the direction of an applied force is sometimes termed the *active* deformation, and that normal to the direction of the force is the *passive* deformation. Poisson's ratio is defined as the ratio of *passive strain*, ε_{jj}, to *active strain*, ε_{ii}, and thus,

$$-\nu_{ij} = \frac{\varepsilon_{jj}}{\varepsilon_{ii}}, \tag{2.16}$$

where summation is not implied on repeated indices. By substituting Equations (2.9), (2.10) and (2.11) independently into Equation (2.16) and also substituting the three moduli of elasticity into the resulting expression, the following are established,

$$\begin{aligned} S_{12} &= -\frac{\nu_{21}}{E_2}, & S_{13} &= -\frac{\nu_{31}}{E_3}, \\ S_{21} &= -\frac{\nu_{12}}{E_1}, & S_{23} &= -\frac{\nu_{32}}{E_3}, \\ S_{31} &= -\frac{\nu_{13}}{E_1}, & S_{32} &= -\frac{\nu_{23}}{E_2}. \end{aligned}$$

The compliance form of the constitutive relations, for an orthotropic material, may thus be written,

$$\begin{bmatrix} \varepsilon_{11} \\ \varepsilon_{22} \\ \varepsilon_{33} \\ 2\varepsilon_{12} \\ 2\varepsilon_{13} \\ 2\varepsilon_{23} \end{bmatrix} = \begin{bmatrix} \frac{1}{E_1} & -\frac{\nu_{21}}{E_2} & -\frac{\nu_{31}}{E_3} & 0 & 0 & 0 \\ -\frac{\nu_{12}}{E_1} & \frac{1}{E_2} & -\frac{\nu_{32}}{E_3} & 0 & 0 & 0 \\ -\frac{\nu_{13}}{E_1} & -\frac{\nu_{23}}{E_2} & \frac{1}{E_3} & 0 & 0 & 0 \\ 0 & 0 & 0 & \frac{1}{G_{12}} & 0 & 0 \\ 0 & 0 & 0 & 0 & \frac{1}{G_{13}} & 0 \\ 0 & 0 & 0 & 0 & 0 & \frac{1}{G_{23}} \end{bmatrix} \begin{bmatrix} \sigma_{11} \\ \sigma_{22} \\ \sigma_{33} \\ \sigma_{12} \\ \sigma_{13} \\ \sigma_{23} \end{bmatrix}. \tag{2.17}$$

For the stiffness form of the constitutive relations the task is to simply invert $\mathbf{S}$ since we know that,

$$\boldsymbol{\varepsilon} = \mathbf{S}\boldsymbol{\sigma} \quad \Rightarrow \quad \boldsymbol{\sigma} = \mathbf{S}^{-1}\boldsymbol{\varepsilon}.$$

The structure of $\mathbf{S}$ makes this a rather easy task and the result is a matrix $\mathbf{C}$ which is the inverse of $\mathbf{S}$ such that,

$$\boldsymbol{\sigma} = \mathbf{C}\boldsymbol{\varepsilon},$$

where the terms of $\mathbf{C}$ are given as,

$$\begin{aligned} C_{11} &= \frac{1-\nu_{23}\nu_{32}}{DE_2E_3}, & C_{12} &= \frac{\nu_{21}+\nu_{31}\nu_{23}}{DE_2E_3}, & C_{13} &= \frac{\nu_{31}+\nu_{21}\nu_{32}}{DE_2E_3}, \\ C_{21} &= \frac{\nu_{12}+\nu_{13}\nu_{32}}{DE_1E_3}, & C_{22} &= \frac{1-\nu_{13}\nu_{31}}{DE_1E_3}, & C_{23} &= \frac{\nu_{32}+\nu_{12}\nu_{31}}{DE_1E_3}, \\ C_{31} &= \frac{\nu_{13}+\nu_{12}\nu_{23}}{DE_1E_2}, & C_{32} &= \frac{\nu_{23}+\nu_{21}\nu_{13}}{DE_1E_2}, & C_{33} &= \frac{1-\nu_{12}\nu_{21}}{DE_1E_2}, \end{aligned}$$

and where D is equal to,

$$D = \frac{1}{E_1E_2E_3}\left(1-\nu_{23}\nu_{32}-\nu_{13}\nu_{31}-\nu_{12}\nu_{21}-\nu_{13}\nu_{21}\nu_{32}-\nu_{12}\nu_{23}\nu_{31}\right).$$

All remaining terms of $\mathbf{C}$ are zero except C_{44}, C_{55} and C_{66} which are those resulting from the diagonal terms S_{44}, S_{55} and S_{66} of compliance matrix $\mathbf{S}$ and are given as,

$$C_{44} = G_{12}, \quad C_{55} = G_{13} \quad \text{and} \quad C_{66} = G_{23}. \tag{2.18}$$

Isotropic Behaviour

As mentioned previously, isotropic materials do not possess definite internal planes of symmetry and, in fact, may be thought of as containing an infinite number of planes of symmetry about the x_1, x_2 and x_3 axes of Figure (2.3). Modern day materials such as certain wood particleboards and fiberboards may exhibit isotropic properties and, for such materials, the constitutive relations are greatly simplified from those defined in the previous section for orthotropic materials. This simplification arises due to the fact that the actual material can be characterised by less parameters given by,

$$E = E_1 = E_2 = E_3,$$

$$G = G_{12} = G_{13} = G_{23},$$

$$\nu = \nu_{12} = \nu_{21} = \nu_{13} = \nu_{31} = \nu_{23} = \nu_{32}.$$

By substituting for Youngs modulus E and Poisson's ratio ν in Equation (2.17) the compliance form of the constitutive relations is obtained. The stiffness form of the constitutive relations may be similarly obtained by inverting the compliance matrix. In doing so the resulting matrix has the form,

$$\begin{bmatrix} \sigma_{11} \\ \sigma_{22} \\ \sigma_{33} \\ \sigma_{12} \\ \sigma_{13} \\ \sigma_{23} \end{bmatrix} = \begin{bmatrix} \lambda+2\mu & \lambda & \lambda & 0 & 0 & 0 \\ \lambda & \lambda+2\mu & \lambda & 0 & 0 & 0 \\ \lambda & \lambda & \lambda+2\mu & 0 & 0 & 0 \\ 0 & 0 & 0 & \mu & 0 & 0 \\ 0 & 0 & 0 & 0 & \mu & 0 \\ 0 & 0 & 0 & 0 & 0 & \mu \end{bmatrix} \begin{bmatrix} \varepsilon_{11} \\ \varepsilon_{22} \\ \varepsilon_{33} \\ 2\varepsilon_{12} \\ 2\varepsilon_{13} \\ 2\varepsilon_{23} \end{bmatrix}, \tag{2.19}$$

where,

$$\lambda = \frac{E\nu}{(1-2\nu)(1+\nu)} \quad \text{and} \quad \mu = \frac{E}{2(1+\nu)}.$$

The above relations can be described using Hooke's law which relates stress to strain in the following way,

$$\sigma_{ij}(\mathbf{u}) = \lambda \left\{ \sum_{k=1}^{3} \varepsilon_{kk}(\mathbf{u}) \right\} \delta_{ij} + 2\mu\varepsilon_{ij}(\mathbf{u}), \quad 1 \leq i, j \leq 3, \tag{2.20}$$

where the parameters $\lambda > 0$ and $\mu > 0$ in Equation (2.20) are known as the Lamé coefficients. Hooke's law may alternatively be expressed as,

$$\boldsymbol{\sigma} = \lambda \mathbf{I} \operatorname{div} \mathbf{u} + 2\mu\boldsymbol{\varepsilon},$$

where $\mathbf{I} = (\delta_{ij})_{i,j=1}^{3}$ is the identity tensor with $\delta_{ij} = 1$ if $i = j$ and zero otherwise and $\operatorname{div}\mathbf{u}$ is expressed as,

$$\operatorname{div}\mathbf{u} = \sum_{i=1}^{3} \frac{\partial u_i}{\partial x_i} = \sum_{i=1}^{3} \varepsilon_{ii} \equiv \sum_{i=1}^{3} \varepsilon_i .$$

using the notation of Equation (2.7).

2.1.3 Plane Systems

In the previous section the constitutive relations for isotropic and orthotropic materials in three dimensions have been discussed. For the solution of many problems however, it is both easier and more practical to consider two-dimensional approximations which are called *plane systems*. Such plane systems require corresponding constitutive relations which are obtained by simplifying the three dimensional relations discussed in the previous section. The following two sections detail the simplifications made in order to obtain both plane stress and plane strain approximations to the three dimensional case.

Plane Stress

A plane stress system is one for which only the normal and shear stresses in a single plane are recognised. This situation arises when the applied forces at the boundary all lie in a single plane corresponding to one of the principal planes of the coordinate system. As an illustration of this, consider Figure (2.4). In such a situation, only three components of stress exist, the two normal

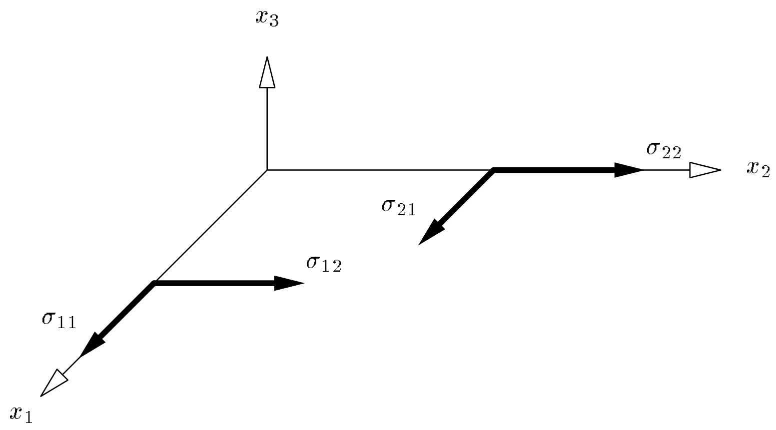

Figure 2.4: Components of stress in two dimensions.

components σ_{11} and σ_{22}, and one shear component σ_{12}. It is not generally true however, that $\sigma_{13} = \sigma_{23} = \sigma_{33} = 0$ but often these are assumed to be so small in relation to the stresses in the x_1, x_2-plane that they may be safely ignored.

For our two-dimensional approximation, by setting $\sigma_{13} = \sigma_{23} = \sigma_{33} = 0$ in the three-dimensional orthotropic compliance relation, we obtain,

$$
\begin{aligned}
\varepsilon_{11} &= \frac{1}{E_1}\sigma_{11} - \frac{\nu_{21}}{E_2}\sigma_{22} \\
\varepsilon_{22} &= \frac{-\nu_{12}}{E_1}\sigma_{11} + \frac{1}{E_2}\sigma_{22} \\
\varepsilon_{33} &= \frac{-\nu_{13}}{E_1}\sigma_{11} - \frac{-\nu_{23}}{E_2}\sigma_{22} \\
2\varepsilon_{12} &= \frac{1}{G_{12}}\sigma_{12}
\end{aligned} \tag{2.21}
$$

It can be seen from Equation (2.21) that there will exist a strain ε_{33} in addition to the expected strains in the x_1, x_2-plane. This strain will result in a decrease or increase in the thickness of, say, a plate of material. In many cases the ε_{33} normal strain is relatively unimportant to the overall problem and can be safely ignored. By ignoring ε_{33} a simplified compliance matrix will result in the compliance relation, which may now be expressed as,

$$
\begin{bmatrix} \varepsilon_{11} \\ \varepsilon_{22} \\ 2\varepsilon_{12} \end{bmatrix} = \begin{bmatrix} \frac{1}{E_1} & -\frac{\nu_{21}}{E_2} & 0 \\ -\frac{\nu_{12}}{E_1} & \frac{1}{E_2} & 0 \\ 0 & 0 & \frac{1}{G_{12}} \end{bmatrix} \begin{bmatrix} \sigma_{11} \\ \sigma_{22} \\ \sigma_{12} \end{bmatrix}. \tag{2.22}
$$

The stiffness form of Hooke's law in the plane for orthotropic materials is obtained by calculating the inverse of the compliance matrix of Equation (2.22). Thus, by letting,

$$
\mathbf{S} = \begin{bmatrix} \frac{1}{E_1} & -\frac{\nu_{21}}{E_2} & 0 \\ -\frac{\nu_{12}}{E_1} & \frac{1}{E_2} & 0 \\ 0 & 0 & \frac{1}{G_{12}} \end{bmatrix},
$$

then,

$$
\mathbf{S}^{-1} = \begin{bmatrix} \mathbf{A}^{-1} & \mathbf{0} \\ \mathbf{0}^T & G_{12} \end{bmatrix}.
$$

Where $\mathbf{0}^T$ above is the transpose of the 2×1 zero column vector and the matrix $\mathbf{A}$ has the form,

$$
\mathbf{A} = \begin{bmatrix} \frac{1}{E_1} & -\frac{\nu_{21}}{E_2} \\ -\frac{\nu_{12}}{E_1} & \frac{1}{E_2} \end{bmatrix}.
$$

Thus,

$$
\mathbf{A}^{-1} = \frac{E_1 E_2}{1 - \nu_{12}\nu_{21}} \begin{bmatrix} \frac{1}{E_2} & \frac{\nu_{21}}{E_2} \\ \frac{\nu_{12}}{E_1} & \frac{1}{E_1} \end{bmatrix},
$$

and so we may write,

$$
\begin{bmatrix} \sigma_{11} \\ \sigma_{22} \\ \sigma_{12} \end{bmatrix} = \begin{bmatrix} X_{11} & X_{12} & 0 \\ X_{21} & X_{22} & 0 \\ 0 & 0 & X_{33} \end{bmatrix} \begin{bmatrix} \varepsilon_{11} \\ \varepsilon_{22} \\ 2\varepsilon_{12} \end{bmatrix},
$$

where,

$$X_{11} = \frac{E_1}{1-\nu_{12}\nu_{21}}, \qquad X_{12} = \frac{E_1\nu_{21}}{1-\nu_{12}\nu_{21}},$$
$$X_{21} = \frac{E_2\nu_{12}}{1-\nu_{12}\nu_{21}}, \qquad X_{22} = \frac{E_2}{1-\nu_{12}\nu_{21}},$$

and $X_{33} = G_{12}$. Since $\mathbf{A}$ is symmetric, $\mathbf{A}^{-1}$ must also be symmetric and so $X_{12} = X_{21}$ since,

$$\frac{\nu_{21}}{E_2} = \frac{\nu_{12}}{E_1},$$

Plane Strain

This plane system is a deformation state restricted to a single plane and is approximated in a continuum when boundary loads are applied in a plane normal to the long axis of an elongated body. Plane strain sometimes occurs in wood composites although it is not as common as plane stress. In a similar way to that of plane stress, let us make the two-dimensional approximation to the three-dimensional stiffness matrix. When strain is restricted to the x_1, x_2-plane only components ε_{11},ε_{22} and ε_{12} are non-zero, this results in,

$$\begin{aligned}
\sigma_{11} &= C_{11}\varepsilon_{11} + C_{12}\varepsilon_{22}, \\
\sigma_{22} &= C_{21}\varepsilon_{11} + C_{22}\varepsilon_{22}, \\
\sigma_{33} &= C_{31}\varepsilon_{11} + C_{32}\varepsilon_{22}, \\
\sigma_{12} &= C_{44}2\varepsilon_{12}.
\end{aligned}$$

Since the normal stress σ_{33} developed in the x_3 direction is only a fraction of either σ_{11} or σ_{22} in plane strain problems, it is frequently ignored. Consequently, to a first approximation, only the σ_{11}, σ_{22} and σ_{12} stresses exist, giving a stiffness relation of the form,

$$\begin{bmatrix} \sigma_{11} \\ \sigma_{22} \\ \sigma_{12} \end{bmatrix} = \begin{bmatrix} C_{11} & C_{12} & 0 \\ C_{21} & C_{22} & 0 \\ 0 & 0 & C_{44} \end{bmatrix} \begin{bmatrix} \varepsilon_{11} \\ \varepsilon_{22} \\ 2\varepsilon_{12} \end{bmatrix}.$$

Isotropic Behaviour in Plane Systems

Thus far both plane stress and plane strain have been described. Both of these can be described by Hooke's law which was first introduced in Equation (2.20) in three dimensions and relates stress to strain in the following way,

$$\sigma_{ij}(\mathbf{u}) = \lambda \left\{ \sum_{k=1}^{2} \varepsilon_{kk}(\mathbf{u}) \right\} \delta_{ij} + 2\mu\varepsilon_{ij}(\mathbf{u}), \quad 1 \leq i, j \leq 2. \tag{2.23}$$

Once again the parameters $\lambda > 0$ and $\mu > 0$ above are known as the Lamé coefficients. Each of these can be expressed in terms of the Youngs modulus E and the Poisson ratio ν of the material.

For plane stress they have the form,

$$\lambda = \frac{E\nu}{1-\nu^2} \quad \text{and} \quad \mu = \frac{E}{2(1+\nu)}, \tag{2.24}$$

and in the case of plane strain,

$$\lambda = \frac{E\nu}{(1-2\nu)(1+\nu)} \quad \text{and} \quad \mu = \frac{E}{2(1+\nu)}. \tag{2.25}$$

This is a convenient form as it enables the constitutive relationship between stress and strain to be written in terms of λ and μ as,

$$\begin{bmatrix} \sigma_{11} \\ \sigma_{22} \\ \sigma_{12} \end{bmatrix} = \begin{bmatrix} C_{11} & C_{12} & C_{14} \\ C_{21} & C_{22} & C_{24} \\ C_{41} & C_{42} & C_{44} \end{bmatrix} \begin{bmatrix} \varepsilon_{11} \\ \varepsilon_{22} \\ 2\varepsilon_{12} \end{bmatrix} = \begin{bmatrix} \lambda+2\mu & \lambda & 0 \\ \lambda & \lambda+2\mu & 0 \\ 0 & 0 & \mu \end{bmatrix} \begin{bmatrix} \varepsilon_{11} \\ \varepsilon_{22} \\ 2\varepsilon_{12} \end{bmatrix}, \tag{2.26}$$

where λ and μ are defined appropriately in terms of either plane stress or strain. Plane system formulations will be used in the forthcoming problems of two-dimensional linear elasticity and plate theory.

2.2 Plate Theory

In this section an introduction to the theory of plates will be made. Plates can generally be split into two types and are characterised by their thickness. Thus a plate can be classed as either of thick or thin type. The classical model for thin a plate will firstly be discussed along with the assumptions and approximations. Following this, the refinements for the modelling of thick plates using first-order shear deformation theory (FSDT) as described by Reddy, [40], will be detailed. It is worth noting that plates in this work will be modelled using FSDT formulations although classical plate theory is included here for completeness and to introduce key concepts and assumptions.

2.2.1 Classical Theory of Plates

A plate is a solid body, bounded by two parallel flat surfaces and whose lateral dimensions are large compared to the distance between the flat surfaces. This distance between the flat surfaces is what is known as the plate thickness and may be used to characterise the type of plate. The theory of elastic plates is an approximation of three-dimensional elasticity to two dimensions. Thus the plate problem is treated as a two-dimensional problem defined over a typical domain $\Omega \in \mathbb{R}^2$ which corresponds to the plate midplane at $x_3 = 0$ and which has boundary $\partial\Omega$. The reduction in the number of dimensions of the problem is obtained by the integration of the material properties contained in the underlying constitutive relations over the thickness in the third dimension. As previously mentioned, a plate can be classed as either being of thick or thin thickness type. There does not seem to be a well defined rule of thumb for differentiating between the two but Reddy in [40] states that a thin plate is one for which the ratio of thickness to the smaller span length is less than 1/20. Although this is a commonly accepted ratio and not a universally noted standard it is felt that this is an important aspect of the model and one which illustrates the physical considerations to the reader. As stated in [40] the classical thin plate theory or Kirchhoff-Love theory is based on the following four fundamental assumptions:

- The displacements of the midsurface are small compared with the thickness of the plate and, therefore, the slope of the deflected surface is very small and the square of the slope is negligible compared to unity.
- The midplane of the plate remains unstrained, that is, the midplane of the plate is the neutral plane, after the bending.
- *The Kirchhoff-Love assumption.* Plane sections initially normal to the midsurface remain *plane* and *normal* to the midsurface after bending. This assumption implies that the transverse shear strains ε_{13} and ε_{23} depicted in Figure (2.2) are negligible. The deflection of the plate is thus associated principally with bending strains. Consequently, the transverse normal strain ε_{33} resulting from transverse loading can be neglected.
- The transverse normal stress σ_{33} is small compared with the other stress components of the plate and, therefore, can be neglected.

When the transverse deflection is comparable to the thickness and in-plane gradients are small, the first two assumptions are replaced by the single assumption that the products and squares of the slopes of in-plane displacements are small compared with unity and can be neglected to give what is known as the von Karman theory of plates as detailed in [40]. From the second two assumptions the plate problem can be classified as a plane stress problem and, from the third assumption and using Equation (2.6) the following normal strains must hold,

$$\varepsilon_1 \equiv \varepsilon_{11} = \frac{\partial u_1}{\partial x_1}, \quad \varepsilon_2 \equiv \varepsilon_{22} = \frac{\partial u_2}{\partial x_2}, \quad \varepsilon_3 \equiv \varepsilon_{33} = \frac{\partial u_3}{\partial x_3} = 0,$$

where shear strains are also given as,

$$\varepsilon_4 \equiv 2\varepsilon_{12} = \frac{\partial u_1}{\partial x_2} + \frac{\partial u_2}{\partial x_1}, \quad \varepsilon_5 \equiv 2\varepsilon_{13} = \frac{\partial u_1}{\partial x_3} + \frac{\partial u_3}{\partial x_1} = 0, \quad \varepsilon_6 \equiv 2\varepsilon_{23} = \frac{\partial u_2}{\partial x_3} + \frac{\partial u_3}{\partial x_2} = 0,$$

by again using Equation (2.6). It can be seen that since $\partial u_3/\partial x_3 = 0$, this implies that u_3 is a function of x_1 and x_2 only. Thus,

$$u_3 = u_3(x_1, x_2) \equiv w(x_1, x_2),$$

where w is the transverse displacement which does not vary over the plate thickness. By integrating $2\varepsilon_{13}$ and $2\varepsilon_{23}$ with respect to x_3 gives,

$$u_1 = -\frac{\partial w}{\partial x_1}x_3 + p(x_1, x_2), \quad u_2 = -\frac{\partial w}{\partial x_2}x_3 + q(x_1, x_2),$$

where p and q denote the functions of integration. By setting $x_3 = 0$ these give,

$$p(x_1, x_2) = u_1(x_1, x_2, 0), \quad q(x_1, x_2) = u_2(x_1, x_2, 0),$$

indicating that p and q are the in-plane displacements along the x_1 and x_2 axes of the plate midplane (the $x_3 = 0$ plane). These in-plane displacements shall be denoted by u and v respectively giving the following displacement expressions,

$$\begin{aligned} u_1(x_1, x_2, x_3) &= u(x_1, x_2) - x_3 \frac{\partial w}{\partial x_1}, \\ u_2(x_1, x_2, x_3) &= v(x_1, x_2) - x_3 \frac{\partial w}{\partial x_2}. \end{aligned} \tag{2.27}$$

The equilibrium equations for classical plate theory as given in Equation (A.9) of Appendix A are of the form,

$$\frac{\partial N_1}{\partial x_1} + \frac{\partial N_4}{\partial x_2} = 0, \tag{2.28}$$

$$\frac{\partial N_4}{\partial x_1} + \frac{\partial N_2}{\partial x_2} = 0, \tag{2.29}$$

$$\left(\frac{\partial^2 M_1}{\partial x_1^2} + 2 \frac{\partial^2 M_4}{\partial x_1 \partial x_2} + \frac{\partial^2 M_2}{\partial x_2^2} \right) + q = 0, \tag{2.30}$$

where the in-plane stress resultants N_1, N_2 and N_4 and bending moment resultants M_1, M_2 and M_4 are defined in terms of the displacements as,

$$N_1 = A_{11} \frac{\partial u}{\partial x_1} + A_{12} \frac{\partial v}{\partial x_2}, \quad N_2 = A_{12} \frac{\partial u}{\partial x_1} + A_{22} \frac{\partial v}{\partial x_2}, \quad N_4 = A_{44} \left(\frac{\partial u}{\partial x_2} + \frac{\partial v}{\partial x_1} \right), \tag{2.31}$$

and,

$$M_1 = -\left(D_{11} \frac{\partial^2 w}{\partial x_1^2} + D_{12} \frac{\partial^2 w}{\partial x_2^2} \right), \quad M_2 = -\left(D_{12} \frac{\partial^2 w}{\partial x_1^2} + D_{22} \frac{\partial^2 w}{\partial x_2^2} \right), \quad M_4 = -2 D_{44} \frac{\partial^2 w}{\partial x_1 \partial x_2}, \tag{2.32}$$

with q the applied force. Note that Equations (2.28) and (2.29) are uncoupled from Equation (2.30). This implies that u and v can be determined from (2.28) and (2.29) with the transverse displacement determined from (2.30) which, for an isotropic elastic body reduces to the biharmonic equation for w given by,

$$\nabla^4 w = \frac{q}{D},$$

where,

$$\nabla^4 = \nabla^2 \nabla^2 = \frac{\partial^4}{\partial x_1^4} + 2 \frac{\partial^4}{\partial x_1^2 \partial x_2^2} + \frac{\partial^4}{\partial x_2^4}, \quad \text{and} \quad D = \frac{E h^3}{12(1 - \nu^2)}.$$

In the above expressions, terms A_{ij} and D_{ij} for $i, j = 1, 2, 4$ arise from integrating terms in the constitutive equations of the type defined in Equation (2.26) over the thickness t in the following way,

$$A_{ij} = \int_{-\frac{t}{2}}^{\frac{t}{2}} C_{ij} \, dx_3, \quad D_{ij} = \int_{-\frac{t}{2}}^{\frac{t}{2}} x_3^2 C_{ij} \, dx_3, \quad i, j = 1, 2, 4, \tag{2.33}$$

where the C_{ij} are terms of the constitutive matrix. The natural boundary conditions for the equilibrium equations (2.28) to (2.30) as given by Equation (A.10) are of the form,

$$N_n - \hat{N}_n = 0, \quad \text{on} \quad \partial\Omega \setminus \Gamma_1 \equiv \hat{\Gamma}_1,$$

$$
\begin{aligned}
N_s - \hat{N}_s &= 0, \quad \text{on} \quad \partial\Omega \setminus \Gamma_2 \equiv \hat{\Gamma}_2, \\
Q_n - \hat{Q}_n &= 0, \quad \text{on} \quad \partial\Omega \setminus \Gamma_3 \equiv \hat{\Gamma}_3, \\
M_n - \hat{M}_n &= 0, \quad \text{on} \quad \partial\Omega \setminus \Gamma_4 \equiv \hat{\Gamma}_4, \\
M_s - \hat{M}_s &= 0, \quad \text{on} \quad \partial\Omega \setminus \Gamma_5 \equiv \hat{\Gamma}_5,
\end{aligned} \tag{2.34}
$$

where Γ_i for $i = 1, 2, 3, 4, 5$ are the portions of the boundary on which u_n, u_s, w, $\partial w/\partial n$ and $\partial w/\partial s$ are specified respectively. In the above the subscripts n and s denote the normal and tangential components to the boundary whilst $\hat{N}_n$, $\hat{N}_s$, $\hat{Q}_n$, $\hat{M}_n$ and $\hat{M}_s$ are as given in Equation (A.5) and N_n, N_s, Q_n, M_n and M_s as in Equation (A.7). The essential boundary conditions are,

$$
u_n = \hat{u}_n, \quad u_s = \hat{u}_s, \quad w = \hat{w}, \quad \frac{\partial w}{\partial n} = \hat{\theta}_n, \quad \text{and} \quad \frac{\partial w}{\partial s} = \hat{\theta}_s, \tag{2.35}
$$

on boundary portions Γ_i for $i = 1, 2, 3, 4, 5$ respectively as given in Equation (A.11).

2.2.2 First-Order Shear Deformation Theory

Unlike the thin plate theory of Kirchhoff described in the previous section, the theory for thick plates differs in one main area. This area is concerned with the rotation of plane sections initially normal to the plate midplane which, in thin plate theory are assumed to remain normal to the midplane after deformation. Thick plate theory on the other hand makes no such assumption and plane sections initially normal to the midplane remain straight but not necessarily normal to the midplane after deformation thus enabling the effects of transverse shear strains and stresses to come into being. The term first-order arises due to the order of approximation of the three global displacements which will be denoted u_1, u_2 and u_3. The approximation is written in power series of the thickness coordinate and unknown functions in the following way,

$$
\begin{aligned}
u_1(x_1, x_2, x_3) &= u(x_1, x_2) + x_3\psi_1(x_1, x_2), \\
u_2(x_1, x_2, x_3) &= v(x_1, x_2) + x_3\psi_2(x_1, x_2), \\
u_3(x_1, x_2, x_3) &= w(x_1, x_2).
\end{aligned} \tag{2.36}
$$

Here the unknowns are the in-plane displacements u, v and w and the two rotations ψ_1 and ψ_2. These rotations are measured about the x_2-axis and x_1-axis respectively with the ψ_1 rotation measured in the x_1, x_3-plane and the ψ_2 rotation measured in the x_2, x_3-plane. This formulation is also known as Reissner-Mindlin plate theory, [35], [42]. A feature of FSDT is that it yields a constant value of transverse shear strain through the thickness of the plate and thus shear correction factors are required. These factors are dimensionless quantities which are employed to account for the discrepancy between the constant state of transverse shear strains in the first-order theory and the quadratic or higher-order distribution of transverse shear strains in the elasticity theory.

The strains associated with the above displacement field are given, by using Equation (2.6), as,

$$
\varepsilon_1 \equiv \varepsilon_{11} = \frac{\partial u}{\partial x_1} + x_3\frac{\partial \psi_1}{\partial x_1}, \quad \varepsilon_2 \equiv \varepsilon_{22} = \frac{\partial v}{\partial x_2} + x_3\frac{\partial \psi_2}{\partial x_2}, \quad \varepsilon_3 \equiv \varepsilon_{33} = \frac{\partial w}{\partial x_3} = 0,
$$

and,

$$\varepsilon_4 \equiv 2\varepsilon_{12} = \frac{\partial u}{\partial x_2} + \frac{\partial v}{\partial x_1} + x_3\left(\frac{\partial \psi_1}{\partial x_2} + \frac{\partial \psi_2}{\partial x_1}\right), \quad \varepsilon_5 \equiv 2\varepsilon_{13} = \psi_1 + \frac{\partial w}{\partial x_1}, \quad \varepsilon_6 \equiv 2\varepsilon_{23} = \psi_2 + \frac{\partial w}{\partial x_2}.$$

Here the transverse shear terms are not zero as they were in the classical theory. Classical or Kirchhoff theory for thin plates may be regained, however, by setting,

$$\psi_1 = -\frac{\partial w}{\partial x_1}, \quad \psi_2 = -\frac{\partial w}{\partial x_2}. \tag{2.37}$$

Before proceeding, we will write the above strains in contracted notation as given in Equation (2.7). By doing this the strains may be expressed as,

$$\varepsilon_i = \varepsilon_i^{(0)} + x_3\varepsilon_i^{(1)} \quad i = 1, 2, 4, 5, 6. \tag{2.38}$$

The equilibrium equations as given in Equation (B.5) of Appendix B are of the form,

$$\frac{\partial N_1}{\partial x_1} + \frac{\partial N_4}{\partial x_2} = 0, \tag{2.39}$$

$$\frac{\partial N_4}{\partial x_1} + \frac{\partial N_2}{\partial x_2} = 0, \tag{2.40}$$

$$\frac{\partial Q_5}{\partial x_1} + \frac{\partial Q_6}{\partial x_2} + q = 0, \tag{2.41}$$

$$\frac{\partial M_1}{\partial x_1} + \frac{\partial M_4}{\partial x_2} - Q_5 = 0, \tag{2.42}$$

$$\frac{\partial M_4}{\partial x_1} + \frac{\partial M_2}{\partial x_2} - Q_6 = 0. \tag{2.43}$$

Again the definitions for the stress resultants are given by,

$$\begin{bmatrix} N_1 \\ N_2 \\ N_4 \end{bmatrix} = \begin{bmatrix} A_{11} & A_{12} & A_{14} \\ A_{12} & A_{22} & A_{24} \\ A_{14} & A_{24} & A_{44} \end{bmatrix} \begin{bmatrix} \varepsilon_1^{(0)} \\ \varepsilon_2^{(0)} \\ \varepsilon_4^{(0)} \end{bmatrix}, \tag{2.44}$$

where A_{ij} for $i, j = 1, 2, 4$ are as given in Equation (2.33). The definition of the bending moment resultants, however, differs from that for classical plate theory in the following way,

$$\begin{bmatrix} M_1 \\ M_2 \\ M_4 \end{bmatrix} = \begin{bmatrix} D_{11} & D_{12} & D_{14} \\ D_{12} & D_{22} & D_{24} \\ D_{14} & D_{24} & D_{44} \end{bmatrix} \begin{bmatrix} \varepsilon_1^{(1)} \\ \varepsilon_2^{(1)} \\ \varepsilon_4^{(1)} \end{bmatrix}, \tag{2.45}$$

where D_{ij} for $i, j = 1, 2, 4$ are again as given in Equation (2.33). The transverse shear forces are defined as,

$$\begin{bmatrix} Q_5 \\ Q_6 \end{bmatrix} = \int_{-\frac{t}{2}}^{\frac{t}{2}} \begin{bmatrix} \sigma_5 \\ \sigma_6 \end{bmatrix} dx_3 = \begin{bmatrix} A_{55} & A_{56} \\ A_{56} & A_{66} \end{bmatrix} \begin{bmatrix} \varepsilon_5^{(0)} \\ \varepsilon_6^{(0)} \end{bmatrix}, \tag{2.46}$$

with,

$$A_{ij} = K_i K_j \int_{-\frac{t}{2}}^{\frac{t}{2}} C_{ij}\, dx_3, \quad \text{for } i, j = 5, 6. \tag{2.47}$$

In the above, C_{ij} for $i,j = 1,2,4$ are as given in Equation (2.26) whilst C_{ij} for $i,j = 5,6$ have the form described in either Equation (2.18) or Equation (2.19) for orthotropic or isotropic materials respectively. The terms K_i and K_j are the aforementioned shear correction coefficients which, for FSDT are taken to be $K_i^2 = K_j^2 = 5/6$ as detailed in Ochoa and Reddy, [37]. In this instance it may be observed that the in-plane displacements u and v which arise in the equilibrium equations via Equations (2.39) and (2.40) are not coupled to w, ψ_1 or ψ_2 which, in turn are coupled by Equations (2.41), (2.42) and (2.43). As given by Equation (B.6) the natural boundary conditions for the FSDT modelled plate have the same form as in classical plate theory, namely,

$$\begin{aligned} N_n - \hat{N}_n &= 0, \quad \text{on} \quad \partial\Omega \setminus \Gamma_1 \equiv \hat{\Gamma}_1, \\ N_s - \hat{N}_s &= 0, \quad \text{on} \quad \partial\Omega \setminus \Gamma_2 \equiv \hat{\Gamma}_2, \\ Q_n - \hat{Q}_n &= 0, \quad \text{on} \quad \partial\Omega \setminus \Gamma_3 \equiv \hat{\Gamma}_3, \\ M_n - \hat{M}_n &= 0, \quad \text{on} \quad \partial\Omega \setminus \Gamma_4 \equiv \hat{\Gamma}_4, \\ M_s - \hat{M}_s &= 0, \quad \text{on} \quad \partial\Omega \setminus \Gamma_5 \equiv \hat{\Gamma}_5, \end{aligned} \tag{2.48}$$

where Γ_i for $i = 1,2,3,4,5$ are the portions of the boundary on which u_n, u_s, w, ψ_n and ψ_s are specified respectively. Subscripts n and s again denote the normal and tangential components to the boundary whilst $\hat{N}_n$, $\hat{N}_s$, $\hat{Q}_n$, $\hat{M}_n$ and $\hat{M}_s$ are as given in Equation (B.1) and N_n, N_s, Q_n, M_n and M_s as in Equation (B.3). The essential boundary conditions are,

$$u_n = \hat{u}_n, \quad u_s = \hat{u}_s, \quad w = \hat{w}, \quad \psi_n = \hat{\psi}_n \quad \text{and} \quad \psi_s = \hat{\psi}_s, \tag{2.49}$$

on boundary portions Γ_i for $i = 1,2,3,4,5$ respectively as given in Equation (B.7). Alternatively, it is possible to express the above boundary conditions in terms of the displacement coordinates. When this is done it is found that in the above,

$$\begin{aligned} N_n &= N_1 n_1 + N_4 n_2, \\ N_s &= N_4 n_1 + N_2 n_2, \\ Q_n &= Q_5 n_1 + Q_6 n_2, \\ M_n &= M_1 n_1 + M_4 n_2, \\ M_s &= M_4 n_1 + M_2 n_2, \end{aligned}$$

on $\hat{\Gamma}_i$ for $i = 1,2,3,4,5$ respectively whilst essential boundary conditions are given by specifying u, v, w, ψ_1 and ψ_2 on boundary portions Γ_i for $i = 1,2,3,4,5$ respectively. Plates modelled in this work will be of rectangular shape and thus the coordinate axes will be parallel to the edges of the plate. In such a situation, the natural and essential boundary conditions simplify to that below.

	Natural		Essential
Specify	N_1	or	u
	N_2	or	v
	Q_5 (or Q_6)	or	w
	M_1	or	ψ_1
	M_2	or	ψ_2

Laminate Plate Considerations

It is of interest here to consider what changes must be made to the FSDT model in order to model laminated composite plates. A laminated plate can be thought of as a number of individual plates bonded together. This results in a 'sandwich' of plates. The term 'composite material' refers to material that is obtained by combining two or more materials on a macroscopic scale. Such materials are man-made and so constituents of the composite material can be selected and combined in order to achieve desirable properties such as high strength and low weight for example. Hitherto the plate has been considered to consist of only one material of thickness t measured in the x_3-direction from $x_3 = -t/2$ to $x_3 = t/2$. The laminate setup is a plate consisting of $\mathcal{M}$ layers, each one located between $x_3 = t_m$ and $x_3 = t_{m+1}$ for $m = 1, \ldots, \mathcal{M}$ and such that $t_1 = -t/2$ and $t_{\mathcal{M}+1} = t/2$. The form of the equilibrium equations is as given in Equations (2.39) to (2.43). In addition the stress and moment resultants N_i, Q_i and M_i are given by,

$$(N_i, M_i) = \int_{-\frac{t}{2}}^{\frac{t}{2}} (1, x_3)\, \sigma_i \, dx_3, \;\; i = 1, 2, 4 \quad \text{and} \quad (Q_5, Q_6) = \int_{-\frac{t}{2}}^{\frac{t}{2}} (\sigma_5, \sigma_6)\, dx_3.$$

Clearly, the equations thus far described vary little from previous ones. Differences do exist, however, in the description of the constitutive behaviour. As the laminated plate now consists of a set of layers, each layer will have a set of constitutive equations describing the material properties. Thus for a typical lamina m,

$$\boldsymbol{\sigma}^m = \mathbf{C}^m \boldsymbol{\varepsilon}^m,$$

where $\boldsymbol{\sigma}^m$ and $\boldsymbol{\varepsilon}^m$ result from the lamina material coordinates which may or may not lie parallel to those of the plate and where $\mathbf{C}^m$ denotes the constitutive matrix of lamina m. To derive the plate constitutive equations, the above constitutive equations for the lamina are transformed to stresses in plate coordinates as described by Reddy, [40]. This results in,

$$\boldsymbol{\sigma} = \mathbf{Q}^m \boldsymbol{\varepsilon},$$

where $\boldsymbol{\sigma}$ and $\boldsymbol{\varepsilon}$ are the stresses and strains for the mth lamina in terms of the plate coordinates. Thus for the stress resultants,

$$\begin{aligned} N_i &= \int_{-\frac{t}{2}}^{\frac{t}{2}} \sigma_i \, dx_3 = \sum_{m=1}^{\mathcal{M}} \int_{t_m}^{t_{m+1}} \sigma_i \, dx_3 \\ &= \sum_{m=1}^{\mathcal{M}} \int_{t_m}^{t_{m+1}} Q_{ij}^m \varepsilon_j \, dx_3 = \sum_{m=1}^{\mathcal{M}} \int_{t_m}^{t_{m+1}} Q_{ij}^m \left(\varepsilon_j^{(0)} + x_3 \varepsilon_j^{(1)} \right) dx_3 \\ &= A_{ij} \varepsilon_j^{(0)} + B_{ij} \varepsilon_j^{(1)}, \end{aligned}$$

where, to recap, $\mathcal{M}$ is the number of laminates in the plate. Similarly, for the bending moment resultants,

$$M_i = \int_{-\frac{t}{2}}^{\frac{t}{2}} x_3 \sigma_i \, dx_3 = \sum_{m=1}^{\mathcal{M}} \int_{t_m}^{t_{m+1}} x_3 \sigma_i \, dx_3$$

$$= \sum_{m=1}^{\mathcal{M}} \int_{t_m}^{t_{m+1}} Q_{ij}^m x_3 \varepsilon_j \, dx_3 = \sum_{m=1}^{\mathcal{M}} \int_{t_m}^{t_{m+1}} Q_{ij}^m \left(x_3 \varepsilon_j^{(0)} + x_3^2 \varepsilon_j^{(1)} \right) \, dx_3$$
$$= B_{ij} \varepsilon_j^{(0)} + D_{ij} \varepsilon_j^{(1)},$$

where A_{ij}, B_{ij} and D_{ij} for $i, j = 1, 2, 4$ are the in-plane, bending-stretching and bending stiffnesses of the plate respectively and are defined as,

$$(A_{ij}, B_{ij}, D_{ij}) = \sum_{m=1}^{\mathcal{M}} \int_{t_m}^{t_{m+1}} Q_{ij}^m \left(1, x_3, x_3^2\right) \, dx_3, \quad i, j = 1, 2, 4. \tag{2.50}$$

In addition the shear force resultants will have the form,

$$\begin{bmatrix} Q_5 \\ Q_6 \end{bmatrix} = K_i K_j \int_{-\frac{t}{2}}^{\frac{t}{2}} \begin{bmatrix} \sigma_5 \\ \sigma_6 \end{bmatrix} dx_3 = K_i K_j \sum_{m=1}^{\mathcal{M}} \int_{t_m}^{t_{m+1}} \begin{bmatrix} \sigma_5 \\ \sigma_6 \end{bmatrix} dx_3$$
$$= K_i K_j \sum_{m=1}^{\mathcal{M}} \int_{t_m}^{t_{m+1}} \begin{bmatrix} Q_{55}^m & Q_{56}^m \\ Q_{56}^m & Q_{66}^m \end{bmatrix} \begin{bmatrix} \varepsilon_5 \\ \varepsilon_6 \end{bmatrix} dx_3 = K_i K_j \sum_{m=1}^{\mathcal{M}} \int_{t_m}^{t_{m+1}} \begin{bmatrix} Q_{55}^m & Q_{56}^m \\ Q_{56}^m & Q_{66}^m \end{bmatrix} \begin{bmatrix} \varepsilon_5^{(0)} \\ \varepsilon_6^{(0)} \end{bmatrix} dx_3$$
$$= \begin{bmatrix} A_{55} & A_{56} \\ A_{56} & A_{66} \end{bmatrix} \begin{bmatrix} \varepsilon_5^{(0)} \\ \varepsilon_6^{(0)} \end{bmatrix},$$

where,

$$A_{ij} = K_i K_j \sum_{m=1}^{\mathcal{M}} \int_{t_m}^{t_{m+1}} Q_{ij}^m \, dx_3 \quad i, j = 5, 6. \tag{2.51}$$

Thus by writing these laminate constitutive relationships out in the same format as that used for the single lamina scenario and expressed in Equations (2.44) and (2.45),

$$\begin{bmatrix} N_1 \\ N_2 \\ N_4 \end{bmatrix} = \begin{bmatrix} A_{11} & A_{12} & A_{14} \\ A_{12} & A_{22} & A_{24} \\ A_{14} & A_{24} & A_{44} \end{bmatrix} \begin{bmatrix} \varepsilon_1^{(0)} \\ \varepsilon_2^{(0)} \\ \varepsilon_4^{(0)} \end{bmatrix} + \begin{bmatrix} B_{11} & B_{12} & B_{14} \\ B_{12} & B_{22} & B_{24} \\ B_{14} & B_{24} & B_{44} \end{bmatrix} \begin{bmatrix} \varepsilon_1^{(1)} \\ \varepsilon_2^{(1)} \\ \varepsilon_4^{(1)} \end{bmatrix}, \tag{2.52}$$

$$\begin{bmatrix} M_1 \\ M_2 \\ M_4 \end{bmatrix} = \begin{bmatrix} B_{11} & B_{12} & B_{14} \\ B_{12} & B_{22} & B_{24} \\ B_{14} & B_{24} & B_{44} \end{bmatrix} \begin{bmatrix} \varepsilon_1^{(0)} \\ \varepsilon_2^{(0)} \\ \varepsilon_4^{(0)} \end{bmatrix} + \begin{bmatrix} D_{11} & D_{12} & D_{14} \\ D_{12} & D_{22} & D_{24} \\ D_{14} & D_{24} & D_{44} \end{bmatrix} \begin{bmatrix} \varepsilon_1^{(1)} \\ \varepsilon_2^{(1)} \\ \varepsilon_4^{(1)} \end{bmatrix}, \tag{2.53}$$

and,

$$\begin{bmatrix} Q_5 \\ Q_6 \end{bmatrix} = \begin{bmatrix} A_{55} & A_{56} \\ A_{56} & A_{66} \end{bmatrix} \begin{bmatrix} \varepsilon_5^{(0)} \\ \varepsilon_6^{(0)} \end{bmatrix}. \tag{2.54}$$

It is often the case in composites that layers display strongly orthotropic material properties. This means that a single lamina will be capable of resisting large stresses in one direction but not in another. The plate in this context will consequently comprise of a number of such laminates which are bonded together in a sandwich type construction with the principal material property directions oriented at differing angles to maximise the strength of the plate for a given application.

Note that in the case of a plate of one single lamina or layer, we simply have that $B_{ij} = 0$ and that by assuming an isotropic material the original FSDT formulation results. For the case where the material coordinates coincide with those of the plate, the transformation stage from material constitutive equations to plate constitutive equations via coordinate transformations is obviously not required.

2.2.3 Problem Domain

As mentioned previously all plates modelled in this work will be rectangular or square in shape. A typical example is that of Figure (2.5) which is a plan view of a square shaped plate centred on the origin O. The shaded region in Figure (2.5) corresponds to the plate midplane at $x_3 = 0$ which

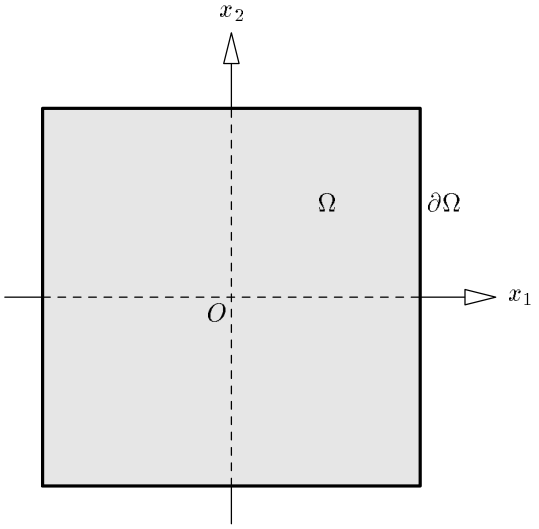

Figure 2.5: Typical plate problem domain Ω (shaded).

we shall denote as Ω and the plate edge or boundary as $\partial\Omega$ illustrated by a thick line around Ω.

For some loading scenarios it may be possible to analyse the behaviour of a plate by only modelling a portion of it and exploiting lines of symmetry in the problem. For example, consider the transverse distributed loading of the square plate in Figure (2.5) which is simply supported on the boundary $\partial\Omega$. In this case it is possible to model just one quarter of the whole plate geometry by exploiting expected lines of symmetry in the solution. This produces a new smaller problem domain Ω and corresponding boundary $\partial\Omega$.

As can be seen in Figure (2.6), the modified domain of the problem now consists only of the top right-hand corner of the previous whole plate domain given in Figure (2.5). Thus the problem has been reduced in size by exploiting two expected lines of symmetry in the solution. These lie along the x_1 and x_2 axes which coincide with the plate centre lines, ℄, or lines of symmetry and correspond to the Southern and Western faces of the new problem boundary $\partial\Omega \equiv \Gamma_N \cup \Gamma_E \cup \Gamma_S \cup \Gamma_W$ which we shall denote as Γ_S and Γ_W respectively. The boundary faces Γ_N and Γ_E are in fact boundaries of the plate and thus have zero transverse displacement conditions attached to them.

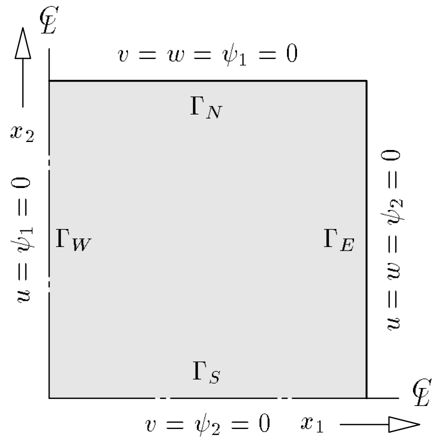

Figure 2.6: Plate geometry for problem.

The restrictions of $v = 0$ on the North and South faces are to stop rigid body translation of the geometry in that direction, as is the restriction of $u = 0$ on the East and West faces. As the rotation ψ_1 is to be interpreted as a rotation about the x_2-axis, it is necessary to stipulate that there be no rotation in this manner along the North face as this face lies on the support. Additionally the same is performed on the East face by setting $\psi_2 = 0$. Finally, dealing with the rotations on the lines of symmetry faces (Γ_S and Γ_W) it is required that the solution be symmetric across these faces. To ensure this the rotations on these faces are set accordingly. This set of boundary conditions provides the essential conditions for a simply supported plate. As illustrated in Figure (2.6) essential boundary conditions have been defined on portions of $\partial\Omega$ for the displacements u, v, w, ψ_1 and ψ_2 in order to simulate a simply supported quadrant of the plate. Where these displacement degrees of freedom are not stipulated on the boundary, zero natural boundary conditions are implied. The relationships between essential and natural boundary conditions in terms of the boundary portions $\Gamma_N, \Gamma_E, \Gamma_S$ and Γ_W are,

		Essential		Natural
$u = 0$	on	$\Gamma_1 = \Gamma_W \cup \Gamma_E$	$\Rightarrow$	$\hat{\Gamma}_1 = \partial\Omega \setminus \Gamma_1$
$v = 0$	on	$\Gamma_2 = \Gamma_N \cup \Gamma_S$	$\Rightarrow$	$\hat{\Gamma}_2 = \partial\Omega \setminus \Gamma_2$
$w = 0$	on	$\Gamma_3 = \Gamma_N \cup \Gamma_E$	$\Rightarrow$	$\hat{\Gamma}_3 = \partial\Omega \setminus \Gamma_3$
$\psi_1 = 0$	on	$\Gamma_4 = \Gamma_N \cup \Gamma_W$	$\Rightarrow$	$\hat{\Gamma}_4 = \partial\Omega \setminus \Gamma_4$
$\psi_2 = 0$	on	$\Gamma_5 = \Gamma_E \cup \Gamma_S$	$\Rightarrow$	$\hat{\Gamma}_5 = \partial\Omega \setminus \Gamma_5$

Thus, for example, on the portion of the boundary $\hat{\Gamma}_1$ where displacement component u is not stipulated, we have a natural boundary condition implied.

Chapter 3

Finite Element Considerations

The Finite Element Method is usually applied to a weak formulation of the problem which, in turn, is itself arrived at from the equilibrium equations of a given problem. In the previous chapter the problems of linear elasticity and plate theory were introduced using Equations (2.1) and (2.39)-(2.43) respectively and the models described. Thus in order to proceed it is now necessary to derive the weak formulations of both the linear elasticity and plate formulations. In the case of elasticity the derivation will be performed along two alternate routes. Each route will yield the same weak formulation however and the two are included as an illustration that the route taken need not be unique. In addition the second route is not commonly performed and is included for completeness.

Once the weak formulations have been obtained, the finite element method will be introduced and used to discuss the forms of the element stiffness matrices. In the context of plates, further discussion will be given as it is important to highlight the necessity for and effect of reduced integration. This numerical tool is required in the computation of the transverse shear terms of the element stiffness matrix and enables the FSDT to model the thin plate limit by avoiding the undesirable effect of locking where the model can severely underpredict the plate deformation.

3.1 Function Spaces and Norms

Before the derivation of the weak formulations, however, some useful mathematical fundamentals are defined. The first task is to define, for $1 \leq p < \infty$, the space of all functions whose pth powers are integrable over Ω. Such spaces will be denoted by $L_p(\Omega)$ where,

$$\int_\Omega |v(\mathbf{x})|^p \, d\mathbf{x} < \infty, \quad \forall \; v(\mathbf{x}) \in L_p(\Omega),$$

and where $\mathbf{x} = [x_1, x_2, \ldots, x_n]^T$ for $\Omega \in \mathbb{R}^n$ with $n = 1, 2$ or 3 ordinarily. This leads to the definition of the $L_p(\Omega)$ norm,

$$\|v\|_{L_p(\Omega)} = \left(\int_\Omega |v(\mathbf{x})|^p \, d\mathbf{x} \right)^{1/p} < \infty, \quad \forall \; v(\mathbf{x}) \in L_p(\Omega).$$

Of particular interest here will be the $L_2(\Omega)$ space for which the inner product $(\cdot, \cdot)$ is given as,

$$(u(\mathbf{x}), v(\mathbf{x})) = \int_\Omega u(\mathbf{x}) v(\mathbf{x}) \, d\mathbf{x}, \quad \forall \; u(\mathbf{x}), v(\mathbf{x}) \in L_2(\Omega), \tag{3.1}$$

and which enables the $L_2(\Omega)$-norm to be expressed as,

$$\|v(\mathbf{x})\|_{L_2(\Omega)} = (v(\mathbf{x}), v(\mathbf{x}))^{\frac{1}{2}}, \quad \forall \; v(\mathbf{x}) \in L_2(\Omega). \tag{3.2}$$

Dropping the $\mathbf{x}$ notation for convenience, a sequence $\{v_r\}_{r=1}^\infty \subset L_2(\Omega)$ converges in the mean to $v \in L_2(\Omega)$ if,

$$\lim_{r \to \infty} \|v - v_r\|_{L_2(\Omega)} = 0,$$

such a sequence is said to be Cauchy if,

$$\lim_{s,r \to \infty} \|v_s - v_r\|_{L_2(\Omega)} = 0.$$

Suppose that the sequence does converge in the mean to $v \in L_2(\Omega)$, then,

$$\begin{aligned} \|v_s - v_r\|_{L_2(\Omega)} &= \|v_s - v + v - v_r\|_{L_2(\Omega)}, \\ &\leq \|v_s - v\|_{L_2(\Omega)} + \|v - v_r\|_{L_2(\Omega)}, \end{aligned} \tag{3.3}$$

and thus it follows that the sequence must also be Cauchy. For $L_2(\Omega)$ the converse is also true. That is, if the sequence $\{v_r\}_{r=1}^\infty \subset L_2(\Omega)$ is a Cauchy sequence then it will converge in the mean to a unique $v \in L_2(\Omega)$. This property implies that the $L_2(\Omega)$ space is complete. A linear space with an inner product defined as in Equation (3.1) and a norm as defined in Equation (3.2) which is complete is a Hilbert space. It follows therefore that $L_2(\Omega)$ is a Hilbert space.

The general Sobolev spaces $W_p^k(\Omega)$ with $1 \leq p < \infty$ and $k \geq 0$ are those consisting of functions which, together with their generalized derivatives of up to and including order k belong to $L_p(\Omega)$. Such generalized derivatives may be described by considering the multi-index α where $\alpha = (\alpha_1, \alpha_2, \ldots, \alpha_n)$ and where each $\alpha_i, i = 1, \ldots, n$ are non-negative. It follows then that the generalized partial derivative in $\mathbb{R}^n$ may be expressed as,

$$D^\alpha v = \frac{\partial^{|\alpha|} v}{\partial x_1^{\alpha_1} \partial x_2^{\alpha_2} \ldots \partial x_n^{\alpha_n}},$$

where $|\alpha| = \alpha_1 + \alpha_2 + \ldots + \alpha_n$ and where again $n = 1, 2$ or 3 in most cases. It follows then that,

$$W_p^k(\Omega) \equiv \{ v : D^\alpha v \in L_p(\Omega), \; \forall \; \alpha \text{ such that } |\alpha| \leq k \}.$$

The spaces $W_2^1(\Omega) \equiv H^1(\Omega)$ and $W_2^2(\Omega) \equiv H^2(\Omega)$ are Hilbert spaces of 'L_2-type' but which only involve respectively first order and first and second order generalized derivatives. Thus, for the general Hilbert space of the form $H^k(\Omega)$ where,

$$W_2^k(\Omega) \equiv H^k(\Omega) \equiv \{ v : D^\alpha v \in L_2(\Omega), \; \forall \; \alpha \text{ such that } |\alpha| \leq k \},$$

the inner product, $(\cdot,\cdot)_{k,\Omega}$, is expressed as,

$$(u,v)_{k,\Omega} = \sum_{|\alpha|\leq k} \left(D^{\alpha}u, D^{\alpha}v\right), \quad \forall\ u,v \in H^k(\Omega),$$

where $(\cdot,\cdot)$ is the $L_2(\Omega)$ inner product as given in Equation (3.1) and the corresponding norm defined on $H^k(\Omega)$ is expressed as,

$$||v||_{H^k(\Omega)} \equiv ||v||_{k,\Omega} = \left[\sum_{|\alpha|\leq k} ||D^{\alpha}v||^2_{L_2(\Omega)}\right]^{\frac{1}{2}}.$$

For the case of boundary value problems with homogeneous boundary conditions on Lipschitz-continuous boundary $\partial\Omega$, define,

$$\mathring{H}^k(\Omega) \equiv \left\{v : v \in H^k(\Omega) \text{ and } D^{\alpha}v|_{\partial\Omega} = 0, |\alpha| \leq k-1\right\}.$$

The corresponding seminorm defined on $\mathring{H}^k(\Omega)$ is defined as,

$$|v|_{\mathring{H}^k(\Omega)} \equiv |v|_{k,\Omega} = \left[\sum_{|\alpha|=k} ||D^{\alpha}v||^2_{L_2(\Omega)}\right]^{\frac{1}{2}},$$

which is in fact the norm, $||v||_{k,0,\Omega}$. This section has thus far been concerned with scalar valued functions. For the problems defined in Chapter 2, it is clear that vector valued formulations will result. Thus the definitions at the beginning of this section will now be extended for such cases. We thus define the L_2-norm of a vector valued function $\mathbf{v} \in [L_2(\Omega)]^n$, where,

$$[L_2(\Omega)]^n = L_2(\Omega) \times \ldots \times L_2(\Omega), \quad (n \text{ times}),$$

as,

$$||\mathbf{v}||_{L_2(\Omega)} = \left[\sum_{i=1}^{n} ||v_i||^2_{L_2(\Omega)}\right]^{\frac{1}{2}},$$

and where the L_2-norm for the scalar valued v_i are as defined above. Similarly, for $\mathbf{v} \in \left[H^k(\Omega)\right]^n$ we have,

$$||\mathbf{v}||_{H^k(\Omega)} \equiv ||\mathbf{v}||_{k,\Omega} = \left[\sum_{i=1}^{n} ||v_i||^2_{H^k(\Omega)}\right]^{\frac{1}{2}}.$$

Finally, for the case of boundary value problems with homogeneous boundary conditions on $\partial\Omega$, we have for $\mathbf{v} \in \left[\mathring{H}^k(\Omega)\right]^n$,

$$||\mathbf{v}||_{k,0,\Omega} \equiv |\mathbf{v}|_{k,\Omega} = \left[\sum_{i=1}^{n} |v_i|^2_{k,\Omega}\right]^{\frac{1}{2}}.$$

Having defined the above mathematical fundamentals we are now able to proceed by obtaining the weak formulations for the models described in Chapter 2. It should be noted that, once the weak formulations and corresponding bilinear forms $a(\cdot,\cdot)$ of the problems at hand have been obtained, we shall express the energy norm $||\cdot||_{E(\Omega)}$, taken over Ω as,

$$||\cdot||_{E(\Omega)} = a(\cdot,\cdot)^{\frac{1}{2}}.$$

For completeness, use will be made in this work of Green's formula, [19], which for $u, v \in H^1(\Omega)$ may be expressed as,

$$\int_\Omega v\frac{\partial w}{\partial x_i} + w\frac{\partial v}{\partial x_i}\,d\mathbf{x} = \int_{\partial\Omega} wv_i n_i\,ds,$$

for any $i \in [1, n]$ and where $\mathbf{n} = (n_1, \ldots, n_n)$ is the unit outward normal to $\partial\Omega$. Rearranging this yields,

$$-\int_\Omega v\frac{\partial w}{\partial x_i}\,d\mathbf{x} = \int_\Omega w\frac{\partial v}{\partial x_i}\,d\mathbf{x} - \int_{\partial\Omega} wvn_i\,ds, \tag{3.4}$$

which illustrates the integration by parts of the left-hand side.

3.2 Weak Formulation of the Elasticity Model

For a three-dimensional linear elastic material, the constitutive relations in the stiffness form can be expressed as detailed in Section (2.1.2) as,

$$\boldsymbol{\sigma}(\mathbf{u}(\mathbf{x})) = \mathbf{C}\varepsilon(\mathbf{u}(\mathbf{x})),$$

where $\mathbf{C}$ is a matrix consisting of six rows and six columns. For simplicity consider the case of an isotropic material in two dimensions. In such a case the constitutive relations once again takes on the form of Hooke's law as described in Equation (2.20) but now given for two dimensions as,

$$\sigma_{ij}(\mathbf{u}) = \lambda\left\{\sum_{k=1}^{2}\varepsilon_{kk}(\mathbf{u})\right\}\delta_{ij} + 2\mu\varepsilon_{ij}(\mathbf{u}), \quad 1 \le i, j \le 2, \tag{3.5}$$

where λ and μ are the previously described Lamé coefficients which may be expressed in either the plane stress or plane strain contexts as given by Equation (2.24) and (2.25) respectively. Substitution of Equations (3.5) and (2.6) into the equilibrium equations recast in the two-dimensional context from Equation (2.1) yields the Lamé equations,

$$-\mu\Delta\mathbf{u} - (\lambda+\mu)\nabla(\nabla\cdot\mathbf{u}) = \mathbf{f}, \tag{3.6}$$

where,

$$\Delta\mathbf{u} \equiv \nabla^2\mathbf{u} = \left(\frac{\partial^2 u_i}{\partial x_1^2} + \frac{\partial^2 u_i}{\partial x_2^2}\right), \quad \text{for } i = 1, 2,$$

and,

$$\nabla(\nabla\cdot\mathbf{u}) = \left(\frac{\partial}{\partial x_i}\left(\frac{\partial u_1}{\partial x_1} + \frac{\partial u_2}{\partial x_2}\right)\right), \quad \text{for } i = 1, 2,$$

and also $\mathbf{f} = (f_1, f_2)^T$. The finite element method is applied to the linear elasticity problem given by Equations (2.1)-(2.3) via a weak formulation and the Galerkin technique. It is possible to obtain the weak formulation of the problem by using either the equilibrium equations (2.1) or the Lamé equations (3.6). These two routes shall now be described in Sections (3.2.1) and (3.2.2) respectively for the two-dimensional linear elasticity problem.

3.2.1 Weak Formulation from the Equilibrium Equations

By starting with Equation (2.1) the first step along this route is to take the scalar product of the equation with a test vector function $\mathbf{v} \in V$, where,

$$V \equiv \left\{ \mathbf{v} : \mathbf{v} \in \left[H^1(\Omega)\right]^2, v_i|_{\partial\Omega_C} = 0, \quad i = 1, 2 \right\},$$

is the space of admissible displacement vectors. This gives,

$$\left(\frac{\partial\sigma_{11}}{\partial x_1} + \frac{\partial\sigma_{12}}{\partial x_2}\right) v_1 + \left(\frac{\partial\sigma_{21}}{\partial x_1} + \frac{\partial\sigma_{22}}{\partial x_2}\right) v_2 + f_1 v_1 + f_2 v_2 = 0. \tag{3.7}$$

This quantity is then integrated over the problem domain Ω. For this, consider the first two terms of Equation (3.7),

$$\left(\frac{\partial\sigma_{11}}{\partial x_1} + \frac{\partial\sigma_{12}}{\partial x_2}\right) v_1 + \left(\frac{\partial\sigma_{21}}{\partial x_1} + \frac{\partial\sigma_{22}}{\partial x_2}\right) v_2 = v_1\frac{\partial\sigma_{11}}{\partial x_1} + v_2\frac{\partial\sigma_{21}}{\partial x_1} + v_1\frac{\partial\sigma_{12}}{\partial x_2} + v_2\frac{\partial\sigma_{22}}{\partial x_2}.$$

Integration of these terms by parts over Ω yields,

$$\begin{aligned}
\int_\Omega v_1\frac{\partial\sigma_{11}}{\partial x_1}\,d\mathbf{x} &= -\int_\Omega \sigma_{11}\frac{\partial v_1}{\partial x_1}\,d\mathbf{x} + \int_{\partial\Omega} \sigma_{11} n_1 v_1\,ds,\\
\int_\Omega v_2\frac{\partial\sigma_{21}}{\partial x_1}\,d\mathbf{x} &= -\int_\Omega \sigma_{21}\frac{\partial v_2}{\partial x_1}\,d\mathbf{x} + \int_{\partial\Omega} \sigma_{21} n_1 v_2\,ds,\\
\int_\Omega v_1\frac{\partial\sigma_{12}}{\partial x_2}\,d\mathbf{x} &= -\int_\Omega \sigma_{12}\frac{\partial v_1}{\partial x_2}\,d\mathbf{x} + \int_{\partial\Omega} \sigma_{12} n_2 v_1\,ds,
\end{aligned}$$

and,

$$\int_\Omega v_2\frac{\partial\sigma_{22}}{\partial x_2}\,d\mathbf{x} = -\int_\Omega \sigma_{22}\frac{\partial v_2}{\partial x_2}\,d\mathbf{x} + \int_{\partial\Omega} \sigma_{22} n_2 v_2\,ds.$$

Substitution back into Equation (3.7) integrated over Ω gives,

$$\begin{aligned}
0 = &-\int_\Omega \sigma_{11}\frac{\partial v_1}{\partial x_1} + \sigma_{22}\frac{\partial v_2}{\partial x_2} + \sigma_{12}\left(\frac{\partial v_1}{\partial x_2} + \frac{\partial v_2}{\partial x_1}\right) d\mathbf{x}\\
&+ \int_{\partial\Omega} \left(\sigma_{11}n_1 + \sigma_{12}n_2\right) v_1 + \left(\sigma_{21}n_1 + \sigma_{22}n_2\right) v_2\,ds\\
&+ \int_\Omega \mathbf{f}\cdot\mathbf{v}\,d\mathbf{x},
\end{aligned}$$

where the shear stress terms have been gathered, the symmetry of the tensors has been exploited and $\mathbf{f} = (f_1, f_2)^T$. From the boundary conditions of Equations (2.2) and (2.3) the boundary integral in the above formulation on the boundary part $\partial\Omega_C$ equals zero. We are thus left with the formulation,

$$\int_\Omega \left(\sigma_{11}\frac{\partial v_1}{\partial x_1} + \sigma_{22}\frac{\partial v_2}{\partial x_2} + \sigma_{12}\left(\frac{\partial v_1}{\partial x_2} + \frac{\partial v_2}{\partial x_1}\right)\right) d\mathbf{x} = \int_\Omega \mathbf{f}\cdot\mathbf{v}\,d\mathbf{x} + \int_{\partial\Omega_T} \mathbf{g}\cdot\mathbf{v}\,ds.$$

Using the previously defined strain tensor components given by,

$$\varepsilon_{ij} = \frac{1}{2}\left(\frac{\partial v_i}{\partial x_j} + \frac{\partial v_j}{\partial x_i}\right), \quad i, j = 1, 2,$$

we have finally that the weak formulation for the analogous two-dimensional linear elastic problem is to seek $\mathbf{u} \in V$ such that,

$$\int_\Omega \boldsymbol{\sigma}(\mathbf{u})\cdot\varepsilon(\mathbf{v})\,d\mathbf{x} = \int_\Omega \mathbf{f}\cdot\mathbf{v}\,d\mathbf{x} + \int_{\partial\Omega_T} \mathbf{g}\cdot\mathbf{v}\,ds, \quad \forall\,\mathbf{v} \in V, \tag{3.8}$$

where $\boldsymbol{\sigma} = (\sigma_{11}, \sigma_{22}, \sigma_{12})^T$, $\boldsymbol{\varepsilon} = (\varepsilon_{11}, \varepsilon_{22}, 2\varepsilon_{12})^T$ and the displacement $\mathbf{u}$ is involved in Equation (3.8) through $\boldsymbol{\sigma}$ via the constitutive relation as now illustrated. From Hooke's Law it is known that, using Equation (2.20),

$$\begin{aligned}
\sigma_{11}(\mathbf{u}) &= (\lambda + 2\mu)\varepsilon_{11}(\mathbf{u}) + \lambda\varepsilon_{22}(\mathbf{u}), \\
\sigma_{22}(\mathbf{u}) &= \lambda\varepsilon_{11}(\mathbf{u}) + (\lambda + 2\mu)\varepsilon_{22}(\mathbf{u}), \\
\sigma_{12}(\mathbf{u}) &= 2\mu\varepsilon_{12}(\mathbf{u}).
\end{aligned}$$

Thus, by considering the left-hand side of Equation (3.8),

$$\begin{aligned}
\boldsymbol{\sigma}(\mathbf{u}) \cdot \boldsymbol{\varepsilon}(\mathbf{v}) = 2\mu \sum_{i,j=1}^{2} \varepsilon_{ij}(\mathbf{u})\varepsilon_{ij}(\mathbf{v}) \; &+ \; \lambda \left[\varepsilon_{11}(\mathbf{u})\varepsilon_{11}(\mathbf{v}) + \varepsilon_{22}(\mathbf{u})\varepsilon_{11}(\mathbf{v})\right. \\
&+ \; \left.\varepsilon_{11}(\mathbf{u})\varepsilon_{22}(\mathbf{v}) + \varepsilon_{22}(\mathbf{u})\varepsilon_{22}(\mathbf{v})\right],
\end{aligned}$$

which may be expressed as,

$$\begin{aligned}
\boldsymbol{\sigma}(\mathbf{u}) \cdot \boldsymbol{\varepsilon}(\mathbf{v}) &= 2\mu \sum_{i,j=1}^{2} \varepsilon_{ij}(\mathbf{u})\varepsilon_{ij}(\mathbf{v}) + \lambda \left[\frac{\partial u_1}{\partial x_1} + \frac{\partial u_2}{\partial x_2}\right] \left[\frac{\partial v_1}{\partial x_1} + \frac{\partial v_2}{\partial x_2}\right], \\
&= 2\mu \sum_{i,j=1}^{2} \varepsilon_{ij}(\mathbf{u})\varepsilon_{ij}(\mathbf{v}) + \lambda \left(\nabla \cdot \mathbf{u}\right) \left(\nabla \cdot \mathbf{v}\right).
\end{aligned}$$

Thus the weak formulation is now that of finding $\mathbf{u} \in V$ such that,

$$a(\mathbf{u}, \mathbf{v}) = F(\mathbf{v}) \quad \forall\ \mathbf{v} \in V, \tag{3.9}$$

where,

$$a(\mathbf{u}, \mathbf{v}) \equiv \int_\Omega \lambda \left(\nabla \cdot \mathbf{u}\right) \left(\nabla \cdot \mathbf{v}\right) + 2\mu \sum_{i,j=1}^{2} \varepsilon_{ij}(\mathbf{u})\varepsilon_{ij}(\mathbf{v}) \, d\mathbf{x}, \tag{3.10}$$

and,

$$F(\mathbf{v}) \equiv \int_\Omega \mathbf{f} \cdot \mathbf{v} \, d\mathbf{x} + \int_{\partial\Omega_T} \mathbf{g} \cdot \mathbf{v} \, ds. \tag{3.11}$$

3.2.2 Weak Formulation from the Lamé Equations

As noted previously, the weak formulation may also be obtained from the Lamé equations introduced in Equation (3.6). This may be done as follows by firstly expressing the Lamé equations as,

$$-\mu\nabla^2\mathbf{u} - (\lambda + \mu)\nabla\left(\nabla \cdot \mathbf{u}\right) = \mathbf{f}. \tag{3.12}$$

By taking the scalar product of Equation (3.12) with a test vector function $\mathbf{v} \in V$ and integrating, the ith component gives,

$$-\mu \int_\Omega v_i \left(\frac{\partial^2 u_i}{\partial x_1^2} + \frac{\partial^2 u_i}{\partial x_2^2}\right) d\mathbf{x} - (\lambda + \mu) \int_\Omega v_i \frac{\partial}{\partial x_i} \left(\frac{\partial u_1}{\partial x_1} + \frac{\partial u_2}{\partial x_2}\right) d\mathbf{x} = \int_\Omega f_i v_i \, d\mathbf{x}. \tag{3.13}$$

As performed previously, Equation (3.13) is now integrated by parts over Ω, giving,

$$\begin{aligned}
&\mu \int_\Omega \frac{\partial u_i}{\partial x_1}\frac{\partial v_i}{\partial x_1} + \frac{\partial u_i}{\partial x_2}\frac{\partial v_i}{\partial x_2}\,d\mathbf{x} + (\lambda+\mu)\int_\Omega \frac{\partial v_i}{\partial x_i}\left(\frac{\partial u_1}{\partial x_1} + \frac{\partial u_2}{\partial x_2}\right)\,d\mathbf{x} \\
&- \mu \int_{\partial\Omega} \frac{\partial u_i}{\partial x_1} v_i n_i + \frac{\partial u_i}{\partial x_2} v_i n_2\,ds - (\lambda+\mu)\int_{\partial\Omega} v_i \left(\frac{\partial u_1}{\partial x_1} + \frac{\partial u_2}{\partial x_2}\right) n_i\,ds \\
&= \int_\Omega f_i v_i\,d\mathbf{x}.
\end{aligned}$$

Summing for all components $i = 1,2$ produces, letting L.H.S. and R.H.S. denote the left and right hand sides of the above equation summed, and neglecting momentarily integrals over $\partial\Omega$,

$$\begin{aligned}
\text{L.H.S.} &= \mu \int_\Omega \frac{\partial u_1}{\partial x_1}\frac{\partial v_1}{\partial x_1} + \frac{\partial u_2}{\partial x_1}\frac{\partial v_2}{\partial x_1} + \frac{\partial u_1}{\partial x_2}\frac{\partial v_1}{\partial x_2} + \frac{\partial u_2}{\partial x_2}\frac{\partial v_2}{\partial x_2}\,d\mathbf{x} \\
&+ (\lambda+\mu)\int_\Omega \frac{\partial v_1}{\partial x_1}\frac{\partial u_1}{\partial x_1} + \frac{\partial v_1}{\partial x_1}\frac{\partial u_2}{\partial x_2} + \frac{\partial v_2}{\partial x_2}\frac{\partial u_1}{\partial x_1} + \frac{\partial v_2}{\partial x_2}\frac{\partial u_2}{\partial x_2}\,d\mathbf{x},
\end{aligned}$$

which may be expressed as,

$$\begin{aligned}
\text{L.H.S.} &= 2\mu \int_\Omega \varepsilon_{11}(\mathbf{u})\varepsilon_{11}(\mathbf{v}) + \varepsilon_{22}(\mathbf{u})\varepsilon_{22}(\mathbf{v})\,d\mathbf{x} \\
&+ \lambda \int_\Omega \nabla\cdot\mathbf{u}\,\nabla\cdot\mathbf{v}\,d\mathbf{x} \\
&+ \mu \int_\Omega \frac{\partial u_2}{\partial x_1}\frac{\partial v_2}{\partial x_1} + \frac{\partial u_1}{\partial x_2}\frac{\partial v_1}{\partial x_2} + \frac{\partial v_1}{\partial x_1}\frac{\partial u_2}{\partial x_2} + \frac{\partial v_2}{\partial x_2}\frac{\partial u_1}{\partial x_1}\,d\mathbf{x}.
\end{aligned} \tag{3.14}$$

Consider the last two terms in the integrand of the last integral. By using integrating by parts twice on each of these terms it may be shown that,

$$\begin{aligned}
\mu \int_\Omega \frac{\partial v_1}{\partial x_1}\frac{\partial u_2}{\partial x_2}\,d\mathbf{x} &= \mu \int_{\partial\Omega} \frac{\partial u_2}{\partial x_2} v_1 n_1\,ds - \mu \int_{\partial\Omega} \frac{\partial u_2}{\partial x_1} v_1 n_2\,ds \\
&+ \mu \int_\Omega \frac{\partial v_1}{\partial x_2}\frac{\partial u_2}{\partial x_1}\,d\mathbf{x},
\end{aligned} \tag{3.15}$$

and,

$$\begin{aligned}
\mu \int_\Omega \frac{\partial v_2}{\partial x_2}\frac{\partial u_1}{\partial x_1}\,d\mathbf{x} &= \mu \int_{\partial\Omega} \frac{\partial u_1}{\partial x_1} v_2 n_2\,ds - \mu \int_{\partial\Omega} \frac{\partial u_1}{\partial x_2} v_2 n_1\,ds \\
&+ \mu \int_\Omega \frac{\partial v_2}{\partial x_1}\frac{\partial u_1}{\partial x_2}\,d\mathbf{x}.
\end{aligned} \tag{3.16}$$

Thus, substituting Equations (3.15) and (3.16) into Equation (3.14) gives,

$$\begin{aligned}
\text{L.H.S.} &= \lambda \int_\Omega \nabla\cdot\mathbf{u}\,\nabla\cdot\mathbf{v}\,d\mathbf{x} + 2\mu \int_\Omega \varepsilon_{11}(\mathbf{u})\varepsilon_{11}(\mathbf{v}) + \varepsilon_{22}(\mathbf{u})\varepsilon_{22}(\mathbf{v})\,d\mathbf{x} \\
&+ \mu \int_\Omega \frac{\partial u_2}{\partial x_1}\frac{\partial v_2}{\partial x_1} + \frac{\partial u_1}{\partial x_2}\frac{\partial v_1}{\partial x_2} + \frac{\partial v_1}{\partial x_2}\frac{\partial u_2}{\partial x_1} + \frac{\partial v_2}{\partial x_1}\frac{\partial u_1}{\partial x_2}\,d\mathbf{x} \\
&+ \mu \int_{\partial\Omega} \frac{\partial u_2}{\partial x_2} v_1 n_1\,ds - \mu \int_{\partial\Omega} \frac{\partial u_2}{\partial x_1} v_1 n_2\,ds \\
&+ \mu \int_{\partial\Omega} \frac{\partial u_1}{\partial x_1} v_2 n_2\,ds - \mu \int_{\partial\Omega} \frac{\partial u_1}{\partial x_2} v_2 n_1\,ds.
\end{aligned} \tag{3.17}$$

Neglecting momentarily the boundary integrals of Equation (3.17),

$$\begin{aligned}
\text{L.H.S.} &= \lambda \int_\Omega \nabla\cdot\mathbf{u}\,\nabla\cdot\mathbf{v}\,d\mathbf{x} + 2\mu \int_\Omega \varepsilon_{11}(\mathbf{u})\varepsilon_{11}(\mathbf{v}) + \varepsilon_{22}(\mathbf{u})\varepsilon_{22}(\mathbf{v})\,d\mathbf{x} \\
&+ 4\mu \int_\Omega \varepsilon_{12}(\mathbf{u})\varepsilon_{12}(\mathbf{v})\,d\mathbf{x}, \\
&= \lambda \int_\Omega \nabla\cdot\mathbf{u}\,\nabla\cdot\mathbf{v}\,d\mathbf{x} + 2\mu \int_\Omega \sum_{i,j=1}^{2} \varepsilon_{ij}(\mathbf{u})\varepsilon_{ij}(\mathbf{v})\,d\mathbf{x}.
\end{aligned} \tag{3.18}$$

which is clearly the bilinear form obtained previously in Equation (3.10). Taking all remaining terms onto the right-hand side of the formulation,

$$\begin{aligned}
\text{R.H.S.} = {} & \mu \int_{\partial\Omega} \frac{\partial u_1}{\partial x_1} v_1 n_1 + \frac{\partial u_2}{\partial x_1} v_2 n_1 + \frac{\partial u_1}{\partial x_2} v_1 n_2 + \frac{\partial u_2}{\partial x_2} v_2 n_2 \, ds \\
& + (\lambda + \mu) \int_{\partial\Omega} v_1 \left(\frac{\partial u_1}{\partial x_1} + \frac{\partial u_2}{\partial x_2} \right) n_1 + v_2 \left(\frac{\partial u_1}{\partial x_1} + \frac{\partial u_2}{\partial x_2} \right) n_2 \, ds \\
& - \mu \int_{\partial\Omega} \frac{\partial u_2}{\partial x_2} v_1 n_1 - \frac{\partial u_2}{\partial x_1} v_1 n_2 + \frac{\partial u_1}{\partial x_1} v_2 n_2 - \frac{\partial u_1}{\partial x_2} v_2 n_1 \, ds \\
& + \int_{\Omega} f_1 v_1 + f_2 v_2 \, d\mathbf{x}.
\end{aligned} \tag{3.19}$$

This may be expressed as,

$$\begin{aligned}
\text{R.H.S.} = {} & \int_{\partial\Omega} \left[\left((\lambda + 2\mu)\varepsilon_{11}(\mathbf{u}) + \lambda\varepsilon_{22}(\mathbf{u}) \right) n_1 + \left(2\mu\varepsilon_{12}(\mathbf{u}) \right) n_2 \right] v_1 \, ds \\
& + \int_{\partial\Omega} \left[\left(\lambda\varepsilon_{11}(\mathbf{u}) + (\lambda + 2\mu)\varepsilon_{22}(\mathbf{u}) \right) n_2 + \left(2\mu\varepsilon_{12}(\mathbf{u}) \right) n_1 \right] v_2 \, ds \\
& + \int_{\Omega} f_1 v_1 + f_2 v_2 \, d\mathbf{x},
\end{aligned} \tag{3.20}$$

by definition of the tensor ε_{ij}. Applying the boundary conditions of Equations (2.2) and (2.3) simplifies the above expression giving,

$$\begin{aligned}
\text{R.H.S.} &= \int_{\partial\Omega_T} g_1 v_1 + g_2 v_2 \, ds + \int_{\Omega} f_1 v_1 + f_2 v_2 \, d\mathbf{x}, \\
&= \int_{\partial\Omega_T} \mathbf{g} \cdot \mathbf{v} \, ds + \int_{\Omega} \mathbf{f} \cdot \mathbf{v} \, d\mathbf{x}.
\end{aligned} \tag{3.21}$$

This is clearly identical to the result obtained in Equation (3.11). Thus it has been shown that the weak formulation of the Lamé equations results again in finding $\mathbf{u} \in V$ such that,

$$a(\mathbf{u}, \mathbf{v}) = F(\mathbf{v}) \quad \forall\ \mathbf{v} \in V, \tag{3.22}$$

where $a(\mathbf{u}, \mathbf{v})$ is given in both Equations (3.10) and (3.18) and $F(\mathbf{v})$ is defined in both Equations (3.11) and (3.21).

3.2.3 Simplification of the Bilinear Form

It has been shown in Equation (3.8) of Section (3.2.1) that,

$$a(\mathbf{u}, \mathbf{v}) \equiv \int_{\Omega} \boldsymbol{\sigma}(\mathbf{u}) \cdot \boldsymbol{\varepsilon}(\mathbf{v}) \, d\mathbf{x}. \tag{3.23}$$

In addition, it was subsequently shown in Equation (3.10) that the bilinear form may also be expressed as,

$$a(\mathbf{u}, \mathbf{v}) \equiv \int_{\Omega} \lambda \, (\nabla \cdot \mathbf{u}) \, (\nabla \cdot \mathbf{v}) + 2\mu \sum_{i,j=1}^{2} \varepsilon_{ij}(\mathbf{u}) \varepsilon_{ij}(\mathbf{v}) \, d\mathbf{x},$$

and that this in turn was equal to the bilinear form obtained via the Lamé route in Section (3.2.2). It is possible to make a slight simplification to the bilinear form given in Equation (3.23). This simplified form will be used later in the linear elasticity problem and so shall now be described. From the constitutive relations given by Equation (2.26) it is clear that stress is related to strain in the following way,

$$\boldsymbol{\sigma} = \mathbf{C}\boldsymbol{\varepsilon}.$$

Thus the integrand of the bilinear form may be expressed as,

$$\boldsymbol{\sigma}(\mathbf{u}) \cdot \boldsymbol{\varepsilon}(\mathbf{v}) = \boldsymbol{\varepsilon}(\mathbf{u})^T \mathbf{C}\, \boldsymbol{\varepsilon}(\mathbf{v}),$$

since $\mathbf{C}$ is symmetric with structure as given in Equation (2.26). For a problem of linear elasticity there are two displacement degrees of freedom u_1 and u_2, these are the displacements in the x_1 and x_2 axis directions respectively. Thus from Equation (2.6) the strain $\boldsymbol{\varepsilon}(\mathbf{u})$ may be expressed as,

$$\boldsymbol{\varepsilon}(\mathbf{u}) = \begin{bmatrix} \dfrac{\partial u_1}{\partial x_1} \\ \dfrac{\partial u_2}{\partial x_2} \\ \dfrac{\partial u_1}{\partial x_2} + \dfrac{\partial u_2}{\partial x_1} \end{bmatrix} = \begin{bmatrix} \dfrac{\partial}{\partial x_1} & 0 \\ 0 & \dfrac{\partial}{\partial x_2} \\ \dfrac{\partial}{\partial x_2} & \dfrac{\partial}{\partial x_1} \end{bmatrix} \begin{bmatrix} u_1 \\ u_2 \end{bmatrix} = \mathbf{B}\mathbf{u}, \tag{3.24}$$

with $\mathbf{B}$ a differential operator acting on the displacement $\mathbf{u} = [u_1, u_2]^T$. It is thus possible to write the bilinear form for the linear elasticity problem as,

$$a(\mathbf{u}, \mathbf{v}) \equiv \int_\Omega (\mathbf{B}\mathbf{u})^T\, \mathbf{C}\, (\mathbf{B}\mathbf{v})\; d\mathbf{x}. \tag{3.25}$$

3.3 Weak Formulation of the Plate Model

Turning now to the plate problem, the equilibrium equations are again used to produce a weak formulation and finite element model. As defined in Equations (2.39)-(2.43) the equilibrium equations of the first-order plate theory have the form,

$$\begin{aligned}
-\left(\frac{\partial N_1}{\partial x_1} + \frac{\partial N_4}{\partial x_2}\right) &= 0, \\
-\left(\frac{\partial N_4}{\partial x_1} + \frac{\partial N_2}{\partial x_2}\right) &= 0, \\
-\left(\frac{\partial Q_5}{\partial x_1} + \frac{\partial Q_6}{\partial x_2} + q\right) &= 0, \\
-\left(\frac{\partial M_1}{\partial x_1} + \frac{\partial M_4}{\partial x_2} - Q_5\right) &= 0, \\
-\left(\frac{\partial M_4}{\partial x_1} + \frac{\partial M_2}{\partial x_2} - Q_6\right) &= 0.
\end{aligned}$$

In order to obtain the weak form of the problem, each equation is multiplied by an appropriate test function and integrated by parts over the problem domain. Consider a test function vector $\mathbf{v} \in V$ where,

$$V = \left\{ \mathbf{v} \in \left[H^1(\Omega)\right]^5 : \text{ and } \mathbf{v} \text{ satisfies essential boundary conditions in Section (2.2.3)} \right\}. \tag{3.26}$$

The equations of motion can be thought of as a system of equations. Taking the scalar product with $\mathbf{v}$ and integrating by parts trades differentiation from the resultants to the test functions giving,

$$\begin{aligned}
0 = & \int_\Omega \left(N_1 \frac{\partial v_1}{\partial x_1} + N_4 \frac{\partial v_1}{\partial x_2} \right) d\mathbf{x} - \int_{\hat{\Gamma}_1} N_n v_1 \, ds \\
+ & \int_\Omega \left(N_4 \frac{\partial v_2}{\partial x_1} + N_2 \frac{\partial v_2}{\partial x_2} \right) d\mathbf{x} - \int_{\hat{\Gamma}_2} N_s v_2 \, ds \\
+ & \int_\Omega \left(Q_5 \frac{\partial v_3}{\partial x_1} + Q_6 \frac{\partial v_3}{\partial x_2} - v_3 q \right) d\mathbf{x} - \int_{\hat{\Gamma}_3} Q_n v_3 \, ds \\
+ & \int_\Omega \left(M_1 \frac{\partial v_4}{\partial x_1} + M_4 \frac{\partial v_4}{\partial x_2} + v_4 Q_5 \right) d\mathbf{x} - \int_{\hat{\Gamma}_4} M_n v_4 \, ds \\
+ & \int_\Omega \left(M_4 \frac{\partial v_5}{\partial x_1} + M_2 \frac{\partial v_5}{\partial x_2} + v_5 Q_6 \right) d\mathbf{x} - \int_{\hat{\Gamma}_5} M_s v_5 \, ds,
\end{aligned} \tag{3.27}$$

where as previously,

$$\begin{gathered}
N_n = N_1 n_1 + N_4 n_2, \quad N_s = N_4 n_1 + N_2 n_2, \\
M_n = M_1 n_1 + M_4 n_2, \quad M_s = M_4 n_1 + M_2 n_2, \\
Q_n = Q_5 n_1 + Q_6 n_2,
\end{gathered} \tag{3.28}$$

and $\mathbf{n} = n_1 \mathbf{i} + n_2 \mathbf{j}$ is the unit outward normal in each boundary integral to the corresponding boundary edge. Using the definitions of the force, moment and shear force resultants from Section (2.2.2) and combining the integrals over Ω, Equation (3.27) may be expressed as,

$$a(\mathbf{u}, \mathbf{v}) = F(\mathbf{v}), \quad \forall\ \mathbf{v} \in V, \tag{3.29}$$

where now,

$$a(\mathbf{u}, \mathbf{v}) \equiv \int_\Omega \left(\mathbf{B}^b \mathbf{u}\right)^T \mathbf{C}^b \left(\mathbf{B}^b \mathbf{v}\right) \, d\mathbf{x} + \int_\Omega \left(\mathbf{B}^s \mathbf{u}\right)^T \mathbf{C}^s \left(\mathbf{B}^s \mathbf{v}\right) d\mathbf{x}, \tag{3.30}$$

and,

$$F(\mathbf{v}) \equiv \int_\Omega v_3 q \, d\mathbf{x} + \int_{\hat{\Gamma}_1} N_n v_1 \, ds + \int_{\hat{\Gamma}_2} N_s v_2 \, ds + \int_{\hat{\Gamma}_3} Q_n v_3 \, ds + \int_{\hat{\Gamma}_4} M_n v_4 \, ds + \int_{\hat{\Gamma}_5} M_s v_5 \, ds. \tag{3.31}$$

In Equation (3.30) the matrices $\mathbf{B}^b, \mathbf{B}^s, \mathbf{C}^b$ and $\mathbf{C}^s$ have been introduced. This is due to the fact that there are terms in the formulation which arise from plate bending terms and transverse shear terms. The matrices arising from plate bending terms are denoted by a superscript b and those arising from transverse shear terms by a superscript s. The first two of the above matrices are differential operators acting on $\mathbf{u}$ and $\mathbf{v}$ and have the form,

$$\mathbf{B}^b = \begin{bmatrix}
\frac{\partial}{\partial x_1} & 0 & 0 & 0 & 0 \\
0 & \frac{\partial}{\partial x_2} & 0 & 0 & 0 \\
\frac{\partial}{\partial x_2} & \frac{\partial}{\partial x_1} & 0 & 0 & 0 \\
0 & 0 & 0 & \frac{\partial}{\partial x_1} & 0 \\
0 & 0 & 0 & 0 & \frac{\partial}{\partial x_2} \\
0 & 0 & 0 & \frac{\partial}{\partial x_2} & \frac{\partial}{\partial x_1}
\end{bmatrix}, \quad \mathbf{B}^s = \begin{bmatrix}
0 & 0 & \frac{\partial}{\partial x_1} & 1 & 0 \\
0 & 0 & \frac{\partial}{\partial x_2} & 0 & 1
\end{bmatrix}. \tag{3.32}$$

The second two of these matrices are dependent upon the material properties involved and arise from the definitions of the force and moment resultants and the definitions of the transverse shear forces in the previous chapter. The matrices have the forms,

$$\mathbf{C}^b = \begin{bmatrix} A_{11} & A_{12} & A_{14} & B_{11} & B_{12} & B_{14} \\ A_{12} & A_{22} & A_{24} & B_{12} & B_{22} & B_{24} \\ A_{14} & A_{24} & A_{44} & B_{14} & B_{24} & B_{44} \\ B_{11} & B_{12} & B_{14} & D_{11} & D_{12} & D_{14} \\ B_{12} & B_{22} & B_{24} & D_{12} & D_{22} & D_{24} \\ B_{14} & B_{24} & B_{44} & D_{14} & D_{24} & D_{44} \end{bmatrix}, \quad \mathbf{C}^s = \begin{bmatrix} A_{55} & A_{56} \\ A_{56} & A_{66} \end{bmatrix}, \tag{3.33}$$

where A_{ij}, B_{ij}, D_{ij} for $i, j = 1, 2, 4$ are as defined in Equation (2.50) and A_{ij} for $i, j = 5, 6$ are as defined in Equation (2.51). The quantity $a(\mathbf{u}, \mathbf{v})$ is now the plate bilinear form and the plate problem now reads as follows: Find $\mathbf{u} \in V$ such that,

$$a(\mathbf{u}, \mathbf{v}) = F(\mathbf{v}) \quad \forall\ \mathbf{v} \in V,$$

where $a(\mathbf{u}, \mathbf{v})$ and $F(\mathbf{v})$ are as defined above in Equations (3.30) and (3.31) respectively. To recap, the energy norm $\|\cdot\|_E$ is expressed in the usual way as,

$$\|\cdot\|_E = \sqrt{a(\cdot,\cdot)}.$$

From Equation (3.30) it is clear that the plate bilinear form may be expressed as,

$$a(\mathbf{u}, \mathbf{v}) = a_b(\mathbf{u}, \mathbf{v}) + a_s(\mathbf{u}, \mathbf{v}),$$

where,

$$a_b(\mathbf{u}, \mathbf{v}) = \int_\Omega \left(\mathbf{B}^b\mathbf{u}\right)^T \mathbf{C}^b \left(\mathbf{B}^b\mathbf{v}\right)\, d\mathbf{x} \quad \text{and} \quad a_s(\mathbf{u}, \mathbf{v}) = \int_\Omega \left(\mathbf{B}^s\mathbf{u}\right)^T \mathbf{C}^s \left(\mathbf{B}^s\mathbf{v}\right)\, d\mathbf{x},$$

and where $a_b(\cdot,\cdot)$ and $a_s(\cdot,\cdot)$ are the portions of the bilinear form $a(\cdot,\cdot)$ arising from the plate bending and transverse shear terms respectively. Using Equation (3.32) along with the displacement vector $\mathbf{u} = [u_1, u_2, u_3, u_4, u_5]^T$ it is also clear that,

$$\mathbf{B}^b\mathbf{u} = \left[\frac{\partial u_1}{\partial x_1}, \frac{\partial u_2}{\partial x_2}, \frac{\partial u_1}{\partial x_2} + \frac{\partial u_2}{\partial x_1}, \frac{\partial u_4}{\partial x_1}, \frac{\partial u_5}{\partial x_2}, \frac{\partial u_4}{\partial x_2} + \frac{\partial u_5}{\partial x_1}\right]^T,$$

and,

$$\mathbf{B}^s\mathbf{u} = \left[\frac{\partial u_3}{\partial x_1} + u_4, \frac{\partial u_3}{\partial x_2} + u_5\right]^T.$$

Hence,

$$a(\mathbf{u}, \mathbf{u}) \geq \lambda_{\min}\left(\mathbf{C}^b\right) \int_\Omega I + II\, d\mathbf{x} + \lambda_{\min}\left(\mathbf{C}^s\right) \int_\Omega III\, d\mathbf{x},$$

where, $\lambda_{\min}\left(\mathbf{C}^b\right)$ and $\lambda_{\min}\left(\mathbf{C}^s\right)$ denote the minimum eigenvalues of matrices $\mathbf{C}^b$ and $\mathbf{C}^s$ respectively and I, II and III are integrands of the form,

$$I = \left(\frac{\partial u_1}{\partial x_1}\right)^2 + \left(\frac{\partial u_2}{\partial x_2}\right)^2 + \left(\frac{\partial u_1}{\partial x_2} + \frac{\partial u_2}{\partial x_1}\right)^2,$$

$$II = \left(\frac{\partial u_4}{\partial x_1}\right)^2 + \left(\frac{\partial u_5}{\partial x_2}\right)^2 + \left(\frac{\partial u_4}{\partial x_2} + \frac{\partial u_5}{\partial x_1}\right)^2,$$

and,

$$III = \left(\frac{\partial u_3}{\partial x_1} + u_4\right)^2 + \left(\frac{\partial u_3}{\partial x_2} + u_5\right)^2.$$

Using the Green's formula given in Equation (3.4) twice and assuming zero Dirichlet boundary data,

$$\int_\Omega \frac{\partial u_j}{\partial x_i}\frac{\partial u_i}{\partial x_j}\,d\mathbf{x} = \int_\Omega \frac{\partial u_i}{\partial x_i}\frac{\partial u_j}{\partial x_j}\,d\mathbf{x},$$

hence integrand I may be expressed as,

$$\begin{aligned}
I &= \left(\frac{\partial u_1}{\partial x_1}\right)^2 + \left(\frac{\partial u_2}{\partial x_2}\right)^2 + \left(\frac{\partial u_1}{\partial x_2}\right)^2 + \left(\frac{\partial u_2}{\partial x_1}\right)^2 + \frac{\partial u_2}{\partial x_1}\frac{\partial u_1}{\partial x_2} + \frac{\partial u_1}{\partial x_1}\frac{\partial u_2}{\partial x_2},\\
&= \frac{1}{2}\left[\left(\frac{\partial u_1}{\partial x_1}\right)^2 + \left(\frac{\partial u_1}{\partial x_2}\right)^2 + \left(\frac{\partial u_2}{\partial x_1}\right)^2 + \left(\frac{\partial u_2}{\partial x_2}\right)^2\right]\\
&\quad + \frac{1}{2}\left[\left(\frac{\partial u_1}{\partial x_1}\right)^2 + 2\frac{\partial u_1}{\partial x_1}\frac{\partial u_2}{\partial x_2} + \left(\frac{\partial u_2}{\partial x_2}\right)^2\right]\\
&\quad + \frac{1}{2}\left[\left(\frac{\partial u_1}{\partial x_2}\right)^2 + 2\frac{\partial u_2}{\partial x_1}\frac{\partial u_1}{\partial x_2} + \left(\frac{\partial u_2}{\partial x_1}\right)^2\right],\\
&= \frac{1}{2}\left[\left(\frac{\partial u_1}{\partial x_1}\right)^2 + \left(\frac{\partial u_1}{\partial x_2}\right)^2 + \left(\frac{\partial u_2}{\partial x_1}\right)^2 + \left(\frac{\partial u_2}{\partial x_2}\right)^2\right]\\
&\quad + \frac{1}{2}\left(\frac{\partial u_1}{\partial x_1} + \frac{\partial u_2}{\partial x_2}\right)^2 + \frac{1}{2}\left(\frac{\partial u_1}{\partial x_2} + \frac{\partial u_2}{\partial x_1}\right)^2,\\
&\geq \frac{1}{2}\left[\left(\frac{\partial u_1}{\partial x_1}\right)^2 + \left(\frac{\partial u_1}{\partial x_2}\right)^2 + \left(\frac{\partial u_2}{\partial x_1}\right)^2 + \left(\frac{\partial u_2}{\partial x_2}\right)^2\right].
\end{aligned}$$

Thus it follows that,

$$\int_\Omega I\,d\mathbf{x} \geq \frac{1}{2}\int_\Omega |\nabla u_1|^2 + |\nabla u_2|^2\,d\mathbf{x},$$

and by the same argument,

$$\int_\Omega II\,d\mathbf{x} \geq \frac{1}{2}\int_\Omega |\nabla u_4|^2 + |\nabla u_5|^2\,d\mathbf{x},$$

enabling the plate bending part of the bilinear form to be bounded below as,

$$\begin{aligned}
a_b(\mathbf{u},\mathbf{u}) &\geq \frac{\lambda_{\min}\left(\mathbf{C}^b\right)}{2}\int_\Omega |\nabla u_1|^2 + |\nabla u_2|^2 + |\nabla u_4|^2 + |\nabla u_5|^2\,d\mathbf{x},\\
&= \frac{\lambda_{\min}\left(\mathbf{C}^b\right)}{2}\left(\|\nabla u_1\|^2_{L_2(\Omega)} + \|\nabla u_2\|^2_{L_2(\Omega)} + \|\nabla u_4\|^2_{L_2(\Omega)} + \|\nabla u_5\|^2_{L_2(\Omega)}\right).
\end{aligned} \tag{3.34}$$

For the plate transverse shear part of the bilinear form, the integrand III has the form,

$$\begin{aligned}
III &= \left(\frac{\partial u_3}{\partial x_1}\right)^2 + 2u_4\frac{\partial u_3}{\partial x_1} + u_4^2 + \left(\frac{\partial u_3}{\partial x_2}\right)^2 + 2u_5\frac{\partial u_3}{\partial x_2} + u_5^2,\\
&= |\nabla u_3|^2 + u_4^2 + u_5^2 + 2u_4\frac{\partial u_3}{\partial x_1} + 2u_5\frac{\partial u_3}{\partial x_2}.
\end{aligned} \tag{3.35}$$

Use will now be made of the fact that, for real $a, b \in \mathbb{R}$ and $\epsilon > 0$,

$$\left(\frac{a}{\sqrt{\epsilon}} + b\sqrt{\epsilon}\right)^2 \geq 0 \text{ and thus } -\left(\frac{a^2}{\epsilon} + b^2\epsilon\right) \leq 2ab.$$

Substitution of this into Equation (3.35) yields,

$$
\begin{aligned}
III &\geq |\nabla u_3|^2 + u_4^2 + u_5^2 - \epsilon u_4^2 - \frac{1}{\epsilon}\left(\frac{\partial u_3}{\partial x_1}\right)^2 - \epsilon u_5^2 - \frac{1}{\epsilon}\left(\frac{\partial u_3}{\partial x_2}\right)^2, \\
&= |\nabla u_3|^2 + u_4^2 + u_5^2 - \epsilon\left(u_4^2 + u_5^2\right) - \frac{1}{\epsilon}|\nabla u_3|^2, \\
&= \left(1 - \frac{1}{\epsilon}\right)|\nabla u_3|^2 + (1-\epsilon)(u_4^2 + u_5^2).
\end{aligned}
$$

Thus,

$$
\begin{aligned}
\int_\Omega III \, d\mathbf{x} &\geq \int_\Omega \left(1 - \frac{1}{\epsilon}\right)|\nabla u_3|^2 - (\epsilon - 1)(u_4^2 + u_5^2)\, d\mathbf{x}, \\
&= \left(1 - \frac{1}{\epsilon}\right)||\nabla u_3||^2_{L_2(\Omega)} - (\epsilon - 1)\left(||u_4||^2_{L_2(\Omega)} + ||u_5||^2_{L_2(\Omega)}\right).
\end{aligned}
$$

Using Friedrich's inequality, which is given by Oden and Reddy in [39] as,

$$
||v||_{L_2(\Omega)} \leq C_F ||\nabla v||_{L_2(\Omega)} \quad \text{for } v \in \mathring{H}^1(\Omega),
$$

where C_F is a constant yields,

$$
a_s(\mathbf{u},\mathbf{u}) \geq \left(1 - \frac{1}{\epsilon}\right)||\nabla u_3||^2_{L_2(\Omega)} - (\epsilon - 1)C_F^2\left(||\nabla u_4||^2_{L_2(\Omega)} + ||\nabla u_5||^2_{L_2(\Omega)}\right). \tag{3.36}
$$

Combining Equations (3.34) and (3.36) enables the bilinear form $a(\mathbf{u},\mathbf{u})$ to be bounded below as,

$$
\begin{aligned}
a(\mathbf{u},\mathbf{u}) \geq{}& \frac{\lambda_{\min}\left(\mathbf{C}^b\right)}{2}\left(||\nabla u_1||^2_{L_2(\Omega)} + ||\nabla u_2||^2_{L_2(\Omega)} + ||\nabla u_4||^2_{L_2(\Omega)} + ||\nabla u_5||^2_{L_2(\Omega)}\right) \\
&+\lambda_{\min}\left(\mathbf{C}^s\right)\left(\left(1 - \frac{1}{\epsilon}\right)||\nabla u_3||^2_{L_2(\Omega)} - (\epsilon-1)C_F^2\left(||\nabla u_4||^2_{L_2(\Omega)} + ||\nabla u_5||^2_{L_2(\Omega)}\right)\right), \\
={}& \frac{\lambda_{\min}\left(\mathbf{C}^b\right)}{2}\left(||\nabla u_1||^2_{L_2(\Omega)} + ||\nabla u_2||^2_{L_2(\Omega)}\right) + \left(1 - \frac{1}{\epsilon}\right)\lambda_{\min}\left(\mathbf{C}^s\right)||\nabla u_3||^2_{L_2(\Omega)} \\
&+\left(\frac{\lambda_{\min}\left(\mathbf{C}^b\right)}{2} - C_F^2(\epsilon-1)\lambda_{\min}\left(\mathbf{C}^s\right)\right)\left(||\nabla u_4||^2_{L_2(\Omega)} + ||\nabla u_5||^2_{L_2(\Omega)}\right), \\
\geq{}& C\left(||\nabla u_1||^2_{L_2(\Omega)} + ||\nabla u_2||^2_{L_2(\Omega)} + ||\nabla u_3||^2_{L_2(\Omega)} + ||\nabla u_4||^2_{L_2(\Omega)} + ||\nabla u_5||^2_{L_2(\Omega)}\right),
\end{aligned}
$$

where C is a constant such that,

$$
C = \min\left\{\frac{\lambda_{\min}\left(\mathbf{C}^b\right)}{2}, \left(1 - \frac{1}{\epsilon}\right)\lambda_{\min}\left(\mathbf{C}^s\right), \frac{\lambda_{\min}\left(\mathbf{C}^b\right)}{2} - C_F^2(\epsilon-1)\lambda_{\min}\left(\mathbf{C}^s\right)\right\},
$$

and where ϵ is such that,

$$
1 < \epsilon < 1 + \frac{\lambda_{\min}\left(\mathbf{C}^b\right)}{2C_F^2\lambda_{\min}\left(\mathbf{C}^s\right)}.
$$

It follows that,

$$
a(\mathbf{u},\mathbf{u}) \equiv ||\mathbf{u}||_E \geq C||\nabla\mathbf{u}||^2_{L_2} \quad \forall \mathbf{u} \in \left[\mathring{H}^1\right]^5,
$$

showing the plate bilinear form $a(\mathbf{u},\mathbf{u})$ to be coercive for use in Chapter 4.

3.4 The Finite Element Method

Having derived the weak formulations for the problems in the context of both linear elasticity and plate theory it is now time to discuss the application of the finite element method. From the previous section the weak formulations yield the task of finding $\mathbf{v} \in V$ such that,

$$a(\mathbf{u}, \mathbf{v}) = F(\mathbf{v}) \quad \forall\ \mathbf{v} \in V. \tag{3.37}$$

The application of the finite element method to a given problem results in an approximation $\mathbf{u}_h$ to the exact solution $\mathbf{u}$ of the problem posed. This finite element solution arises from the discretisation of the problem domain Ω. Such a discretisation is obtained by partitioning Ω into non-overlapping regions or elements, the size of which is indicated by a mesh parameter h. In order to solve the above weak formulation numerically, a finite dimensional subspace S^h is chosen. This subspace is such that $S^h \subset V$ and the corresponding problem formulation which approximates that of Equation (3.37) requires one to find $\mathbf{u}_h \in S^h$ such that,

$$a(\mathbf{u}_h, \mathbf{v}_h) = F(\mathbf{v}_h) \quad \forall\ \mathbf{v}_h \in S^h. \tag{3.38}$$

The condition $S^h \subset V$ is the conforming condition and is fundamental to finite element analysis since it ensures continuity and satisfaction of the boundary conditions. The finite element test $(\mathbf{v}_h)$ and trial $(\mathbf{u}_h)$ functions will invariably be piecewise polynomial functions over the partition of Ω and the global continuity over $\overline{\Omega} \equiv \Omega \cup \partial\Omega$ of these functions is important. The problem formulation of Equation (3.38) is a Galerkin problem and it is via this route that the following finite element description will proceed.

For this section a scalar valued solution will be used so that the finite element method can be described in a clear way with minimal complexity. Once this has been done the details can be refined to encompass vector valued solutions such as those of elasticity and plate theory. In order to obtain u_h the elements in the partitioned region Ω each contain n nodes. However, some of these nodes may coincide and so the concept of multiple nodes is allowed. Suppose that there are $\mathcal{N}$ nodes, $z_1, z_2, \ldots, z_{\mathcal{N}}$ in $\overline{\Omega}$ where, for boundary nodes, those associated with essential boundary conditions are not included in the set $\{z_i\}_{i=1}^{\mathcal{N}}$.

Consider the *interpolant* $\pi u_h(\mathbf{x})$, $\mathbf{x} \in \overline{\Omega}$, which for any element takes on values of u, and some or all of the derivatives of u, of order $\leq m$, at the n nodes of the element. The interpolant may thus be expressed in each element Ω_k as,

$$\pi u_h(\mathbf{x})|_{\Omega_k} = \sum_{i=1}^{n} (M_i u)\, \phi_i(\mathbf{x}), \tag{3.39}$$

where the $(M_i u)$ are function or derivative point evaluations of u at the nodal positions in the element, and the $\phi_i(\mathbf{x})$ are the *cardinal basis functions* of the Lagrange or Hermite interpolation. The selection of nodes and point evaluations are chosen so that the interpolant is unique. The finite element solution $u_h(\mathbf{x})$ which approximates u may be expressed in each element Ω_k as,

$$u_h(\mathbf{x})|_{\Omega_k} = \sum_{i=1}^{n} (M_i u_h)\, \phi_i(\mathbf{x}), \tag{3.40}$$

where the $(M_i u_h)$ are the point evaluations of u_h corresponding to those of u in Equation (3.39). The cardinal basis functions are *local* to each element, but, taken over the totality of elements in the region $\Omega \cup \partial\Omega_N$ they together determine a linearly independent set of functions $\{\Phi_i(\mathbf{x})\}_{i=1}^{\mathcal{N}}$. These $\Phi_i(\mathbf{x})$ functions, which are chosen such that global test and trial functions will both be in S^h, are the *finite element basis functions* at the $\mathcal{N}$ nodes in the region $\Omega \cup \partial\Omega_N$. This region is the interior Ω, plus the boundary part $\partial\Omega_N$ where there is a natural boundary condition. For the boundary part $\partial\Omega_D$ where there is an essential boundary condition and $\partial\Omega \equiv \partial\Omega_N \cup \partial\Omega_D$, there is a further set $\{\Phi_i(\mathbf{x})\}_{i=\mathcal{N}+1}^{\mathcal{M}}$ of basis functions. Thus each $\Phi_i(\mathbf{x})$, $i = 1, 2, \ldots, \mathcal{N}, \mathcal{N}+1, \ldots, \mathcal{M}$ is associated with a single node z_i and is non-zero only in elements which have z_i as a node. Further,

$$(M_j \Phi_i) = \delta_{ij}, \quad \text{for } i = 1, 2, \ldots, \mathcal{M}, \tag{3.41}$$

with δ_{ij} the Kronecker delta. All the functions $\Phi_i(\mathbf{x})$ at nodes interior to Ω are thus zero at nodes of $\partial\Omega$, whilst those at nodes of $\partial\Omega$ are zero at nodes of Ω.

Consider the differential problem which has the scalar form of Equation (3.37) as the weak formulation. Assume that there are Dirichlet boundary conditions and so the approximating problem is of the form $a(u_h, v_h) = F(v_h)$. Using the above notation, the finite element solution may be expressed as,

$$u_h(\mathbf{x}) = \sum_{i=1}^{\mathcal{N}} (M_i u_h)\, \Phi_i(\mathbf{x}) + \sum_{i=\mathcal{N}+1}^{\mathcal{M}} (M_i u_h)\, \Phi_i(\mathbf{x}).$$

The Galerkin problem is set up as,

$$a\left(\sum_{i=1}^{\mathcal{N}} (M_i u_h)\, \Phi_i(\mathbf{x}) + \sum_{i=\mathcal{N}+1}^{\mathcal{M}} (M_i u_h)\, \Phi_i(\mathbf{x}), \Phi_j(\mathbf{x}) \right) = F\left(\Phi_j(\mathbf{x})\right),$$

for $j = 1, 2, \ldots, \mathcal{N}$. Since the $(M_i u_h)$ are known for nodes on $\partial\Omega_D$, the problem may be rewritten as,

$$\sum_{i=1}^{\mathcal{N}} (M_i u_h)\, a\left(\Phi_i(\mathbf{x}), \Phi_j(\mathbf{x})\right) = F\left(\Phi_j(\mathbf{x})\right) - \sum_{i=\mathcal{N}+1}^{\mathcal{M}} (M_i u_h)\, a\left(\Phi_i(\mathbf{x}), \Phi_j(\mathbf{x})\right)$$

for $j = 1, 2, \ldots, \mathcal{N}$. This set of $\mathcal{N}$ equations is a linear system and may be written in the form,

$$\mathbf{K}_g \mathbf{u}_h = \mathbf{F}, \tag{3.42}$$

where the $\mathcal{N} \times \mathcal{N}$ matrix $\mathbf{K}_g$ is the *global stiffness matrix*, defined as,

$$\mathbf{K}_g = \begin{bmatrix} a\left(\Phi_1(\mathbf{x}), \Phi_1(\mathbf{x})\right) & a\left(\Phi_2(\mathbf{x}), \Phi_1(\mathbf{x})\right) & \ldots & a\left(\Phi_{\mathcal{N}}(\mathbf{x}), \Phi_1(\mathbf{x})\right) \\ a\left(\Phi_1(\mathbf{x}), \Phi_2(\mathbf{x})\right) & a\left(\Phi_2(\mathbf{x}), \Phi_2(\mathbf{x})\right) & \ldots & a\left(\Phi_{\mathcal{N}}(\mathbf{x}), \Phi_2(\mathbf{x})\right) \\ \vdots & \vdots & \ddots & \vdots \\ a\left(\Phi_1(\mathbf{x}), \Phi_{\mathcal{N}}(\mathbf{x})\right) & a\left(\Phi_2(\mathbf{x}), \Phi_{\mathcal{N}}(\mathbf{x})\right) & \ldots & a\left(\Phi_{\mathcal{N}}(\mathbf{x}), \Phi_{\mathcal{N}}(\mathbf{x})\right) \end{bmatrix}.$$

The vector $\mathbf{u}_h \equiv \{(M_i u_h)\}$ is found by solving Equation (3.42), and substitution of this into Equation (3.40) gives the required finite element approximation $u_h(\mathbf{x})$. Having illustrated the finite element fundamentals for a scalar partial differential equation we now proceed to problems of linear elasticity and plate theory.

3.5 Finite Element Elasticity Model

As described in the previous section the problem domain is firstly discretised into elements. As this is now a problem of linear elasticity, the weak formulation takes on the form of Equation (3.37) where the bilinear form and linear functional are as described by the Equations (3.25) and (3.21) respectively. To recap, these are given as,

$$a(\mathbf{u},\mathbf{v}) \equiv \int_\Omega (\mathbf{B}\mathbf{u})^T \mathbf{C}\,(\mathbf{B}\mathbf{v})\,d\mathbf{x} \quad \text{and} \quad F(\mathbf{v}) \equiv \int_\Omega \mathbf{f}\cdot\mathbf{v}\,d\mathbf{x} + \int_{\partial\Omega} \mathbf{g}\cdot\mathbf{v}\,ds.$$

To aid notation, let the two displacement degrees of freedom per node be u and v respectively. In the finite element model the two displacement degrees of freedom will be approximated over each element Ω_k consisting of n nodes as,

$$u(x_1,x_2) \approx u_h(\mathbf{x}) := \sum_{j=1}^{n} u_j^h \phi_j(\mathbf{x}) \quad \text{and} \quad v(x_1,x_2) \approx v_h(\mathbf{x}) := \sum_{j=1}^{n} v_j^h \phi_j(\mathbf{x}), \tag{3.43}$$

where u_j^h and v_j^h denote the finite element solution of u and v respectively at node j and ϕ_j are the element shape functions of Lagrange type. It is thus possible to express the finite element solution vector $\mathbf{u}_k^h$ at any point $\mathbf{x}$ in the element Ω_k as,

$$\mathbf{u}_k^h(\mathbf{x}) = \begin{bmatrix} u_k^h(\mathbf{x}) \\ v_k^h(\mathbf{x}) \end{bmatrix} = \mathbf{L}_k \mathbf{u}_k^h$$

where $\mathbf{L}_k$ is the array of element shape functions evaluated at point $\mathbf{x}$ and defined as,

$$\mathbf{L}_k = \begin{bmatrix} \phi_1(\mathbf{x}) & 0 & \phi_2(\mathbf{x}) & 0 & \ldots\ \phi_n(\mathbf{x}) & 0 \\ 0 & \phi_1(\mathbf{x}) & 0 & \phi_2(\mathbf{x})\ \ldots & 0 & \phi_n(\mathbf{x}) \end{bmatrix},$$

and $\mathbf{u}_k^h$ is the vector of nodal displacements for the element, defined as,

$$\mathbf{u}_k^h = \left[u_1^h, v_1^h, u_2^h, v_2^h, \ldots, u_n^h, v_n^h\right]^T.$$

Thus the finite element approximation to the strain defined in Equation (3.24) can be expressed at a point $\mathbf{x}$ on the element as,

$$\varepsilon(\mathbf{x}) \approx \varepsilon(\mathbf{u}_k^h(\mathbf{x})) = \varepsilon_h = \mathbf{B}\mathbf{L}_k\mathbf{u}_k^h.$$

As described in the previous section, the element shape functions are local to each element Ω_k but, taken over the totality of elements in the region $\Omega \cup \partial\Omega_N$ they together determine a linearly independent set of functions $\{\Phi_i(\mathbf{x})\}_{i=1}^{\mathcal{N}}$ with a further set $\{\Phi_i(\mathbf{x})\}_{i=\mathcal{N}+1}^{\mathcal{M}}$ of basis functions arising from the part of the boundary Ω_D where there are essential boundary conditions. In this way we may consider the finite element solution at any point $\mathbf{x}$ in the Ω as,

$$\mathbf{u}_h(\mathbf{x}) = \begin{bmatrix} u_h(\mathbf{x}) \\ v_h(\mathbf{x}) \end{bmatrix} = \mathbf{L}_g \mathbf{u}_h + \mathbf{L}_g^D \mathbf{u}_h^D,$$

where $\mathbf{L}_g$ is defined as,

$$\mathbf{L}_g = \begin{bmatrix} \Phi_1(\mathbf{x}) & 0 & \Phi_2(\mathbf{x}) & 0 & \ldots & \Phi_{\mathcal{N}}(\mathbf{x}) & 0 \\ 0 & \Phi_1(\mathbf{x}) & 0 & \Phi_2(\mathbf{x}) & \ldots & 0 & \Phi_{\mathcal{N}}(\mathbf{x}) \end{bmatrix},$$

$\mathbf{L}_g^D$ is defined as,

$$\mathbf{L}_g^D = \begin{bmatrix} \Phi_{\mathcal{N}+1}(\mathbf{x}) & 0 & \Phi_{\mathcal{N}+2}(\mathbf{x}) & 0 & \ldots & \Phi_{\mathcal{M}}(\mathbf{x}) & 0 \\ 0 & \Phi_{\mathcal{N}+1}(\mathbf{x}) & 0 & \Phi_{\mathcal{N}+2}(\mathbf{x}) & \ldots & 0 & \Phi_{\mathcal{M}}(\mathbf{x}) \end{bmatrix},$$

$\mathbf{u}_h$ is the vector of nodal displacements,

$$\mathbf{u}_h = \left[u_1^h, v_1^h, u_2^h, v_2^h, \ldots, u_{\mathcal{N}}^h, v_{\mathcal{N}}^h\right]^T.$$

and $\mathbf{u}_h^D$ is the vector of known nodal displacements on $\partial\Omega_D$ defined as,

$$\mathbf{u}_h^D = \left[u_{\mathcal{N}+1}^h, v_{\mathcal{N}+1}^h, u_{\mathcal{N}+2}^h, v_{\mathcal{N}+2}^h, \ldots, u_{\mathcal{M}}^h, v_{\mathcal{M}}^h\right]^T.$$

As in the previous section, the Galerkin problem is set up as,

$$a(\mathbf{u}_h, \mathbf{\Phi}_j) = F(\mathbf{\Phi}_j) \quad \text{for } j = 1, \ldots, 2\mathcal{N}$$

where $\mathbf{\Phi}_j$ is the jth column of $\mathbf{L}_g$. Since the components of $\mathbf{u}_h^D$ are known, the problem may be rewritten as,

$$a\left(\mathbf{L}_g \mathbf{u}_h, \mathbf{\Phi}_j\right) = F(\mathbf{\Phi}_j) - a\left(\mathbf{L}_g^D \mathbf{u}_h^D, \mathbf{\Phi}_j\right) \quad \text{for } j = 1, \ldots, 2\mathcal{N}.$$

It is from the left-hand side of this expression that the global stiffness matrix $\mathbf{K}_g$ is obtained which has the form,

$$\mathbf{K}_g = (K_{ij})_{ij=1}^{2\mathcal{N}} \quad \text{where } K_{ij} = a\left(\mathbf{\Phi}_{\boldsymbol{i}}, \mathbf{\Phi}_{\boldsymbol{j}}\right) \text{ for } i, j = 1, \ldots, 2\mathcal{N},$$

and where,

$$\left.\begin{aligned} \mathbf{\Phi}_{2m-1} &= [\Phi_m, 0]^T \\ \mathbf{\Phi}_{2m} &= [0, \Phi_m]^T \end{aligned}\right\} \quad \text{for } m = 1, \ldots, \mathcal{N}.$$

By solving the resulting system of equations as in Equation (3.42) the required nodal displacements $\mathbf{u}_h$ are obtained.

In practice the global stiffness matrix is assembled from the element stiffness matrices $\mathbf{K}_k$. The stiffness matrix for a typical element Ω_k is defined as follows,

$$\mathbf{K}_k = (K_{ij})_{i,j=1}^{2n},$$

where each K_{ij} is defined as,

$$K_{ij} = a(\boldsymbol{\phi}_i, \boldsymbol{\phi}_j)|_{\Omega_k} = \int_{\Omega_k} (\mathbf{B}\boldsymbol{\phi}_i)^T \, \mathbf{C} \, (\mathbf{B}\boldsymbol{\phi}_j) \; d\mathbf{x},$$

for $i, j = 1, \ldots, 2n$ and where the vectors $\boldsymbol{\phi}_i$ for $i = 1, \ldots, 2n$ are defined as,

$$\left.\begin{aligned} \boldsymbol{\phi}_{2m-1} &= [\phi_m, 0]^T \\ \boldsymbol{\phi}_{2m} &= [0, \phi_m]^T \end{aligned}\right\} \quad \text{for } m = 1, \ldots, n.$$

The element stiffness matrix may be further inspected to reveal that it has the structure,

$$\mathbf{K}_k = \begin{bmatrix} \mathbf{K}_{11} & \mathbf{K}_{12} & \ldots & \mathbf{K}_{1n} \\ \mathbf{K}_{21} & \mathbf{K}_{22} & \ldots & \mathbf{K}_{2n} \\ \vdots & \vdots & \ddots & \vdots \\ \mathbf{K}_{n1} & \mathbf{K}_{n2} & \ldots & \mathbf{K}_{nn} \end{bmatrix},$$

where each $\mathbf{K}_{ij}, i, j = 1, \ldots, n$ is a 2×2 sub-matrix of the form,

$$\mathbf{K}_{ij} = \int_{\Omega_k} (\mathbf{B}\mathbf{I}_2\phi_i)^T \, \mathbf{C} \, (\mathbf{B}\mathbf{I}_2\phi_j) \; d\mathbf{x},$$

where the matrix $\mathbf{B}$ is as previously defined in Equation (3.24), $\phi_i, i = 1, \ldots, n$ are the element shape functions and $\mathbf{I}_2$ is the 2×2 identity matrix. Thus, over the whole element, we may write,

$$\mathbf{K}_k = \int_{\Omega_k} (\mathbf{B}\boldsymbol{\phi}_k)^T \, \mathbf{C} \, (\mathbf{B}\boldsymbol{\phi}_k) \; d\mathbf{x},$$

where now, for an element with nodes $1, 2, \ldots, n$,

$$\boldsymbol{\phi}_k = [\mathbf{I}_2\phi_1, \mathbf{I}_2\phi_2, \ldots, \mathbf{I}_2\phi_n] \, .$$

3.6 Finite Element Plate Model

The finite element formulation, corresponding to the continuous case defined in Section (3.3) seeks a solution $\mathbf{u}_h \in V^h \subset V$ such that,

$$a(\mathbf{u}_h, \mathbf{v}_h) = F(\mathbf{v}_h) \quad \forall \; \mathbf{v}_h \in V^h, \tag{3.44}$$

as previously discussed. Since the force and moment resultants contain, at most, only the first derivatives of the dependent variables u, v, w, ψ_1 and ψ_2, all may be approximated using Lagrange interpolation functions. This means that the plate bending element of the first-order plate theory is a C^0 element and thus each of the displacements u, v, w, ψ_1 and ψ_2 are approximated over each element as,

$$u(x_1, x_2) \approx u_h(\mathbf{x}) := \sum_{j=1}^{n} u_j^h \phi_j(\mathbf{x}), \quad v(x_1, x_2) \approx v_h(\mathbf{x}) := \sum_{j=1}^{n} v_j^h \phi_j(\mathbf{x}),$$

$$w(x_1, x_2) \approx w_h(\mathbf{x}) := \sum_{j=1}^{n} w_j^h \phi_j(\mathbf{x}), \tag{3.45}$$

$$\psi_1(x_1, x_2) \approx \psi_{1,h}(\mathbf{x}) := \sum_{j=1}^{n} \psi_{1j}^h \phi_j(\mathbf{x}), \quad \psi_2(x_1, x_2) \approx \psi_{2,h}(\mathbf{x}) := \sum_{j=1}^{n} \psi_{2j}^h \phi_j(\mathbf{x}),$$

where n is the number of nodes per element, α_j^h denotes the finite element solution value of $\alpha = u, v, w, \psi_1$ or ψ_2 at node j and ϕ_j are the element shape functions of Lagrange type. The finite element model is then obtained by substituting expressions (3.45) for u, v, w, ψ_1 and ψ_2 and the components of the test function vector into Equation (3.44). Due to the fact that the degrees of freedom are interpolated using identical Lagrange basis functions the procedure in applying the Galerkin problem follows the same route as that of linear elasticity in Section (3.5) with the only difference being that there are now five degrees of freedom per node instead of two. Thus the element stiffness matrix for a typical element Ω_k may be expressed as,

$$\mathbf{K}_k = (K_{ij})_{i,j=1}^{5n},$$

where each K_{ij} is defined as,

$$K_{ij} = a(\boldsymbol{\phi}_i, \boldsymbol{\phi}_j)|_{\Omega_k} = \int_{\Omega_k} \left(\mathbf{B}^b \boldsymbol{\phi}_i\right)^T \mathbf{C}^b \left(\mathbf{B}^b \boldsymbol{\phi}_j\right) \, d\mathbf{x} + \int_{\Omega_k} \left(\mathbf{B}^s \boldsymbol{\phi}_i\right)^T \mathbf{C}^s \left(\mathbf{B}^s \boldsymbol{\phi}_j\right) \, d\mathbf{x},$$

for $i, j = 1, \ldots, 5n$ and where the vectors $\boldsymbol{\phi}_i$ for $i = 1, \ldots, 5n$ are defined as,

$$\left.\begin{aligned} \boldsymbol{\phi}_{5m-4} &= [\phi_m, 0, 0, 0, 0]^T \\ \boldsymbol{\phi}_{5m-3} &= [0, \phi_m, 0, 0, 0]^T \\ \boldsymbol{\phi}_{5m-2} &= [0, 0, \phi_m, 0, 0]^T \\ \boldsymbol{\phi}_{5m-1} &= [0, 0, 0, \phi_m, 0]^T \\ \boldsymbol{\phi}_{5m} &= [0, 0, 0, 0, \phi_m]^T \end{aligned}\right\} \quad \text{for } m = 1, \ldots, n.$$

The stiffness matrix may be written more clearly as,

$$\mathbf{K}_k = \mathbf{K}_k^b + \mathbf{K}_k^s,$$

where $\mathbf{K}_k^b$ and $\mathbf{K}_k^s$ are matrices arising from the bending and transverse shear terms within Equation (3.44) respectively. The matrices $\mathbf{K}_k^b$ and $\mathbf{K}_k^s$ may be further inspected to reveal the structure,

$$\mathbf{K}_k = \begin{bmatrix} \mathbf{K}_{11}^b & \mathbf{K}_{12}^b & \ldots & \mathbf{K}_{1n}^b \\ \mathbf{K}_{21}^b & \mathbf{K}_{22}^b & \ldots & \mathbf{K}_{2n}^b \\ \vdots & \vdots & \ddots & \vdots \\ \mathbf{K}_{n1}^b & \mathbf{K}_{n2}^b & \ldots & \mathbf{K}_{nn}^b \end{bmatrix} + \begin{bmatrix} \mathbf{K}_{11}^s & \mathbf{K}_{12}^s & \ldots & \mathbf{K}_{1n}^s \\ \mathbf{K}_{21}^s & \mathbf{K}_{22}^s & \ldots & \mathbf{K}_{2n}^s \\ \vdots & \vdots & \ddots & \vdots \\ \mathbf{K}_{n1}^s & \mathbf{K}_{n2}^s & \ldots & \mathbf{K}_{nn}^s \end{bmatrix},$$

where each $\mathbf{K}_{ij}^l, i, j = 1, \ldots, n$, $l = b$ or s, is a 5×5 sub-matrix of the form,

$$\mathbf{K}_{ij}^b = \int_{\Omega_k} \left(\mathbf{B}^b \mathbf{I}_5 \phi_i\right)^T \mathbf{C}^b \left(\mathbf{B}^b \mathbf{I}_5 \phi_j\right) \, d\mathbf{x},$$

and,

$$\mathbf{K}_{ij}^s = \int_{\Omega_k} \left(\mathbf{B}^s \mathbf{I}_5 \phi_i\right)^T \mathbf{C}^s \left(\mathbf{B}^s \mathbf{I}_5 \phi_j\right) \, d\mathbf{x},$$

where $\mathbf{B}^b$, $\mathbf{B}^s$, $\mathbf{C}^b$ and $\mathbf{C}^s$ are as previously defined, $\phi_i, i = 1, \ldots, n$ are the element shape functions and $\mathbf{I}_5$ is the 5×5 identity matrix. Thus, over the whole element, we may write,

$$\mathbf{K}_k = \int_{\Omega_k} \left(\mathbf{B}^b \boldsymbol{\phi}_k\right)^T \mathbf{C}^b \left(\mathbf{B}^b \boldsymbol{\phi}_k\right) \, d\mathbf{x} + \int_{\Omega_k} \left(\mathbf{B}^s \boldsymbol{\phi}_k\right)^T \mathbf{C}^s \left(\mathbf{B}^s \boldsymbol{\phi}_k\right) \, d\mathbf{x}, \tag{3.46}$$

where now, for an element with nodes $1, 2, \ldots, n$,

$$\boldsymbol{\phi}_k = \left[\mathbf{I}_5 \phi_1, \mathbf{I}_5 \phi_2, \ldots, \mathbf{I}_5 \phi_n\right].$$

The element stiffness matrix may alternatively be represented in a more detailed form and in a similar way to that given in [37] as,

$$\sum_{\beta=1}^{5} \sum_{j=1}^{n} K_{ij}^{\alpha\beta} \Delta_j^\beta - F_j^\alpha = 0, \quad \alpha = 1, 2, \ldots, 5, \quad i = 1, 2, \ldots, n\,, \tag{3.47}$$

where Δ_j^β for $\beta = 1, 2, 3, 4, 5$ denotes the nodal degrees of freedom at node j. This results in an element stiffness matrix $\mathbf{K}_k$ of the form,

$$\mathbf{K}_k = \begin{bmatrix} \mathbf{K}_{11} & \mathbf{K}_{12} & \ldots & \mathbf{K}_{1n} \\ \mathbf{K}_{21} & \mathbf{K}_{22} & \ldots & \mathbf{K}_{2n} \\ \vdots & \vdots & \ddots & \vdots \\ \mathbf{K}_{n1} & \mathbf{K}_{n2} & \ldots & \mathbf{K}_{nn} \end{bmatrix},$$

where each $\mathbf{K}_{ij}$ for $i, j = 1, \ldots, n$ is a 5×5 sub-matrix of the form,

$$\mathbf{K}_{ij} = \begin{bmatrix} K_{ij}^{11} & K_{ij}^{12} & \ldots & K_{ij}^{15} \\ K_{ij}^{21} & K_{ij}^{22} & \ldots & K_{ij}^{25} \\ \vdots & \vdots & \ddots & \vdots \\ K_{ij}^{51} & K_{ij}^{52} & \ldots & K_{ij}^{55} \end{bmatrix}.$$

Within each sub-matrix the elements $K_{ij}^{\alpha\beta}$ are given for $\alpha = 1, 2, 3, 4$ and 5 as,

$$K_{ij}^{1\beta} = \int_{\Omega_k} \left(\frac{\partial \phi_i}{\partial x_1} N_{1j}^\beta + \frac{\partial \phi_i}{\partial x_2} N_{4j}^\beta \right) d\mathbf{x},$$

$$K_{ij}^{2\beta} = \int_{\Omega_k} \left(\frac{\partial \phi_i}{\partial x_1} N_{4j}^\beta + \frac{\partial \phi_i}{\partial x_2} N_{2j}^\beta \right) d\mathbf{x},$$

$$K_{ij}^{3\beta} = \int_{\Omega_k} \left(\frac{\partial \phi_i}{\partial x_1} Q_{5j}^\beta + \frac{\partial \phi_i}{\partial x_2} Q_{6j}^\beta \right) d\mathbf{x},$$

$$K_{ij}^{4\beta} = \int_{\Omega_k} \left(\frac{\partial \phi_i}{\partial x_1} M_{1j}^\beta + \frac{\partial \phi_i}{\partial x_2} M_{4j}^\beta + \phi_i Q_{1j}^\beta \right) d\mathbf{x},$$

$$K_{ij}^{5\beta} = \int_{\Omega_k} \left(\frac{\partial \phi_i}{\partial x_1} M_{4j}^\beta + \frac{\partial \phi_i}{\partial x_2} M_{2j}^\beta + \phi_i Q_{2j}^\beta \right) d\mathbf{x}.$$

The coefficients N^{β}_{Ij}, M^{β}_{Ij}, and Q^{β}_{Ij} in the above for $\beta = 1,2,3,4,5$ and $I = 1,2,4$ are thus,

$$\begin{aligned}
N^1_{1j} &= A_{11}\frac{\partial\phi_j}{\partial x_1} + A_{14}\frac{\partial\phi_j}{\partial x_2}, \quad N^2_{1j} = A_{12}\frac{\partial\phi_j}{\partial x_2} + A_{14}\frac{\partial\phi_j}{\partial x_1},\\
N^4_{1j} &= B_{11}\frac{\partial\phi_j}{\partial x_1} + B_{14}\frac{\partial\phi_j}{\partial x_2}, \quad N^5_{1j} = B_{12}\frac{\partial\phi_j}{\partial x_2} + B_{14}\frac{\partial\phi_j}{\partial x_1},\\
N^1_{2j} &= A_{12}\frac{\partial\phi_j}{\partial x_1} + A_{24}\frac{\partial\phi_j}{\partial x_2}, \quad N^2_{2j} = A_{22}\frac{\partial\phi_j}{\partial x_2} + A_{24}\frac{\partial\phi_j}{\partial x_1},\\
N^4_{2j} &= B_{12}\frac{\partial\phi_j}{\partial x_1} + B_{24}\frac{\partial\phi_j}{\partial x_2}, \quad N^5_{2j} = B_{22}\frac{\partial\phi_j}{\partial x_2} + B_{24}\frac{\partial\phi_j}{\partial x_1},\\
N^1_{4j} &= A_{14}\frac{\partial\phi_j}{\partial x_1} + A_{44}\frac{\partial\phi_j}{\partial x_2}, \quad N^2_{4j} = A_{24}\frac{\partial\phi_j}{\partial x_2} + A_{44}\frac{\partial\phi_j}{\partial x_1},\\
N^4_{4j} &= B_{14}\frac{\partial\phi_j}{\partial x_1} + B_{44}\frac{\partial\phi_j}{\partial x_2}, \quad N^5_{4j} = B_{24}\frac{\partial\phi_j}{\partial x_2} + B_{44}\frac{\partial\phi_j}{\partial x_1},\\
&N^3_{1j} = 0, \quad N^3_{2j} = 0, \quad N^3_{4j} = 0,\\
M^1_{1j} &= B_{11}\frac{\partial\phi_j}{\partial x_1} + B_{14}\frac{\partial\phi_j}{\partial x_2}, \quad M^2_{1j} = B_{12}\frac{\partial\phi_j}{\partial x_2} + B_{14}\frac{\partial\phi_j}{\partial x_1},\\
M^4_{1j} &= D_{11}\frac{\partial\phi_j}{\partial x_1} + D_{14}\frac{\partial\phi_j}{\partial x_2}, \quad M^5_{1j} = D_{12}\frac{\partial\phi_j}{\partial x_2} + D_{14}\frac{\partial\phi_j}{\partial x_1},\\
M^1_{2j} &= B_{12}\frac{\partial\phi_j}{\partial x_1} + B_{24}\frac{\partial\phi_j}{\partial x_2}, \quad M^2_{2j} = B_{22}\frac{\partial\phi_j}{\partial x_2} + B_{24}\frac{\partial\phi_j}{\partial x_1},\\
M^4_{2j} &= D_{12}\frac{\partial\phi_j}{\partial x_1} + D_{24}\frac{\partial\phi_j}{\partial x_2}, \quad M^5_{2j} = D_{22}\frac{\partial\phi_j}{\partial x_2} + D_{24}\frac{\partial\phi_j}{\partial x_1},\\
M^1_{4j} &= B_{14}\frac{\partial\phi_j}{\partial x_1} + B_{44}\frac{\partial\phi_j}{\partial x_2}, \quad M^2_{4j} = B_{24}\frac{\partial\phi_j}{\partial x_2} + B_{44}\frac{\partial\phi_j}{\partial x_1},\\
M^4_{4j} &= D_{14}\frac{\partial\phi_j}{\partial x_1} + D_{44}\frac{\partial\phi_j}{\partial x_2}, \quad M^5_{4j} = D_{24}\frac{\partial\phi_j}{\partial x_2} + D_{44}\frac{\partial\phi_j}{\partial x_1},\\
&M^3_{1j} = 0, \quad M^3_{2j} = 0, \quad M^3_{4j} = 0,\\
Q^3_{1j} &= A_{55}\frac{\partial\phi_j}{\partial x_1} + A_{45}\frac{\partial\phi_j}{\partial x_2}, \quad Q^4_{1j} = A_{55}\phi_j, \quad Q^5_{1j} = A_{45}\phi_j,\\
Q^3_{2j} &= A_{45}\frac{\partial\phi_j}{\partial x_1} + A_{44}\frac{\partial\phi_j}{\partial x_2}, \quad Q^4_{2j} = A_{45}\phi_j, \quad Q^5_{2j} = A_{44}\phi_j,\\
&Q^1_{1j} = 0, \quad Q^2_{1j} = 0, \quad Q^1_{2j} = 0, \quad Q^2_{2j} = 0.
\end{aligned}$$

For the element load vector, in addition to the integral of the transverse load over the element domain, there exist terms where the boundary of the element $\partial\Omega_k$ coincides with a part of the boundary of the domain where essential boundary conditions have not been specified. Thus the terms take on the form,

$$\begin{aligned}
F^1_i &= \int_{\partial\Omega_k \cap \hat{\Gamma}_1} N_n \phi_i \, ds, \quad F^2_i = \int_{\partial\Omega_k \cap \hat{\Gamma}_2} N_s \phi_i \, ds,\\
F^3_i &= \int_{\Omega_k} q\phi_i \, d\mathbf{x} + \int_{\partial\Omega_k \cap \hat{\Gamma}_3} Q_n \phi_i \, ds,\\
F^4_i &= \int_{\partial\Omega_k \cap \hat{\Gamma}_4} M_n \phi_i \, ds, \quad F^5_i = \int_{\partial\Omega_k \cap \hat{\Gamma}_5} M_s \phi_i \, ds.
\end{aligned}$$

3.7 Numerical and Reduced Integration

It has been shown in the illustration of the finite element models that integrations will be required over the element domains. Such integrations will be performed numerically and the aim of this section is to detail how this will be done. Special consideration will be given here to the plate problem as it will be shown that there is a need for *reduced integration* on certain terms in the element stiffness matrix. This numerical tool enables solutions to be found for plates whose thickness is considered thin by fighting their desire to lock. This *locking effect* is undesirable as it results in the underprediction of displacements in the finite element solution with the plate appearing stiffer than the material properties would suggest.

We shall begin by introducing the idea of numerical integration in one dimension. A general integral of a function $f(x)$ may be mapped or transformed onto a standard region in the following way,

$$\int_a^b f(x)\,dx = \int_{-1}^{1} \hat{f}(\xi)\,d\xi,$$

where,

$$\hat{f}(\xi) = f(x(\xi))\,J(\xi),$$

and where $J(\xi)$ is known as the Jacobian of the transformation. In setting up this transformation it is required that $\xi = -1$ when $x = a$ and $\xi = 1$ when $x = b$. It is thus possible to write ξ in terms of x as,

$$\xi = \xi(x) = \frac{(x-a)-(b-x)}{b-a} = \frac{2x-(a+b)}{b-a}. \qquad (3.48)$$

Therefore,

$$d\xi = \frac{2}{b-a}dx \Rightarrow dx = \frac{b-a}{2}d\xi = J(\xi)d\xi,$$

and from Equation (3.48) we have that,

$$x = x(\xi) = \frac{1}{2}\left[(b-a)\xi + (a+b)\right].$$

It should be noted that $J(\xi)$ is simply the ratio of the two lengths defined by the two integral bounds. Once a general integral has been transformed onto a standard region, the integral may then be evaluated using a Gauss-Legendre quadrature formula. Thus,

$$\int_a^b f(x)\,dx = \int_{-1}^{1} \hat{f}(\xi)\,d\xi \approx \sum_{i=1}^{k} w_i \hat{f}(\xi_i),$$

where w_i are known as the Gauss weights and ξ_i are known as the base points which are themselves roots of the Legendre polynomial $P_k(\xi)$. In this way a polynomial $f(x)$ of degree p may be integrated exactly by employing $n = (p+1)/2$ Gauss points. When $p+1$ is odd, one should pick the nearest larger integer.

In two dimensions the region of integration in global coordinates must be transformed onto a standard two-dimensional region in local coordinates. Such integrations have been met in the finite element methods earlier in this chapter and thus we may consider, for example, an integral over a typical element Ω_k of the domain of interest. Such elements may be triangular or quadrilateral in this work as depicted in Figure (3.1). The standard local regions are called standard elements and will be denoted as $\hat{\Omega}$. In considering the transformation from the global to local coordinates it is important to consider how we would like the transformation to be performed. Since we will

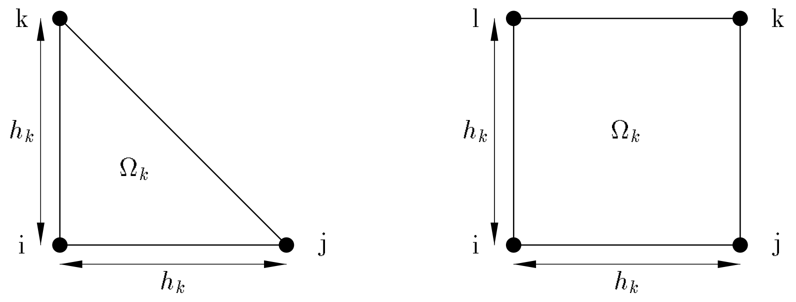

Figure 3.1: General triangular and rectangular elements.

be using linear elements in this work, it is natural to have straight lines in global coordinates transformed onto straight lines in local coordinates. As in the one-dimensional case we would like to be able to express the global coordinates x and y each in terms of the local coordinates ξ and η. By using what is called an isoparametric approximation this is ensured and we are able to write,

$$x = x(\xi,\eta) = \sum_{i=1}^{n} x_i \phi_i(\xi,\eta), \quad \text{and} \quad y = y(\xi,\eta) = \sum_{i=1}^{n} y_i \phi_i(\xi,\eta), \tag{3.49}$$

where the $\phi_i(\xi,\eta), i = 1,\ldots,n$ are the element shape functions in local coordinates (ξ,η). Thus, for the standard triangular element $\hat{\Omega}_T$ with horizontal and vertical edges of unit length corresponding to the general triangular element Ω_k in Figure (3.1) we have that,

$$\phi_i(\xi,\eta) = 1 - \xi - \eta, \quad \phi_j(\xi,\eta) = \xi, \quad \text{and} \quad \phi_k(\xi,\eta) = \eta.$$

Alternatively, for the standard quadrilateral element $\hat{\Omega}_Q$ with side lengths two and centred on the origin we have that,

$$\begin{aligned} \phi_i(\xi,\eta) &= \frac{1}{4}(1-\xi)(1-\eta), \quad \phi_j(\xi,\eta) = \frac{1}{4}(1+\xi)(1-\eta), \\ \phi_k(\xi,\eta) &= \frac{1}{4}(1+\xi)(1+\eta), \quad \phi_l(\xi,\eta) = \frac{1}{4}(1-\xi)(1+\eta), \end{aligned} \tag{3.50}$$

where, for both standard elements the node numbering is as shown for the general cases in Figure (3.1). Thus as an illustration, consider the line $\xi = 1$ in the standard element $\hat{\Omega}_Q$. Setting $\xi = 1$ in Equation (3.49) for x and y results in,

$$x = x(1,\eta) = \frac{1}{2}\left[x_j + x_k + (x_k - x_j)\eta\right] \quad \text{and} \quad y = y(1,\eta) = \frac{1}{2}\left[y_j + y_k + (y_k - y_j)\eta\right],$$

where (x_α, y_α) for $\alpha = i, j, k$ or l are the global coordinates at node $\alpha = i, j, k$ or l. It can be seen that both x and y are linear functions of η and thus define a straight line. In fact, when Ω_k is as shown in Figure (3.1), $x = x_j = x_k$ is a constant and y traces out the line from node j to node k as η varies from -1 to 1. The same may be done for $\xi = -1$ and $\eta = \pm 1$, in each case linear functions and hence a straight line will result for the global coordinates. As in the case for one dimension, the transformation must transform functions of x and y to functions of ξ and η. We thus require to establish the Jacobian of the transformation and this is done by considering the relation between differentials of a typical function $r(x,y)$ in the global coordinates and those of its transformed counterpart $\hat{r}(\xi,\eta)$ in local coordinates. Using the chain rule these may be expressed as,

$$\begin{bmatrix} \dfrac{\partial r}{\partial x} \\ \dfrac{\partial r}{\partial y} \end{bmatrix} = \begin{bmatrix} \dfrac{\partial \xi}{\partial x} & \dfrac{\partial \eta}{\partial x} \\ \dfrac{\partial \xi}{\partial y} & \dfrac{\partial \eta}{\partial y} \end{bmatrix} \begin{bmatrix} \dfrac{\partial \hat{r}}{\partial \xi} \\ \dfrac{\partial \hat{r}}{\partial \eta} \end{bmatrix} \quad \text{and} \quad \begin{bmatrix} \dfrac{\partial \hat{r}}{\partial \xi} \\ \dfrac{\partial \hat{r}}{\partial \eta} \end{bmatrix} = \begin{bmatrix} \dfrac{\partial x}{\partial \xi} & \dfrac{\partial y}{\partial \xi} \\ \dfrac{\partial x}{\partial \eta} & \dfrac{\partial y}{\partial \eta} \end{bmatrix} \begin{bmatrix} \dfrac{\partial r}{\partial x} \\ \dfrac{\partial r}{\partial y} \end{bmatrix}.$$

Upon inspection it can be seen that in fact the two matrices are inverses of each other. One maps the global derivatives onto the local and the other from local to global. Thus we have identified the Jacobian $\mathbf{J}$ of the transformation, given by,

$$\mathbf{J} = \begin{bmatrix} \dfrac{\partial x}{\partial \xi} & \dfrac{\partial y}{\partial \xi} \\ \dfrac{\partial x}{\partial \eta} & \dfrac{\partial y}{\partial \eta} \end{bmatrix}.$$

From Equation (3.49) it is possible to calculate the terms of $\mathbf{J}$ which for the standard element $\hat{\Omega}_Q$ are given as,

$$\mathbf{J} = \begin{bmatrix} \frac{1}{4}(x_j - x_i + x_k - x_l) & 0 \\ 0 & \frac{1}{4}(y_l - y_i + y_k - y_j) \end{bmatrix},$$

and using Figure (3.1) it is clear that the Jacobian can thus be expressed as,

$$\mathbf{J} = \begin{bmatrix} \dfrac{h_k}{2} & 0 \\ 0 & \dfrac{h_k}{2} \end{bmatrix}, \quad \text{and thus,} \quad \mathbf{J}^{-1} = \begin{bmatrix} \dfrac{2}{h_k} & 0 \\ 0 & \dfrac{2}{h_k} \end{bmatrix},$$

where h_k is the side length of the element in the global coordinates. We are now in a position to transform an integral over the general element Ω_k to one over the standard element $\hat{\Omega}_Q$ as follows,

$$\int_{\Omega_k} r(x,y)\, dydx = \int_{\hat{\Omega}_Q} \hat{r}(\xi,\eta)\, d\eta d\xi,$$

where,

$$\hat{r}(\xi,\eta) = r(x(\xi,\eta), y(\xi,\eta))|\mathbf{J}|,$$

and where it is of interest to note that, for rectangular or square elements in the global coordinates, the value of $|\mathbf{J}| = h_k^2/4$ is merely the area ratio of the two elements Ω_k and $\hat{\Omega}_Q$ which is an analogous result to the one-dimensional case. The integral over the standard element can now be performed by using a Gauss-Legendre quadrature formula since,

$$\int_{\hat{\Omega}_Q} \hat{r}(\xi,\eta)\, d\eta d\xi = \int_{-1}^{1}\int_{-1}^{1} \hat{r}(\xi,\eta)\, d\eta d\xi.$$

The quadrature formula in this case may be derived from the one-dimensional quadrature formula in the following way,

$$\begin{aligned} \int_{-1}^{1}\left(\int_{-1}^{1} \hat{r}(\xi,\eta)\, d\eta\right) d\xi &\approx \int_{-1}^{1}\left(\sum_{j=1}^{n} \hat{r}(\xi,\eta_j)w_j\right) d\xi, \\ &\approx \sum_{i=1}^{m}\sum_{j=1}^{n} \hat{r}(\xi_i,\eta_j)w_iw_j, \end{aligned} \tag{3.51}$$

where m and n denote the number of quadrature points in the ξ and η directions, (ξ_i, η_j) denote the Gauss points and w_i and w_j denote the corresponding Gauss weights. As in the one-dimensional case, a polynomial of degree p is integrated exactly by employing $n = (p+1)/2$ Gauss points. For the case when $p+1$ is odd, one should pick $n = p/2 + 1$. It is normally the case that the interpolation functions are of the same degree in both ξ and η and thus $m = n$ in the quadrature formula.

The form of the finite element formulation of FSDT in the plate context requires only C^0 continuity of the solution which means that only the generalized displacement degrees of freedom must be continuous across element interfaces. Consequently this enables a suitable shear deformable plate element to be chosen easily and, as in the case of this work, simple Lagrange type elements with linear basis functions can be used. The disadvantage however, lies in the fact that such elements become too stiff when used to model thin plates and some elements become completely rigid as their span-to-thickness ratio tends towards infinity. This behaviour is called artificial stiffening, or locking, and much work in the past has been aimed at identifying more clearly and eliminating the source of this undesirable effect.

Averill and Reddy, [5], have investigated the behaviour of shear deformable elements when used to analyse thin structures. Therein it has been shown that, by using a penalty formulation, in the thin plate limit the penalty parameter enforces the Kirchhoff or Classical Plate Theory constraints,

$$\psi_1 + \frac{\partial w}{\partial x_1} = 0 \quad \text{and} \quad \psi_2 + \frac{\partial w}{\partial x_2} = 0, \tag{3.52}$$

as previously given in Equation (2.37). As described in [5], the finite element method may be expressed in the form,

$$(\mathbf{K}_b + \delta \mathbf{K}_s)\,\mathbf{u} = \mathbf{f},$$

where $\mathbf{K}_b$ is the bending stiffness matrix, $\mathbf{K}_s$ is the shearing stiffness matrix, $\mathbf{u}$ is the displacement vector, $\mathbf{f}$ is the load vector and δ is the penalty parameter. When δ tends to infinity, as it does for thin plates, $\mathbf{K}_s\mathbf{u}$ must go to zero in order for the potential energy to remain bounded. This is equivalent to the Kirchhoff constraints being enforced and implies that the shearing strain in each element should vanish as its thickness is decreased. Shear deformable finite elements are unable to model a state of zero transverse shearing strain such as this and consequently an overstiff element and the phenomenon known as shear locking is created.

In [5] a technique for identifying shear constraints is proposed, this firstly looks at the approximation of the Kirchhoff constraints in the finite element model. Thus the approximations of the constraints given in Equation (3.52) over a rectangular element consisting of n nodes are,

$$\sum_{i=1}^{n} \psi_{1i}^h \phi_i(\mathbf{x}) + \sum_{i=1}^{n} w_i^h \frac{\partial \phi_i(\mathbf{x})}{\partial x_1} = 0 \quad \text{and} \quad \sum_{i=1}^{n} \psi_{2i}^h \phi_i(\mathbf{x}) + \sum_{i=1}^{n} w_i^h \frac{\partial \phi_i(\mathbf{x})}{\partial x_2} = 0, \tag{3.53}$$

where ψ_{1i}^h, ψ_{2i}^h and w_i^h are the rotations and transverse displacement at node i, $\phi_i(\mathbf{x})$ are the shape functions and $\mathbf{x} = [x_1, x_2]^T$. As previously outlined the element stiffness matrices are integrated numerically, hence it is necessary for Equation (3.53) to be satisfied exactly only at the Gauss points which correspond to the integration rule being used. Assuming that we are using a quadrature rule employing N points we thus require that,

$$\sum_{i=1}^{n} \psi_{1i}^h \phi_i(\mathbf{x}_k) + \sum_{i=1}^{n} w_i^h \frac{\partial \phi_i(\mathbf{x}_k)}{\partial x_1} = 0 \quad \text{and} \quad \sum_{i=1}^{n} \psi_{2i}^h \phi_i(\mathbf{x}_k) + \sum_{i=1}^{n} w_i^h \frac{\partial \phi_i(\mathbf{x}_k)}{\partial x_2} = 0, \tag{3.54}$$

at each Gauss point $\mathbf{x}_k$ for $k = 1, \ldots, N$. As described in [5], Equation (3.54) represents the shearing constraints which are imposed on an element in the thin plate limit. These constraints can be interpreted as either discretised equivalents of the Kirchhoff constraints or some other condition which represents a spurious locking constraint. In order to proceed, we will investigate the effect when full integration is employed to evaluate the transverse shear strain terms above. It is reported in [5] that, "If the Gaussian rule which is employed is sufficient to integrate the stiffness coefficients exactly, then the shear constraints which arise in thin elements can be derived in a different manner to that above. In this case, the shearing strains must vanish everywhere within the element, so the shear constraints can be obtained by setting to zero the coefficients of each polynomial term in " Equation (3.53). This would involve a quadrature rule in which $m = n = 2$ in the two-dimensional scheme of Equation (3.51) and will impose eight shear constraints on the element which are given as,

$$\begin{aligned}
\varepsilon_{5_i} &= \psi_{1i}^h + \frac{1}{2}\left(w_j^h - w_i^h\right) = 0, & \varepsilon_{6_i} &= \psi_{2i}^h + \frac{1}{2}\left(w_l^h - w_i^h\right) = 0,\\
\varepsilon_{5_j} &= \psi_{1j}^h + \frac{1}{2}\left(w_j^h - w_i^h\right) = 0, & \varepsilon_{6_j} &= \psi_{2j}^h + \frac{1}{2}\left(w_k^h - w_j^h\right) = 0,\\
\varepsilon_{5_k} &= \psi_{1k}^h + \frac{1}{2}\left(w_k^h - w_l^h\right) = 0, & \varepsilon_{6_k} &= \psi_{2k}^h + \frac{1}{2}\left(w_k^h - w_j^h\right) = 0,\\
\varepsilon_{5_l} &= \psi_{1l}^h + \frac{1}{2}\left(w_k^h - w_l^h\right) = 0, & \varepsilon_{6_l} &= \psi_{2l}^h + \frac{1}{2}\left(w_l^h - w_i^h\right) = 0,
\end{aligned} \tag{3.55}$$

where ε_{5_α} and ε_{6_α} are the components of the transverse shearing strain at node $\alpha = i, j, k, l$ and which can be rearranged to yield the following expressions,

$$\begin{aligned}
\psi_{1i}^h &= \psi_{1j}^h, & \psi_{2i}^h &= \psi_{2l}^h,\\
\psi_{1k}^h &= \psi_{1l}^h, & \psi_{2j}^h &= \psi_{2k}^h.
\end{aligned}$$

These constraints mean that ψ_1 and ψ_2 are required to be constant with respect to x_1 and x_2 respectively. When such conditions are enforced, terms in the bending strain vanish (see Section (3.6)) and the element becomes stiff. In addition, because the rotational degrees of freedom must be continuous across the element interfaces, the entire mesh is forced to act as a rigid body. This will lead to trivial deflections and thus the system will seem to be locked or stiff.

In order to combat the effect of locking, a reduced integration scheme can be used. For the bilinear element this amounts to using a one point Gauss quadrature to integrate the transverse shear terms. Thus the quadrature rule of Equation (3.51) is again used but now with $m = n = 1$. The location of this point is at the origin of the standard element and so by evaluating the constraints using the original method of Equation (3.54) the first constraint has the form,

$$\frac{1}{4}\left(\psi_{1i}^h + \psi_{1j}^h + \psi_{1k}^h + \psi_{1l}^h\right) - w_i^h\left(\frac{1}{4}\right) + w_j^h\left(\frac{1}{4}\right) + w_k^h\left(\frac{1}{4}\right) - w_l^h\left(\frac{1}{4}\right) = 0.$$

Following slight manipulation, this may be written as,

$$\frac{1}{4}\left(\psi^h_{1i}+\psi^h_{1j}+\psi^h_{1k}+\psi^h_{1l}\right)+\frac{1}{4}\left(\frac{1}{2}(w^h_j-w^h_i)+\frac{1}{2}(w^h_j-w^h_i)+\frac{1}{2}(w^h_k-w^h_l)+\frac{1}{2}(w^h_k-w^h_l)\right)=0,$$

and finally as,

$$\begin{aligned}\frac{1}{4}\left(\psi^h_{1i}+\frac{1}{2}(w^h_j-w^h_i)\right)&+\frac{1}{4}\left(\psi^h_{1j}+\frac{1}{2}(w^h_j-w^h_i)\right)\\ \frac{1}{4}\left(\psi^h_{1k}+\frac{1}{2}(w^h_k-w^h_l)\right)&+\frac{1}{4}\left(\psi^h_{1l}+\frac{1}{2}(w^h_k-w^h_l)\right)=0.\end{aligned}$$

Similarly, the second constraint may be expressed as,

$$\begin{aligned}\frac{1}{4}\left(\psi^h_{2i}+\frac{1}{2}(w^h_l-w^h_i)\right)&+\frac{1}{4}\left(\psi^h_{2j}+\frac{1}{2}(w^h_k-w^h_j)\right)\\ \frac{1}{4}\left(\psi^h_{2k}+\frac{1}{2}(w^h_k-w^h_j)\right)&+\frac{1}{4}\left(\psi^h_{2l}+\frac{1}{2}(w^h_l-w^h_i)\right)=0.\end{aligned}$$

From Equation (3.55) the reduced integration constraints may be expressed as,

$$\begin{aligned}\frac{1}{4}\varepsilon_{5_i}+\frac{1}{4}\varepsilon_{5_j}+\frac{1}{4}\varepsilon_{5_k}+\frac{1}{4}\varepsilon_{5_l}&=0,\\ \frac{1}{4}\varepsilon_{6_i}+\frac{1}{4}\varepsilon_{6_j}+\frac{1}{4}\varepsilon_{6_k}+\frac{1}{4}\varepsilon_{6_l}&=0,\end{aligned}$$

which are discretised equivalents of the Kirchhoff constraints in Equation (3.52). It can be seen that in the reduced integration scenario the Kirchhoff constraints are approximated in the finite element model by 'lumping' the constraints at the nodes. Although the reduced integration constraints contain the same expressions that caused locking in the full integration investigation, the excess stiffness is eliminated by enforcing the constraints in a weighted averaged form. In this way a bilinear element which uses reduced integration to integrate the transverse shear strain terms in the element stiffness matrix should also accurately model thin plate behaviour. The bending terms however will still be treated using the original quadrature rule with $m = n = 2$ and so the element as a whole is said to be selectively integrated.

Table (3.1) shows the effect upon the computed element stiffness matrix upon varying the quadrature used. It can be seen that changing the integration scheme produces a subsequent change in the number of zero eigenvalues of the element stiffness matrix. It is important to note that

Integration Scheme		Number of zero eigenvalues		
Bending Terms	Shear Terms	$\mathbf{K}^b_k$	$\mathbf{K}^s_k$	$\mathbf{K}_k = \mathbf{K}^b_k + \mathbf{K}^s_k$
exact	exact	7	4	3
2×2	2×2	7	4	3
2×2	1×1	7	10	5
1×1	1×1	9	10	7

Table 3.1: Counts of zero eigenvalues for element stiffness matrix $\mathbf{K}_k$.

shear locking does not involve membrane deformation and so in-plane displacements u and v are assumed to be zero. Following such an assumption the element stiffness matrix will have three zero eigenvalues. These correspond to the three rigid body motions which are a transverse displacement and two rotations, each of which can be taken to rotate around the x_1 or x_2 coordinate axes. From Table (3.1) it can be seen that by using selective integration the element stiffness matrix $\mathbf{K}_k$ will have five zero eigenvalues where the results have been obtained by using Mathematica, [59]. Thus the reduced integration has introduced two extra zero eigenvalues. As previously mentioned, it is required that the product of the shear stiffness matrix and the displacement vector be zero as the span-to-thickness ratio tends to infinity. The use of reduced integration enables this by making the shear stiffness matrix singular. In such a situation a non-trivial displacement may be obtained since the product of the non-trivial displacement and the singular matrix can be zero.

3.8 Master Element Considerations

For the task of modelling the behaviour of the plate using first order shear deformation theory, the standard and well known quadrilateral element as illustrated in Figure (3.2) is chosen as the 'parent' master element type. The main reasons for selecting such an element are born out of the

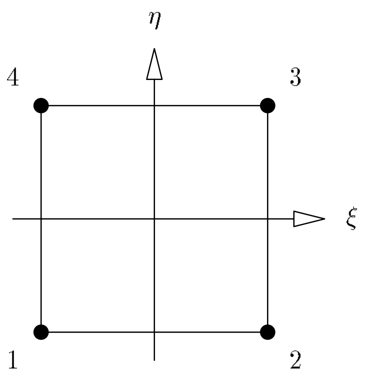

Figure 3.2: Standard quadrilateral 'parent' master element.

physical model developed in Section (2.2.2) and the finite element plate model of Section (3.6). One of the main features is the requirement of only a C^0 element in the modelling and thus the simplest form of this element may be employed by using bilinear shape functions. The previously discussed necessity of reduced integration in Section (3.7) for the thin plate limit must also be employed and due to the fact that Gaussian quadrature rules lend themselves particularly well to quadrilateral type elements the reduced integration requirement can be easily adopted.

It is thought that due to the square or rectangular nature of the plates to be modelled, the aspect ratios of the quadrilateral elements can be retained at an optimal or near optimal value close to unity. This is significant as it will be shown in Chapter 4 that a large aspect ratio may have a detrimental effect upon the error convergence although it should be noted here that Ženíšek and Vanmaele, [60], have shown that the order of convergence can be retained in the case of such thin or anisotropic elements. In reducing the errors it is one of the aims of this work to incorporate transition elements into the mesh for adaptive purposes. As will be discussed in the next section, such elements retain the aspect ratio of their 'parent' elements and so, beginning an analysis with square elements, the optimal unity element aspect ratio will be preserved.

To recap, the master element can thus be thought of as a square element centred on the origin with side length $h = 2$. We will consider such an element with node numbering as detailed in Figure (3.2). The bilinear shape functions for the element in terms of the local coordinates ξ and η are then given by,

$$\phi_1(\xi,\eta) = \frac{1}{4}(1-\xi)(1-\eta), \qquad \phi_2(\xi,\eta) = \frac{1}{4}(1+\xi)(1-\eta),$$
$$\phi_3(\xi,\eta) = \frac{1}{4}(1+\xi)(1+\eta), \qquad \phi_4(\xi,\eta) = \frac{1}{4}(1-\xi)(1+\eta),$$

as in Equation (3.50). Plots of the four shape functions can be seen in Figure (3.3).

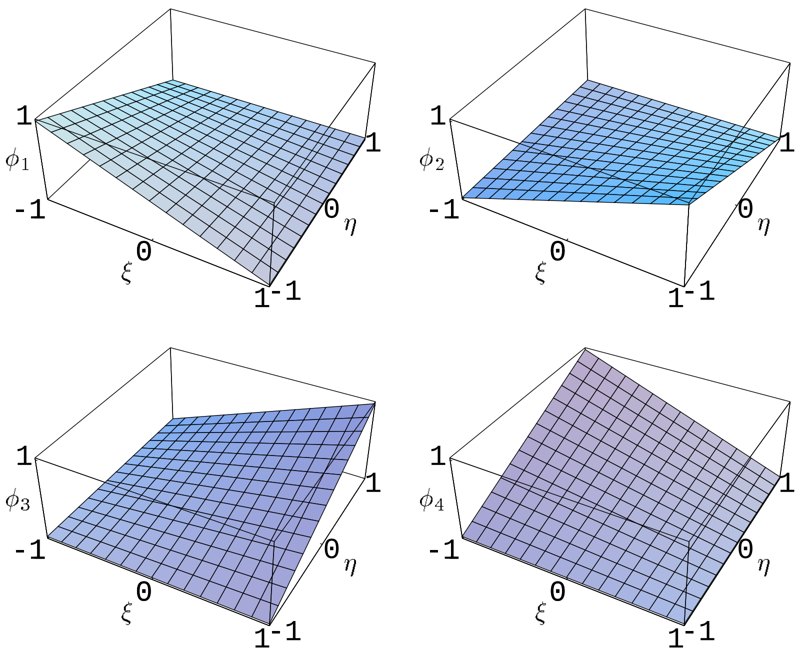

Figure 3.3: Standard bilinear shape functions ϕ_1, ϕ_2, ϕ_3 and ϕ_4 of the 'parent' master element.

3.9 Mesh Adaptivity - Transition Elements

As the main purpose of this study is to develop a robust and efficient a posteriori error estimator for the plate problem we must now consider how best to refine the mesh in order to utilize the estimator predictions. It is here that we introduce the idea of the transition element. As described by Choi and Park, [17], [18] and Gupta [22], the transition elements can have five, six or seven nodes and are used to provide a transition in the mesh from elements of side length $h = m/2$ to elements of side length $h = m$ for some m. A typical scenario is illustrated in Figure (3.4) where a transition element (shaded) with an irregular mid-side node on the western edge is used to provide a transition in the mesh from finer elements to coarser ones. For convenience let this

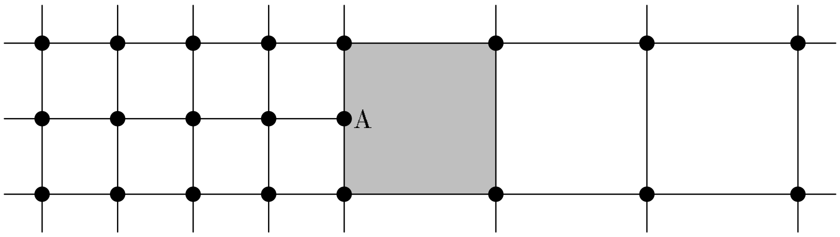

Figure 3.4: 1-irregular transition element (shaded).

type of transition element be known as a 1-irregular transition element due to the presence of the single irregular node A. Similarly, for a transition element having six nodes, let this be known as a 2-irregular transition element and that of seven nodes a 3-irregular transition element. In addition, the irregular node positions at the edge midpoints will be denoted as on the North, East, South or West element edge. Thus the transition element in Figure (3.4) will be known as a 1-irregular transition element with Western irregular node.

3.9.1 Shape Function Modification

The presence of irregular nodes means that there are modifications to be made to the parent master element shape functions. Consider the new master element as shown in Figure (3.5), this

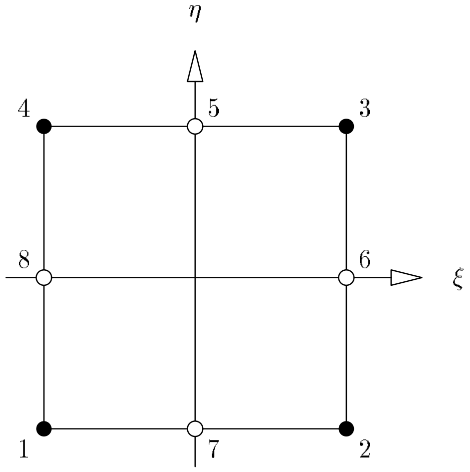

Figure 3.5: Modified master element.

element has the same four nodes as the parent master element of Figure (3.2) but, in addition, the shape functions for the possible irregular nodes must now be considered. These irregular nodes are indicated by an empty circle at nodes 5, 6, 7 and 8 which reside on the North, East, South and

West element edges respectively. It should be noted that the transition element will never contain all four irregular nodes, instead the element will be bisected into four smaller bilinear elements. Figure (3.5) is thus an illustration of the possible nodal locations of the irregular nodes and up to three may appear on the transition element at any one time. The shape functions in terms of local coordinates ξ and η firstly for the irregular nodes are given as,

$$\phi_5(\xi,\eta) = \frac{1}{2}(1-|\xi|)(1+\eta), \qquad \phi_6(\xi,\eta) = \frac{1}{2}(1+\xi)(1-|\eta|),$$
$$\phi_7(\xi,\eta) = \frac{1}{2}(1-|\xi|)(1-\eta), \qquad \phi_8(\xi,\eta) = \frac{1}{2}(1-\xi)(1-|\eta|).$$

The presence of an irregular node will also have an effect upon the shape functions of the ordinary nodes. These are modified as follows,

$$\phi_1(\xi,\eta) = \frac{1}{4}(1-\xi)(1-\eta) - \frac{1}{2}\left[\phi_7+\phi_8\right], \tag{3.56}$$
$$\phi_2(\xi,\eta) = \frac{1}{4}(1+\xi)(1-\eta) - \frac{1}{2}\left[\phi_6+\phi_7\right], \tag{3.57}$$
$$\phi_3(\xi,\eta) = \frac{1}{4}(1+\xi)(1+\eta) - \frac{1}{2}\left[\phi_5+\phi_6\right], \tag{3.58}$$
$$\phi_4(\xi,\eta) = \frac{1}{4}(1-\xi)(1+\eta) - \frac{1}{2}\left[\phi_5+\phi_8\right]. \tag{3.59}$$

It is important to note that the shape function ϕ_i for the irregular node i is only non-zero when there exists an irregular node at position i on the element. Thus, for example, $\phi_6 = \phi_7 = \phi_8 = 0$ in the case of a five node or 1-irregular transition element. In the case of a 1-irregular transition element with irregular Northern node, the shape function ϕ_5 has the form as depicted in Figure (3.6). The presence of this irregular node means that the standard bilinear shape functions are

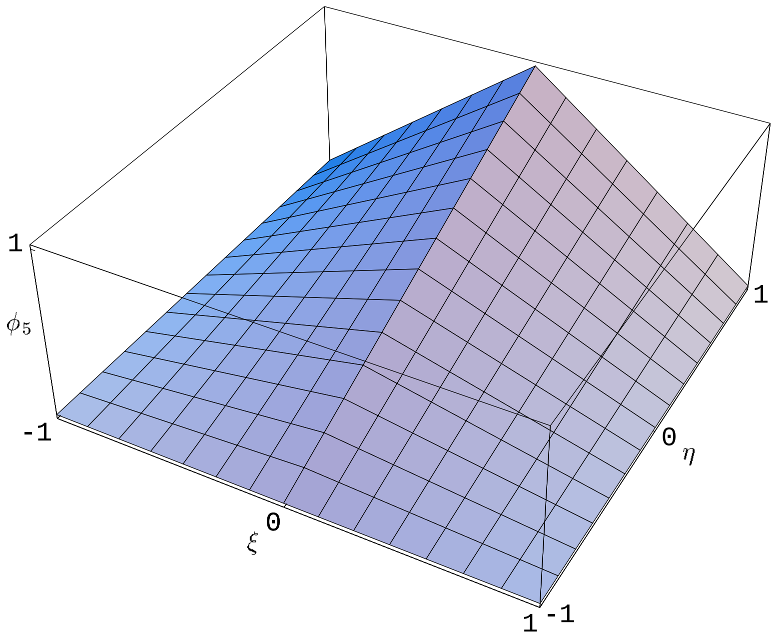

Figure 3.6: Northern irregular node shape function ϕ_5.

modified according to Equations (3.56)-(3.59). These shape functions then differ from those in Figure (3.3) to those illustrated in Figure (3.7). In this way we can ensure that the displacements are continuous across all element boundaries and that we have a smooth transition from coarse

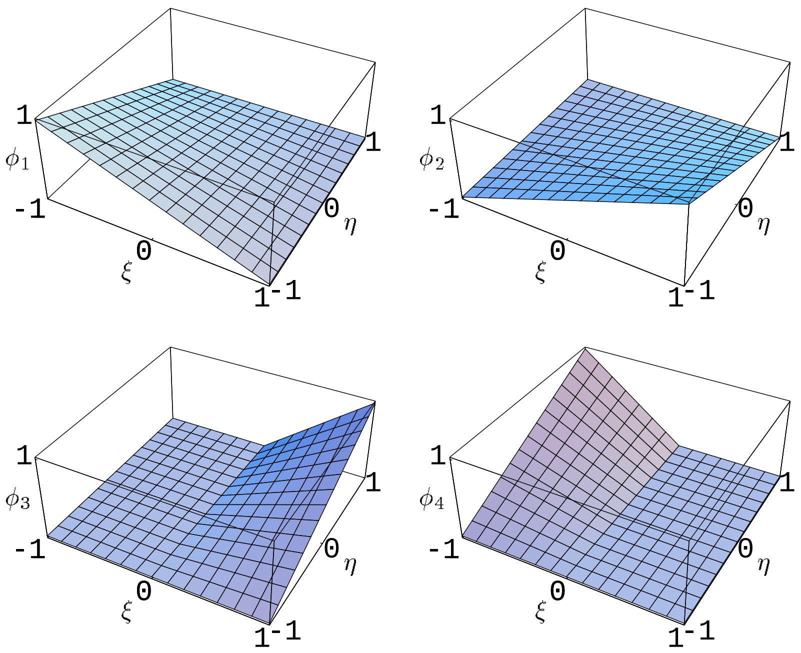

Figure 3.7: Modified shape functions ϕ_1, ϕ_2, ϕ_3 and ϕ_4 of a 1-irregular master element with irregular Northern node.

to finer mesh subdomains. In addition the elements retain their initial aspect ratios throughout the finite element analysis. Upon commencing the finite element analysis with square elements, the final refined or adapted mesh will also consist only of square elements, some of which will be transition elements.

3.9.2 Quadrature Modification

From Section (3.7) it has been shown that for the bending terms of the stiffness matrix the standard bilinear element will require a 2×2 quadrature rule whilst the transverse shear terms will be integrated by a 1×1 rule to enable the thin plate limit to be modelled by preventing locking. When transition elements are used these quadrature schemes must also be modified to take into account the fact that there may exist a displacement slope discontinuity running through the element centre between the North and South edges, between East and West edges or even both. A modification originally proposed by Gupta, [22], will now be detailed for use in such scenarios. Section (3.7) introduced the idea of numerical integration over a typical quadrilateral element $\hat{\Omega}_Q$. It was shown that the quadrature rule could be defined by considering two one-dimensional quadrature formulae along the local coordinates ξ and η. Since the quadrature is applied independently in the ξ and η directions, it is possible to consider any one direction for the following discussion without loss of generality. Thus consider the one-dimensional integral in the direction of the ξ coordinate. It has been seen in Section (3.7) that,

$$I = \int_a^b f(x)\,dx \equiv \int_{-1}^1 \hat{f}(\xi)\,d\xi, \tag{3.60}$$

where,

$$\hat{f}(\xi) = f(x(\xi))J(\xi),$$

with,

$$x(\xi) = \frac{1}{2}\left[a + b + \xi(b-a)\right],$$

and where $J(\xi)$ is known as the Jacobian of the transformation, itself given as,

$$J(\xi) = \frac{b-a}{2}.$$

In turn it is possible to express,

$$\int_{-1}^1 \hat{f}(\xi)\,d\xi \approx \sum_{i=1}^k w_i \hat{f}(\xi_i),$$

where w_i are known as Gauss weights and ξ_i are known as the Gauss points which are themselves roots of the Legendre polynomial $P_k(\xi)$. As previously noted, a polynomial of degree p may be integrated exactly by employing $n = (p+1)/2$ Gauss points and when $p+1$ is odd one should pick the nearest larger integer.

In the case of a transition element however, with an irregular node at $\xi = 0$, the integrand will be discontinuous at $\xi = 0$. Due to this feature the quadrature formula cannot be applied directly and instead the integral on the right-hand side of Equation (3.60) must be split into two integrals,

$$I = \int_{-1}^0 \hat{f}(\xi)\,d\xi + \int_0^1 \hat{f}(\xi)\,d\xi = I_1 + I_2. \tag{3.61}$$

Applying the transformation of Equation (3.60) on integral I_1 gives,

$$I_1 = \int_{-1}^0 \hat{f}(\xi)\,d\xi = \int_{-1}^1 F_1(t)\,dt, \tag{3.62}$$

where, in a similar manner,

$$F_1(t) = \hat{f}(\xi_1(t))J(t),$$

with,

$$\xi_1(t) = \frac{1}{2}\left[t-1\right] \quad \text{and} \quad J(t) = \frac{1}{2}.$$

Since Equation (3.62) represents a continuous integral in the range $(-1, 1)$ we may write,

$$\int_{-1}^1 F_1(t)\,dt \approx \sum_{i=1}^k F_1(t_i)w_i,$$

where t_i and w_i are the previously mentioned Gauss points and weights respectively. Thus the integral I_1 may be expressed as,

$$I_1 \approx \sum_{i=1}^{k} F_1(t_i)w_i = \frac{1}{2}\sum_{i=1}^{k} \hat{f}(\xi_1(t_i))w_i \equiv \sum_{i=1}^{k} \overline{F}_i \overline{w}_i, \tag{3.63}$$

where we have that,

$$\overline{F}_i = \hat{f}(\xi_1(t_i)), \quad \text{and} \quad \overline{w}_i = \frac{1}{2}w_i.$$

Performing the same transformation on integral I_2 yields,

$$I_2 = \int_0^1 \hat{f}(\xi)\, d\xi = \int_{-1}^1 F_2(t)\, dt,$$

where again,

$$F_2(t) = \hat{f}(\xi_2(t))J(t),$$

but this time with,

$$\xi_2(t) = \frac{1}{2}[t+1] \quad \text{and} \quad J(t) = \frac{1}{2}.$$

This ultimately enables the integral I_2 to be expressed as,

$$I_2 \approx \sum_{i=1}^{k} \overline{F}_i \overline{w}_i, \tag{3.64}$$

where,

$$\overline{F}_i = \hat{f}(\xi_2(t_i)), \quad \text{and} \quad \overline{w}_i = \frac{1}{2}w_i.$$

Equations (3.63) and (3.64) replace the original k point quadrature by a $2k$ point quadrature. We thus have,

$$I = \int_{-1}^1 \hat{f}(\xi)\, d\xi \approx \sum_{i=1}^{2k} \overline{F}_i \overline{w}_i, \tag{3.65}$$

where,

$$\overline{F}_i = \hat{f}(\xi_j(t_i)), \quad i = 1, \ldots, 2k, \tag{3.66}$$

and where $j = 1$ for $i = 1, \ldots, k$ and $j = 2$ for $i = k+1, \ldots, 2k$. For the $j = 1$ scenario, we have,

$$\xi_1(t_i) = \frac{1}{2}[t_i - 1], \quad i = 1, \ldots, k, \tag{3.67}$$

along with,

$$\overline{w}_i = \frac{1}{2}w_i, \quad i = 1, \ldots, k. \tag{3.68}$$

Similarly, for the $j = 2$ scenario,

$$\xi_2(t_i) = \frac{1}{2}[t_{i-k} + 1], \quad i = k+1, \ldots, 2k, \tag{3.69}$$

along with,

$$\overline{w}_i = \frac{1}{2}w_{i-k}, \quad i = k+1, \ldots, 2k. \tag{3.70}$$

As an example, consider the one and two point Gauss quadrature rules to be applied on an integral in the range $(-1, 1)$. The standard locations and weight values for the Gauss points are as given

Number of points (k)	Point locations (t_i)	Point weights (w_i)
1	0	2
2	$-\frac{1}{\sqrt{3}}$	1
	$+\frac{1}{\sqrt{3}}$	1

Table 3.2: Standard Gaussian quadrature point locations and weights.

in Table (3.2) and are as detailed in Zienkiewicz, [65]. Modification of these two quadrature rules using Equations (3.65) to (3.70) for the case where there exists a displacement slope discontinuity yields the modified two and four point schemes respectively as given in Table (3.3). For integration in two dimensions the quadrature rules are applied as described in Equation (3.51). In the standard Gaussian quadrature guise, this yields the quadrature point locations and weights as illustrated in

Number of points ($2k$)	Point locations ($\xi_j(t_i)$)	Point weights ($\overline{w}_i$)
2	$-\frac{1}{2}$	1
	$+\frac{1}{2}$	1
4	$\frac{1}{2}\left[-\frac{1}{\sqrt{3}}-1\right]$	$\frac{1}{2}$
	$\frac{1}{2}\left[+\frac{1}{\sqrt{3}}-1\right]$	$\frac{1}{2}$
	$\frac{1}{2}\left[-\frac{1}{\sqrt{3}}+1\right]$	$\frac{1}{2}$
	$\frac{1}{2}\left[+\frac{1}{\sqrt{3}}+1\right]$	$\frac{1}{2}$

Table 3.3: Modified Gaussian quadrature point locations and weights.

Figure (3.8) in which the locations for the point locations are denoted by $\star$ and $\diamond$ for the 2×2 and 1×1 quadrature rules respectively. Figure (3.8) also includes the weight values, shown in square brackets, for each quadrature point. The modified quadrature rules which arise, for example, in the 1-irregular transition element with an irregular Northern node are as detailed in Figure (3.9). In this case the same format has been adopted as in Figure (3.8) with Gauss point locations being denoted by $\star$ and $\diamond$ for the two schemes respectively and weights included in square brackets. As can be seen, the presence of the irregular node on the North edge forces the quadrature schemes to be modified. Thus the 2×2 scheme is modified to give a 4×2 scheme. Similarly, the 1×1 scheme undergoes a 'points doubling' across the possible displacement slope discontinuity running between

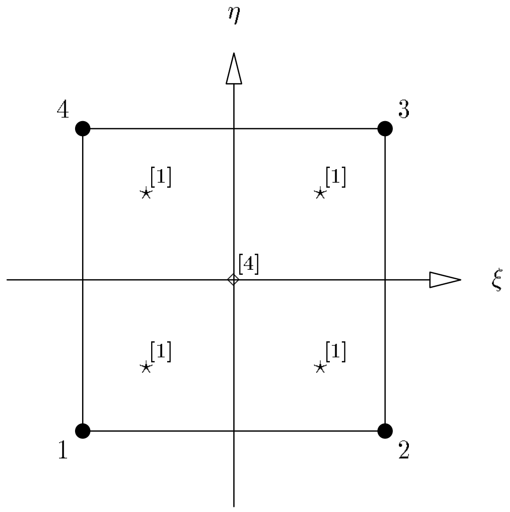

Figure 3.8: 2×2 and 1×1 quadrature points and weights for standard element.

the North and South edges of the element and through the element centroid which is caused by the presence of the irregular node. Exactly the same two integration schemes will result in the case of a 2-irregular transition element having irregular nodes on both the North and South edges. This is due to the fact that the presence in this instance of the Southern irregular node along with the Northern node would introduce no further possible slope discontinuities. In the case of a 1-irregular

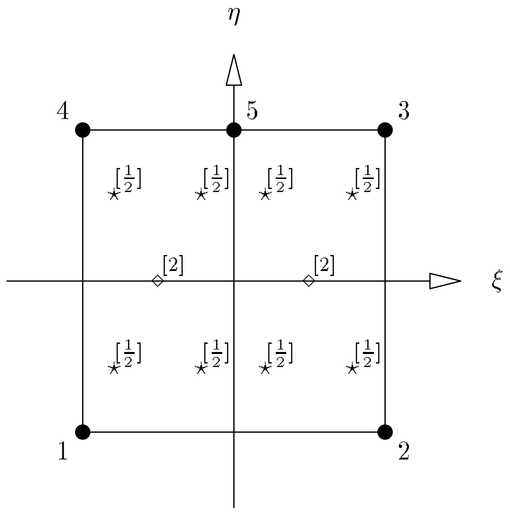

Figure 3.9: Modified 2×2 and 1×1 quadrature points and weights for 1-irregular element.

transition element with Eastern or Western irregular node, the two schemes in Figure (3.9) would undergo a 'points doubling' across the possible slope discontinuity running between the East and West edges and through the element centroid. Thus the schemes would take on the appearance of those in Figure (3.9) but rotated through $\pm\pi/2$ about the element centroid. Finally, Figure (3.10) shows the modified integration schemes in the case of a 2-irregular transition element where the irregular nodes reside on adjacent edges or for any 3-irregular transition element. Once again the same format has been adopted as for Figures (3.8) and (3.9) with Gauss point locations being

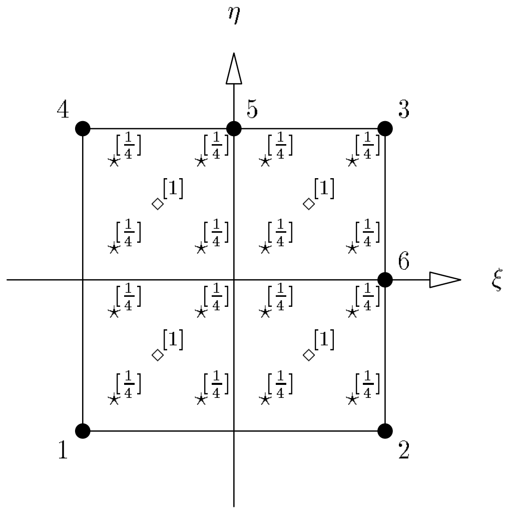

Figure 3.10: Modified 2×2 and 1×1 quadrature points and weights for 2-irregular element.

denoted by $\star$ and $\diamond$ for the two schemes respectively and weights included in square brackets. In Figure (3.10) it can be seen that both the standard 2×2 and 1×1 schemes have undergone 'points doubling' in both the ξ and η directions. This is due to the fact that now there are 2 irregular nodes which lie on adjacent edges. This means that there is the possibility of two lines of slope discontinuity, one running between the North and South edges and the other running between the East and West edges with both passing through the element centroid. These integration schemes will arise for any 2-irregular transition element with irregular nodes on adjacent edges or for any 3-irregular transition element.

Chapter 4

Error Analysis and Estimation

The following section provides an analysis of the theoretical error in the finite element solution. It will be shown that it is possible to bound the finite element error above by the interpolation error and thus recast the problem as one of approximation theory.

The chapter will then proceed to describe two a posteriori error estimators. The first of these is that of Zinekiewicz and Zhu as presented in [69] and [70] whilst the second is that of Johnson and Hansbo as presented in [27] which are of the recovery and residual types described in Chapter 1 respectively. In the case of the Zienkiewicz-Zhu estimator the complication arising from the use of transition elements is detailed along with the modified patch selection problem. For the Johnson-Hansbo estimator, the estimator itself will be firstly applied to the plate problem. The proposed estimator will then be extended in order to cope with the presence of transition elements.

4.1 Theoretical Error Analysis

In the previous chapter the weak formulations for the problems of interest were derived. In both cases the formulation results in the task of finding $\mathbf{u} \in V$ such that,

$$a(\mathbf{u}, \mathbf{v}) = F(\mathbf{v}) \quad \forall\ \mathbf{v} \in V. \tag{4.1}$$

As also detailed, the finite element approximation to the above continuous case requires the finding of $\mathbf{u}_h \in V^h \subset V$ such that,

$$a(\mathbf{u}_h, \mathbf{v}_h) = F(\mathbf{v}_h) \quad \forall\ \mathbf{v}_h \in V^h. \tag{4.2}$$

The solution of the finite element formulation will result in an approximating solution $\mathbf{u}_h \in V^h \subset V$ and so it is important to be able to measure how good the approximation is. In order to proceed it is necessary to define what is meant by the bilinear form, $a(\cdot,\cdot) : V \times V \mapsto \mathbb{R}$, being V-elliptic and also continuous. Consider the general bilinear form $a(\mathbf{u},\mathbf{v})$ as given above:

- $a(\mathbf{u},\mathbf{v})$ is V-elliptic (or V-coercive) if there exists a constant $\rho > 0$ such that,

$$a(\mathbf{v},\mathbf{v}) \geq \rho \|\mathbf{v}\|_V^2 \quad \forall\ \mathbf{v} \in V. \tag{4.3}$$

- $a(\mathbf{u},\mathbf{v})$ is continuous on V if there exists a constant $\gamma > 0$ such that,

$$|a(\mathbf{u},\mathbf{v})| \leq \gamma \|\mathbf{u}\|_V \|\mathbf{v}\|_V \quad \forall\ \mathbf{u},\mathbf{v} \in V. \tag{4.4}$$

Proceeding now with the error analysis, since Equation (4.1) holds for all $\mathbf{v} \in V$ it must also hold for $\mathbf{v}_h \in V^h \subset V$. Thus it is true that,

$$a(\mathbf{u},\mathbf{v}_h) = F(\mathbf{v}_h) \quad \forall\ \mathbf{v}_h \in V^h. \tag{4.5}$$

The bilinear form then enables Equation (4.2) to be subtracted from Equation (4.5), giving the orthogonality condition,

$$a(\mathbf{u}-\mathbf{u}_h,\mathbf{v}_h) = 0 \quad \forall\ \mathbf{v}_h \in V^h. \tag{4.6}$$

Assuming that $a(\mathbf{u},\mathbf{v})$ is V-elliptic, then from Equation (4.3) there exists a $\rho > 0$ such that,

$$\rho\|\mathbf{u}-\mathbf{u}_h\|_V^2 \leq a(\mathbf{u}-\mathbf{u}_h,\mathbf{u}-\mathbf{u}_h).$$

Choosing a $\mathbf{w}_h \in V^h$ and including in the above yields,

$$\rho\|\mathbf{u}-\mathbf{u}_h\|_V^2 \leq a(\mathbf{u}-\mathbf{u}_h,\mathbf{u}-\mathbf{w}_h+\mathbf{w}_h-\mathbf{u}_h).$$

Expanding this expression,

$$\begin{aligned}\rho\|\mathbf{u}-\mathbf{u}_h\|_V^2 &\leq a(\mathbf{u}-\mathbf{u}_h,\mathbf{u}-\mathbf{w}_h) + a(\mathbf{u}-\mathbf{u}_h,\mathbf{w}_h-\mathbf{u}_h),\\ &= a(\mathbf{u}-\mathbf{u}_h,\mathbf{u}-\mathbf{w}_h) + a(\mathbf{u}-\mathbf{u}_h,\mathbf{W}_h),\end{aligned}$$

where $\mathbf{W}_h = \mathbf{w}_h - \mathbf{u}_h \in V^h$. From the orthogonality condition of Equation (4.6) it is true that,

$$a(\mathbf{u}-\mathbf{u}_h,\mathbf{W}_h) = 0, \quad \forall\ \mathbf{W}_h \in V^h.$$

Thus we have that,

$$\rho\|\mathbf{u}-\mathbf{u}_h\|_V^2 \leq a(\mathbf{u}-\mathbf{u}_h,\mathbf{u}-\mathbf{w}_h), \quad \forall\ \mathbf{w}_h \in V^h.$$

If $a(\mathbf{u},\mathbf{v})$ is continuous on V, application of Equation (4.4) yields,

$$\begin{aligned}\rho\|\mathbf{u}-\mathbf{u}_h\|_V^2 &\leq |a(\mathbf{u}-\mathbf{u}_h,\mathbf{u}-\mathbf{w}_h)|\\ &\leq \gamma\|\mathbf{u}-\mathbf{u}_h\|_V\|\mathbf{u}-\mathbf{w}_h\|_V, \quad \forall\ \mathbf{w}_h \in V^h.\end{aligned}$$

This finally gives the result that,

$$\|\mathbf{u}-\mathbf{u}_h\|_V \leq \frac{\gamma}{\rho}\|\mathbf{u}-\mathbf{w}_h\|_V, \quad \forall\ \mathbf{w}_h \in V^h. \tag{4.7}$$

Equation (4.7) holds in particular when $\mathbf{w}_h$ is the interpolant $\pi_h \mathbf{u} \in V^h$ to $\mathbf{u}$, so that,

$$||\mathbf{u} - \mathbf{u}_h||_V \leq \frac{\gamma}{\rho} ||\mathbf{u} - \pi_h \mathbf{u}||_V. \tag{4.8}$$

In such a scenario, the problem of estimating the error $\mathbf{u} - \mathbf{u}_h$ becomes one of approximation theory requiring now an estimation of the interpolation error $\mathbf{u} - \pi_h \mathbf{u}$. This task is by no means trivial and a related problem will be detailed in a forthcoming chapter. Squaring both sides of Equation (4.8) and writing V now as the general space $\left[H^k(\Omega)\right]^n$ we have that, by definition, the norm containing the interpolant can be expressed as,

$$||\mathbf{u} - \pi_h^p \mathbf{u}||^2_{H^k(\Omega)} = \sum_{i=1}^{n} ||u_i - \pi_h^p u_i||^2_{H^k(\Omega)}, \tag{4.9}$$

where we have introduced the term π_h^p in place of π_h which is merely to denote that the interpolant is a piecewise pth order polynomial. Let $\Omega \in \mathbb{R}^2$ be a bounded rectangular domain with a partition of rectangular elements and let h and β denote respectively the largest edge length and smallest edge ratio for elements of the mesh. Let V^h consist of piecewise 'bi-functions' such that in any element the interpolant is a pth order polynomial. Then, from [55] there exists a constant C such that,

$$|u_i - \pi_h^p u_i|_{s,\Omega} \leq C \frac{1}{\beta} h^{\min(p,k)+1-s} |u_i|_{k+1,\Omega}, \quad \forall\ u_i \in H^{k+1}(\Omega),\ s = 0, 1. \tag{4.10}$$

For an analogous result in the case of a partition of triangular elements see [55]. It is important to note at this stage the recommendation that rectangular elements of small aspect ratios be avoided in the model so that β remains close to unity. In this way the error bounds remain as accurate or 'sharp' as possible. This is again analogous to the recommendation that triangular elements with small internal angles should be avoided. In the context of a rectangular partition, the β in Equation (4.10) may be incorporated into the constant C as it is independent of h. By doing this we have, for $s = 0$,

$$|u_i - \pi_h^p u_i|_{0,\Omega} \leq C h^{\min(p,k)+1} |u_i|_{k+1,\Omega}, \tag{4.11}$$

whilst, for $s = 1$,

$$|u_i - \pi_h^p u_i|_{1,\Omega} \leq C h^{\min(p,k)} |u_i|_{k+1,\Omega}. \tag{4.12}$$

Now, by definition,

$$||u_i - \pi_h^p u_i||^2_{1,\Omega} = |u_i - \pi_h^p u_i|^2_{0,\Omega} + |u_i - \pi_h^p u_i|^2_{1,\Omega},$$

and so, substituting the bounds of Equations (4.11) and (4.12) in the above gives,

$$||u_i - \pi_h^p u_i||^2_{1,\Omega} \leq C^2 h^{2(\min(p,k))} |u_i|^2_{k+1,\Omega}.$$

Thus in Equation (4.9) we have that,

$$\begin{aligned} ||\mathbf{u} - \pi_h^p \mathbf{u}||^2_{H^k(\Omega)} &\leq C^2 h^{2(\min(p,k))} \sum_{i=1}^{n} |u_i|^2_{k+1,\Omega}, \\ &= C^2 h^{2(\min(p,k))} |\mathbf{u}|^2_{k+1,\Omega}, \end{aligned}$$

by definition and where again C incorporates the constants which are independent of h. Consequently the general result for the error is of the form,

$$\|\mathbf{u} - \mathbf{u}_h^p\|_{H^k(\Omega)} \leq C h^{\min(p,k)} |\mathbf{u}|_{k+1,\Omega}. \tag{4.13}$$

For $\mathbf{u} \in \left[H^2(\Omega)\right]^2$ and in the case of a piecewise bilinear interpolant on the rectangular partition of Ω which means that $p = 1$ in the above,

$$\|\mathbf{u} - \mathbf{u}_h\|_{H^1(\Omega)} \leq C h |\mathbf{u}|_{2,\Omega},$$

whereas, moving to the L_2-norm,

$$\|\mathbf{u} - \mathbf{u}_h\|_{0,\Omega} \leq C h^2 |\mathbf{u}|_{2,\Omega},$$

as shown by Johnson, [26]. Thus the convergence gain with change from $\|\cdot\|_{1,\Omega}$ to $\|\cdot\|_{0,\Omega}$ is h for regular $\mathbf{u} \in \left[H^2(\Omega)\right]^2$, this is known as the 'Nitsche lift' as described in [55]. The exponent of h is often referred to as the rate of convergence and the error in a series of uniformly refined meshes (with h being successively halved) can be expected to decrease with the same order of convergence as h.

4.2 The Zienkiewicz-Zhu Error Estimator

In this section the error estimator of Zienkiewicz and Zhu, [69], [70], also often referred to as the Z-Z or Z^2 estimator, will be introduced. As previously mentioned, this estimator has received much attention since publication and researchers have busied themselves in a bid to develop and enhance certain aspects, particularly in the recovery procedure employed and the question of strategy to be taken for gradient recovery at boundary nodes of the problem domain.

Consider the problem of linear elasticity defined previously in Chapter 2, we shall define the error of the finite element approximation $\mathbf{u}_h$ with respect to the exact solution $\mathbf{u}$ as,

$$\mathbf{e} = \mathbf{u} - \mathbf{u}_h, \tag{4.14}$$

and the error of the gradients (stresses) as,

$$\mathbf{e}_\sigma = \boldsymbol{\sigma} - \boldsymbol{\sigma}_h. \tag{4.15}$$

In practical computations the true solutions $\mathbf{u}$ and $\boldsymbol{\sigma}$ will generally not be known and so it is at this point that [70] recommends substituting the value of $\mathbf{e}_\sigma$ in Equation (4.15) by an approximation. This approximation encompasses the essence of the estimator and entails replacing $\boldsymbol{\sigma}$ with $\boldsymbol{\sigma}_h^*$ which is a recovered or post-processed value of $\boldsymbol{\sigma}_h$ and which is interpolated between the nodal values by the finite element displacement basis functions. We thus have that,

$$\mathbf{e}_\sigma \approx \mathbf{e}_\sigma^* = \boldsymbol{\sigma}_h^* - \boldsymbol{\sigma}_h.$$

Measured in the energy norm, the true error is expressed as,

$$||\mathbf{e}||_{E(\Omega)} = ||\mathbf{u} - \mathbf{u}_h||_{E(\Omega)} = \left(\int_\Omega \mathbf{e}_\sigma^T \mathbf{C}^{-1} \mathbf{e}_\sigma \, d\Omega \right)^{\frac{1}{2}},$$

where the integral arises from the definition of the bilinear form, $a(\cdot, \cdot)$ for linear elasticity as given in Equation (3.25). Thus the approximation of the error measured again in the energy norm is given as,

$$||\tilde{\mathbf{e}}||_{E(\Omega)} = \left(\int_\Omega \mathbf{e}_\sigma^{*T} \mathbf{C}^{-1} \mathbf{e}_\sigma^* \, d\Omega \right)^{\frac{1}{2}},$$

which is known as the error estimator. We thus have that, by substitution into Equation (1.2) with $E = ||\tilde{\mathbf{e}}||_{E(\Omega)}$, the effectivity index is given by,

$$\theta = \frac{||\tilde{\mathbf{e}}||_{E(\Omega)}}{||\mathbf{e}||_{E(\Omega)}}. \tag{4.16}$$

As previously mentioned, it is required that this quantity tends asymptotically to unity as the true or exact error $||\mathbf{e}||$ tends to zero, implying that the estimator converges to the exact error. It has been shown in [70] that if $||\mathbf{e}^*|| = ||\mathbf{u} - \mathbf{u}^*||$ is some error norm of the recovered solution, then the error estimator $||\tilde{\mathbf{e}}||$ will be asymptotically exact if,

$$\frac{||\mathbf{e}^*||}{||\mathbf{e}||} \rightarrow 0.$$

The proof of this is as follows. The estimator may be expressed as,

$$||\tilde{\mathbf{e}}|| = ||\mathbf{u}^* - \mathbf{u}_h|| \equiv ||(\mathbf{u} - \mathbf{u}_h) - (\mathbf{u} - \mathbf{u}^*)||.$$

Using the triangle inequality, we have that,

$$||\mathbf{u} - \mathbf{u}_h|| - ||\mathbf{u} - \mathbf{u}^*|| \leq ||\tilde{\mathbf{e}}|| \leq ||\mathbf{u} - \mathbf{u}_h|| + ||\mathbf{u} - \mathbf{u}^*||,$$

and using Equation (4.14) and the definition of $||\mathbf{e}^*||$, this can be expressed as,

$$||\mathbf{e}|| - ||\mathbf{e}^*|| \leq ||\tilde{\mathbf{e}}|| \leq ||\mathbf{e}|| + ||\mathbf{e}^*||.$$

Dividing through by $||\mathbf{e}||$ and using Equation (4.16) we have that,

$$\left(1 - \frac{||\mathbf{e}^*||}{||\mathbf{e}||}\right) \leq \theta \leq \left(1 + \frac{||\mathbf{e}^*||}{||\mathbf{e}||}\right),$$

showing that the effectivity index, θ, will approach unity as the ratio $||\mathbf{e}^*||/||\mathbf{e}||$ tends to zero $\Box$.

In order for the ratio $||\mathbf{e}^*||/||\mathbf{e}||$ to tend to zero, $||\mathbf{e}^*||$ must converge at a higher rate than $||\mathbf{e}||$. Thus, if $||\mathbf{e}^*||$ is superconvergent then asymptotic exactness of the estimator is guaranteed. It may be the case, however, that superconvergent convergence of $||\mathbf{e}^*||$ itself cannot be guaranteed. This may arise from the fact that some sampling points in the recovery procedure may not be superconvergent sampling points themselves. In such a scenario the estimator will still be applicable according to [70] providing that the recovered values are more accurate (though not necessarily superconvergent) than those obtained in the finite element computations.

4.2.1 Recovery Procedure

As detailed by Zienkiewicz and Zhu, [69], the aim of this procedure is to recover more accurate nodal values of derivatives from the original finite element solution. The technique is also often referred to as 'smoothing' and may be thought of as one in which the discontinuous derivatives are post-processed to give a piecewise continuous polynomial across the domain Ω, interpolating the recovered values at the nodes using the finite element displacement basis functions. It is stated in [69] that the quality of the estimator is obviously dependent upon the accuracy of the recovered solutions. These solutions in turn rely upon the accuracy of the sampling points taken in the procedure but, as observed in the previous section, the sampling points need not necessarily be superconvergent sampling points. When this is the case and the sampling points are simply of high accuracy, the estimator cannot be guaranteed as superconvergent and in all probability will not be.

Firstly let us define the idea of an element patch. This is merely a collection of elements which share a common node. The common shared node will be known henceforth as the patch assembly node and will be denoted in the figures as a ringed node. An example of a typical patch can be seen in Figure (4.1) for a quadrilateral mesh. By denoting the resulting finite element nodal

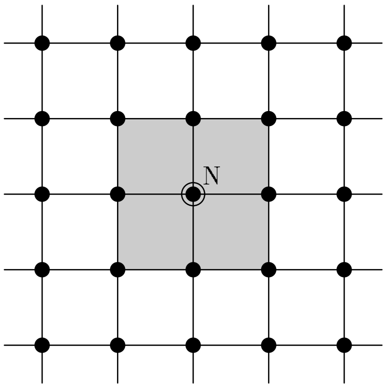

Figure 4.1: Example of a general element patch surrounding patch assembly node N.

displacement vector as $\overline{\mathbf{u}}$ we may express the finite element solution $\mathbf{u}_h(\mathbf{x})$ at any point $\mathbf{x} \in \Omega$ as,

$$\mathbf{u}_h(\mathbf{x}) = \mathbf{L}\overline{\mathbf{u}},$$

where $\mathbf{L}$ is the array of finite element basis functions as described in Section (3.5). As also defined previously, the stresses (or gradients) are given by,

$$\boldsymbol{\sigma}_h = \mathbf{C}\mathbf{B}\mathbf{u}_h, \tag{4.17}$$

with $\mathbf{C}$ the constitutive matrix and $\mathbf{B}$ the differential operator matrix which defines the strain as,

$$\boldsymbol{\varepsilon}_h = \mathbf{B}\mathbf{u}_h.$$

It is clear that the stresses $\boldsymbol{\sigma}_h$ will be discontinuous across element boundaries. Thus it is the objective of the recovery procedure to find nodal parameters $\overline{\boldsymbol{\sigma}}_h^*$, such that the smoothed continuous stress field $\boldsymbol{\sigma}_h^*$ defined as,

$$\boldsymbol{\sigma}_h^* = \mathbf{L}\overline{\boldsymbol{\sigma}}_h^*,$$

where $\mathbf{L}$ is again the same array of finite element basis functions which is used to interpolate the nodal displacements, is more accurate than $\boldsymbol{\sigma}_h$. In the recovery process outlined in [69], it is assumed that the nodal values $\overline{\boldsymbol{\sigma}}_h^*$ belong to a polynomial expansion $\boldsymbol{\sigma}_p^*$ of the same complete order p as that present in the basis functions of $\mathbf{L}$ and which is valid over an element patch surrounding the patch assembly node considered, as shown in Figure (4.1). The same polynomial expansion is used for each component of $\boldsymbol{\sigma}_p^*$ (or the derivatives) and for each of which may be expressed as,

$$\sigma_p^* = \mathbf{Pa}, \tag{4.18}$$

where $\mathbf{P}$ contains the appropriate polynomial terms and $\mathbf{a}$ is a set of unknown parameters. For the case of a one-dimensional element of order p we will have that,

$$\mathbf{P} = \left[1, x, x^2, \ldots, x^p\right],$$

and,

$$\mathbf{a} = \left[a_0, a_1, \ldots, a_p\right]^T.$$

For the case of a quadrilateral element we have, in addition to the complete polynomials, terms involving x and y. Thus, in the case of a bilinear element, we have that,

$$\mathbf{P} = [1, x, y, xy].$$

The task is thus to determine the unknown parameters of $\mathbf{a}$ given in Equation (4.18) for each component of $\boldsymbol{\sigma}_p^*$ (or the derivatives). This is done by ensuring a least square fit of this to the set of superconvergent or at least high accuracy sampling points existing on the element patch considered. In order to do this, it is required that we minimize,

$$\begin{aligned} F(\mathbf{a}) &= \sum_{i=1}^{s}\left(\sigma_h\left(x_i, y_i\right) - \sigma_p^*\left(x_i, y_i\right)\right)^2 \\ &= \sum_{i=1}^{s}\left(\sigma_h\left(x_i, y_i\right) - \mathbf{P}\left(x_i, y_i\right)\mathbf{a}\right)^2 \end{aligned} \tag{4.19}$$

where (x_i, y_i) are the coordinates of the sampling points and s is the total number of sampling points. The minimization of Equation (4.19) implies that $\mathbf{a}$ satisfies,

$$\sum_{i=1}^{s}\mathbf{P}^T(x_i, y_i)\mathbf{P}(x_i, y_i)\mathbf{a} = \sum_{i=1}^{s}\mathbf{P}^T(x_i, y_i)\sigma_h(x_i, y_i).$$

This can be solved in matrix form as,

$$\mathbf{a} = \mathbf{G}^{-1}\mathbf{b}, \tag{4.20}$$

where

$$\mathbf{G} = \sum_{i=1}^{s}\mathbf{P}^T(x_i, y_i)\mathbf{P}(x_i, y_i) \quad \text{and} \quad \mathbf{b} = \sum_{i=1}^{s}\mathbf{P}^T(x_i, y_i)\sigma_h(x_i, y_i).$$

For a regular quadrilateral mesh it is known, and indeed it shall be shown in Section (4.3.1), that the optimal sampling point lies at the element centroid. Thus, for the patch shown in Figure (4.2) we

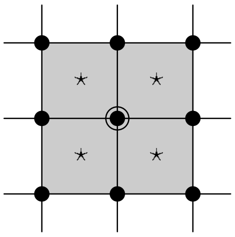

Figure 4.2: Sampling point locations, $\star$, for regular mesh.

have four sampling points in total. Since the same sampling points are used for each component of $\boldsymbol{\sigma}_p^*$ it is clear that the same matrix $\mathbf{G}$ will result for a given patch. Thus, as mentioned in [69], only a single inversion of the matrix is required to solve for $\mathbf{a}$ in Equation (4.20). Once the parameters of $\mathbf{a}$ have been obtained, the recovered values are obtained by insertion of the appropriate coordinates into Equation (4.18). It is claimed in [69] that, in this way, all values of $\boldsymbol{\sigma}_p^*$ in the domain of the patch are superconvergent as it fits closely to local sampling points which exhibit this property and is also of the correct polynomial order.

Zienkiewicz and Zhu state in [69] that the locations of superconvergent points for triangular elements at the time of publication was still a matter which had not been fully explored mathematically. In order to test the recovery procedure Zienkiewicz and Zhu subsequently elected to sample at the triangular element centroid although it was known that this was not rigorously correct. It appears that in numerical studies $O(h^{1.5})$ convergence is obtained in the energy norm using triangular elements for a Poisson type problem. This may be due to the fact that the sampling points used were not the optimal superconvergent points but illustrates that an improvement of the convergence rate is still possible.

4.3 Zienkiewicz-Zhu Estimator for Plates

The application of the Zienkiewicz-Zhu estimator to the plate problem follows a similar approach to that described above for linear elasticity. As done in the previous section, it is again possible to define the finite element error $\mathbf{e}$ as,

$$\mathbf{e} = \mathbf{u} - \mathbf{u}_h.$$

From Section (3.3), however, the bilinear form of the plate problem has been found to be,

$$a(\mathbf{u}, \mathbf{v}) = \int_\Omega \left(\mathbf{B}^b\mathbf{u}\right)^T \mathbf{C}^b \left(\mathbf{B}^b\mathbf{v}\right)\, d\mathbf{x} + \int_\Omega \left(\mathbf{B}^s\mathbf{u}\right)^T \mathbf{C}^s \left(\mathbf{B}^s\mathbf{v}\right)\, d\mathbf{x},$$

where the presence of $\mathbf{B}^b$ and $\mathbf{B}^s$ arise from the fact that there are terms in the formulation which result from plate bending terms and transverse shear terms and are thus signified by the superscripts b and s respectively. These operators are analogous to the operator $\mathbf{B}$ in Equation (4.17) and enable the resulting bending and transverse shear strains to be expressed as,

$$\varepsilon^b(\mathbf{u}) = \mathbf{B}^b\mathbf{u} \quad \text{and} \quad \varepsilon^s(\mathbf{u}) = \mathbf{B}^s\mathbf{u}.$$

Consequently these give rise to stresses $\boldsymbol{\sigma}^b$ and $\boldsymbol{\sigma}^s$ expressed by multiplying with material matrices $\mathbf{C}^b$ and $\mathbf{C}^s$ which give,

$$\boldsymbol{\sigma}^b(\mathbf{u}) = \mathbf{C}^b \varepsilon^b(\mathbf{u}) \quad \text{and} \quad \boldsymbol{\sigma}^s(\mathbf{u}) = \mathbf{C}^s \varepsilon^s(\mathbf{u}).$$

Thus the error of the gradients (stresses) can be expressed in an analogous manner to that in the linear elasticity scenario as,

$$\mathbf{e}_{\sigma^b} = \boldsymbol{\sigma}^b - \boldsymbol{\sigma}_h^b \quad \text{and} \quad \mathbf{e}_{\sigma^s} = \boldsymbol{\sigma}^s - \boldsymbol{\sigma}_h^s. \tag{4.21}$$

where now we have $\boldsymbol{\sigma}^b$ and $\boldsymbol{\sigma}^s$ instead of the single $\boldsymbol{\sigma}$ present in the linear elasticity case. In the same way as for linear elasticity, the quantities $\mathbf{u}$, $\boldsymbol{\sigma}^b$ and $\boldsymbol{\sigma}^s$ will generally not be known. Thus substitution of the values $\mathbf{e}_{\sigma^b}$ and $\mathbf{e}_{\sigma^s}$ in Equation (4.21) is made by an approximation to each. The quantities $\boldsymbol{\sigma}^b$ and $\boldsymbol{\sigma}^s$ are replaced with $\boldsymbol{\sigma}_h^{*b}$ and $\boldsymbol{\sigma}_h^{*s}$ respectively which are recovered values of $\boldsymbol{\sigma}_h^b$ and $\boldsymbol{\sigma}_h^s$ and which are interpolated between their nodal values by the finite element displacement basis functions. We thus have that,

$$\mathbf{e}_{\sigma^b} \approx \mathbf{e}^*_{\sigma^b} = \boldsymbol{\sigma}_h^{*b} - \boldsymbol{\sigma}_h^b \quad \text{and} \quad \mathbf{e}_{\sigma^s} \approx \mathbf{e}^*_{\sigma^s} = \boldsymbol{\sigma}_h^{*s} - \boldsymbol{\sigma}_h^s.$$

The true error can now be expressed as,

$$||\mathbf{e}||_{E(\Omega)} = ||\mathbf{u} - \mathbf{u}_h||_{E(\Omega)} = \left(\int_\Omega \left(\mathbf{e}^b_\sigma\right)^T \left(\mathbf{C}^b\right)^{-1} \left(\mathbf{e}^b_\sigma\right) \, d\mathbf{x} + \int_\Omega \left(\mathbf{e}^s_\sigma\right)^T \left(\mathbf{C}^s\right)^{-1} \left(\mathbf{e}^s_\sigma\right) \, d\mathbf{x} \right)^{\frac{1}{2}},$$

whilst the approximation of the error, also measured in the energy norm is given as,

$$||\tilde{\mathbf{e}}||_{E(\Omega)} = \left(\int_\Omega \left(\mathbf{e}^*_{\sigma^b}\right)^T \left(\mathbf{C}^b\right)^{-1} \left(\mathbf{e}^*_{\sigma^b}\right) d\mathbf{x} + \int_\Omega \left(\mathbf{e}^*_{\sigma^s}\right)^T \left(\mathbf{C}^s\right)^{-1} \left(\mathbf{e}^*_{\sigma^s}\right) \, d\mathbf{x} \right)^{\frac{1}{2}},$$

which is known as the error estimator. The recovery procedure for plates is as detailed for the linear elasticity case and now attention must be switched to the problem of determining where to make the samples on each element patch. Due to the fact that transition elements will be employed in the plate model this is not clear and the presence of irregular nodes on the element will destroy the local symmetry of the mesh. The locations of optimal sampling points on the elements are strongly affected by the local symmetry and it is thus necessary to observe how the desirable sampling areas change as the irregular nodes are added to a typical element. In this way one can develop a strategy for sampling on the mesh in the vicinity of irregular nodes which is well justified.

At this point it is interesting to recap on the results from Section (3.9.2) in which the effects upon the quadrature schemes for integrating the stiffness matrix terms were derived for the transition element family. There it was shown that a 'points doubling' effect was seen across any possible line of slope discontinuity on the element, itself emanating from the presence of a mid-side node. As will be reported in the following section, researchers have found that the optimal sampling point locations for stresses are at what have come to be known as the 'Barlow points'. These points are located at the reduced integration Gauss points on an element as detailed in Section (3.7) and which lie on 'Gauss lines' which, themselves will be illustrated in the following section. Although this phenomenon is well documented, there is little knowledge for the case of transition elements and thus it is the aim of the following section to address this problem.

4.3.1 Optimal Sample Point Locations - A Taylor Series Analysis

As stated in [69], the quality and reliability of the error estimator is obviously dependent on the accuracy of the recovered solutions and therefore on the smoothing procedures. These in turn depend upon the sampling points used in a typical element patch surrounding the patch assembly node at which the recovered solutions are to be evaluated. It is thus desirable for the sampling points to be 'superconvergent' points. These are points at which the normal rate of theoretical convergence as defined in Section (4.1) is exceeded by one order. The location of such points has been the subject of much investigation following the pioneering work of Barlow [14] which led to the idea of 'Barlow points' highlighted by Ochoa and Reddy, [37], and Reddy and Miravete, [41], for the use in sampling optimal stresses. Later work has been produced by Zhang, [61], and also Zhang and Zhang, [63], for differing types of problem formulations and more recently Babuška et al, [9] and [10], in which a computer based proof is provided for the existence of superconvergent points for many problems and mesh geometries.

Attention here will be focused on research by Mackinnon and Carey, [33], which highlights a particularly appealing approach for predicting the locations of superconvergent points on a typical element. Such analysis is based on the use of Taylor series expansions and developed to determine accuracy estimates for derivatives in one and two dimensions computed by differentiation of a finite element interpolant or approximation. Although research has been performed on standard elements by the authors mentioned in the previous paragraph, the present literature does not contain superconvergent point location predictions for the general transition element as described in Section (3.9). The use of such elements is central to this work and thus the task here is to investigate the transition element family in order to determine whether such points exist and, if so, to calculate their location. Babuška et al. [9] and [10] investigate the properties of a certain type of transition element but in such cases the irregular nodes on the elements have their displacements constrained. This is usually performed by interpolating between the displacements of the irregular node's neighbour nodes. In this way the irregular nodes are not 'active' in the finite element model unlike in the case of the transition elements used here where the irregular nodes have the same 'active' degrees of freedom as the regular nodes. It is thus the aim of this section to firstly introduce the ideas of Mackinnon and Carey [33], to replicate the well known predictions for the standard bilinear element and then to apply the analysis to the family of transition elements.

The following analysis is based on [33] where the analysis of optimal sampling point locations is determined using Taylor series. The methodology is extended to problems which are more specific to the current work, namely the treatment of situations arising from the presence of irregular mid-side nodes and the subsequent modification of shape functions as detailed in Section (3.9.1).

Recall that, using master element shape functions $\phi_i(\mathbf{x})$, the finite element solution can be evaluated at any point $\mathbf{x}$ on an element Ω_k in the following way,

$$u_h(\mathbf{x}) = \sum_{i=1}^{n} u_i^h \phi_i(\mathbf{x}), \quad \mathbf{x} \in \Omega_k, \tag{4.22}$$

where u_i^h are the n nodal degrees of freedom for the element, h denotes the mesh size, $\mathbf{x} \in \mathbb{R}^n$ with $n = 1$ or 2 here and u_h has been taken to be scalar valued. For the case where we have vector valued $\mathbf{u}_h$ as in the case of the elasticity and plate models in Chapter 2, the above formulations hold true for each component of $\mathbf{u}_h$ provided that each degree of freedom is interpolated by the same set of shape functions on the element. An approximation to the true derivative may be obtained by differentiating Equation (4.22) giving, for the jth component,

$$\frac{\partial u_h(\mathbf{x})}{\partial x_j} = \sum_{i=1}^{n} u_i^h \frac{\partial \phi(\mathbf{x})}{\partial x_j}. \tag{4.23}$$

It is usual to evaluate Equation (4.23) at specific points in the element at which highest accuracy occurs. These points are the aforementioned superconvergent or high accuracy sampling points and our immediate task is to establish their locations.

One-Dimensional Analysis

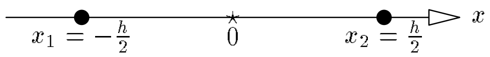

Figure 4.3: One-dimensional linear reference element Ω_k of length $h = x_2 - x_1$.

Considering the linear one-dimensional analysis of scalar valued $u(x)$ we have, for the element of length h depicted in Figure (4.3) the shape functions,

$$\phi_1(x) = \frac{1}{h}\left(\frac{h}{2} - x\right), \quad \phi_2(x) = \frac{1}{h}\left(\frac{h}{2} + x\right).$$

In this way, the value of the linear interpolant $\pi_h u$ to u at any point $x \in \Omega_k$ can be expressed by using Equation (4.22) which gives the expression,

$$\pi_h u(x) = \sum_{i=1}^{2} u(x_i)\phi_i(x) \equiv \sum_{i=1}^{2} u_i \phi_i.$$

Thus the derivative of the interpolant, using Equation (4.23), is expressed as,

$$\frac{\partial \pi_h u(x)}{\partial x} = \sum_{i=1}^{2} u_i \frac{\partial \phi_i(x)}{\partial x} \equiv \sum_{i=1}^{2} u_i \varphi_i, \tag{4.24}$$

where we have introduced the notation $\varphi_i(x) \equiv \partial\phi_i(x)/\partial x$. Consider the Taylor series expansion of $u(x_i)$ about a general point $x \in \Omega_k$, then,

$$u(x_i) \equiv u_i = u(x) + (x_i - x)u_x(x) + \frac{1}{2!}(x_i - x)^2 u_{xx}(x) + \frac{1}{3!}(x_i - x)^3 u_{xxx}(x) + \ldots \tag{4.25}$$

where we are using subscript x to denote differentiation with respect to x. Introducing also the notation $\delta_i \equiv (x_i - x)$ we then have, dropping the x notation, that,

$$u_i = u + \delta_i u_x + \frac{1}{2!}\delta_i^2 u_{xx} + \frac{1}{3!}\delta_i^3 u_{xxx} + \dots \tag{4.26}$$

for $i = 1$ or 2 in the case for the linear element Ω_k above. Multiplying Equation (4.26) by φ_i and summing each term over all the nodes yields,

$$\sum_{i=1}^{2} \varphi_i u_i = u \sum_{i=1}^{2} \varphi_i + u_x \sum_{i=1}^{2} \varphi_i \delta_i + u_{xx} \frac{1}{2!} \sum_{i=1}^{2} \varphi_i \delta_i^2 + u_{xxx} \frac{1}{3!} \sum_{i=1}^{2} \varphi_i \delta_i^3 + \dots \tag{4.27}$$

As interest lies in the first-order derivative, by rearranging the above we have that,

$$u_x \sum_{i=1}^{2} \varphi_i \delta_i = \sum_{i=1}^{2} \varphi_i u_i - u \sum_{i=1}^{2} \varphi_i - u_{xx} \frac{1}{2!} \sum_{i=1}^{2} \varphi_i \delta_i^2 - u_{xxx} \frac{1}{3!} \sum_{i=1}^{2} \varphi_i \delta_i^3 - \dots \tag{4.28}$$

Since we know all the terms in the summations these may be evaluated. Using Mathematica, [59], to do this, Equation (4.28) is found to reduce to,

$$u_x = \sum_{i=1}^{2} \varphi_i u_i + x u_{xx} - \frac{1}{24}(h^2 + 12x^3) u_{xxx} + \mathrm{O}(h^3). \tag{4.29}$$

The right-hand side of Equation (4.29) can therefore be thought of as an approximation to the derivative u_x when truncated at some point. Upon inspection it can be seen that the summation is in fact the derivative of the interpolant to u as given by Equation (4.24). Thus it can be seen that Equation (4.24) is an $\mathrm{O}(h)$ approximation to u_x since we know that $-h/2 \leq x \leq h/2$ for $x \in \Omega_k$. It is important to note here that, at specific points in the element, the order of approximation can be higher. In this particular case it can be seen that by evaluating Equation (4.29) at $x = 0$, the $\mathrm{O}(h)$ term is effectively knocked out, resulting in,

$$u_x = \sum_{i=1}^{2} \varphi_i u_i - \frac{h^2}{24} u_{xxx} + \mathrm{O}(h^3), \tag{4.30}$$

which is an $\mathrm{O}(h^2)$ approximation to u_x. It has thus been shown that at certain points in the element the order of accuracy of the approximation may be higher. This has been done by establishing a suitable sampling point which, in the case of the linear one-dimensional element, lies at the element centre as shown in Figure (4.3) by the $\star$ symbol. Exactly the same analysis may be applied to the quadratic one-dimensional element as shown in [33]. In this case it is found that, by taking the element to be the reference element $[-1, 1]$, the optimal sampling points lie at positions $x = \pm 1/\sqrt{3}$. At this juncture it should be noted that the optimal sampling points detailed thus far for both the linear and quadratic one-dimensional elements lie at exactly the Gauss points for the unmodified one and two point quadrature schemes respectively as detailed in Section (3.9.2).

Introduction of the Irregular Node

The one-dimensional analogue of the transition element involves the introduction of a node at the centre of the element. Thus the original element of Figure (4.3) will now have three nodes as

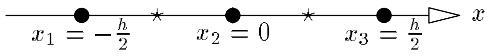

Figure 4.4: One-dimensional modified reference element Ω_k of length $h = x_3 - x_1$.

illustrated in Figure (4.4). In accordance with the shape function modification of Section (3.9.1) the linearly independent shape functions for the three nodes are now given as,

$$
\begin{aligned}
\phi_1(x) &= \frac{1}{h}\left(\frac{h}{2} - x\right) - \frac{1}{h}\left(\frac{h}{2} - |x|\right), \\
\phi_2(x) &= \frac{2}{h}\left(\frac{h}{2} - |x|\right), \\
\phi_3(x) &= \frac{1}{h}\left(\frac{h}{2} + x\right) - \frac{1}{h}\left(\frac{h}{2} - |x|\right).
\end{aligned}
$$

Proceeding with the same analysis as detailed for the standard linear element, the following expression for the derivative is obtained,

$$
u_x \sum_{i=1}^{3} \varphi_i \delta_i = \sum_{i=1}^{3} \varphi_i u_i - u \sum_{i=1}^{3} \varphi_i - u_{xx}\frac{1}{2!}\sum_{i=1}^{3} \varphi_i \delta_i^2 - u_{xxx}\frac{1}{3!}\sum_{i=1}^{3} \varphi_i \delta_i^3 - \ldots \tag{4.31}
$$

which is similar to that of Equation (4.28) but now with three shape functions in each summation. It is important to note, however, that due to the presence of the $|x|$ terms in the shape functions, the element must now be split into 'zones'. By doing this the $|x|$ terms can be given a value of $\pm x$ which then enables the differentiation of the shape functions to be made easily. In the current case there will be two zones, zone 1 for $x < 0$ and zone 2 for $x > 0$. Due to the fact that there may well be a slope discontinuity at $x = 0$ arising from the additional node, a value for the derivative may not exist at that point.

Consider zone 1, in this zone $|x| = -x$ and so Equation (4.31) has the form,

$$
u_x = \sum_{i=1}^{3} \varphi_i u_i + \left(x + \frac{h}{4}\right) u_{xx} - \frac{1}{24}\left(h^2 + 6hx + 12x^2\right) u_{xxx} + \mathrm{O}(h^3).
$$

Again we can see that at $x = -h/4$ the above summation will be an $\mathrm{O}(h^2)$ approximation to u_x. Similarly, for the zone 2 in which $|x| = x$, Equation (4.31) has the form,

$$
u_x = \sum_{i=1}^{3} \varphi_i u_i + \left(x - \frac{h}{4}\right) u_{xx} - \frac{1}{24}\left(h^2 - 6hx + 12x^2\right) u_{xxx} + \mathrm{O}(h^3).
$$

At $x = h/4$ the summation will again be $\mathrm{O}(h^2)$ accurate. It has thus been shown that, by the addition of the extra node onto the one-dimensional linear reference element $[-1, 1]$, the optimal sampling point at $x = 0$ has changed to two optimal sampling points at $x = \pm 1/2$ for the case where $h = 2$ as shown in Figure (4.4). This result is as expected since the modified element in Figure (4.4) acts as two linear elements each of which share the node at $x = x_2$. Since it has previously been established that the optimal sampling point for the standard element was at the element centre it is entirely consistent that the sampling points for the two zones 1 and 2 lie at the centres of each linear zone. It is of importance to note that a 'points doubling' is evident here as similarly detailed in the quadrature modification of Section (3.9.2).

Two-Dimensional Analysis

The analysis will now be performed on the quadrilateral reference element with bilinear shape functions as described at the beginning of Section (3.8). Such an element has side lengths h, has four nodes and is centred on the origin. The optimal sampling points are well known for the this element and [69] for example states that such a point resides at the element centroid. This result will now be verified before extending the investigation as in the one-dimensional case to problems in the transition element family. As in the case of the one-dimensional analysis, the value of the interpolant $\pi_h u(\mathbf{x})$ to $u(\mathbf{x})$ at any point $\mathbf{x}$ in the element may be expressed as,

$$\pi_h u(\mathbf{x}) = \sum_{i=1}^{4} u(\mathbf{x}_i)\phi_i(\mathbf{x}) \equiv \sum_{i=1}^{4} u_i\phi_i.$$

It follows that the derivative with respect to $j = x$ or y, where $\mathbf{x} \equiv (x,y)^T \in \mathbb{R}^2$, can thus be expressed as,

$$\frac{\partial \pi_h u(\mathbf{x})}{\partial j} = \sum_{i=1}^{4} u_i \frac{\partial \phi_i(\mathbf{x})}{\partial j} \equiv \sum_{i=1}^{4} u_i \varphi_i^j,$$

where now the notation, $\varphi_i^j \equiv \partial\phi_i(\mathbf{x})/\partial j$ for $j = x$ or y has been used. Note here that we are using x and y as coordinate variables. This is simply in order to make the Taylor series analysis clearer in terms of expressing derivatives. The Taylor series expansion of $u(x_i, y_i)$ about a general point (x, y) in the element is given by, using the notation $\delta_i^j \equiv (j_i - j)$ for $j = x$ or y,

$$\begin{aligned} u(x_i, y_i) \equiv u_i \; &= \; u + \delta_i^x u_x + \delta_i^y u_y + \frac{1}{2!}\left[(\delta_i^x)^2 u_{xx} + 2\delta_i^x\delta_i^y u_{xy} + (\delta_i^y)^2 u_{yy}\right] \\ &+ \; \frac{1}{3!}\left[(\delta_i^x)^3 u_{xxx} + 3(\delta_i^x)^2\delta_i^y u_{xxy} + 3\delta_i^x(\delta_i^y)^2 u_{xyy} + (\delta_i^y)^3 u_{yyy}\right] \\ &+ \; \ldots \end{aligned} \tag{4.32}$$

for $i = 1, 2, 3$ or 4. Multiplying Equation (4.32) by φ_i^x and summing each term over the nodes yields,

$$\begin{aligned} \sum_{i=1}^{4}\varphi_i^x u_i \; &= \; u\sum_{i=1}^{4}\varphi_i^x + u_x\sum_{i=1}^{4}\varphi_i^x\delta_i^x + u_y\sum_{i=1}^{4}\varphi_i^x\delta_i^y \\ &+ \; \frac{1}{2!}\left[u_{xx}\sum_{i=1}^{4}\varphi_i^x(\delta_i^x)^2 + u_{xy}2\sum_{i=1}^{4}\varphi_i^x\delta_i^x\delta_i^y + u_{yy}\sum_{i=1}^{4}\varphi_i^x(\delta_i^y)^2\right] \\ &+ \; \frac{1}{3!}\left[u_{xxx}\sum_{i=1}^{4}\varphi_i^x(\delta_i^x)^3 + u_{xxy}3\sum_{i=1}^{4}\varphi_i^x(\delta_i^x)^2\delta_i^y \right. \\ &\qquad\qquad \left. + \; u_{xyy}3\sum_{i=1}^{4}\varphi_i^x\delta_x^i(\delta_i^y)^2 + u_{yyy}\sum_{i=1}^{4}\varphi_i^x(\delta_i^y)^3\right] \\ &+ \; \ldots \end{aligned} \tag{4.33}$$

This can be rearranged as in the one-dimensional case to give, for the x derivative,

$$u_x\sum_{i=1}^{4}\varphi_i^x\delta_i^x \; = \; \sum_{i=1}^{4}\varphi_i^x u_i - u\sum_{i=1}^{4}\varphi_i^x - u_y\sum_{i=1}^{4}\varphi_i^x\delta_i^y$$

$$
\begin{aligned}
& - \frac{1}{2!}\left[u_{xx}\sum_{i=1}^{4}\varphi_i^x\left(\delta_i^x\right)^2 + u_{xy}2\sum_{i=1}^{4}\varphi_i^x\delta_i^x\delta_i^y + u_{yy}\sum_{i=1}^{4}\varphi_i^x\left(\delta_i^y\right)^2\right] \\
& - \frac{1}{3!}\left[u_{xxx}\sum_{i=1}^{4}\varphi_i^x\left(\delta_i^x\right)^3 + u_{xxy}3\sum_{i=1}^{4}\varphi_i^x\left(\delta_i^x\right)^2\delta_i^y\right. \\
& \qquad \left. + u_{xyy}3\sum_{i=1}^{4}\varphi_i^x\delta_x^i\left(\delta_i^y\right)^2 + u_{yyy}\sum_{i=1}^{4}\varphi_i^x\left(\delta_i^y\right)^3\right] \\
& - \ldots
\end{aligned}
\tag{4.34}
$$

Evaluation of the summations yield,

$$u_x = \sum_{i=1}^{4}\varphi_i^x u_i + x u_{xx} - \left(\frac{h^2}{24} + \frac{x^2}{2}\right)u_{xxx} - \frac{1}{8}\left(h^2 - 4y^2\right)u_{xyy} + \mathrm{O}(h^3).$$

It can be seen that along the line $x = 0$ the above summation will be an $\mathrm{O}(h^2)$ approximation to u_x. This result mimics the previous result for the derivative in one-dimension and is not unexpected due to the fact that the bilinear element has a linear profile along any section taken through it parallel to the x-axis. The line $x = 0$ passes through the element centroid and is parallel to the y-axis on the reference element studied, this is often referred to as a 'Gauss line'.

As work is being performed in two dimensions it is natural now to consider the y derivative. The methodology is as above but now Equation (4.32) is multiplied by φ_i^y and each term summed. Upon rearranging, the y derivative is given to be,

$$
\begin{aligned}
u_y\sum_{i=1}^{4}\varphi_i^y\delta_i^y = & \sum_{i=1}^{4}\varphi_i^y u_i - u\sum_{i=1}^{4}\varphi_i^y - u_x\sum_{i=1}^{4}\varphi_i^y\delta_i^x \\
& - \frac{1}{2!}\left[u_{xx}\sum_{i=1}^{4}\varphi_i^y\left(\delta_i^x\right)^2 + u_{xy}2\sum_{i=1}^{4}\varphi_i^y\delta_i^x\delta_i^y + u_{yy}\sum_{i=1}^{4}\varphi_i^y\left(\delta_i^y\right)^2\right] \\
& - \frac{1}{3!}\left[u_{xxx}\sum_{i=1}^{4}\varphi_i^y\left(\delta_i^x\right)^3 + u_{xxy}3\sum_{i=1}^{4}\varphi_i^y\left(\delta_i^x\right)^2\delta_i^y\right. \\
& \qquad \left. + u_{xyy}3\sum_{i=1}^{4}\varphi_i^y\delta_x^i\left(\delta_i^y\right)^2 + u_{yyy}\sum_{i=1}^{4}\varphi_i^y\left(\delta_i^y\right)^3\right] \\
& - \ldots
\end{aligned}
\tag{4.35}
$$

Evaluation of the summations yield,

$$u_y = \sum_{i=1}^{4}\varphi_i^y u_i + y u_{yy} - \frac{1}{8}\left(h^2 - 4x^2\right)u_{xxy} - \left(\frac{h^2}{24} + \frac{x^2}{2}\right)u_{yyy} + \mathrm{O}(h^3).$$

In this case it can be seen that along the line $y = 0$ the above summation is in fact an $\mathrm{O}(h^2)$ approximation to the derivative u_y.

Thus two lines have been identified on the reference element, the line $x = 0$ and the line $y = 0$ which denote superconvergent sampling points for the u_x and u_y derivatives respectively. If a general point is required for both x and y derivatives then the intersection of these two lines must be taken. We thus have the anticipated result that the centroid of the element is the optimal superconvergent sampling point for derivative evaluation in the case of bilinear shape functions.

Transition Element Family

The introduction of midside irregular nodes as discussed in Section (3.9) on the standard bilinear element produces transition elements. It is thus now the aim to apply the Taylor series analysis to such elements in order to predict the optimal sampling points on the family, ranging from 1-irregular to the 3-irregular members. The analysis will follow the same route as in the case for the standard bilinear example in the previous Section. However, care must be taken here - as was done in the one-dimensional case - to establish zones on the element in order to cater for the possible complications arising from the $|x|$ and $|y|$ terms. As detailed previously, the inclusion of such terms in the element shape functions can result in possible slope discontinuities across the element, running between the North and South edges and or the East and West edges and passing through the element centroid. Work will be performed once again on a reference element as illustrated in Figure (3.5).

1-irregular Element

We begin the analysis of the transition elements with the 1-irregular element with additional Northern node as illustrated in Figure (4.5). Due to the presence of the irregular node on the North edge of the element there exists the possibility of a slope discontinuity in the derivative of the interpolant across the line $x = 0$. In order to combat this, we consider the element as consisting of two zones as was done in the one-dimensional case. Figure (4.5) illustrates the choice of zones 1 and 2. The choice of these zones is such that we will be able to give the $|x|$ terms in the element

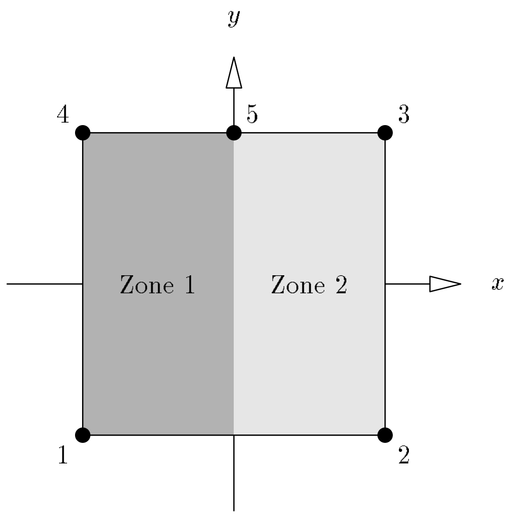

Figure 4.5: Zones 1 and 2 on 1-irregular transition element with Northern irregular node.

shape functions definite values. Thus, in zone 1, inspection of the x derivative yields an equation as given by Equation (4.34) but with summations now over the five shape functions. Upon evaluation of these we obtain,

$$
\begin{aligned}
u_x = & \sum_{i=1}^{5} \varphi_i^x u_i + \frac{1}{8}(h + 8x + 2y)\, u_{xx} - \left(\frac{h^2}{24} + \frac{hx}{8} + \frac{x^2}{2} + \frac{xy}{4}\right) u_{xxx} \\
& - \frac{1}{16}\left(-h^2 + 4y^2\right) u_{xxy} - \frac{1}{8}\left(h^2 - 4y^2\right) u_{xyy} + \mathrm{O}(h^3).
\end{aligned} \tag{4.36}
$$

In a now familiar way, by solving the $\mathrm{O}(h)$ term after the interpolant derivative summation equal to zero, one obtains,

$$
y = -\frac{h}{2} - 4x, \tag{4.37}
$$

which is a line of superconvergent points. By sampling on this line we see that the interpolant derivative is once again an $\mathrm{O}(h^2)$ approximation to u_x. Correspondingly, in zone 2 it is found that,

$$
\begin{aligned}
u_x = & \sum_{i=1}^{5} \varphi_i^x u_i - \frac{1}{8}(h - 8x + 2y)\, u_{xx} - \left(\frac{h^2}{24} - \frac{hx}{8} + \frac{x^2}{2} - \frac{xy}{4}\right) u_{xxx} \\
& - \frac{1}{16}\left(h^2 - 4y^2\right) u_{xxy} - \frac{1}{8}\left(h^2 - 4y^2\right) u_{xyy} + \mathrm{O}(h^3).
\end{aligned} \tag{4.38}
$$

which yields another line of superconvergent sampling points given by,

$$
y = -\frac{h}{2} + 4x. \tag{4.39}
$$

Plots of these lines are included in Figure (4.6). It can be seen that along the south edge of the element we have the normal single optimal point located at the midpoint. As we then sweep up the element this single point splits into two lines given by Equations (4.37) and (4.39). The two lines continue until they meet the North edge of the element. Here they meet the top of zones 1 and 2 at $(-h/4, h/2)$ and $(h/4, h/2)$ respectively. These locations are exactly at the midpoints of the upper edges of zones 1 and 2 which agrees with the results from the one-dimensional analysis which included the irregular node. Such a result seems to be intuitively correct as, along the North edge of the transition element we actually have two linear profiles for which we have previously noted each should have optimal sampling points at their centres. Analysis of the y derivative in zone 1 yields the following,

$$
\begin{aligned}
u_y = & \sum_{i=1}^{5} \varphi_i^y u_i + \frac{1}{8}(h + 2x)\, u_{xx} + y u_{yy} - \frac{1}{8}x\,(h + 2x)\, u_{xxx} \\
& - \frac{1}{16}(h + 2x)(h - 4x + 2y)\, u_{xxy} - \frac{1}{24}\left(h^2 + 12y^2\right) u_{xyy} + \mathrm{O}(h^3).
\end{aligned} \tag{4.40}
$$

Thus for the interpolant derivative to be an $\mathrm{O}(h^2)$ approximation to u_y the sampling point must be at $(-h/2, 0)$ in order to knock out the $\mathrm{O}(h)$ terms. In zone 2 it is found that,

$$
\begin{aligned}
u_y = & \sum_{i=1}^{5} \varphi_i^y u_i - \frac{1}{8}(-h + 2x)\, u_{xx} + y u_{yy} - \frac{1}{8}x\,(h - 2x)\, u_{xxx} \\
& - \frac{1}{16}(h - 2x)(h + 4x + 2y)\, u_{xxy} - \frac{1}{24}\left(h^2 + 12y^2\right) u_{xyy} + \mathrm{O}(h^3).
\end{aligned} \tag{4.41}
$$

Here it can be seen that, for the interpolant derivative to be $\mathrm{O}(h^2)$ accurate, the sampling must be made at position $(h/2, 0)$. Thus the superconvergent line of the standard bilinear element has

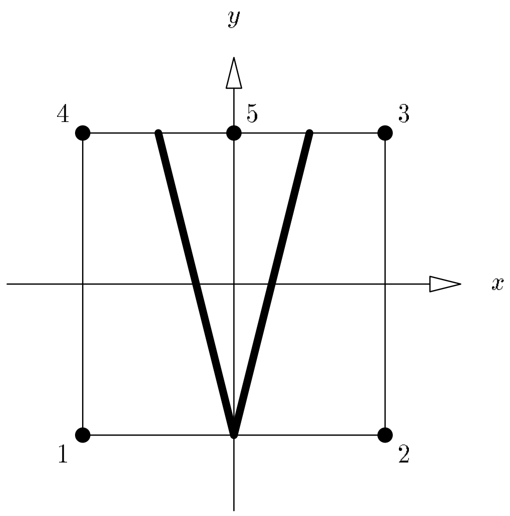

Figure 4.6: Transition element superconvergent lines for the x derivative.

been reduced to two points upon the introduction of the Northern irregular node. If the analysis of Barlow, [14], is applied to this transition element for a class of known u, it is found that there still exists a line of high accuracy sampling points for the y derivative. A typical line for the y derivative is as detailed in Figure (4.7). It can be seen that the line has been affected by the presence of the

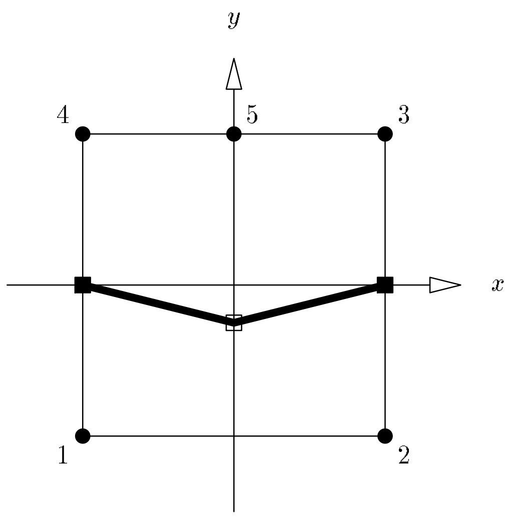

Figure 4.7: 1-irregular transition element high accuracy lines for the y derivative.

irregular node. The point at which the line crosses the y-axis denoted here by an empty box can move along the axis depending upon the function u being interpolated but will always pass through the superconvergent points $(\pm h/2, 0)$ found by the Taylor series analysis and which are denoted by filled boxes. An interesting point to note here is that both of the superconvergent points found for the y derivative lie at exactly the anticipated points along the Eastern and Western edges of the element as the transition element has linear profiles along both of these edges.

2-irregular Elements

The analysis will now be applied to a typical 2-irregular element. Here the configuration of the irregular nodes may either be on adjacent edges or opposite edges. In the former case, consider such an element with irregular nodes on both the North and East edges. For this element we have possibly two lines of slope discontinuity, one running between the North and South edges and the other running between the East and West edges. Consequently, we thus consider the element as having four zones instead of two as in the previous analysis. The four zones are as shown in Figure (4.8). By performing the analysis as detailed in the previous cases, we obtain the results detailed

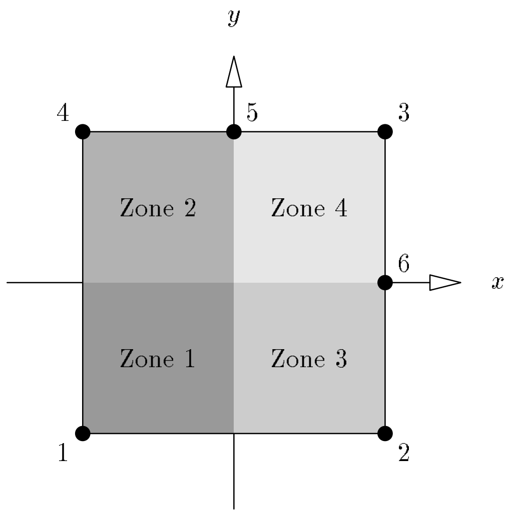

Figure 4.8: Zones 1,2,3 and 4 on 2-irregular transition element with adjacent irregular nodes.

in Table (4.1) for the approximation to the u_x derivative. It can be seen from Table (4.1) that,

Zone	Solutions of O(h) terms = 0	Resulting superconvergent point
1	$y = -\frac{h}{2} - 4x$ and $y = -\frac{h}{2}$	$\left(0, -\frac{h}{2}\right)$
2	$y = -\frac{h}{2} - 4x$ and $y = \frac{h}{2}$	$\left(-\frac{h}{4}, \frac{h}{2}\right)$
3	$y = -\frac{h}{2} + 4x$ and $y = -\frac{h}{2}$	$\left(0, -\frac{h}{2}\right)$
4	$y = -\frac{h}{2} + 4x$ and $y = \frac{h}{2}$	$\left(\frac{h}{4}, \frac{h}{2}\right)$

Table 4.1: Approximation to u_x using 2-irregular transition element with adjacent irregular nodes.

although the familiar lines are still present in the solution of the O(h) terms, there are additional terms which need to be knocked out in order to give a true O(h^2) approximation to the derivative. These combine in each of the four zones to give superconvergent points as seen previously for interpolation of u_y in the 1-irregular transition element case. Inspection of the resulting points in this case yield again expected results on the edges of the element with all superconvergent points lying at the midpoints of their linear portions on the element boundary. Application of the Barlow analysis as described in [14] also yields high accuracy regions. For an example, consider the case when the function being interpolated is simply,

$$u(x, y) = x^2 + y^2. \tag{4.42}$$

Figure (4.9) shows the high accuracy regions on the reference element $[-1, 1] \times [-1, 1]$ which are denoted by dark lines for the derivative u_x. It can be seen from Figure (4.9) that the lines do in

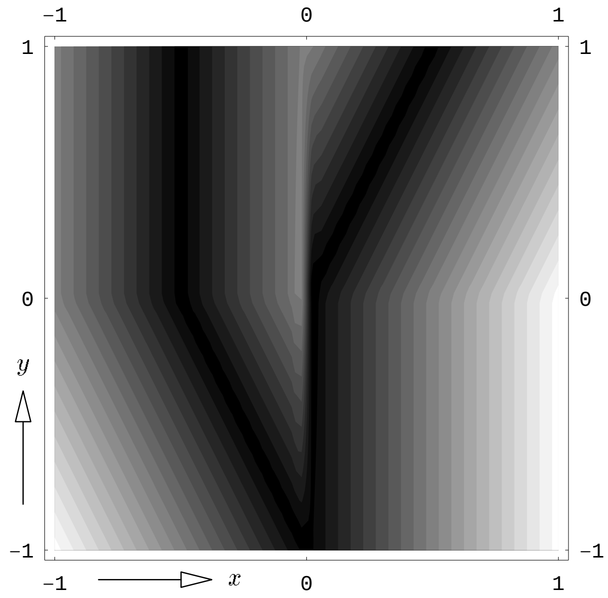

Figure 4.9: High accuracy regions for interpolant to u_x for known u.

fact pass through the predicted superconvergent points of the extended Taylor series analysis. It has been observed that, for varying functions $u(x, y)$ the numerical plots of the Barlow analysis can change but the resulting lines will always pass through the aforementioned superconvergent point locations.

For the derivative u_y, the results are as detailed in Table (4.2) Again it can be seen that there

Zone	Solutions of O(h) terms = 0	Resulting superconvergent point
1	$x = -\frac{h}{2}$ and $y = -\frac{h}{8} - \frac{x}{4}$	$\left(-\frac{h}{2}, 0\right)$
2	$x = -\frac{h}{2}$ and $y = \frac{h}{8} + \frac{x}{4}$	$\left(-\frac{h}{2}, 0\right)$
3	$x = \frac{h}{2}$ and $y = -\frac{h}{8} - \frac{x}{4}$	$\left(\frac{h}{2}, -\frac{h}{4}\right)$
4	$x = \frac{h}{2}$ and $y = \frac{h}{8} + \frac{x}{4}$	$\left(\frac{h}{2}, \frac{h}{4}\right)$

Table 4.2: Approximation to u_y using 2-irregular transition element with adjacent irregular nodes.

are familiar lines which could well be expected in the case of a 1-irregular element with irregular

Eastern node. In addition to these are O(h) terms which force the superconvergent lines to become points as detailed in the last column of Table (4.2). As expected, these superconvergent points lie at the midpoints of the element boundary portions which are linear. The corresponding plots from the Barlow approach for the derivative u_y are as shown in Figure (4.10). It has been observed

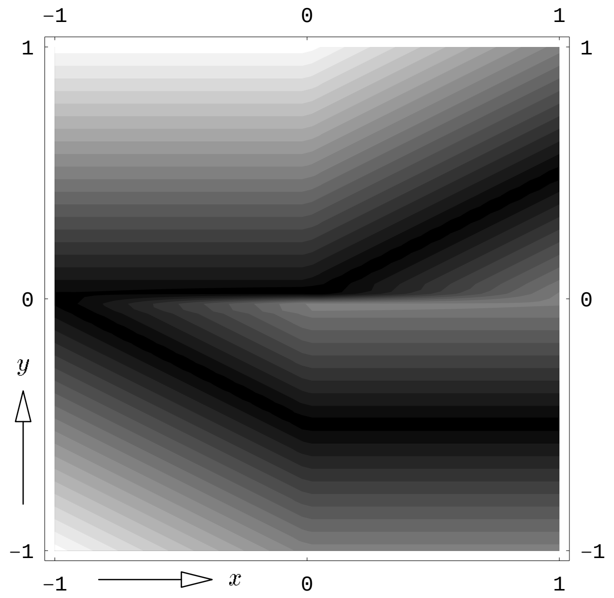

Figure 4.10: High accuracy regions for interpolant to u_y for known u.

again that, for varying $u(x, y)$, the lines may move around but will always pass through the superconvergent points given in Table (4.2). It is interesting to note that there is a strong similarity between Figures (4.9) and (4.10) and the results reported by Babuška et. al. in [9] for certain mesh configurations.

It was mentioned at the beginning of this section dealing with 2-irregular elements that there is also the 2-irregular element with opposing irregular nodes. In this case consider the element with irregular nodes on the North and South edges. In such a scenario it is necessary to split the element into only two zones as depicted in Figure (4.5). By doing this we effectively have two standard bilinear elements placed beside each other. The Taylor series approach then predicts that there will be superconvergent sampling lines for the derivative u_x at locations $x = \pm h/4$ on the element. Similarly for the derivative u_y there is a superconvergent sampling line running across the element at the location $y = 0$. This results in superconvergent sampling points for both the interpolation of u_x and u_y existing at $(\pm h/4, 0)$. Since we effectively have two bilinear elements placed beside each other this result is as expected with a superconvergent point found to exist at the centroid of each 'element'.

3-irregular Element

For this final scenario, consider a typical 3-irregular element with irregular nodes on the North, East and South edges. In this case the element will be once again split into four zones as shown in Figure (4.8). Results for the Taylor series analysis are shown for the derivative u_x in Table (4.3). These results show that for such an element, the interpolant derivative will be $O(h^2)$ accurate at

Zone	Solutions of $O(h)$ terms $= 0$	Resulting superconvergent point
1	$\frac{1}{4}(h+4x)$ and $\frac{1}{8}(h+2y)$	$\left(-\frac{h}{4}, -\frac{h}{2}\right)$
2	$\frac{1}{4}(h+4x)$ and $-\frac{1}{8}(-h+2y)$	$\left(-\frac{h}{4}, \frac{h}{2}\right)$
3	$-\frac{1}{4}(h-4x)$ and $\frac{1}{8}(h+2y)$	$\left(\frac{h}{4}, -\frac{h}{2}\right)$
4	$-\frac{1}{4}(h-4x)$ and $-\frac{1}{8}(-h+2y)$	$\left(\frac{h}{4}, \frac{h}{2}\right)$

Table 4.3: Approximation to u_x for 3-irregular transition element.

certain points on the boundary of the element. These points follow the now familiar pattern having locations at the midpoints of the linear portion of the element boundary upon which they reside. Application of the Barlow analysis for the interpolant to any quadratic $u(x, y)$ in both x and y confirms the locations of these points. Similar observations can be seen here as were seen in the case of the u_y derivative approximation for the 1-irregular transition element. Here though there are two lines of high accuracy as shown in Figure (4.11). It has been observed that, by varying a known function u, the points denoted by the empty squares are free to slide along the x-axis whilst the filled squares remain at the known superconvergent points found by using the Taylor series analysis and detailed in Table (4.3). For the derivative u_y we obtain results as detailed in

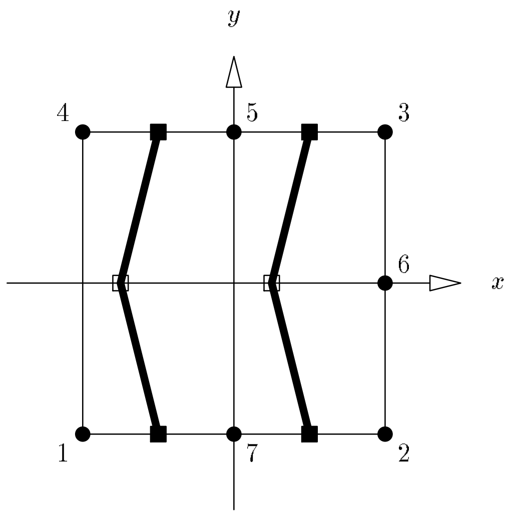

Figure 4.11: 3-irregular transition element high accuracy lines for the x derivative.

Table (4.4). Here we can see that there exist lines as were seen earlier in the analysis. Plots from the Barlow analysis can be seen in Figure (4.12) for the case when the known u is as described

Zone	Solutions of O(h) terms = 0	Resulting superconvergent line
1	$\frac{1}{8}(h+2x+8y)$	$y=-\frac{h}{8}-\frac{x}{4}$
2	$-\frac{1}{8}(h+2x-8y)$	$y=\frac{h}{8}+\frac{x}{4}$
3	$\frac{1}{8}(h+2x+8y)$	$y=-\frac{h}{8}-\frac{x}{4}$
4	$-\frac{1}{8}(h+2x-8y)$	$y=\frac{h}{8}+\frac{x}{4}$

Table 4.4: Approximation to u_y for 3-irregular transition element.

in Equation (4.42), plot (a) shows the high accuracy regions for sampling u_x and (b) for u_y. For plot (a) it is clear that the plotted lines mimic those of Figure (4.11). The plot also shows clearly that the lines pass through the established superconvergent points which on the reference element $[-1,1]\times[-1,1]$ are at locations specified in Table (4.3) with $h=2$. Plot (b) shows that the Barlow results for this particular known u lie on the established superconvergent lines of the Taylor series for the approximation to u_y as given in Table (4.4).

(a)

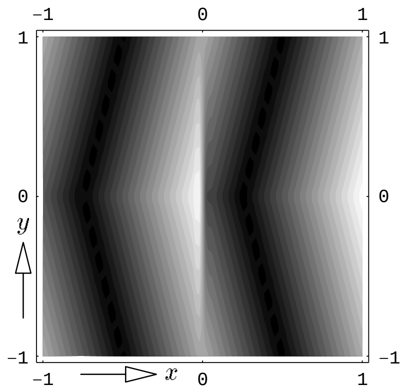

(b)

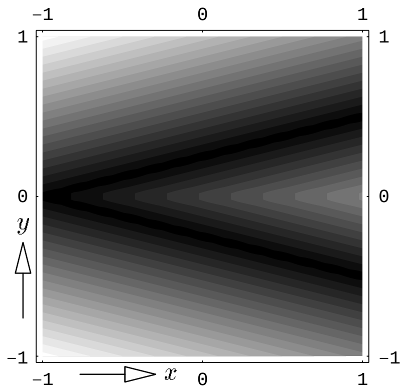

Figure 4.12: High accuracy regions for interpolant, (a) to u_x and (b) to u_y for known u.

For completeness an analysis has also been performed on the 4-irregular element. Having stated that this element will never arise in practice, it is still of interest and may in fact be of use to see what happens to the superconvergent points in such a scenario. It is found that, in such a case the element behaves as if it were four standard bilinear elements placed next to each other with edge length $h/2$. For the approximation to the derivative u_x two lines of superconvergence result. These have the appearance of Gauss lines and are given by $x=\pm h/4$. Similarly, for the u_y derivative approximation, two further lines are found. These reside along the lines $y=\pm h/4$. The two sets of lines combine as in the case of the two Gauss lines for the standard bilinear element to give superconvergent points at the locations $(\pm h/4, \pm h/4)$ for both approximations to the u_x and u_y derivatives.

At this point the transition family of elements has been analysed. In each case an attempt has been made to identify the superconvergent or high accuracy sampling points which exist on the element. In the standard cases we have obtained the expected results but, for the cases where the outcome was unknown, it has been shown that the locations of the sought after points may be strongly affected by the presence of irregular nodes. The aim of this section was to establish the locations of the sampling points for meshes containing transition elements so that a strategy could be built up for the recovery procedure of the Z-Z error estimator. In order to have some automated set of rules it is inevitable that compromises in some areas may have to be made so that the algorithm, which rapidly becomes complicated by these considerations, does not become cumbersome and inefficient. As mentioned at the beginning of this section it has been reported by previous researchers that for the standard quadrilateral element the optimal locations for sampling stresses or derivatives are at the reduced integration Gauss points. Indeed, results of this section have shown this to be true and for the case of transition elements this is also true for certain node configurations. We thus proceed to describe the resulting algorithms for the recovery procedure on meshes containing transition elements.

4.3.2 Element Patch Strategies for Non-Symmetric Meshes

In the previous section it was established that for the standard elements in both one and two dimensions the optimal sampling points lie on the reduced integration points of the element. This is in agreement with previous research findings and means that for uniform meshes of quadrilateral elements employing bilinear shape functions the sampling point locations for a typical element patch are clearly defined to lie at the centroids of the elements forming the patch. For the case of transition elements the findings were mixed with some node configurations yielding optimal sampling points at the modified reduced integration points for transition elements whilst in other cases the agreement was found to be not as strong. In such cases where the agreement was less conclusive however, it is felt that sampling can still be made at the modified reduced integration points as the samples here are of a higher accuracy due to their close proximity to the optimal areas. This means that an improvement can still be expected for the recovered stresses or gradients at the nodes although there will be no guarantee of superconvergence. What now follows is the patch assembly node algorithm which will detail how the assembly nodes are determined for each node n where the stresses or gradients are to be recovered. It will be seen that sometimes the node where recovery is desired and the patch assembly node coincide but this is by no means true for all nodes. In fact the only case where the two always coincide will be for the nodes of a uniform mesh which do not lie on the boundary $\partial\Omega$ of the problem domain.

Patch Assembly Node Assignment

Before proceeding it may be necessary to define the meaning of some terms. For a typical node n say, the term 'surrounding nodes' means the nodes of all the elements who share n. Alternatively, the term 'neighbouring nodes' are those nodes connected to n by an element edge. Further, if node n has element count four then this means that there are four elements surrounding n and will be denoted in the algorithm as elcount(n) $= 4$. A final point to note is that any irregular mid-side node will always have element count equal to three.

This algorithm details the identification of the patch assembly node. This will be referred to as the p.a.n. during the algorithm. It is worth noting that, for all nodes $n = 1, \ldots, N$ a patch assembly node must be identified.

1. For node n, compute elcount(n) and store element numbers, Element1 to Element4 maximum.
2. If elcount(n) ≥ 3 then p.a.n. $= n$.
   - Stop if $n = N$ or increment n and return to Step 1.
3. Arrive here if elcount(n) equals one (or two).
   Count number of irregular nodes on the surrounding element(s), Element1 (and Element2). Label as Nodes1 (and Nodes2) for the one (or two) possible surrounding element(s).
4. If elcount(n) $= 1$ and Nodes1 $= 2$ then p.a.n. $= n$.
   - Stop if $n = N$ or increment n and return to Step 1.
5. Compute surrounding nodes $m = 1, \ldots, p$ for node n and elcount(m) for $m = 1, \ldots, p$.
6. Loop over $m = 1, \ldots, p$. If elcount(m) $= 3$ and $m \notin \partial\Omega$ then,
   (a) If elcount(n) $= 1$ then p.a.n. $= m$.
      - Stop if $n = N$ or increment n and return to Step 1.

   (b) If elcount(n) $= 2$ then,

   (c) If m is a neighbour of n then p.a.n. $= m$.
      - Stop if $n = N$ or increment n and return to Step 1.
7. Arrive here if there are no suitable irregular nodes in the surrounding node set.
8. Establish node r where elcount(r) $= \max(elcount(m))$ for $m = 1, \ldots, p$.
9. If elcount(n) $= 1$ then p.a.n. $= r$.
   - Stop if $n = N$ or increment n and return to Step 1.
10. If elcount(n) $= 2$ then there may be more than one node with element count equal to elcount(r).

11. Select from short list the node which is a neighbour of node n. If this is node q say then p.a.n. $= q$.
    - Stop if $n = N$ or increment n and return to Step 1.

The above algorithm will identify the patch assembly nodes for all nodes $n = 1, \ldots, N$. A few comments may now clarify some of the less obvious points. If the element count for node n is initially found to be three or more then the patch assembly node is trivially n itself as stated in Step 2 of the algorithm. This is due to the fact that, for the case where elcount(n)=4, the patch consists of the surrounding elements and the possibility that some of these may or may not be transition elements does not matter as samples are made on particular zones of such elements. For the case where elcount(n)=3, this means that n is an irregular node. Due to the fact that we will be sampling at the reduced integration points for the recovery scheme, two samples will come from the transition element and one from each of the other two elements. Figure (4.13) shows these two scenarios in parts (a) and (b) respectively. In both cases the patch assembly node is ringed,

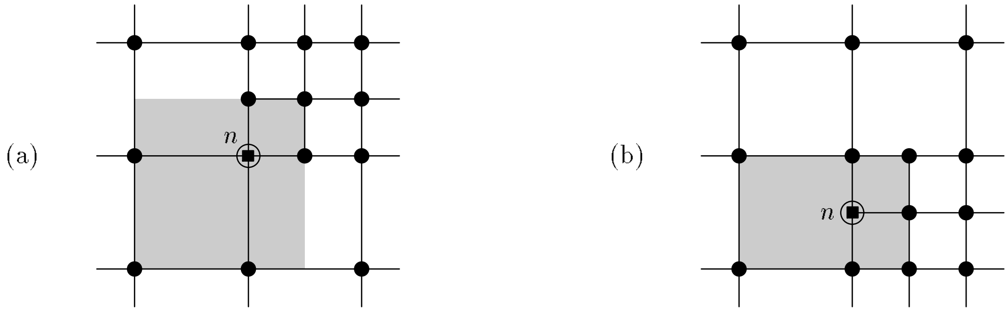

Figure 4.13: Patch examples for node n where (a) elcount(n) = 4 and (b) elcount(n) = 3.

the current node n is denoted by a filled square and the patches are also shown as shaded areas for clarity. It can be seen in Figure (4.13) that in these two instances the patch assembly node coincides with node n. This will always be the case for elcount(n) = 4 and elcount(n) = 3 with n an irregular node.

For elcount(n) = 1 or elcount(n) = 2 the situation is different. As can be seen from the algorithm if there is only one element surrounding node n then we have that node n is a corner node. In such a scenario the number of irregular nodes on the element becomes important. If there is only one irregular node we proceed through the algorithm but for the case where there are two such irregular nodes then we have the situation depicted in part (a) of Figure (4.14) and at Step 4 of the algorithm. Again the patch assembly node is node n but the patch chosen is simply the 2-irregular transition element as shown. This is due to the fact that there are four zones on such an element, as shown in Figure (4.8) of Section (4.3.1), which yield a valid sampling point each from the reduced integration points. Proceeding through the algorithm, the next situation which can arise is that the element count for node n is one and the element is a 1-irregular element. In such a scenario the irregular node is chosen as the patch assembly node as instructed in Step 6(a) of the algorithm. This is also indicated in part (a) of Figure (4.14) by broken rings depending

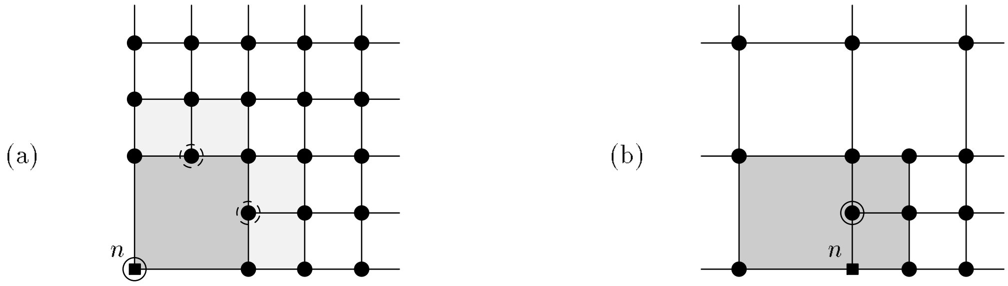

Figure 4.14: Patch examples for node n where (a) elcount(n) = 1 with two irregular nodes and (b) elcount(n) = 2 with a suitable neighbour.

upon whether the 1-irregular corner transition element has irregular Northern or Eastern node. In addition, lighter shading is extended around both possible patch assembly nodes which will give patch configurations of the type illustrated in part (b) of Figure (4.13) when taken in union with the darker shaded region.

For the case depicted in part (b) of Figure (4.14) it can be seen that node n has element count equal to two. This means that n must also lie on the boundary of the problem domain but in this case on a side of the domain. Although at first glance this looks the same as that shown in part (b) of Figure (4.13) it can be seen on closer inspection that this is not the case. In this situation n is now a boundary node and the algorithm states in Step 6(c) that if any of the surrounding nodes which have element count equal to three and do not lie on the boundary are also neighbours of node n then they are chosen as the patch assembly node. This is shown in part (b) of Figure (4.14) with the ringed patch assembly node lying in the domain interior as required.

We now arrive at the final steps of the algorithm. At Step 7 we have established, by a process of elimination, that there are no suitable irregular nodes in the surrounding elements which may be used as patch assembly nodes. The process now embarks on establishing which node of the surrounding node set has the largest element count. If the element count for node n is one then the patch assembly node is then the surrounding node with largest element count. For the case where the mesh is locally uniform in the area of the corner node n, this means that the node diagonally opposing n with element count equal to four is chosen as the patch assembly node. This can be envisaged by imagining that, in part (a) of Figure (4.15), the top right element has not been refined. In this instance the patch will consist of the four corner elements all of which have same edge length. For the case where the top right element has been refined however part (a) of Figure (4.15) depicts exactly the choice made. It can be seen here that the node n is a corner node and the patch assembly node is again the diagonally opposing node. Although this patch choice is the same as that shown in part (a) of Figure (4.13) it is worth noting that in each situation the fit made to the sample points is evaluated at different positions, namely the positions of node n. A typical mesh scenario for reaching Step 10 in the algorithm can be seen in part (b) of Figure (4.15). Here it can be seen that none of the irregular nodes are neighbours of node n. The resulting patch assembly node is then chosen by finding the maximum of all element counts of the surrounding

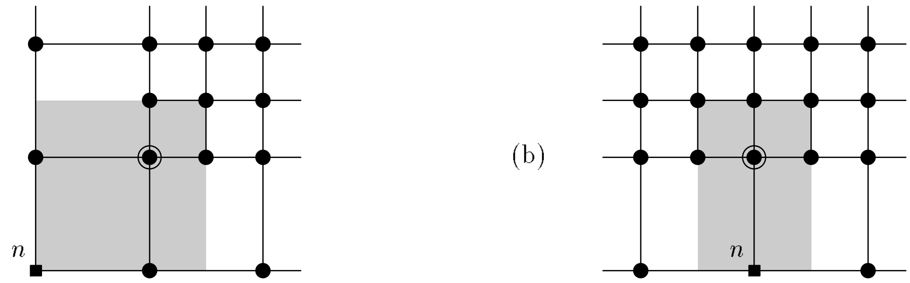

Figure 4.15: Patch examples for node n where (a) elcount(n) = 1 and (b) elcount(n) = 2. Both cases have no suitable neighbouring irregular node.

nodes as done in the previous case but this time selecting the one which is a neighbour of node n.

4.4 The Johnson-Hansbo Error Estimator

An illustration of the a posteriori error estimator of Johnson and Hansbo, [27], will now be presented for linear elasticity in two dimensions. Such a problem has been chosen here due to the fact that the resulting estimator formulation will then be enhanced to cater for meshes containing possible transition elements. Finally an adaptation to plate theory will be proposed.

In [27], the scene is set by considering a boundary value problem $\mathcal{P}$ with given data f and corresponding exact solution u. We then have that $\mathcal{P}_{h,p}$ is a finite element method for $\mathcal{P}$ based on piecewise polynomial approximation on a family $\{\Upsilon_{h,p}\}$ of meshes with characteristic mesh size $h = h(\mathbf{x})$ and local order $p = p(\mathbf{x})$ of the polynomial approximations as functions of space $\mathbf{x}$. Such a family of meshes will produce a corresponding family of finite element solutions $\{u_{h,p}\}$. The task is then to construct an algorithm for finding a mesh $\Upsilon_{h,p}$ such that, for the corresponding finite element solution $u_{h,p}$,

$$||u - u_{h,p}|| \leq \text{TOL},$$

where TOL > 0 is a given error tolerance and the work to compute $u_{h,p}$ is 'nearly minimal' as stated in [27]. In developing such algorithms, it is essential to develop robust error estimates. The error estimates of Johnson and Hansbo which shall be referred to as the Johnson-Hansbo error estimates are based upon a posteriori estimates of the form,

$$||u - u_{h,p}|| \leq E_1(h, p, u_{h,p}, f),$$

where the error $||u - u_{h,p}||$ is estimated in terms of a directly computable quantity $E_1(h, p, u_{h,p}, f)$. It will be shown that the Johnson-Hansbo estimator is a residual based estimator. These residual quantities provide a measure of how much the approximate finite element solution $u_{h,p}$ fails to satisfy the governing differential equations or equivalently 'the deviation from equality obtained by inserting $u_{h,p}$ into the given continuous equation' as described in [27].

It will be seen that two types of constant will arise in the derivation of the error estimates. These are the interpolation error constants and will be denoted by $C^i_{1,k}$ and $C^i_{2,k}$ for a typical element Ω_k. These constants arise from the analysis of local polynomial interpolation error on the element and depend on the shape of the element and the local order of the polynomial approximation used in the finite element method. The difference between $C^i_{1,k}$ and $C^i_{2,k}$, as detailed by their subscripts 1 and 2 respectively, is that they are concerned with interpolation error on the interior and boundary of element Ω_k respectively. It is stated in [27] that these constants may be determined computationally, this will be performed in Chapters 5 and 6.

In preparation for the following sections we now recap on the definitions of Section (3.1). The L_q-norm of a vector valued function $\mathbf{v}(\mathbf{x}) \in [L_q(\Omega)]^n$ is defined as,

$$||\mathbf{v}(\mathbf{x})||_{L_q(\Omega)} = \left[\sum_{i=1}^{n} ||v_i(\mathbf{x})||^q_{L_q(\Omega)} \right]^{\frac{1}{q}},$$

where, as usual, for the scalar valued function $v_i(\mathbf{x})$,

$$||v_i(\mathbf{x})||^q_{L_q(\Omega)} = \int_\Omega |v_i(\mathbf{x})|^q \, d\mathbf{x}.$$

In addition we shall also be meeting here the norm,

$$||\mathbf{v}(\mathbf{x})||_{L_q(\partial\Omega)} = \left[\sum_{i=1}^{n} ||v_i(\mathbf{x})||^q_{L_q(\partial\Omega)} \right]^{\frac{1}{q}},$$

for $\mathbf{v}(\mathbf{x}) \in [L_q(\partial\Omega)]^n$ where again we have, for $v_i(\mathbf{x})$ the norm,

$$||v_i(\mathbf{x})||^q_{L_q(\partial\Omega)} = \int_{\partial\Omega} |v_i(\mathbf{x})|^q \, ds.$$

Let Ω be a domain in $\mathbb{R}^m$ with boundary $\partial\Omega$, for the case of linear elasticity it will be true that $n = m = 2$ or 3 for problems in two or three dimensions respectively. For the case of plates however, it has been seen that $m = 2$ whilst $n = 5$ and thus for generality we make the possible distinction here. In the above we have defined the space $L_q(\partial\Omega)$. To explain this, consider the case when $m = 2$ and $g \in L_q(\partial\Omega)$. It is then possible to express a point with coordinates $\mathbf{x} \equiv (x, y)$ on $\partial\Omega$ in terms of a parameter t as,

$$x = \phi(t), \quad y = \delta(t), \qquad a \leq t \leq b.$$

Then, since $g \in L_q(\partial\Omega)$, we know

$$||g(\mathbf{x})||^2_{L_2(\partial\Omega)} = \int_{\partial\Omega} |g(\mathbf{x})|^2 \, ds \equiv \int_a^b |g(\phi(t), \delta(t))|^2 \sqrt{(\phi'(t))^2 + (\delta'(t))^2} \, dt,$$

where,

$$ds = \sqrt{(\phi'(t))^2 + (\delta'(t))^2} \quad dt.$$

4.4.1 Problem Definition - Elasticity Recap

To illustrate the Johnson-Hansbo estimator we shall consider linear elasticity in two dimensions. As detailed in Chapter 2 the problem may be expressed as one in which it is required to find the displacement $\mathbf{u} = \{u_i\}_{i=1}^2$ such that,

$$-\text{div}\,\boldsymbol{\sigma}(\mathbf{u}(\mathbf{x})) = \mathbf{f}(\mathbf{x}) \quad \text{for } \mathbf{x} \in \Omega,$$

with boundary conditions,

$$\mathbf{u}(\mathbf{x}) = \mathbf{0} \quad \text{for } \mathbf{x} \in \partial\Omega_C,$$

and,

$$\boldsymbol{\sigma}(\mathbf{u}(\mathbf{x})) \cdot \mathbf{n} = \mathbf{g} \quad \text{for } \mathbf{x} \in \partial\Omega_T,$$

where, to recap, Ω is a bounded domain in $\mathbb{R}^2$ with boundary $\partial\Omega \equiv \partial\Omega_C \cup \partial\Omega_T$, $\mathbf{f} \in [L_2(\Omega)]^2$ and $\mathbf{g} \in [L_2(\partial\Omega_T)]^2$ are given loads, $\mathbf{n}$ is the unit outward normal to $\partial\Omega_T$, $\boldsymbol{\sigma}$ is the symmetric stress tensor given by $\boldsymbol{\sigma} = (\sigma_{ij})_{i,j=1}^2$, $\text{div}\,\boldsymbol{\sigma}$ is expressed as,

$$\text{div}\,\boldsymbol{\sigma} = \left(\sum_{j=1}^{2} \frac{\partial \sigma_{ij}}{\partial x_j}\right)_{i=1}^{2} \quad \text{and} \quad \boldsymbol{\sigma}\cdot\mathbf{n} = \left(\sum_{j=1}^{2} \sigma_{ij} n_j\right)_{i=1}^{2}.$$

The relationship between stress and strain is given by the previously defined Hooke's law of Equation (2.20) and which may be expressed as,

$$\boldsymbol{\sigma}(\mathbf{u}(\mathbf{x})) = \lambda\,\mathbf{I}\,\text{div}\,\mathbf{u}(\mathbf{x}) + 2\mu\varepsilon(\mathbf{u}(\mathbf{x})),$$

where λ and μ are again the Lamé coefficients, $\mathbf{I} = (\delta_{ij})_{i,j=1}^2$ is the identity tensor with $\delta_{ij} = 1$ if $i = j$ and zero otherwise and $\text{div}\,\mathbf{u}$ is expressed as,

$$\text{div}\,\mathbf{u} = \sum_{i=1}^{2} \frac{\partial u_i}{\partial x_i},$$

where it is important to note the differing result from application of the divergence operator 'div' on tensors and vectors. As derived in Section (3.2), the variational formulation of this problem is one in which we seek to find $\mathbf{u} \in V$ where,

$$V = \left\{\mathbf{v} \in \left[H^1(\Omega)\right]^2 : \mathbf{v} = \mathbf{0} \text{ on } \partial\Omega_C\right\},$$

such that,

$$a(\mathbf{u},\mathbf{v}) = F(\mathbf{v}) \quad \forall\, \mathbf{v} \in V, \tag{4.43}$$

where,

$$a(\mathbf{u},\mathbf{v}) = \int_\Omega \lambda \text{div}\,\mathbf{u}\,\text{div}\,\mathbf{v} + 2\mu \sum_{i,j=1}^{2} \varepsilon_{ij}(\mathbf{u})\varepsilon_{ij}(\mathbf{v})\,d\mathbf{x}, \tag{4.44}$$

and,

$$F(\mathbf{v}) = \int_\Omega \mathbf{f}\cdot\mathbf{v}\,d\mathbf{x} + \int_{\partial\Omega_T} \mathbf{g}\cdot\mathbf{v}\,ds. \tag{4.45}$$

By defining,

$$\varepsilon(\mathbf{u}) : \varepsilon(\mathbf{v}) = \sum_{i,j=1}^{2} \varepsilon_{ij}(\mathbf{u})\varepsilon_{ij}(\mathbf{v}),$$

Equation (4.44) may be expressed as,

$$a(\mathbf{u}, \mathbf{v}) = \int_{\Omega} \lambda \mathrm{div}\, \mathbf{u}\, \mathrm{div}\, \mathbf{v} + 2\mu\varepsilon(\mathbf{u}) : \varepsilon(\mathbf{v})\, d\mathbf{x} = \int_{\Omega} \boldsymbol{\sigma}(\mathbf{u}) : \varepsilon(\mathbf{v})\, d\mathbf{x}. \tag{4.46}$$

As performed in [27], consider the finite element subdivision $\Upsilon_{h,p}$ of Ω into non-overlapping elements Ω_k of size $h = h_k$. In addition, for each element $\Omega_k \in \Upsilon_{h,p}$ let there exist a positive integer p_k and also let $P_{p_k}(\Omega_k)$ be a space of polynomials on Ω_k containing the set of polynomials over Ω_k of degree at most p_k then the finite element space is given as,

$$V_{h,p} = \left\{ \mathbf{v}_{h,p} \in V : \mathbf{v}_{h,p} \text{ is continuous on } \Omega, \mathbf{v}_{h,p}|_{\Omega_k} \in [P_{p_k}(\Omega_k)]^2\ \forall\ \Omega_k \in \Upsilon_{h,p} \right\},$$

which will be of use in the following section. The approximating finite element formulation is thus one in which it is required to find $\mathbf{u}_{h,p} \in V_{h,p}$ such that,

$$a(\mathbf{u}_{h,p}, \mathbf{v}_{h,p}) = F(\mathbf{v}_{h,p}) \quad \forall\ \mathbf{v}_{h,p} \in V_{h,p}. \tag{4.47}$$

Since Equation (4.43) holds for all $\mathbf{v} \in V$ then it must also hold for $\mathbf{v}_{h,p} \in V_{h,p} \subset V$. Thus it is true that,

$$a(\mathbf{u}, \mathbf{v}_{h,p}) = F(\mathbf{v}_{h,p}) \quad \forall\ \mathbf{v}_{h,p} \in V_{h,p}. \tag{4.48}$$

We are thus able to subtract Equation (4.47) from (4.48) giving the orthogonality condition,

$$a(\mathbf{u} - \mathbf{u}_{h,p}, \mathbf{v}_{h,p}) = 0 \quad \forall\ \mathbf{v}_{h,p} \in V_{h,p}, \tag{4.49}$$

which will be of use in the error analysis of the next section.

In the following section we will drop the subscript p due to the fact that the polynomial degree in our finite element formulation will remain constant. In addition it is necessary to define at this point the set S of edges s of quadrilaterals $\Omega_k \in \Upsilon_h$ which are contained in $\Omega \setminus \partial\Omega$ and, for each edge $s \in S$ common to two elements we define $\mathbf{n}_s$ to be the unit outward normal to s.

4.4.2 Energy Norm Error Estimate

We define the finite element error $\mathbf{e}$ in the usual way as the difference between the true solution and the finite element solution expressed as,

$$\mathbf{e} = \mathbf{u} - \mathbf{u}_h.$$

From our definition of $a(\mathbf{u}, \mathbf{v})$ we may define the energy norm squared of the error $\mathbf{e}$ taken over problem domain Ω as,

$$||\mathbf{e}||^2_{E(\Omega)} = a(\mathbf{e}, \mathbf{e}) = a(\mathbf{u} - \mathbf{u}_h, \mathbf{e}) = a(\mathbf{u} - \mathbf{u}_h, \mathbf{e} - \pi_h \mathbf{e}), \tag{4.50}$$

using the orthogonality condition of Equation (4.49) with $\mathbf{v}_h = \pi_h \mathbf{e} \in V_h$. Thus,

$$||\mathbf{e}||^2_{E(\Omega)} = a(\mathbf{u}, \mathbf{e} - \pi_h \mathbf{e}) - a(\mathbf{u}_h, \mathbf{e} - \pi_h \mathbf{e}),$$

which, by using Equation (4.43) with $\mathbf{v} = \mathbf{e} - \pi_h \mathbf{e} \in V$ enables the error to be written as,

$$||\mathbf{e}||^2_{E(\Omega)} = F(\mathbf{e} - \pi_h \mathbf{e}) - a(\mathbf{u}_h, \mathbf{e} - \pi_h \mathbf{e}). \tag{4.51}$$

From Equation (4.45) we have, with $\mathbf{v} = \mathbf{e} - \pi_h \mathbf{e} \in V$,

$$F(\mathbf{e} - \pi_h \mathbf{e}) = \int_\Omega \mathbf{f} \cdot (\mathbf{e} - \pi_h \mathbf{e})\, d\mathbf{x} + \int_{\partial \Omega_T} \mathbf{g} \cdot (\mathbf{e} - \pi_h \mathbf{e})\, ds. \tag{4.52}$$

Similarly, with Equation (4.46) we have, substituting for the finite element solution and the interpolation error,

$$-a(\mathbf{u}_h, \mathbf{e} - \pi_h \mathbf{e}) = -\int_\Omega \boldsymbol{\sigma}(\mathbf{u}_h) : \varepsilon(\mathbf{e} - \pi_h \mathbf{e})\, d\mathbf{x}.$$

Consider the subdivision Υ_h of Ω into N non-overlapping quadrilateral elements Ω_k each of size h_k. Equation (4.51) may thus be expressed in terms of elements as,

$$||\mathbf{e}||^2_{E(\Omega)} = \sum_{k=1}^N \int_{\Omega_k} \mathbf{f} \cdot (\mathbf{e} - \pi_h \mathbf{e})\, d\mathbf{x} + \int_{\partial \Omega_T} \mathbf{g} \cdot (\mathbf{e} - \pi_h \mathbf{e})\, ds - \sum_{k=1}^N \int_{\Omega_k} \boldsymbol{\sigma}(\mathbf{u}_h) : \varepsilon(\mathbf{e} - \pi_h \mathbf{e})\, d\mathbf{x}. \tag{4.53}$$

Integrating the last integral above using Green's formula given in [19] as,

$$\int_\Omega u \frac{\partial v}{\partial x_i}\, dx = -\int_\Omega \frac{\partial u}{\partial x_i} v\, dx + \int_{\partial \Omega} u\, v\, n_i\, ds,$$

where n_i is the ith component of the unit outward normal to $\partial\Omega$, we obtain,

$$-\sum_{k=1}^N \int_{\Omega_k} \boldsymbol{\sigma}(\mathbf{u}_h) : \varepsilon(\mathbf{e} - \pi_h \mathbf{e})\, d\mathbf{x} = \sum_{k=1}^N \int_{\Omega_k} \operatorname{div} \boldsymbol{\sigma}(\mathbf{u}_h) \cdot (\mathbf{e} - \pi_h \mathbf{e})\, d\mathbf{x} - \sum_{k=1}^N \int_{\partial \Omega_k} \boldsymbol{\sigma}(\mathbf{u}_h) \cdot \mathbf{n}_k \cdot (\mathbf{e} - \pi_h \mathbf{e})\, ds.$$

Substituting this into Equation (4.53) and rearranging gives,

$$\begin{aligned} ||\mathbf{e}||^2_{E(\Omega)} = & \sum_{k=1}^N \int_{\Omega_k} (\mathbf{f} + \operatorname{div} \boldsymbol{\sigma}(\mathbf{u}_h)) \cdot (\mathbf{e} - \pi_h \mathbf{e})\, d\mathbf{x} + \int_{\partial \Omega_T} \mathbf{g} \cdot (\mathbf{e} - \pi_h \mathbf{e})\, ds \\ & - \sum_{k=1}^N \int_{\partial \Omega_k} \boldsymbol{\sigma}(\mathbf{u}_h) \cdot \mathbf{n}_k \cdot (\mathbf{e} - \pi_h \mathbf{e})\, ds, \end{aligned} \tag{4.54}$$

where $\mathbf{n}_k$ denotes the *unit outward normal* to the boundary $\partial\Omega_k$ of $\Omega_k \in \Upsilon_h$, and where,

$$\boldsymbol{\sigma} \cdot \mathbf{n} = \left(\sum_{j=1}^2 \sigma_{ij} n_j \right)_{i=1}^2, \tag{4.55}$$

is the stress on a boundary with unit outward normal $\mathbf{n} = (n_i)_{i=1}^2$ as in [27]. On inspection of the last integral in Equation (4.54) it is clear that upon integrating around the perimeter of each element we are integrating along internal element edges $s \in S$ which lie in $\Omega \setminus \partial\Omega$ as well as those element edges which lie on $\partial\Omega$ and thus not in set S. The integrand can thus be split up into contributions from these two areas. In performing the integration over all elements, it is also clear that the integration will be performed twice along all such internal element edges. For example,

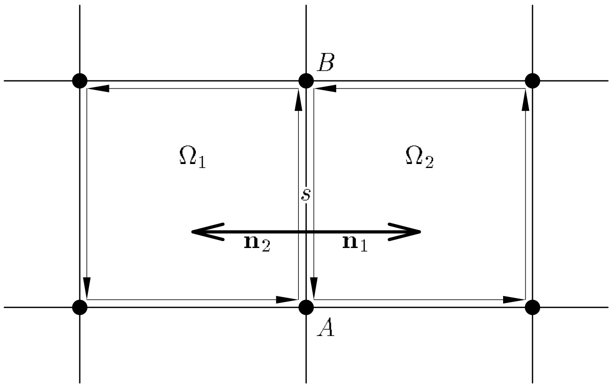

Figure 4.16: Elements Ω_1 and Ω_2 sharing common edge s bounded by nodes A and B.

consider the two neighbouring quadrilateral elements Ω_1 and Ω_2 in Figure (4.16). Integrating around the boundary of Ω_1 will involve the edge s as will the integration around the boundary of Ω_2. Thus, for edge s we have the contribution, $\mathcal{B}$, given as,

$$\mathcal{B} = -\int_A^B (\boldsymbol{\sigma}(\mathbf{u}_h)\cdot\mathbf{n}_1)|_{\Omega_1}\cdot(\mathbf{e}-\pi_h\mathbf{e})\,ds - \int_B^A (\boldsymbol{\sigma}(\mathbf{u}_h)\cdot\mathbf{n}_2)|_{\Omega_2}\cdot(\mathbf{e}-\pi_h\mathbf{e})\,dt,$$

where $dt = -ds$ and the first and second integrals are contributions from elements Ω_1 and Ω_2 respectively. In $\mathcal{B}$ we also have that $\mathbf{n}_2 = -\mathbf{n}_1$ and so we may express $\mathcal{B}$ as,

$$\mathcal{B} = -\int_A^B (\boldsymbol{\sigma}(\mathbf{u}_h)\cdot\mathbf{n}_1)|_{\Omega_1}\cdot(\mathbf{e}-\pi_h\mathbf{e})\,ds - \int_B^A (\boldsymbol{\sigma}(\mathbf{u}_h)\cdot\mathbf{n}_1)|_{\Omega_2}\cdot(\mathbf{e}-\pi_h\mathbf{e})\,ds.$$

Reversing the integration limits on the second integral then gives,

$$\mathcal{B} = -\int_A^B (\boldsymbol{\sigma}(\mathbf{u}_h)\cdot\mathbf{n}_1)|_{\Omega_1}\cdot(\mathbf{e}-\pi_h\mathbf{e})\,ds + \int_A^B (\boldsymbol{\sigma}(\mathbf{u}_h)\cdot\mathbf{n}_1)|_{\Omega_2}\cdot(\mathbf{e}-\pi_h\mathbf{e})\,ds,$$

and it is now possible to bring these contributions together, remembering that the terms will not necessarily cancel due to the fact that the stress is not continuous across a typical edge s. This gives,

$$\mathcal{B} = \int_A^B \left((\boldsymbol{\sigma}(\mathbf{u}_h)\cdot\mathbf{n}_1)|_{\Omega_2} - (\boldsymbol{\sigma}(\mathbf{u}_h)\cdot\mathbf{n}_1)|_{\Omega_1}\right)\cdot(\mathbf{e}-\pi_h\mathbf{e})\,ds, \tag{4.56}$$

This introduces the notion of a stress 'jump' across a typical edge s which shall henceforth be denoted by $[\boldsymbol{\sigma}(\mathbf{u}_h)\cdot\mathbf{n}_s]$ and where $\mathbf{n}_s$ can be considered as the unit outward normal to the edge s. Thus in Equation (4.56) we have that s is the edge running from A to B defined in Figure (4.16) and so $\mathbf{n}_s \equiv \mathbf{n}_1$. The definition of the stress jump $[\boldsymbol{\sigma}(\mathbf{u}_h)\cdot\mathbf{n}_s]$ can be thought of as taking the difference of the quantity defined in Equation (4.55) as we approach the edge from both sides. We thus have, for a point $\mathbf{x}$ on edge s,

$$[\boldsymbol{\sigma}(\mathbf{u}_h)\cdot\mathbf{n}_s](\mathbf{x}) := \lim_{t\to 0^+}\boldsymbol{\sigma}(\mathbf{u}_h(\mathbf{x}+t\mathbf{n}_s))\cdot\mathbf{n}_s(\mathbf{x}) - \lim_{t\to 0^+}\boldsymbol{\sigma}(\mathbf{u}_h(\mathbf{x}-t\mathbf{n}_s))\cdot\mathbf{n}_s(\mathbf{x}).$$

It is thus possible to regroup the terms in Equation (4.54) giving,

$$\begin{aligned}\|\mathbf{e}\|^2_{E(\Omega)} = {} & \sum_{k=1}^{N}\int_{\Omega_k}(\mathbf{f}+\operatorname{div}\boldsymbol{\sigma}(\mathbf{u}_{h,p}))\cdot(\mathbf{e}-\pi_h\mathbf{e})\,d\mathbf{x} + \int_{\partial\Omega_T}\mathbf{g}\cdot(\mathbf{e}-\pi_h\mathbf{e})\,ds \\ & -\int_{\partial\Omega_T}\boldsymbol{\sigma}(\mathbf{u}_h)\cdot\mathbf{n}\cdot(\mathbf{e}-\pi_h\mathbf{e})\,ds + \sum_{s\in S}\int_s[\boldsymbol{\sigma}(\mathbf{u}_h)\cdot\mathbf{n}_s]\cdot(\mathbf{e}-\pi_h\mathbf{e})\,ds,\end{aligned} \tag{4.57}$$

where now we have a summation over all internal element edges $s \in S$. The terms in Equation (4.57) may be grouped further, giving finally,

$$\|\mathbf{e}\|^2_{E(\Omega)} = \sum_{k=1}^{N} \int_{\Omega_k} (\mathbf{f} + \operatorname{div} \boldsymbol{\sigma}(\mathbf{u}_h)) \cdot (\mathbf{e} - \pi_h \mathbf{e})\, d\mathbf{x} + \int_{\partial\Omega_T} (\mathbf{g} - \boldsymbol{\sigma}(\mathbf{u}_h) \cdot \mathbf{n}) \cdot (\mathbf{e} - \pi_h \mathbf{e})\, ds$$
$$+ \sum_{s \in S} \int_s [\boldsymbol{\sigma}(\mathbf{u}_h) \cdot \mathbf{n}_s]\, (\mathbf{e} - \pi_h \mathbf{e})\, ds. \tag{4.58}$$

It is now possible to express the form of the error estimate, measured in the energy norm, in the following way,

$$\|\mathbf{e}\|^2_{E(\Omega)} = E_1 + E_2, \tag{4.59}$$

where,

$$E_1 \equiv \sum_{k=1}^{N} \int_{\Omega_k} \mathcal{R}_1(\mathbf{u}_h) \cdot (\mathbf{e} - \pi_h \mathbf{e})\, d\mathbf{x}, \tag{4.60}$$

and,

$$E_2 \equiv \sum_{k=1}^{N} \int_{\partial\Omega_k} h_k \mathcal{R}_2(\mathbf{u}_h) \cdot (\mathbf{e} - \pi_h \mathbf{e})\, ds. \tag{4.61}$$

Where,

$$\mathcal{R}_1(\mathbf{u}_h) = \mathbf{f} + \operatorname{div} \boldsymbol{\sigma}(\mathbf{u}_h) \text{ on } \Omega_k \in \Upsilon_h, \tag{4.62}$$

and,

$$\mathcal{R}_2(\mathbf{u}_h) = \begin{cases} \dfrac{1}{2\,h_k} [\boldsymbol{\sigma}(\mathbf{u}_h) \cdot \mathbf{n}_s] & \text{on } s \subset \partial\Omega_k \text{ if } s \in S \text{ with } \Omega_k \in \Upsilon_h, \\ \dfrac{1}{h_k} (\mathbf{g} - \boldsymbol{\sigma}(\mathbf{u}_h) \cdot \mathbf{n}_k) & \text{on } \partial\Omega_k \cap \partial\Omega_T \text{ with } \Omega_k \in \Upsilon_h. \end{cases} \tag{4.63}$$

The quantities $\mathcal{R}_1(\mathbf{u}_h)$ and $\mathcal{R}_2(\mathbf{u}_h)$ represent *residuals* of the finite element solution $\mathbf{u}_h$ related to the interior and boundary respectively of each element $\Omega_k \in \Upsilon_h$. In [27] bounds are given for the interpolation error $\mathbf{e} - \pi_h \mathbf{e}$ used in the above expressions. These bound the interpolation error, measured in the L_2-norm above by the energy norm. Thus, for a typical element Ω_k and using [27] and Appendix E,

$$\|\mathbf{e} - \pi_h \mathbf{e}\|_{L_2(\Omega_k)} \leq C^i_{1,k} h_k \|\mathbf{e}\|_{E(\Omega_k)}, \tag{4.64}$$

and,

$$\|\mathbf{e} - \pi_h \mathbf{e}\|_{L_2(\partial\Omega_k)} \leq C^i_{2,k} h_k^{\frac{1}{2}} \|\mathbf{e}\|_{E(\Omega_k)}. \tag{4.65}$$

Where,

$$C^i_{1,k} = \sup_{\boldsymbol{\tau} \in V_e} \frac{h_k^{-1} \|\boldsymbol{\tau} - \pi_h \boldsymbol{\tau}\|_{L_2(\Omega_k)}}{\|\boldsymbol{\tau}\|_{E(\Omega_k)}}, \tag{4.66}$$

$$C^i_{2,k} = \sup_{\boldsymbol{\tau} \in V_e} \frac{h_k^{-\frac{1}{2}} \|\boldsymbol{\tau} - \pi_h \boldsymbol{\tau}\|_{L_2(\partial\Omega_k)}}{\|\boldsymbol{\tau}\|_{E(\Omega_k)}}, \tag{4.67}$$

and also where,

$$\|\boldsymbol{\tau}\|_{E(\Omega_k)} = \left(\int_{\Omega_k} \boldsymbol{\sigma}(\boldsymbol{\tau}) : \varepsilon(\boldsymbol{\tau})\, d\mathbf{x} \right)^{1/2}.$$

Note that in the above, the interpolation error constants $C^i_{1,k}$ and $C^i_{2,k}$ are considered for a typical element Ω_k. The interpolation error constants will always have a superscript i in this work to denote that they are interpolation error constants. Further, the subscript 1 or 2 is to signify whether the constant is for the element interior or boundary respectively as prescribed by the integration of the L_2-norm in Equations (4.66) and (4.67). The second subscript denotes the element dependence and in the following work the constants will be considered for the general element Ω_k.

From Equation (4.60), application of the Cauchy-Schwarz integral inequality yields,

$$\begin{aligned}
|E_1| &\leq \sum_{k=1}^{N} ||\mathcal{R}_1(\mathbf{u}_h)||_{L_2(\Omega_k)} ||\mathbf{e} - \pi_h \mathbf{e}||_{L_2(\Omega_k)}, \\
&\leq \sum_{k=1}^{N} ||\mathcal{R}_1(\mathbf{u}_h)||_{L_2(\Omega_k)} C^i_{1,k} h_k ||\mathbf{e}||_{E(\Omega_k)}, \text{ using Equation (4.64), with } \tilde{\Omega}_k = \Omega_k \\
&\leq \left[\sum_{k=1}^{N} \left[C^i_{1,k} h_k ||\mathcal{R}_1(\mathbf{u}_h)||_{L_2(\Omega_k)}\right]^2\right]^{\frac{1}{2}} \left[\sum_{k=1}^{N} ||\mathbf{e}||^2_{E(\Omega_k)}\right]^{\frac{1}{2}}, \text{ by Cauchy-Schwarz sum inequality,} \\
&\equiv ||C^i_1 h \mathrm{R}_1(\mathbf{u}_h)||_{L_2(\Omega)} ||\mathbf{e}||_{E(\Omega)},
\end{aligned} \tag{4.68}$$

where,

$$\mathrm{R}_1(\mathbf{u}_h) = |\mathcal{R}_1(\mathbf{u}_h)|, \text{ on each } \Omega_k, \tag{4.69}$$

and also where $h = h_k$ and $C^i_1 = C^i_{1,k}$ on Ω_k. From Equation (4.61), application again of the Cauchy-Schwarz integral inequality yields,

$$\begin{aligned}
|E_2| &\leq \sum_{k=1}^{N} || \; h_k \mathcal{R}_2(\mathbf{u}_h)||_{L_2(\partial\Omega_k)} ||\mathbf{e} - \pi_h \mathbf{e}||_{L_2(\partial\Omega_k)}, \\
&\leq \sum_{k=1}^{N} ||h_k \mathcal{R}_2(\mathbf{u}_h)||_{L_2(\partial\Omega_k)} C^i_{2,k} h_k^{\frac{1}{2}} ||\mathbf{e}||_{E(\Omega_k)}, \text{ using Equation (4.65), with } \tilde{\Omega}_k = \Omega_k \\
&\leq \left[\sum_{k=1}^{N} \left[C^i_{2,k} h_k^{\frac{1}{2}} ||h_k \mathcal{R}_2(\mathbf{u}_h)||_{L_2(\partial\Omega_k)}\right]^2\right]^{\frac{1}{2}} \left[\sum_{k=1}^{N} ||\mathbf{e}||^2_{E(\Omega_k)}\right]^{\frac{1}{2}}, \text{ by Cauchy-Schwarz sum inequality,} \\
&\equiv ||C^i_2 h \mathrm{R}_2(\mathbf{u}_h)||_{L_2(\Omega)} ||\mathbf{e}||_{E(\Omega)},
\end{aligned} \tag{4.70}$$

where,

$$\mathrm{R}_2(\mathbf{u}_h) = \frac{h^{\frac{1}{2}} ||\mathcal{R}_2(\mathbf{u}_h)||_{L_2(\partial\Omega_k)}}{A(\Omega_k)^{\frac{1}{2}}}, \text{ on } \Omega_k, \tag{4.71}$$

$h = h_k$ and $C^i_2 = C^i_{2,k}$ on Ω_k and $A(\Omega_k)$ is the area of Ω_k. Equation (4.71) defines $\mathrm{R}_2(\mathbf{u}_h)$ in the interior of Ω_k so that,

$$||h \mathrm{R}_2(\mathbf{u}_h)||_{L_2(\Omega_k)} = h_k^{\frac{1}{2}} ||h \mathcal{R}_2(\mathbf{u}_h)||_{L_2(\partial\Omega_k)}. \tag{4.72}$$

This gives a convenient way of expressing the estimate for E_2. It is emphasised in [27] that with the definitions of $\mathrm{R}_1(\mathbf{u}_h)$ and $\mathrm{R}_2(\mathbf{u}_h)$ on each element Ω_k they are considered as functions defined on Ω. Thus using Equation (4.59) along with the triangle inequality, it is possible to express,

$$||\mathbf{e}||^2_{E(\Omega)} = E_1 + E_2 = |E_1 + E_2| \leq |E_1| + |E_2|.$$

Equations (4.68) and (4.70) may now be substituted into the above expression giving a final bound on the error $\mathbf{e} = \mathbf{u} - \mathbf{u}_h$, measured in the energy norm as,

$$||\mathbf{u} - \mathbf{u}_h||_{E(\Omega)} \leq \sum_{j=1}^{2} ||h C^i_j \mathrm{R}_j(\mathbf{u}_h)||_{L_2(\Omega)}, \tag{4.73}$$

where C_j^i, $j = 1, 2$ are defined by Equations (4.66) and (4.67) and $\mathrm{R}_j(\mathbf{u}_h)$, $j = 1, 2$ are defined by Equations (4.62), (4.63), (4.69), and (4.71).

4.4.3 Extension of Johnson-Hansbo Estimator for Transition Element Effects

It has been seen previously in this work that the presence of transition elements and irregular nodes produces a variety of complications ranging from the modification of shape functions and quadrature rules to the sampling problems discussed for the Zienkiewicz-Zhu error estimator implementation. It is thus no surprise to learn that the effect upon the Johnson-Hansbo error estimator is also significant.

In the previous section the Johnson-Hansbo estimator was illustrated for problems of linear elasticity in two dimensions. It was shown in Equation (4.54) that the error, expressed in the usual way as,

$$\mathbf{e} = \mathbf{u} - \mathbf{u}_h,$$

could be measured in the energy norm as a sum over elemental contributions as,

$$\begin{aligned}||\mathbf{e}||^2_{E(\Omega)} = &\sum_{k=1}^{N} \int_{\Omega_k} (\mathbf{f} + \operatorname{div} \boldsymbol{\sigma}(\mathbf{u}_h)) \cdot (\mathbf{e} - \pi_h \mathbf{e})\, d\mathbf{x} + \int_{\partial\Omega_T} \mathbf{g} \cdot (\mathbf{e} - \pi_h \mathbf{e})\, ds \\ &- \sum_{k=1}^{N} \int_{\partial\Omega_k} \boldsymbol{\sigma}(\mathbf{u}_h) \cdot \mathbf{n}_k \cdot (\mathbf{e} - \pi_h \mathbf{e})\, ds. \end{aligned} \tag{4.74}$$

At this point is is important to consider the effect on the above when the partition of Ω possibly contains transition elements. It is proposed that in such a case all elements be considered as illustrated in Figure (4.17) where the element Ω_k is shown as what we shall call here a 'composite' element, consisting of four 'sub-element' regions denoted Ω_{kl} for $l = 1, 2, 3$ and 4. This configuration is to combat the effect of possible lines of slope discontinuity running across the element and included in the figure as broken lines. Such lines arise, as previously described, from the presence

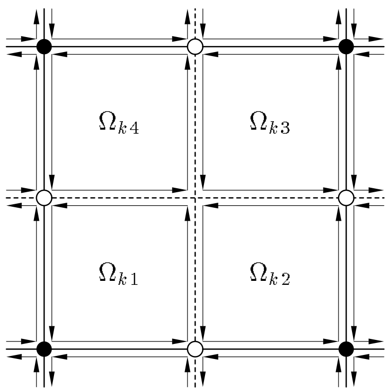

Figure 4.17: General element Ω_k depicted as a possible composite of four sub-element regions.

of irregular mid-side nodes on the element which are illustrated at their four possible locations by empty circles whilst the standard corner nodes are illustrated in the usual way by filled circles. It should be noted at this point that although the recommendation is for all elements to be considered as 'composite' elements, in some cases four sub-element regions are not necessary. Such cases arise whenever the element is not a transition element or when it is a 1-irregular element. In such cases the regions are retained but may or may not have slope discontinuities between them. This will not affect the computations over the element but by considering the most general case we are taking into account the whole transition family along with the standard non-transition element configurations.

The introduction of the sub-element regions in turn introduces modifications to the error measure given above. The integration over the elements for example, given as,

$$\sum_{k=1}^{N}\int_{\Omega_k}(\mathbf{f}+\operatorname{div}\boldsymbol{\sigma}(\mathbf{u}_h))\cdot(\mathbf{e}-\pi_h\mathbf{e})\,d\mathbf{x}, \quad \text{now becomes} \quad \sum_{k=1}^{N}\sum_{l=1}^{4}\int_{\Omega_{kl}}(\mathbf{f}+\operatorname{div}\boldsymbol{\sigma}(\mathbf{u}_h))\cdot(\mathbf{e}-\pi_h\mathbf{e})\,d\mathbf{x}, \tag{4.75}$$

which involves an additional summation over the sub-element regions. The effect upon the integration over transition elements has been discussed in Section (3.9.2) and so the summation over each sub-element region can be done by a modification to the quadrature scheme which is applied over the element as a whole. This integral can thus still be considered as a sum over all elements Ω_k, noting that, for the case where Ω_k is a transition element, the integration is modified accordingly to cope with the sub-element region features.

The effect of sub-element regions must now also be considered for the integral around the element boundary given in the error measure at the start of this section. Thus, as in the above modification for the element interior integral,

$$-\sum_{k=1}^{N}\int_{\partial\Omega_k}\boldsymbol{\sigma}(\mathbf{u}_h)\cdot\mathbf{n}_k\cdot(\mathbf{e}-\pi_h\mathbf{e})\,ds, \quad \text{now becomes} \quad -\sum_{k=1}^{N}\sum_{l=1}^{4}\int_{\partial\Omega_{kl}}\boldsymbol{\sigma}(\mathbf{u}_h)\cdot\mathbf{n}_{kl}\cdot(\mathbf{e}-\pi_h\mathbf{e})\,ds, \tag{4.76}$$

where $\mathbf{n}_{kl}$ denotes the unit outward normal to the boundary $\partial\Omega_{kl}$ of sub-element region Ω_{kl} spawned from 'parent' element Ω_k.

Considering the integration around each perimeter $\partial\Omega_{kl}$ as illustrated in Figure (4.17) it is clear that integration will be performed twice along each element edge $s \in (\partial\Omega_k \cap \partial\Omega_{kl}) \setminus \partial\Omega \equiv S_k$ where $S \equiv \cup_k S_k$ which corresponds to the set S in the previous section and defined as the set of internal element edges contained in $\Omega \setminus \partial\Omega$. In addition, integration will also be performed twice along each edge $t \in \partial\Omega_{kl} \setminus \partial\Omega_k \equiv T_k$ which coincides with the interior lines of slope discontinuity in the element Ω_k and the set $T \equiv \cup_k T_k$. Here we have used the terms 'internal' and 'interior', the meanings of these are not the same. We shall use the term 'internal' when describing element edges which are internal as far as the problem domain is concerned. These are true element edges and belong to set S. The term 'interior' will be used to describe the interior features of a transition element, thus a 1-irregular element will have one interior line of possible slope discontinuity which belongs to set T. It was seen in the previous section that integration around the element boundaries produced stress jumps across common internal element edges. These jumps will again arise here and for the case of transition elements additional 'interior' stress jumps will arise. Expanding the boundary integral in Equation (4.76) to illustrate this yields,

$$
\begin{aligned}
-\sum_{k=1}^{N}\sum_{l=1}^{4}\int_{\partial\Omega_{kl}} \boldsymbol{\sigma}(\mathbf{u}_h)\cdot\mathbf{n}_{kl}\cdot(\mathbf{e}-\pi_h\mathbf{e})\,ds \;=\; & \sum_{s\in S}\int_s [\boldsymbol{\sigma}(\mathbf{u}_h)\cdot\mathbf{n}_s]\cdot(\mathbf{e}-\pi_h\mathbf{e})\,ds \\
& + \sum_{t\in T}\int_t [\boldsymbol{\sigma}(\mathbf{u}_h)\cdot\mathbf{n}_t]\cdot(\mathbf{e}-\pi_h\mathbf{e})\,ds \qquad (4.77) \\
& - \int_{\partial\Omega_T} \boldsymbol{\sigma}(\mathbf{u}_h)\cdot\mathbf{n}\cdot(\mathbf{e}-\pi_h\mathbf{e})\,ds,
\end{aligned}
$$

where again $[\boldsymbol{\sigma}(\mathbf{u}_h)\cdot\mathbf{n}_\alpha]$ is the jump of $\boldsymbol{\sigma}(\mathbf{u}_h)\cdot\mathbf{n}_\alpha$ across edge α expressed as,

$$
[\boldsymbol{\sigma}(\mathbf{u}_h)\cdot\mathbf{n}_\alpha](\mathbf{x}) := \lim_{z\to 0+}\boldsymbol{\sigma}(\mathbf{u}_h(\mathbf{x}+z\mathbf{n}_\alpha))\cdot\mathbf{n}_\alpha(\mathbf{x}) - \lim_{z\to 0+}\boldsymbol{\sigma}(\mathbf{u}_h(\mathbf{x}-z\mathbf{n}_\alpha))\cdot\mathbf{n}_\alpha(\mathbf{x}), \ \text{for } \mathbf{x}\in\alpha,
$$

where α with unit normal $\mathbf{n}_\alpha$ may be either $s\in S$ or $t\in T$. It can be seen in Equation (4.77) that the integral over set S coincides with the integration over internal edges whilst integration over set T is due to the interior element features which yield jumps themselves. Obviously for an element Ω_k which is not a transition element the contributions from the latter integration will be zero due to there being no such lines of slope discontinuity and thus no jumps across them. In practice this means that for this term the integrals, when computed, will have zero contribution.

Substitution of Equations (4.75) and (4.77) into the error measure of Equation (4.74) and rearranging gives the error, measured in the energy norm and over a mesh which may contain transition elements, as,

$$
\begin{aligned}
\|\mathbf{e}\|^2_{E(\Omega)} = & \sum_{k=1}^{N}\sum_{l=1}^{4}\int_{\Omega_{kl}}(\mathbf{f}+\operatorname{div}\boldsymbol{\sigma}(\mathbf{u}_h))\cdot(\mathbf{e}-\pi_h\mathbf{e})\,d\mathbf{x} + \int_{\partial\Omega_T}(\mathbf{g}-\boldsymbol{\sigma}(\mathbf{u}_h)\cdot\mathbf{n})\cdot(\mathbf{e}-\pi_h\mathbf{e})\,ds \\
& + \sum_{s\in S}\int_s[\boldsymbol{\sigma}(\mathbf{u}_h)\cdot\mathbf{n}_s]\cdot(\mathbf{e}-\pi_h\mathbf{e})\,ds + \sum_{t\in T}\int_t[\boldsymbol{\sigma}(\mathbf{u}_h)\cdot\mathbf{n}_t]\cdot(\mathbf{e}-\pi_h\mathbf{e})\,ds. \qquad (4.78)
\end{aligned}
$$

In the above, the integral over the sub-element region interiors can be considered over the element interiors without the extra summation over l. This is due to the previously mentioned quadrature modification detailed in Section (3.9.2). Thus the first two terms of Equation (4.78) have previously been seen in the error measure of Equation (4.58) in Section (4.4.2). Additionally, the third integral over set S has also been seen previously as it coincides with the integral over internal element edges $s\in S$ of Equation (4.58). Thus the only new term here is the last integral over set T which itself has non-zero contribution only for the case where the element Ω_k is a transition element. It can be also seen that the integrands for the two integrals over sets S and T are the same. The integrals may thus be now combined noting now that the resulting integral will encompass all jump integrals over all edges $s\in S\cup T$.

The task now is to express the new form of the error estimate. This is begun by firstly noting that, as in Equation (4.59), the error measured in the energy norm can be expressed as,

$$
\|\mathbf{e}\|^2_{E(\Omega)} = E_1 + E_2,
$$

where now,

$$E_1 \equiv \sum_{k=1}^{N}\sum_{l=1}^{4}\int_{\Omega_{kl}} \mathcal{R}_1(\mathbf{u}_h)\cdot(\mathbf{e}-\pi_h\mathbf{e})\,d\mathbf{x}, \tag{4.79}$$

and,

$$E_2 \equiv \sum_{k=1}^{N}\sum_{l=1}^{4}\int_{\partial\Omega_{kl}} h_k\mathcal{R}_2(\mathbf{u}_h)\cdot(\mathbf{e}-\pi_h\mathbf{e})\,ds. \tag{4.80}$$

Where,

$$\mathcal{R}_1(\mathbf{u}_h) = \mathbf{f} + \operatorname{div}\boldsymbol{\sigma}(\mathbf{u}_h) \text{ on } \Omega_{kl}, \tag{4.81}$$

and,

$$\mathcal{R}_2(\mathbf{u}_h) = \begin{cases} \dfrac{1}{2h_k}\left[\boldsymbol{\sigma}(\mathbf{u}_h)\cdot\mathbf{n}_s\right] & \text{on } s \in (\partial\Omega_{kl}\cap\partial\Omega_k)\setminus\partial\Omega \equiv S_k \text{ for each } \Omega_k, \\ \dfrac{1}{h_k}\left[\boldsymbol{\sigma}(\mathbf{u}_h)\cdot\mathbf{n}_s\right] & \text{on } s \in \partial\Omega_{kl}\setminus\partial\Omega_k \equiv T_k \text{ for each } \Omega_k, \\ \dfrac{1}{h_k}(\mathrm{g}-\boldsymbol{\sigma}(\mathbf{u}_h)\cdot\mathbf{n}_{kl}) & \text{on } \partial\Omega_{kl}\cap\partial\Omega_T \text{ for each } \Omega_k, \end{cases} \tag{4.82}$$

where the factor of two arising in the first expression for $\mathcal{R}_2(\mathbf{u}_h)$ in Equation (4.82) arises due to the fact that the jump contribution on edge $s \in S$ is shared between two neighbouring elements. This does not occur for the jump contribution on edge $t \in T$ in the second expression of Equation (4.82), however, as this is an interior jump which is specific to an element interior and so the element receives the full jump value. The interpolation error bounds given in Equations (4.64) and (4.65) may now be expressed for a typical element Ω_k and taking into account the possible sub-element regions as,

$$\left[\sum_{l=1}^{4}\|\mathbf{e}-\pi_h\mathbf{e}\|^2_{L_2(\Omega_{kl})}\right]^{\frac{1}{2}} \le C^i_{1,k}h_k\|\mathbf{e}\|_{E(\Omega_k)}, \tag{4.83}$$

and,

$$\left[\sum_{l=1}^{4}\|\mathbf{e}-\pi_h\mathbf{e}\|^2_{L_2(\partial\Omega_{kl})}\right]^{\frac{1}{2}} \le C^i_{2,k}h_k^{\frac{1}{2}}\|\mathbf{e}\|_{E(\Omega_k)}. \tag{4.84}$$

Where now,

$$C^i_{1,k} = \sup_{\boldsymbol{\tau}\in V_e} \frac{h_k^{-1}\left[\displaystyle\sum_{l=1}^{4}\|\boldsymbol{\tau}-\pi_h\boldsymbol{\tau}\|^2_{L_2(\Omega_{kl})}\right]^{\frac{1}{2}}}{\|\boldsymbol{\tau}\|_{E(\Omega_k)}}, \tag{4.85}$$

and,

$$C^i_{2,k} = \sup_{\boldsymbol{\tau}\in V_e} \frac{h_k^{\frac{1}{2}}\left[\displaystyle\sum_{l=1}^{4}\|\boldsymbol{\tau}-\pi_h\boldsymbol{\tau}\|^2_{L_2(\partial\Omega_{kl})}\right]^{\frac{1}{2}}}{\|\boldsymbol{\tau}\|_{E(\Omega_k)}}. \tag{4.86}$$

From Equation (4.79), application of the Cauchy-Schwarz integral inequality yields,

$$\begin{aligned} |E_1| &\le \sum_{k=1}^{N}\left[\sum_{l=1}^{4}\|\mathcal{R}_1(\mathbf{u}_h)\|^2_{L_2(\Omega_{kl})}\right]^{\frac{1}{2}}\left[\sum_{l=1}^{4}\|\mathbf{e}-\pi_h\mathbf{e}\|^2_{L_2(\Omega_{kl})}\right]^{\frac{1}{2}}, \\ &\le \sum_{k=1}^{N}\left[\sum_{l=1}^{4}\|\mathcal{R}_1(\mathbf{u}_h)\|^2_{L_2(\Omega_{kl})}\right]^{\frac{1}{2}} C^i_{1,k}h_k\|\mathbf{e}\|_{E(\Omega_k)} \quad \text{using Equation (4.83)}, \end{aligned}$$

$$\leq \left[\sum_{k=1}^{N}\sum_{l=1}^{4}\left[C_{1,k}^{i} h_k \|\mathcal{R}_1(\mathbf{u}_h)\|_{L_2(\Omega_{kl})}\right]^2\right]^{\frac{1}{2}} \left[\sum_{k=1}^{N} \|\mathbf{e}\|_{E(\Omega_k)}^2\right]^{\frac{1}{2}}, \tag{4.87}$$

which will reduce to Equation (4.68) if there are no transition elements. Additionally, from Equation (4.80),

$$\begin{aligned}
|E_2| &\leq \sum_{k=1}^{N}\left[\sum_{l=1}^{4} \|h_k \mathcal{R}_2(\mathbf{u}_h)\|_{L_2(\partial\Omega_{kl})}^2\right]^{\frac{1}{2}} \left[\sum_{l=1}^{4} \|\mathbf{e} - \pi_h \mathbf{e}\|_{L_2(\partial\Omega_{kl})}^2\right]^{\frac{1}{2}}, \\
&\leq \sum_{k=1}^{N}\left[\sum_{l=1}^{4} \|h_k \mathcal{R}_2(\mathbf{u}_h)\|_{L_2(\partial\Omega_{kl})}^2\right]^{\frac{1}{2}} C_{2,k}^{i} h_k^{\frac{1}{2}} \|\mathbf{e}\|_{E(\Omega_k)} \quad \text{using Equation (4.84)}, \\
&\leq \left[\sum_{k=1}^{N}\sum_{l=1}^{4}\left[C_{2,k}^{i} h_k^{\frac{1}{2}} \|h_k \mathcal{R}_2(\mathbf{u}_h)\|_{L_2(\partial\Omega_{kl})}\right]^2\right]^{\frac{1}{2}} \left[\sum_{k=1}^{N} \|\mathbf{e}\|_{E(\Omega_k)}^2\right]^{\frac{1}{2}},
\end{aligned} \tag{4.88}$$

this again will reduce to Equation (4.70) if there are no transition elements. In Equations (4.87) and (4.88) we have that,

$$\left[\sum_{k=1}^{N} \|\mathbf{e}\|_{E(\Omega_k)}^2\right]^{\frac{1}{2}} = \|\mathbf{e}\|_{E(\Omega)},$$

thus we have that the error, measured in the energy norm can be bounded,

$$\|\mathbf{e}\|_{E(\Omega)} \leq \left[\sum_{k=1}^{N}\sum_{l=1}^{4}\left[C_{1,k}^{i} h_k \|\mathcal{R}_1(\mathbf{u}_h)\|_{L_2(\Omega_{kl})}\right]^2\right]^{\frac{1}{2}} + \left[\sum_{k=1}^{N}\sum_{l=1}^{4}\left[C_{2,k}^{i} h_k^{\frac{1}{2}} \|h_k \mathcal{R}_2(\mathbf{u}_h)\|_{L_2(\partial\Omega_{kl})}\right]^2\right]^{\frac{1}{2}}. \tag{4.89}$$

Thus for the case where there are no transition elements, the estimator will reduce to that of the previous section since there will be no interior jumps on the elements and the sub-element region considerations will not be necessary.

4.4.4 Interpolation Error Constant Discussions and Previous Results

It has been briefly discussed at the beginning of Section (4.4) that the interpolation constants given in Equations (4.66), (4.67), (4.85) and (4.86) must be computed for the implementation of the error estimator. Indeed, Johnson and Hansbo report in [27] that,

> 'One way of computing $C_{j,k}^{i}$ in the case of energy and L_2-norms, is to restrict the supremum to be taken over polynomials of degree $p+1$ where p is the maximal degree occurring in $P_p(\Omega_k)$, which leads to a finite dimensional eigenvalue problem on the element Ω_k soluble by some standard numerical routine.'

Where the mathematical notation in the above extract has been changed in order to agree with the notation in this work. The above extract is, however, followed shortly thereafter with, 'To obtain an idea of the size of the interpolation constants in the case $P_p(\Omega_k) = P_1(\Omega_k)$ with Ω_k a triangle, we have instead sought an approximate supremum over all $\boldsymbol{\tau} \in [P_2(\Omega_k)]^2$ (by trial and error). Here, $P_p(\Omega_k)$ denotes the set of polynomials on Ω_k of degree at most p. We then find the following approximate bounds of the $C^i_{j,k}$ in the case of energy norm:

$$C^i_{1,k} \lesssim \frac{0.4}{\sqrt{\lambda + 5\mu}}, \qquad C^i_{2,k} \lesssim \frac{1.1}{\sqrt{\lambda + 5\mu}}, \tag{4.90}$$

where λ and μ are the Lamé coefficients.'

At the time of writing, it seems that these are the only existing estimates for the interpolation error constants of this type in the literature although the related work of Handscomb, [23], should be noted here. It also seems, however, that these bounds are not rigorous in the sense that they are derived from an 'approximate supremum' which itself is found 'by trial and error'. A necessary task therefore is to devote effort into the computation of such interpolation error constants in the hope that both an accurate method and results can be established for the first time. Chapters 5 and 6 detail the work performed in this area. It can be seen therein that interpolation error constant values are presented for various problems and for triangular, quadrilateral and transition elements.

Enhancements made in the previous section gave the resulting modified error estimator the capability of handling the possible occurrence of transition elements in the mesh. Consequently there is now also the need for interpolation error constant values to be obtained for the transition element family as well as for the standard elements. In this way the enhanced error estimator can be applied on meshes which contain transition elements with varying numbers of irregular mid-side nodes. Upon encountering such elements the estimator will then be able to select specific interpolation error constant values which are correct for that element. For example, upon encountering a 1-irregular transition element the corresponding interpolation error constant for 1-irregular elements can be selected. In addition, it has been shown that the need exists for two types of interpolation error constant. These are $C^i_{1,k}$ and $C^i_{2,k}$ which will become known as the 'interior' and 'boundary' interpolation error constants respectively. In the context of transition elements these two types of constant remain but must now incorporate the sub-element region effects. Thus Chapters 5 and 6 also detail the work performed in this area for the transition element family.

4.5 Application of Johnson-Hansbo Theory to Plates

In this section we shall apply the Johnson-Hansbo estimator to the plate model which was introduced in Chapter 2. The estimator will firstly be obtained for uniform meshes as in Section (4.4.2) and then be modified as detailed for linear elasticity in Section (4.4.3) in order to cope with meshes which may contain transition elements. As previously, an estimator will be sought which measures the error in the energy norm.

In Section (3.3) the weak formulation of the plate problem was found to be one in which it is required to find $\mathbf{u} \in V$ where,

$$a(\mathbf{u}, \mathbf{v}) = F(\mathbf{v}), \quad \forall\ \mathbf{v} \in V, \tag{4.91}$$

and where V is as described in Equation (3.26). The bilinear form given in Equation (4.91) has the form,

$$a(\mathbf{u}, \mathbf{v}) \equiv \int_\Omega \left(\mathbf{B}^b\mathbf{u}\right)^T \mathbf{C}^b \left(\mathbf{B}^b\mathbf{v}\right)\, d\mathbf{x} + \int_\Omega \left(\mathbf{B}^s\mathbf{u}\right)^T \mathbf{C}^s \left(\mathbf{B}^s\mathbf{v}\right) d\mathbf{x}, \tag{4.92}$$

along with,

$$F(\mathbf{v}) \equiv \int_\Omega v_3 q\, d\mathbf{x} + \int_{\hat\Gamma_1} N_n v_1\, ds + \int_{\hat\Gamma_2} N_s v_2\, ds + \int_{\hat\Gamma_3} Q_n v_3\, ds + \int_{\hat\Gamma_4} M_n v_4\, ds + \int_{\hat\Gamma_5} M_s v_5\, ds. \tag{4.93}$$

where terms above are as defined in Sections (3.3) and (3.6). From Equation (4.51) it has been shown that the error $\mathbf{e} = \mathbf{u} - \mathbf{u}_h$, measured in the energy norm may be expressed as,

$$||\mathbf{e}||^2_{E(\Omega)} = F(\mathbf{e} - \pi_h\mathbf{e}) - a(\mathbf{u}_h, \mathbf{e} - \pi_h\mathbf{e}), \tag{4.94}$$

where π_h is the interpolation operator defined in Section (4.4.2). From Section (4.4.2) it is known that the bilinear form will need to be integrated by parts over each element in order to trade the differentiation from the interpolation error terms in Equation (4.94). In order to make this process clearer consider firstly the bilinear form given in Equation (4.92) but expressed now as,

$$a(\mathbf{u}, \mathbf{v}) \equiv \int_\Omega \mathcal{A}\, d\mathbf{x} + \int_\Omega \mathcal{B}\, d\mathbf{x}.$$

where the substitutions,

$$\mathcal{A} = \left(\mathbf{B}^b\mathbf{u}\right)^T \mathbf{C}^b \left(\mathbf{B}^b\mathbf{v}\right) \quad \text{and} \quad \mathcal{B} = \left(\mathbf{B}^s\mathbf{u}\right)^T \mathbf{C}^s \left(\mathbf{B}^s\mathbf{v}\right),$$

have been made. By using Equations (3.32) and (3.33) it can be shown that,

$$\begin{aligned}
\mathcal{A} \;=\; & \left[\frac{\partial u}{\partial x_1}A_{11} + \frac{\partial v}{\partial x_2}A_{12} + \left(\frac{\partial u}{\partial x_2} + \frac{\partial v}{\partial x_1}\right)A_{14} + \frac{\partial \psi_1}{\partial x_1}B_{11} + \frac{\partial \psi_2}{\partial x_2}B_{12} + \left(\frac{\partial \psi_1}{\partial x_2} + \frac{\partial \psi_2}{\partial x_1}\right)B_{14}\right]\frac{\partial v_1}{\partial x_1} \\
+ & \left[\frac{\partial u}{\partial x_1}A_{12} + \frac{\partial v}{\partial x_2}A_{22} + \left(\frac{\partial u}{\partial x_2} + \frac{\partial v}{\partial x_1}\right)A_{24} + \frac{\partial \psi_1}{\partial x_1}B_{12} + \frac{\partial \psi_2}{\partial x_2}B_{22} + \left(\frac{\partial \psi_1}{\partial x_2} + \frac{\partial \psi_2}{\partial x_1}\right)B_{24}\right]\frac{\partial v_2}{\partial x_2} \\
+ & \left[\frac{\partial u}{\partial x_1}A_{14} + \frac{\partial v}{\partial x_2}A_{24} + \left(\frac{\partial u}{\partial x_2} + \frac{\partial v}{\partial x_1}\right)A_{44} + \frac{\partial \psi_1}{\partial x_1}B_{14} + \frac{\partial \psi_2}{\partial x_2}B_{24} + \left(\frac{\partial \psi_1}{\partial x_2} + \frac{\partial \psi_2}{\partial x_1}\right)B_{44}\right]\frac{\partial v_1}{\partial x_2} \\
+ & \left[\frac{\partial u}{\partial x_1}A_{14} + \frac{\partial v}{\partial x_2}A_{24} + \left(\frac{\partial u}{\partial x_2} + \frac{\partial v}{\partial x_1}\right)A_{44} + \frac{\partial \psi_1}{\partial x_1}B_{14} + \frac{\partial \psi_2}{\partial x_2}B_{24} + \left(\frac{\partial \psi_1}{\partial x_2} + \frac{\partial \psi_2}{\partial x_1}\right)B_{44}\right]\frac{\partial v_2}{\partial x_1} \\
+ & \left[\frac{\partial u}{\partial x_1}B_{11} + \frac{\partial v}{\partial x_2}B_{12} + \left(\frac{\partial u}{\partial x_2} + \frac{\partial v}{\partial x_1}\right)B_{14} + \frac{\partial \psi_1}{\partial x_1}D_{11} + \frac{\partial \psi_2}{\partial x_2}D_{12} + \left(\frac{\partial \psi_1}{\partial x_2} + \frac{\partial \psi_2}{\partial x_1}\right)D_{14}\right]\frac{\partial v_4}{\partial x_1} \\
+ & \left[\frac{\partial u}{\partial x_1}B_{12} + \frac{\partial v}{\partial x_2}B_{22} + \left(\frac{\partial u}{\partial x_2} + \frac{\partial v}{\partial x_1}\right)B_{24} + \frac{\partial \psi_1}{\partial x_1}D_{12} + \frac{\partial \psi_2}{\partial x_2}D_{22} + \left(\frac{\partial \psi_1}{\partial x_2} + \frac{\partial \psi_2}{\partial x_1}\right)D_{24}\right]\frac{\partial v_5}{\partial x_2} \\
+ & \left[\frac{\partial u}{\partial x_1}B_{14} + \frac{\partial v}{\partial x_2}B_{24} + \left(\frac{\partial u}{\partial x_2} + \frac{\partial v}{\partial x_1}\right)B_{44} + \frac{\partial \psi_1}{\partial x_1}D_{14} + \frac{\partial \psi_2}{\partial x_2}D_{24} + \left(\frac{\partial \psi_1}{\partial x_2} + \frac{\partial \psi_2}{\partial x_1}\right)D_{44}\right]\frac{\partial v_4}{\partial x_2} \\
+ & \left[\frac{\partial u}{\partial x_1}B_{14} + \frac{\partial v}{\partial x_2}B_{24} + \left(\frac{\partial u}{\partial x_2} + \frac{\partial v}{\partial x_1}\right)B_{44} + \frac{\partial \psi_1}{\partial x_1}D_{14} + \frac{\partial \psi_2}{\partial x_2}D_{24} + \left(\frac{\partial \psi_1}{\partial x_2} + \frac{\partial \psi_2}{\partial x_1}\right)D_{44}\right]\frac{\partial v_5}{\partial x_1},
\end{aligned}$$

where the displacement vector $\mathbf{u} = (u, v, w, \psi_1, \psi_2)^T$ and test vector $\mathbf{v} = (v_1, v_2, v_3, v_4, v_5)^T$ have been used. Similarly, for the transverse shear terms in the bilinear form, integrand $\mathcal{B}$ may be expressed as,

$$\begin{aligned}\mathcal{B} = & \left[\left(\frac{\partial w}{\partial x_1} + \psi_1\right) A_{55} + \left(\frac{\partial w}{\partial x_2} + \psi_2\right) A_{56}\right] \left(\frac{\partial v_3}{\partial x_1} + v_4\right) \\ & + \left[\left(\frac{\partial w}{\partial x_1} + \psi_1\right) A_{56} + \left(\frac{\partial w}{\partial x_2} + \psi_2\right) A_{66}\right] \left(\frac{\partial v_3}{\partial x_2} + v_5\right).\end{aligned}$$

Now that terms in the integrand have been determined it is possible to integrate by parts as required. Before this is done however, it is worth noting that the above the terms enclosed in square brackets can be substituted by the stress resultants, bending moment resultants and transverse shear terms given in Equations (2.52), (2.53) and (2.54) respectively. For $\mathcal{A}$ this yields,

$$\mathcal{A} = N_1\frac{\partial v_1}{\partial x_1} + N_2\frac{\partial v_2}{\partial x_2} + N_4\frac{\partial v_1}{\partial x_2} + N_4\frac{\partial v_2}{\partial x_1} + M_1\frac{\partial v_4}{\partial x_1} + M_2\frac{\partial v_5}{\partial x_2} + M_4\frac{\partial v_4}{\partial x_2} + M_4\frac{\partial v_5}{\partial x_1}.$$

By performing the same substitutions for $\mathcal{B}$ we obtain,

$$\mathcal{B} = Q_5\left(\frac{\partial v_3}{\partial x_1} + v_4\right) + Q_6\left(\frac{\partial v_3}{\partial x_2} + v_5\right).$$

Considering the integrals of $\mathcal{A}$ and $\mathcal{B}$ over Ω now as summations of integral contributions taken over each element Ω_k for $k = 1, \ldots, N$ it is possible to obtain, via integration by parts,

$$\begin{aligned}-\sum_{k=1}^{N}\int_{\Omega_k} \mathcal{A}\, d\mathbf{x} = & \sum_{k=1}^{N}\int_{\Omega_k} \left(\frac{\partial}{\partial x_1}N_1 + \frac{\partial}{\partial x_2}N_4\right) v_1 + \left(\frac{\partial}{\partial x_1}N_4 + \frac{\partial}{\partial x_2}N_2\right) v_2 \\ & \qquad + \left(\frac{\partial}{\partial x_1}M_1 + \frac{\partial}{\partial x_2}M_4\right) v_4 + \left(\frac{\partial}{\partial x_1}M_4 + \frac{\partial}{\partial x_2}M_2\right) v_5\ d\mathbf{x} \\ & - \sum_{k=1}^{N}\int_{\partial\Omega_k} (N_1n_1 + N_4n_2)\, v_1 + (N_4n_1 + N_2n_2)\, v_2 \\ & \qquad + (M_1n_1 + M_4n_2)\, v_4 + (M_4n_1 + M_2n_2)\, v_5\ ds.\end{aligned}$$

Similarly, for $\mathcal{B}$ the resulting expression after integration is,

$$\begin{aligned}-\sum_{k=1}^{N}\int_{\Omega_k} \mathcal{B}\, d\mathbf{x} = & \sum_{i=1}^{N}\int_{\Omega_k} \left(\frac{\partial}{\partial x_1}Q_5 + \frac{\partial}{\partial x_2}Q_6\right) v_3 - (Q_5)\, v_4 - (Q_6)\, v_5\ d\mathbf{x} \\ & - \sum_{k=1}^{N}\int_{\partial\Omega_k} (Q_5n_1 + Q_6n_2)\, v_3\ ds.\end{aligned}$$

By now combining these terms to give an expression for $-a(\mathbf{u}, \mathbf{v})$ we obtain,

$$\begin{aligned}-a(\mathbf{u}, \mathbf{v}) = & -\sum_{k=1}^{N}\int_{\Omega_k} \mathcal{A}\, d\mathbf{x} - \sum_{k=1}^{N}\int_{\Omega_k} \mathcal{B}\, d\mathbf{x} \\ = & \sum_{k=1}^{N}\int_{\Omega_k} \left(\frac{\partial}{\partial x_1}N_1 + \frac{\partial}{\partial x_2}N_4\right) v_1 + \left(\frac{\partial}{\partial x_1}N_4 + \frac{\partial}{\partial x_2}N_2\right) v_2 \\ & \qquad + \left(\frac{\partial}{\partial x_1}Q_5 + \frac{\partial}{\partial x_2}Q_6\right) v_3 + \left(\frac{\partial}{\partial x_1}M_1 + \frac{\partial}{\partial x_2}M_4\right) v_4 \\ & \qquad + \left(\frac{\partial}{\partial x_1}M_4 + \frac{\partial}{\partial x_2}M_2\right) v_5 - (Q_5)\, v_4 - (Q_6)\, v_5\ d\mathbf{x} \\ & - \sum_{k=1}^{N}\int_{\partial\Omega_k} (N_1n_1 + N_4n_2)\, v_1 + (N_4n_1 + N_2n_2)\, v_2 \\ & \qquad + (Q_5n_1 + Q_6n_2)\, v_3 + (M_1n_1 + M_4n_2)\, v_4 \\ & \qquad + (M_4n_1 + M_2n_2)\, v_5\ ds.\end{aligned}$$

For convenience and clearer notation, the above expression can be expressed as,

$$-a(\mathbf{u},\mathbf{v}) = \sum_{k=1}^{N} \int_{\Omega_k} \operatorname{div} \mathbf{T}(\mathbf{u}) \cdot \mathbf{v} - \mathbf{q}(\mathbf{u}) \cdot \mathbf{v} \, d\mathbf{x} - \sum_{k=1}^{N} \int_{\partial\Omega_k} \mathbf{T}(\mathbf{u})\, \mathbf{n}_k \cdot \mathbf{v} \, ds, \tag{4.95}$$

where $\mathbf{v} = (v_1, v_2, v_3, v_4, v_5)^T$ as previously defined, $\mathbf{n}_k = (n_1, n_2)^T$ is the unit outward normal to the boundary $\partial\Omega_k$ and $\mathbf{T}(\mathbf{u})$ and $\mathbf{q}(\mathbf{u})$ are of the form,

$$\mathbf{T}(\mathbf{u}) \equiv \mathbf{T} = \begin{bmatrix} T_{11} & T_{12} \\ T_{21} & T_{22} \\ T_{31} & T_{32} \\ T_{41} & T_{42} \\ T_{51} & T_{52} \end{bmatrix} \equiv \begin{bmatrix} N_1 & N_4 \\ N_4 & N_2 \\ Q_5 & Q_6 \\ M_1 & M_4 \\ M_4 & M_2 \end{bmatrix} \quad \text{and} \quad \mathbf{q}(\mathbf{u}) \equiv \mathbf{q} = \begin{bmatrix} 0 \\ 0 \\ 0 \\ Q_5 \\ Q_6 \end{bmatrix} \tag{4.96}$$

where we now define,

$$\operatorname{div} \mathbf{T} := \left(\sum_{j=1}^{2} \frac{\partial T_{ij}}{\partial x_j} \right)_{i=1}^{5} \quad \text{and} \quad \mathbf{T}\,\mathbf{n}_k := \left(\sum_{j=1}^{2} T_{ij} n_j \right)_{i=1}^{5},$$

and where $\mathbf{u}$ is contained in the terms N_i, M_i for $i = 1, 2, 4$ and Q_i for $i = 5, 6$ given by Equations (2.52), (2.53) and (2.54) respectively. The task is now to use this result to help find a bound for the error in energy defined in Equation (4.94). Thus it is necessary to express $a(\mathbf{u}, \mathbf{v})$ and $F(\mathbf{v})$ with $\mathbf{u} = \mathbf{u}_h$ and $\mathbf{v} = \mathbf{e} - \pi_h\mathbf{e}$. It is possible to do this by simply substituting $\mathbf{u} = \mathbf{u}_h$ and $\mathbf{v} = \mathbf{e} - \pi_h\mathbf{e}$ in the above as the integrals are now being considered as summations over each elemental contribution. Thus, for the bilinear form,

$$\begin{aligned} -a(\mathbf{u}_h, \mathbf{e} - \pi_h\mathbf{e}) &= \sum_{k=1}^{N} \int_{\Omega_k} (\operatorname{div} \mathbf{T}(\mathbf{u}_h) - \mathbf{q}(\mathbf{u}_h)) \cdot (\mathbf{e} - \pi_h\mathbf{e}) \, d\mathbf{x} \\ &\quad - \sum_{k=1}^{N} \int_{\partial\Omega_k} (\mathbf{T}(\mathbf{u}_h)\, \mathbf{n}_k) \cdot (\mathbf{e} - \pi_h\mathbf{e}) \, ds, \end{aligned}$$

where it is important to now note in the above that the finite element solution $\mathbf{u}_h$ has been used in Equations (2.52), (2.53) and (2.54). Substituting this into Equation (4.94) gives, for the error $\mathbf{e} = \mathbf{u} - \mathbf{u}_h$,

$$\begin{aligned} ||\mathbf{e}||^2_{E(\Omega)} &= \sum_{k=1}^{N} \int_{\Omega_k} (\mathbf{f} + \operatorname{div} \mathbf{T}(\mathbf{u}_h) - \mathbf{q}(\mathbf{u}_h)) \cdot (\mathbf{e} - \pi_h\mathbf{e}) \, d\mathbf{x} \\ &- \sum_{k=1}^{N} \int_{\partial\Omega_k} (\mathbf{T}(\mathbf{u}_h)\, \mathbf{n}_k) \cdot (\mathbf{e} - \pi_h\mathbf{e}) \, ds \\ &+ \int_{\hat{\Gamma}_1} N_n(e_1 - \pi_h e_1) \, ds + \int_{\hat{\Gamma}_2} N_s(e_2 - \pi_h e_2) \, ds + \int_{\hat{\Gamma}_3} Q_n(e_3 - \pi_h e_3) \, ds \\ &+ \int_{\hat{\Gamma}_4} M_n(e_4 - \pi_h e_4) \, ds + \int_{\hat{\Gamma}_5} M_s(e_5 - \pi_h e_5) \, ds, \end{aligned} \tag{4.97}$$

where $\mathbf{f}$ is the applied load and which has the form $\mathbf{f} = (0, 0, q, 0, 0)^T$ for a transverse load, $\mathbf{n}_k$ is again the unit outward normal to the boundary $\partial\Omega_k$ of element Ω_k and, for the integrals over boundary portions $\hat{\Gamma}_i$ for $i = 1, 2, 3, 4, 5$ of $\partial\Omega$, the interpolation error vector has been separated into component form. The left side of the integrand for the element boundary integral has the form,

$$\mathbf{T}(\mathbf{u}_h)\,\mathbf{n}_k = \begin{bmatrix} N_1^h & N_4^h \\ M_4^h & N_2^h \\ Q_5^h & Q_6^h \\ M_1^h & M_4^h \\ M_4^h & M_2^h \end{bmatrix} \begin{bmatrix} n_1 \\ n_2 \end{bmatrix}, \tag{4.98}$$

for the interior element edges whilst, for edges which coincide with the boundary portions $\hat{\Gamma}_i$ for $i = 1, 2, 3, 4, 5$ we have,

$$\mathbf{T}(\mathbf{u}_h)\,\mathbf{n}_k = \begin{bmatrix} N_n^h & N_s^h & Q_n^h & M_n^h & M_s^h \end{bmatrix}^T, \tag{4.99}$$

the terms of which are defined as in Equation (3.28). As described in Section (4.4.2), it is clear that upon integrating around the perimeter of each element we are integrating along element edges $s \in S$ which lie in $\Omega \setminus \partial\Omega$ as well as those edges which lie on $\partial\Omega$ and thus not in set S. For each internal edge $s \in S$ it is illustrated in Section (4.4.2) that integration will be performed twice along the edge length. This arises from the fact that s is shared between two neighbouring elements and the same feature arises here. Consequently an analogous jump term $[\mathbf{T}(\mathbf{u}_h)\,\mathbf{n}_s]$ is obtained across side $s \in S$ which, for a point $\mathbf{x}$ on edge s is defined as,

$$[\mathbf{T}(\mathbf{u}_h)\,\mathbf{n}_s](\mathbf{x}) := \lim_{t\to 0^+} \mathbf{T}(\mathbf{u}_h(\mathbf{x}+t\mathbf{n}_s))\,\mathbf{n}_s(\mathbf{x}) - \lim_{t\to 0^+} \mathbf{T}(\mathbf{u}_h(\mathbf{x}-t\mathbf{n}_s))\,\mathbf{n}_s(\mathbf{x}). \tag{4.100}$$

It is thus possible to express Equation (4.97) as,

$$\begin{aligned} ||\mathbf{e}||^2_{E(\Omega)} &= \sum_{k=1}^{N} \int_{\Omega_k} (\mathbf{f} + \operatorname{div} \mathbf{T}(\mathbf{u}_h) - \mathbf{q}(\mathbf{u}_h)) \cdot (\mathbf{e} - \pi_h \mathbf{e})\, d\mathbf{x} \\ &+ \sum_{s\in S} \int_s [\mathbf{T}(\mathbf{u}_h)\,\mathbf{n}_s] \cdot (\mathbf{e} - \pi_h \mathbf{e})\, ds \\ &+ \int_{\hat{\Gamma}_1} (N_n - N_n^h)(e_1 - \pi_h e_1)\, ds + \int_{\hat{\Gamma}_2} (N_s - N_s^h)(e_2 - \pi_h e_2)\, ds \\ &+ \int_{\hat{\Gamma}_3} (Q_n - Q_n^h)(e_3 - \pi_h e_3)\, ds + \int_{\hat{\Gamma}_4} (M_n - M_n^h)(e_4 - \pi_h e_4)\, ds \\ &+ \int_{\hat{\Gamma}_5} (M_s - M_s^h)(e_5 - \pi_h e_5)\, ds. \end{aligned}$$

As before we now obtain the following error representation, from which the a posteriori error estimate will follow by using suitable estimates for the interpolation error $\mathbf{e} - \pi_h\mathbf{e}$. The final error representation then takes on the form of that arrived at in the previous chapter in the case for linear elasticity in two dimensions,

$$||\mathbf{e}||^2_{E(\Omega)} = E_1 + E_2, \tag{4.101}$$

where,

$$E_1 = \sum_{k=1}^{N} \int_{\Omega_k} \mathcal{R}_1(\mathbf{u}_h) \cdot (\mathbf{e} - \pi_h \mathbf{e})\, d\mathbf{x}, \tag{4.102}$$

$$E_2 = \sum_{k=1}^{N} \int_{\partial\Omega_k} h_k \mathcal{R}_2(\mathbf{u}_h) \cdot (\mathbf{e} - \pi_h \mathbf{e})\, ds, \tag{4.103}$$

with,

$$\mathcal{R}_1(\mathbf{u}_h) = \mathbf{f} + \operatorname{div}\mathbf{T}(\mathbf{u}_h) - \mathbf{q}(\mathbf{u}_h), \quad \text{on } \Omega_k, \tag{4.104}$$

and,

$$\mathcal{R}_2(\mathbf{u}_h) = \begin{cases} \frac{1}{2h_k}\left[\mathbf{T}(\mathbf{u}_h)\mathbf{n}_s\right], & \text{on } s \subset \partial\Omega_k \text{ if } s \in S, \\ \frac{1}{h_k}\left[N_n - N_n^h, 0, 0, 0, 0\right]^T, & \text{on } \partial\Omega_k \cap \hat{\Gamma}_1, \\ \frac{1}{h_k}\left[0, N_s - N_s^h, 0, 0, 0\right]^T, & \text{on } \partial\Omega_k \cap \hat{\Gamma}_2, \\ \frac{1}{h_k}\left[0, 0, Q_n - Q_n^h, 0, 0\right]^T, & \text{on } \partial\Omega_k \cap \hat{\Gamma}_3, \\ \frac{1}{h_k}\left[0, 0, 0, M_n - M_n^h, 0\right]^T, & \text{on } \partial\Omega_k \cap \hat{\Gamma}_4, \\ \frac{1}{h_k}\left[0, 0, 0, 0, M_s - M_s^h\right]^T, & \text{on } \partial\Omega_k \cap \hat{\Gamma}_5, \end{cases} \tag{4.105}$$

where $\mathbf{q}(\mathbf{u}_h) = \left[0, 0, 0, Q_5^h, Q_6^h\right]^T$. We now proceed as described in detail in Section (4.4.2) and obtain the required a posteriori error estimate. From Equation (4.101),

$$||\mathbf{e}||^2_{E(\Omega)} = |E_1 + E_2| \leq |E_1| + |E_2|, \tag{4.106}$$

and so now we need only work with the definitions of E_1 and E_2 in order to change the error estimate into one of a more useful form. Before doing this, however, interpolation error bounds will now be given in the plate context so that, in a similar way to those met earlier for the linear elasticity problem and using Appendix E,

$$||\mathbf{e} - \pi_h\mathbf{e}||_{L_2(\Omega_k)} \leq C^i_{1,k} h_k ||\mathbf{e}||_{E(\Omega_k)}, \tag{4.107}$$

and,

$$||\mathbf{e} - \pi_h\mathbf{e}||_{L_2(\partial\Omega_k)} \leq C^i_{2,k} h_k^{\frac{1}{2}} ||\mathbf{e}||_{E(\Omega_k)}. \tag{4.108}$$

Where,

$$C^i_{1,k} = \sup_{\boldsymbol{\tau}\in V_e} \frac{h_k^{-1}||\boldsymbol{\tau} - \pi_h\boldsymbol{\tau}||_{L_2(\Omega_k)}}{||\boldsymbol{\tau}||_{E(\Omega_k)}}, \tag{4.109}$$

$$C^i_{2,k} = \sup_{\boldsymbol{\tau}\in V_e} \frac{h_k^{-\frac{1}{2}}||\boldsymbol{\tau} - \pi_h\boldsymbol{\tau}||_{L_2(\partial\Omega_k)}}{||\boldsymbol{\tau}||_{E(\Omega_k)}}, \tag{4.110}$$

and where now the energy norm term is defined in terms of the plate bilinear form. Using the Cauchy-Schwarz inequality on Equation (4.102) gives,

$$\begin{aligned} |E_1| &\leq \sum_k ||\mathcal{R}_1(\mathbf{u}_h)||_{L_2(\Omega_k)} ||\mathbf{e} - \pi_h\mathbf{e}||_{L_2(\Omega_k)}, \\ &\leq \sum_k ||\mathcal{R}_1(\mathbf{u}_h)||_{L_2(\Omega_k)} C^i_{1,k} h_k ||\mathbf{e}||_{E(\Omega_k)}, \quad \text{using Equation (4.107) with } \tilde{k} = k, \\ &\leq \left(\sum_k \left[C^i_{1,k} h_k ||\mathcal{R}_1(\mathbf{u}_h)||_{L_2(\Omega_k)}\right]^2\right)^{\frac{1}{2}} \left(\sum_k ||\mathbf{e}||^2_{E(\Omega_k)}\right)^{\frac{1}{2}} \\ &= \left(\sum_k \left[C^i_{1,k} h_k ||\mathcal{R}_1(\mathbf{u}_h)||_{L_2(\Omega_k)}\right]^2\right)^{\frac{1}{2}} ||\mathbf{e}||_{E(\Omega)}, \end{aligned} \tag{4.111}$$

where the Ω_k subscript notation denotes norms taken over element Ω_k. By applying Cauchy-Schwarz to the definition of E_2 in Equation (4.103),

$$\begin{aligned}
|E_2| &\leq \sum_k ||h_k \mathcal{R}_2(\mathbf{u}_h)||_{L_2(\partial\Omega_k)} ||\mathbf{e} - \pi_h \mathbf{e}||_{L_2(\partial\Omega_k)}, \\
&\leq \sum_k ||h_k \mathcal{R}_2(\mathbf{u}_h)||_{L_2(\partial\Omega_k)} C^i_{2,k} h_k^{\frac{1}{2}} ||\mathbf{e}||_{E(\Omega_k)}, \quad \text{using Equation (4.108) with } \tilde{k} = k, \\
&\leq \left(\sum_k \left[C^i_{2,k} h_k^{\frac{1}{2}} ||h_k \mathcal{R}_2(\mathbf{u}_{h,p})||_{L_2(\partial\Omega_k)} \right]^2 \right)^{\frac{1}{2}} \left(\sum_k ||\mathbf{e}||^2_{E(\Omega_k)} \right)^{\frac{1}{2}}, \\
&= \left(\sum_k \left[C^i_{2,k} h_k^{\frac{1}{2}} ||h_k \mathcal{R}_2(\mathbf{u}_{h,p})||_{L_2(\partial\Omega_k)} \right]^2 \right)^{\frac{1}{2}} ||\mathbf{e}||_{E(\Omega)}.
\end{aligned} \tag{4.112}$$

Using the inequalities (4.111) and (4.112) the error may be bounded above as,

$$||\mathbf{e}||_{E(\Omega)} \leq \left(\sum_k \left[C^i_{1,k} h_k ||\mathcal{R}_1(\mathbf{u}_h)||_{L_2(\Omega_k)} \right]^2 \right)^{\frac{1}{2}} + \left(\sum_k \left[C^i_{2,k} h_k^{\frac{1}{2}} ||h_k \mathcal{R}_2(\mathbf{u}_{h,p})||_{L_2(\partial\Omega_k)} \right]^2 \right)^{\frac{1}{2}}, \tag{4.113}$$

where it is possible to evaluate all terms on the right hand side. This formulation may be simplified as performed for the linear elasticity problem in two dimensions yielding again an expression of the form given in Equation (4.73) but now with the residual terms given by Equations (4.104) and (4.105). The theory thus far applied is rigorous but it can be seen that the estimated error relies upon the values of the interpolation error constants. In one dimension the values of these constants can be determined analytically but analytical results for problems in two dimensions are not as readily obtained. Consequently the constants for such problems shall be obtained computationally and a technique developed for this will be discussed in Chapters 5 and 6.

4.5.1 Transition Element Effects

The modifications required for the plate estimator introduced in Section (4.5) are the same as those detailed for the problem of linear elasticity in Section (4.4.3). Consequently we again consider the possibility of transition elements in the mesh by considering elements as illustrated in Figure (4.17) where it can be seen that each element Ω_k for $k = 1, \ldots, N$ is considered as a composite element, consisting of four sub-element regions Ω_{kl} where $l = 1, 2, 3, 4$. This means that integrals over Ω_k are considered over each sub-element region so that, as before,

$$\int_{\Omega_k} \mathcal{F}(\mathbf{x})\, d\mathbf{x} \quad \text{now becomes} \quad \sum_{l=1}^{4} \int_{\Omega_{kl}} \mathcal{F}(\mathbf{x})\, d\mathbf{x},$$

for any $\mathcal{F}(\mathbf{x})$. Similarly, for integrals around the element boundary, the modifications mean that,

$$\int_{\partial\Omega_k} \mathcal{F}(\mathbf{x})\, ds \quad \text{now becomes} \quad \sum_{l=1}^{4} \int_{\partial\Omega_{kl}} \mathcal{F}(\mathbf{x})\, ds,$$

which entails the introduction of interior jumps arising from possible lines of slope discontinuity. It is thus found that performing the above modified integration around each $\partial\Omega_{kl}$ for $k = 1, \ldots, N$

and $l = 1, 2, 3, 4$ will result in the integration being shared between adjacent elements along each element edge $s \in (\partial\Omega_k \cap \partial\Omega_{kl}) \setminus \partial\Omega \equiv S_k$ where again, $S \equiv \cup_k S_k$, which is the set of all internal element edges. This is not the case for each $t \in \partial\Omega_{lk} \setminus \partial\Omega_k \equiv T_k$ where again, $T \equiv \cup_k T_k$, which is the set of all interior lines of slope discontinuity and which are specific for the corresponding transition element in which they reside. Following the modifications detailed in Section (4.4.3) the error for the plate may thus be expressed as,

$$||\mathbf{e}||^2_{E(\Omega)} = E_1 + E_2,$$

where now,

$$E_1 \equiv \sum_{k=1}^{N} \sum_{l=1}^{4} \int_{\Omega_{kl}} \mathcal{R}_1(\mathbf{u}_h) \cdot (\mathbf{e} - \pi_h \mathbf{e})\, d\mathbf{x}, \tag{4.114}$$

and,

$$E_2 \equiv \sum_{k=1}^{N} \sum_{l=1}^{4} \int_{\partial\Omega_{kl}} h_k \mathcal{R}_2(\mathbf{u}_h) \cdot (\mathbf{e} - \pi_h \mathbf{e})\, ds, \tag{4.115}$$

with,

$$\mathcal{R}_1(\mathbf{u}_h) = \mathbf{f} + \mathrm{div}\, \mathbf{T}(\mathbf{u}_h) - \mathbf{q}(\mathbf{u}_h), \text{ on } \Omega_{kl}, \tag{4.116}$$

and,

$$\mathcal{R}_2(\mathbf{u}_h) = \begin{cases} \dfrac{1}{2h_k}[\mathbf{T}(\mathbf{u}_h)\mathbf{n}_s], & \text{on } s \in (\partial\Omega_{kl} \cap \partial\Omega_k) \setminus \partial\Omega \equiv S_k \text{ for each } \Omega_k, \\ \dfrac{1}{h_k}[\mathbf{T}(\mathbf{u}_h)\mathbf{n}_s], & \text{on } s \in \partial\Omega_{kl} \setminus \partial\Omega_k \equiv T_k \text{ for each } \Omega_k, \\ \dfrac{1}{h_k}\left[N_n - N_n^h, 0, 0, 0, 0\right]^T, & \text{on } \partial\Omega_{kl} \cap \hat{\Gamma}_1, \\ \dfrac{1}{h_k}\left[0, N_s - N_s^h, 0, 0, 0\right]^T, & \text{on } \partial\Omega_{kl} \cap \hat{\Gamma}_2, \\ \dfrac{1}{h_k}\left[0, 0, Q_n - Q_n^h, 0, 0\right]^T, & \text{on } \partial\Omega_{kl} \cap \hat{\Gamma}_3, \\ \dfrac{1}{h_k}\left[0, 0, 0, M_n - M_n^h, 0\right]^T, & \text{on } \partial\Omega_{kl} \cap \hat{\Gamma}_4, \\ \dfrac{1}{h_k}\left[0, 0, 0, 0, M_s - M_s^h\right]^T, & \text{on } \partial\Omega_{kl} \cap \hat{\Gamma}_5, \end{cases} \tag{4.117}$$

where $\mathbf{f}$ is the applied load which again has the form $\mathbf{f} = [0, 0, q, 0, 0]^T$ for a transverse load, $\mathbf{q}(\mathbf{u}_h) = \left[0, 0, 0, Q_5^h, Q_6^h\right]^T$ and the jump terms are as described by Equations (4.98), (4.99) and (4.100).

As performed in Section (4.4.3) the interpolation error bounds given in Equations (4.107) and (4.108) may now be expressed for a typical element Ω_k and taking into account the possible sub-element regions as,

$$\left[\sum_{l=1}^{4} ||\mathbf{e} - \pi_h \mathbf{e}||^2_{L_2(\Omega_{kl})}\right]^{\frac{1}{2}} \leq C^i_{1,k} h_k ||\mathbf{e}||_{E(\Omega_k)}, \tag{4.118}$$

and,

$$\left[\sum_{l=1}^{4} ||\mathbf{e} - \pi_h \mathbf{e}||^2_{L_2(\partial\Omega_{kl})}\right]^{\frac{1}{2}} \leq C^i_{2,k} h_k^{\frac{1}{2}} ||\mathbf{e}||_{E(\Omega_k)}. \tag{4.119}$$

Where now,

$$C^i_{1,k} = \sup_{\boldsymbol{\tau} \in V_e} \frac{h_k^{-1}\left[\sum_{l=1}^{4} ||\boldsymbol{\tau} - \pi_h \boldsymbol{\tau}||^2_{L_2(\Omega_{kl})}\right]^{\frac{1}{2}}}{||\boldsymbol{\tau}||_{E(\Omega_k)}}, \tag{4.120}$$

and,

$$C^i_{2,k} = \sup_{\boldsymbol{\tau} \in V_e} \frac{h_k^{\frac{1}{2}}\left[\sum_{l=1}^{4} ||\boldsymbol{\tau} - \pi_h \boldsymbol{\tau}||^2_{L_2(\partial\Omega_{kl})}\right]^{\frac{1}{2}}}{||\boldsymbol{\tau}||_{E(\Omega_k)}}. \tag{4.121}$$

By employing the same techniques as in Sections (4.4.3) and the first part of Section (4.5) the error, measured in the energy norm, can be bounded above as,

$$||\mathbf{e}||_{E(\Omega)} \leq \left[\sum_{k=1}^{N}\sum_{l=1}^{4}\left[C^i_{1,k} h_k ||\mathcal{R}_1(\mathbf{u}_h)||_{L_2(\Omega_{kl})}\right]^2\right]^{\frac{1}{2}} + \left[\sum_{k=1}^{N}\sum_{l=1}^{4}\left[C^i_{2,k} h_k^{\frac{1}{2}} ||h_k \mathcal{R}_2(\mathbf{u}_h)||_{L_2(\partial\Omega_{kl})}\right]^2\right]^{\frac{1}{2}}. \tag{4.122}$$

As previously, for the case where there are no transition elements the estimator will reduce to that of Equation (4.113) since there will be no interior jumps on the elements and the sub-element region considerations will not be necessary.

In order to be able to implement this error estimator, the immediate task is to obtain the interpolation error constants $C^i_{1,k}$ and $C^i_{2,k}$. These will be obtained computationally and details of the work performed in this area are included in Chapters 5 and 6.

Chapter 5

Interpolation Error

In Section (4.4) of Chapter 4 the a posteriori error estimator of Johnson and Hansbo, [27], was introduced for linear elasticity in two dimensions and applied on a mesh consisting of quadrilateral elements. The estimator was then enhanced in Section (4.4.3) in order to cope with the occurrence of transition elements in the mesh and finally, in Section (4.5) an adaptation of the estimator for plate theory was proposed. In each occurrence of the estimator a reliance upon interpolation error constants is seen. The existence of this type of constant is as given by Scott and Zhang, [47], and upper bounds for use in the Johnson-Hansbo estimator are given in [27] for linear elasticity and quoted in Section (4.4.4) along with comments and observations. It seems that computed values of the constants in the form in which we require do not exist in the current literature and so it is the aim of this chapter to develop computational methods for obtaining them. In addition, the resulting numerical values for the interpolation error constants will be included and commented upon. To recap, the interpolation error constants $C^i_{1,k}$ and $C^i_{2,k}$ occur as given in Equations (4.64) and (4.65) and Equations (4.107) and (4.108) in both the linear elasticty and plate contexts respectively. Their generic definitions are repeated here in Equations (5.1) and (5.2) respectively as,

$$||\mathbf{e} - \pi_h \mathbf{e}||_{L_2(\Omega_k)} \leq C^i_{1,k} h_k ||\mathbf{e}||_{E(\Omega_k)}, \tag{5.1}$$

and,

$$||\mathbf{e} - \pi_h \mathbf{e}||_{L_2(\partial\Omega_k)} \leq C^i_{2,k} h_k^{\frac{1}{2}} ||\mathbf{e}||_{E(\Omega_k)}, \tag{5.2}$$

where, from Appendix E,

$$C^i_{1,k} = \sup_{\boldsymbol{\alpha} \in V_e} \frac{h_k^{-1} ||\boldsymbol{\alpha} - \pi_h \boldsymbol{\alpha}||_{L_2(\Omega_k)}}{||\boldsymbol{\alpha}||_{E(\Omega_k)}}, \tag{5.3}$$

and,

$$C^i_{2,k} = \sup_{\boldsymbol{\alpha} \in V_e} \frac{h_k^{-\frac{1}{2}} ||\boldsymbol{\alpha} - \pi_h \boldsymbol{\alpha}||_{L_2(\partial\Omega_k)}}{||\boldsymbol{\alpha}||_{E(\Omega_k)}}, \tag{5.4}$$

and where we have used the notation $||\cdot||_{E(\Omega_k)}$ to denote the energy norm evaluated on element Ω_k. In [27] it is recommended that for the computation of the above constants the supremum be taken over polynomials of degree $p+1$ where p is the degree of the piecewise polynomials used in the finite element method. The finite element analyses performed in this work will employ elements consisting of linear or bilinear shape functions with slight modification for transition elements as detailed in Section (3.9.1) and so this requirement merely means stepping up to the spaces of quadratic and biquadratic polynomials respectively. The aim of this chapter is to develop methods for calculating the interpolation error constants for various problems. Currently such information is not readily available and this is a strong motivation for providing results in some detail.

It can be seen above that there are two types of interpolation error constant. These will be known as the interior and boundary constants, denoted by $C^i_{1,k}$, and $C^i_{2,k}$ for a typical element Ω_k as shown in Equations (5.3) and (5.4) respectively. The differences between the two lie in the contents of the numerators with the interior interpolation error constant integrated over the whole domain of element Ω_k whilst that of the boundary constant is integrated only over the boundary $\partial\Omega_k$ of the element. Attention in the following sections will be mainly focused upon the determination of the interior constant. This is due to the fact that the computational procedures developed for the interior constant evaluation can be directly used for the boundary constant. In doing so there will be only one necessary modification. This lies in the aforementioned interpolation error integration where, in the case of the boundary constant, integration of the yet to be defined mass matrix $\mathbf{M}$ must be performed over the boundary of the element instead of over the whole element as is the case for the interior constant. Section (5.1) begins by considering a one-dimensional case where the need for the boundary constant does not arise. The numerical results, once verified against the theoretical result, are then found for problems in two-dimensions as detailed in Section (5.6) by modifying the original computational method. It is in Section (5.6) that details of the modification to the computational procedure in order to establish the boundary constant are included along with numerical results. This is followed by a further enhancement of the computational method in order to cater for the case of transition elements.

5.1 Interpolation Error Constant Calculation in One Dimension

Consider the following problem in one dimension,

$$-s''(x)=f(x), \quad x\in(0,1), \tag{5.5}$$

with boundary conditions $s'(1)=g$ and $s(0)=0$. The weak formulation for this problem may be derived in the usual manner by multiplying by a suitable test function $v\in V$, where we define,

$$V=\{v\in H^1(0,1):v(0)=0\},$$

and integrating by parts. This gives,

$$\begin{aligned}\int_0^1 f\,v\,dx &= -\int_0^1 v\,s''\,dx\\ &= -\left[v\,s'\right]_0^1 + \int_0^1 v'\,s'\,dx\\ &= \int_0^1 v'\,s'\,dx - v(1)\,g.\end{aligned}$$

Hence we have the weak formulation where we seek $s \in V$ such that,

$$a(s,v) = (f,v) + g\,v(1) \quad \forall\ v \in V, \tag{5.6}$$

where,

$$a(s,v) = \int_0^1 v'\,s'\,dx \quad \text{and} \quad (f,v) = \int_0^1 f\,v\,dx.$$

Consider the finite element discretisation $\Upsilon_{h,p}$ of the problem domain Ω which will comprise a number N of elements Ω_k each of size $h_k = x_k - x_{k-1}$ and let, for each Ω_k, p_k be a positive integer and $P_{p_k}(\Omega_k)$ be a space of polynomials on Ω_k of degree at most p_k. For the case of a piecewise linear finite element method we have that $p_k = 1$ and $P_1(\Omega_k)$ is thus the space of linear polynomials defined on Ω_k. Thus the finite element space is described as,

$$V^h = \{v_h \in V : v_h \text{ is continuous on } \Omega, v_h|_{\Omega_k} \in P_1(\Omega_k)\ \forall\ \Omega_k \in \Upsilon_h\}.$$

Application of the piecewise linear finite element method to the above weak formulation yields an approximating solution $s_h \in V^h \subset V$ to the true solution $s \in V$ where,

$$a(s_h, v_h) = (f, v_h) + g\,v_h(1), \quad \forall\ v_h \in V^h. \tag{5.7}$$

Since Equation (5.6) holds for all $v \in V$ then it must also hold for $v_h \in V^h \subset V$. Thus it is true that,

$$a(s, v_h) = (f, v_h) + g\,v_h(1), \quad \forall\ v_h \in V^h. \tag{5.8}$$

We are thus able to subtract Equation (5.7) from (5.8) giving the orthogonality condition,

$$a(s - s_h, v_h) = 0, \quad \forall\ v_h \in V^h. \tag{5.9}$$

This orthogonality property will be of use in the error analysis of the following section.

5.1.1 Error Analysis

Once s_h is known it is possible to define the error e in the finite element approximation as $e = s - s_h$. It follows then that the error, measured in the energy norm, may be expressed as,

$$||e||^2_{E(0,1)} = a(e,e) = a(s - s_h, e) = a(s - s_h, e - \pi_h e),$$

using Equation (5.9) with $v_h = \pi_h e \in V^h$ the interpolant of the error e. Thus,

$$||e||^2_{E(0,1)} = a(s, e - \pi_h e) - a(s_h, e - \pi_h e),$$

which, by using Equation (5.6) with $v = e - \pi_h e \in V$, enables the error to be expressed as,

$$||e||^2_{E(0,1)} = (f, e - \pi_h e) + g\,(e - \pi_h e)(1) - a(s_h, e - \pi_h e). \tag{5.10}$$

As previously stated, the finite element discretisation will comprise a finite number N of elements Ω_k each of size $h_k = x_k - x_{k-1}$ where each x_k for $k = 0, \ldots, N$, denotes a node in the interval $[0, 1]$. Thus, we may now consider Equation (5.10) in terms of elements as,

$$\begin{aligned}
||e||^2_{E(0,1)} &= \sum_{k=1}^{N} \int_{x_{k-1}}^{x_k} (e - \pi_h e)\, f\, dx + (e - \pi_h e)(1)\, g - \sum_{k=1}^{N} \left[\int_{x_{k-1}}^{x_k} (e - \pi_h e)'\, s_h'\, dx \right] \\
&= \sum_{k=1}^{N} \int_{x_{k-1}}^{x_k} (e - \pi_h e)\, f\, dx + (e - \pi_h e)(1)\, g \\
&\qquad - \sum_{k=1}^{N} \left[[(e - \pi_h e) s_h']_{x_{k-1}}^{x_k} - \int_{x_{k-1}}^{x_k} (e - \pi_h e)\, s_h''\, dx \right] \\
&= \sum_{k=1}^{N} \int_{x_{k-1}}^{x_k} (e - \pi_h e)\, f\, dx + 0 - \sum_{k=1}^{N} \left[0 - \int_{x_{k-1}}^{x_k} (e - \pi_h e)\, s_h''\, dx \right].
\end{aligned}$$

Where the first zero arises due to the fact that since we have nodal interpolation, the quantity $e - \pi_h e$ at $x = 1$ due to the presence of a node there is zero. Similarly, the zero term within the square brackets also arises due to the fact that the interpolant is exact at the nodes x_k for $k = 0, \ldots, N$. This gives finally,

$$\begin{aligned}
||e||^2_{E(0,1)} &= \sum_{k=1}^{N} \int_{x_{k-1}}^{x_k} (f + s_h'')\, (e - \pi_h e)\, dx \\
&= \sum_{k=1}^{N} \int_{x_{k-1}}^{x_k} (e - \pi_h e) f\, dx,
\end{aligned} \tag{5.11}$$

since we have a piecewise linear finite element approximation. Applying Cauchy-Schwarz to Equation (5.11) yields,

$$\begin{aligned}
||e||^2_{E(0,1)} &\le \sum_{k=1}^{N} ||h_k f||_{L_2(x_{k-1},x_k)} ||h_k^{-1}(e - \pi_h e)||_{L_2(x_{k-1},x_k)} \\
&\le \left[\sum_{k=1}^{N} ||h_k^{-1}(e - \pi_h e)||^2_{L_2(x_{k-1},x_k)} \right]^{\frac{1}{2}} ||h_k f||_{L_2(0,1)},
\end{aligned} \tag{5.12}$$

where we have used the notation $||\cdot||_{L_2(x_{k-1},x_k)}$ to denote the L_2-norm over the element $\Omega_k \equiv [x_{k-1}, x_k]$. In order to proceed we need to bound the interpolation error measured in the L_2-norm in the above inequality by the error e measured in the energy norm. This requirement gives rise to the inequality,

$$||e - \pi_h e||_{L_2(x_{k-1},x_k)} \le C^i_{1,k}\, h_k\, ||e||_{E(x_{k-1},x_k)}, \tag{5.13}$$

in which accurate estimates of the interpolation error constant $C^i_{1,k}$ on each element Ω_k must be obtained.

5.1.2 Determination of Interpolation Error Constant

As illustrated in the previous section, the task is now to find the interpolation constant $C^i_{1,k}$ for an element Ω_k of length $h_k = x_k - x_{k-1}$ where, in one dimension and using Equation (5.3),

$$C^i_{1,k} = \sup_{a \in V} \frac{h_k^{-1} \|a - \pi_h a\|_{L_2(x_{k-1},x_k)}}{\|a\|_{E(x_{k-1},x_k)}} = \sup_{a \in V} \frac{h_k^{-1}\left[\displaystyle\int_{x_{k-1}}^{x_k} (a - \pi_h a)^2 \, dx\right]^{\frac{1}{2}}}{\left[\displaystyle\int_{x_{k-1}}^{x_k} (a')^2 \, dx\right]^{\frac{1}{2}}}.$$

Before proceeding it is useful to transform this problem - in a similar way to that described in Section (3.7) - onto a standard element of length unity in order to obtain an expression for $C^i_{1,k}$ independent of h_k. In doing this the task becomes that of finding,

$$(C^i_{1,k})^2 \equiv (C^i_1)^2 = \sup_{\hat{a} \in H^1(0,1)} \frac{h_k^{-2} \displaystyle\int_0^1 (\hat{a} - \pi\hat{a})^2 |J| \, d\hat{x}}{\displaystyle\int_0^1 (J^{-1}\hat{a}')(J^{-1}\hat{a}')|J| \, d\hat{x}},$$

where J is the usual Jacobian of the transformation and which in one dimension, mapping the general element (x_{k-1}, x_k) onto the standard element $(0,1)$, has value $(x_k - x_{k-1})/1 = h_k/1$. Thus substituting for J and J^{-1} the problem becomes,

$$(C^i_1)^2 = \sup_{\hat{a} \in H^1(0,1)} \frac{h_k^{-2} \displaystyle\int_0^1 (\hat{a} - \pi\hat{a})^2 h_k \, d\hat{x}}{\displaystyle\frac{1}{h_k^2} \int_0^1 (\hat{a}')^2 h_k \, d\hat{x}} = \sup_{\hat{a} \in H^1(0,1)} \frac{\displaystyle\int_0^1 (\hat{a} - \pi\hat{a})^2 \, d\hat{x}}{\displaystyle\int_0^1 (\hat{a}')^2 \, d\hat{x}} = \sup_{\hat{a} \in H^1(0,1)} \frac{\|\hat{a} - \pi\hat{a}\|^2_{L_2(0,1)}}{\|\hat{a}'\|^2_{L_2(0,1)}}, \tag{5.14}$$

where, in the above, $\pi\hat{a}$ is used instead of $\pi_h\hat{a}$ since the interpolant is now defined on the standard element with $\hat{h} = 1$. Thus the problem has been transformed to one on the unit length $(0,1)$ and, dropping the 'hat' notation for functions on the standard element for convenience, we require to find C^i_1 where,

$$(C^i_1)^2 = \sup_{a \in H^1(0,1)} \left\{ \frac{\|a - \pi a\|^2_{L_2(0,1)}}{\|a'\|^2_{L_2(0,1)}}; \pi a \in P_1(0,1), \pi a(0) = a(0), \pi a(1) = a(1) \right\}.$$

We now find the value of C^i_1. To begin we define $b = a - \pi a$ and since the interpolant is exact at the nodes it is immediately clear that $b(0) = b(1) = 0$. Differentiating and rearranging it can be seen that,

$$a' = b' + (\pi a)' = b' + c, \quad c \in \mathbb{R},$$

where c is obtained from the derivative of the linear interpolant. From this result it follows that,

$$\|a'\|^2_{L_2(0,1)} = \|b' + c\|^2_{L_2(0,1)} = \int_0^1 (b' + c)^2 \, dx = \int_0^1 (b')^2 + 2b'c + c^2 \, dx \geq \|b'\|^2_{L_2(0,1)},$$

since $b(0) = b(1)$ and $c \in \mathbb{R}$. It is of interest to note here that equality will hold if $c = 0$ which would arise if $a(0) = a(1)$. It is now possible to reformulate the problem into,

$$(C^i_1)^2 = \sup_{b \in \mathring{H}^1(0,1)} \left\{ \frac{\|b\|^2_{L_2(0,1)}}{\|b' + c\|^2_{L_2(0,1)}} \right\} = \sup_{b \in \mathring{H}^1(0,1)} \left\{ \frac{\|b\|^2_{L_2(0,1)}}{\|b'\|^2_{L_2(0,1)} + c^2} \right\}$$

$$\leq (C^i)^2 = \sup_{b\in \mathring{H}^1(0,1)} \left\{ \frac{||b||^2_{L_2(0,1)}}{||b'||^2_{L_2(0,1)}} \right\},$$

where, since $a(x) - \pi a(x) = 0$ at $x = 0$ and $x = 1$ we have that $b \in \mathring{H}^1(0,1)$. Thus it is now required to find C^i such that,

$$||b||_{L_2(0,1)} \leq C^i ||b'||_{L_2(0,1)}, \quad \forall\, b \in \mathring{H}^1(0,1),$$

which is a version of the Poincaré-Friedrichs inequality as described in [19] and [39].

Define $Aw := -w''$ and consider the eigenvalue problem,

$$Aw = \lambda w \quad \Rightarrow \quad -w'' = \lambda w, \quad \text{with} \quad w(0) = w(1) = 0, \tag{5.15}$$

where this problem has been chosen so that, via the weak formulation, we are able to bound the above supremum. The solution of Equation (5.15) involves, as usual, the solution of the auxiliary equation which for this problem has the form,

$$-m^2 = \lambda \quad \Rightarrow \quad m = \pm i\sqrt{\lambda}.$$

Substitution into the general solution yields,

$$w(x) = S\sin(x\sqrt{\lambda}) + T\cos(x\sqrt{\lambda}),$$

with S and T constants. Application of the boundary condition $w(0) = 0$ yields $T = 0$ in the above whilst $w(1) = 0$ provides the result (neglecting the trivial solution where S=0) that,

$$\begin{aligned} \sin(\sqrt{\lambda}) = 0 \quad &\Rightarrow \quad \sqrt{\lambda_n} = n\pi, \quad n = 0, \pm 1, \pm 2, \ldots, \\ &\Rightarrow \quad \lambda_n = n^2\pi^2, \quad n = 0, 1, 2, \ldots. \end{aligned}$$

It follows that the solution of Equation (5.15) is the eigensystem,

$$\{\lambda_n, w_n\}_{n=0}^{\infty} = \left\{ n^2\pi^2, \sin x\sqrt{\lambda_n} \right\}_{n=0}^{\infty},$$

where the w_n form a complete orthogonal system in $\mathring{H}^1(0,1) \subset L_2(0,1)$,

$$(w_n, w_m) \propto \delta_{mn} \quad \text{and} \quad (w_n', w_m') \propto \delta_{mn} \quad \text{for } m, n = 0, \ldots \infty,$$

where δ_{mn} is the Kronecker delta, equal to unity when $m = n$ and zero otherwise. The weak formulation of this eigenvalue problem is to find $(\lambda, w) \in \mathbb{R} \times \mathring{H}^1(0,1)$ such that,

$$(w', \gamma') = \lambda(w, \gamma), \quad \forall\, \gamma \in \mathring{H}^1(0,1). \tag{5.16}$$

Due to the orthogonality, it is possible to express any $b \in \mathring{H}^1(0,1)$ as

$$b = \sum_{i=1}^{\infty} \alpha_i w_i \tag{5.17}$$

with $\{\alpha_i\}_{i=1}^{\infty}$ scalars. It follows then that,

$$b' = \sum_{i=1}^{\infty} \alpha_i w_i' \tag{5.18}$$

and also that,

$$||b||^2_{L_2(0,1)} = \sum_{i=1}^{\infty} \alpha_i^2 (w_i, w_i) \quad \text{and} \quad ||b'||^2_{L_2(0,1)} = \sum_{i=1}^{\infty} \alpha_i^2 (w_i', w_i').$$

Substitution of Equations (5.17) and (5.18) into Equation (5.16) and taking $\gamma = b$ yields,

$$\left(\sum_{i=1}^{\infty} \alpha_i w_i', \sum_{j=1}^{\infty} \alpha_j w_j' \right) = \left(\sum_{k=1}^{\infty} \lambda_k \alpha_k w_k, \sum_{l=1}^{\infty} \alpha_l w_l \right)$$

by linearity. Using the orthogonality property it is then possible to write,

$$\sum_{i=1}^{\infty} \alpha_i^2 (w_i', w_i') = \sum_{j=1}^{\infty} \lambda_j \alpha_j^2 (w_j, w_j) \geq \lambda_1 \left(\sum_{j=1}^{\infty} \alpha_j^2 (w_j, w_j) \right)$$

where we have chosen λ_1 since it is the smallest non-trivial eigenvalue. The above may thus be expressed as,

$$||b'||^2_{L_2(0,1)} \geq \lambda_1 ||b||^2_{L_2(0,1)}.$$

Thus an upper bound for C^i has been found since it has been shown that,

$$(C^i)^2 = \sup_{b \in \mathring{H}^1(0,1)} \frac{||b||^2_{L_2(0,1)}}{||b'||^2_{L_2(0,1)}} \leq \frac{1}{\lambda_1}.$$

Now, for λ_1 in the eigenvalue problem it is possible to select $b = w_1$. In such a scenario it is clear that equality will hold in the above expression giving the best possible value,

$$(C^i)^2 = \frac{1}{\lambda_1} = \frac{1}{\pi^2} \quad \Rightarrow \quad C^i = \pi^{-1}.$$

However, for a general $b \in \mathring{H}^1(0,1)$ we have that $C_1^i \leq \pi^{-1}$. This finally gives the known result for the one dimensional problem considered here that,

$$||a - \pi a||_{L_2(0,1)} \leq \pi^{-1} ||a'||_{L_2(0,1)}, \quad \forall\ a \in V.$$

Such an analysis is not feasible for plates and so we need to develop a numerical procedure. As we now know the theoretical result for this one-dimensional problem, a numerical procedure will firstly be developed which may be verified against the known result. This is proposed in the following section.

5.2 Numerical Computation of Interpolation Error Constant

Having obtained a theoretical value for the interpolation error constant we now embark upon computational methods to test the numerical results for C_1^i. As described in [27] the interpolation error constant may be computed by taking the supremum of Equations (5.3) and (5.4) over a space of functions one degree higher than that used in the finite element model as described at the beginning of this chapter. This leads to a finite dimensional eigenvalue problem on the element, solvable by some standard numerical routine. Thus the problem here is to obtain a numerical estimate for the interpolation error constant when a linear interpolant is used to approximate any quadratic function over the element. We have shown this value to be $C_1^i \leq \pi^{-1}$ in the previous section and the task is now to develop a computational technique for obtaining numerical approximations to this value. Figure (5.1) shows the nodal configurations taken for a one-dimensional standard element in both linear and quadratic shape function contexts.

Any quadratic function may be defined over the quadratic element as,

$$u(x) = \sum_{i=1}^{3} u(x_i)\phi_i(x) = \sum_{i=1}^{3} u_i\phi_i(x),$$

where $\{u_i\}_{i=1}^3$ are the nodal values of u at node i with coordinate x_i and $\{\phi_i\}_{i=1}^3$ are the quadratic Lagrange shape functions associated with these nodes. Thus it is possible to express the interpo-

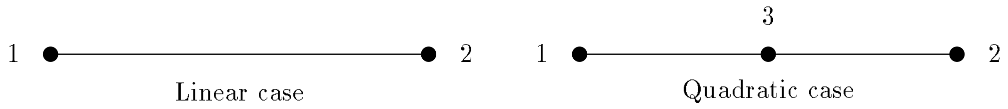

Figure 5.1: Nodal arrangement of linear and quadratic line elements.

lation error $u - \pi u$ at any point x in the domain as,

$$u(x) - \pi u(x) = \sum_{i=1}^{3} [u_i - \pi u_i]\, \phi_i(x) = [u_3 - \pi u_3]\, \phi_3(x), \tag{5.19}$$

where πu_i is the value of the interpolant πu at node i. The expression on the right-hand side of Equation (5.19) arises due to the fact that the interpolation error is zero at nodes 1 and 2 but we shall proceed here with the interpolation error in the most general form and given by the summation.

Since interest lies in evaluating the L_2-norm of this interpolation error, it is appropriate to look at this value squared. Thus,

$$\begin{aligned} |u(x) - \pi u(x)|^2 &= \left(\sum_{i=1}^{3} [u_i - \pi u_i]\, \phi_i(x)\right) \left(\sum_{j=1}^{3} [u_j - \pi u_j]\, \phi_j(x)\right), \\ &= \sum_{i,j=1}^{3} [u_i - \pi u_i]\, \phi_i(x)\phi_j(x)\, [u_j - \pi u_j]\,, \\ &= \mathbf{w}^T \mathbf{\Phi}(x)\, \mathbf{w}, \end{aligned} \tag{5.20}$$

where,

$$\mathbf{\Phi}(x) = \left(\phi_i(x)\, \phi_j(x)\right)_{i,j=1}^{3}, \quad \text{and} \quad \mathbf{w} = \mathbf{u} - \pi\mathbf{u},$$

and where now we have defined $\mathbf{u}$ and $\pi\mathbf{u}$ to be the vectors of nodal displacements for the quadratic function u and the linear interpolant πu respectively. The interpolant πu will interpolate the quadratic exactly at nodes 1 and 2. Thus it is possible to state that,

$$\pi u_i = u_i, \qquad \text{for } i = 1, 2.$$

By simple linear interpolation, the interpolant will have a value of $\frac{1}{2}(u_1 + u_2)$ at the midpoint. Thus the interpolant may be expressed in terms of u at the nodes by invoking a 'transformation' matrix $\mathbf{T}$ defined as,

$$\pi\mathbf{u} = \begin{bmatrix} \pi u_1 \\ \pi u_2 \\ \pi u_3 \end{bmatrix} = \begin{bmatrix} 1 & 0 & 0 \\ 0 & 1 & 0 \\ \frac{1}{2} & \frac{1}{2} & 0 \end{bmatrix} \begin{bmatrix} u_1 \\ u_2 \\ u_3 \end{bmatrix} = \mathbf{Tu}.$$

This allows $\mathbf{w}$ to be expressed as,

$$\mathbf{w} = \mathbf{u} - \pi\mathbf{u} = (\mathbf{I} - \mathbf{T})\mathbf{u},$$

where $\mathbf{I}$ is the identity matrix. From the previous section it was shown in Equation (5.14) that the task is to find C_1^i where,

$$(C_1^i)^2 = \sup_{u \in H^1(0,1)} \frac{||u - \pi u||^2_{L_2(0,1)}}{||u||^2_{E(0,1)}} = \sup_{u \in H^1(0,1)} \frac{(u - \pi u, u - \pi u)}{a(u, u)}, \tag{5.21}$$

where we recall that,

$$||\beta||_{L_2(0,1)} := (\beta, \beta)^{\frac{1}{2}} = \left(\int_0^1 |\beta|^2 \, dx \right)^{\frac{1}{2}},$$

and,

$$||\beta||_{E(0,1)} := a(\beta, \beta)^{\frac{1}{2}},$$

and we are able to use the bilinear form in the denominator due to the fact that the standard element coincides with that of the original region although this will generally not be the case. Thus it is possible to express (5.21) as,

$$(C_1^i)^2 = \sup_{\mathbf{u} \in \mathbb{R}^3} \frac{\mathbf{u}^T \left(\mathbf{I} - \mathbf{T}\right)^T \mathbf{M} \left(\mathbf{I} - \mathbf{T}\right) \mathbf{u}}{\mathbf{u}^T \mathbf{E} \mathbf{u}},$$

where $\mathbf{M}$ is the mass matrix and $\mathbf{E}$ is the stiffness matrix for the element, for which the definitions are given as,

$$\mathbf{M} = \left(M_{ij}\right)^3_{i,j=1} = \int_0^1 \mathbf{\Phi}(x) \, dx = \int_0^1 \left(\phi_i(x)\phi_j(x)\right)^3_{i,j=1} \, dx,$$

and,

$$\mathbf{E} = \left(E_{ij}\right)^3_{i,j=1} = \left(a(\phi_i, \phi_j)\right)^3_{i,j=1}.$$

By defining the matrix $\mathbf{F}$ to be,

$$\mathbf{F} = \left(\mathbf{I} - \mathbf{T}\right)^T \mathbf{M} \left(\mathbf{I} - \mathbf{T}\right),$$

the task may finally be expressed as one in which it is required to find C_1^i where,

$$(C_1^i)^2 = \sup_{\mathbf{u} \in \mathbb{R}^3} \left\{ \frac{\mathbf{u}^T \mathbf{F} \mathbf{u}}{\mathbf{u}^T \mathbf{E} \mathbf{u}} \right\}. \tag{5.22}$$

The terms in matrices $\mathbf{E}$ and $\mathbf{F}$ are easily computed now since we know the form of the problem being solved and the region of the element over which to integrate. The remaining task is to find the required supremum.

5.3 Numerical Results for Interpolation Error Constant

For the one-dimensional problem defined in Equation (5.5) the terms in matrices **E** and **F** are calculated. Denoting the quotient on the right of Equation (5.22) as Q, the task is thus to find the maximum of Q. Three methods will be used to test whether the numerical results for the interpolation error constant in the one dimensional problem are close to the theoretical value of $C_1^i \leq \pi^{-1}$.

5.3.1 Sampling Method - Mathematica

For this method many evaluations of the quotient Q are made at random sampling points. The number of samples made, N, is increased from 10^2 to 10^5. It is hoped that this 'Monte Carlo' type method will be able to pick out some sort of maximum value. After the quotient evaluation at the sampling points, the maximum value is found. As a check, the same procedure is also performed for the reciprocal of the quotient Q and in this case the minimum value of the reciprocal evaluations is found. In theory, the maximum of the quotient evaluations and the minimum of the reciprocal evaluations should be the reciprocals of each other approximately and tend to a common value as the number of sampling points increases. The results to six decimal places are as detailed in Table (5.1). As can be seen, for a given value of N the maximum and minimum values are close to

N	100	1000	10000	100000
Max(Q)	0.099996	0.100000	0.100000	0.100000
Min(1/Q)	10.000099	10.000000	10.000000	10.000000

Table 5.1: Sampling method results in one dimension.

reciprocals of each other as expected and in fact are reciprocals of each other when the accuracy is restricted to six decimal places. Thus, assuming that the most accurate result is when N is largest, the maximum value of the quotient is found to be 0.100000 to six decimal places. Since the work has been performed over a standard linear element and $h = 1$, we are able to calculate, by taking the square root in accordance with Equation (5.22), that this crude method yields a value for the interpolation error constant which is,

$$C_1^i = 0.316228 \text{ to six decimal places,}$$

which agrees well with the theoretical answer which states that the value is $C_1^i \leq \pi^{-1} = 0.318310$ to six decimal places.

5.3.2 Minimization Method - Mathematica

Mathematica, [59], has the facility to find the local minimum of a function f given a starting value. In the case of the current problem, we have that $f = 1/Q$ is a function of three variables, u_1, u_2 and u_3 and so it is necessary to specify the starting position in three dimensions. Mathematica also has a useful random number generator and so this may be used each time to obtain starting values for 40 executions of the minimization routine as shown in Table (5.2). As interest lies in finding the maximum of the quotient Q, the minimization routine is thus performed on the reciprocal of the quotient Thus by considering $f = 1/\mathrm{Q}$ in Table (5.2), partial derivative values of f are displayed along with the value of f at the minimum point found. These derivatives should obviously all be close to zero to ensure that a minimum has actually been found. From the table it is clear that

Run No.	Min. value	$\frac{\partial f}{\partial u_1}$	$\frac{\partial f}{\partial u_2}$	$\frac{\partial f}{\partial u_3}$
1	10.000000	$-5.09369(-8)$	$5.09369(-8)$	0
2	10.000000	$-5.20154(-10)$	$5.20154(-10)$	0
3	10.000000	$1.04157(-8)$	$-1.04157(-8)$	$7.10543(-15)$
4	10.000000	$-2.52236(-10)$	$2.52232(-10)$	0
5	10.000000	$1.78226(-7)$	$-1.78226(-7)$	$7.10543(-15)$
$\vdots$	$\vdots$	$\vdots$	$\vdots$	$\vdots$
36	10.000000	0	0	0
37	10.000000	$-2.54925(-9)$	$2.54922(-9)$	$2.13163(-14)$
38	10.000000	$-6.37901(-9)$	$6.37901(-9)$	$-3.55271(-15)$
39	10.000000	$6.41975(-12)$	$-6.40910(-12)$	$-7.10543(-15)$
40	10.000000	$5.29710(-12)$	$-5.29710(-12)$	0

Table 5.2: Minimization routine results for $f = 1/\mathrm{Q}$.

the value of the minimum of the reciprocal of the quotient is 10.000000 to six decimal places. The claim that this is a minimum is strengthened by the fact that the derivative values are all close to zero at the minimum points found. Thus, reciprocating this and taking the square root yields again the value of the interpolation error constant which is found to be,

$$C_1^i = 0.316228 \text{ to six decimal places,}$$

this again agrees well with the exact value, $\pi^{-1} = 0.318310$, to six decimal places, and is in total agreement with the numerical answer obtained in the previous section.

5.4 The Generalized Eigenvalue Problem

In this section it is proposed that the relationship between the quotient to be maximized and an associated generalized eigenvalue problem will be shown. It is shown that the maximum of a quotient of the type shown in Equation (5.22) is, in fact, the maximum eigenvalue of the generalized eigenvalue problem given by,

$$\lambda \mathbf{E}\mathbf{x} = \mathbf{F}\mathbf{x}, \tag{5.23}$$

in which matrices $\mathbf{E}$ and $\mathbf{F}$ are both real, symmetric and singular $n \times n$ matrices and where the task is to find scalars λ and non-zero vectors $\mathbf{x}$ such that Equation (5.23) holds. The general case of Equation (5.22) is thus one in which it is required to find,

$$\left(C_1^i\right)^2 = \sup_{\mathbf{x} \in \mathbb{R}^n} \left\{ \frac{\mathbf{x}^T \mathbf{F} \mathbf{x}}{\mathbf{x}^T \mathbf{E} \mathbf{x}} \right\}, \tag{5.24}$$

where again $\mathbf{E}$ and $\mathbf{F}$ are real, symmetric, and singular $n \times n$ matrices. The fact that both $\mathbf{E}$ and $\mathbf{F}$ are singular is potentially a problem. Matrix $\mathbf{E}$ is the element stiffness matrix and so the eigenvectors corresponding to zero eigenvalues are the rigid body motions of the problem. Specific to this problem however is the fact that eigenvectors of $\mathbf{E}$ corresponding to zero eigenvalues will also be eigenvectors of $\mathbf{F}$ which themselves correspond to zero eigenvalues of $\mathbf{F}$. This is due to the fact that the rigid body motions are linear displacements which the finite element interpolant is able to capture exactly. Thus,

$$\mathbf{E}\mathbf{v}_i = \mathbf{0} \quad \Rightarrow \quad \mathbf{F}\mathbf{v}_i = \mathbf{0} \quad \text{for} \quad i = n-r+1, \ldots, n,$$

where $\mathbf{v}_i$ for $i = n-r+1, \ldots, n$ are the r eigenvectors of $\mathbf{E}$ which correspond to zero eigenvalues. The matrix $\mathbf{F}$ will in fact have at least r zero eigenvalues since any linear displacement will be interpolated exactly by the finite element space which here is linear.

It will now be shown that the maximum of the quotient given in Equation (5.24) is in fact the maximum eigenvalue of the associated eigenvalue problem given in Equation (5.23). This is firstly done by proving the equality between Equation (5.24) where $\mathbf{x} \in \mathbb{R}^n$ and an equivalent quotient having $(n-r) \times (n-r)$ matrices $\tilde{\mathbf{E}}$ and $\tilde{\mathbf{F}}$ where $\tilde{\mathbf{E}}$ is a symmetric positive definite matrix and $\tilde{\mathbf{F}}$ is symmetric.

Since $\mathbf{E}$ is symmetric, real and $n \times n$, using [20] p379, there exists an orthogonal matrix $\mathbf{V}$ such that,

$$\mathbf{V}^T \mathbf{E} \mathbf{V} = \mathbf{D}_{\mathrm{E}}, \tag{5.25}$$

where $\mathbf{D}_{\mathrm{E}}$ is a diagonal matrix. Matrices $\mathbf{E}$ and $\mathbf{D}_{\mathrm{E}}$ are thus by definition similar matrices and consequently the diagonal terms of $\mathbf{D}_{\mathrm{E}}$ are the eigenvalues of $\mathbf{E}$. Additionally, since $\mathbf{V}$ is orthogonal it follows that $\mathbf{V}^T\mathbf{V} = \mathbf{I}$ and so premultiplying both sides of Equation (5.25) by $\mathbf{V}$ gives,

$$\mathbf{E}\mathbf{V} = \mathbf{V}\mathbf{D}_{\mathrm{E}}.$$

By now considering the columns of $\mathbf{V}$ the above may be expressed as,

$$\mathbf{E}\left[\mathbf{v}_1 \mathbf{v}_2 \ldots \mathbf{v}_n\right] = \left[\mathbf{v}_1 \mathbf{v}_2 \ldots \mathbf{v}_n\right] \mathbf{D}_{\mathrm{E}}.$$

It follows then that,

$$\mathbf{E}\mathbf{v}_i = d_{ii} \mathbf{v}_i, \ \text{for } i = 1, \ldots, n\,,$$

where d_{ii} are the diagonal entries of $\mathbf{D}_{\mathrm{E}}$. Clearly the vectors $\mathbf{v}_i$ for $i = 1, \ldots, n$ are the corresponding eigenvectors of $\mathbf{E}$ and since $\mathbf{V}$ is an orthogonal matrix then the eigenvectors must be orthonormal and span $\mathbb{R}^n$. However, $\mathbf{E}$ is also singular and as previously detailed there will exist r eigenvectors such that,

$$\mathbf{E}\mathbf{v}_i = \mathbf{0} \quad \text{for} \quad i = n - r + 1, \ldots, n.$$

This in turn implies that for the other $n - r$ eigenvectors,

$$\mathbf{E}\mathbf{v}_i \neq \mathbf{0} \quad \text{for} \quad i = 1, \ldots, n - r.$$

Any $\mathbf{x} \in \mathbb{R}^n$ may thus be expressed as a linear combination of the orthonormal eigenvectors $\{\mathbf{v}_i\}_{i=1}^n$ and so it is possible to express $\mathbf{x}$, using the substitution $k = n - r + 1$ for convenience, as,

$$\begin{aligned} \mathbf{x} &= \sum_{i=1}^{k-1} \alpha_i \mathbf{v}_i + \sum_{i=k}^{n} \alpha_i \mathbf{v}_i, \\ &= \quad \mathbf{x}_1 \quad + \quad \mathbf{x}_2. \end{aligned} \tag{5.26}$$

It follows then that,

$$\mathbf{E}\mathbf{x} = \mathbf{E}\mathbf{x}_1 + \mathbf{E}\mathbf{x}_2 = \mathbf{E}\mathbf{x}_1,$$

since $\mathbf{E}\mathbf{x}_2 = \mathbf{0}$ due to the fact that $\mathbf{x}_2$ is a linear combination of eigenvectors $\{\mathbf{v}_i\}_{i=k}^n$ where $\mathbf{E}\mathbf{v}_i = \mathbf{0}$. Thus, considering the denominator of Equation (5.24),

$$\begin{aligned} \mathbf{x}^T \mathbf{E}\mathbf{x} &= (\mathbf{x}_1 + \mathbf{x}_2)^T \mathbf{E} (\mathbf{x}_1 + \mathbf{x}_2), \\ &= \mathbf{x}_1^T \mathbf{E}\mathbf{x}_1, \quad \text{since } \mathbf{E} = \mathbf{E}^T, \\ &= \left(\sum_{i=1}^{n-r} \alpha_i \mathbf{v}_i \right)^T \mathbf{E} \left(\sum_{j=1}^{n-r} \alpha_j \mathbf{v}_j \right), \\ &= \sum_{i=1}^{n-r} \sum_{j=1}^{n-r} \alpha_i \alpha_j \mathbf{v}_i^T \mathbf{E} \mathbf{v}_j, \\ &= \boldsymbol{\alpha}^T \tilde{\mathbf{E}} \boldsymbol{\alpha}, \end{aligned}$$

where,

$$\tilde{\mathbf{E}} = \left(\tilde{E}_{ij} \right)_{i,j=1}^{n-r} \quad \text{and} \quad \tilde{E}_{ij} = \mathbf{v}_i^T \mathbf{E} \mathbf{v}_j \quad \text{for} \quad i, j = 1, \ldots, n - r. \tag{5.27}$$

The matrix $\mathbf{F}$ is also symmetric, real and $n \times n$. Thus, as for matrix $\mathbf{E}$ there must again exist an orthogonal matrix $\mathbf{U}$ such that,

$$\mathbf{U}^T \mathbf{F} \mathbf{U} = \mathbf{D}_{\mathrm{F}},$$

where $\mathbf{D}_{\mathrm{F}}$ is a diagonal matrix. Matrices $\mathbf{F}$ and $\mathbf{D}_{\mathrm{F}}$ are thus similar matrices and so the diagonal terms of $\mathbf{D}_{\mathrm{F}}$ are the eigenvalues of $\mathbf{F}$. As previously noted, the r eigenvectors $\{\mathbf{v}_i\}_{i=k}^n$ of $\mathbf{E}$ which correspond to zero eigenvalues are also eigenvectors of $\mathbf{F}$ which correspond to zero eigenvalues. By denoting $\{\mathbf{u}_i\}_{i=1}^{n-r}$ to be the other $n - r$ orthonormal eigenvectors of $\mathbf{F}$ then,

$$\operatorname{span}\{\mathbf{u}_1, \ldots, \mathbf{u}_{n-r}\} = \operatorname{span}\{\mathbf{v}_1, \ldots, \mathbf{v}_{n-r}\},$$

and thus it is possible to similarly express,

$$\mathbf{x}^T \mathbf{F} \mathbf{x} = \mathbf{x}_1^T \mathbf{F} \mathbf{x}_1 = \boldsymbol{\alpha}^T \tilde{\mathbf{F}} \boldsymbol{\alpha},$$

where,

$$\tilde{\mathbf{F}} = \left(\tilde{F}_{ij}\right)_{i,j=1}^{n-r} \quad \text{and} \quad \tilde{F}_{ij} = \mathbf{v}_i^T \mathbf{F} \mathbf{v}_j \quad \text{for} \quad i,j = 1, \ldots, n-r. \tag{5.28}$$

Thus, for $\mathbf{x} \in V \equiv \text{span}\{\mathbf{v}_1, \ldots, \mathbf{v}_{n-r}\}$ there exists an $\boldsymbol{\alpha} \in V_R \equiv \mathbb{R}^{n-r}$ using Equation (5.26) such that,

$$\frac{\mathbf{x}^T \mathbf{F} \mathbf{x}}{\mathbf{x}^T \mathbf{E} \mathbf{x}} = \frac{\boldsymbol{\alpha}^T \tilde{\mathbf{F}} \boldsymbol{\alpha}}{\boldsymbol{\alpha}^T \tilde{\mathbf{E}} \boldsymbol{\alpha}}, \tag{5.29}$$

and so,

$$\sup_{\mathbf{x} \in V} \frac{\mathbf{x}^T \mathbf{F} \mathbf{x}}{\mathbf{x}^T \mathbf{E} \mathbf{x}} \leq \sup_{\boldsymbol{\alpha} \in V_R} \frac{\boldsymbol{\alpha}^T \tilde{\mathbf{F}} \boldsymbol{\alpha}}{\boldsymbol{\alpha}^T \tilde{\mathbf{E}} \boldsymbol{\alpha}}.$$

It is possible to bound this 'tilde' quotient above and below as,

$$\tilde{\lambda}_{\min} \leq \frac{\boldsymbol{\alpha}^T \tilde{\mathbf{F}} \boldsymbol{\alpha}}{\boldsymbol{\alpha}^T \tilde{\mathbf{E}} \boldsymbol{\alpha}} \leq \tilde{\lambda}_{\max}, \tag{5.30}$$

where the 'tilde' quotient is known as the generalized Rayleigh quotient and $\tilde{\lambda}_{\min}$ and $\tilde{\lambda}_{\max}$ are respectively the smallest and largest eigenvalues of the generalized eigenvalue problem,

$$\tilde{\lambda} \tilde{\mathbf{E}} \boldsymbol{\alpha} = \tilde{\mathbf{F}} \boldsymbol{\alpha},$$

as detailed by Datta, [20]. Concentrating on the upper eigenvalue bound $\tilde{\lambda}_{\max}$ there exists a corresponding eigenvector $\boldsymbol{\alpha}_{\max}$ such that,

$$\tilde{\lambda}_{\max} \tilde{\mathbf{E}} \boldsymbol{\alpha}_{\max} = \tilde{\mathbf{F}} \boldsymbol{\alpha}_{\max}.$$

It follows that,

$$\frac{\boldsymbol{\alpha}_{\max}^T \tilde{\mathbf{F}} \boldsymbol{\alpha}_{\max}}{\boldsymbol{\alpha}_{\max}^T \tilde{\mathbf{E}} \boldsymbol{\alpha}_{\max}} = \tilde{\lambda}_{\max},$$

and so, given $\boldsymbol{\alpha} = \boldsymbol{\alpha}_{\max}$, it is possible via Equation (5.26) to find $\mathbf{x} = \mathbf{x}_{\text{m}}$ with $\mathbf{x}_2 = \mathbf{0}$ since $\mathbf{E}\mathbf{x}_2 = \mathbf{F}\mathbf{x}_2 = \mathbf{0}$ so that,

$$\frac{\mathbf{x}_{\text{m}}^T \mathbf{F} \mathbf{x}_{\text{m}}}{\mathbf{x}_{\text{m}}^T \mathbf{E} \mathbf{x}_{\text{m}}} = \frac{\boldsymbol{\alpha}_{\max}^T \tilde{\mathbf{F}} \boldsymbol{\alpha}_{\max}}{\boldsymbol{\alpha}_{\max}^T \tilde{\mathbf{E}} \boldsymbol{\alpha}_{\max}} = \tilde{\lambda}_{\max}. \tag{5.31}$$

Thus it is in fact true that,

$$\sup_{\mathbf{x} \in \mathbb{R}^n} \frac{\mathbf{x}^T \mathbf{F} \mathbf{x}}{\mathbf{x}^T \mathbf{E} \mathbf{x}} = \sup_{\boldsymbol{\alpha} \in V_R} \frac{\boldsymbol{\alpha}^T \tilde{\mathbf{F}} \boldsymbol{\alpha}}{\boldsymbol{\alpha}^T \tilde{\mathbf{E}} \boldsymbol{\alpha}},$$

showing the required supremum of the original quotient to be equal to the maximum eigenvalue of the 'tilde' quotient. To now investigate further, consider $\mathcal{F}(\mathbf{x})$ where,

$$\mathcal{F}(\mathbf{x}) = \frac{\mathbf{x}^T \mathbf{F} \mathbf{x}}{\mathbf{x}^T \mathbf{E} \mathbf{x}}.$$

The maximum of $\mathcal{F}(\mathbf{x})$ at $\mathbf{x} = \mathbf{x}_{\text{m}}$ will exist where $\nabla \mathcal{F}(\mathbf{x}_{\text{m}}) = \mathbf{0}$. Thus, considering the ith component,

$$\frac{\partial \mathcal{F}(\mathbf{x})}{\partial x_i} = \frac{1}{\left(\mathbf{x}^T \mathbf{E} \mathbf{x}\right)^2} \left[\left(\mathbf{x}^T \mathbf{E} \mathbf{x}\right) \frac{\partial}{\partial x_i} \left(\mathbf{x}^T \mathbf{F} \mathbf{x}\right) - \left(\mathbf{x}^T \mathbf{F} \mathbf{x}\right) \frac{\partial}{\partial x_i} \left(\mathbf{x}^T \mathbf{E} \mathbf{x}\right) \right],$$

it thus follows that,

$$\nabla \mathcal{F}(\mathbf{x}) = \frac{1}{\left(\mathbf{x}^T \mathbf{E} \mathbf{x}\right)^2} \left[\left(\mathbf{x}^T \mathbf{E} \mathbf{x}\right) \nabla \left(\mathbf{x}^T \mathbf{F} \mathbf{x}\right) - \left(\mathbf{x}^T \mathbf{F} \mathbf{x}\right) \nabla \left(\mathbf{x}^T \mathbf{E} \mathbf{x}\right) \right]. \tag{5.32}$$

For symmetric matrices $\mathbf{E}$ and $\mathbf{F}$,

$$\nabla\left(\mathbf{x}^T\mathbf{E}\mathbf{x}\right) = 2\mathbf{E}\mathbf{x} \quad \text{and} \quad \nabla\left(\mathbf{x}^T\mathbf{F}\mathbf{x}\right) = 2\mathbf{F}\mathbf{x},$$

this enables a simplification upon substitution into Equation (5.32) giving,

$$\nabla\mathcal{F}(\mathbf{x}) = \frac{2}{\left(\mathbf{x}^T\mathbf{E}\mathbf{x}\right)^2}\left[\left(\mathbf{x}^T\mathbf{E}\mathbf{x}\right)\mathbf{F}\mathbf{x} - \left(\mathbf{x}^T\mathbf{F}\mathbf{x}\right)\mathbf{E}\mathbf{x}\right]. \tag{5.33}$$

At $\mathbf{x} = \mathbf{x}_{\mathrm{m}}$, $\nabla\mathcal{F}(\mathbf{x}_{\mathrm{m}}) = \mathbf{0}$. For this to be true then from Equation (5.33),

$$\left(\mathbf{x}_{\mathrm{m}}^T\mathbf{E}\mathbf{x}_{\mathrm{m}}\right)\mathbf{F}\mathbf{x}_{\mathrm{m}} - \left(\mathbf{x}_{\mathrm{m}}^T\mathbf{F}\mathbf{x}_{\mathrm{m}}\right)\mathbf{E}\mathbf{x}_{\mathrm{m}} = \mathbf{0},$$

must hold. By using Equation (5.31),

$$\mathbf{F}\mathbf{x}_{\mathrm{m}} = \tilde{\lambda}_{\max}\mathbf{E}\mathbf{x}_{\mathrm{m}},$$

which implies that $\tilde{\lambda}_{\max}$ is also an eigenvalue of the generalized eigenvalue problem,

$$\lambda\mathbf{E}\mathbf{x} = \mathbf{F}\mathbf{x},$$

which is the eigenvalue problem of Equation (5.23) associated with the original quotient of Equation (5.24). In fact $\tilde{\lambda}_{\max}$ equals the maximum eigenvalue of Equation (5.23) as the following proof by contradiction will illustrate.

Assume that there exists an eigenvalue $\lambda_{\max}$ and corresponding eigenvector $\mathbf{x}_{\max}$ of the generalized eigenvalue problem given in Equation (5.23) such that $\lambda_{\max} > \tilde{\lambda}_{\max}$. Thus we may write,

$$\begin{aligned}\lambda_{\max}\mathbf{E}\mathbf{x}_{\max} = \mathbf{F}\mathbf{x}_{\max} \quad &\Rightarrow \quad \lambda_{\max}\mathbf{x}_{\max}^T\mathbf{E}\mathbf{x}_{\max} = \mathbf{x}_{\max}^T\mathbf{F}\mathbf{x}_{\max}, \\ &\Rightarrow \quad \lambda_{\max} = \frac{\mathbf{x}_{\max}^T\mathbf{F}\mathbf{x}_{\max}}{\mathbf{x}_{\max}^T\mathbf{E}\mathbf{x}_{\max}} > \tilde{\lambda}_{\max}.\end{aligned} \tag{5.34}$$

Given $\mathbf{x}_{\max}$ it is possible to find $\boldsymbol{\alpha} = \boldsymbol{\alpha}_{\mathrm{m}}$ since, as in Equation (5.26), for any $\mathbf{x} \in \mathbb{R}^n$ with orthonormal basis $\{\mathbf{v}_i\}_{i=1}^n$, $\mathbf{x}$ may be expressed as,

$$\mathbf{x} = \alpha_1\mathbf{v}_1 + \alpha_2\mathbf{v}_2 + \ldots + \alpha_n\mathbf{v}_n.$$

Thus using the orthonormal property,

$$\begin{aligned}(\mathbf{x}, \mathbf{v}_i) &= \alpha_1(\mathbf{v}_1, \mathbf{v}_i) + \alpha_2(\mathbf{v}_2, \mathbf{v}_i) + \ldots + \alpha_i(\mathbf{v}_i, \mathbf{v}_i) + \ldots + \alpha_n(\mathbf{v}_n, \mathbf{v}_i), \\ &= \alpha_i,\end{aligned}$$

and so it is possible to find each scalar α_i for $i = 1, \ldots, n$ given a general $\mathbf{x}$. This means that for $\mathbf{x} = \mathbf{x}_{\max}$ we have that,

$$\mathbf{x}_{\max} = \sum_{i=1}^{n}\left(\mathbf{x}_{\max}^T\mathbf{v}_i\right)\mathbf{v}_i,$$

which in turn gives us $\boldsymbol{\alpha}_{\mathrm{m}}$ such that,

$$\tilde{\lambda}_{\max} < \lambda_{\max} = \frac{\mathbf{x}_{\max}^T\mathbf{F}\mathbf{x}_{\max}}{\mathbf{x}_{\max}^T\mathbf{E}\mathbf{x}_{\max}} = \frac{\boldsymbol{\alpha}_{\mathrm{m}}^T\tilde{\mathbf{F}}\boldsymbol{\alpha}_{\mathrm{m}}}{\boldsymbol{\alpha}_{\mathrm{m}}^T\tilde{\mathbf{E}}\boldsymbol{\alpha}_{\mathrm{m}}} \leq \tilde{\lambda}_{\max} \text{ from Equation (5.30).}$$

Thus we have that $\tilde{\lambda}_{\max} < \tilde{\lambda}_{\max}$ which is a contradiction and so $\lambda_{\max}$ cannot be greater than $\tilde{\lambda}_{\max}$.

It has thus been shown that there is no eigenvalue of the original quotient that is larger than $\tilde{\lambda}_{\max}$ and that $\tilde{\lambda}_{\max}$ is in fact an eigenvalue of the original quotient. By using these results and Equations (5.29) and (5.30) it follows, assuming from this point on that $\mathbf{x}^T\mathbf{E}\mathbf{x} \neq 0$, that,

$$\sup_{\mathbf{x}\in\mathbb{R}^n} \left\{ \frac{\mathbf{x}^T\mathbf{F}\mathbf{x}}{\mathbf{x}^T\mathbf{E}\mathbf{x}} \right\} = \lambda_{\max}$$

where $\lambda_{\max}$ is the maximum eigenvalue of the associated generalized eigenvalue problem,

$$\lambda\mathbf{E}\mathbf{x} = \mathbf{F}\mathbf{x},$$

as claimed at the beginning of this section. Thus instead of trying to maximize the quotient as was done in the previous two sections, it is possible simply to solve the generalized eigenvalue problem using some numerical routine. One such routine which may be employed to solve the generalized eigenvalue problem is the QZ algorithm. This transforms the matrices $\mathbf{E}$ and $\mathbf{F}$ into reduced forms from which the eigenvalues are extracted with less difficulty. The simultaneous reduction of $\mathbf{E}$ and $\mathbf{F}$ to triangular forms is guaranteed by the following theorem which is taken from [20].

Theorem 1 (The Generalized Real Schur Decomposition) *Given two real $n \times n$ matrices $\mathbf{E}$ and $\mathbf{F}$, there exist orthogonal matrices $\mathbf{Q}$ and $\mathbf{Z}$ such that:*

$$\mathbf{F}' = \mathbf{Q}^T\mathbf{F}\mathbf{Z} : \quad \mathbf{F}' = \text{ an upper real Schur matrix,}$$

$$\mathbf{E}' = \mathbf{Q}^T\mathbf{E}\mathbf{Z} : \quad \mathbf{E}' = \text{ an upper triangular matrix.}$$

Denoting $\mathbf{F} - \lambda\mathbf{E}$ to be the pair $(\mathbf{E}, \mathbf{F})$, then the pair $(\mathbf{E}', \mathbf{F}')$ is said to be in generalized real Schur form. The pair $(\mathbf{E}', \mathbf{F}')$ has the same eigenvalues as the pair $(\mathbf{E}, \mathbf{F})$.

For a proof of the above theorem, see [20] p497. In addition, for a matrix to be in real Schur form, Datta, [20] (p434), states the following theorem.

Theorem 2 (The Real Schur Triangularization Theorem) *Let $\mathbf{E}$ be a real $n \times n$ matrix. Then there exists an orthogonal $n \times n$ matrix $\mathbf{Q}$ such that:*

$$\mathbf{Q}^T\mathbf{E}\mathbf{Q} = \mathbf{R} = \begin{bmatrix} R_{11} & R_{12} & \dots & R_{1k} \\ 0 & R_{22} & \dots & R_{2k} \\ \vdots & \vdots & \ddots & \vdots \\ 0 & 0 & \dots & R_{kk} \end{bmatrix},$$

where each R_{ii} for $i = 1, \dots, k$ is either a scalar or a 2×2 matrix. The scalar diagonal entries correspond to real eigenvalues and the 2×2 matrices on the diagonal correspond to complex conjugate eigenvalues. The matrix $\mathbf{R}$ is said to be the real Schur form of $\mathbf{E}$.

A proof of this can once again be found in [20], p434. A corollary of the above real Schur triangularization theorem is that for real, symmetric matrices the eigenvalues are real and so each R_{ii} for $i = 1, \ldots, k(= n)$ will be scalar. In fact the matrix $\mathbf{R}$ will be a diagonal matrix with diagonal elements equal to the eigenvalues of $\mathbf{E}$ and the columns of orthogonal matrix $\mathbf{Q}$ equal to the orthonormal eigenvectors of $\mathbf{E}$.

5.4.1 Numerical Solution of the Generalized Eigenvalue Problem

As defined in Equation (5.23) the general eigenvalue problem considered here is of the form,

$$\lambda \mathbf{E}\mathbf{x} = \mathbf{F}\mathbf{x}.$$

In solving the above equation, the task is to seek the solutions, λ, of the characteristic equation,

$$\det(\mathbf{F} - \lambda\mathbf{E}) = 0. \tag{5.35}$$

Matlab has the facility to apply the QZ algorithm, described briefly in the previous section, to two square matrices $\mathbf{E}$ and $\mathbf{F}$. The Matlab User's Guide, [34], states that the QZ algorithm for square matrices $\mathbf{E}$ and $\mathbf{F}$ produces upper triangular matrices $\mathbf{E}'$ and $\mathbf{F}'$ and matrices $\mathbf{R}$ and $\mathbf{S}$ containing the products of the left and right transformations such that,

$$\mathbf{RES} = \mathbf{E}' \quad \text{and} \quad \mathbf{RFS} = \mathbf{F}'.$$

By Theorem 1 the roots of the new characteristic equation,

$$\det(\mathbf{F}' - \lambda\mathbf{E}') = 0, \tag{5.36}$$

are the same as those of Equation (5.35). In this form it is easy to spot the values for λ for which Equation (5.36) will hold due to the fact that the matrices are now upper triangular. Such values for λ will be when there exists a zero diagonal term in the matrix $(\mathbf{F}' - \lambda\mathbf{E}')$. The general form of these diagonal terms can be expressed as,

$$\alpha_{ii} = f'_{ii} - \lambda e'_{ii}, \quad i = 1, \ldots, n.$$

where α_{ii} are the diagonal terms of the matrix $(\mathbf{F}' - \lambda\mathbf{E}')$ and the diagonal terms of $\mathbf{E}'$ and $\mathbf{F}'$ are defined as e'_{ii} and f'_{ii} respectively. This yields n values of λ for which the above is satisfied given by,

$$\lambda_i = \frac{f'_{ii}}{e'_{ii}}, \quad i = 1, \ldots, n\,,$$

where care must be taken to exclude the cases where $e'_{ii} = f'_{ii} = 0$ due to the fact that possible computer rounding error may yield spurious λ_i values. As we have previously shown, the required supremum value will remain unaffected by this and using the result from the previous section the maximum of these eigenvalues is equal to the supremum of the quotient given by Equation (5.24).

By performing the QZ algorithm in Matlab, [34], the maximum eigenvalue for the one dimensional problem was thus found to be,

$$\lambda_{\max} = 0.100000 \text{ to six decimal places.}$$

Thus, in accordance with Equation (5.22) this yields a value for the interpolation error constant which is,

$$C_1^i = 0.316228 \text{ to six decimal places,}$$

which again agrees well with the theoretical prediction and is in total agreement with results from the previously described numerical methods used in Sections (5.3.1) and (5.3.2).

5.5 Interpolation of Higher Order Functions

Hitherto, three methods have been described for numerically computing the interpolation error constant C_1^i and in addition it has been shown that the results from each method agree well with the theoretical value for the current problem. Such agreement is achieved by merely investigating how well a linear interpolant is able to approximate a quadratic function over the region $[0, 1]$. This is as recommended by Johnson and Hansbo, [27], where it is stated that it should be sufficient to look for approximations to functions in a richer polynomial space of one degree higher than the interpolant. The order of this richer space will, however, now be increased in order to observe the true effect upon the interpolation error constant value and it is hoped that the values will tend to the known theoretical value for the current one-dimensional problem of $C_1^i \leq \pi^{-1} = 0.318310$ to six decimal places. Table (5.3) illustrates the results obtained for the numerical calculation of C_1^i upon varying the degree of the polynomial u to be linearly interpolated. All values are given to six

Degree of u	Sampling Method	Minimization Method	QZ Method
2	0.316228	0.316228	0.316228
3	0.316221	0.316228	0.316228
4	0.318063	0.318308	0.318308
10	0.220468	0.318236	0.318310

Table 5.3: Effect on C_1^i in one dimension upon varying degree of u.

decimal places and the sampling method results are for $N = 10^4$. As can be seen from the table, increasing the degree of u correspondingly increases the computed value of the interpolation error constant for the QZ method as expected. Indeed, for the scenario where the linear interpolant is evaluated for polynomials u of degree 10, it can be seen that the QZ method actually does give $C_1^i = \pi^{-1}$ to six decimal places. Thus it has been shown that by increasing the degree of u the three methods seem to tend to the expected theoretical value.

Due to the fact that the number of sampling points is retained at $\mathrm{N} = 10^4$ it can also be seen that the sampling method begins to become less accurate as the degree of u is increased. This is to be expected as the order of the problem increases with the degree of u and will consequently require more samples taken in order to retain accuracy. A similar trend can be seen in the minimization method results although the effect is less severe and an increase in the number of samples made will again improve results. Although these results are of use in terms of validating the methods used, it is thought that the extra computational effort involved does not justify the slight increase in accuracy. Indeed, it is possible that for both the sampling and minimization methods there may well be a decrease in accuracy for fixed N and increasing degree of u. Alternatively, the QZ method seems to perform consistently well and behaves exactly as expected. At this early stage it is clear that this is the more robust method here and indeed the one with strong justification for future use. Due to the increase in computational effort required to obtain results for the higher degree problems it is agreed that, as mentioned by Johnson [27], spaces of only one degree richer will be investigated from this point on as there seems to be little gain from the higher degree cases.

5.6 Interpolation Error Constant Calculation in Two Dimensions

The first part of this chapter addressed the problem of determining the interpolation error constant for a one dimensional problem. Here attention is now switched to problems in two dimensions. The test problem chosen is Poisson's equation which is defined as,

$$\begin{aligned} -\Delta u &= f(\mathbf{x}), \qquad \text{for } \mathbf{x} \in \Omega, \\ u(\mathbf{x}) &= 0, \qquad \text{for } \mathbf{x} \in \partial\Omega, \end{aligned} \tag{5.37}$$

where $\Omega \in \mathbb{R}^2$. Multiplying in the usual way with a suitable test function $v \in \mathring{H}^1(\Omega)$ and integrating by parts yields the weak formulation of the problem in which it is required to find $u \in \mathring{H}^1(\Omega)$ where,

$$a(u, v) = (f, v) \quad \forall\ v \in \mathring{H}^1(\Omega),$$

where the bilinear form $a(u, v)$ is given as,

$$a(u, v) \equiv \int_\Omega \nabla u \cdot \nabla v \, d\mathbf{x}.$$

In the course notes of Eriksson, Estep, Hansbo and Johnson, [21] the value given for the interpolation constant $C^i_{1,k}$ for this problem using triangular elements is that of *approximately* 0.5 ([21], page 51). From Appendix E with $V_\epsilon = H^{1+\epsilon}(\Omega_k)$,

$$C^i_{1,k} = \sup_{u \in V_\epsilon} \frac{h_k^{-1} ||u - \pi_h u||_{L_2(\Omega_k)}}{||u||_{E(\Omega_k)}},$$

and with this information it is now possible to test the numerical methods used in the one dimensional problem for use in two dimensions. Before this is done however, it is important to map this problem to a reference element and show that a value for $C^i_{1,k}$ may be obtained which is independent of h_k.

5.6.1 Mapping from Global to Local Elements

Consider the mapping or transformation from global coordinates (x, y) to local coordinates (ξ, η). Under such a mapping, it is possible to express derivatives in the global space in terms of those in the local space and vice versa as described in Section (3.7). Using the chain rule it is clear that,

$$\begin{bmatrix} \dfrac{\partial u}{\partial x} \\ \dfrac{\partial u}{\partial y} \end{bmatrix} = \begin{bmatrix} \dfrac{\partial \xi}{\partial x} & \dfrac{\partial \eta}{\partial x} \\ \dfrac{\partial \eta}{\partial y} & \dfrac{\partial \xi}{\partial y} \end{bmatrix} \begin{bmatrix} \dfrac{\partial \hat{u}}{\partial \xi} \\ \dfrac{\partial \hat{u}}{\partial \eta} \end{bmatrix} = \mathbf{J}^{-1} \begin{bmatrix} \dfrac{\partial \hat{u}}{\partial \xi} \\ \dfrac{\partial \hat{u}}{\partial \eta} \end{bmatrix},$$

and,

$$\begin{bmatrix} \dfrac{\partial \hat{u}}{\partial \xi} \\ \dfrac{\partial \hat{u}}{\partial \eta} \end{bmatrix} = \begin{bmatrix} \dfrac{\partial x}{\partial \xi} & \dfrac{\partial y}{\partial \xi} \\ \dfrac{\partial x}{\partial \eta} & \dfrac{\partial y}{\partial \eta} \end{bmatrix} \begin{bmatrix} \dfrac{\partial u}{\partial x} \\ \dfrac{\partial u}{\partial y} \end{bmatrix} = \mathbf{J} \begin{bmatrix} \dfrac{\partial u}{\partial x} \\ \dfrac{\partial u}{\partial y} \end{bmatrix},$$

where $\mathbf{J}$ is the Jacobian of the transformation. Considering isoparametric transformation of either the quadrilateral element Ω_k of size h_k or the triangular element Ω_k shown in Figure (5.2) onto

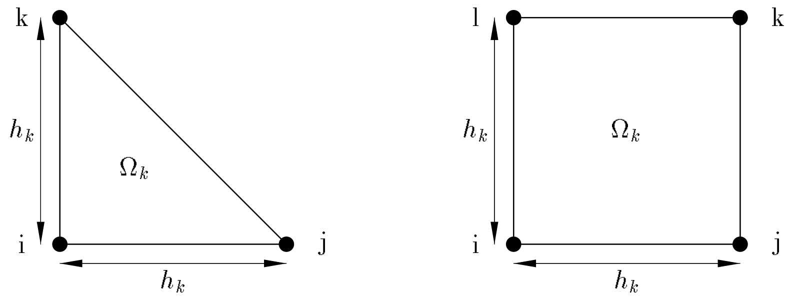

Figure 5.2: General triangular and quadrilateral elements.

their standard unit counterparts $\hat{\Omega}$ it is possible to show that,

$$\mathbf{J} = \begin{bmatrix} h_k & 0 \\ 0 & h_k \end{bmatrix}, \qquad \text{and so,} \qquad \mathbf{J}^{-1} = \frac{1}{h_k^2} \begin{bmatrix} h_k & 0 \\ 0 & h_k \end{bmatrix}.$$

where we have used the fact that $|\mathbf{J}| = h_k^2$. It follows that the bilinear form and the L_2 inner product can also be expressed on the standard unit element $\hat{\Omega}$ so that,

$$(C^i_{1,k})^2 = \sup_{u \in V_\epsilon} \frac{h_k^{-2} \|u - \pi_h u\|^2_{L_2(\Omega_k)}}{\|u\|^2_{E(\Omega_k)}} = \sup_{\hat{u} \in \hat{V}_\epsilon} \frac{h_k^{-2} \displaystyle\int_{\hat{\Omega}} |\hat{u} - \pi \hat{u}|^2 |\mathbf{J}| \, d\hat{\mathbf{x}}}{\displaystyle\int_{\hat{\Omega}} \left(\mathbf{J}^{-1} \hat{\nabla} \hat{u}\right) \cdot \left(\mathbf{J}^{-1} \hat{\nabla} \hat{u}\right) |\mathbf{J}| \, d\hat{\mathbf{x}}} = (C^i_1)^2 \text{ say.}$$

Using the above definitions of $\mathbf{J}$ and $\mathbf{J}^{-1}$ this may be expressed as,

$$(C^i_1)^2 = \sup_{\hat{u} \in \hat{V}_\epsilon} \frac{\displaystyle\int_{\hat{\Omega}} |\hat{u} - \pi \hat{u}|^2 \, d\hat{\mathbf{x}}}{\displaystyle\int_{\hat{\Omega}} \hat{\nabla} \hat{u} \cdot \hat{\nabla} \hat{u} \, d\hat{\mathbf{x}}}. \tag{5.38}$$

Thus, dropping the 'hat' notation for convenience except to denote the integration bounds and working on the standard element, we can now find the required interpolation error constant which is independent of element size and given as,

$$(C_1^i)^2 = \sup_{u \in \hat{V}_e} \frac{||u - \pi u||^2_{L_2(\hat{\Omega})}}{||u||^2_{E(\hat{\Omega})}}. \tag{5.39}$$

For the boundary interpolation error constant $C_{2,k}^i$ on element Ω_k of the type shown in Figure (5.2) and of size h_k, a transformation may again be made onto a standard element. Thus the original task of finding $C_{2,k}^i$ where,

$$\left(C_{2,k}^i\right)^2 = \sup_{u \in V_e} \frac{h_k^{-1}||u - \pi u||^2_{L_2(\partial\Omega_k)}}{||u||^2_{E(\Omega_k)}},$$

can be re-cast on a standard element and the dependence upon h_k removed. Firstly though, consider the integration around the element perimeter as the sum of a number of contributions arising from the integration along each edge Γ_j^k of element Ω_k where $j = 1, \ldots, e$ and e is the number of element edges. This gives,

$$\left(C_{2,k}^i\right)^2 = \sup_{u \in V_e} \frac{h_k^{-1} \displaystyle\int_{\partial\Omega_k} |u - \pi u|^2 \, ds}{\displaystyle\int_{\Omega_k} \nabla u \cdot \nabla u \, d\mathbf{x}} = \sup_{u \in V_e} \frac{h_k^{-1} \displaystyle\sum_{j=1}^{e} \int_{\Gamma_j^k} |u - \pi u|^2 \, d\Gamma_j^k}{\displaystyle\int_{\Omega_k} \nabla u \cdot \nabla u \, d\mathbf{x}},$$

where, for a triangular element $e = 3$ and for quadrilaterals we have $e = 4$ as illustrated in Figure (5.2). Mapping now onto the standard element $\hat{\Omega}$, we have,

$$\left(C_{2,k}^i\right)^2 \equiv \left(C_2^i\right)^2 = \sup_{\hat{u} \in \hat{V}_e} \frac{h_k^{-1} \displaystyle\sum_{j=1}^{e} \int_{\hat{\Gamma}_j} |\hat{u} - \pi\hat{u}|^2 \frac{d\Gamma_j^k}{d\hat{\Gamma}_j} \, d\hat{\Gamma}_j}{\displaystyle\int_{\hat{\Omega}} \left(\mathbf{J}^{-1}\hat{\nabla}\hat{u}\right) \cdot \left(\mathbf{J}^{-1}\hat{\nabla}\hat{u}\right) |\mathbf{J}| \, d\hat{\mathbf{x}}},$$

where, for the general triangular and quadrilateral elements of Figure (5.2) mapped onto their unit counterparts as shown in Figure (5.3) we have that,

$$\frac{d\Gamma_j^k}{d\hat{\Gamma}_j} = \frac{h_k}{1},$$

and where $\mathbf{J}$ and $\mathbf{J}^{-1}$ are as defined for the interior boundary constant. Substitution of these values gives a formulation for the boundary interpolation error constant independent of h_k as,

$$\left(C_2^i\right)^2 = \sup_{\hat{u} \in \hat{V}_e} \frac{\displaystyle\sum_{j=1}^{e} \int_{\hat{\Gamma}_j} |\hat{u} - \pi\hat{u}|^2 \, d\hat{\Gamma}_j}{\displaystyle\int_{\hat{\Omega}} \hat{\nabla}\hat{u} \cdot \hat{\nabla}\hat{u} \, d\hat{\mathbf{x}}}. \tag{5.40}$$

An interesting point to note here is that, in practice, when integrating around the perimeter of the standard elements it is advised that the same direction is kept. In this way the jumps across common edges is found between neighbouring elements. Thus, considering the standard elements

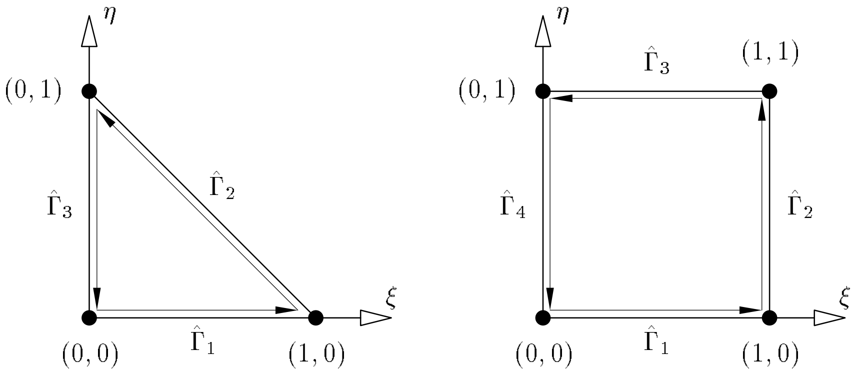

Figure 5.3: Standard unit triangular and quadrilateral elements $\hat{\Omega}$.

depicted in Figure (5.3) we have, for the triangular element,

$$\begin{aligned}\int_{\partial\hat{\Omega}} f(\xi,\eta)\,d\Gamma &= \int_0^1 f(\xi,0)\,d\xi - \int_1^0 f(\xi,1-\xi)\sqrt{2}\,d\xi - \int_1^0 f(0,\eta)\,d\eta,\\ &= \int_0^1 f(\xi,0)\,d\xi + \sqrt{2}\int_0^1 f(\xi,1-\xi)\,d\xi + \int_0^1 f(0,\eta)\,d\eta, \qquad (5.41)\end{aligned}$$

where the integral along $\hat{\Gamma}_2$ has been expressed in terms of ξ. For the quadrilateral element the integration is simpler and can be expressed as,

$$\begin{aligned}\int_{\partial\hat{\Omega}} f(\xi,\eta)\,d\Gamma &= \int_0^1 f(\xi,0)\,d\xi + \int_0^1 f(1,\eta)\,d\eta - \int_1^0 f(\xi,1)\,d\xi - \int_1^0 f(0,\eta)\,d\eta,\\ &= \int_0^1 f(\xi,0)\,d\xi + \int_0^1 f(1,\eta)\,d\eta + \int_0^1 f(\xi,1)\,d\xi + \int_0^1 f(0,\eta)\,d\eta.\end{aligned}$$

Thus, dropping the 'hat' notation from the integrands of Equation (5.40) and working on the standard element, we can now find the required interpolation error constant which is independent of element size and given as,

$$(C_2^i)^2 = \sup_{u\in\hat{V}_e} \frac{||u-\pi u||^2_{L_2(\partial\hat{\Omega})}}{||u||^2_{E(\hat{\Omega})}}, \qquad (5.42)$$

which is similar to the result for the interior constant given in Equation (5.39)

5.6.2 Numerical Computation of Interpolation Error Constant for Triangles

In this scenario a linear interpolant is again taken, but this time defined over a standard unit triangular domain $\hat{\Omega}$. As shown in the previous section this will yield an interpolation error constant independent of the element size $\hat{h}$ as it is unity. The problem will consist of a linear interpolant which interpolates a quadratic defined over the same triangular domain. Figure (5.4) shows the nodal configurations taken for both a typical linear and quadratic triangular element. Any quadratic function may be defined over the quadratic element as,

$$u(\mathbf{x}) = \sum_{i=1}^{6} u(\mathbf{x}_i)\phi_i(\mathbf{x}) = \sum_{i=1}^{6} u_i\phi_i(\mathbf{x}),$$

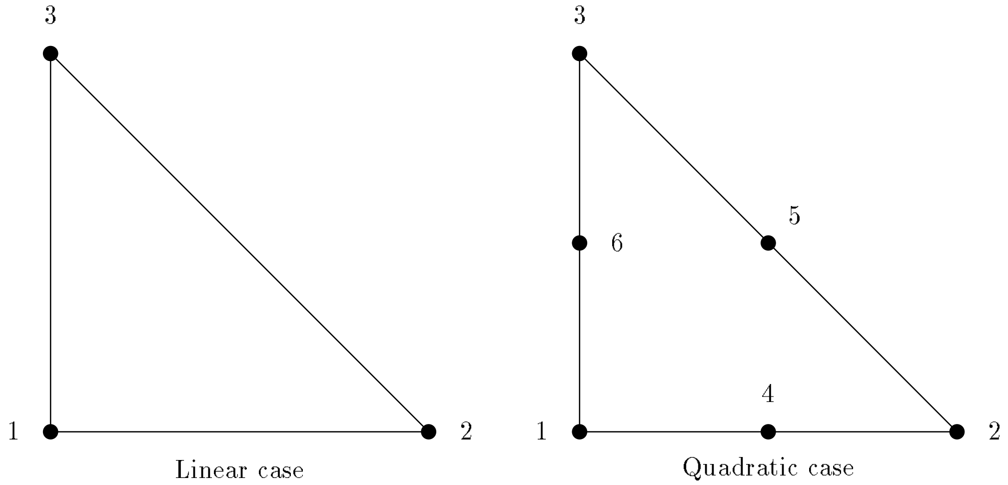

Figure 5.4: Nodal arrangement of linear and quadratic triangular elements.

where $\{u_i\}_{i=1}^6$ are the values of u at nodal locations $\mathbf{x}_i$ for $i = 1, \ldots, 6$ and $\{\phi_i\}_{i=1}^6$ are the quadratic Lagrange shape functions defined over the triangle. It is thus possible to express the interpolation error $u - \pi u$ at any point $\mathbf{x}$ in the domain as,

$$u(\mathbf{x}) - \pi u(\mathbf{x}) = \sum_{i=1}^{6} [u_i - \pi u_i]\, \phi_i(\mathbf{x}).$$

This is a direct extension of the procedure described in Section (5.2) except that now the interpolant πu will interpolate the quadratic exactly at nodes 1,2 and 3. Thus,

$$\pi u_i = u_i, \quad \text{for } i = 1, 2, 3.$$

Similarly, by linear interpolation on the triangle, the interpolant may be expressed in terms of u at the nodes as,

$$\pi\mathbf{u} = \begin{bmatrix} \pi u_1 \\ \pi u_2 \\ \pi u_3 \\ \pi u_4 \\ \pi u_5 \\ \pi u_6 \end{bmatrix} = \begin{bmatrix} 1 & 0 & 0 & 0 & 0 & 0 \\ 0 & 1 & 0 & 0 & 0 & 0 \\ 0 & 0 & 1 & 0 & 0 & 0 \\ \frac{1}{2} & \frac{1}{2} & 0 & 0 & 0 & 0 \\ 0 & \frac{1}{2} & \frac{1}{2} & 0 & 0 & 0 \\ \frac{1}{2} & 0 & \frac{1}{2} & 0 & 0 & 0 \end{bmatrix} \begin{bmatrix} u_1 \\ u_2 \\ u_3 \\ u_4 \\ u_5 \\ u_6 \end{bmatrix} = \mathbf{Tu}.$$

This yields the task of finding the interpolation error constant C_1^i for a two dimensional problem where,

$$(C_1^i)^2 = \sup_{\mathbf{u} \in \mathbb{R}^6} \frac{\mathbf{u}^T(\mathbf{I} - \mathbf{T})^T \mathbf{M}(\mathbf{I} - \mathbf{T})\mathbf{u}}{\mathbf{u}^T \mathbf{E}\mathbf{u}},$$

and again $\mathbf{M}$ and $\mathbf{E}$ are the mass and element stiffness matrices respectively which are defined as,

$$\mathbf{M} = (M_{ij})_{i,j=1}^6 \text{ with } M_{ij} = \int_{\hat{\Omega}} \phi_i(\mathbf{x})\phi_j(\mathbf{x})\, d\mathbf{x}, \quad \text{for } i, j = 1, \ldots, 6\,,$$

and,

$$\mathbf{E} = (E_{ij})_{i,j=1}^6 \text{ with } E_{ij} = \int_{\hat{\Omega}} \nabla\phi_i(\mathbf{x}) \cdot \nabla\phi_j(\mathbf{x})\, d\mathbf{x}, \quad \text{for } i, j = 1, \ldots, 6.$$

5.6.3 Numerical Results of the Interpolation Error Constant for Triangles

All three methods developed for the one dimensional problem can be used for problems in two or even three dimensions. The only difference which results from doing this is the dimension of the matrices **E** and **F** and the transformation matrix **T**. Below are the results of the methods applied to the two dimensional problem.

Sampling Method

As before, the sampling method was applied to both the quotient and the reciprocal. The number of samples taken was varied from N = 10^2 to N = 10^5 as in the one dimensional case. As can be seen

N	100	1000	10000	100000
Max(Q)	0.230040	0.258916	0.271974	0.275509
Min(1/Q)	3.871343	3.764889	3.694663	3.638739

Table 5.4: Sampling method results for varying N on triangular element.

in Table (5.4), for a given value of N, the maximum and minimum values are close to reciprocals of each other as expected although convergence in this case to a common value is slower. This is due to the fact that we are now working with larger matrices and working in six-dimensional space. Assuming that the most accurate result is when N is largest, the maximum value of the quotient is found to be 0.275509 to six decimal places. Since the work has been performed over a standard triangular element and $h = 1$, we are able to calculate, by taking the square root that this crude method yields a value for the interpolation error constant which is,

$$C_1^i = 0.524889 \text{ to six decimal places,}$$

which agrees well with that of [21] where it is stated that the value is *approximately* 0.5.

Minimization Method

For the current problem the quotient may be regarded as a function f of six variables. As previously, random starting points are again given to the minimization routine in Mathematica, [59]. Table (5.5) shows the resulting partial derivative values computed at the minimum position found along with the minimum value itself. From Table (5.5) it is clear that the value of the minimum of the reciprocal of the quotient is 3.6254 correct to four decimal places. The claim that this is a minimum is strengthened by the fact that the derivative values are all close to zero at the minimum points found. Taking an average value from all 40 runs of the minimization routine gives a value of

Run	Min. value	$\frac{\partial f}{\partial x_1}$	$\frac{\partial f}{\partial x_2}$	$\frac{\partial f}{\partial x_3}$	$\frac{\partial f}{\partial x_4}$	$\frac{\partial f}{\partial x_5}$	$\frac{\partial f}{\partial x_6}$
1	3.625415	0.00076	−0.00039	0.00033	−0.00050	0.00021	−0.00040
2	3.625414	−0.00035	−0.00077	0.00074	−0.00032	−0.00034	0.00103
3	3.625414	−0.00001	−0.00001	0.00000	−0.00002	−0.00001	0.00004
4	3.625418	−0.00209	0.00271	−0.00407	0.00453	−0.00761	0.00653
5	3.625414	−0.00007	−0.00005	0.00010	−0.00005	0.00017	−0.00010
⋮	⋮	⋮	⋮	⋮	⋮	⋮	⋮
36	3.625414	0.00006	−0.00021	0.00014	0.00005	−0.00029	0.00024
37	3.625418	0.00486	−0.00311	0.00305	−0.00550	0.00275	−0.00206
38	3.625414	−0.00002	−0.00000	0.00002	0.00031	0.00006	−0.00037
39	3.625416	0.00253	0.00161	−0.00122	−0.00018	0.00345	−0.00618
40	3.625416	0.00011	0.00029	−0.00018	−0.00007	0.00058	−0.00073

Table 5.5: Minimization results for the Poisson problem over a triangular element.

3.625414 to six decimal places. Thus, taking the reciprocal of this and then the square root yields again the value of the interpolation error constant which is,

$$C_1^i = 0.525196 \text{ to six decimal places,}$$

which again agrees well with the approximate value 0.5 of [21] and also with the previous estimate.

QZ Method

The final method yields a value of $\lambda_{\max} = 0.275830$ to six decimal places. Thus taking the square root of this value gives the interpolation error constant as,

$$C_1^i = 0.525196 \text{ to six decimal places,}$$

which again agrees well with both the result of approximately 0.5 as given by Johnson and Hansbo in [21] and with our previous estimates.

5.6.4 Numerical Computation of Interpolation Error Constant for Quadrilaterals

The transformation mapping process described in Section (5.6.1) is also valid for a general quadrilateral element Ω_k of size h_k and so we are able to work here on a standard unit quadrilateral domain $\hat{\Omega}$. The problem will consist of a bilinear interpolant which interpolates a biquadratic defined over the same quadrilateral domain. Figure (5.5) shows the nodal configurations taken for both a typical bilinear and biquadratic quadrilateral element. Any biquadratic function may be

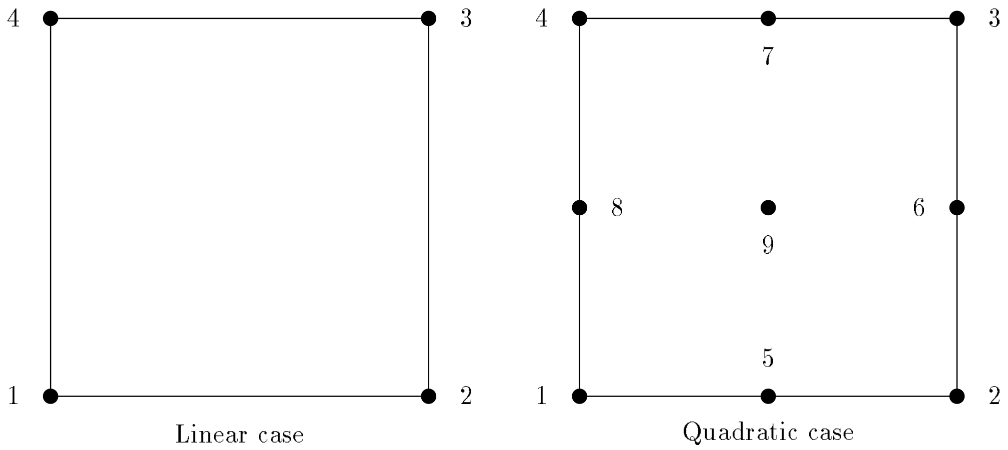

Figure 5.5: Nodal arrangement of bilinear and biquadratic quadrilateral elements.

defined over the biquadratic element as,

$$u(\mathbf{x}) = \sum_{i=1}^{9} u(\mathbf{x}_i)\phi_i(\mathbf{x}) = \sum_{i=1}^{9} u_i\phi_i(\mathbf{x}),$$

where $\{u_i\}_{i=1}^{9}$ are the values of u at nodal locations $\mathbf{x}_i$ for $i = 1, \ldots, 9$ and $\{\phi_i\}_{i=1}^{9}$ are the biquadratic Lagrange shape functions defined over the quadrilateral. It is thus possible to express the interpolation error $u - \pi u$ at any point $\mathbf{x}$ in the domain as,

$$u(\mathbf{x}) - \pi u(\mathbf{x}) = \sum_{i=1}^{9} [u_i - \pi u_i]\,\phi_i(\mathbf{x}).$$

This is a direct extension of the procedure described in Section (5.2) except that now the interpolant πu will interpolate the quadratic exactly at nodes 1,2,3 and 4. Thus,

$$\pi u_i = u_i, \qquad \text{for } i = 1, 2, 3, 4.$$

Similarly, by linear interpolation on the quadrilateral, the interpolant may be expressed in terms of u at the nodes as,

$$\pi\mathbf{u} = \begin{bmatrix} \pi u_1 \\ \pi u_2 \\ \pi u_3 \\ \pi u_4 \\ \pi u_5 \\ \pi u_6 \\ \pi u_7 \\ \pi u_8 \\ \pi u_9 \end{bmatrix} = \begin{bmatrix} 1 & 0 & 0 & 0 & 0 & 0 & 0 & 0 & 0 \\ 0 & 1 & 0 & 0 & 0 & 0 & 0 & 0 & 0 \\ 0 & 0 & 1 & 0 & 0 & 0 & 0 & 0 & 0 \\ 0 & 0 & 0 & 1 & 0 & 0 & 0 & 0 & 0 \\ \frac{1}{2} & \frac{1}{2} & 0 & 0 & 0 & 0 & 0 & 0 & 0 \\ 0 & \frac{1}{2} & \frac{1}{2} & 0 & 0 & 0 & 0 & 0 & 0 \\ 0 & 0 & \frac{1}{2} & \frac{1}{2} & 0 & 0 & 0 & 0 & 0 \\ \frac{1}{2} & 0 & 0 & \frac{1}{2} & 0 & 0 & 0 & 0 & 0 \\ \frac{1}{4} & \frac{1}{4} & \frac{1}{4} & \frac{1}{4} & 0 & 0 & 0 & 0 & 0 \end{bmatrix} \begin{bmatrix} u_1 \\ u_2 \\ u_3 \\ u_4 \\ u_5 \\ u_6 \\ u_7 \\ u_8 \\ u_9 \end{bmatrix} = \mathbf{T}\mathbf{u}.$$

This yields the task of finding the interpolation error constant C_1^i for a two dimensional problem where,

$$(C_1^i)^2 = \sup_{\mathbf{u}\in\mathbb{R}^9} \frac{\mathbf{u}^T(\mathbf{I}-\mathbf{T})^T\mathbf{M}(\mathbf{I}-\mathbf{T})\mathbf{u}}{\mathbf{u}^T\mathbf{E}\mathbf{u}},$$

where again $\mathbf{M}$ is the mass matrix and $\mathbf{E}$ is the element stiffness matrix which are defined by,

$$\mathbf{M} = (M_{ij})_{i,j=1}^{9} \text{ with } M_{ij} = \int_{\hat{\Omega}} \phi_i(\mathbf{x})\phi_j(\mathbf{x})\,d\mathbf{x}, \quad \text{for } i,j = 1,\ldots,9\,, \tag{5.43}$$

and,

$$\mathbf{E} = (E_{ij})_{i,j=1}^{9} \text{ with } E_{ij} = \int_{\hat{\Omega}} \nabla\phi_i(\mathbf{x}) \cdot \nabla\phi_j(\mathbf{x})\,d\mathbf{x}, \quad \text{for } i,j = 1,\ldots,9.$$

5.6.5 Numerical Results of the Interpolation Error Constant for Quadrilaterals

Using the same Poisson test problem defined in Equation (5.37) and tested using triangular elements, the interpolation problem may be set up for standard unit quadrilateral elements as described in the previous section. Here a bilinear interpolant to general biquadratic functions is analysed. The results for both the interior and boundary interpolation constants will now be detailed.

Interior Constant

It is found that both the minimization and QZ methods yield a value for the interpolation error constant which is $C_1^i = 0.622160$ to six decimal places. However, for the sampling method it is found that the value for the interpolation error is not in such strong agreement with an estimated value of $C_1^i = 0.610611$ arising from 10^5 samples. This behaviour has been seen before and it is thought that it is due to the fact that the problem is now posed in nine-dimensional space and the random samples need to be made at a larger number of locations in order to retain the same level of agreement with the other two methods as seen earlier in the chapter.

Boundary Constant

It was mentioned at the beginning of the chapter that, for the boundary interpolation constant, the computational procedure involved is similar to that for the interior constant. The only difference lies in the integration of the mass matrix terms which, in this case, is performed along the element boundary instead of over the whole element domain as in Equation (5.43). We thus have instead that,

$$\mathbf{M} = (M_{ij})_{i,j=1}^{9} \text{ with } M_{ij} = \int_{\partial\hat{\Omega}} \phi_i(\mathbf{x})\phi_j(\mathbf{x})\,ds, \quad \text{for } i,j = 1,\ldots,9. \tag{5.44}$$

It is found that this results in a value of $C_2^i = 1.095445$ in the case of the QZ and minimization methods. Predictably the sampling method is not in such close agreement and yields a value of $C_2^i = 1.088469$ when 10^5 samples are taken.

5.7 Transition Element Complications

The computational method developed in the previous sections of this chapter has been shown to perform well, particularly when used in conjunction with the QZ algorithm to solve the resulting generalized eigenvalue problem. The underlying assumption of the method is that one is able to write the interpolant in terms of the shape functions employed to describe the function from the higher order space. This has meant in the past that a linear interpolant could be described in terms of the quadratic shape functions in the one-dimensional case and for triangles in two dimensions and similarly a bilinear interpolant in terms of the biquadratic shape functions in two dimensions on a quadrilateral element. This in turn enabled the construction of transformation matrices $\mathbf{T}$ and the solution of the interpolation error problems. In the case of transition elements of the type described in Section (3.9) it is clearly not possible to express the interpolant in terms of the shape functions from the higher order space due to the modifications they must undergo as described in Section (3.9.1). It is thus necessary to develop an enhanced version of the original computational method which has been shown to work in the case of standard bilinear interpolants. In addition to retaining this capability the new method will also perform correctly in the case of transition elements and the modified interpolants emanating from them.

Consider the interpolation error $u - \pi u$ as previously defined on the standard quadrilateral element shown in Figure (5.5). The standard element to be considered here is centred on the origin with side length $\hat{h} = 2$ and with shape functions as described in Section (3.9.1). As also seen previously, u is a function from the higher order space and may be evaluated at any point $\mathbf{x}$ in the element as,

$$u(\mathbf{x}) = \sum_{i=1}^{n} u(\mathbf{x}_i)\phi_i(\mathbf{x}) = \sum_{i=1}^{n} u_i\phi_i(\mathbf{x}),$$

where $\{u_i\}_{i=1}^{n}$ are the values of u at nodal locations $\mathbf{x}_i$ for $i = 1, \ldots, n$ and $\{\phi_i\}_{i=1}^{n}$ are the Lagrange shape functions defined over the quadrilateral and used to describe u. The interpolant πu evaluated also at any point $\mathbf{x}$ in the element is similarly given by,

$$\pi u(\mathbf{x}) = \sum_{i=1}^{m} \pi u(\mathbf{x}_i)\vartheta_i(\mathbf{x}) = \sum_{i=1}^{m} \pi u_i\vartheta_i(\mathbf{x}),$$

where now $\{\vartheta_i\}_{i=1}^{m}$ are the shape functions defined over the quadrilateral and used to describe πu. For the interpolation of a biquadratic function u on the standard element, we have that $n = 9$ where $\{\phi_i\}_{i=1}^{9}$ are the usual biquadratic shape functions. Similarly, for the bilinear interpolant for example, we have that $m = 4$ where $\{\vartheta_i\}_{i=1}^{4}$ are the usual bilinear shape functions. It is important to note, however, that it is possible for m to equal five, six or seven in the case of interpolants defined over transition elements. For the general case let us consider $m = 4$, 5, 6 or 7, with $\vartheta_i = 0$ for $m < i \leq n$. The interpolation error may then be expressed as,

$$u(\mathbf{x}) - \pi u(\mathbf{x}) = \sum_{i=1}^{n} \left(\phi_i(\mathbf{x}) - \vartheta_i(\mathbf{x})\right) u_i,$$

since we know that, at the nodes, the value of the interpolant will be that of the function for $i = 1, \ldots, m$ and for $m < i \leq n$ we note that $\vartheta_i = 0$. Thus for the case where we are considering the interpolation of a biquadratic function u we have,

$$\begin{aligned} |u(\mathbf{x}) - \pi u(\mathbf{x})|^2 &= \left[\sum_{i=1}^{9} (\phi_i(\mathbf{x}) - \vartheta_i(\mathbf{x}))\, u_i \right] \left[\sum_{j=1}^{9} (\phi_j(\mathbf{x}) - \vartheta_j(\mathbf{x}))\, u_j \right] \\ &= \sum_{i,j=1}^{9} u_i \left(\phi_i(\mathbf{x}) - \vartheta_i(\mathbf{x})\right) \left(\phi_j(\mathbf{x}) - \vartheta_j(\mathbf{x})\right) u_j, \end{aligned}$$

which should be compared with Equation (5.20). It can be seen that now we are considering the difference between shape functions instead of the differences in the nodal displacements between the function and interpolant. It is thus possible to write the square of the interpolation error as,

$$|u(\mathbf{x}) - \pi u(\mathbf{x})|^2 = \mathbf{u}^T \mathbf{\Phi}(\mathbf{x})\, \mathbf{u},$$

where,

$$\mathbf{\Phi}(\mathbf{x}) = \left(\left(\phi_i(\mathbf{x}) - \vartheta_i(\mathbf{x})\right) \left(\phi_j(\mathbf{x}) - \vartheta_j(\mathbf{x})\right) \right)_{i,j=1}^{9},$$

and where now we have defined $\mathbf{u}$ to be the vector of nodal displacements for the quadratic function u. Consequently we may define a modified mass matrix $\mathbf{M}'$ whose terms are obtained from integrating each term of $\mathbf{\Phi}(\mathbf{x})$. For the interior interpolation error constant calculation, $\mathbf{M}'$ is defined as,

$$\mathbf{M}' = \left(M'_{ij}\right)_{i,j=1}^{9} \text{ with } M'_{ij} = \int_{\hat{\Omega}} \left(\phi_i(\mathbf{x}) - \vartheta_i(\mathbf{x})\right) \left(\phi_j(\mathbf{x}) - \vartheta_j(\mathbf{x})\right) d\mathbf{x}, \quad \text{for } i,j = 1, \ldots, 9.$$

The interior interpolation error constant C_1^i is then given by,

$$\left(\hat{h} C_1^i\right)^2 = \sup_{\mathbf{u} \in \mathbb{R}^9} \frac{\mathbf{u}^T \mathbf{M}' \mathbf{u}}{\mathbf{u}^T \mathbf{E} \mathbf{u}},$$

where it should be noted there is now no need for the troublesome transition matrix and the appearance of $\hat{h}$ on the left-hand side is due to the fact that we have taken the standard element $\hat{\Omega}$ to be of side length $\hat{h}$. If it is decided to take $\hat{\Omega}$ to be of side length unity then the $\hat{h} = 1$ and the quotient appears independent of $\hat{h}$ as earlier in this work. In such a case however, the modified transition element shape functions will differ from those given in Section (3.9.1) in which $\hat{h} = 2$ and so for consistency we include the $\hat{h}$ term here since the choice of standard element $\hat{\Omega}$ has no effect upon the resulting value for C_1^i. This claim will now be illustrated by considering two standard elements which differ in size. Consider a standard element of side length $\hat{h}$ with corresponding maximum eigenvalue of the associated generalized eigenvalue problem given as $\lambda_{\max}$, an element of side length $2\hat{h}$ will have corresponding maximum eigenvalue $4\lambda_{\max}$. Thus when taking the square root and dividing by the element side length in order to obtain the required constant, we have either,

$$C_1^i = \frac{\sqrt{\lambda_{\max}}}{\hat{h}} \quad \text{or} \quad C_1^i = \frac{\sqrt{4\lambda_{\max}}}{2\hat{h}}.$$

Thus both elements yield the same interpolation error constant value. We have thus developed an enhancement of the original computational method which will calculate the interior interpolation error constants for the family of transition elements and also the original case of the standard bilinear interpolant. The remaining task is now to consider the further modifications needed for the computation of the boundary interpolation error constant.

As was the case for the original method, the enhanced method must also be modified slightly in order to be able to compute the boundary interpolation error constants for bilinear interpolants and those emanating from the transition element family. Such modifications are slight and involve again merely a change of the integration limits for matrix $\mathbf{M}'$.

In the case of transition elements however, as illustrated in part (b) of Figure (5.6), a further feature must be addressed. The boundary interpolation error constants were introduced in Section

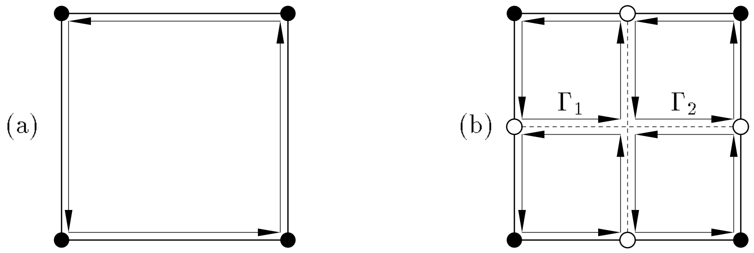

Figure 5.6: Integration routes for C_2^i computation for (a) bilinear interpolant and (b) transition element interpolant.

(4.4) and arose from the consideration of inter-element 'jumps' across shared element edges. Such terms are of interest since, in an adapted mesh, there should be smooth transitions and a large coefficient jump across neighbouring element boundaries indicates that the mesh is not acceptable and in need of further refinement. In the case of transition elements we not only have to consider the inter-element jumps but also the possibility of interior jumps which arise from the existence of previously mentioned lines of slope discontinuity which can be seen in part (b) of Figure (5.6) as broken lines. Thus it is recommended that for all elements the integration is performed not only around the element boundary as illustrated in part (a) of Figure (5.6) but also along the possible internal lines of slope discontinuity as shown in part (b). It should be noted that for transition elements which only have one line of slope discontinuity, the integrals across the element interior which do not follow a line of slope discontinuity sum to zero. Thus for the 1-irregular northern element with line of slope discontinuity running from North to South face, integration along Γ_1 and Γ_2 portions in Figure (5.6) will sum to zero and thus have no effect upon the computed value of C_2^i. This is also the case for the standard bilinear interpolant where there are no lines of slope discontinuity and the resulting value for C_2^i will be identical whether the integration route of (a) or (b) is used.

5.7.1 Transition Element Interior and Boundary Interpolation Error Constants

The enhanced method for computing the interior interpolation error constant values will now be used for the transition element family. As previously we will call a transition element having i irregular nodes an i-irregular element. The results for 1-irregular elements is identical whether the irregular node lies on the North, East, South or West face and similarly this property holds for the 2-irregular and 3-irregular type elements with the placing of irregular nodes yielding no numerical difference in the result. An important point to note here is that there are two types of 2-irregular element. The first type arises when the irregular nodes lie on adjacent edges of the element whilst the second type arises when the irregular nodes lie on opposite element edges. We thus have 2_{adj}-irregular and 2_{opp}-irregular elements respectively for such scenarios.

Table (5.6) shows the results of the enhanced method in the computation of C_1^i and C_2^i for the Poisson problem defined in Equation (5.37). It should be noted at this stage that, in addition to

Element type	Computed C_1^i	Computed C_2^i	C_2^i (no interior)
Standard	0.622160	1.095445	1.095445
1-irregular	0.512232	1.216914	1.007056
2_{adj}-irregular	0.436739	1.237296	0.927089
2_{opp}-irregular	0.350518	0.855615	0.850296
3-irregular	0.334147	1.035273	0.784267

Table 5.6: Computed C_1^i and C_2^i values for the transition element family.

having results columns for computed C_1^i and C_2^i values, a third results column has been included. This column shows the computed C_2^i values without the interior contributions taken into account and is included to highlight the important role they play. The results in Table (5.6) were obtained using the QZ algorithm, it can be seen that the value for C_1^i on a standard element is the same as those detailed in Section (5.6.5). This is expected and shows that the enhanced method does indeed duplicate the results of the previous method as required. The addition of irregular nodes in the case of C_1^i produces a gradual decrease in the computed values. This is thought to be a consequence of the transition element interpolant being able to interpolate the function from the higher order space more accurately as the nodes are added.

As briefly commented upon earlier, Table (5.6) has two columns of results for C_2^i. The first of these columns shows the computed values of C_2^i when the interior jumps are taken into account and the second 'no interior' column when the interior jumps are not taken into account. The inclusion of this final column is merely to highlight the effect of the internal jumps on the computation and it can be seen that that the two columns show identical computed values for the standard element due to the fact that there are no internal jumps present. As observed for the C_1^i value on the standard element, the value of C_2^i matches that given before by the QZ method in Section (5.6.5) showing once again that the enhanced method duplicates the required results. Upon the addition of the irregular nodes the values for C_2^i show a steady decrease for the 'no interior' case. This is as expected due to similar reasons described for the C_1^i scenario.

In contrast, the C_2^i values incorporating the interior jumps show a sharp increase upon the addition of one irregular node. This is due to the fact that, in addition to the element boundary, we now also consider the internal jump term arising from the line of slope discontinuity running across the element. For the 2_{adj}-irregular element there are now two such lines and consequently more jump terms producing again a higher computed C_2^i value. It is the opposite case for the 2_{opp}-irregular element which has the same single line of slope discontinuity as the 1-irregular element but now has more accurate interpolation on the boundary due to the extra node. Thus we see a drop from the result for the 1-irregular element to that of the 2_{opp}-irregular element. We again see a drop from the 2_{adj}-irregular element to the 3-irregular element which is again due to the latter having an extra node on the boundary.

5.8 Summary

In this chapter initial investigations into the computation of the interpolation error constants C_1^i and C_2^i have been presented for scalar differential equation problems in both one and two dimensions. Where possible, numerical findings have been verified with both theoretical and existing results from the literature and beyond this the numerical methods have been extended to provide results which have thus far not been detailed in the literature. It has been shown that the numerical methods developed here agree well with each other and also with expected values where known. The methods will thus now be used in the next chapter to predict interpolation error constant values for problems of both linear elasticity and plate theory.

Chapter 6

Interpolation Error II

It has been shown in the previous chapter that the task of finding the interpolation error constants C_1^i and C_2^i can be posed as a problem in which we seek,

$$\left(C_j^i\right)^2 = \sup_{\mathbf{u}\in\mathbb{R}^n} \left\{ \frac{\mathbf{u}^T \mathbf{F}\,\mathbf{u}}{\mathbf{u}^T \mathbf{E}\,\mathbf{u}} \right\} \qquad \text{for } j = 1 \text{ or } 2,$$

where $\mathbf{E}$ is the element stiffness matrix and the matrix $\mathbf{F}$ can be expressed in two different forms. The first form arose from the computational method initially developed in Chapter 5 and is given as,

$$\mathbf{F} = (\mathbf{I} - \mathbf{T})^T\, \mathbf{M}\, (\mathbf{I} - \mathbf{T}),$$

for interpolants not associated with transition elements, with $\mathbf{T}$ the appropriately defined 'transformation' matrix and $\mathbf{I}$ the identity matrix. Alternatively $\mathbf{M}$ may have the form,

$$\mathbf{M} = \mathbf{M}',$$

as described for the enhanced method in Section (5.7) which was developed in order to cope with interpolants belonging to transition elements as well as the standard case. Since we are concerned with calculating the interpolation error constants for both transition and standard types of elements we will use the latter definition from this point on. The previous chapter also detailed three methods for finding the required supremum of the above quotient. It was shown that these performed well, particularly the QZ method which is used to find the largest eigenvalue of the associated generalized eigenvalue problem. In this chapter the aim is to extend the work of the previous chapter to calculate the interpolation error constant values for problems of linear elasticity and plate theory.

6.1 Linear Elasticity in Two Dimensions

As described in Section (4.4.1) the two-dimensional isotropic linear elasticity analogue of that described in Section (2.1) is one in which it is required to find the displacement $\mathbf{u} = (u_i)_{i=1}^2$ and symmetric stress tensor $\boldsymbol{\sigma} = (\sigma_{ij})_{i,j=1}^2$ such that,

$$\boldsymbol{\sigma} = \lambda \mathbf{I} \operatorname{div} \mathbf{u} + 2\mu\varepsilon(\mathbf{u}) \quad \text{in} \quad \Omega, \tag{6.1}$$

$$-\text{div } \boldsymbol{\sigma} = \mathbf{f} \quad \text{in} \quad \Omega, \tag{6.2}$$

$$\mathbf{u} = \mathbf{0} \quad \text{on} \quad \partial\Omega_C, \tag{6.3}$$

$$\boldsymbol{\sigma}\mathbf{n} = \mathbf{g} \quad \text{on} \quad \partial\Omega_T, \tag{6.4}$$

where Ω is a bounded domain in $\mathbb{R}^2$ with boundary $\partial\Omega \equiv \partial\Omega_C \cup \partial\Omega_T$, λ and μ are the Lamé coefficients and $\boldsymbol{\varepsilon}(\mathbf{u}) = (\varepsilon_{ij}(\mathbf{u}))_{i,j=1}^2$ is the strain tensor with components,

$$\varepsilon_{ij} = \frac{1}{2}\left(\frac{\partial u_i}{\partial x_j} + \frac{\partial u_j}{\partial x_i}\right) = \frac{1}{2}(u_{i,j} + u_{j,i}) \quad \text{for } i, j = 1, 2\,,$$

as introduced in Section (2.1.1). In the above, $\mathbf{I} = (\delta_{ij})_{i,j=1}^2$ is the identity tensor with $\delta_{ij} = 1$ if $i = j$ and zero otherwise, $\mathbf{f} \in [L_2(\Omega)]^2$ and $\mathbf{g} \in [L_2(\partial\Omega_T)]^2$ are given loads and $\mathbf{n}$ is the unit outward normal to $\partial\Omega_T$. Also, define the action of the divergence operator differently according to whether it acts on a tensor or vector in two dimensions as,

$$\text{div } \boldsymbol{\sigma} = \left(\sum_{j=1}^{2} \frac{\partial \sigma_{ij}}{\partial x_j}\right)_{i=1}^{2}, \qquad \text{div } \mathbf{u} = \sum_{i=1}^{2} \frac{\partial u_i}{\partial x_i}.$$

The weak formulation of Equations (6.1)-(6.4) and derived in Section (3.2) reads as follows: Find $\mathbf{u} \in V$ where,

$$V = \left\{\mathbf{v} \in \left[H^1(\Omega)\right]^2 \; : \; \mathbf{v} = 0 \text{ on } \partial\Omega_C\right\},$$

such that,

$$a(\mathbf{u}, \mathbf{v}) = F(\mathbf{v}) \quad \forall\, \mathbf{v} \in V. \tag{6.5}$$

Where, as derived in Section (3.2),

$$a(\mathbf{u}, \mathbf{v}) = \int_\Omega \lambda \text{ div } \mathbf{u} \text{ div } \mathbf{v} + 2\mu\, \boldsymbol{\varepsilon}(\mathbf{u}) : \boldsymbol{\varepsilon}(\mathbf{v})\, \mathrm{d}\mathbf{x},$$

and also,

$$F(\mathbf{v}) = \int_\Omega \mathbf{f}.\mathbf{v}\, d\mathbf{x} + \int_{\partial\Omega_T} \mathbf{g}.\mathbf{v}\, ds. \tag{6.6}$$

To recap, note that the bilinear form $a(\mathbf{u}, \mathbf{v})$ may be written as,

$$a(\mathbf{u}, \mathbf{v}) = \int_\Omega \boldsymbol{\sigma}(\mathbf{u}) : \boldsymbol{\varepsilon}(\mathbf{v})\, d\mathbf{x}, \tag{6.7}$$

where $\boldsymbol{\sigma}(\mathbf{u})$ is as defined in Equation (6.1) and,

$$\boldsymbol{\sigma} : \varepsilon = \sum_{i,j=1}^{2} \sigma_{ij}\varepsilon_{ij}.$$

Alternatively, in vector notation this has the form,

$$a(\mathbf{u}, \mathbf{v}) = \int_\Omega \boldsymbol{\sigma}(\mathbf{u}) \cdot \boldsymbol{\varepsilon}(\mathbf{v})\, d\mathbf{x},$$

where $\boldsymbol{\sigma}$ and $\boldsymbol{\varepsilon}$ are now stress and strain vectors respectively which have been defined for the three-dimensional scenario in Chapter 2.

Equation (6.1) is known as Hooke's law for an isotropic material which, as described in Section (2.1.3), allows the relationship between stress and strain to be written using the constitutive matrix $\mathbf{C}$ as,

$$\boldsymbol{\sigma} = \mathbf{C}\boldsymbol{\varepsilon} = \begin{bmatrix} \lambda + 2\mu & \lambda & 0 \\ \lambda & \lambda + 2\mu & 0 \\ 0 & 0 & \mu \end{bmatrix} \begin{bmatrix} \varepsilon_{11} \\ \varepsilon_{22} \\ 2\varepsilon_{12} \end{bmatrix}. \tag{6.8}$$

In the above λ and μ are referred to as the Lamé coefficients which, in the plane stress context take the form,

$$\lambda = \frac{E\nu}{1-\nu^2} \quad \text{and} \quad \mu = \frac{E}{2(1+\nu)}, \tag{6.9}$$

whilst in the plane strain context,

$$\lambda = \frac{E\nu}{(1-2\nu)(1+\nu)} \quad \text{and} \quad \mu = \frac{E}{2(1+\nu)}, \tag{6.10}$$

where E is Young's modulus of elasticity for the material and ν is Poisson's ratio. Transformation from a plane stress system to that of a plane strain system can be performed by simultaneously making the substitutions,

$$E \leftarrow \frac{E}{1-\nu^2} \quad \text{and} \quad \nu \leftarrow \frac{\nu}{1-\nu},$$

in Equation (6.9). In addition, an equivalent plane strain system having same constitutive matrix $\mathbf{C}$ as that arising from a plane stress system having $E = E_{\text{stress}}$ and $\nu = \nu_{\text{stress}}$ may be obtained by setting ,

$$E = E_{\text{strain}} = \frac{E_{\text{stress}}}{1-\nu_{\text{stress}}^2} \quad \text{and} \quad \nu = \nu_{\text{strain}} = \frac{\nu_{\text{stress}}}{1-\nu_{\text{stress}}},$$

in Equation (6.10). Transformation from a plane strain system to that of a plane stress system on the other hand can similarly be performed by simultaneously making the substitutions,

$$E \leftarrow \frac{E(1+2\nu)}{(1+\nu)^2} \quad \text{and} \quad \nu \leftarrow \frac{\nu}{1+\nu},$$

in Equation (6.10). In addition, an equivalent plane stress system having the same constitutive matrix $\mathbf{C}$ as that arising from a plane strain system having $E = E_{\text{strain}}$ and $\nu = \nu_{\text{strain}}$ may also be obtained by setting,

$$E = E_{\text{stress}} = \frac{E_{\text{strain}}(1+2\nu_{\text{strain}})}{(1+\nu_{\text{strain}})^2} \quad \text{and} \quad \nu = \nu_{\text{stress}} = \frac{\nu_{\text{strain}}}{1+\nu_{\text{strain}}},$$

in Equation (6.9). The forthcoming interpolation error constant results for linear elasticity shall be obtained using a plane strain assumption in the model. Using the above transformations it is thus clear that results may also be obtained in the plane stress context if required. To recap, by defining an operator $\mathbf{B}$ acting on the displacement vector $\mathbf{u}$ where,

$$\boldsymbol{\varepsilon} = \begin{bmatrix} \varepsilon_{11} \\ \varepsilon_{22} \\ 2\varepsilon_{12} \end{bmatrix} = \begin{bmatrix} \frac{\partial}{\partial x_1} & 0 \\ 0 & \frac{\partial}{\partial x_2} \\ \frac{\partial}{\partial x_2} & \frac{\partial}{\partial x_1} \end{bmatrix} \begin{bmatrix} u_1 \\ u_2 \end{bmatrix} = \mathbf{Bu}, \tag{6.11}$$

it is possible to express the bilinear form of the linear elasticity problem as,

$$a(\mathbf{u}, \mathbf{v}) = \int_\Omega (\mathbf{Bu})^T \, \mathbf{C} \, (\mathbf{Bv}) \, d\mathbf{x}. \tag{6.12}$$

For the application of the finite element method the region Ω is partitioned into elements Ω_k with generic mesh size h_k. A finite dimensional space $V^h \subset V$ consisting of piecewise polynomial functions defined over the partition is set up and the Galerkin problem approximating Equation (6.5) is that of finding $\mathbf{u}_h \in V^h$ such that

$$a(\mathbf{u}_h, \mathbf{v}_h) = F(\mathbf{v}_h) \quad \forall \; \mathbf{v}_h \in V^h.$$

It is thus required that the interpolation error constant value is found for a typical element Ω_k of such a partition. Before doing this however, it is necessary to firstly map the element onto a standard element $\hat{\Omega}$ in order to simplify the task.

6.1.1 Mapping from Global to Local Elements

For this problem the task of finding the interpolation error constant $C^i_{1,k}$ for a general element Ω_k is one in which, as described in Section (4.4),

$$C^i_{1,k} = \sup_{\mathbf{u} \in V_\epsilon} \frac{h_k^{-1} ||\mathbf{u} - \pi_h \mathbf{u}||_{L_2(\Omega_k)}}{||\mathbf{u}||_{E(\Omega_k)}}.$$

Considering the mapping again of a general triangular or quadrilateral element as described in Section (5.6.1) we will now show that the interpolation error constant may be expressed independent of element size h_k for problems of linear elasticity. Recall that for a general element Ω_k of size h_k as shown in Figure (5.2) the Jacobian of the mapping onto a standard unit element $\hat{\Omega}$ may be expressed as,

$$\mathbf{J} = \begin{bmatrix} h_k & 0 \\ 0 & h_k \end{bmatrix}, \quad \text{and} \quad \mathbf{J}^{-1} = \frac{1}{h_k^2} \begin{bmatrix} h_k & 0 \\ 0 & h_k \end{bmatrix}.$$

where we have used the fact that $|\mathbf{J}| = h_k^2$. Thus the derivative operator $\mathbf{B}$ defined above can be expressed as,

$$\mathbf{B} = \begin{bmatrix} \frac{\partial}{\partial x_1} & 0 \\ 0 & \frac{\partial}{\partial x_2} \\ \frac{\partial}{\partial x_2} & \frac{\partial}{\partial x_1} \end{bmatrix} = \frac{1}{h_k} \begin{bmatrix} \frac{\partial}{\partial \xi} & 0 \\ 0 & \frac{\partial}{\partial \eta} \\ \frac{\partial}{\partial \eta} & \frac{\partial}{\partial \xi} \end{bmatrix} = \frac{1}{h_k} \hat{\mathbf{B}}.$$

It follows that the bilinear form and the L_2 inner product can also be expressed on the standard unit element $\hat{\Omega}$ so that,

$$(C^i_{1,k})^2 = \sup_{\mathbf{u}\in V_\epsilon} \frac{h_k^{-2}\|\mathbf{u}-\pi_h\mathbf{u}\|^2_{L_2(\Omega_k)}}{\|\mathbf{u}\|^2_{E(\Omega_k)}} = \sup_{\hat{\mathbf{u}}\in \hat{V}_\epsilon} \frac{h_k^{-2}\displaystyle\int_{\hat{\Omega}} |\hat{\mathbf{u}}-\pi\hat{\mathbf{u}}|^2 |\mathbf{J}|\, d\hat{\mathbf{x}}}{\dfrac{1}{h_k^2}\displaystyle\int_{\hat{\Omega}} (\hat{\mathbf{B}}\hat{\mathbf{u}})^T \mathbf{C}\,(\hat{\mathbf{B}}\hat{\mathbf{u}})|\mathbf{J}|\, d\hat{\mathbf{x}}},$$

where $\hat{V}_\epsilon = [H^{1+\epsilon}(\hat{\Omega})]^2$ from Appendix E. Thus, substituting $|\mathbf{J}| = h_k^2$ this may be expressed as,

$$(C^i_1)^2 = \sup_{\hat{u}\in \hat{V}_\epsilon} \frac{\displaystyle\int_{\hat{\Omega}} |\hat{\mathbf{u}}-\pi\hat{\mathbf{u}}|^2\, d\hat{\mathbf{x}}}{\displaystyle\int_{\hat{\Omega}} (\hat{\mathbf{B}}\hat{\mathbf{u}})^T \mathbf{C}\,(\hat{\mathbf{B}}\hat{\mathbf{u}})\, d\hat{\mathbf{x}}} = \sup_{\hat{\mathbf{u}}\in \hat{V}_\epsilon} \frac{\|\hat{\mathbf{u}}-\pi\hat{\mathbf{u}}\|^2_{L_2(\hat{\Omega})}}{\|\hat{\mathbf{u}}\|^2_{E(\hat{\Omega})}}. \tag{6.13}$$

Similarly, for the boundary constant formulation, mapping onto the standard unit element yields,

$$(C^i_2)^2 = \sup_{\hat{u}\in \hat{V}_\epsilon} \frac{\displaystyle\sum_{j=1}^{e}\int_{\hat{\Gamma}_j} |\hat{\mathbf{u}}-\pi\hat{\mathbf{u}}|^2\, d\hat{\Gamma}_j}{\displaystyle\int_{\hat{\Omega}} (\hat{\mathbf{B}}\hat{\mathbf{u}})^T \mathbf{C}\,(\hat{\mathbf{B}}\hat{\mathbf{u}})\, d\hat{\mathbf{x}}} = \sup_{\hat{\mathbf{u}}\in \hat{V}_\epsilon} \frac{\|\hat{\mathbf{u}}-\pi\hat{\mathbf{u}}\|^2_{L_2(\partial\hat{\Omega})}}{\|\hat{\mathbf{u}}\|^2_{E(\hat{\Omega})}}, \tag{6.14}$$

where again the edges of the standard element are denoted by $\hat{\Gamma}_j$ for $j = 1,\ldots,e$ as in Section (5.6). By dropping the 'hat' notation and working on the standard element we can now find the required interpolation error constants which are independent of element size.

6.1.2 Numerical Computation of Interpolation Error Constant for Elasticity

It is clear that the task of finding the interpolation error constants in the context of linear elasticity will be similar to that described in the previous chapter for two-dimensional problems. The main difference here is that the bilinear form has now changed and that the problem now has two degrees of freedom per node on any given element. Working with the standard elements as done in the previous chapter in two dimensions, the task is again to find the supremum of quotients of the type given in Equations (6.13) and (6.14). In a similar way to that described in the previous chapter for the scalar case, a triangular or quadrilateral Lagrange type element $\hat{\Omega}$ having n nodes, can have now a vector valued function $\mathbf{u}$ from the higher order space V defined over it. Thus $\mathbf{u}$ may be evaluated at any point $\mathbf{x}$ in the element as,

$$\mathbf{u}(\mathbf{x}) = \begin{bmatrix} u_1(\mathbf{x}) \\ u_2(\mathbf{x}) \end{bmatrix} = \sum_{i=1}^{n} \begin{bmatrix} u_1(\mathbf{x}_i) \\ u_2(\mathbf{x}_i) \end{bmatrix} \phi_i(\mathbf{x}) = \sum_{i=1}^{n} \begin{bmatrix} u_1^i \\ u_2^i \end{bmatrix} \phi_i(\mathbf{x}), \tag{6.15}$$

where now $u_1(\mathbf{x}_i) \equiv u_1^i$ and $u_2(\mathbf{x}_i) \equiv u_2^i$ are the displacements at the nodes $i = 1,\ldots,n$ for the two degrees of freedom u_1 and u_2 respectively and $\{\phi_i(\mathbf{x})\}_{i=1}^n$ are the appropriate element shape functions. The interpolant $\pi\mathbf{u}$ evaluated also at any point $\mathbf{x}$ in the element is similarly expressed as,

$$\pi\mathbf{u}(\mathbf{x}) = \begin{bmatrix} \pi u_1(\mathbf{x}) \\ \pi u_2(\mathbf{x}) \end{bmatrix} = \sum_{i=1}^{m} \begin{bmatrix} \pi u_1(\mathbf{x}_i) \\ \pi u_2(\mathbf{x}_i) \end{bmatrix} \vartheta_i(\mathbf{x}) = \sum_{i=1}^{m} \begin{bmatrix} \pi u_1^i \\ \pi u_2^i \end{bmatrix} \vartheta_i(\mathbf{x}),$$

where now $\{\vartheta_i(\mathbf{x})\}_{i=1}^m$ are the shape functions defined over the element and used to describe $\pi\mathbf{u}$. As in the scalar valued case, we have that $\vartheta_i(\mathbf{x}) = 0$ for $m < i \leq n$. The interpolation error may then be expressed as,

$$\mathbf{u}(\mathbf{x}) - \pi\mathbf{u}(\mathbf{x}) = \sum_{i=1}^{n} \begin{bmatrix} u_1^i \\ u_2^i \end{bmatrix} \phi_i(\mathbf{x}) - \sum_{i=1}^{m} \begin{bmatrix} \pi u_1^i \\ \pi u_2^i \end{bmatrix} \vartheta_i(\mathbf{x}) = \sum_{i=1}^{n} \begin{bmatrix} u_1^i \\ u_2^i \end{bmatrix} (\phi_i(\mathbf{x}) - \vartheta_i(\mathbf{x})), \tag{6.16}$$

since we know that, at the nodes, the value of the interpolant will be that of the function $\mathbf{u}$ for $i = 1, \ldots, m$ and for $m < i \leq n$ we have $\vartheta_i(\mathbf{x}) = 0$. Thus, considering the interpolation error squared,

$$\begin{aligned} |\mathbf{u}(\mathbf{x}) - \pi\mathbf{u}(\mathbf{x})|^2 &= [u_1(\mathbf{x}) - \pi u_1(\mathbf{x}), u_2(\mathbf{x}) - \pi u_2(\mathbf{x})] \begin{bmatrix} u_1(\mathbf{x}) - \pi u_1(\mathbf{x}) \\ u_2(\mathbf{x}) - \pi u_2(\mathbf{x}) \end{bmatrix} \\ &= \left(\sum_{i=1}^{n} [u_1^i, u_2^i] (\phi_i(\mathbf{x}) - \vartheta_i(\mathbf{x})) \right) \left(\sum_{j=1}^{n} \begin{bmatrix} u_1^j \\ u_2^j \end{bmatrix} (\phi_j(\mathbf{x}) - \vartheta_j(\mathbf{x})) \right) \\ &= \sum_{i,j=1}^{n} [u_1^i, u_2^i] \begin{bmatrix} \Phi_{ij}(\mathbf{x}) & 0 \\ 0 & \Phi_{ij}(\mathbf{x}) \end{bmatrix} \begin{bmatrix} u_1^j \\ u_2^j \end{bmatrix}, \end{aligned} \tag{6.17}$$

where, $\Phi_{ij}(\mathbf{x})$ has the form,

$$\Phi_{ij}(\mathbf{x}) = (\phi_i(\mathbf{x}) - \vartheta_i(\mathbf{x}))\,(\phi_j(\mathbf{x}) - \vartheta_j(\mathbf{x})). \tag{6.18}$$

Thus Equation (6.17) can be expressed in the form,

$$|\mathbf{u}(\mathbf{x}) - \pi\mathbf{u}(\mathbf{x})|^2 = \mathbf{u}^T \mathbf{\Phi}(\mathbf{x})\,\mathbf{u},$$

where,

$$\mathbf{u}^T = [u_1^1, u_2^1, u_1^2, u_2^2, \ldots, u_1^n, u_2^n],$$

and the matrix $\mathbf{\Phi}(\mathbf{x})$ has the form,

$$\mathbf{\Phi}(\mathbf{x}) = \begin{bmatrix} \Phi_{11}(\mathbf{x}) & 0 & \Phi_{12}(\mathbf{x}) & 0 & \ldots & \Phi_{1n}(\mathbf{x}) & 0 \\ 0 & \Phi_{11}(\mathbf{x}) & 0 & \Phi_{12}(\mathbf{x}) & \ldots & 0 & \Phi_{1n}(\mathbf{x}) \\ \vdots & \vdots & \vdots & \vdots & \ddots & \vdots & \vdots \\ \Phi_{n1}(\mathbf{x}) & 0 & \Phi_{n2}(\mathbf{x}) & 0 & \ldots & \Phi_{nn}(\mathbf{x}) & 0 \\ 0 & \Phi_{n1}(\mathbf{x}) & 0 & \Phi_{n2}(\mathbf{x}) & \ldots & 0 & \Phi_{nn}(\mathbf{x}) \end{bmatrix} \equiv (\Phi_{ij}(\mathbf{x})\mathbf{I}_2)_{i,j=1}^n, \tag{6.19}$$

where $\Phi_{i,j}(\mathbf{x})$ for $i, j = 1, \ldots, n$ is as defined in Equation (6.18) and $\mathbf{I}_2$ is the 2×2 identity matrix. Here it can be seen that there exist strong similarities with matrix $\mathbf{\Phi}(\mathbf{x})$ above and that defined in Section (5.7). In addition we may define now a matrix $\mathbf{M}'$ similar to that in Section (5.7) but whose terms are obtained by integrating those of matrix $\mathbf{\Phi}(\mathbf{x})$ given in Equation (6.19). Thus we have that,

$$\mathbf{M}' = (M'_{ij}\mathbf{I}_2)_{i,j=1}^n,$$

where, for the interior interpolation error constant C_1^i,

$$M'_{ij} = \int_{\hat{\Omega}} \Phi_{i,j}\, d\mathbf{x} \text{ for } i, j = 1, \ldots, n, \tag{6.20}$$

whilst, for the boundary interpolation error constant C_2^i,

$$M'_{ij} = \int_{\partial\hat{\Omega}} \Phi_{i,j}\, ds \text{ for } i,j = 1,\ldots,n, \tag{6.21}$$

on a standard triangular or quadrilateral element $\hat{\Omega}$ and with extra terms as described in Section (5.7) for the case of transition element interpolants. The task of finding the interpolation error constant can be thus now be written as one in which we seek,

$$(C_j^i)^2 = \sup_{\mathbf{u}\in\mathbb{R}^{2n}} \frac{\mathbf{u}^T\mathbf{F}\,\mathbf{u}}{\mathbf{u}^T\mathbf{E}\,\mathbf{u}}, \quad \text{for } j = 1 \text{ or } 2, \tag{6.22}$$

where $\mathbf{F} = \mathbf{M}'$ and $\mathbf{E}$ is the element stiffness matrix which may be expressed as,

$$\mathbf{E} = (E_{ij})_{i,j=1}^{2n} \text{ with } E_{ij} = \int_{\hat{\Omega}} (\mathbf{B}\boldsymbol{\phi}_i)^T\, \mathbf{C}\, \left(\mathbf{B}\boldsymbol{\phi}_j\right)\, d\mathbf{x}, \quad \text{for } i,j = 1,\ldots,2n, \tag{6.23}$$

where,

$$\left.\begin{array}{ll} \boldsymbol{\phi}_{2l-1} & = [\phi_l, 0]^T \\ \boldsymbol{\phi}_{2l} & = [0, \phi_l]^T \end{array}\right\} \quad \text{for } l = 1,\ldots,n.$$

6.1.3 Numerical Results of Interpolation Error Constants for Elasticity

The computational method of the previous section will now be used to obtain the interpolation error constant values for linear elasticity on both triangular and quadrilateral elements. The interpolants are respectively linear and bilinear for these two types of elements and, for the latter, investigation into the interpolation error constant values for transition element interpolants will be considered. The computational results will be obtained using the three numerical methods introduced in the previous chapter and in all following sections the QZ method results will be considered to be the 'optimal' results. Unless stated otherwise it will be these results which are used in subsequent calculations and discussions. Results from the other two methods are included in order to primarily reinforce the QZ results but also to show the limitations in their capabilities as the problem complexity increases

Triangular Elements

Table (6.1) shows the interior interpolation error constant results for the three methods on triangular elements. It can be seen that the sampling method again seems to be less accurate even with 10^5 samples being taken. Both the minimization and QZ methods agree well however and although the interpolation error constant is different to that observed for triangles in the case of Poisson's problem it is important to consider that the values here are strongly affected by the choice of material properties in the constitutive matrix $\mathbf{C}$. The table shows the variation of the computed interpolation constant values with λ and μ. These variations were obtained by varying Young's modulus E but keeping $\nu = 0.3$ constant. It can be seen that as the Young's modulus

E	λ	μ	Sampling Method	Minimization Method	QZ Method
1	0.576923	0.384615	0.999558	1.197708	1.197708
10	5.769231	3.846154	0.279528	0.378748	0.378748
10^2	57.69231	38.46154	0.073390	0.119771	0.119771
10^3	576.9231	384.6154	0.025711	0.037875	0.037875
10^4	5769.231	3846.154	0.009207	0.011977	0.011977
10^5	57692.31	38461.54	0.002759	0.003787	0.003787

Table 6.1: Computed C_1^i for trangles in linear elasticity with varying E and fixed ν.

value is increased, this in turn increases the λ and μ values given in Equation (6.10). This results in larger terms in the element stiffness matrix $\mathbf{E}$ of Equation (6.22) whilst those of matrix $\mathbf{F}$ remain constant. It is thus clear that we should, and indeed do, see a drop in the computed C_1^i values as the material properties increase.

An interesting observation for the results (Minimization and QZ) in Table (6.1) is that, upon increasing the Young's modulus value E by a factor of 10, a corresponding decrease by a factor of $\sqrt{10}$ is observed in the value of the computed interpolation error constant. The reason for this can be given by inspection of the terms in Equation (6.22). The problem being solved is that of Equation (6.22) with $j = 1$ and where $\mathbf{E}$ and $\mathbf{F}$ are the previously defined interpolation error and element stiffness matrices respectively. The terms of $\mathbf{F}$ are independent of material properties and thus remain constant upon varying such parameters. However, the element stiffness matrix terms do vary with changing material properties and it is this term which we now require to inspect. The element stiffness matrix is as defined in Equation (6.23) where the material property matrix $\mathbf{C}$ is,

$$\mathbf{C} = \begin{bmatrix} \lambda + 2\mu & \lambda & 0 \\ \lambda & \lambda + 2\mu & 0 \\ 0 & 0 & \mu \end{bmatrix},$$

and where, in the case of plane strain,

$$\lambda = \frac{\nu E}{(1-2\nu)(1+\nu)} \quad \text{and} \quad \mu = \frac{E}{2(1+\nu)}.$$

It is clear that for fixed ν, as in the case of Table (6.1), both λ and μ are proportional to E. Considering Young's modulus E_1 it follows therefore that λ_1 and μ_1 can be expressed as,

$$\lambda_1 = KE_1 \quad \text{and} \quad \mu_1 = LE_1,$$

with K and L constants. In addition, by considering $E_2 = 10E_1$ say, it follows that the corresponding λ_2 and μ_2 can be expressed as,

$$\lambda_2 = 10KE_1 \quad \text{and} \quad \mu_2 = 10LE_1.$$

The material property matrices $\mathbf{C}_1$ and $\mathbf{C}_2$ arising from the use of E_1 and E_2 respectively will therefore be such that,

$$\mathbf{C}_2 = 10\mathbf{C}_1,$$

and the resulting element stiffness matrices will also be affected similarly and given by,

$$\mathbf{E}_2 = 10\mathbf{E}_1.$$

It follows that, by using Equation (6.22),

$$\sup_{\mathbf{u}\in\mathbb{R}^{2n}} \frac{\mathbf{u}^T\mathbf{F}\,\mathbf{u}}{\mathbf{u}^T\mathbf{E}_2\,\mathbf{u}} \equiv \sup_{\mathbf{u}\in\mathbb{R}^{2n}} \frac{\mathbf{u}^T\mathbf{F}\,\mathbf{u}}{10\,\mathbf{u}^T\mathbf{E}_1\,\mathbf{u}}.$$

Thus by taking the required square root of the above it is now clear that the computed interpolation error constant value for a material with Young's modulus E_2 will be a factor of $\sqrt{10}$ smaller than with Young's modulus E_1. This explains the previously mentioned trend observed in Table (6.1) where an increase of a factor of 10 in the Young's modulus values resulted in a decrease by a factor of $\sqrt{10}$ in the computed interpolation error constant values. It may thus be argued that, knowing the interpolation error constant for just one value of E, it is possible to predict the interpolation error constant for any E providing that ν is fixed. In such a case we must have 'datum' values for both the Young's modulus and the corresponding interpolation error constant which shall be denoted here as E_d and C_d^i respectively. Suppose that we now require to predict the interpolation error constant C_p^i for a material with Young's modulus E and same value of ν where $E = ME_d$ with M some constant. In such a case, we know that,

$$(C_d^i)^2 = \sup_{\mathbf{u}\in\mathbb{R}^{2n}} \frac{\mathbf{u}^T\mathbf{F}\,\mathbf{u}}{\mathbf{u}^T\mathbf{E}_d\,\mathbf{u}},$$

where $\mathbf{E}_d$ is the element stiffness matrix arising from the datum material properties. Also, it is known from above that,

$$\left(C_p^i\right)^2 = \sup_{\mathbf{u}\in\mathbb{R}^{2n}} \frac{\mathbf{u}^T\mathbf{F}\,\mathbf{u}}{\mathbf{u}^T\mathbf{E}\,\mathbf{u}} \equiv \sup_{\mathbf{u}\in\mathbb{R}^{2n}} \frac{\mathbf{u}^T\mathbf{F}\,\mathbf{u}}{M\,\mathbf{u}^T\mathbf{E}_d\,\mathbf{u}} = \frac{(C_d^i)^2}{M}.$$

Thus, the predicted interpolation error constant C_p^i is given as,

$$C_p^i = \frac{C_d^i}{\sqrt{M}}, \tag{6.24}$$

provided that ν remains fixed throughout. The above observation for the results of Table (6.1) is clearly an example of the case when $M = 10$. As a further example consider the task of finding the interior interpolation error constant value for a material with $E = 12745$ and $\nu = 0.3$. Before performing the computations let us attempt to predict what the interpolation error constant will be. As above we shall denote the predicted interpolation error constant C_p^i and use as our datum value, C_d^i, the interpolation error constant arising from the $E = 1$ scenario in Table (6.1). Thus,

$$C_p^i = \frac{C_d^i}{\sqrt{M}} = \frac{1.197708}{\sqrt{12745}} = 0.010609 \text{ to six decimal places.}$$

The computed interpolation error constant is found to be $C_1^i = 0.010609$ to six decimal places which is in complete agreement with the predicted value. It should be noted that although the datum value chosen here is for the case where $E = 1$ this is not mandatory and indeed any of the results of Table (6.1) can be used as datum values.

Due to the fact that we have thus far fixed ν we shall now present results for fixed E and varying ν. These results can be seen in Table (6.2) where a fixed Young's modulus value of $E = 1$ has been chosen. From Table (6.2) it can be seen that within the usual operating range $0 \leq \nu < 0.5$, the interpolation error constant has a small variation. Even as ν approaches the upper limit of 0.5 we still obtain 'sensible' interpolation error constant values. By the term 'sensible', we mean that the interpolation error constant value does no increase dramatically as $\nu \rightarrow 0.5$. For example, when $\nu = 0.49999$ the computed interpolation error constant is found to be $C_1^i = 1.237806$ to six decimal places.

ν	λ	μ	Sampling Method	Minimization Method	QZ Method
0.1	0.113636	0.454545	0.908498	1.143177	1.143177
0.2	0.277778	0.416667	0.944910	1.172415	1.172415
0.3	0.576923	0.384615	0.890735	1.197708	1.197708
0.4	1.428571	0.357143	0.958710	1.219404	1.219404

Table 6.2: Computed C_1^i for trangles in linear elasticity with varying ν and fixed E.

Using the previous analyses for fixed ν and the above results for fixed E we are able to propose a general method for *estimating* the interior interpolation error constant for any E and ν in problems of linear elasticity. The method will consist of two parts, the first of which involves linear interpolation between the results of Table (6.2). In this way an estimated interpolation error constant is obtained for $E = 1$ and the required ν value and which shall be denoted as the datum value C_d^i. It should be noted that the value of C_d^i will, however, now inevitably contain an error due to the interpolation employed to determine it. The second part of the proposed method then scales C_d^i to the predicted interpolation error constant value C_p^i for the required value of E as described in Equation (6.24).

To test this let us attempt to predict the interior interpolation error constant for a random material with $\nu = 0.24$ and $E = 14263$. The results interpolation will obviously have to be carried out between the $\nu = 0.2$ and $\nu = 0.3$ results from Table (6.2). This gives,

$$\begin{aligned} C_d^i &= 0.6C_{1,\nu=0.2}^i + 0.4C_{1,\nu=0.3}^i, \\ &= 0.6(1.172415) + 0.4(1.197708), \\ &= 1.182532\,. \end{aligned} \tag{6.25}$$

Scaling this now using Equation (6.24) with the above value of C_d^i and $M = 14263$ gives,

$$C_p^i = \frac{C_d^i}{\sqrt{M}} = \frac{1.182532}{\sqrt{14263}} = 0.009902 \text{ to six decimal places.}$$

The computed interpolation error constant is found to be $C_1^i = 0.009905$ to six decimal places which agrees well with the predicted value. The possible error in the predicted value is due to interpolation step of Equation (6.25) between selected results of Table (6.2).

We will now present results for the computation of the boundary interpolation error constant C_2^i. As detailed previously in Section (6.1.2) this differs from the computation of the interior interpolation error constant due to the fact that Equation (6.21) is employed in place of Equation (6.20) for the calculation of the interpolation error matrix $\mathbf{F}$ in Equation (6.22).

The results for the computation of C_2^i can be seen in Table (6.3). Again, it can be seen that, for

E	λ	μ	Sampling Method	Minimization Method	QZ Method
1	0.576923	0.384615	2.120251	2.734093	2.734093
10	5.769231	3.846154	0.673799	0.864596	0.864596
10^2	57.69231	38.46154	0.212116	0.273409	0.273409
10^3	576.9231	384.6154	0.063968	0.086460	0.086460
10^4	5769.231	3846.154	0.022797	0.027341	0.027341
10^5	57692.31	38461.54	0.006435	0.008646	0.008646

Table 6.3: Computed C_2^i for trangles in linear elasticity with varying E and fixed ν.

both the Minimization and QZ Method results, a factor of 10 increase in the Young's modulus value results in a factor of $\sqrt{10}$ decrease in the computed interpolation error constant value. The reason for this is exactly as for the interior constant described above and due to the fact that we are again solving Equation (6.22) but now with $j = 2$. As established previously it is the element stiffness matrix which dictates the results trend upon the variation of E whilst the terms of $\mathbf{F}$ remain fixed. It should be emphasised that the terms of $\mathbf{F}$ are now computed using Equation (6.21) and thus differ from those computed for the interior interpolation error constant. This difference consequently produces different interpolation error constant values for the boundary case.

As detailed for the interior interpolation constant results, it is possible to predict the boundary interpolation error constant for a general Young's modulus E provided the value of ν is the same value as that used for the datum results. Thus we again have that the predicted interpolation error constant C_p^i may be calculated by Equation (6.24), given as,

$$C_p^i = \frac{C_d^i}{\sqrt{M}},$$

where C_d^i is the interpolation error constant arising from the datum Young's modulus value E_d with ν fixed and where $E = ME_d$ with M a constant. Performing the same example as for the interior case, consider the task of finding the boundary interpolation error constant value for a material with $E = 12745$ and $\nu = 0.3$. Using the datum values from $E \equiv E_d = 1$ in Table (6.3) the predicted value is,

$$C_p^i = \frac{2.734093}{\sqrt{12745}} = 0.024218 \text{ to six decimal places.}$$

The computed interpolation error constant is found to be $C_2^i = 0.024218$ to six decimal places which agrees with the predicted value. Thus, as previously seen, it is possible to predict the boundary interpolation error constant value for any E provided that we have one computed interpolation error constant value, C_d^i, resulting from datum value E_d and ν remains fixed.

We shall now present results for $E = 1$ and varying ν as done for the interior interpolation error constant. Table (6.4) shows the interpolation error constant values obtained for such cases. By

ν	λ	μ	Sampling Method	Minimization Method	QZ Method
0.1	0.113636	0.454545	2.244281	2.683068	2.683068
0.2	0.277778	0.416667	2.076315	2.715093	2.715093
0.3	0.576923	0.384615	2.182510	2.734093	2.734093
0.4	1.428571	0.357143	2.183471	2.741194	2.741196

Table 6.4: Computed C_2^i for trangles in linear elasticity with varying ν and fixed E.

applying the estimation method introduced for interior interpolation error constants in order to find an estimated C_d^i value for $\nu = 0.24$, gives,

$$\begin{aligned} C_d^i &= 0.6C_{1,\nu=0.2}^i + 0.4C_{1,\nu=0.3}^i, \\ &= 0.6(2.715093) + 0.4(2.734093), \\ &= 2.722693\,. \end{aligned}$$

If the interpolation error constant is required for, $E = 14263$, as for the the interior case, it will be necessary to scale the value of C_d^i. This is done as before by using Equation (6.24) with the above value of C_d^i and $M = 14263$ to give,

$$C_p^i = \frac{C_d^i}{\sqrt{M}} = \frac{2.722693}{\sqrt{14263}} = 0.022798 \text{ to six decimal places.}$$

The computed interpolation error constant is found to be $C_1^i = 0.022810$ to six decimal places which agrees well with the predicted value. The possible error in the predicted value is due again to the interpolation of the results presented in Table (6.4).

A global observation for this section is that the computed C_2^i values are consistently larger than their corresponding C_1^i values for given λ and μ. Although this is merely an observation it is consistent with the results of Table (5.6) for the Poisson problem.

Quadrilateral Elements

Table (6.5) shows the interior interpolation error constant results for the three methods on quadrilateral elements. It can be seen that the sampling method again seems to be less accurate even with 10^5 samples made. As illustrated beforehand, both the minimization and QZ methods agree well. Again the results are affected by changing material properties and the table depicts what happens when these are varied. The table shows the variation of the interpolation constant with λ and

μ. These variations were obtained by varying Young's modulus E but keeping $\nu = 0.3$ constant. The results show, as previously, that an increase in E by a factor of 10 results in a corresponding

E	λ	μ	Sampling Method	Minimization Method	QZ Method
1	0.576923	0.384615	0.746750	0.844513	0.844513
10	5.769231	3.846154	0.222800	0.267058	0.267058
10^2	57.69231	38.46154	0.067587	0.084451	0.084451
10^3	576.9231	384.6154	0.022294	0.026706	0.026706
10^4	5769.231	3846.154	0.007138	0.008445	0.008445
10^5	57692.31	38461.54	0.002357	0.002671	0.002671

Table 6.5: Computed C_1^i for quadrilaterals in linear elasticity with varying E and fixed ν.

decrease of a factor of $\sqrt{10}$ in the computed interpolation error constant value. This behaviour is due to the same effect observed for the interior constant values calculated over the triangular element in the previous section. It is clear again that it is possible to predict the interpolation error constant value for any value of E now over quadrilateral elements by using a result from Table (6.5) as a datum and Equation (6.24).

The computed interior interpolation error constant value with varying ν and $E = 1$ fixed is now presented in Table (6.6). Application of the estimation method to predict the interpolation error

ν	λ	μ	Sampling Method	Minimization Method	QZ Method
0.1	0.113636	0.454545	0.704600	0.824727	0.824727
0.2	0.277778	0.416667	0.707714	0.841202	0.841202
0.3	0.576923	0.384615	0.706232	0.844513	0.844513
0.4	1.428571	0.357143	0.650359	0.824061	0.824061

Table 6.6: Computed C_1^i for quadrilaterals in linear elasticity with varying ν and fixed E.

constant for a material with $E = 14263$ and $\nu = 0.24$ yields, from part one,

$$C_d^i = 0.842526 \text{ to six decimal places.}$$

Scaling this now, as given in Equation (6.24),

$$C_p^i = \frac{0.842526}{\sqrt{14263}} = 0.007055 \text{ to six decimal places.}$$

For comparison, the corresponding computed result is found to be $C_1^i = 0.007071$ to six decimal places which agrees well with the predicted value. As before, any error may be attributed to the results interpolation performed in order to obtain C_d^i.

The results for the boundary interpolation error constant C_2^i are detailed in Table (6.7) for varying material properties. Both Tables (6.5) and (6.7) depict a now familiar trend with the sampling method requiring an increasing number of samples made in order to yield even only comparable results with those of the other two methods. The results for this method here were established with 10^5 samples made. Due to the run-times involved, the sampling method is rapidly becoming less efficient as the size of the problem increases and will consequently not be used in following sections. Similarly, the minimization method, although still in strong agreement with the QZ method will

E	λ	μ	Sampling Method	Minimization Method	QZ Method
1	0.576923	0.384615	1.175856	1.492840	1.492840
10	5.769231	3.846154	0.367745	0.472077	0.472077
10^2	57.69231	38.46154	0.111793	0.149284	0.149284
10^3	576.9231	384.6154	0.036573	0.047208	0.047208
10^4	5769.231	3846.154	0.011523	0.014928	0.014928
10^5	57692.31	38461.54	0.003644	0.004721	0.004721

Table 6.7: Computed C_2^i for quadrilaterals in linear elasticity with varying E and fixed ν.

not be used in following sections and we shall continue analysis of the two constants by using the QZ method alone which has shown itself to be reliable in all cases thus far. The interpolation error constant results of Table (6.7) again show the trend observed previously, with a factor of 10 increase in E yielding a corresponding factor of $\sqrt{10}$ decrease in interpolation error constant value. This is again due to the reasons given earlier in this section for a triangular element.

Results for varying ν can be found in Table (6.8). It can be seen here that the computed interpolation error constant values seem to vary more than previously observed. We shall see how this

ν	λ	μ	Sampling Method	Minimization Method	QZ Method
0.1	0.113636	0.454545	1.189793	1.712698	1.712698
0.2	0.277778	0.416667	1.163583	1.643168	1.643168
0.3	0.576923	0.384615	1.123308	1.492840	1.492840
0.4	1.428571	0.357143	1.027924	1.196478	1.196479

Table 6.8: Computed C_2^i for quadrilaterals in linear elasticity with varying ν and fixed E.

effects the method for estimating the interpolation error constant by trying once again to predict the interpolation error constant value for the material with properties $E = 14263$ and $\nu = 0.24$. Part one of the method yields,

$$C_d^i = 1.583037 \text{ to six decimal places.}$$

Scaling this result in order to be an estimate for $E = 14263$ gives the predicted interpolation error constant, C_p^i as,

$$C_p^i = \frac{1.583037}{\sqrt{14263}} = 0.013255 \text{ to six decimal places.}$$

For comparison, the corresponding computed result is found to be $C_2^i = 0.009446$ to six decimal places. The agreement here is not as good as previously seen and may be attributed to the results interpolation performed in order to obtain C_d^i.

It is interesting to note that, as seen in the case of triangular elements, the values for C_2^i are larger than their corresponding C_1^i values for a given λ and μ.

Before proceeding to the plate problem, we shall finally consider the effect of quadrilateral transition elements on the interior and boundary interpolation error constants in the context of two-dimensional linear elasticity. As in the case for the Poisson problem, the integration for matrix $\mathbf{M}'$ is modified according to Section (5.7) in order to take account of the possible internal jump terms. The material properties chosen for this are $E = 1000$ and $\nu = 0.3$ and the results are from the QZ method. The values of C_1^i and C_2^i for the standard element in Table (6.9) can be seen to agree

Element type	Computed C_1^i	Computed C_2^i
Standard	0.026706	0.047208
1-irregular	0.023493	0.058351
2_{adj}-irregular	0.023109	0.066476
2_{opp}-irregular	0.019654	0.039221
3-irregular	0.018586	0.053713

Table 6.9: Computed C_1^i and C_2^i for transition elements in linear elasticity with fixed E and ν.

with those on the fourth row in Tables (6.5) and (6.7) respectively due to the fact that these are the material properties employed. As was observed in Table (5.6), the addition of irregular nodes produces a decrease in the computed C_1^i values as the interpolant becomes successively more able to interpolate the higher order functions. For the C_2^i values we again see a sharp increase upon the addition of a single irregular node thought to be due to the internal line of slope discontinuity producing an internal jump which must now be considered in addition to the boundary jumps. The value of C_2^i increases further for the 2_{adj}-irregular element due now to the presence of two internal lines of slope discontinuity and the resulting increase in internal jump terms. In contrast the 2_{opp}-irregular element C_2^i value shows a drop from that of the result for the 1-irregular element due to the fact that, although there still exists the internal jump to consider, the element is more accurate on the element boundary due to the presence of the extra node. A similar drop is apparent from the result for the 2_{adj}-irregular element to that for the 3-irregular element. This is again due to the latter being more accurate on the boundary due to the extra node.

6.2 Interpolation Error Constant for Plates

We finally arrive at the calculation of the interpolation error constants for the plate problem. The techniques produced thus far have served as a series of tests so that, at this stage, we have a reliable and robust technique for computing the interpolation error constants for use ultimately in the error estimator. The method is now extended to the problem of first-order shear deformation theory of plates. In a similar way to the extension from the scalar differential problem to the problem of linear elasticity, the same points are now to be considered for the step from linear elasticity to the plate problem.

Recall from Section (3.3) that the weak formulation for the plate problem requires finding the displacement vector $\mathbf{u} \in V$ comprising five unknowns u, v, w, ψ_1 and ψ_2 where,

$$a(\mathbf{u}, \mathbf{v}) = F(\mathbf{v}) \quad \forall\ \mathbf{v} \in V,$$

and where V is as defined in Equation (3.26). The terms in the weak formulation are defined as,

$$a(\mathbf{u}, \mathbf{v}) = \int_\Omega \left(\mathbf{B}^b\mathbf{u}\right)^T \mathbf{C}^b \ \left(\mathbf{B}^b\mathbf{v}\right)\, d\mathbf{x} + \int_\Omega \left(\mathbf{B}^s\mathbf{u}\right)^T \mathbf{C}^s \ \left(\mathbf{B}^s\mathbf{v}\right)\, d\mathbf{x},$$

and,

$$F(\mathbf{v}) = \int_\Omega v_3 q\, d\mathbf{x} + \int_{\hat{\Gamma}_1} N_n v_1\, ds + \int_{\hat{\Gamma}_2} N_s v_2\, ds + \int_{\hat{\Gamma}_3} Q_n v_3\, ds + \int_{\hat{\Gamma}_4} M_n v_4\, ds + \int_{\hat{\Gamma}_5} M_s v_5\, ds,$$

where Ω is the plate midplane and all remaining terms are as defined in Section (3.3). It can be seen that we now have both differential operators $\mathbf{B}^b$ and $\mathbf{B}^s$ acting on the displacement vectors. These are analogous to differential operator $\mathbf{B}$ in the linear elasticity case as previously noted.

It can be seen in the plate bilinear form that two material property matrices $\mathbf{C}^b$ and $\mathbf{C}^s$ are employed which yield from bending and transverse shear terms respectively in the model. Physical aspects of the plate mean that plane stress assumptions are adopted in the construction of these material property matrices as described in Section (2.1.3) which differs from the plane strain assumptions used in linear elasticity. Such assumptions lead to different Lamé coefficients as detailed in Equations (2.24) and (2.25) for plane stress and strain respectively. The material property matrices may be expressed as,

$$\mathbf{C}^b = \begin{bmatrix} A_{11} & A_{12} & A_{14} & B_{11} & B_{12} & B_{14} \\ A_{12} & A_{22} & A_{24} & B_{12} & B_{22} & B_{24} \\ A_{14} & A_{24} & A_{44} & B_{14} & B_{24} & B_{44} \\ B_{11} & B_{12} & B_{14} & D_{11} & D_{12} & D_{14} \\ B_{12} & B_{22} & B_{24} & D_{12} & D_{22} & D_{24} \\ B_{14} & B_{24} & B_{44} & D_{14} & D_{24} & D_{44} \end{bmatrix}, \tag{6.26}$$

and,

$$\mathbf{C}^s = \begin{bmatrix} A_{55} & A_{56} \\ A_{56} & A_{66} \end{bmatrix}, \tag{6.27}$$

where,

$$(A_{ij}, B_{ij}, D_{ij}) = \int_{-\frac{t}{2}}^{\frac{t}{2}} C_{ij}\left(1, x_3, x_3^2\right)\, dx_3 \quad \text{for} \quad i,j = 1,2,4 \tag{6.28}$$

and,

$$A_{ij} = K_i K_j \int_{-\frac{t}{2}}^{\frac{t}{2}} C_{ij}\, dx_3 \quad \text{for} \quad i,j = 5,6\,, \tag{6.29}$$

for a plate of thickness t and where K_i and K_j are the shear correction coefficients introduced in Equation (2.47). For a plate manufactured from isotropic material, values for C_{ij} are given by,

$$\begin{bmatrix} C_{11} & C_{12} & C_{14} \\ C_{12} & C_{22} & C_{24} \\ C_{14} & C_{24} & C_{44} \end{bmatrix} = \begin{bmatrix} \lambda + 2\mu & \lambda & 0 \\ \lambda & \lambda + 2\mu & 0 \\ 0 & 0 & \mu \end{bmatrix}, \tag{6.30}$$

and,

$$\begin{bmatrix} C_{55} & C_{56} \\ C_{56} & C_{66} \end{bmatrix} = \begin{bmatrix} \mu & 0 \\ 0 & \mu \end{bmatrix}. \tag{6.31}$$

Where now in the plane stress case we define,

$$\lambda = \frac{E\nu}{1-\nu^2} \quad \text{and} \quad \mu = \frac{E}{2\,(1+\nu)}.$$

Application of the finite element method as described in Section (3.6) to the weak formulation yields an approximate solution to the problem under consideration arising from a partition of the problem domain into elements. The task is now to consider the calculation of the interpolation error constant for these elements as performed in the previous section for linear elasticity in two dimensions.

6.2.1 Mapping from Global to Local Elements

As described in Section (4.5) the task here of finding the interpolation error constant $C^i_{1,k}$ for a typical element Ω_k is one in which,

$$C^i_{1,k} = \sup_{\mathbf{u}\in V_\epsilon} \frac{h_k^{-1} \|\mathbf{u} - \pi_h \mathbf{u}\|_{L_2(\Omega_k)}}{\|\mathbf{u}\|_{E(\Omega_k)}}.$$

Considering the mapping again of a triangular or quadrilateral element as described in Section (6.1.1) we will attempt to show that the interpolation error constant formulation may be bounded independent of element size for this plate problem. Recall from Figure (5.2) that for an element Ω_k of size h_k the Jacobian of the mapping onto a standard unit element $\hat{\Omega}$ may be expressed as,

$$\mathbf{J} = \begin{bmatrix} h_k & 0 \\ 0 & h_k \end{bmatrix}, \quad \text{and} \quad \mathbf{J}^{-1} = \frac{1}{h_k^2} \begin{bmatrix} h_k & 0 \\ 0 & h_k \end{bmatrix}.$$

where we have used the fact that $|\mathbf{J}| = h_k^2$. Thus the derivative operators $\mathbf{B}^b$ and $\mathbf{B}^s$ defined above must be expressed in terms of local coordinate variables ξ and η as performed in the case of linear elasticity. Beginning with $\mathbf{B}^b$, this may be expressed as,

$$\mathbf{B}^b = \begin{bmatrix} \frac{\partial}{\partial x_1} & 0 & 0 & 0 & 0 \\ 0 & \frac{\partial}{\partial x_2} & 0 & 0 & 0 \\ \frac{\partial}{\partial x_2} & \frac{\partial}{\partial x_1} & 0 & 0 & 0 \\ 0 & 0 & 0 & \frac{\partial}{\partial x_1} & 0 \\ 0 & 0 & 0 & 0 & \frac{\partial}{\partial x_2} \\ 0 & 0 & 0 & \frac{\partial}{\partial x_2} & \frac{\partial}{\partial x_1} \end{bmatrix} = \frac{1}{h_k} \begin{bmatrix} \frac{\partial}{\partial \xi} & 0 & 0 & 0 & 0 \\ 0 & \frac{\partial}{\partial \eta} & 0 & 0 & 0 \\ \frac{\partial}{\partial \eta} & \frac{\partial}{\partial \xi} & 0 & 0 & 0 \\ 0 & 0 & 0 & \frac{\partial}{\partial \xi} & 0 \\ 0 & 0 & 0 & 0 & \frac{\partial}{\partial \eta} \\ 0 & 0 & 0 & \frac{\partial}{\partial \eta} & \frac{\partial}{\partial \xi} \end{bmatrix} = \frac{1}{h_k}\hat{\mathbf{B}}^b, \tag{6.32}$$

Similarly, for $\mathbf{B}^s$ we may write,

$$\mathbf{B}^s = \begin{bmatrix} 0 & 0 & \frac{\partial}{\partial x_1} & 1 & 0 \\ 0 & 0 & \frac{\partial}{\partial x_2} & 0 & 1 \end{bmatrix} = \frac{1}{h_k} \begin{bmatrix} 0 & 0 & \frac{\partial}{\partial \xi} & h_k & 0 \\ 0 & 0 & \frac{\partial}{\partial \eta} & 0 & h_k \end{bmatrix} = \frac{1}{h_k}\hat{\mathbf{B}}^s. \tag{6.33}$$

Thus considering mapping of the bilinear form evaluated over an element Ω_k to the standard element $\hat{\Omega}$ we obtain,

$$a(\mathbf{u},\mathbf{v})|_{\Omega_k} \equiv \frac{1}{h_k^2}\int_{\hat{\Omega}} \left(\hat{\mathbf{B}}^b\hat{\mathbf{u}}\right)^T \mathbf{C}^b \left(\hat{\mathbf{B}}^b\hat{\mathbf{v}}\right) |\mathbf{J}|\, d\hat{\mathbf{x}} + \frac{1}{h_k^2}\int_{\hat{\Omega}} \left(\hat{\mathbf{B}}^s\hat{\mathbf{u}}\right)^T \mathbf{C}^s \left(\hat{\mathbf{B}}^s\hat{\mathbf{v}}\right) |\mathbf{J}|\, d\hat{\mathbf{x}}.$$

Using the fact that $|\mathbf{J}| = h_k^2$ the above expression can be rewritten as,

$$a(\mathbf{u},\mathbf{v})|_{\Omega_k} \equiv \int_{\hat{\Omega}} \left(\hat{\mathbf{B}}^b\hat{\mathbf{u}}\right)^T \mathbf{C}^b \left(\hat{\mathbf{B}}^b\hat{\mathbf{v}}\right) d\hat{\mathbf{x}} + \int_{\hat{\Omega}} \left(\hat{\mathbf{B}}^s\hat{\mathbf{u}}\right)^T \mathbf{C}^s \left(\hat{\mathbf{B}}^s\hat{\mathbf{v}}\right) d\hat{\mathbf{x}}.$$

Although this removes the immediate presence of h_k in the expression it can be seen in Equation (6.33) that $\hat{\mathbf{B}}^s$ has terms involving h_k. This is due to the fact that shear terms in the second integral of the bilinear form contain terms themselves which are not derivatives. We shall now investigate the occurrence of h_k in the denominator by inspecting the contribution from the second integrand. Taking $\hat{\mathbf{u}} = [\hat{u}_1, \hat{u}_2, \hat{u}_3, \hat{u}_4, \hat{u}_5]^T$ and $\hat{\mathbf{B}}^s$ as given in Equation (6.33) we have that,

$$\hat{\mathbf{B}}^s\hat{\mathbf{u}} = \begin{bmatrix} 0 & 0 & \frac{\partial}{\partial \xi} & h_k & 0 \\ 0 & 0 & \frac{\partial}{\partial \eta} & 0 & h_k \end{bmatrix} \begin{bmatrix} \hat{u}_1 \\ \hat{u}_2 \\ \hat{u}_3 \\ \hat{u}_4 \\ \hat{u}_5 \end{bmatrix} = \begin{bmatrix} \frac{\partial \hat{u}_3}{\partial \xi} + h_k\hat{u}_4 \\ \frac{\partial \hat{u}_3}{\partial \eta} + h_k\hat{u}_5 \end{bmatrix}.$$

Thus the contribution of the integrand, $\mathcal{I}$, to the energy norm, using Equation (6.27) may be expressed as,

$$\mathcal{I} = A_{55}\left(\frac{\partial \hat{u}_3}{\partial \xi} + h_k\hat{u}_4\right)^2 + 2A_{56}\left(\frac{\partial \hat{u}_3}{\partial \xi} + h_k\hat{u}_4\right)\left(\frac{\partial \hat{u}_3}{\partial \eta} + h_k\hat{u}_5\right) + A_{66}\left(\frac{\partial \hat{u}_3}{\partial \eta} + h_k\hat{u}_5\right)^2.$$

The interpolation error constants are to be used in adapted meshes with varying values of h_k and ideally we would like them to be independent of h_k. As illustrated above it is not possible to obtain such a formulation in this case. It is advantageous however, for the constants to be most accurate as $h_k \to 0$. In this way, as the mesh is refined, the error estimate becomes increasingly accurate and gives reliable estimates near the critical endpoint of the analysis and in areas of high refinement. Thus it is proposed that the terms involving h_k in the above expression for $\mathcal{I}$ be set to zero in order to provide constants accurate for the limiting case as $h_k \to 0$. Denoting the resulting contribution $\mathcal{I}^*$ we thus have that,

$$\mathcal{I}^* = A_{55}\left(\frac{\partial \hat{u}_3}{\partial \xi}\right)^2 + 2A_{56}\left(\frac{\partial \hat{u}_3}{\partial \xi}\right)\left(\frac{\partial \hat{u}_3}{\partial \eta}\right) + A_{66}\left(\frac{\partial \hat{u}_3}{\partial \eta}\right)^2.$$

This operation is equivalent to setting the h_k terms in $\hat{\mathbf{B}}^s$ to zero in Equation (6.33). In doing so we obtain $\hat{\mathbf{B}}^*$ which, when used in the bilinear form in place of $\hat{\mathbf{B}}^s$ yields the modified bilinear form $a^*(\mathbf{u}, \mathbf{v})$, defined as,

$$a^*(\mathbf{u}, \mathbf{v})|_{\hat{\Omega}} := \int_{\hat{\Omega}} \left(\hat{\mathbf{B}}^b \hat{\mathbf{u}}\right)^T \mathbf{C}^b \left(\hat{\mathbf{B}}^b \hat{\mathbf{v}}\right) d\hat{\mathbf{x}} + \int_{\hat{\Omega}} \left(\hat{\mathbf{B}}^* \hat{\mathbf{u}}\right)^T \mathbf{C}^s \left(\hat{\mathbf{B}}^* \hat{\mathbf{v}}\right) d\hat{\mathbf{x}}.$$

Thus we obtain, for the mapped interpolation error constant quotient,

$$(C_1^i)^2 = \sup_{\hat{\mathbf{u}} \in \hat{V}_\epsilon} \frac{\displaystyle\int_{\hat{\Omega}} |\hat{\mathbf{u}} - \pi \hat{\mathbf{u}}|^2 \, d\hat{\mathbf{x}}}{\displaystyle\int_{\hat{\Omega}} \left(\hat{\mathbf{B}}^b \hat{\mathbf{u}}\right)^T \mathbf{C}^b \left(\hat{\mathbf{B}}^b \hat{\mathbf{u}}\right) d\hat{\mathbf{x}} + \int_{\hat{\Omega}} \left(\hat{\mathbf{B}}^* \hat{\mathbf{u}}\right)^T \mathbf{C}^s \left(\hat{\mathbf{B}}^* \hat{\mathbf{u}}\right) d\hat{\mathbf{x}}},$$

where $\hat{V}_\epsilon = [H^{1+\epsilon}(\hat{\Omega})]^5$. The interpolation error constant is now independent of h_k and correct for the limiting case as $h_k \to 0$. Thus, denoting the resulting energy norm arising from the modified bilinear form as $||\cdot||_{E^*(\hat{\Omega})}$ we may express,

$$(C_1^i)^2 = \sup_{\hat{\mathbf{u}} \in \hat{V}_\epsilon} \frac{||\hat{\mathbf{u}} - \pi \hat{\mathbf{u}}||^2_{L_2(\hat{\Omega})}}{||\hat{\mathbf{u}}||^2_{E^*(\hat{\Omega})}}. \tag{6.34}$$

The mapping for the boundary interpolation error constant onto the standard unit element similarly yields,

$$(C_2^i)^2 = \sup_{\hat{\mathbf{u}} \in \hat{V}_\epsilon} \frac{||\hat{\mathbf{u}} - \pi \hat{\mathbf{u}}|^2_{L_2(\partial\hat{\Omega})}}{||\hat{\mathbf{u}}||^2_{E^*(\hat{\Omega})}}. \tag{6.35}$$

By dropping the 'hat' notation and working on the standard element we can now find the required interpolation error constant which is independent of element size.

6.2.2 Numerical Computation of Interpolation Error Constant for Plates

The task of finding the interpolation error constant in the plate context will be similar to that described for linear elasticity. Points of concern here are the bilinear form which differs from the linear elasticity case and the fact that there are now five degrees of freedom per node on any given element. As described in Section (3.6) the elements are of Lagrange type and the task is to is to find the supremum of quotients of the type given in Equations (6.34) and (6.35). We are thus concerned with interpolating the vector valued function $\mathbf{u}$ by $\pi\mathbf{u}$ where, using appropriate shape functions we may express $\mathbf{u}(\mathbf{x})$ at any point $\mathbf{x}$ in the element as,

$$\mathbf{u}(\mathbf{x}) = \sum_{i=1}^{n} \mathbf{u}(\mathbf{x}_i)\phi_i(\mathbf{x}) = \sum_{i=1}^{n} \mathbf{u}_i\phi_i(\mathbf{x}),$$

where $\mathbf{u}_i$ is the displacement vector evaluated at the nodes $i = 1, \ldots, n$ and $\{\phi_i(\mathbf{x})\}_{i=1}^{n}$ are the appropriate element shape functions. The interpolant $\pi\mathbf{u}$ evaluated also at any point $\mathbf{x}$ in the element can be similarly expressed as,

$$\pi\mathbf{u}(\mathbf{x}) = \sum_{i=1}^{m} \pi\mathbf{u}(\mathbf{x}_i)\vartheta_i(\mathbf{x}) = \sum_{i=1}^{m} \pi\mathbf{u}_i\vartheta_i(\mathbf{x}),$$

where now $\{\vartheta_i(\mathbf{x})\}_{i=1}^{m}$ are the shape functions defined over the element and used to describe $\pi\mathbf{u}$. Again we have the condition that $\vartheta_i(\mathbf{x}) = 0$ for $m < i \leq n$ which enables the interpolation error to be expressed as,

$$\mathbf{u}(\mathbf{x}) - \pi\mathbf{u}(\mathbf{x}) = \sum_{i=1}^{n} \mathbf{u}_i\phi_i(\mathbf{x}) - \sum_{i=1}^{m} \pi\mathbf{u}_i\vartheta_i(\mathbf{x}) = \sum_{i=1}^{n} \mathbf{u}_i \left(\phi_i(\mathbf{x}) - \vartheta_i(\mathbf{x})\right),$$

since we have that, at the nodes, the value of the interpolant will equal that of $\mathbf{u}$ for $i = 1, \ldots, m$ and for $m < i \leq n$ we have that $\vartheta_i(\mathbf{x}) = 0$. Thus, considering the interpolation error squared,

$$\begin{aligned}
|\mathbf{u}(\mathbf{x}) - \pi\mathbf{u}(\mathbf{x})|^2 &= \left(\mathbf{u}(\mathbf{x}) - \pi\mathbf{u}(\mathbf{x})\right)^T \left(\mathbf{u}(\mathbf{x}) - \pi\mathbf{u}(\mathbf{x})\right) \\
&= \left(\sum_{i=1}^{n} \mathbf{u}_i^T \left(\phi_i(\mathbf{x}) - \vartheta_i(\mathbf{x})\right)\right) \left(\sum_{j=1}^{n} \mathbf{u}_j \left(\phi_j(\mathbf{x}) - \vartheta_j(\mathbf{x})\right)\right) \\
&= \sum_{i,j=1}^{n} \mathbf{u}_i^T \begin{bmatrix} \Phi_{ij}(\mathbf{x}) & 0 & 0 & 0 & 0 \\ 0 & \Phi_{ij}(\mathbf{x}) & 0 & 0 & 0 \\ 0 & 0 & \Phi_{ij}(\mathbf{x}) & 0 & 0 \\ 0 & 0 & 0 & \Phi_{ij}(\mathbf{x}) & 0 \\ 0 & 0 & 0 & 0 & \Phi_{ij}(\mathbf{x}) \end{bmatrix} \mathbf{u}_j,
\end{aligned} \tag{6.36}$$

where, as before,

$$\Phi_{ij}(\mathbf{x}) = \left(\phi_i(\mathbf{x}) - \vartheta_i(\mathbf{x})\right)\left(\phi_j(\mathbf{x}) - \vartheta_j(\mathbf{x})\right).$$

This is very similar to the result for linear elasticity, the only difference here being that there are now five degrees of freedom per node instead of two. Thus Equation (6.36) can be expressed in the form,

$$|\mathbf{u}(\mathbf{x}) - \pi\mathbf{u}(\mathbf{x})|^2 = \mathbf{u}^T \mathbf{\Phi}(\mathbf{x})\, \mathbf{u},$$

where $\mathbf{u}$ is the element displacement vector and can be expressed in terms of the nodal displacement vectors $\mathbf{u}_i$ for $i = 1, \ldots, n$ as,

$$\mathbf{u}^T = \left[\mathbf{u}_1^T, \mathbf{u}_2^T, \ldots, \mathbf{u}_n^T\right],$$

and the matrix $\mathbf{\Phi}(\mathbf{x})$ has the form,

$$\mathbf{\Phi}(\mathbf{x}) = \left(\Phi_{ij}(\mathbf{x})\mathbf{I}_5\right)_{i,j=1}^{n}, \tag{6.37}$$

where $\Phi_{ij}(\mathbf{x})$ is as previously defined and $\mathbf{I}_5$ is the 5×5 identity matrix. The integration of the terms of $\mathbf{\Phi}(\mathbf{x})$ once again give matrix $\mathbf{M}'$ defined as,

$$\mathbf{M}' = \left(M'_{ij}\mathbf{I}_5\right)^n_{i,j=1}, \tag{6.38}$$

where, for the interior interpolation error constant C^i_1,

$$M'_{ij} = \int_{\hat{\Omega}} \Phi_{i,j}(\mathbf{x})\, d\mathbf{x} \text{ for } i,j = 1,\ldots,n, \tag{6.39}$$

whilst, for the boundary interpolation error constant C^i_2,

$$M'_{ij} = \int_{\partial\hat{\Omega}} \Phi_{ij}(\mathbf{x})\, d\Gamma \text{ for } i,j = 1,\ldots,n, \tag{6.40}$$

on a standard triangular or quadrilateral element $\hat{\Omega}$ and with extra terms as described in Section (5.7) for the case of transition element interpolants. We thus have the now familiar task of finding the interpolation error constants where we seek,

$$(C^i_j)^2 = \sup_{\mathbf{u}\in\mathbb{R}^{5n}} \frac{\mathbf{u}^T\mathbf{F}\,\mathbf{u}}{\mathbf{u}^T\mathbf{E}\,\mathbf{u}}, \quad \text{for } j = 1 \text{ or } 2, \tag{6.41}$$

where $\mathbf{F} = \mathbf{M}'$ and $\mathbf{E}$ is the element stiffness matrix arising from the modified bilinear form and which may be expressed as,

$$\mathbf{E} = (E_{ij})^{5n}_{i,j=1} \text{ with } E_{ij} = \int_{\hat{\Omega}} \left(\mathbf{B}^b\boldsymbol{\phi}_i\right)^T \mathbf{C}^b \left(\mathbf{B}^b\boldsymbol{\phi}_j\right)\, d\mathbf{x} + \int_{\hat{\Omega}} \left(\mathbf{B}^*\boldsymbol{\phi}_i\right)^T \mathbf{C}^s \left(\mathbf{B}^*\boldsymbol{\phi}_j\right)\, d\mathbf{x}, \tag{6.42}$$

for $i,j = 1,\ldots,5n$ where,

$$\left.\begin{aligned} \boldsymbol{\phi}_{lk-4} &= [\phi_l,0,0,0,0]^T \\ \boldsymbol{\phi}_{lk-3} &= [0,\phi_l,0,0,0]^T \\ \boldsymbol{\phi}_{lk-2} &= [0,0,\phi_l,0,0]^T \\ \boldsymbol{\phi}_{lk-1} &= [0,0,0,\phi_l,0]^T \\ \boldsymbol{\phi}_{lk} &= [0,0,0,0,\phi_l]^T \end{aligned}\right\} \quad \text{for } l = 1,\ldots,n\,,$$

and where the bilinear form has been modified slightly via the operator $\hat{\mathbf{B}}^*$ in Section (6.2.1) to give a value of C^i_j for $j = 1,2$ independent of element size h_k.

6.2.3 Numerical Results of Interpolation Error Constants for Plates

The following results were obtained using the now familiar technique described in the previous section. Results are firstly presented for a triangular element in order to compare with previous results and then for a standard quadrilateral element with corresponding bilinear interpolant. The results end with an analysis of the interpolation error constant values performed over the transition element family of elements. All results are obtained, as previously, for a range of material properties and for fixed plate thickness $t = 0.5$. Results for varying t are presented in the Section (6.2.4) along with a discussion on the 'thickness effect' upon the interpolation error constant values for plates.

Triangular Elements

Although triangular elements will not be used in the plate analysis, the results for the interpolation error constants are provided here over a triangular element for comparison with previous results. Table (6.10) shows results for both the interior and boundary interpolation error constants. The

E	λ	μ	C_1^i	C_2^i
1	0.329670	0.384615	11.88836	27.41264
10	3.296703	3.846154	3.759430	8.668636
10^2	32.96703	38.46154	1.188836	2.741263
10^3	329.6703	384.6154	0.375943	0.866864
10^4	3296.703	3846.154	0.118884	0.274126
10^5	32967.03	38461.54	0.037594	0.086686

Table 6.10: Computed C_1^i and C_2^i for trangles in plate theory with varying E and fixed ν.

results are again sensitive to changing material properties and the table depicts what happens when these are varied. The table shows the variation of the interpolation constant with λ and μ by varying E but keeping $\nu = 0.3$ constant. It can be seen from Table (6.10) that again, as the material properties are increased, the interior interpolation error constant shows a gradual decrease. This is due to the effect seen previously for elasticity.

It can also be seen in Table (6.10) that the results for the boundary interpolation error constant are larger than those for the interior for a given λ and μ as seen for elasticity results. In fact some quite large computed constant values are presented for both the interior and boundary particularly for smaller λ and μ values. This is due to the inclusion of the plate thickness in the model which, when small, will produce larger interpolation error constants due to the corresponding decrease in the element stiffness matrix terms in Equation (6.41). These decreases arise from the material properties which are integrated over the plate thickness as shown in Equations (6.28) and (6.29). The effect of varying thickness will be illustrated in greater detail in Section (6.2.4).

For fixed t, however, the interpolation error constant value depends upon the variation in material properties alone. Thus it can be seen in Table (6.10) that, with the thickness fixed at $t = 0.5$ and for small λ and μ, the terms of the element stiffness matrix of Equation (6.41) are small and the resulting interpolation error constants largest. As the values of λ and μ increase due to the increases made in E, they compensate the effect of the fixed thickness and the terms in the element stiffness matrix increase, causing a decrease in the interpolation error constant values. This trend has been previously observed and discussed for the linear elasticity results of Section (6.1.3).

Results for varying ν with fixed thickness t and $E = 1$ are presented in Table (6.11). From these results estimated interpolation error constant values can be obtained for any E and ν by

ν	λ	μ	C_1^i	C_2^i
0.1	0.101010	0.454545	11.219158	26.362497
0.2	0.208333	0.416667	11.557922	26.888600
0.3	0.329670	0.384615	11.888361	27.412635
0.4	0.476190	0.357143	12.210937	27.933751

Table 6.11: Computed C_1^i and C_2^i for triangles in plate theory with varying ν and fixed E.

interpolating the results of Table(6.11) and scaling the resulting constant value using Equation (6.24) as detailed for elasticity.

Quadrilateral Elements

Table (6.12) shows the interpolation error results for both the interior and boundary for quadrilateral elements. Again it is interesting to note that all results have smaller computed interpolation error constant values than for the triangle. This is not totally unexpected as the bilinear inter-

E	λ	μ	C_1^i	C_2^i
1	0.329670	0.384615	8.498284	16.18889
10	3.296703	3.846154	2.687393	5.119375
10^2	32.96703	38.46154	0.849828	1.618889
10^3	329.6703	384.6154	0.268739	0.511937
10^4	3296.703	3846.154	0.084983	0.161889
10^5	32967.03	38461.54	0.026874	0.051194

Table 6.12: Computed C_1^i and C_2^i for quadrilaterals in plate theory with varying E and fixed ν.

polant has an extra term in it over the standard linear interpolant on the triangle and thus can be expected to be more capable of interpolating functions from a higher order space. In addition we again see that the boundary values are larger than the interior for a given λ and μ. For the lower valued λ and μ we also see rather large interpolation error constant values. This is once again due to the thickness effect as described for triangles and which will be explained in greater detail in the following section.

As has been the case for all such results we again see the factor of 10 increase in E producing a corresponding decrease in the computed interpolation error constants of a factor of $\sqrt{10}$. This is due to the same reason outlined for elasticity.

Results for varying ν and with fixed thickness t and $E = 1$ are presented in Table (6.13). Again, estimated interpolation error constant values can be obtained for any E and ν by interpolating the relevant results of Table (6.13) and scaling the resulting constant value using Equation (6.24).

ν	λ	μ	C_1^i	C_2^i
0.1	0.101010	0.454545	8.094878	16.885497
0.2	0.208333	0.416667	8.315975	16.627688
0.3	0.329670	0.384615	8.498284	16.188885
0.4	0.476190	0.357143	8.640842	15.553778

Table 6.13: Computed C_1^i and C_2^i for quadrilaterals in plate theory with varying ν and fixed E.

Finally, Table (6.14) shows the interior and boundary constant results for transition elements in plates. The plate modelled here is of thickness $t = 0.5$ and with material properties $E = 1000$ and

Element type	Computed C_1^i	Computed C_2^i
Standard	0.268739	0.511937
1-irregular	0.244574	0.615689
2_{adj}-irregular	0.240599	0.697942
2_{opp}-irregular	0.194673	0.405421
3-irregular	0.192143	0.559246

Table 6.14: Computed C_1^i and C_2^i for transition elements in plate theory with fixed E and ν.

$\nu = 0.3$. As previously observed the interior constants show a gradual decrease in value as the irregular nodes are added due to the fact that the interpolant is gradually able to interpolate the function more accurately each time. The boundary constants also show a now familiar trend with the addition of irregular nodes not necessarily producing a drop in the computed constant value due, again, to the additional internal jumps arising from the lines of slope discontinuity across the element.

6.2.4 Comparison with Elasticity

From the results in the previous section it can be seen that the values of interpolation error constants for plates are larger than those for elasticity. In fact the values for plate interpolation error constants are strongly reliant upon the plate thickness t as previously noted. In order to see how the thickness effects the computed interpolation error constant values we shall now provide results of interior interpolation error constant C_1^i for plates with varying thickness as shown in Table (6.15) which also includes elasticity results in the context of plane stress on quadrilateral elements for comparison. In all cases $\nu = 0.3$ is used and the QZ method used to calculate the interpolation error constant values.

From Table (6.15) it is clear that as the thickness is decreased the computed values of the interpolation error constant increase. The reason for this can be found by inspecting the bilinear form

E	λ	μ	Elasticity	Plate, $t = 0.5$	Plate, $t = 0.25$	Plate, $t = 0.125$
1	0.329670	0.384615	0.867352	8.498284	24.036777	67.986272
10	3.296703	3.846154	0.274281	2.687393	7.601096	21.499147
10^2	32.96703	38.46154	0.086735	0.849828	2.403678	6.798627
10^3	329.6703	384.6154	0.027428	0.268739	0.760110	2.149915
10^4	3296.703	3846.154	0.008674	0.084983	0.240368	0.679863
10^5	32967.03	38461.54	0.002743	0.026874	0.076011	0.214991

Table 6.15: Comparison of C_1^i for quadrilaterals in both linear elasticity and plate theory with varying plate thickness t.

for plates which, from Equation (3.30), may be expressed as,

$$a(\mathbf{u}, \mathbf{v}) = \int_{\Omega} \left(\mathbf{B}^b \mathbf{u}\right)^T \mathbf{C}^b \left(\mathbf{B}^b \mathbf{v}\right) \, d\mathbf{x} + \int_{\Omega} \left(\mathbf{B}^s \mathbf{u}\right)^T \mathbf{C}^s \left(\mathbf{B}^s \mathbf{v}\right) \, d\mathbf{x},$$

where the thickness of the plate is involved in material property matrices $\mathbf{C}^b$ and $\mathbf{C}^s$ which are of the form,

$$\mathbf{C}^b = \begin{bmatrix} \mathbf{A} & \mathbf{B} \\ \mathbf{B} & \mathbf{D} \end{bmatrix}, \quad \text{and} \quad \mathbf{C}^s = \begin{bmatrix} A_{55} & A_{56} \\ A_{56} & A_{66} \end{bmatrix},$$

where $\mathbf{A}$, $\mathbf{B}$ and $\mathbf{D}$ are 3×3 matrices with structure as shown in Equation (6.26). The terms of these matrices are as given in Equation (6.28) and involve the integration of material properties over powers of the plate thickness. By evaluating these integrals for a thickness t it is found for a single laminate that $\mathbf{B}$ is a zero matrix and,

$$\mathbf{A} = t \begin{bmatrix} C_{11} & C_{12} & C_{14} \\ C_{12} & C_{22} & C_{24} \\ C_{14} & C_{24} & C_{44} \end{bmatrix} \equiv t\mathbf{C}_1, \quad \text{and} \quad \mathbf{D} = \frac{t^3}{12} \begin{bmatrix} C_{11} & C_{12} & C_{14} \\ C_{12} & C_{22} & C_{24} \\ C_{14} & C_{24} & C_{44} \end{bmatrix} \equiv \frac{t^3}{12}\mathbf{C}_1.$$

For the transverse shear terms given by Equation (6.29), the material property matrix $\mathbf{C}^s$ may be expressed as,

$$\mathbf{C}^s = t \begin{bmatrix} K_5 K_5 C_{55} & K_5 K_6 C_{56} \\ K_5 K_6 C_{56} & K_6 K_6 C_{66} \end{bmatrix} \equiv t\mathbf{C}_2,$$

where K_i for $i = 5, 6$ are the shear correction coefficients introduced in Equation (2.47). For the calculation of the interpolation error constants the bilinear form is modified as discussed in Section (6.2.1) so that the constants can be calculated independent of element size h_k. This results in Equation (6.41) and in order to show the effect of the thickness, Equation (6.41) may be decomposed into three integrals since we have that $\mathbf{B}$ is a zero matrix. This results in,

$$a^*(\mathbf{u}, \mathbf{v})|_{\hat{\Omega}} = t \int_{\hat{\Omega}} \left(\mathbf{B}_1^b \mathbf{u}\right)^T \mathbf{C}_1 \left(\mathbf{B}_1^b \mathbf{v}\right) \, d\mathbf{x} + \frac{t^3}{12} \int_{\hat{\Omega}} \left(\mathbf{B}_2^b \mathbf{u}\right)^T \mathbf{C}_1 \left(\mathbf{B}_2^b \mathbf{v}\right) \, d\mathbf{x} + t \int_{\hat{\Omega}} \left(\mathbf{B}^* \mathbf{u}\right)^T \mathbf{C}_2 \left(\mathbf{B}^* \mathbf{v}\right) \, d\mathbf{x},$$

where now $\mathbf{C}_1$ and $\mathbf{C}_2$ have the form described in Equations (6.30) and (6.31) respectively and

$\mathbf{B}_1^b$, $\mathbf{B}_2^b$ and $\mathbf{B}^*$ have the forms,

$$\mathbf{B}_1^b = \begin{bmatrix} \frac{\partial}{\partial x} & 0 & 0\ 0\ 0 \\ 0 & \frac{\partial}{\partial y} & 0\ 0\ 0 \\ \frac{\partial}{\partial y} & \frac{\partial}{\partial x} & 0\ 0\ 0 \end{bmatrix}, \quad \mathbf{B}_2^b = \begin{bmatrix} 0\ 0\ 0 & \frac{\partial}{\partial x} & 0 \\ 0\ 0\ 0 & 0 & \frac{\partial}{\partial y} \\ 0\ 0\ 0 & \frac{\partial}{\partial y} & \frac{\partial}{\partial x} \end{bmatrix} \quad \text{and} \quad \mathbf{B}^* = \begin{bmatrix} 0\ 0 & \frac{\partial}{\partial x} & 0\ 0 \\ 0\ 0 & \frac{\partial}{\partial y} & 0\ 0 \end{bmatrix}.$$

Recall that, from Equation (6.41) the task here is to find,

$$(C_1^i)^2 = \sup_{\mathbf{u}\in\mathbb{R}^{5n}} \frac{\mathbf{u}^T\mathbf{F}\,\mathbf{u}}{\mathbf{u}^T\mathbf{E}\,\mathbf{u}},$$

where $\mathbf{F} \equiv \mathbf{M}'$ as defined in Equation (6.38) and $\mathbf{E}$ is the element stiffness matrix, defined here as,

$$\mathbf{E} = (E_{ij})_{i,j=1}^{5n} \text{ with } E_{ij} = a^*(\boldsymbol{\phi}_i, \boldsymbol{\phi}_j)|_{\hat{\Omega}} \text{ for } i, j = 1, \ldots, 5n\,,$$

and where the vectors $\boldsymbol{\phi}_i$ for $i = 1, \ldots, 5n$ are defined as,

$$\left.\begin{aligned} \boldsymbol{\phi}_{5l-4} &= [\phi_l, 0, 0, 0, 0]^T \\ \boldsymbol{\phi}_{5l-3} &= [0, \phi_l, 0, 0, 0]^T \\ \boldsymbol{\phi}_{5l-2} &= [0, 0, \phi_l, 0, 0]^T \\ \boldsymbol{\phi}_{5l-1} &= [0, 0, 0, \phi_l, 0]^T \\ \boldsymbol{\phi}_{5l} &= [0, 0, 0, 0, \phi_l]^T \end{aligned}\right\} \quad \text{for } l = 1, \ldots, n.$$

It can thus be seen that the thickness t features in each term of the element stiffness matrix $\mathbf{E}$. Thus, when t is small the terms of $\mathbf{E}$ will consequently be small. The terms in matrix $\mathbf{F}$ will, however, remain constant as they are independent of both the material properties and the thickness. In this way it is clear that, for a given interpolation error, a larger interpolation error constant value will be obtained for small t than that for larger t assuming material properties remain fixed throughout.

6.3 Summary

In this chapter the interpolation error constants for problems of linear elasticity and plate theory have been investigated using a natural extension of the methods developed in the previous chapter. Such computations cannot be readily found in the literature and it is believed that this is the first time that such a catalogue of results has been presented, certainly for the case of plates. A major finding in this chapter is the fact that for plate problems the thickness can have a large influence upon the interpolation error constant value due to its presence in the bilinear form.

In [27], Johnson and Hansbo provide approximate bounds for both the interior and boundary interpolation error constants over triangular elements in the context of two-dimensional linear elasticity. The interpolants taken are linear and evaluated against the space of quadratic functions defined over a triangular element domain as performed in Section (6.1.2). It is reported, however, that the bounds themselves are derived from an 'approximate' supremum value, itself found 'by trial and error'. Apparently, such a technique results in the bounds,

$$C_1^i \lesssim \frac{0.4}{\sqrt{\lambda + 5\mu}} \quad \text{and} \quad C_2^i \lesssim \frac{1.1}{\sqrt{\lambda + 5\mu}}. \tag{6.43}$$

In order to check these bounds against what are considered in this work to be accurate results, we include again the numerical results of Section (6.1.3) for triangular elements in the context of two-dimensional linear elasticity. Table (6.16) shows the computed values and also the Johnson

Material properties			Interior constant		Boundary constant	
E	λ	μ	QZ Method	J-H	QZ Method	J-H
1	0.576923	0.384615	1.197708	0.252982	2.734093	0.695701
10	5.769231	3.846154	0.378748	0.080000	0.864596	0.220000
10^2	57.69231	38.46154	0.119771	0.025298	0.273409	0.069570
10^3	576.9231	384.6154	0.037875	0.008000	0.086460	0.022000
10^4	5769.231	3846.154	0.011977	0.002530	0.027341	0.006957
10^5	57692.31	38461.54	0.003787	0.000800	0.008646	0.002200

Table 6.16: Comparison of computed C_1^i values with J-H bound.

and Hansbo (J-H) interpolation error constant values for both the interior and boundary cases. A range of values has been obtained by varying the material properties in the two-dimensional linear elasticity model where again, $\nu = 0.3$ and Young's modulus is varied from $E = 1$ to 10^5. It can be seen that the computed interpolation error constant values do not agree well with the Johnson values. Closer inspection reveals however that the ratios of the results are approximately constant. For the interior constant results it is found that the ratio of our results to those of the Johnson bound is 4.734 to three decimal places whilst, for the boundary results, we get 3.930. This implies that the bounds seem to be predicting the correct trends for the constants as the Lamé coefficients are varied but not the correct magnitudes.

In order to reinforce the integrity of our results we will now show that it is possible to select displacement polynomials from the higher order space of polynomials for which the value of the interpolation error constant is larger than that of the relevant Johnson upper bound.

Recall that, from Equation (6.15), the vector valued displacement $\mathbf{u}$ for problems of linear elasticity can be evaluated at any point $\mathbf{x}$ in the element as,

$$\mathbf{u}(\mathbf{x}) = \begin{bmatrix} u_1(\mathbf{x}) \\ u_2(\mathbf{x}) \end{bmatrix} = \sum_{i=1}^{n} \begin{bmatrix} u_1(\mathbf{x}_i) \\ u_2(\mathbf{x}_i) \end{bmatrix} \phi_i(\mathbf{x}) = \sum_{i=1}^{n} \begin{bmatrix} u_1^i \\ u_2^i \end{bmatrix} \phi_i(\mathbf{x}), \tag{6.44}$$

where $u_1(\mathbf{x}_i) \equiv u_1^i$ and $u_2(\mathbf{x}_i) \equiv u_2^i$ are the displacements at the nodes $i = 1, \ldots, n$ for the two degrees of freedom u_1 and u_2 respectively and $\{\phi_i(\mathbf{x})\}_{i=1}^n$ are the appropriate shape functions. Recall also that the computed interpolation error constant values are obtained by taking the square root of the maximum eigenvalue, $\lambda_{\max}$, of the generalized eigenvalue problem associated with Equation (6.22). It follows that, by substituting the corresponding eigenvector $\mathbf{v}_{\max}$ as nodal displacements in the above we will obtain corresponding displacement polynomials for both $u_1(\mathbf{x})$ and $u_2(\mathbf{x})$ from the higher order space of polynomials over which the supremum, or equivalently $\lambda_{\max}$, is required. Denoting the resulting displacement polynomials as $u_{1,\max}(\mathbf{x})$ and $u_{2,\max}(\mathbf{x})$ we thus have the displacement $\mathbf{u}_{\max}(\mathbf{x})$, expressed as,

$$\mathbf{u}_{\max}(\mathbf{x}) = \begin{bmatrix} u_{1,\max}(\mathbf{x}) \\ u_{2,\max}(\mathbf{x}) \end{bmatrix} = \sum_{i=1}^{n} \begin{bmatrix} v_1^i \\ v_2^i \end{bmatrix} \phi_i(\mathbf{x}),$$

where the eigenvector $\mathbf{v}_{\max}$ has the form,

$$\mathbf{v}_{\max} = \left[v_1^1, v_2^1, v_1^2, v_2^2, \ldots, v_1^n, v_2^n\right]^T.$$

Once the displacement polynomials have been established it is then possible to calculate the interpolation error explicity. This is done by using Equation (6.16) in which the interpolation error may be expressed as,

$$\mathbf{u}_{\max}(\mathbf{x}) - \pi\mathbf{u}_{\max}(\mathbf{x}) = \sum_{i=1}^{n} \begin{bmatrix} v_1^i \\ v_2^i \end{bmatrix} (\phi_i(\mathbf{x}) - \vartheta_i(\mathbf{x})), \tag{6.45}$$

since it is known that the value of the interpolant will be that of $\mathbf{u}_{\max}$ for $i = 1, \ldots, m$ and for $m < i \leq n$ we have that the interpolant shape functions $\vartheta_i(\mathbf{x}) = 0$. It should be noted that v_j^i for $j = 1$ or 2 and $i = 1, \ldots, n$ are known terms of the eigenvector $\mathbf{v}_{\max}$ and so the interpolation error $\mathbf{u}_{\max}(\mathbf{x}) - \pi\mathbf{u}_{\max}(\mathbf{x})$ may thus now be explicitly measured in the L_2-norm. This measure may be obtained by integrating the resulting interpolation error over either the whole element as in Equation (6.13) for interior constants or over the element boundary as required in Equation (6.14) for boundary constants. This will result in either the quantity,

$$||\mathbf{u}_{\max} - \pi\mathbf{u}_{\max}||_{L_2(\hat{\Omega})} \quad \text{or} \quad ||\mathbf{u}_{\max} - \pi\mathbf{u}_{\max}||_{L_2(\partial\hat{\Omega})},$$

where $\hat{\Omega}$ is the standard element over which the integration is performed. The quantity $||\mathbf{u}_{\max}||_{E(\hat{\Omega})}$ can also be evaluated using the bilinear form given in Equation (6.12). By then evaluating either,

$$\frac{||\mathbf{u}_{\max} - \pi\mathbf{u}_{\max}||_{L_2(\hat{\Omega})}}{||\mathbf{u}_{\max}||_{E(\hat{\Omega})}} \quad \text{or} \quad \frac{||\mathbf{u}_{\max} - \pi\mathbf{u}_{\max}||_{L_2(\partial\hat{\Omega})}}{||\mathbf{u}_{\max}||_{E(\hat{\Omega})}}, \tag{6.46}$$

depending upon whether the interpolation error over either the element interior or boundary is being investigated, one should obtain the original interpolation error constant. This test will enhance the integrity of the results presented in this work by showing that it is possible to select a valid displacement profile which in turn yields the computed result for the interpolation error constant. Furthermore, it will show that the same displacement profile, when substituted into the relevant expression of Equation (6.46), actually produces a value greater than that predicted by the Johnson and Hansbo bounds given in Equation (6.43) which are supposed to be upper bounds for the interpolation error constants.

The above test will now be applied to a result from both the interior and boundary constant results presented in Table (6.16). It will be shown in both cases that by using the terms of eigenvector $\mathbf{v}_{\max}$ the resulting values of the quantities presented in Equation (6.46) are not only larger than those predicted by the Johnson and Hansbo bounds of Equation (6.43) but also equal to the interpolation error constant value given in Table (6.16) as required.

6.3.1 Verification of Interior Interpolation Error Constant

Consider the case when $E = 1000$ for example, the QZ method gives an interior interpolation error constant value of $C_1^i = 0.037875$ to six decimal places, which is the square root of the largest eigenvalue of the associated generalized eigenvalue problem. Taking the corresponding eigenvector, **vmax** $\equiv \mathbf{v}_{\max}$, as nodal displacement values it is possible to find two displacement polynomials which we shall call **u1max** $\equiv u_{1,\max}(\mathbf{x})$ and **u2max** $\equiv u_{2,\max}(\mathbf{x})$ where $\mathbf{x} \in \mathrm{I\!R}^2$. These polynomials are constructed by using the shape functions denoted as $\{\phi_i(\mathbf{x})\}_{i=1}^n$ in Equation (6.44) which are defined on the element and are used to describe the displacement in the higher order space. Thus for two dimensions we have six quadratic shape functions described on a typical triangular element giving (in Mathematica syntax, [59]),

```
In[9]:=  u1max = Expand[u1shape.vmax]

Out[9]=  0.15698411375118 - 0.151894 x - 0.122644 x**2 + 0.329542 y +
         0.700969 x*y - 1.30766 y**2

In[10]:= u2max = Expand[u2shape.vmax]

Out[10]= 0.12131963284348 + 0.946689 x - 1.30766 x**2 - 0.151894 y +
         0.700969 x*y - 0.122644 y**2
```

where the above output is taken from a typical Mathematica analysis and shows the displacement polynomials **u1max** and **u2max** as '`Out[9]`' and '`Out[10]`' respectively which are obtained by performing the dot (inner) product with the eigenvector **vmax** and the shape functions for u_1 and u_2 on the element which have been denoted as vectors **u1shape** and **u2shape** respectively. It can be seen that both **u1max** and **u2max** are quadratic in **x** and **y** as required and thus both valid displacements from the higher order space.

Once the displacement polynomials have been found it is possible to calculate the interpolation error for each component by using Equation (6.16) and the fact that the interpolant is known to be of linear type. This is done by expressing the further polynomials **u1error** $\equiv u_{1,\max} - \pi u_{1,\max}$ and **u2error** $\equiv u_{2,\max} - \pi u_{2,\max}$ which are the components of Equation (6.45) and are given as,

```
In[12]:= u1error = (u1shape-u1interp).vmax

Out[12]= -0.11755340871436 (-x+x (-1+2 x))+
          0.201505 x (1-x-y)+0.2539 x y-0.0206371 (1-x-y) y+
```

```
          0.15698411375118 (-1+x+(1-2 x-2 y) (1-x-y)+y)-
          0.82113164631506 (-y+y (-1+2 y))

In[13]:= u2error = (u2shape-u2interp).vmax

Out[13]= -0.23964905776064 (-x+x (-1+2 x))+
          1.071 x (1-x-y)+1.34554 x y+0.0588473 (1-x-y) y+
          0.12131963284348 (-1+x+(1-2 x-2 y) (1-x-y)+y)-
          0.15321788962206 (-y+y (-1+2 y))
```

where `u1interp` and `u2interp` are the shape functions describing u_1 and u_2 of the interpolant respectively. Thus the L_2-norm squared of the interpolation error may now be calculated by performing the following integration of the squares of the two displacement error components over the element domain,

```
In[14]:= numer = Integrate[u1error^2+u2error^2,{x,0,1},{y,0,1-x}]

Out[14]= 0.105290
```

This quantity is denoted `numer` since it is equal to the numerator of the quotient in Equation (6.13). Similarly, the denominator term is the energy norm for the displacement polynomials `u1max` and `u2max` detailed above. This term squared will be denoted `denom` but firstly the two-dimensional strain vectors, `strain`, as described by Equation (6.11) and the corresponding transpose `straint` are defined as,

```
In[15]:= strain  = {
                    D[u1max,x],
                    D[u2max,y],
                    D[u1max,y]+D[u2max,x]
                   };
In[16]:= straint = {
                    {D[u1max,x]},
                    {D[u2max,y]},
                    {D[u1max,y]+D[u2max,x]}
                   };
```

These strain vectors can now be used to evaluate the energy norm squared of the displacements. This entails, by definition of the energy norm, the evaluation of the bilinear form which is given in Equation (6.12). The integrand of the bilinear form is denoted `energy` where,

```
In[17]:= energy = straint.C.strain;

In[18]:= denom = Integrate[energy,{x,0,1},{y,0,1-x}]

Out[18]= {73.397881}
```

and where `C` is the constitutive matrix as given in Equation (6.8) and which was introduced in Chapter 2. Integrating over the element domain yields the corresponding value for `denom`. Thus we may now evaluate the quantity on the left-hand side of Equation (6.46) in order to give the value of the interior interpolation error constant for the specified displacement polynomials `u1max` and `u2max`. Taking the square root this gives,

```
In[19]:= Sqrt[numer/denom]

Out[19]= {0.037875}
```

It can be seen that the above choice of displacement polynomials gives exactly the interpolation error constant in Table (6.16). This is not surprising since the displacement polynomials were derived from the eigenvector corresponding to the largest eigenvalue. These polynomials, however, do in fact belong to the higher order space of polynomials as required and it has been shown that these result in an interpolation error constant which is larger than the bound given by Johnson and Hansbo, [27], for C_1^i and included in Equation (6.43). The reason for this difference is not clear although in this work the supremum is obtained over all functions in the richer space whilst the bounds of [27] are obtained using a finite set of functions as detailed in Appendix D. Such a finite set of functions may not be able to adequately capture the worst case scenario and thus may lead to smaller interpolation error constant bounds as observed.

6.3.2 Verification of Boundary Interpolation Error Constant

Considering the case of the boundary interpolation error constant results and again taking the $E = 1000$ case, the computed value is $C_2^i = 0.086460$ to six decimal places. Performing the same analysis now for the boundary constant as that performed for the interior constant above yields displacement polynomials `u1max` and `u2max` as follows,

```
In[9]:=  u1max = Expand[u1shape.vmax]

Out[9]=  0.15851226221691 - 0.196364 x - 0.0806432 x**2 + 0.26358 y +
         0.750379 x*y - 1.25045 y**2

In[10]:= u2max = Expand[u2shape.vmax]

Out[10]= 0.12694636774844 + 0.903429 x - 1.25045 x**2 - 0.196364 y +
         0.750379 x*y - 0.0806432 y**2
```

where now `vmax` is a different eigenvector and corresponds to the maximum eigenvalue of the associated eigenvalue problem for the boundary constant. The construction of the numerator value `numer` is complicated by the fact that we have an integral along the diagonal of the element as detailed in Section (5.6.1). Thus as before it is possible to define the interpolation error for each component given by,

```
In[12]:= u1error = (u1shape-u1interp).vmax

Out[12]= -0.11849500518487 (-x+x (-1+2 x))+0.160678 x (1-x-y)+
          0.18777 x y-0.0892373 (1-x-y) y+
          0.15851226221691 (-1+x+(1-2 x-2 y) (1-x-y)+y)-
          0.82835381413738 (-y+y (-1+2 y))

In[13]:= u2error = (u2shape-u2interp).vmax
```

```
Out[13]= -0.22007045151112 (-x+x (-1+2 x))+1.0642 x (1-x-y)+
          1.3412 x y+0.0344142 (1-x-y) y+
          0.12694636774844 (-1+x+(1-2 x-2 y) (1-x-y)+y)-
          0.15006089965334 (-y+y (-1+2 y))
```

whilst, along the diagonal we now define `u1errord` and `u2errord` which are defined as above but with `y` replaced by `1-x`.

```
In[14]:= u1errord = u1error/.y->1-x;

In[15]:= u2errord = u2error/.y->1-x;
```

The quantity `numer` is then computed from three integrations along the element boundary as detailed in Equation (5.41). These are given as,

```
In[16]:= numer1 = Integrate[u1error^2+u2error^2,{x,0,1}]/.y->0;
         numer2 = N[Sqrt[2],16]*Integrate[u1errord^2+u2errord^2,{x,0,1}];
         numer3 = Integrate[u1error^2+ u2error^2,{y,0,1}]/.x->0;
         numer = numer1 + numer2 + numer3

Out[16]= 0.513147
```

The calculation of the denominator term `denom` is exactly as detailed for the interior term although now with eigenvector `vmax` changed to that for the boundary constant calculation. This results in a value of,

```
In[19]:= energy = straint.C.strain;

In[20]:= denom = Integrate[energy,{x,0,1},{y,0,1-x}]

Out[21]= {68.646035}
```

Thus we may now evaluate the quantity on the right-hand side of Equation (6.46) in order to give the value of the boundary interpolation error constant for the specified displacement polynomials `u1max` and `u2max`. Again taking the square root this gives,

```
In[22]:= Sqrt[numer/denom]

Out[23]= {0.086460}
```

It can be seen that the above choice of displacement polynomials gives exactly the interpolation error constant in Table (6.16). Again, this is to be expected since the displacement polynomials were derived from the eigenvector corresponding to the largest eigenvalue. As in the case of the interior constant these polynomials do in fact belong to the higher order space of polynomials as required and it has once again been shown that these result in an interpolation error constant which is larger than the Johnson-Hansbo bound included in Equation (6.43).

It has thus been shown that it is possible to select displacement polynomials of the correct order which give interpolation error constants larger than the bounds provided in [27] for both the element interior and boundary. This may be due to the fact that, as stated in [27], the bounds were previously derived from an 'approximate' supremum value, itself found by 'trial and error' and also due to the fact that a finite number of functions were used instead of all functions from the richer space as detailed in Appendix D. It is felt that the constants obtained in this work and the computational method developed have removed the possibility of error in the results and consequently provide reliable interpolation error constant values for use in the error estimator.

Chapter 7

Numerical Experiments

The aim of this chapter is to detail the results of numerical experiments applied to both the linear elasticity and plate problems outlined in the previous chapters. It is hoped that the chapter will provide an illustration of where the error estimators excel and also highlight potential problem areas.

The chapter will begin by considering a linear elasticity problem for which the true solution is known. This problem is as it appeared in both Johnson and Hansbo, [27], and Li and Wiberg, [30], and is included here for two reasons. The first of these is due to the fact that in [30] a refined version of the Zienkiewicz-Zhu (Z-Z) error estimator is proposed and it is mentioned therein that numerical comparisons between the standard and refined Z-Z estimator had not then been performed. Consequently the standard Z-Z results for the same problem are provided in this work so that a comparison can be made and also to verify that the finite element solution results compliment each other. The second reason for including the known linear elasticity problem is to attempt to duplicate the Johnson-Hansbo (J-H) error estimator results presented in [27] and to use the interpolation error constant results given in Chapter 6. Attention will then be focused on a second test problem in which the necessity for mesh adaptivity will be demonstrated. This will include the refined error estimators of Z-Z and J-H as proposed in Chapter 4 and show their effectivity in meshes which include transition elements and irregular nodes.

The chapter will then present numerical results for the error estimators in the plate theory context and modelled using first-order shear deformation theory. Once again the analysis will begin with a test problem for which the solution is known enabling the error estimator performance to be analysed. This will be followed by an attempt to duplicate real-life experimental results which have been taken from the concentrated loading and three and four point bending tests performed on particle board samples. These experimental results were obtained from the Forest Products Research Centre (FPRC) located at Buckinghamshire College in High Wycombe.

7.1 Linear Elasticity Experiments

In this section concern will focus on two problems for which the solution is known. For the second problem the meshes will be adaptively refined and in all cases the estimator performance will be analysed.

7.1.1 Bubble Problem

The problem of interest is taken from [27] and [30] and is cast in two dimensions over the unit square $(0,1) \times (0,1) \equiv \Omega$ with $\mathbf{u} = \mathbf{0}$ on the boundary $\partial\Omega$ and with the exact displacement $\mathbf{u}$,

$$\mathbf{u} = \begin{bmatrix} u_1 \\ u_2 \end{bmatrix} = \begin{bmatrix} 0 \\ -x_1 x_2 (1-x_1)(1-x_2) \end{bmatrix}, \tag{7.1}$$

where $\mathbf{x} = [x_1, x_2]^T \in \Omega$ and u_2 exhibits a 'bubble' like profile. Substitution of this displacement into the two-dimensional analogues of the model equilibrium equations given by Equation (2.1) yields body force $\mathbf{f}$ where,

$$\mathbf{f} = \begin{bmatrix} f_1 \\ f_2 \end{bmatrix} = \begin{bmatrix} (\lambda+\mu)(1-2x_1)(1-2x_2) \\ -2\mu x_2(1-x_2) - 2(\lambda+2\mu)x_1(1-x_1) \end{bmatrix}. \tag{7.2}$$

The energy and L_2 norms of the known displacement may be expressed respectively as,

$$||\mathbf{u}||_{E(\Omega)} = \sqrt{\frac{\lambda+3\mu}{90}} \quad \text{and} \quad ||\mathbf{u}||_{L_2(\Omega)} = \frac{1}{30}.$$

In the plane strain context a material with Young's modulus, $E = 1$, and Poisson's ratio, $\nu = 3/10$, is chosen for the problem as done in Li and Wiberg, [30]. With this initial data it can be shown that,

$$\lambda = \frac{15}{26}, \quad \mu = \frac{5}{13}, \quad ||\mathbf{u}||_{E(\Omega)} \approx 1.38675049 \times 10^{-1} \quad \text{and} \quad ||\mathbf{u}||_{L_2(\Omega)} = 3.33\bar{3} \times 10^{-2}. \tag{7.3}$$

In order to attempt to firstly duplicate the results of [30] a series of uniform meshes will be used. The meshes will consist of elements which are right angled isosceles triangles employing linear shape functions and orientated in a unidirectional way as shown in Figure (7.1). It can be seen in

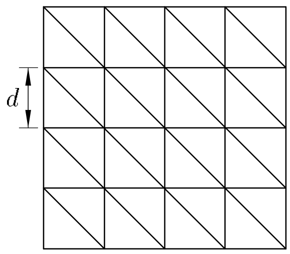

Figure 7.1: Typical unidirectional uniform mesh of triangular elements.

Figure (7.1) that the elements have two edges of the same length and a larger diagonal one. The shorter edge lengths will henceforth be denoted by d, the discretisation value of the domain.

7.1.2 Estimator Results and Discussion

For this initial problem, Table (7.1) shows the numerical results for the Zienkiewicz-Zhu estimator detailed in [69] and [70] and discussed at the beginning of Section (4.3). The recovery procedure is that proposed in [69] and can be compared directly with that discussed in Section (4.2.1) for quadrilateral elements. From Table (7.1) it can be seen that the computed energy norm of the

d	$\|\|\mathbf{u}\|\|_{E(\Omega)}$	$\|\|\mathbf{u}_h\|\|_{E(\Omega)}$	$\|\|\mathbf{u}_h\|\|_{L_2(\Omega)}$	$\|\|\mathbf{u}-\mathbf{u}_h\|\|_{E(\Omega)}$	Z-Z	θ
1/2	1.386407(−1)	9.834972(−2)	1.962190(−2)	9.771675(−2)	1.216631(−1)	1.245
1/4	1.386745(−1)	1.276257(−1)	2.872431(−2)	5.424300(−2)	7.754710(−2)	1.430
1/8	1.386750(−1)	1.358215(−1)	3.206566(−2)	2.798734(−2)	3.809960(−2)	1.361
1/16	1.386750(−1)	1.379551(−1)	3.300759(−2)	1.411259(−2)	1.756371(−2)	1.245
1/32	1.386750(−1)	1.384946(−1)	3.325130(−2)	7.071589(−3)	8.096948(−3)	1.145
1/64	1.386750(−1)	1.386299(−1)	3.331279(−2)	3.537722(−3)	3.819104(−3)	1.080

Table 7.1: Performance of Z-Z estimator for uniform refinement of triangular elements in linear elasticity.

known displacement $\mathbf{u}$ tends to the exact solution given in (7.3). This shows that the quadrature used is capable of accurately integrating the displacement profile and this is seen as d decreases and both the computed energy and L_2-norm of the finite element solution tend to the exact solutions.

From the computed finite element error column measured in the energy norm it can be seen that close agreement is obtained between the results here and that of Li and Wiberg, [30]. The small differences arising between the two computed sets of values is probably due to the differing quadrature schemes employed. As the mesh is refined the expected order of convergence is observed for both the computed finite element error measured in the energy norm and also for the Z-Z column which is the Zienkiewicz-Zhu global estimated error. In addition it can also be seen that the effectivity index θ tends to unity. Comparing the results here with those presented in [30] it is clear that the main difference lies in the fact that for the standard Z-Z estimator θ tends to unity from above whilst the results in [30] show θ tending to unity from below for the three noded triangle. This may be due to the fact that in [30] the basis $\mathbf{P}(\mathbf{x})$ used in obtaining the $\boldsymbol{\sigma}_p^*$ described in Section (4.2.1) is two orders higher than that used here. Thus whilst $\mathbf{P}(\mathbf{x}) = [1, x_1, x_2]$ here, $\mathbf{P}(\mathbf{x}) = [1, x_1, x_2, x_1^2, x_1x_2, x_2^2]$ is used in [30].

Table (7.2) shows the results using a set of uniform meshes consisting of square elements and employing bilinear shape functions. The recovery procedure is as described in Section (4.2.1) and for the uniform meshes considered here is the same as that proposed in Zienkiewicz and Zhu, [69], for quadrilateral element meshes. The meshes used here may now be thought of as those illustrated in Figure (7.1) but without the diagonal lines. Thus the discretisation value d now becomes the global element edge length. In this way a mesh of given d has the same number of unknowns as the uniform triangular counterpart mesh in Table (7.1) with the same value of d but only half the number of elements. It can be seen in Table (7.2) that for the true solution measured in the

d	$\|\|\mathbf{u}\|\|_{E(\Omega)}$	$\|\|\mathbf{u}_h\|\|_{E(\Omega)}$	$\|\|\mathbf{u}_h\|\|_{L_2(\Omega)}$	$\|\|\mathbf{u}-\mathbf{u}_h\|\|_{E(\Omega)}$	Z-Z	θ
1/2	1.379510(−1)	1.186804(−1)	2.604167(−2)	7.032363(−2)	8.391971(−2)	1.193
1/4	1.386299(−1)	1.341930(−1)	3.161069(−2)	3.479219(−2)	3.616844(−2)	1.040
1/8	1.386722(−1)	1.375828(−1)	3.291021(−2)	1.734833(−2)	1.756995(−2)	1.013
1/16	1.386749(−1)	1.384037(−1)	3.322809(−2)	8.668869(−3)	8.703381(−3)	1.004
1/32	1.386750(−1)	1.386073(−1)	3.330706(−2)	4.333802(−3)	4.338670(−3)	1.001
1/64	1.386750(−1)	1.386581(−1)	3.332677(−2)	2.166823(−3)	2.167470(−3)	1.000

Table 7.2: Performance of Z-Z estimator for uniform refinement of square elements in linear elasticity.

energy norm the computed value takes longer to reach the same level of accuracy as was attained in the case of triangular elements of linear type. It is thought that this is due to the lower accuracy quadrature rule employed for the square elements. Elsewhere it is clear that similar results are obtained compared with the test runs for triangular elements. This is to be expected due to the fact that the problems are of the same size for a given d. The similarity of results can also be attributed to the fact that any two triangles which are joined by their longest edges in a mesh of the type illustrated in Figure (7.1) can interpolate the same degrees of freedom at the nodes as the square element defined over the same nodes and also around the boundary of the square element. Again the anticipated orders of convergence are observed for both the finite element and estimated error and the effectivity index θ tends to unity as d is decreased.

From Tables (7.1) and (7.2) it is clear that the code is giving the expected finite element solutions and so we shall now attempt to duplicate the result of Johnson and Hansbo using the J-H estimator as presented in [27].

For the same problem as that given in Section (7.1.1) the task is now to duplicate the results presented by Johnson and Hansbo, [27]. Due to the fact that the elements are of linear type, this results in the divergence of the finite element stress tensor becoming zero and consequently Equation (4.62) reduces to $\mathcal{R}_1(\mathbf{u}_h) = \mathbf{f}$. If $\mathbf{f}$ is smooth, it is stated in [27] that the R_1 terms of the estimator given in Equation (4.73) can then be replaced by $||h^3 C_1^i D^2 \mathbf{f}||_{L_2(\Omega)}$ with suitably modified interpolation constants. It is also stated in [27] that, in the case of a piecewise linear approximation and a smooth $\mathbf{f}$, the R_1 terms in the error estimate may then be neglected. In this way the the $\mathbf{f}$-dependence in the error estimator is dropped and the estimator is simplified giving, from Equation (4.73),

$$||\mathbf{u} - \mathbf{u}_h||_{E(\Omega)} \le ||hC_2^i \mathrm{R}_2(\mathbf{u}_h)||_{L_2(\Omega)}.$$

Using Equations (4.71) and (4.72) and also the fact that $h = h_k$ and $C_2^i = C_{2,k}^i$ on each element

Ω_k it is possible to express the error, measured in the energy norm as,

$$\|\mathbf{u}-\mathbf{u}_h\|_{E(\Omega)} \le \left[\sum_{k=1}^{N}\int_{\Omega_k} h_k^2 (C_{2,k}^i)^2 \left|\frac{h_k^{\frac{1}{2}}\|\mathcal{R}_2(\mathbf{u}_h)\|_{L_2(\partial\Omega_k)}}{A(\Omega_k)^{\frac{1}{2}}}\right|^2 d\mathbf{x}\right]^{\frac{1}{2}},$$

$$= \left[\sum_{k=1}^{N}\int_{\Omega_k} \frac{h_k^3 (C_{2,k}^i)^2}{A(\Omega_k)}\|\mathcal{R}_2(\mathbf{u}_h)\|^2_{L_2(\partial\Omega_k)}\, d\mathbf{x}\right]^{\frac{1}{2}},$$

where, as previously, $A(\Omega_k)$ is the area of element Ω_k. Using Equation (4.63) we may write,

$$\|\mathbf{u}-\mathbf{u}_h\|_{E(\Omega)} \le \left[\sum_{k=1}^{N}\int_{\Omega_k} \frac{h_k^3 (C_{2,k}^i)^2}{A(\Omega_k)}\left[\int_{\partial\Omega_k}\left|\frac{1}{2h_k}\left[\boldsymbol{\sigma}\cdot\mathbf{n}_k\right]\right|^2 ds\right] d\mathbf{x}\right]^{\frac{1}{2}},$$

where again $\mathbf{n}_k$ is taken to be the unit outward normal to the element boundary $\partial\Omega_k$. Due to the linear elements used, the jump terms across the element edges in the $\mathcal{R}_2$ terms will be constant. Thus the integration can be performed by multiplying the constant jump integrand by the length over which it resides. In addition, the integral over the element Ω_k can be carried out by simply multiplying the constant integrand by the element area. Once this has been performed the simplified estimator takes on the form,

$$\|\mathbf{u}-\mathbf{u}_h\|_{E(\Omega)} \le \left[\sum_{k=1}^{N}(C_{2,k}^i)^2 h_k \sum_{i=1}^{e}\left|\frac{\left[\boldsymbol{\sigma}\cdot\mathbf{n}_k^i\right]}{2}\right|^2 h_k^i\right]^{\frac{1}{2}}, \tag{7.4}$$

where we have denoted h_k^i for $i = 1, \ldots, e$ to be the edge lengths of element Ω_k with corresponding unit outward normals $\mathbf{n}_k^i$ and where $e = 1, 2$ or 3 denotes the number of edges of element Ω_k which do not lie on $\partial\Omega$ and hence have jumps associated with them between the coefficients of element Ω_k and a neighbouring element. For uniform meshes, the diameter of the element h_k can be characterised by a global mesh size h and similarly, the interpolation error constant $C_{2,k}^i$ can be replaced by C_2^i as all the elements are the same and thus have the same interpolation characteristics. Thus Equation (7.4) may be expressed as,

$$\|\mathbf{u}-\mathbf{u}_h\|_{E(\Omega)} \le C_2^i h^{\frac{1}{2}}\left[\sum_{k=1}^{N}\sum_{i=1}^{e}\left|\frac{\left[\boldsymbol{\sigma}\cdot\mathbf{n}_k^i\right]}{2}\right|^2 h_k^i\right]^{\frac{1}{2}} = C_2^i h^{\frac{1}{2}}\kappa \text{ say.} \tag{7.5}$$

Here we simply have the jump terms integrated over each edge of element Ω_k which lies in the domain interior. This could also be written as a sum over all the internal edges $s \in S$ as presented in Section (4.4.2). In the above we have introduced the term κ which corresponds to the jump contributions of the error estimator only. It is possible to distinguish this from the quantities C_2^i and h since we are presently dealing only with uniform meshes and so the quantities $C_{2,k}^i = C_2^i$ and $h_k = h$ for all elements Ω_k for $i = 1, \ldots, N$.

Table (7.3) shows the computed values of κ for the same meshes used in Table (7.1) and for the same material properties. As expected, the same norm measures are obtained as in Table (7.1). Recall that κ is such that,

$$\|\mathbf{u}-\mathbf{u}_h\|_{E(\Omega)} \le C_2^i h^{\frac{1}{2}}\kappa,$$

d	$\|\|\mathbf{u}\|\|_{E(\Omega)}$	$\|\|\mathbf{u}_h\|\|_{E(\Omega)}$	$\|\|\mathbf{u}_h\|\|_{L_2(\Omega)}$	$\|\|\mathbf{u}-\mathbf{u}_h\|\|_{E(\Omega)}$	κ
1/2	1.386407(−1)	9.834972(−2)	1.962190(−2)	9.771675(−2)	1.911534(−1)
1/4	1.386745(−1)	1.276257(−1)	2.872431(−2)	5.424300(−2)	2.359721(−1)
1/8	1.386750(−1)	1.358215(−1)	3.206566(−2)	2.798734(−2)	1.989748(−1)
1/16	1.386750(−1)	1.379551(−1)	3.300759(−2)	1.411259(−2)	1.498678(−1)
1/32	1.386750(−1)	1.384946(−1)	3.325130(−2)	7.071589(−3)	1.086544(−1)
1/64	1.386750(−1)	1.386299(−1)	3.331279(−2)	3.537722(−3)	7.766450(−2)

Table 7.3: κ values for uniform refinement of triangular elements in linear elasticity.

and so we are now in a position to calculate the J-H error estimator values. In [27], h_k is referred to as the element 'diameter'. It is not clear how this is exactly defined but in a private communication with Professor Hansbo, included in Appendix D, it is established that,

$$h_k = \sqrt{2A\left(\Omega_k\right)}, \tag{7.6}$$

with $A\left(\Omega_k\right)$ the element area. For the meshes currently being used, Equation (7.6) reduces to $h_k = d$ and so we have that $h = h_k = d$. For the element boundary interpolation error constant $C_2^i = C_{2,k}^i$ the bound given in [27] is used. This bound was introduced in Equation (4.90) along with that for the element interior interpolation error constant $C_{1,k}^i$. For this problem,

$$\lambda = \frac{15}{26} \quad \text{and} \quad \mu = \frac{5}{13},$$

and so the value for the element boundary interpolation error constant from Equation (4.90) is,

$$C_2^i = \frac{1.1}{\sqrt{\lambda + 5\mu}} = 0.695701, \tag{7.7}$$

to six decimal places although it is noted that such accuracy is not required in practice. Table (7.4) shows the resulting J-H estimator performance when the above C_2^i and h are used. It can be

h	κ	J-H	θ
1/2	1.911534(−1)	9.403504(−2)	0.962
1/4	2.359721(−1)	8.208302(−2)	1.513
1/8	1.989748(−1)	4.894133(−2)	1.749
1/16	1.498678(−1)	2.606580(−2)	1.847
1/32	1.086544(−1)	1.336272(−2)	1.890
1/64	7.766450(−2)	6.753910(−3)	1.909

Table 7.4: Performance of J-H estimator for uniform refinement of triangular elements in linear elasticity.

seen from Table (7.4) that the correct order of convergence is seen for the J-H estimator values as the mesh is refined. In the case of the J-H estimator it can be seen that the effectivity index value does not tend to unity as seen in the Z-Z estimator results. This is not unexpected as there is no guarantee that the effectivity index will be close to unity for this estimator and indeed a value of approximately two as seen above should not be viewed as unacceptable. In [27] the authors themselves state that is difficult to guarantee effectivity indices close to unity and add that it could very well be possible to obtain values in the range $1-3$. This is due to the fact that the interpolation error constants are not optimal for the specific problem being solved as discussed in Appendix D.

From the previous test for the Z-Z estimator it has been established that the code is giving reliable finite element solutions for the set of meshes and it has been shown that the energy norm measure of the finite element error compares well with that of Li and Wiberg, [30]. Thus assuming this to be true, the overestimation of the error must be due to the estimator itself. In the simplest form the estimator has three components, h, C_2^i and κ as shown in Equation (7.5). The forms of the first two of these are given in Equations (7.6) and (7.7) respectively. These are as used in [27] and thus it seems that the only area where the overestimation could be coming from is the computation of κ. The computation of quantity κ has, however, itself been verified by firstly a hand calculation of κ for the coarse mesh $d = 1/2$ and secondly by writing a portion of Mathematica code, [59], which is included in Appendix C. In both instances it is found that the computation of κ agrees with the original code computations and consequently an attempt shall now be made to duplicate the results of [27] in order to verify the implementation of the estimator.

As previously mentioned, Johnson and Hansbo use the same problem in [27] as Li and Wiberg in [30]. The only difference being that in [27] a plot is given which illustrates the behaviour of the effectivity index, θ, (or efficiency index as it is called in [27]) for varying ν. This is done by plotting the effectivity index value against $\log(\lambda/\mu)$. Although it is not stated in [27] we shall assume that this is $\log_{10}(\lambda/\mu)$ since this is usual for the notation 'log' and also since this gives a spread of ν between zero and one half which is physically meaningful. The results for a uniform, unidirectional mesh of triangular elements with $d = 1/32$ can be seen in Table (7.5) for varying values of $\log_{10}(\lambda/\mu)$. It can be seen in Table (7.5) that the computed J-H results agree well with

$\log_{10}(\lambda/\mu)$	Computed J-H	Mathematica	θ	θ [27]
-4	$1.067426(-2)$	$1.067426(-2)$	1.621	1.448
-3	$1.067474(-2)$	$1.067474(-2)$	1.621	1.448
-2	$1.067980(-2)$	$1.067980(-2)$	1.623	1.448
-1	$1.075194(-2)$	$1.075194(-2)$	1.643	1.465
0	$1.232306(-2)$	$1.232306(-2)$	1.812	1.618
1	$2.749623(-2)$	$2.749623(-2)$	2.420	2.165
2	$8.681017(-2)$	$8.681017(-2)$	2.753	2.453
3	$2.752147(-1)$	$2.752147(-1)$	2.801	2.500
4	$8.705623(-1)$	$8.705623(-1)$	2.806	2.506
5	2.753028	2.753028	2.807	2.506
6	8.705904	8.705904	2.807	2.506

Table 7.5: Performance of J-H estimator for $d = 1/32$ mesh and varying ν.

that of the Mathematica code in Appendix C and which have been included under the column labelled 'Mathematica'. The resulting effectivity index values for the computed J-H estimates can also be seen in the table as well as the results from [27] which are included under the column labelled 'θ [27]'. Upon inspection it is clear that the computed J-H estimator values seem to be larger than those taken from [27], the reason for this is not clear. Figure (7.2) gives a visual comparison of the two sets of values for θ by plotting the values of θ against the corresponding $\log_{10}(\lambda/\mu)$ value. It can be seen that the same trends are present between the two sets of θ values

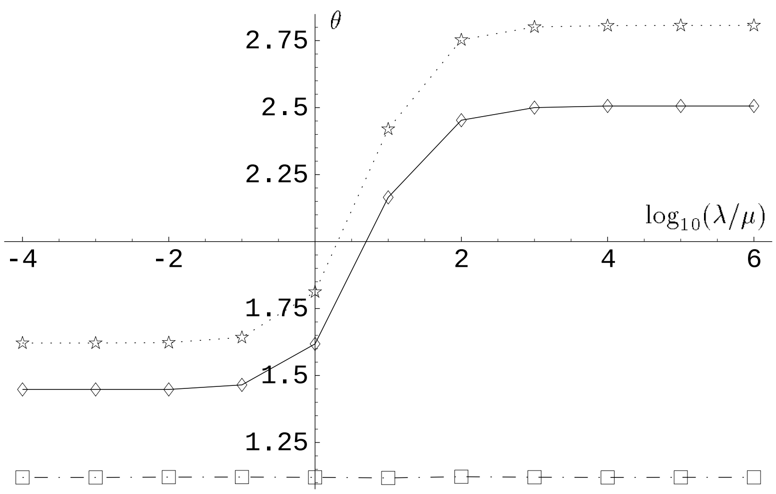

Figure 7.2: Comparison plots of θ versus $\log_{10}(\lambda/\mu)$.

with the computed values marked by star icons and those of [27] by diamond icons. The third line in Figure (7.2) is the ratio of the two θ values for each $\log_{10}(\lambda/\mu)$ value, these are marked with box icons. It can be seen that this remains at a constant value of approximately 1.125 across the range of ν showing the computed θ values to be approximately a factor of 9/8 times those of [27].

Although an overestimation of approximately 12% is not considered catastrophic it is nevertheless surprising that there seems to be such difficulty in reproducing the results of [27]. Results from the code have been checked against those of Li and Wiberg [30] earlier in this section and found to give very similar values for the energy norm measure of the finite element error. Unfortunately no such energy norm measures are given in [27] but it is not unreasonable to assume that this quantity should not change appreciably between the three sets of results given that both the mesh used and the problem solved are identical. The effectivity index θ relies strongly on this quantity as shown in Equation (1.2) and so by assuming that the energy norm measure of the finite element solution is the same in [27] as that obtained here then the overestimation can only be due to the estimator calculation itself as previously mentioned. Using the formulation given in Equation (7.5), however, it is believed that there is little or no possibility of an error having been made. The interpolation error constant and element diameter are as used in [27] and the computation of the estimator itself has been checked firstly by hand on a coarse mesh and secondly by the Mathematica code included in Appendix C. In addition, since the computation of the estimator in the simple form given by Equation (7.5) can be done without the need for quadrature this eliminates a further possible source of discrepancy.

The alternative train of thought is to assume that the estimator implementation and computation is correct and that the energy norm measure of the finite element error differs between that presented here and that used in obtaining the θ value of [27]. This discrepancy could arise from the quadrature schemes used to compute this value and indeed the quadrature schemes used elsewhere in the codes for evaluating the element stiffness matrices and load vectors. In addition, the method used for solving the resulting system of equations may also play a part in producing a finite element solution which differs from that obtained here. As an illustration, consider the results presented in Table (7.6) which shows how the effectivity index value changes with varying quadrature schemes (taken from [65]) on the now familiar $d = 1/32$ mesh and with $\nu = 1/4$. This value of ν yields $\lambda = \mu$ which in turn implies that $\log_{10}(\lambda/\mu) = 0$ and so the resulting θ values can be compared easily with that for $\log_{10}(\lambda/\mu) = 0$ in Table (7.5). It can be seen from Table (7.6) that as the quadrature

Quadrature Scheme	$\lVert\mathbf{u} - \mathbf{u}_h\rVert_{E(\Omega)}$	J-H	θ
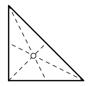	5.004922(−3)	1.232032(−2)	2.461641
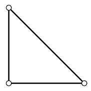	1.048094(−2)	1.233130(−2)	1.176546
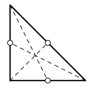	6.799736(−3)	1.232306(−2)	1.812286
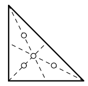	6.799258(−3)	1.232306(−2)	1.812413
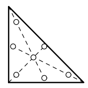	6.799424(−3)	1.232306(−2)	1.812369
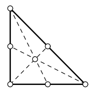	6.7996311(−3)	1.232306(−2)	1.812314

Table 7.6: Effect on θ upon varying the quadrature scheme.

is varied the energy norm measure of the finite element error changes by large amounts for the lower order quadrature schemes and less so for the higher order schemes as expected. This is due to the higher order schemes being able to integrate the error exactly. It can also be seen that the J-H estimator changes little, regardless of the quadrature change. This is due to the fact that the form of the estimator is as given in Equation (7.5) and consequently it is not necessary to employ quadrature to evaluate the estimator. The small variations which do appear in the estimator value are due to the changing finite element solutions themselves which in turn arise from the element stiffness matrix and load vector terms being evaluated with different quadrature.

The effect upon the effectivity index values can be seen in the last column of Table (7.6). Here it is clear that quite different values can be obtained merely by the choice of quadrature. There are no details in [27] on either the choice of quadrature or the choice of solver used and these are both possible sources from which a discrepancy such as that illustrated in Figure (7.2) can arise.

The aim of this section was to duplicate the previous results of both Li and Wiberg [30] and Johnson and Hansbo [27]. In the case of Li and Wiberg the Z-Z estimator results compare well with those of [30] even though the recovery procedure differs. In addition, the energy norm measure of the finite element error was also shown to compare well. This is reassuring as it indicates that the code written for this work is performing as expected and solves the supplied problem. In the case of Johnson and Hansbo an attempt was made to duplicate the effectivity index plot as illustrated in Figure (7.2). Unfortunately it is felt that in order to duplicate this exactly it would be necessary to gather more information than is readily available in [27]. The results here show that the J-H estimator overestimates that in [27] by approximately 12%. This is considered to be acceptable considering the amount of information which is unknown with regard to the analyses performed in [27]. The reasons for the discrepancy, however, are not clear but a likely candidate is the possibility of differing quadrature schemes being employed. It has been shown that by merely changing the quadrature scheme used in the code a large variation in the resulting effectivity index can result.

The next section will introduce a new problem. This is one in which it may well be necessary to adaptively refine the mesh and this will be demonstrated on both meshes of triangular elements and square elements employing linear and bilinear shape functions respectively.

7.1.3 Spike Problem

Now that the code implementation has been checked we shall move on to the problem of mesh adaptivity. In the following problem the results from Chapter 4 will be used and comments will be made upon the applications of both the Z-Z and J-H error estimators and their performance.

Consider again the problem of linear elasticity in two dimensions but now with the known displacements having the form,

$$\mathbf{u} = \begin{bmatrix} u_1 \\ u_2 \end{bmatrix} = \frac{1}{2} \begin{bmatrix} \exp\left(-\alpha\left(x_1 - x_1^c\right)^2 + \left(x_2 - x_2^c\right)^2\right) \\ \exp\left(-\alpha\left(x_1 - x_1^c\right)^2 + \left(x_2 - x_2^c\right)^2\right) \end{bmatrix}, \tag{7.8}$$

where the point (x_1^c, x_2^c) lies at the centre of the problem domain Ω which, if taken to be the unit square with the origin located at the bottom left corner, has $(x_1^c, x_2^c) = (1/2, 1/2)$.

Figure (7.3) illustrates one component of the above displacement, plotted as a function of x_1 and x_2 with constant $\alpha = 200$. This figure shows the displacement acting in the x_3 direction simply for clarity. It can be seen that the displacements exhibit a 'spike' profile and also that at the boundary the displacement is virtually zero which will be the boundary condition for both

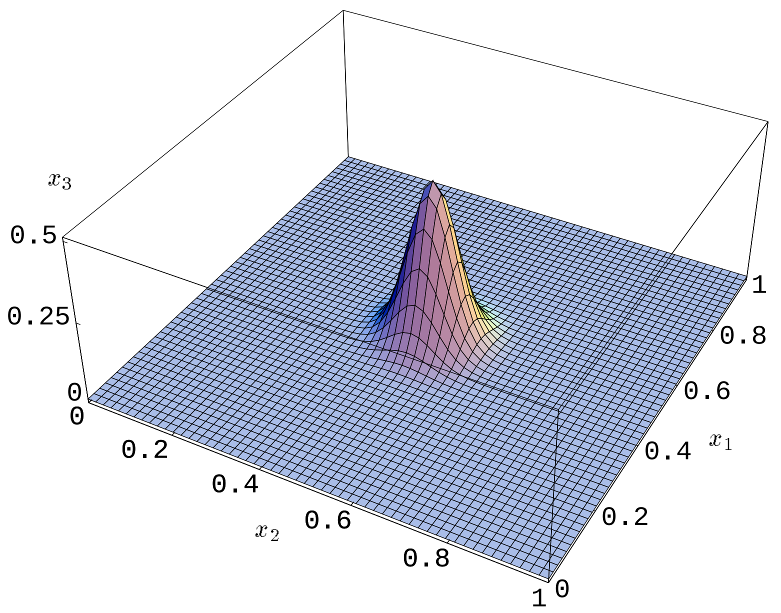

Figure 7.3: 'Spike' displacement as a function of x_1 and x_2.

displacement components. The code will be firstly run using the meshes of the previous section in order to test the error estimators on uniform meshes. Once this has been done, the meshes will be adaptively refined and the subsequent estimator performance analysed.

The material properties for the following numerical tests will be taken to be Young's modulus, $E = 1$ and Poisson's ratio $\nu = 1/4$. For such a material the energy and L_2-norm measure of the true solution calculated using Mathematica, [59], is,

$$||\mathbf{u}||_{E(\Omega)} \approx 1.12099824 \quad \text{and} \quad ||\mathbf{u}||_{L_2(\Omega)} \approx 6.26657069 \times 10^{-2}.$$

Table (7.7) shows the convergence of the finite element solution to that given above for a sequence of unidirectional uniform meshes consisting of triangular elements. Here it can be seen that the

d	$\|\|\mathbf{u}\|\|_{E(\Omega)}$	$\|\|\mathbf{u}_h\|\|_{E(\Omega)}$	$\|\|\mathbf{u}_h\|\|_{L_2(\Omega)}$	$\|\|\mathbf{u}-\mathbf{u}_h\|\|_{E(\Omega)}$
1/2	1.475093	1.570545	2.776357(−1)	2.474551
1/4	1.124861	1.135405	1.680754(−1)	1.150024
1/8	1.115850	0.940702	5.054604(−2)	6.042408(−1)
1/16	1.121209	0.987165	5.317357(−2)	5.312084(−1)
1/32	1.120998	1.076688	5.928630(−2)	3.120518(−1)
1/64	1.120998	1.108896	6.169865(−2)	1.642733(−1)
1/128	1.120998	1.117892	6.241393(−2)	8.339967(−2)

Table 7.7: Uniform refinement of triangular element uniform meshes in linear elasticity spike problem.

values tend slowly to their expected values. This is due to the chosen displacement solution which has a sharp feature as illustrated in Figure (7.3). This also has an effect on the expected order of convergence which only approaches the expected rate as the meshes become fine. The behaviour of both the Z-Z and J-H error estimators on the above uniform meshes is as presented in Table (7.8). It can be seen that the Z-Z estimator once again seems to be asymptotically exact whilst

d	Z-Z	θ	J-H	θ
1/2	2.183753	0.882485	1.740675	0.703430
1/4	9.345197(−1)	0.812609	1.226825	1.066781
1/8	7.820816(−1)	1.294321	1.043198	1.726461
1/16	5.340868(−1)	1.005419	7.636690(−1)	1.437607
1/32	3.134853(−1)	1.004594	5.237987(−1)	1.678563
1/64	1.648673(−1)	1.003616	3.003171(−1)	1.828155
1/128	8.349589(−2)	1.001154	1.566839(−1)	1.878711

Table 7.8: Error estimates on uniform meshes of triangular elements for the spike problem.

the J-H estimator overestimates. The form of the J-H estimator here is exactly as in the previous section and again uses both the element diameter given in Equation (7.6) and the interpolation error constant given in Equation (7.7). It is interesting to note that the effectivity index value attained by the J-H estimator of approximately 1.8 for the $d = 1/64$ mesh agrees well with that of the previous problem in Table (7.5) for the case where $\log_{10}(\lambda/\mu) = 0$. This occurs when $\lambda = \mu$ or equivalently when $\nu = 1/4$ in plane strain as is the case here and so it is reassuring to see the J-H estimator overestimating by a similar margin for the same material but on a different problem.

The J-H estimator values have hitherto been computed by dropping the **f**-dependence and by using both the definitions of element diameter and the bound for the interpolation error constant as given by Equations (7.6) and (7.7) respectively. As mentioned previously, the element diameter value was established via a private communication with Professor Hansbo which is included in Appendix D. In this communication the methodology used for computing the interpolation error constants used in [27] was also established. It was found that the constants, bounded above as in Equation (2.25) of [27], were established by inserting a number of functions into the quotients given in Equations (5.3) and (5.4) and computing the worst quotient value. In this 'trial and error' method the constants can only be correct for the functions used in the test. The constants are as given in Equations (5.1) and (5.2) with the corresponding expressions for the interpolation error constants themselves given in Equations (5.3) and (5.4). In practce the constants are computed by considering all polynomials of degree $p + 1$ where p is the degree of the piecewise polynomials used in the finite element method. It is thought that by merely taking a selection of these functions instead of all those of degree $p + 1$ the resulting values of the supremum may consequently be restricted and a smaller interpolation error constant could result.

As pointed out by Professor Hansbo in Appendix D, the interpolation error estimate is a 'worst case scenario', what is really required is an estimate of how well we interpolate the *actual* solution to the problem. Thus much is to be said for 'tuning' the constants which can be done by solving over a set of problems with known exact solutions. This will show how the constants vary over a 'nice' or 'real' set of solutions and can lead to the calibration of the constants.

From this point on the interpolation error constants computed in Chapter 6 will be used due to the fact that it is believed these values are the true constants required by Equations (5.3) and (5.4). In addition the element diameter will be taken to be the element longest edge. Since in this work all triangular elements will be right angled and such that the union of any two trianglular elements sharing a common longest edge forms a square this means that the longest edge corresponds to the diameter of the escribing circle. Similarly, all quadrilateral elements will in fact be square and so this measure will simply be the edge length. The interpolation error constants for the triangular elements in Chapter 6 were obtained by using an element diameter of unity on the standard element which was equivalent to taking either one of the two shorter edge sides as the element diameter. Since we will in practice use the longest edge of the element as the diameter, the constant values for use here are obtained by dividing the constants from Chapter 6 by $\sqrt{2}$ for the interior interpolation constant C_1^i and $2^{1/4}$ for the boundary interpolation error constant C_2^i in accordance with Equations (5.3) and (5.4). This is due to the fact that on the triangular elements, the longest edge is $\sqrt{2}$ times greater than the two shorter edge lengths. For the present material with $E = 1$ and $\nu = 1/4$ we thus have,

$$C_1^i = 0.838298 \quad \text{and} \quad C_2^i = 2.292410, \tag{7.9}$$

to six decimal places where again it is noted that such accuracy is not required in practice. Table (7.9) shows the increase in the computed J-H estimator resulting from using the new element diameter and interpolation error constant values. It can be seen from the table that there are

d	Dropped		Included	
	J-H	θ	J-H	θ
1/2	6.683137	2.700747	17.08528	6.904396
1/4	4.710264	4.095795	13.85492	12.04750
1/8	4.005249	6.628564	8.804433	14.57107
1/16	2.932026	5.519541	5.279814	9.939252
1/32	2.011070	6.444666	3.185732	10.20898
1/64	1.153036	7.019008	1.740367	10.59434
1/128	0.601571	7.213114	0.895237	10.73430

Table 7.9: J-H estimator performance using computed interpolation error constants, longest edge element diameter and showing the effect of dropping the **f**-dependence.

two sets of results, these are those resulting from either dropping the **f**-dependence or including it. Obviously the inclusion of the **f**-dependence results in a rise in the J-H estimator value and consequently in the effectivity index value. Upon comparing the results of the estimator under the 'Dropped' column, however, with that of Table (7.8) it can be seen that the values differ by a multiplicative constant. This is illustrated in Figure (7.4) which shows the effectivity index values plotted against their corresponding values of d. The original data points from Table (7.8)

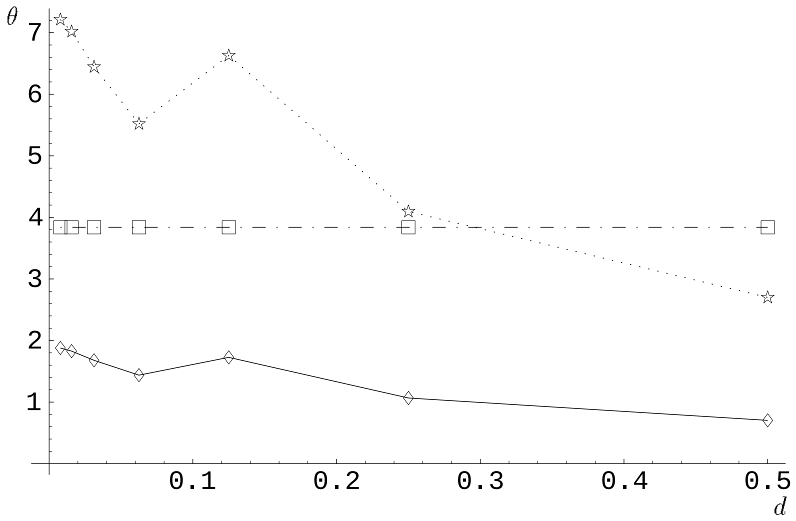

Figure 7.4: Comparison plots of effectivity index values θ versus d using computed interpolation error constants C_2^i and longest edge element diameter.

are marked with diamonds whilst the above data under the 'Dropped' column of Table (7.9) are marked with stars. Taking the ratio of these two sets of numbers produces the third line in Figure (7.4) whose actual values are marked by boxes. It can be seen that this shows the 'Dropped' data to be approximately 3.8 times that of the original data. This is as expected since the only parameters to have been changed are the element diameter values and the interpolation error constant C_2^i. In the 'Dropped' data the interpolation error constant is a factor of 3.228533 larger whilst that of the element diameter is a factor of $\sqrt{2}$ larger. From Equation (7.5) this means that the estimator should be a factor of,

$$3.228533\left(2^{1/4}\right) = 3.839394 \text{ to six decimal places,}$$

larger. This value agrees well with both the figure and the computed ratio values themselves.

The 'Included' column results of Table (7.9) show the increase in effectivity index θ upon including the $\mathbf{f}$-dependence in the error estimator. Here it is clear that there is now no multiplicative factor between the results and those of Table (7.8). This is as expected since we are now using the interior interpolation error constant C_1^i given in Equation (7.9) and including the $\mathbf{f}$-dependence in addition to computing the 'Dropped' part of the estimator.

By performing two final runs with the current data but now solving the initial problem of Section (7.1.1) with the $d = 1/64$ mesh it is interesting to observe that the 'Dropped' estimator yields $\theta = 7.029891$ whilst the 'Included' estimator yields $\theta = 10.43566$. These are very similar to the above two sets of θ values for the 'Spike' problem given in Table (7.9) and thus again it can be observed that the estimator is overestimating by similar amounts for differing problems providing the same material properties are used. This feature was seen previously and it suggests that the constant requires calibrating or tuning in order to obtain effectivity index values close to unity.

Using now a sequence of uniform meshes comprising of square elements, the analogous results to those given in Table (7.7) are given in Table (7.10). Again similarities can be seen between

d	$\|\|\mathbf{u}\|\|_{E(\Omega)}$	$\|\|\mathbf{u}_h\|\|_{E(\Omega)}$	$\|\|\mathbf{u}_h\|\|_{L_2(\Omega)}$	$\|\|\mathbf{u}-\mathbf{u}_h\|\|_{E(\Omega)}$
1/2	0.217277	1.919539	4.380729(−1)	2.074023
1/4	1.547274	0.690679	1.525982(−1)	1.970478
1/8	1.064705	1.525943	1.801691(−1)	7.262640(−1)
1/16	1.115801	1.043222	5.738226(−2)	4.338294(−1)
1/32	1.120998	1.094761	6.105451(−2)	2.437425(−1)
1/64	1.120998	1.114228	6.224677(−2)	1.233519(−1)
1/128	1.120998	1.119292	6.255993(−2)	6.186405(−2)

Table 7.10: Uniform refinement of square element uniform meshes in linear elasticity spike problem.

the results tables as was observed between Tables (7.1) and (7.2) in Section (7.1.2) for the initial problem. The performance of both the Z-Z and J-H estimators are as given in Table (7.11). It can be seen again that the Z-Z estimator produces an effectivity index value which tends to unity whilst the J-H estimator has larger effectivity index values. Upon comparison with the 'Included'

d	Z-Z	θ	J-H	θ
1/2	1.357319	0.654437	8.330550	4.016614
1/4	4.044677(−1)	0.205264	5.553873	2.818541
1/8	1.172104	1.613882	6.257627	8.616187
1/16	6.192369(−1)	1.427374	3.069229	7.074735
1/32	2.949940(−1)	1.210269	1.672244	6.860701
1/64	1.326033(−1)	1.075000	8.659815(−1)	7.020412
1/128	6.314910(−2)	1.020772	4.370280(−1)	7.064328

Table 7.11: Error estimates on uniform meshes of square elements for the spike problem.

results of the uniform meshes comprising of triangular elements in Table (7.9) it can be seen that the effectivity index values here tend to lower values. The reason for this is due to the fact that the square element meshes seem to produce smaller energy norm measures of the finite element error indicating a higher quality finite element solution itself as d is decreased. Consequently this results in a smaller error estimate and this in turn produces a smaller effectivity index value. By now solving the initial problem introduced in Section (7.1.1) but retaining the current material properties it is found that for the $d = 1/64$ mesh an effectivity index value of $\theta = 7.427582$ is obtained. This is again similar to that obtained above in Table (7.11) and is a further indication that the estimator is performing consistently. For an effectivity index close to unity this is a further claim that the interpolation error constant needs to be calibrated as previously discussed. This will be done by introducing the notion of a calibration constant $\mathcal{C}$ to be used in the J-H estimators and defined initially here as the integer part of the 'raw' effectivity index obtained from a series of uniform refinements. Table (7.11) for example would yield $\mathcal{C} = 7$ to be subsequently used to scale the computed interpolation error constants.

7.1.4 Adaptive Scheme, Estimator Results and Discussion

It has been seen that the error estimators provide the user with a global error estimate over Ω. These global error estimates are obtained by summing elemental contributions which are known as error indicators. This may be expressed as,

$$\rho^2 = \sum_{i=1}^{N} \varrho_i^2, \tag{7.10}$$

where ρ denotes the global error estimate obtained by summing error indicator values ϱ_i squared over elements $i = 1, \ldots, N$. The aim of the error estimates is to approximate the true global error. For the energy norm measure of the true error $\mathbf{u} - \mathbf{u}_h$ it is thus required that,

$$\rho^2 \approx ||\mathbf{u} - \mathbf{u}_h||^2_{E(\Omega)} \equiv ||\mathbf{e}||^2_{E(\Omega)}.$$

The percentage error shall be denoted by $R\%$ where the quantity R is expressed as,

$$R = \frac{||\mathbf{e}||_{E(\Omega)}}{||\mathbf{u}||_{E(\Omega)}} \times 100.$$

Ordinarily $||\mathbf{u}||_{E(\Omega)}$ will not be known in practice and so this quantity is approximated by using the error estimate in the following way,

$$||\mathbf{u}||^2_{E(\Omega)} = ||\mathbf{u}_h||^2_{E(\Omega)} + ||\mathbf{e}||^2_{E(\Omega)} \approx ||\mathbf{u}_h||^2_{E(\Omega)} + \rho^2.$$

Using this approximation in the above expression for the percentage error gives,

$$R \approx \frac{\rho}{\sqrt{||\mathbf{u}_h||^2_{E(\Omega)} + \rho^2}} \times 100. \tag{7.11}$$

By rearranging the above and using Equation (7.10) it is possible to obtain the expression,

$$\rho^2 = \sum_{i=1}^{N} \varrho_i^2 \approx \left(\frac{R}{100}\right)^2 \left(||\mathbf{u}_h||^2_{E(\Omega)} + \rho^2\right). \tag{7.12}$$

In order to be able to adapt or refine a uniform mesh it is necessary to know regions on the mesh and subsequently the elements in the mesh which need to be refined. By considering $R\%$ as the required percentage error *tolerance* for the problem it is possible to construct a local tolerance which each element indicator must satisfy. This is done by requiring that,

$$\varrho_i^2 \leq \frac{1}{N} \left(\frac{R}{100}\right)^2 \left(||\mathbf{u}_h||^2_{E(\Omega)} + \rho^2\right), \tag{7.13}$$

with all elements whose indicator values fail this test being candidates for refinement. It should be noted that the error indicator values are not estimates of the local error on each element. By performing the above local tolerance test on the error indicator values we are attempting to 'equilibrate' the error over the region and doing this by making the assumption that the indicators will provide qualitative information of the true error distribution over the region.

It is reported by Li and Wiberg, [30], that is is often difficult to achieve the target tolerance level through a sequence of mesh refinements. This may be remedied by invoking a safety factor K in

Equation (7.12) which typically has a value in the range 1.0-1.5. Upon dividing this into the right-hand side of Equation (7.12) this has the effect of lowering the local tolerance level requirement and causes more elements to be refined. Due to there being no such difficulty observed in attaining the target tolerance there will be no such use of safety factor K in the forthcoming calculations.

The results from adaptive runs can be seen in Table (7.12) for meshes consisting of triangular elements. The required percentage error tolerance was set at 5% and it can be seen that the interpolation error constants have now been calibrated for the J-H estimator in order to give effectivity index values close to unity. The first column in Table (7.12) is labelled I which denotes

Z-Z Estimator				
I	M	$\|\|\mathbf{u}-\mathbf{u}_h\|\|_{E(\Omega)}$	θ	%error
2	18	1.389289	0.476996	54.78
4	98	6.416954(−1)	1.119977	62.00
6	202	4.268852(−1)	1.383801	49.52
8	426	2.786204(−1)	1.100932	27.19
10	954	1.411260(−1)	1.041083	13.10
12	2438	7.221701(−2)	1.017256	6.55
13	3862	5.332946(−2)	1.013214	4.82
J-H Estimator, $\mathcal{C}=10$				
I	M	$\|\|\mathbf{u}-\mathbf{u}_h\|\|_{E(\Omega)}$	θ	%error
2	18	1.389289	0.656571	66.95
4	70	6.417361(−1)	1.297814	67.53
6	126	4.269685(−1)	1.168742	43.39
8	310	2.787671(−1)	0.973856	24.26
10	730	1.432724(−1)	0.982435	12.56
12	1858	7.858502(−2)	0.964540	6.76
14	3058	6.152878(−2)	0.910255	5.00

Table 7.12: Error estimator performance for adaptive run to 5% error requirement on a mesh consisting of triangular elements.

the refinement stage of the mesh. Thus the first row of both the Z-Z and J-H results corresponds to the mesh at the second refinement stage with the initial mesh used in both cases being the unidirectional mesh with $d = 1/2$. The second column is labelled M which denotes the total number of degrees of freedom. The final column of Table (7.12) shows the percentage error computed using Equation (7.11). It can be seen that in order to reach the required 5% tolerance both estimators arrive at similarly sized problems and in a similar number of refinement steps.

The convergence curves for the above data can be seen in Figures (7.5) and (7.6). These figures both show ln(%error) plotted against ln(M). In both cases the solid line marked with diamonds shows the uniform refinement route and the broken line marked with stars denotes the adaptive route taken by the code. From the two figures it is clear that for the coarser meshes the convergence is slow. This is to be expected as the mesh is not able to correctly resolve the spike feature of the displacement and due to the lack of quality in the resulting finite element solutions a reliable error

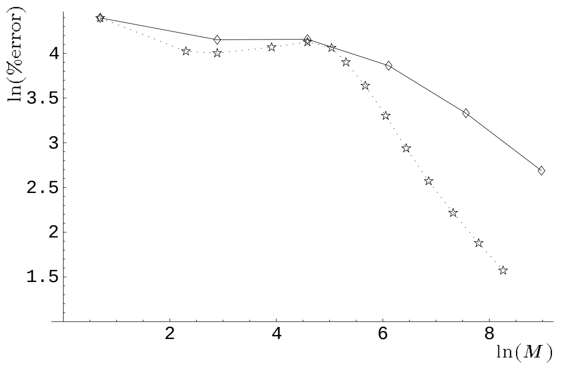

Figure 7.5: Uniform and adaptive refinement convergence curves for Z-Z estimator using triangular elements.

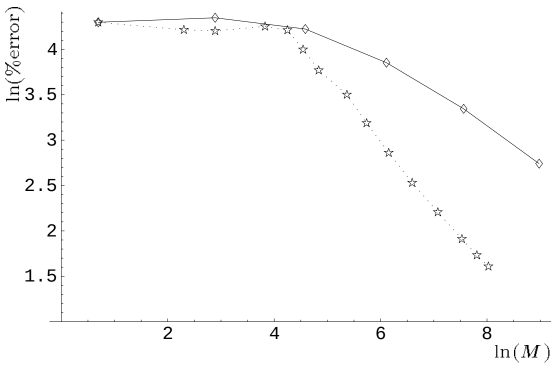

Figure 7.6: Uniform and adaptive refinement convergence curves for J-H estimator using triangular elements.

estimate cannot be expected. As the number of unknowns builds, however, it can be seen that the curves begin to converge to the required tolerance. It is clear that both figures show similar trends with the adaptive route converging to the required 5% error requirement quicker than the uniform refinement cases.

The resulting adapted meshes for the two estimators can be seen in Figures (7.7) and (7.8). It is clear that both figures show heavy refinement around the area where the displacements are changing rapidly. The mesh arising from the Z-Z estimator implementation has a higher degree

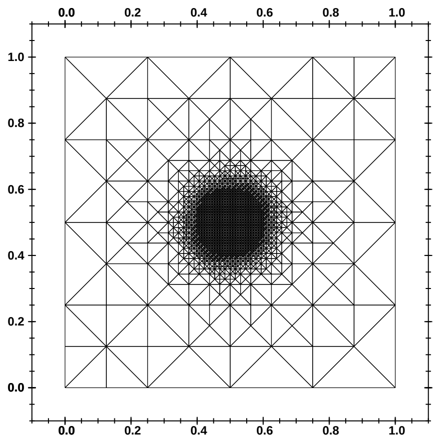

Figure 7.7: Adapted triangular element mesh to achieve 5% error using Z-Z estimator.

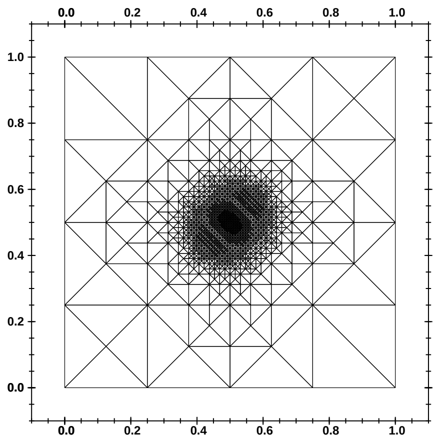

Figure 7.8: Adapted triangular element mesh to achieve 5% error using J-H estimator.

of refinement around the domain boundary. This is due to the patch selection strategy adopted for boundary nodes and it can be seen that the J-H estimator mesh does not have this feature. A further difference between the meshes is a slight dominance in the J-H estimator refinement area along the $x_1 = x_2$ line. It is thought that this is due to the inclusion of the **f**-dependence term in the estimator as the resultant of **f** exhibits the same characteristic.

To complete this section the results for adaptive runs using meshes comprising of square and transition elements is now presented in Table (7.13). Once again a required error tolerance of 5% is requested and the interpolation error constants for the J-H estimator are calibrated. It can be

Z-Z Estimator				
I	M	$\|\|\mathbf{u}-\mathbf{u}_h\|\|_{E(\Omega)}$	θ	%error
2	98	7.262640(−1)	1.613882	60.92
4	562	2.437444(−1)	1.210292	26.02
6	2818	6.268713(−2)	1.026229	5.74
7	5450	3.754892(−2)	1.023160	3.43
J-H Estimator, $\mathcal{C}=7$				
I	M	$\|\|\mathbf{u}-\mathbf{u}_h\|\|_{E(\Omega)}$	θ	%error
2	94	7.262641(−1)	1.231044	50.55
4	422	2.437455(−1)	0.980165	21.32
6	1974	6.607382(−2)	1.051601	6.20
7	3070	4.957090(−2)	0.996308	4.41

Table 7.13: Error estimator performance for adaptive run to 5% error requirement on a mesh consisting of square elements.

seen that the Z-Z and J-H estimators again perform similarly and enable the code to arrive at the required tolerance in the same number of mesh refinements. As detailed in Section (4.2.1) the implementation of the Z-Z estimator requires element patches to be determined for each node. This task is complicated, however, for meshes containing transition elements and irregular nodes and the sample points on the resulting element patches are strongly affected by the presence of these features as detailed in Section (4.3.1). Due to findings in that section an algorithm was developed as given in Section (4.3.2) for patch selection and it is in Table (7.13) that results are presented for the Z-Z estimator for the first time. The original J-H estimator must also undergo some enhancements to cope with the presence of transition elements and irregular nodes. The proposed modifications are as detailed in Section (4.4.3) and Table (7.13) again shows the results from using this enhanced J-H estimator for the first time.

The convergence curves for the above data can be seen in Figures (7.9) and (7.10). As for the case of triangular elements, the figures both show ln(%error) plotted against $\ln(M)$. In the figures the solid line marked with diamonds again denotes the uniform refinement route and the broken line marked with stars denotes the adaptive route. Upon inspection it is again clear that the adaptive route converges to the required error tolerance quicker than the corresponding uniform refinement route. An interesting feature which is common to both figures is that the adaptive scheme, which is driven by the local tolerance test given in Equation (7.13), actually follows the uniform refinement at the start of the analyses. This is to be expected for the coarser meshes due to the lack of quality in the finite element solutions and consequently the lack of accuracy in the error estimates. It is interesting to note that this feature was not apparent in the case of triangular element meshes in Figures (7.5) and (7.6) where a small departure from the uniform refinement route can be seen

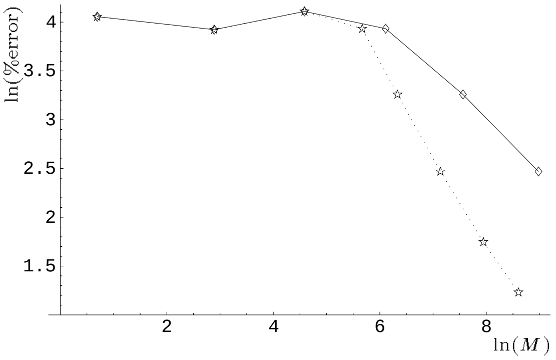

Figure 7.9: Uniform and adaptive refinement convergence curves for Z-Z estimator using square and transition elements.

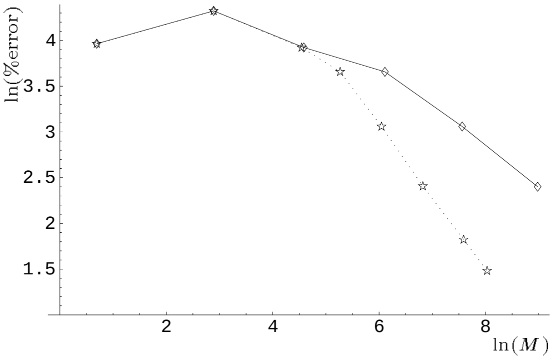

Figure 7.10: Uniform and adaptive refinement convergence curves for J-H estimator using square and transition elements.

immediately. It is thought that this may be due to the fact that there are twice as many triangular elements than square elements in a mesh of given discretisation value d and consequently twice as many error indicator values. These may be better able to give a qualitative representation of the true error distribution for the coarser meshes and enable early adaptive refinement to take place. Another possibility is that the elements have certain orientations in the uniform meshes of triangles as shown in Figure (7.1) which can have either a beneficial or detrimental effect upon the resulting finite element solution and also the error estimate. It may be seen in Figures (7.5) and (7.6), however, that after a small number of refinements over the coarser meshes both the adaptive and uniform routes coincide at a second point. It is from this second point which the two routes separate for the final time as seen in Figures (7.9) and (7.10) for the case of square elements. A further point to note is that the final separation points for the triangular element analyses are in similar locations to those for the square element analyses.

The resulting adapted meshes for the two estimators can be seen in Figures (7.11) and (7.12).

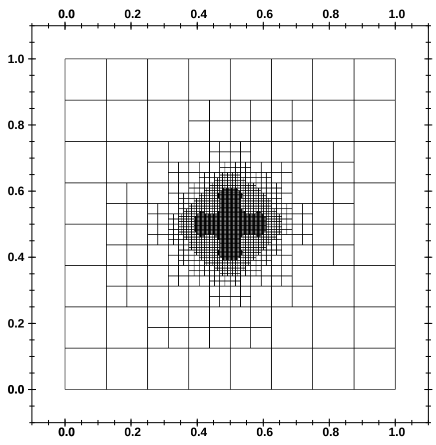

Figure 7.11: Adapted square element mesh to achieve 5% error using Z-Z estimator.

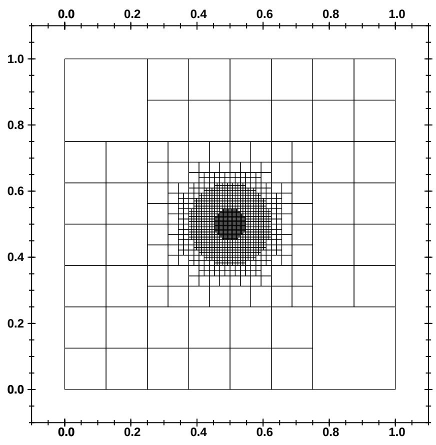

Figure 7.12: Adapted square element mesh to achieve 5% error using J-H estimator.

It can be seen that again the two resulting meshes show heavy refinement where expected. The mesh resulting from the Z-Z estimator implementation in fact yields an estimated error of 3.34% which is considerably lower than the required 5% and this accounts for there being a higher number of degrees of freedom for refinement number seven in Table (7.13). The mesh arising from the J-H implementation yields a less accurate error estimate at 4.41% but by adapting the mesh again and asking for a more stringent tolerance of 4% from the J-H estimator the resulting mesh is as shown in Figure (7.13).

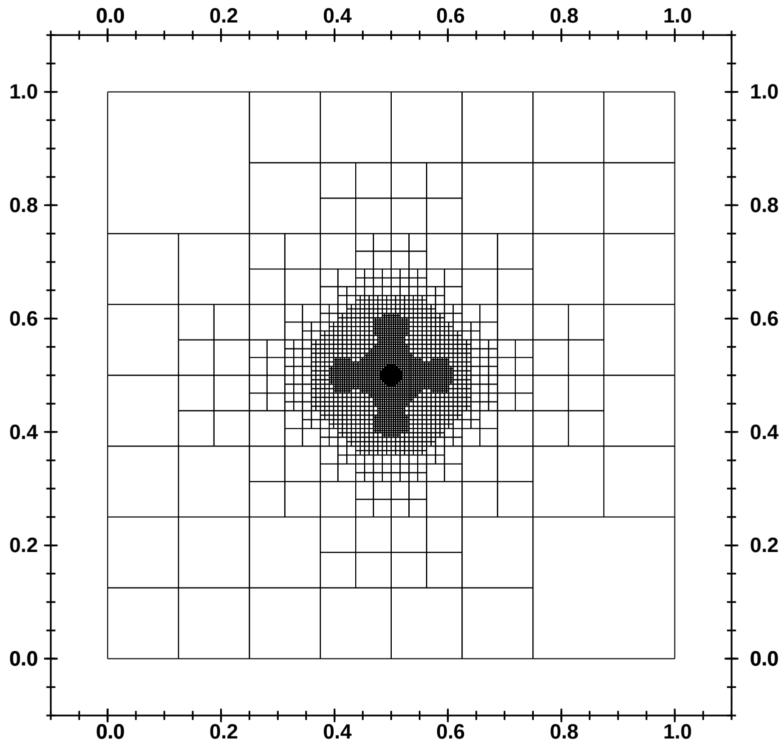

Figure 7.13: Adapted square element mesh to achieve 4% error using J-H estimator.

As a comparison with Table (7.13), the relevant data for this mesh is,

$$M = 5646, \quad \|\mathbf{u} - \mathbf{u}_h\|_{E(\Omega)} = 3.659466(-2), \quad \theta = 1.034410 \quad \text{and} \quad \%\text{error} = 3.38\%,$$

which compares well with the seventh refinement using the Z-Z estimator in Table (7.13). In addition, it can be seen that the above resulting mesh compares well with that arising from the implementation of the Z-Z estimator in Figure (7.9) indicating that the estimators are once again behaving in a similar way.

7.2 Plate Theory Experiments

This section will begin with two problems for which the solutions are known. The problems will be similar to those introduced in the linear elasticity sections and are included so that both the code and estimator robustness can be analysed. This will be followed by the modelling of real-life experiments enabling the level of agreement between computational and experimental results to be analysed.

7.2.1 Bubble Problem

In this problem we shall assume that all five displacement components as detailed in Section (2.2.2) have the form,

$$\zeta(\mathbf{x}) = x_1 x_2 (1 - x_1)(1 - x_2),$$

where $\mathbf{x} \equiv (x_1, x_2)^T \in \Omega$. As done in Section (7.1.3) the displacement profile plotted in the x_3 direction is as shown in Figure (7.14) where it clearly exhibits a 'bubble' shape with peak value of 1/16 at (1/2, 1/2). The plate taken will be square in shape with midplane $\Omega \equiv (0,1) \times (0,1)$

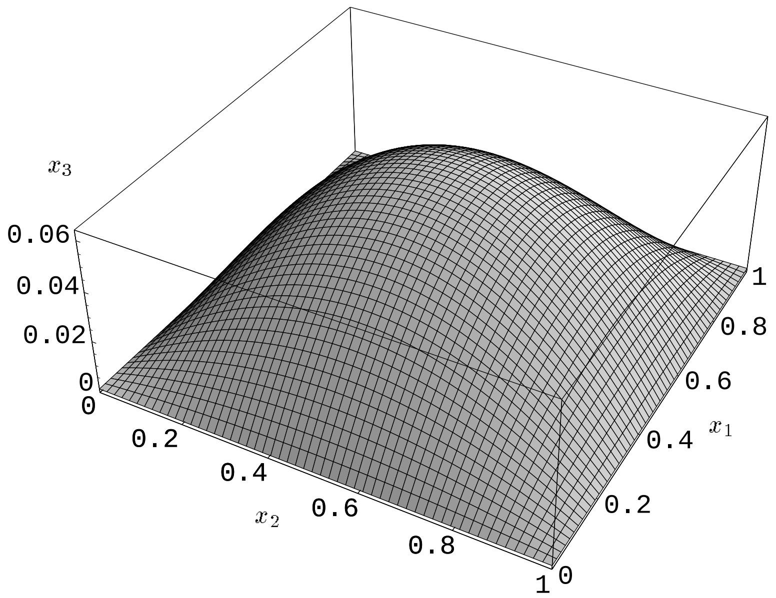

Figure 7.14: 'Bubble' displacement as a function of x_1 and x_2.

and boundary conditions $\mathbf{u}(\mathbf{x}) = \mathbf{0}$ for $\mathbf{x} \in \partial\Omega$. Material properties for the plate will be taken to be $E = 1$ and $\nu = 1/4$ in a plane stress setting along with a plate thickness of $t = 1/10$. Using Mathematica, [59], the following quantities were calculated,

$$\lambda = \frac{4}{15}, \quad \mu = \frac{2}{5}, \quad ||\mathbf{u}||_{E(\Omega)} \approx 6.38497465 \times 10^{-2} \quad \text{and} \quad ||\mathbf{u}||_{L_2(\Omega)} \approx 7.45355992 \times 10^{-2}. \quad (7.14)$$

7.2.2 Estimator Results and Discussion

Successive uniform mesh refinement as performed for the linear elasticity analyses using square elements yields the results presented in Table (7.14). It can be seen from the table that the

d	M	$\|\mathbf{u}\|_{E(\Omega)}$	$\|\mathbf{u}_h\|_{E(\Omega)}$	$\|\mathbf{u}_h\|_{L_2(\Omega)}$	$\|\mathbf{u}-\mathbf{u}_h\|_{E(\Omega)}$
1/2	5	6.351031(−2)	5.972033(−2)	9.346701(−2)	3.360615(−2)
1/4	45	6.382858(−2)	6.264881(−2)	7.706931(−2)	1.601630(−2)
1/8	245	6.384842(−2)	6.354292(−2)	7.499261(−2)	7.928500(−3)
1/16	1125	6.384966(−2)	6.377272(−2)	7.464045(−2)	3.956547(−3)
1/32	4805	6.384974(−2)	6.383047(−2)	7.456125(−2)	1.977384(−3)
1/64	19845	6.384975(−2)	6.384493(−2)	7.454198(−2)	9.885832(−4)
1/128	80625	6.384975(−2)	6.384854(−2)	7.453719(−2)	4.942781(−4)

Table 7.14: Uniform refinement of square element uniform meshes in plate bubble problem.

expected order of convergence is obtained for the finite element error measured in the energy norm. In addition, the computed norm values $\|\mathbf{u}_h\|_{E(\Omega)}$ and $\|\mathbf{u}_h\|_{L_2(\Omega)}$ tend to their expected values given in (7.14) and the computed $\|\mathbf{u}\|_{E(\Omega)}$ quantity tends to the exact value.

Using the Mathematica code developed in Chapter 6 and included in Appendix C the interpolation error constants for the current set of plate data were found to be,

$$C^i_{1,k} = 94.049218 \quad \text{and} \quad C^i_{2,k} = 183.711731,$$

each given correct to six decimal places. It can be seen that these are rather large compared with those used in Section (7.1). This can be attributed to a combination of both the thickness effect present for plates and the material properties chosen as discussed in Section (6.2.4).

Estimator performance for the set of successively refined uniform meshes an be seen in Table (7.15). It is clear that the Z-Z estimator again performs well by displaying the expected order

d	Z-Z	θ	J-H	θ
1/2	4.207608(−2)	1.252035	6.618270	196.936289
1/4	1.693241(−2)	1.057199	3.556231	222.038246
1/8	8.068344(−3)	1.017638	1.837793	231.795810
1/16	3.977229(−3)	1.005227	9.338680(−1)	236.031038
1/32	1.980224(−3)	1.001436	4.707292(−1)	238.056558
1/64	9.889560(−4)	1.000377	2.363236(−1)	239.052839
1/128	4.943259(−4)	1.000097	1.184031(−1)	239.547534

Table 7.15: Error estimates on uniform meshes of square elements for the bubble problem.

of convergence and once again portraying asymptotically exact behaviour. First impressions of the J-H estimator though are slightly alarming due to the large effectivity index present. Further investigation reveals, however, that the J-H estimator also converges at the expected rate. In addition, the effectivity index values do not seem to be growing in an unbounded manner and instead seem to be tending towards a value of approximately 240. Figure (7.15) shows the computed order of convergence for meshes $d = 1/4$ to $1/128$ starting from initial mesh $d = 1/2$ and plotted against $\ln(M)$ using the finite element error data from Table (7.14) and both the Z-Z and J-H estimator data from Table (7.15). The order of convergence values are calculated by using the

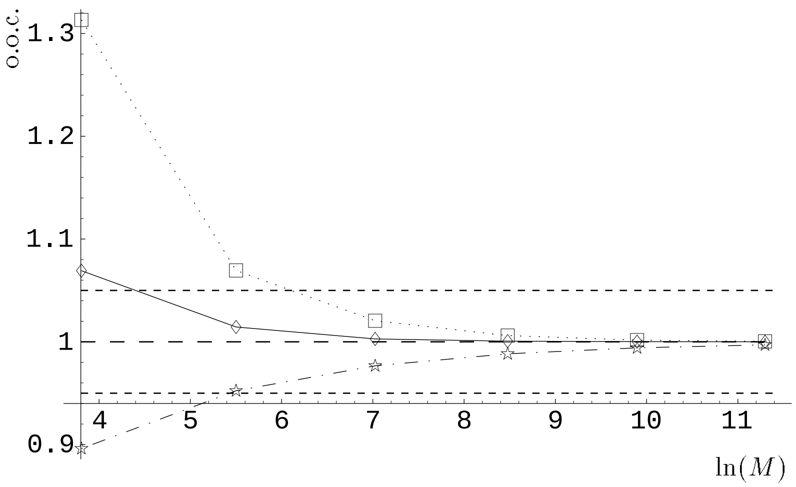

Figure 7.15: Order of convergence values versus $\ln(M)$ for successively refined square element uniform meshes $d = 1/4$ to $d = 1/128$. True, Z-Z and J-H estimator values marked with diamond, box and star icons respectively.

property that the finite element error $\mathbf{u} - \mathbf{u}_{2h}$ on a mesh with $d = 2h$ and measured in the energy norm is such that,

$$||\mathbf{u} - \mathbf{u}_{2h}||_{E(\Omega)} \sim C(2h)^{\alpha},$$

as given in Section (4.1) where C is a constant and α is the order of convergence. For a mesh with $d = h$ it follows that,

$$||\mathbf{u} - \mathbf{u}_h||_{E(\Omega)} \sim Ch^{\alpha},$$

enabling the order of convergence of the finite element error in moving from a mesh with $d = 2h$ to one for which $d = h$ to be expressed as,

$$\alpha = \frac{\ln\left(\dfrac{||\mathbf{u} - \mathbf{u}_{2h}||_{E(\Omega)}}{||\mathbf{u} - \mathbf{u}_h||_{E(\Omega)}}\right)}{\ln(2)} \equiv \alpha_h.$$

In the above α_h has been introduced to denote the mesh size h at which the order of convergence is observed. The same procedure may be performed by using the Z-Z and J-H error estimate values in place of the finite element error. By doing so the three curves shown in Figure (7.15) are obtained. The curve for the finite element error is shown as a solid line with the value at each new mesh point marked with a diamond whilst the Z-Z and J-H estimator curves are shown as a dotted line marked with boxes and a 'dot dash' line marked with stars respectively. For the above uniform meshes the domain discretisation parameter d is in fact the element edge size and also the global mesh size h. Thus Figure (7.15) shows O(h) convergence for the true error and both estimators since all three curves tend to unity as the mesh is refined which is in agreement with the theoretical rate of convergence as outlined in Section (4.1) where $\alpha = 1$. The main reason for including Figure (7.15), however, is in order to determine a suitable point from which a calibration constant $\mathcal{C}$ can be determined for the J-H estimator. As a refinement of that given in Section (7.1.3) it is proposed that a suitable point at which to establish $\mathcal{C}$ will be when it is clear that $\mathrm{O}(h)$ convergence has been attained for the first time by both the finite element error and the estimator. By denoting the order of convergence for the finite element error as α_h and that for the J-H estimator as β_h we thus require that,

$$\max\{|\alpha_h - 1|, |\beta_h - 1|\} \leq \epsilon, \tag{7.15}$$

where ϵ is a tolerance on the deviation from unity of the two orders of convergence and which shall be taken here to be 5%. Once Equation (7.15) has been satisfied $\mathcal{C}$ can be obtained by taking the integer part of the effectivity index obtained for mesh size h. By using Equation (7.15) $\mathrm{O}(h)$ convergence is guaranteed and the potentially troublesome early stages of the uniform refinement analyses are avoided where the order of convergence may well be much larger than unity. Figure (7.15) shows the 5% tolerance bounds on the theoretical order of convergence as dashed lines. It can be seen that the orders of convergence for both the finite element error and the J-H estimator fall within these bounds for the mesh $d = h = 1/8$ at which point we have $\alpha_h = 1.014$ and $\beta_h = 0.952$. From Table (7.15) this corresponds to the integer part of the effectivity index giving $\mathcal{C} = 231$. It is accepted that the use of tolerance value ϵ is a rough rule of thumb but it is necessary to make some decision on this value in order to proceed with a J-H estimator of an acceptable magnitude. In addition, the value of ϵ can be varied at will by the modeller depending upon what is deemed to be appropriate. By using this calibration technique, however, one can expect to obtain global error estimates from the J-H estimator which yield an effectivity index value close to unity. Figure (7.16) shows the convergence curves for the finite element error measured in the energy norm and also for both the Z-Z and calibrated J-H error estimates upon uniform refinement. These curves

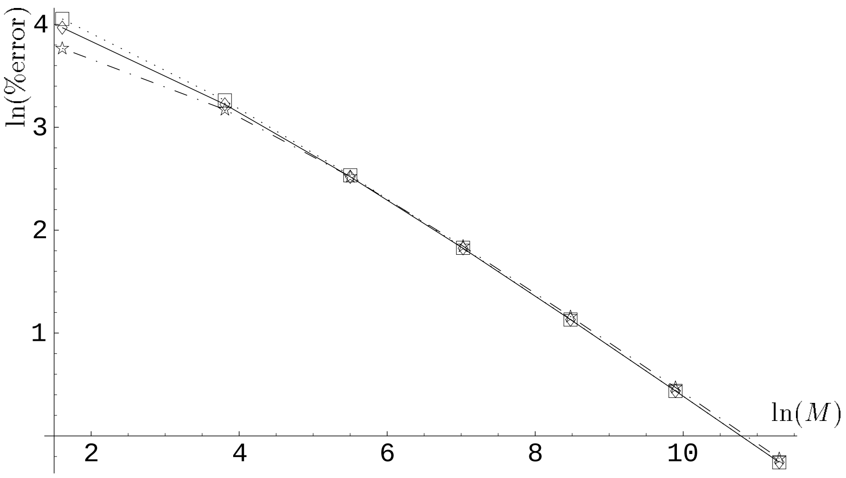

Figure 7.16: Convergence curves on successively refined uniform square element meshes. True error, Z-Z estimator and J-H estimator marked with diamond, box and star icons respectively.

are obtained as before by plotting ln(%error) against $\ln(M)$. In the same format as Figure (7.15) the curve corresponding to the true percentage error is shown as a solid line marked with diamonds whilst the other two percentage error curves for the Z-Z and calibrated J-H estimators appear as a dotted line marked with boxes and a 'dot dash' line marked with stars respectively. It can be seen that all three curves now agree closely with each other as required. Figure (7.17) shows the effectivity index values for both the Z-Z and calibrated J-H estimators plotted against $\ln(M)$. It can be seen that $\theta \to 1$ for the Z-Z estimator. For the case of the calibrated J-H estimator it is

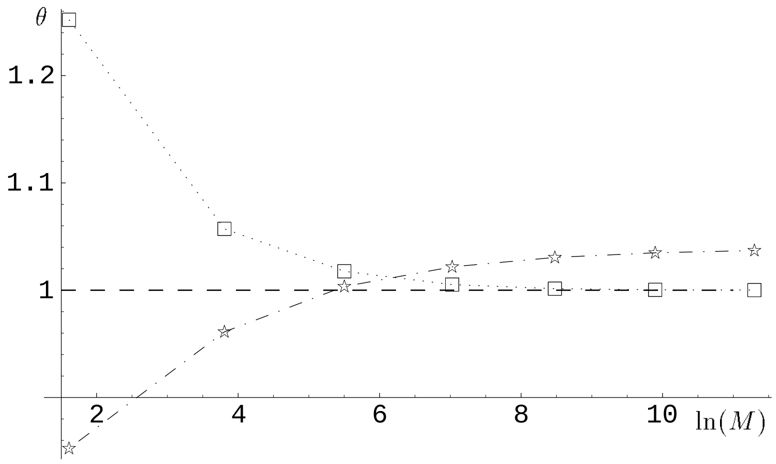

Figure 7.17: Effectivity index θ versus $\ln(M)$ for Z-Z and calibrated J-H estimators represented by a dotted line marked with boxes and a 'dot dash' line marked with stars respectively.

clear that for the $d = 1/8$ mesh $\theta \approx 1$ whilst for coarser meshes $\theta < 1$ and for finer meshes $\theta > 1$. This is as expected due to the fact that the mesh used to obtain the calibration constant was that for $d = 1/8$ and thus the calibration constant is optimal for this mesh. For the coarser meshes the calibration constant is too large leading to an effectivity index of less than unity whilst for the finer meshes the calibration constant is too small leading to an overestimation in the error and an effectivity index value greater than unity. This is a result of choosing $\epsilon = 0.05$ in Equation (7.15). By choosing a smaller ϵ this will result in a calibration constant $\mathcal{C}$ being taken from a later mesh and consequently the calibrated J-H estimator curve will cross unity at a later stage. In this way a calibration constant can be established which can force the calibrated J-H estimator curve to cross unity at any desired point. It is, however, worth noting that it is best for an estimator to overpredict an error rather than underpredict and it is for that precise reason that a tolerance of 5% was chosen for ϵ rather than 1%.

7.2.3 Variation of Calibration Constant with Plate Thickness

The previous section illustrated the proposed method for obtaining a calibration constant $\mathcal{C}$ for the J-H estimator. It was found therein that for the current test problem a calibration constant of $\mathcal{C} = 231$ results. This constant is consequently used to scale the interpolation error constants computed as detailed in Chapter 6. It is clear that by employing such a calibration constant it is possible for the calibrated J-H estimator to attain an effectivity index close to unity as desired.

In Section (6.2.4) it was shown that the interpolation error constants themselves are strongly reliant upon the plate thickness value. Further, it was shown that as the thickness was increased the interpolation error constant values fell dramatically due to the inclusion of the thickness in the plate bilinear form. Figure (7.18) again illustrates this effect on the interpolation error constants C_1^i and C_2^i for varying thickness. It can be seen that for both constants C_1^i and C_2^i, whose values are

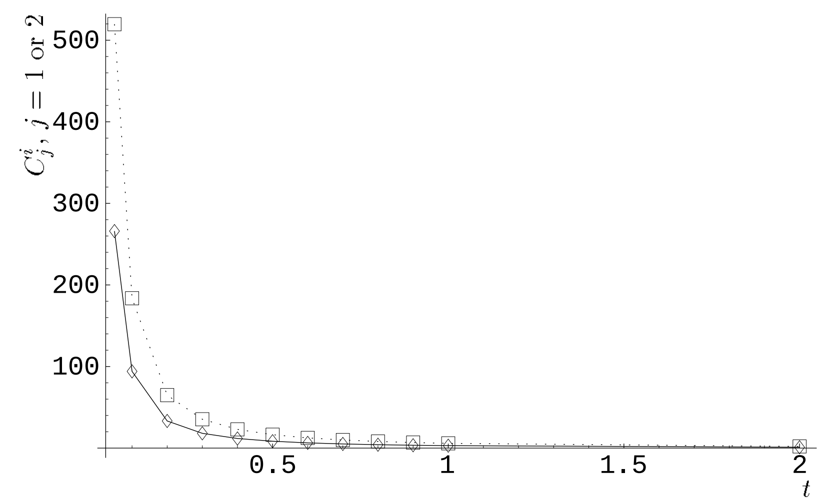

Figure 7.18: Interpolation error constants C_1^i and C_2^i versus thickness t and denoted by a solid line marked with diamonds and dotted line marked with boxes respectively.

marked with diamonds and boxes respectively, there is a decrease in their values as the thickness increases. For the current square plate with side dimensions or span equal to unity it is clear that a thickness value of up to two as shown in Figure (7.18) is excessive. This has been included, however, to show that the decreasing interpolation error constant trend continues for ever increasing thicknesses.

The aim of this section is to illustrate how the calibration constant $\mathcal{C}$ changes with varying plate thickness. This will be done by computing the values of $\mathcal{C}$ for a range of plate thicknesses using the method described in the previous section and Equation (7.15). For this method an accuracy of 5% is chosen on both α_h and β_h which are the orders of convergence for the finite element error and the J-H error estimate respectively. Table (7.16) shows the computed values of $\mathcal{C}$ for varying plate thickness t along with the orders of convergence from the point at which $\mathcal{C}$ is taken. For each test in Table (7.16) the plate material properties of $E = 1$ and $\nu = 1/4$ are retained and a sequence of uniformly refined meshes used to obtain $\mathcal{C}$ as in the previous section. It can be seen that the orders of convergence α_h and β_h remain approximately constant for the thicknesses modelled. Furthermore it is found that these orders of convergence which are the first pair to

t	α_h	β_h	$\mathcal{C}$	t	α_h	β_h	$\mathcal{C}$
1/20	1.019	0.952	463	3	1.008	0.956	7
1/10	1.014	0.952	231	4	1.007	0.956	8
2/10	1.012	0.953	115	5	1.006	0.955	10
3/10	1.011	0.953	77	10	1.005	0.954	22
4/10	1.011	0.953	57	20	1.004	0.954	48
5/10	1.011	0.953	46	30	1.004	0.954	72
6/10	1.010	0.953	38	40	1.004	0.954	97
7/10	1.010	0.953	32	60	1.004	0.954	146
8/10	1.010	0.953	28	80	1.004	0.954	195
9/10	1.010	0.953	25	100	1.004	0.954	244
1	1.010	0.953	22	200	1.004	0.954	488
2	1.009	0.953	10	1000	1.004	0.954	2443

Table 7.16: Variation of calibration constant $\mathcal{C}$ with plate thickness t.

satisfy Equation (7.15) are obtained throughout the analyses at mesh $d = 1/8$ as was the case in the previous section. For realistic thicknesses it can be seen that a decrease is observed for $\mathcal{C}$ as was the case for the interpolation error constants. This is illustrated in Figure (7.19) which shows a plot of the value of $\mathcal{C}$ against the corresponding plate thickness. As for the interpolation

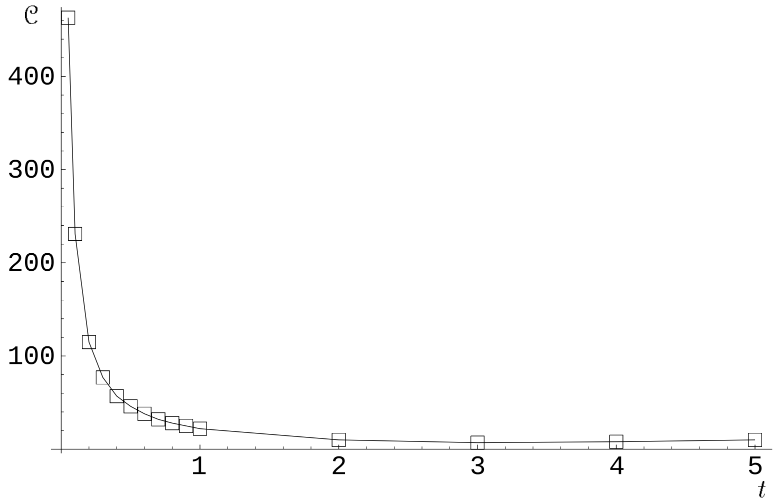

Figure 7.19: Calibration constant $\mathcal{C}$ versus thickness t.

error constant illustration the thickness value is again taken to extremely large values. For these values it is clear that the decrease in $\mathcal{C}$ becomes successively less until an increase is observed at approximately $t = 4$. As the thickness is further increased so does $\mathcal{C}$ and a linear relationship seems to develop between the two as can be seen in Table (7.16). Of course this behaviour occurs at thickness values for which the plate model is no longer appropriate. Indeed the thickness of a plate should never approach the value of the plate span itself since this can no longer be considered a plate and it becomes necessary to model the material using a full three dimensional elasticity model.

7.2.4 Spike Problem

As performed for the case of linear elasticity the 'spike' problem will now be analysed in the plate model. To recap, each displacement term is now assumed to have the form,

$$\zeta(\mathbf{x}) = \frac{1}{2}\exp\left(-\alpha\left((x_1 - x_1^c)^2 + (x_2 - x_2^c)^2\right)\right),$$

where the point (x_1^c, x_2^c) lies at the centre of the plate midplane which shall be taken as in the previous problem to be $\Omega \equiv (0,1)\times(0,1)$. As also in the previous problem $\mathbf{u} = \mathbf{0}$ on the boundary $\partial\Omega$ and a value of $\alpha = 200$ shall be used. Material properties for the plate are again taken to be $E = 1$ and $\nu = 1/4$ along with a plate thickness $t = 1/10$. This data yields energy and L_2-norm measure of the true solution calculated using Mathematica, [59], as,

$$||\mathbf{u}||_{E(\Omega)} \approx 3.76295844 \times 10^{-1} \quad \text{and} \quad ||\mathbf{u}||_{L_2(\Omega)} \approx 9.90831824 \times 10^{-2}.$$

Table (7.17) shows the convergence of the finite element solution to that given above for a sequence of uniformly refined meshes each consisting of square elements of side d. It can be seen from the

d	$\|\|\mathbf{u}\|\|_{E(\Omega)}$	$\|\|\mathbf{u}_h\|\|_{E(\Omega)}$	$\|\|\mathbf{u}_h\|\|_{L_2(\Omega)}$	$\|\|\mathbf{u}-\mathbf{u}_h\|\|_{E(\Omega)}$
1/2	7.290559(−2)	6.886569(−1)	6.026146(−1)	7.400161(−1)
1/4	5.192551(−1)	5.102911(−1)	3.978068	8.435363(−1)
1/8	3.574541(−1)	7.493108(−1)	3.150287	5.473321(−1)
1/16	3.745532(−1)	3.595359(−1)	1.212588(−1)	1.526986(−1)
1/32	3.762958(−1)	3.687299(−1)	9.973897(−2)	8.187458(−2)
1/64	3.762958(−1)	3.743163(−1)	9.881559(−2)	4.139653(−2)
1/128	3.762958(−1)	3.757955(−1)	9.898783(−2)	2.075793(−2)

Table 7.17: Uniform refinement of square element uniform meshes in plate spike problem.

table that once again the expected order of convergence is obtained for the finite element error measure and both the computed energy and L_2-norm quantities are close to their expected true values.

Due to the fact that the plate here is the same as that used for the previous problem the interpolation error constants computed using the code included in Appendix C are also the same as in the previous problem and have the values,

$$C_{1,k}^i = 94.049218 \quad \text{and} \quad C_{2,k}^i = 183.711731,$$

each given correct to six decimal places. Using the now familiar sequence of uniform meshes the estimator performance can be seen in Table (7.18). As was witnessed for the spike problem in the linear elasticity context, the estimators again seem to take longer to approach O(h) convergence. It is interesting to see that again the Z-Z error estimate is beginning to show asymptotic exactness whilst the J-H estimator, although quicker to settle down and exhibit the theoretical rate of convergence, again overestimates the global error. As seen previously for the linear elasticity

d	Z-Z	θ	J-H	θ
1/2	4.869526(−1)	0.658030	8.740314(+1)	118.109788
1/4	4.259990(−1)	0.505016	6.972931(+1)	82.663079
1/8	6.429899(−1)	1.174771	7.758873(+1)	141.758051
1/16	2.180384(−1)	1.427901	3.315386(+1)	217.119603
1/32	9.945070(−2)	1.214671	1.798727(+1)	219.693002
1/64	4.453209(−2)	1.075744	9.311410	224.932104
1/128	2.119222(−2)	1.020922	4.698561	226.350181

Table 7.18: Error estimates on uniform meshes of square elements for the spike problem.

problems the J-H estimator θ value is approximately that found for the bubble problem for plates where $\theta \approx 239$. Using Equation (7.15) with $\epsilon = 0.05$ we obtain a calibration constant of $\mathcal{C} = 224$ here which compares well for the plate bubble problem value of $\mathcal{C} = 231$ considering the differences in the solutions.

Prior to running adaptively, the computed interpolation error constants obtained using the Mathematica code included in Appendix C and developed from Chapters 5 and 6 for the transition element family are as given in Table (7.19). These interpolation error constants when calibrated

Element type	Computed C_1^i	Computed C_2^i
Standard	9.404922(+1)	1.837117(+2)
1-irregular	8.668740(+1)	2.191192(+2)
2_{adj}-irregular	8.526373(+1)	2.480080(+2)
2_{opp}-irregular	6.779471(+1)	1.448804(+2)
3-irregular	6.792558(+1)	1.981567(+2)

Table 7.19: Computed C_1^i and C_2^i values for the transition element family for use in the plate spike problem.

using $\mathcal{C} = 224$ and used in the J-H estimator to obtain an error tolerance of 5% yield results as given in Table (7.20) which also includes the adaptive run results for the Z-Z estimator. These values have been obtained using the extensions to previous error estimators as detailed in Chapter 4 for use in the plate model and in meshes containing transition elements.

It can be seen in Table (7.20) that the Z-Z estimator is performing well. To recap, this estimator was extended for use in first-order shear deformation theory in order to cope with the presence of transition elements and irregular nodes. It was shown in Section (4.3.1) by using the approach of Barlow, [14] and Mackinnon and Carey, [33], that the locations of the superconvergent sampling points can vary wildly over the transition element family. It was based upon these locations that the algorithm for element patch selection as detailed in Section (4.3.2) was developed. Inspection of the Z-Z results in Table (7.20) show that both the algorithm and the selection points chosen seem to be performing well. In addition to this it can be seen that the effectivity index value

Z-Z Estimator				
I	M	$\|\mathbf{u}-\mathbf{u}_h\|_{E(\Omega)}$	θ	%error
2	245	5.473321(−1)	1.174771	65.12
4	2530	8.187460(−2)	1.214672	26.04
6	8580	2.091864(−2)	1.024459	5.69
7	15740	1.223402(−2)	1.020493	3.32
J-H Estimator, $\mathcal{C} = 224$				
I	M	$\|\mathbf{u}-\mathbf{u}_h\|_{E(\Omega)}$	θ	%error
2	245	5.473321(−1)	0.632848	41.96
4	1565	8.187528(−2)	0.980830	21.28
6	6085	2.176806(−2)	1.020241	5.90
7	8825	1.595678(−2)	0.993295	4.21

Table 7.20: Error estimator performance for adaptive run to 5% error requirement on a mesh consisting of square elements.

seems to be tending to unity indicating that the asymptotic exactness feature of the estimator has been retained. The use of transition elements has been detailed previously by Choi and Park, [17]. In a second publication by Choi and Park, [18], the transition elements are implemented in a plate model along with a version of the Z-Z estimator. However, no mention is made of the sampling points taken or indeed the patch selection procedure. It is felt that this is one of the most important areas in the implementation of this type of estimator and it is believed that the Z-Z implementation presented here provides information on these key areas for the first time.

Table (7.20) also shows results for the calibrated J-H estimator. As for the Z-Z estimator this estimator has been extended for use with transition elements and reformulated for use in the plate model as detailed in Sections (4.4.3) and (4.5). It can be seen from the table that this estimator is also performing well with effectivity index value close to unity. A potential area of concern, however, lies in the fact that the effectivity index value is slightly less than unity meaning that the estimator is underestimating the error slightly. It is thought that this is due to the technique used to calibrate the interpolation error constants given in Table (7.19). This is done by scaling the interpolation error constants by the calibration constant $\mathcal{C} = 224$ which is itself found by successive uniform refinement. It may thus be argued that this calibration constant is only correct for uniform meshes and that it is not optimal to scale the transition element family interpolation error constants by the same quantity. The results for uncalibrated adaptive runs, however, seem to settle at effectivity index values of approximately $\theta \approx 225$ for true error values of 10% and smaller. This implies a calibration constant of $\mathcal{C} = 225$ which is very close to that obtained from the uniform refinement analysis of $\mathcal{C} = 224$ and used in the calibrated adaptive analysis shown in Table (7.20). Running the same problem again but now asking for 4% error in order to compare with the Z-Z result and using the calibration constant found from the uncalibrated adaptive run yields the results presented in Table (7.21). The convergence curves for the Z-Z estimator data presented in Table (7.20) and the J-H estimator data in Table (7.21) can be seen in Figures (7.20)

J-H Estimator, $\mathcal{C} = 225$				
I	M	$\|\|\mathbf{u} - \mathbf{u}_h\|\|_{E(\Omega)}$	θ	%error
2	245	5.473321(−1)	0.630036	41.81
4	1645	8.187528(−2)	0.976471	21.19
6	6725	2.123630(−2)	1.015623	5.73
7	11445	1.406744(−2)	1.013795	3.79

Table 7.21: J-H estimator performance for adaptive run to 4% error requirement on a mesh consisting of square elements using calibration constant from uncalibrated adaptive analysis.

and (7.21). As previously these curves show ln(%error) plotted against ln(M) for both uniform and adaptive refinements. In both figures, the solid line marked with diamonds again denotes the uniform refinement route and the dotted line marked with stars denotes the adaptive route. It is

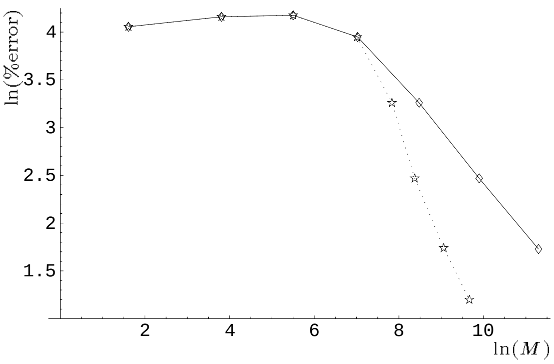

Figure 7.20: Uniform and adaptive refinement convergence curves for Z-Z estimator using square and transition elements in the plate model.

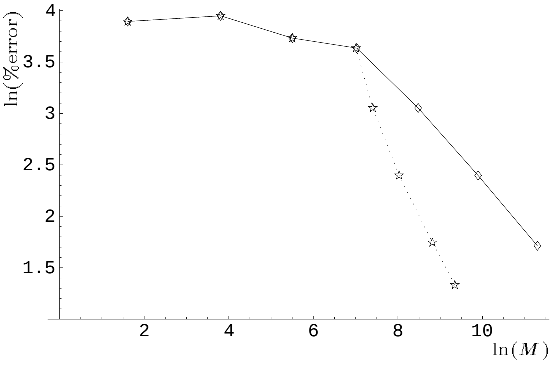

Figure 7.21: Uniform and adaptive refinement convergence curves for J-H estimator using square and transition elements in the plate model.

clear from both figures that the adaptive route converges to the required tolerance quicker than the corresponding uniform refinement route. As seen previously in the case of linear elasticity, the adaptive route follows that of the uniform refinement route at the start of the analyses before branching off to embark on the faster route.

The resulting adapted meshes for the two estimators can be seen in Figures (7.22) and (7.23). It is clear that both figures show heavy refinement around the area where the displacements are changing rapidly. As seen for the linear elasticity problem, the mesh resulting from the Z-Z estimator has a smoother transition from coarse to fine elements. This is another feature which can be observed in the adapted meshes for the linear elasticity spike problem shown in Figures (7.11) and (7.12). It is also worth noting that the mesh produced by the Z-Z estimator yields an estimated error of 3.32% whilst that of the J-H estimator yields 3.79%. Thus it is quite acceptable that there seems to be a higher degree of refinement in the resulting Z-Z mesh due to the higher accuracy it yields. This can be seen clearly upon comparing the number of unknowns M between Tables (7.20) and (7.21).

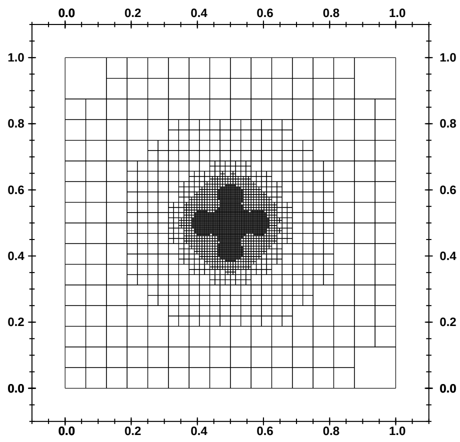

Figure 7.22: Adapted square element mesh to achieve 5% error using Z-Z estimator.

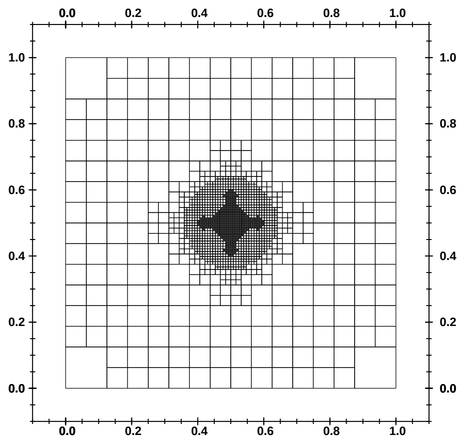

Figure 7.23: Adapted square element mesh to achieve 5% error using J-H estimator.

The previous sections have detailed the importance of obtaining a calibration constant in order to bring the global J-H error estimate down to an acceptable level. The need for such a calibration constant is due to the magnitudes of the computed interpolation error constants which have been shown to depend upon the choice of both material properties and plate thickness. It is thought that the use of a single calibration constant could be improved, however, by obtaining a set of calibration constants. In this way a calibration constant could be obtained for each meber of the transition element family for use in adaptive analyses as will be discussed in Chapter 8.

7.3 Plate Model Agreement with Physical Experiments

The previous two sections have been concerned with the analysis of test problems for which the solutions are known. In this final section, a comparison will be made between the results of the plate model and those obtained from physical experiments performed at the Forrest Products Research Centre located at Buckinghamshire College in High Wycombe. The experimental results have kindly been provided for use as a comparison with the plate model in this work as well as results from Ansys, [4], which is a commercially available finite element package.

The problem of interest will be that of a square plate which is simply supported on two sides and free on the other two. This is in order to simulate the floor boarding in a modern house between the floor beams as illustrated in Figure (7.24). Here it can be seen that the board rests on the

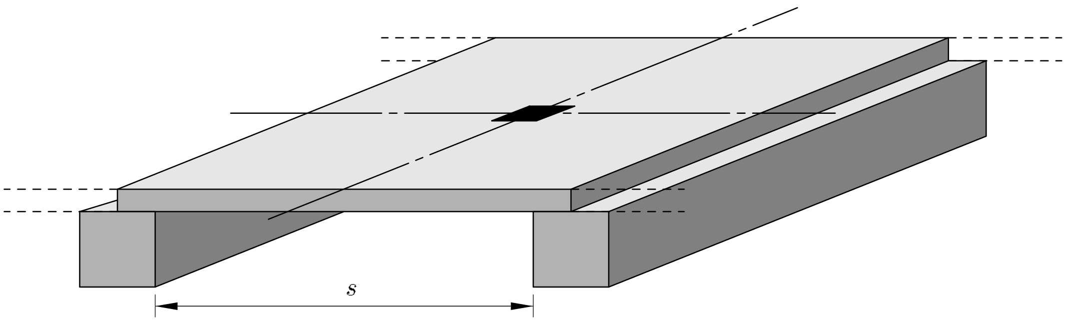

Figure 7.24: Section of a typical floor board resting on two beams.

beams which provide support on two edges. In reality there may be cross beams and the boards may be joined and possibly glued together using what is called a 'tongue and groove' joint. In the model, however, the board will be taken simply as that illustrated in Figure (7.24) with a concentrated load applied to the centre of the board and illustrated in the figure as a black region. This section will thus present the results when the plate model is used to model the board.

As discussed in Section (2.2.3) certain plate problems can be reduced by exploiting lines of symmetry. This was illustrated by reducing the problem domain shown in Figure (2.5) to that illustrated in Figure (2.6). It is clear from Figure (7.24) that this technique can be applied here by using the centre lines marked as usual by 'dot-dash' lines. Once this has been done a quarter of the plate problem domain is obtained as shown in Figure (7.25) which shall henceforth be called the quarter plate model. This figure clearly shows the upper right quadrant of the plate with the plate centre now at the bottom left corner of the domain.

In accordance with the physical experimental conditions the span of the plate, labelled s in Figure (7.24), will be 450mm. In addition the plate will be square which means that the quarter plate problem shown in Figure (7.25) will have edge dimensions $s/2$ and be of 18mm thickness. It can be

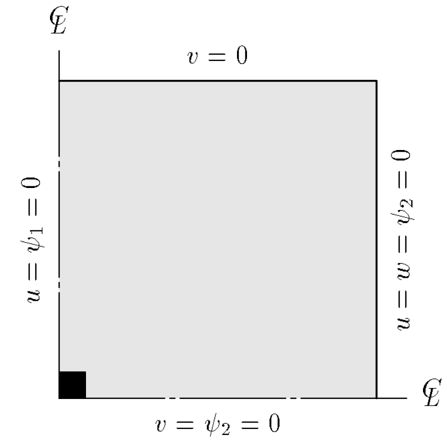

Figure 7.25: Reduced plate geometry for floor problem.

seen in Figure (7.24) that the plate is only supported on two edges by the floor beams. These edges will be modelled as being simply supported and for the quarter plate problem this corresponds to the Eastern edge where it can be seen that the boundary conditions enable rotation about the x_2-axis in turn enabling the plate to essentially pivot along the edge. As previously mentioned the plate will experience a transverse concentrated load acting over a small area at the centre of the plate and illustrated in Figure (7.25) as a square black area. Although the physical experiment is performed with a circular loading head it is not thought that the approximation of this to a square region of equivalent area will effect the computational results to a large extent. The load applied in the physical experiment to the whole plate is 750N which must be reduced by a factor of four for the quarter plate problem. This gives 187.5N to be applied to the quarter plate model over a region 12.5mm square.

Material properties for the plate are obtained from a series of three and four point physical bending tests performed over a selection of board samples. By averaging the results it is found that the Young's modulus value $E = 3943\text{N/mm}^2$ and the Poisson's ratio value $\nu = 0.177$.

7.3.1 Estimator Results and Discussion

Prior to the analysis of the estimator performance for the physical problem it will be firstly necessary to establish the J-H estimator calibration constant $\mathcal{C}$. It has been observed in the previous results sections that the J-H estimator requires such a constant in order to yield a global error estimate which is useful. This is done by scaling the computed interpolation error constants used in the estimator.

It has been shown for the previous test problems that, providing the same material properties are retained, a valid calibration constant can be obtained for the problems. Thus by analysing both the bubble and spike test problems again but this time with the physical plate characteristics and material properties of the current problem it should be possible to obtain a calibration constant which is valid for the current problem. Consequently, both the bubble and spike problems of the previous sections were analysed again but this time with the physical plate characteristics of the current problem. Results from these analyses both required the calibration constant to be $\mathcal{C} = 5$ and this value will be used in the J-H estimator here in order to scale the computed interpolation error constants which, for the transition element family are as given in Table (7.22). Results for

Element type	Computed C_1^i	Computed C_2^i
Standard	3.925059(−3)	6.910904(−3)
1-irregular	3.231552(−3)	7.677230(−3)
2_{adj}-irregular	2.922969(−3)	8.532031(−3)
2_{opp}-irregular	2.269786(−3)	5.397871(−3)
3-irregular	2.321078(−3)	6.791497(−3)

Table 7.22: Computed C_1^i and C_2^i values for the transition element family for use in the physical plate problem.

both the Z-Z and J-H error estimators can be seen in Table (7.23). Once again the results have been obtained by using a sequence of successively refined uniform meshes. However, instead of the domain discretisation parameter d, each mesh shall now be identified by the number of elements along each edge $\sqrt{N}$ where N is the total number of elements in the mesh. It can be seen that

$\sqrt{N}$	$\lVert\mathbf{u}_h\rVert_{L_2(\Omega)}$	$\lVert\mathbf{u}_h\rVert_{E(\Omega)}$	Z-Z Estimator		J-H Estimator, $\mathcal{C} = 5$	
			ρ	%error	ρ	%error
2	2.201511(+2)	6.376210(+1)	6.153161(+1)	69.44	8.954026(+2)	99.75
4	2.417753(+2)	3.668497(+1)	3.205344(+1)	65.80	2.447633(+2)	98.90
8	2.478329(+2)	2.448803(+1)	1.645960(+1)	55.78	6.875181(+1)	94.20
16	2.496243(+2)	1.999527(+1)	8.180485	37.87	2.035103(+1)	71.33
32	2.501049(+2)	1.875717(+1)	4.129323	21.50	7.002726	34.98
64	2.502241(+2)	1.843277(+1)	2.089431	11.26	2.852976	15.30
128	2.502534(+2)	1.834707(+1)	1.029519	5.60	1.311411	7.13
9	2.483031(+2)	2.334109(+1)	1.466696(+1)	53.21	5.566591(+1)	92.22
18	2.497717(+2)	1.965741(+1)	7.281070	34.73	1.678318(+1)	64.93
36	2.501402(+2)	1.866381(+1)	3.657413	19.23	5.926784	30.27
72	2.502323(+2)	1.840627(+1)	1.829396	9.89	2.473366	13.32

Table 7.23: Estimator performance upon successive uniform refinement in physical plate problem.

there are two sets of data in Table (7.23), these are the set of results beginning with $\sqrt{N} = 2$ which is then followed by the set of results beginning with $\sqrt{N} = 9$. It can also be seen that in addition to the %error, Table (7.23) also lists the actual estimated global error ρ. For the first set of data beginning with mesh $\sqrt{N} = 2$ the coarse meshes have large error estimates. It is thought that this is due to the coarse meshes not being able to correctly represent the load area which results in a 'smearing' of the load over a larger area. It is only when the element size is sufficiently small at approximately $\sqrt{N} = 32$ that the load can begin to be correctly represented. Due to the fact that an element edge will never lie exactly on the load application boundary for this set of meshes, however, there will always be a degree of load 'smearing' although this decreases as $\sqrt{N}$ increases and the mesh size consequently decreases. The second set of meshes does not suffer from this problem and from the $\sqrt{N} = 18$ mesh the load area is spanned exactly by an integer number of elements. Comparing the data from the second set of meshes with the first it can be seen that the two become similar as the number of elements increases indicating that the results from the first set do not suffer from not coinciding with the load region of application. This is due to the previously mentioned fact that as the mesh size decreases this effect becomes small and also due to the fact that the computer code generated during this work is able to cope with this problem by being able to integrate the load over regions which do not necessarily coincide with element boundaries. This is done by modifying the quadrature schemes in a similar way to that detailed in Section (3.9.2).

Plots of the error distribution over the quarter plate problem can be seen in Figures (7.26) and (7.27) for the Z-Z and J-H estimators respectively. In each figure the gray levels vary from dark to light with lighter shades being larger as denoted in each case by the legend. It can be seen that the two estimators predict similar error distributions over the domain with both picking out the presence of the concentrated load at the plate centre. Elsewhere on the domain the error

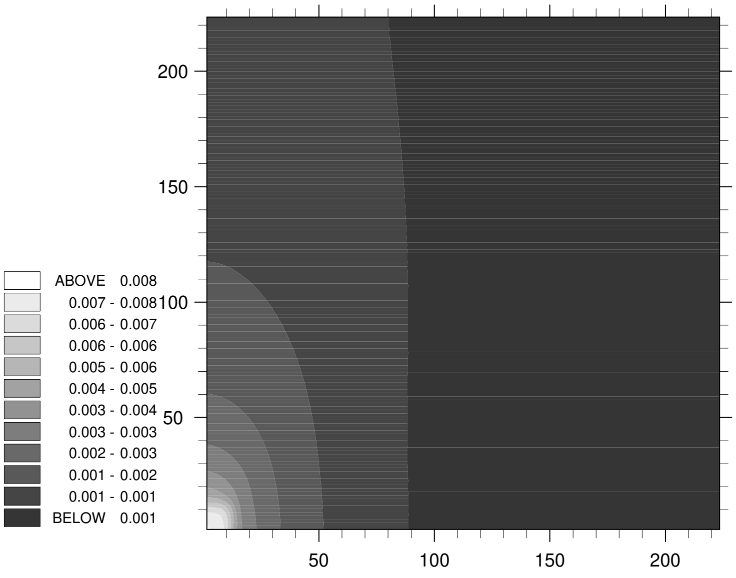

Figure 7.26: Qualitative error distribution from Z-Z estimator over quarter plate problem.

distribution is more uniform with only slight increases appearing as region of the load application is approached. In Figure (7.26) it can be seen that this region is shown as a square area of larger indicated error. Relative to the smaller surrounding error it can be seen that the increase is approximately eight times that which is indicated in the centre of the quarter plate domain. It

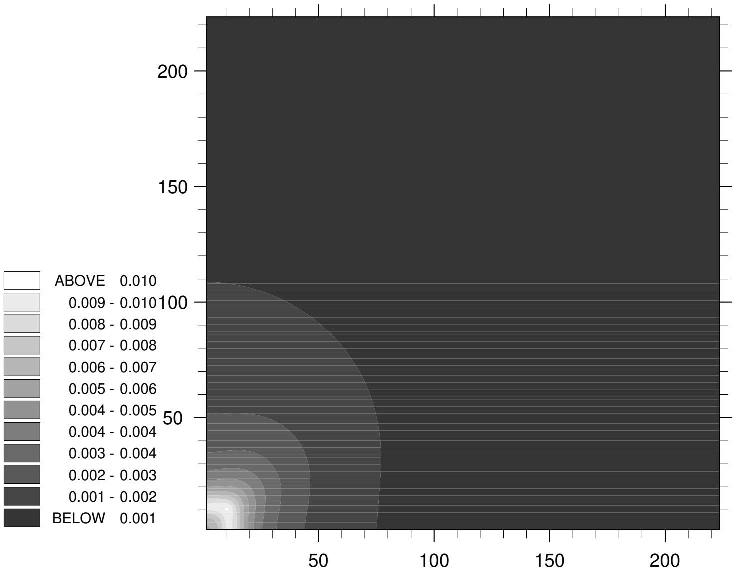

Figure 7.27: Qualitative error distribution from J-H estimator over quarter plate problem.

should be noted once again that these values are not necessarily the actual errors over the domain and instead should be thought of as qualitative representations of the error distribution.

Figure (7.27) shows similar trends in the error distribution. Here it can be seen that once again the error far away from the 12.5mm square load application region is low relative to the error close to it. Upon closer inspection it is clear that within the load application area the error is once again approximately eight times that in the centre of the quarter plate domain. The main difference here, however, is that the J-H estimator is in fact is able to pick out the boundary of the load where it can be seen that there is a higher error still. It is thought that this is due to the inclusion of the jump terms in this estimator which will be large in precisely these regions due to the sudden presence of the concentrated load and also the presence of the load $\mathbf{f}$ itself in the estimator.

The computed transverse displacements at the centre point of the plate, w_c, for the meshes in Table (7.23) are shown in Figure (7.28). It is clear that both sets of data produce similar displacements with the set beginning with $\sqrt{N} = 2$ shown as a solid line marked with diamonds and that beginning with $\sqrt{N} = 9$ as a dashed line marked with stars. Results from an analysis performed at The Forest Products Research Centre (FPRC) using Ansys, [4], gave this displacement to be 1.797mm whilst that of the physical experiment gave 1.71mm. The computed transverse displacements from Figure (7.28) are 1.7967mm for the $\sqrt{N} = 128$ mesh and 1.7966mm for the $\sqrt{N} = 72$ mesh, both given to four decimal places. Good agreement can thus be seen between the results computed here and both the computed and physically observed results provided as a comparison.

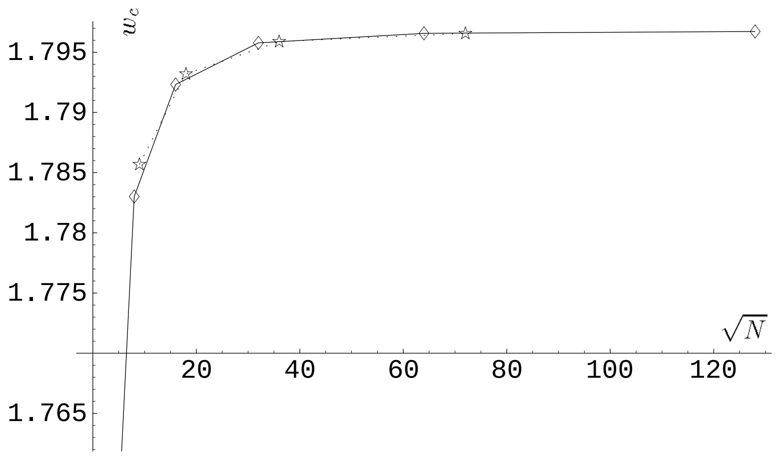

Figure 7.28: Computed transverse displacement w_c upon uniform refinement.

The resulting transverse displacement profile of the quarter plate domain can be seen in Figure (7.29) where it should be noted that the orientation of the axes is as illustrated by Figure (A.1). From the figure it can be seen that the part of the plate which lies on the beam and is simply supported in the model has zero transverse displacement. As we sweep across the plate from this edge the transverse displacements increases until we reach the plate centre line which corresponds to the Western boundary in the quarter plate domain. At this point it can be seen that by traveling down this centre line the transverse displacement continues to increase until the plate centre point has been reached.

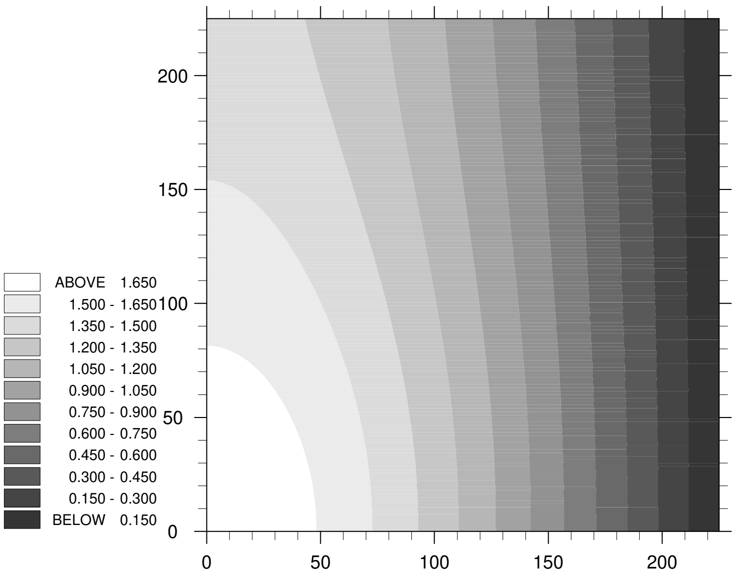

Figure 7.29: Computed transverse displacement for quarter plate model.

Adaptive analysis to 10% error for the problem and beginning with the $\sqrt{N} = 9$ mesh yields results detailed in Table (7.24). It can be seen that both estimators obtain similar error values

Z-Z Estimator			
I	M	ρ	%error
1	1544	7.29583	34.79
2	5788	3.685130	19.37
3	19662	1.924608	10.39
4	46697	1.311369	7.12

J-H Estimator, $\mathcal{C} = 5$			
I	M	ρ	%error
1	1654	16.783180	64.93
2	6550	5.926784	30.27
3	22288	2.628859	14.14
4	40128	1.922115	10.40
5	64283	1.480078	8.04

Table 7.24: Error estimator performance for adaptive run to 10% error requirement on a mesh consisting of square elements.

upon satisfying the tolerance. It can also be seen, however, that the J-H estimator seem to require more elements to reach an acceptable estimated error which is reflected in the total number of unknowns M. This is probably due to the fact that the calibration constant $\mathcal{C}$ used is slightly too small. The method used here to obtain $\mathcal{C}$ will indeed result in a calibration constant slightly less than 'optimal'. This is due to the fact that only the integer part from the selected effectivity index is taken for $\mathcal{C}$ as described in Section (7.2.2).

7.3.2 Laminated Plate

Laminated plates consist of a number of layers or laminates chosen for their particular material properties. This results in a sandwich of layers, an example of which is as illustrated in Figure (7.30) where it can be seen that there are two outer skin layers and an inner core layer. The details for modelling a laminated plate as given by Ochoa and Reddy, [37], can be seen in Section (2.2.2).

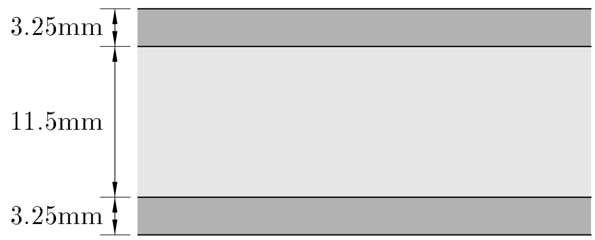

Figure 7.30: Plate section showing three laminates.

For the case of orthotropic laminates it is shown that the first necessary step is to transform the laminate material properties into the global components of the plate. The transformed material properties are then integrated over the thickness of each laminate and summed over all laminates to give a final global plate constitutive matrix. The type of particle board used for flooring has layers or laminates as illustrated in Figure (7.30). Physically the skin layers are of a higher density than the core due to there being a higher number of smaller and tightly packed wood chips or particles present whereas the core consists of relatively large wood chips which consequently are less tightly packed together. This layered structure arises from the manufacturing process and the rolling of the boards in order to obtain uniform thicknesses and in reality the distinction between skin and core layers is not easily made since the transition from high to low density layers is a gradual one. The skin thickness of 3.25mm given in Figure (7.30) must therefore be thought of as an approximate value as it is possible for this to vary between samples.

For this final numerical experiment the layers will be considered to be isotropic which gives rise to Young's modulus values E^s and E^c and Poisson's ratio values ν^s and ν^c where the superscripts s and c denote skin and core material properties respectively. Industry does not currently provide such data for particle boards but recent experimental research at FPRC has provided the values,

$$E^s = 5013.0\text{N/mm}^2,\ \nu^s = 0.207,\ E^c = 1416.9\text{N/mm}^2 \quad \text{and} \quad \nu^c = 0.135,$$

for Schauman C4(M) moisture resistant particle boards, [46]. Using this laminate data as described in Section (2.2.2) yields different material matrices **A**, **B** and **D** and thus it is necessary to compute once again the interpolation error constants but this time for the laminated plate. This is performed as detailed in Section (6.2) with the only change being the integration over each laminate and the subsequent summation through the thickness for the construction of matrices **A**, **B** and **D** to be used in the computation of the element stiffness matrix. Once this has been done the resulting interpolation error constants are as given in Table (7.25). It can be seen that the computed

Element type	Computed C_1^i	Computed C_2^i
Standard	4.739762(−3)	8.345363(−3)
1-irregular	3.902307(−3)	9.270739(−3)
2_{adj}-irregular	3.520467(−3)	1.027313(−2)
2_{opp}-irregular	2.670332(−3)	6.518278(−3)
3-irregular	2.796288(−3)	8.179939(−3)

Table 7.25: Computed C_1^i and C_2^i values for the transition element family for use in the laminated physical plate problem.

interpolation error constants are similar to those computed for the single layer plate and presented in Table (7.22). This is as expected due to the single layer plate being the uniformly isotropic equivalent to the layered plate considered here. This similarity in results is also present in the computation of the calibration constant for the layered plate model. Here it is once again found that by applying the test problems of Section (7.2) a calibration constant of $\mathcal{C} = 5$ results for the layered plate.

As a comparison with Table (7.23), results for both the Z-Z and J-H error estimators can be seen for the layered plate model in Table (7.26). Again two sets of data are presented, these differ in their starting meshes as explained previously with the set starting with $\sqrt{N} = 9$ being those

$\sqrt{N}$	$\|\|\mathbf{u}_h\|\|_{L_2(\Omega)}$	$\|\|\mathbf{u}_h\|\|_{E(\Omega)}$	Z-Z Estimator		J-H Estimator, $\mathcal{C} = 5$	
			ρ	%error	ρ	%error
2	2.113987(+2)	5.160917(+1)	4.894187(+1)	68.81	7.163713(+2)	99.74
4	2.323243(+2)	3.103461(+1)	2.562831(+1)	63.67	1.986734(+2)	98.80
8	2.381818(+2)	2.224961(+1)	1.337173(+1)	51.51	5.753208(+1)	93.27
16	2.399115(+2)	1.904523(+1)	6.531791	32.44	1.732801(+1)	67.30
32	2.403751(+2)	1.824592(+1)	3.320170	17.90	6.267708	32.49
64	2.404901(+2)	1.803897(+1)	1.703641	9.40	2.671640	14.65
128	2.405184(+2)	1.798146(+1)	8.242780(−1)	4.58	1.251730	6.94
9	2.386361(+2)	2.143400(+1)	1.192934(+1)	48.63	4.680152(+1)	90.92
18	2.400535(+2)	1.882425(+1)	5.814466	29.51	1.439323(+1)	60.74
36	2.404091(+2)	1.818334(+1)	2.926774	15.89	5.340556	28.18
72	2.404981(+2)	1.801908(+1)	1.463973	8.10	2.321259	12.78

Table 7.26: Estimator performance upon successive uniform refinement in physical layered plate problem.

able to exactly model the load application area. It can be seen that once again the two sets of data behave in a similar way and also that the results in the two tables show similar trends. This shows that the two estimators can be used for laminated plates in addition to the single layer plate modelled in Table (7.23).

The computed centre point displacements for the meshes in Table (7.26) can be seen in Figure (7.31). As observed for the single layer plate in Figure (7.28) both sets of meshes produce similar

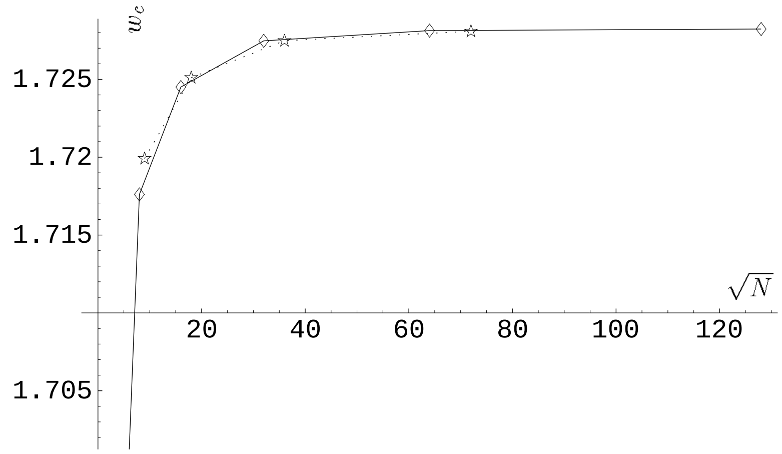

Figure 7.31: Computed transverse displacement w_c upon uniform refinement in layered plate model.

displacements as shown here by a solid line marked with diamonds for the set beginning with the $\sqrt{N} = 2$ mesh and a dashed line marked with stars for that beginning with the $\sqrt{N} = 9$ mesh.

For the final meshes in both sets $\sqrt{N} = 128$ yields a displacement of 1.7282mm whilst $\sqrt{N} = 72$ yields a displacement of 1.7281mm both given to four decimal places. These displacements agree well with the observed experimental displacement of 1.71mm.

The above results show that it is possible to model a plate both with and without layers or laminates and obtain results which agree well with observed physical experimental results. Typically a level of agreement of within 10% error in maximum displacement is considered acceptable at FPRC between experimental and computational results. For the single layer plate results presented here an error of 4.5% is seen, this drops to 1.2% for the laminated plate so both computational models would be acceptable and also be of practical use. The results from the computational models, however, depend strongly upon the quality of the material properties supplied to them and these in turn depend strongly upon the quality of experimental physical testing of the material. It is thus not clear a priori whether a model employing a single layer plate will produce better results than one employing a layered plate since the latter, although being closer to the physical plate, relies strongly upon the quality of a larger number of experimental data. In theory, however, the layered plate should be a more accurate model of the true plate and this is indeed observed in the above results. In addition to this it is interesting to see that both estimators give lower estimated errors for the layered model results.

Chapter 8

Conclusions

This work has been primarily concerned with the application of a variant of the residual based error estimator proposed by Johnson and Hansbo, [27], to plate problems modelled using the first-order shear deformation theory of Reddy, [40]. In addition, a variant of the recovery based estimator proposed by Zienkiewicz and Zhu, [69], [70] has also been applied. It is believed that this is the first such application of the J-H estimator to plates in this context although the estimator 'machinery' has been previously applied by researchers to a wide range of problems as discussed in Chapter 1. Recovery based estimators of the Z-Z type have previously been applied to problems of plate theory with one of the earliest publications being that of Zienkiewicz and Zhu, [67], in which the authors applied their original estimator of [66]. This has since been followed by the work of Liu and Elmaraghy, [31] who combined the original Z-Z estimator of [66] with a mesh generator and the work of Choi and Park, [18], who employed the same estimator along with transition elements for mesh adaptivity. More recently the Z-Z superconvergent patch recovery error estimator used in this work has been applied to plate problems as detailed in Bettess, Bull, Bond and Applegarth, [29], and Mukherjee and Krishnamoorthy, [36] with both cases employing automatic mesh generators and thus retaining a single element type mesh. In both [29] and [36], however, no mention is made of the effects upon the optimal sampling points which the estimator relies upon. It is thus believed that the Z-Z estimator implementation presented in this work is also a novel approach as the superconvergent patch recovery estimator is applied to plate problems over meshes containing transition elements which were introduced in the work of Gupta, [22], and employed by Choi and Park, [18], in their analysis of the original Z-Z estimator as previously mentioned.

It has been observed in this work that the decision to employ transition elements for adaptivity purposes creates additional difficulties for the finite element implementation itself and also the estimator implementations. It was thus found necessary for the standard estimators to be initially extended for use on meshes having such features. Initial results for these estimators have been obtained on test problems of linear elasticity as presented in Section (7.1) where they have been shown to perform well. The difficulties encountered from the presence of transition elements in the meshes will now be summarized for the two estimator implementations.

For the Z-Z error estimator implementation the presence of transition elements produced a complication which manifested itself in the determination of the optimal or superconvergent sample point locations in the elements. It is important to know the locations of these points for use in the recovery process as discussed in Section (4.3.1) and consequently the analysis of Makkinnon and Carey, [33], was applied along with that of Barlow, [14], in an attempt to identify them. This led to the development of an original patch selection strategy for which the final algorithm is as detailed in Section (4.3.2).

For the J-H estimator implementation the presence of the transition elements produced additional jump terms on the interior of each transition element and on the transition element edges as discussed in Section (4.4.3). This complicated the estimator implementation as all transition elements were thus required to be treated as 'composite' elements - a term given in this work to signify that the element consists of a number of 'sub-element' regions. The implementation of the J-H estimator requires the computation of interpolation error constants $C^i_{1,k}$ and $C^i_{2,k}$ as discussed in Section (4.4.4). Upon the addition of transition elements it was thus necessary to also compute the interpolation error constants for the transition element family for use in the J-H estimator. This led to the development of a general technique for computing such constants and progressed to produce a catalogue of results beginning in Chapter 5 with scalar valued problems in both one and two dimensions and continuing in Chapter 6 for vector valued problems in two dimensions, namely those of linear elasticity and plate theory. It is hoped that this will be of use for future modellers and current implementations of this type of estimator as the values are believed to be more accurate than the bounds given by Johnson and Hansbo in [27].

The application to plates for the Z-Z and J-H estimators can be seen in Sections (4.3) and (4.5) respectively. It was found that the Z-Z estimator implementation was straightforward and also that the J-H implementation could be performed whilst retaining some similarities with the original estimator. Results for the two estimators applied to plate test problems can be seen in Section (7.2) where it is shown that again the estimators perform well as observed for the linear elasticity tests. The estimators are finally applied to a physical problem in Section (7.3) and once again shown to be reliable and perform well even when the model is enhanced to consider the layers present in the physical plate.

It has been observed that the plate model is able to cope well with varying material properties and plate thicknesses. This is particularly apparent in the case of the physical problem where the model provides good agreement with the physically observed data. This is a good result especially when considering that the model in this case uses material properties which themselves have been determined experimentally and thus susceptible to experimental error themselves.

Many enhancements have been recommended for the Z-Z estimator as discussed in Chapter 1. For the estimator implementation described in this work it is thought that an area which could be improved lies in the determination of the optimal sampling points and the subsequent patch selection strategy for use in the recovery procedure. Although the analysis of Mackinnon and Carey, [33], was able to highlight regions where the optimal sample point locations reside, the estimator could benefit from an application similar to that described by Babuška et al., [9], where regions over the elements could be identified as having a certain degree of superconvergence or η%-superconvergence. In this way it is possible that new sample point locations could be established leading to a new patch selection strategy. It is felt, however, that any patch selection strategy over meshes of the type met in this work will contain some degree of compromise since the problem of making each patch selection and corresponding set of sampling points optimal is a complex task.

Results from Chapter 7 have highlighted the importance of obtaining a calibration constant, $\mathcal{C}$, in order to decrease the global J-H error estimate which will otherwise overestimate. It has been observed that the degree of overestimation can be quite large but at the same time it has been shown to remain constant for different problems in both linear elasticity and plate theory provided that the material and physical properties are retained across the problems. It is thought that the need for such a calibration constant is due to the magnitudes of the computed interpolation error constants which themselves depend upon the choice of material and physical properties of the problems. In Section (7.2) it was noted that the use of a single calibration constant could be improved, however, by obtaining a set of calibration constants. In this way a calibration constant could be obtained for each of the transition element family of elements for use in adaptive analyses. These calibration constants could be obtained in the same way as the original constant $\mathcal{C}$ is for the standard element using a sequence of successively refined uniform meshes. In the case of transition elements the uniform meshes should be constructed from entirely those elements for which the calibration constant is sought. In this way a calibration constant $\mathcal{C}_1$ for example could be obtained for the interpolation error constants of the 1-irregular element by considering the successive uniform refinement of meshes of the type shown in Figure (8.1a). It can be seen from this figure that the

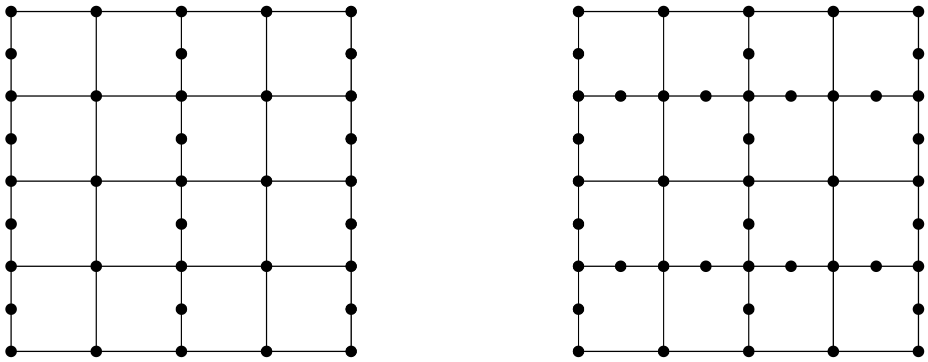

(a) 1-irregular element mesh (b) 2_{adj}-irregular element mesh

Figure 8.1: Uniform meshes constructed from (a) 1-irregular and (b) 2_{adj}-irregular transition elements.

mesh is constructed entirely from 1-irregular elements. Similarly Figure (8.1b) shows a uniform mesh constructed entirely from 2_{adj}-irregular elements. This can also be performed for the 2_{opp}-irregular and 3-irregular elements as illustrated in parts (a) and (b) of Figure (8.2) respectively.

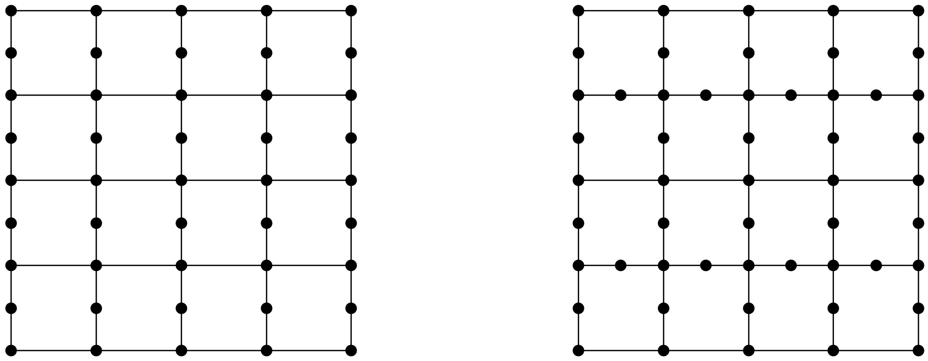

(a) 2_{opp}-irregular element mesh (b) 3-irregular element mesh

Figure 8.2: Uniform meshes constructed from (a) 2_{opp}-irregular and (b) 3-irregular transition elements.

In this way it is felt that a set of calibration constants could be obtained, each of which would be tuned for the corresponding transition element for use in scaling the contributions from each of these elements in the global error estimate.

The refinement procedure of longest edge element bisection adopted for meshes comprising of triangular elements was taken from previous work by the author in [32]. The algorithm for doing this is similar to that proposed by Rivara, [43], [44], and leads to conforming triangulations with no irregular nodes. A possible improvement here would be to use the 'red-green' refinement strategy of Bank, [12], whereby elements required to be refined are split into four 'sons' by connecting the midpoints of the parent triangle in a process known as the red refinement stage. Such a refinement is illustrated in Figure (8.3a) for the darker shaded parent element. The three neighbouring elements

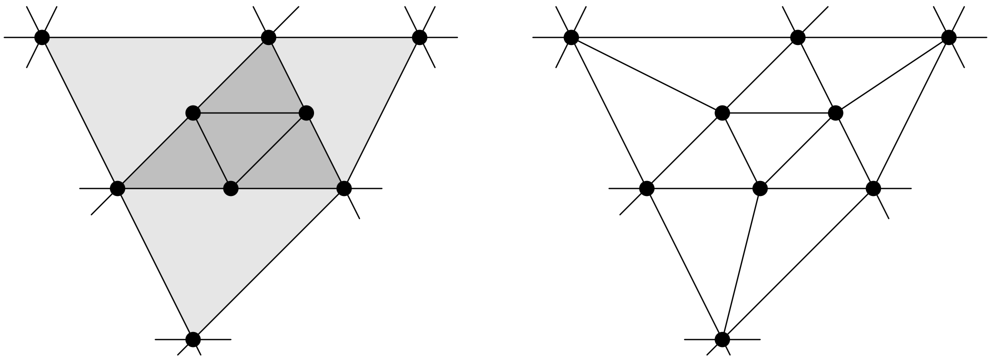

(a) red refinement of parent element (b) Red and green refinements complete

Figure 8.3: Illustration of red-green refinement on a general triangulation.

of the original parent element will thus have irregular midside nodes. These are also shown in Figure (8.3a) as shaded elements. These elements are then bisected in what is termed the green refinement stage to produce two elements each and thus 'removing' the irregular node as illustrated in Figure

(8.3b). The green refinements are, however, temporary and used only to remove the irregular nodes from the mesh, upon subsequent mesh refinements they may thus be removed and replaced if necessary with red refinements. A difficulty which may occur with this adaptive process is in the case where more than one neighbour of an element has been red refined. In such a case this will lead to the element having more than one irregular midside node as illustrated for element T in Figure (8.4a). The solution to this problem is simple and found by immediately adopting

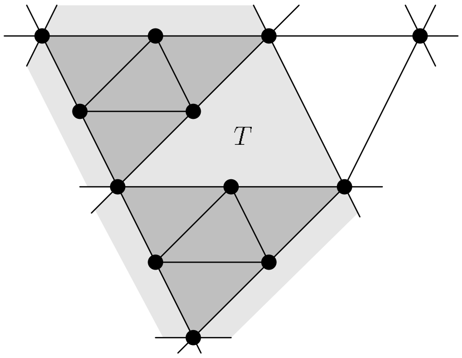

(a) Element T with two midside nodes

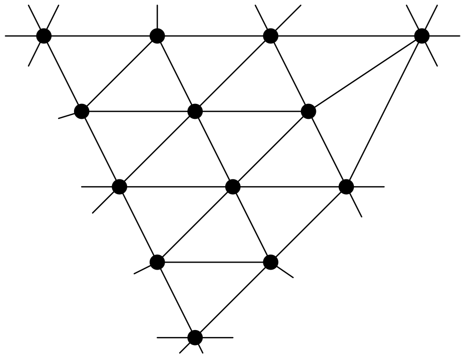

(b) Final red-green refined mesh

Figure 8.4: Red refinement of element T having two irregular midside nodes.

red refinement for element T itself with all neighbours subsequently green refined leading to the mesh shown in Figure (8.4b). This adaptive process has the desirable property in that the shape regularity of the parent element is inherited by the sons upon red refinement as can be clearly seen in Figures (8.3) and (8.4).

For meshes comprising quadrilateral elements a method for refinement is less obvious. In the absence of an automatic mesh generator it was thus decided that transition elements would be used for adaptivity as previously discussed. These elements enable a transition from coarse to fine mesh areas and enable elements in the fine region to be subdivided into four smaller elements which have the same aspect ratios as their parent element. Due to this technique a simple refinement scheme was used as detailed in Section (7.1.4) in which an element was refined if the element indicator value failed a 'local' tolerance test. It is accepted that this technique could be elaborated upon by employing the estimator to give some idea of a new h value for elements but this would not lend itself particularly well to the transition element implementation. A possible enhancement would be to refine the elements into a larger number of smaller elements instead of simply bisecting. Care would be required here, however, due to possible 'pollution' effects in which errors can manifest themselves in areas of the mesh due to inaccuracies elsewhere as noted by Bank, [12].

As a final possible enhancement it is thought that the plate adaptation of the J-H estimator could possibly benefit from being structured in a different way. From the plate equilibrium equations given by Equations (2.39)-(2.43) it can be seen that Equations (2.39) and (2.40) are concerned solely with the in-plane displacements u and v. This may thus be thought of as the in-plane elastic part of the model whilst the more unusual plate degrees of freedom w, ψ_1 and ψ_2 are coupled by

Equations (2.41)-(2.43) which may be thought of as the plate elastic part. In Section (4.5) the plate bilinear form was expressed in terms of a bending and transverse shear part as,

$$a(\mathbf{u}, \mathbf{v}) \equiv \int_\Omega \mathcal{A}\, d\mathbf{x} + \int_\Omega \mathcal{B}\, d\mathbf{x},$$

where,

$$\mathcal{A} = \left(\mathbf{B}^b \mathbf{u}\right)^T \mathbf{C}^b \left(\mathbf{B}^b \mathbf{v}\right) \quad \text{and} \quad \mathcal{B} = \left(\mathbf{B}^s \mathbf{u}\right)^T \mathbf{C}^s \left(\mathbf{B}^s \mathbf{v}\right),$$

and where the components of $\mathcal{A}$ and $\mathcal{B}$ are as given in Equations (3.32) and (3.33). Following the observation on the equilibrium equation coupling it is possible to partition both $\mathbf{u}$ and $\mathbf{v}$ into their respective in-plane elastic and plate elastic parts,

$$\mathbf{u} = \begin{bmatrix} u \\ v \\ w \\ \psi_1 \\ \psi_2 \end{bmatrix} = \mathbf{u}^e + \mathbf{u}^p = \begin{bmatrix} u \\ v \\ 0 \\ 0 \\ 0 \end{bmatrix} + \begin{bmatrix} 0 \\ 0 \\ w \\ \psi_1 \\ \psi_2 \end{bmatrix} \quad \text{and} \quad \mathbf{v} = \begin{bmatrix} v_1 \\ v_2 \\ v_3 \\ v_4 \\ v_5 \end{bmatrix} = \mathbf{v}^e + \mathbf{v}^p = \begin{bmatrix} v_1 \\ v_2 \\ 0 \\ 0 \\ 0 \end{bmatrix} + \begin{bmatrix} 0 \\ 0 \\ v_3 \\ v_4 \\ v_5 \end{bmatrix},$$

where superscripts e and p have been used to signify the in-plane elastic and plate elastic parts respectively. In addition, let $\mathbf{u}_e = [u, v]^T$, $\mathbf{u}_p = [w, \psi_1, \psi_2]^T$, $\mathbf{v}_e = [v_1, v_2]^T$ and $\mathbf{v}_p = [v_3, v_4, v_5]^T$ denote the non-zero parts of $\mathbf{u}^e$, $\mathbf{u}^p$, $\mathbf{v}^e$ and $\mathbf{v}^p$ respectively where use is now made of subscripts e and p. It is thus possible to now express the bilinear form as,

$$\begin{aligned} a(\mathbf{u}, \mathbf{v}) &= a(\mathbf{u}^e + \mathbf{u}^p, \mathbf{v}^e + \mathbf{v}^p) \\ &= a(\mathbf{u}^e, \mathbf{v}^e) + a(\mathbf{u}^e, \mathbf{v}^p) + a(\mathbf{u}^p, \mathbf{v}^e) + a(\mathbf{u}^p, \mathbf{v}^p). \end{aligned}$$

This enables integrands $\mathcal{A}$ and $\mathcal{B}$ to be expressed as,

$$\mathcal{A} = \mathcal{A}_{ee} + \mathcal{A}_{ep} + \mathcal{A}_{pe} + \mathcal{A}_{pp} \quad \text{and} \quad \mathcal{B} = \mathcal{B}_{ee} + \mathcal{B}_{ep} + \mathcal{B}_{pe} + \mathcal{B}_{pp},$$

where the components of $\mathcal{A}$ are given as,

$$\begin{aligned} \mathcal{A}_{ee} &= \left[A_{11}\frac{\partial u}{\partial x_1} + A_{12}\frac{\partial v}{\partial x_2} + A_{14}\left(\frac{\partial u}{\partial x_2} + \frac{\partial v}{\partial x_1}\right)\right]\frac{\partial v_1}{\partial x_1} \\ &+ \left[A_{12}\frac{\partial u}{\partial x_1} + A_{22}\frac{\partial v}{\partial x_2} + A_{24}\left(\frac{\partial u}{\partial x_2} + \frac{\partial v}{\partial x_1}\right)\right]\frac{\partial v_2}{\partial x_2} \\ &+ \left[A_{14}\frac{\partial u}{\partial x_1} + A_{24}\frac{\partial v}{\partial x_2} + A_{44}\left(\frac{\partial u}{\partial x_2} + \frac{\partial v}{\partial x_1}\right)\right]\left(\frac{\partial v_1}{\partial x_2} + \frac{\partial v_2}{\partial x_1}\right), \end{aligned}$$

$$\begin{aligned} \mathcal{A}_{ep} &= \left[B_{11}\frac{\partial u}{\partial x_1} + B_{12}\frac{\partial v}{\partial x_2} + B_{14}\left(\frac{\partial u}{\partial x_2} + \frac{\partial v}{\partial x_1}\right)\right]\frac{\partial v_4}{\partial x_1} \\ &+ \left[B_{12}\frac{\partial u}{\partial x_1} + B_{22}\frac{\partial v}{\partial x_2} + B_{24}\left(\frac{\partial u}{\partial x_2} + \frac{\partial v}{\partial x_1}\right)\right]\frac{\partial v_5}{\partial x_2} \\ &+ \left[B_{14}\frac{\partial u}{\partial x_1} + B_{24}\frac{\partial v}{\partial x_2} + B_{44}\left(\frac{\partial u}{\partial x_2} + \frac{\partial v}{\partial x_1}\right)\right]\left(\frac{\partial v_4}{\partial x_2} + \frac{\partial v_5}{\partial x_1}\right), \end{aligned}$$

$$\begin{aligned} \mathcal{A}_{pe} &= \left[B_{11}\frac{\partial \psi_1}{\partial x_1} + B_{12}\frac{\partial \psi_2}{\partial x_2} + B_{14}\left(\frac{\partial \psi_1}{\partial x_2} + \frac{\partial \psi_2}{\partial x_1}\right)\right]\frac{\partial v_1}{\partial x_1} \\ &+ \left[B_{12}\frac{\partial \psi_1}{\partial x_1} + B_{22}\frac{\partial \psi_2}{\partial x_2} + B_{24}\left(\frac{\partial \psi_1}{\partial x_2} + \frac{\partial \psi_2}{\partial x_1}\right)\right]\frac{\partial v_2}{\partial x_2} \\ &+ \left[B_{14}\frac{\partial \psi_1}{\partial x_1} + B_{24}\frac{\partial \psi_2}{\partial x_2} + B_{44}\left(\frac{\partial \psi_1}{\partial x_2} + \frac{\partial \psi_2}{\partial x_1}\right)\right]\left(\frac{\partial v_1}{\partial x_2} + \frac{\partial v_2}{\partial x_1}\right), \end{aligned}$$

and

$$\begin{aligned}
\mathcal{A}_{pp} &= \left[D_{11}\frac{\partial\psi_1}{\partial x_1} + D_{12}\frac{\partial\psi_2}{\partial x_2} + D_{14}\left(\frac{\partial\psi_1}{\partial x_2} + \frac{\partial\psi_2}{\partial x_1}\right)\right]\frac{\partial v_4}{\partial x_1} \\
&+ \left[D_{12}\frac{\partial\psi_1}{\partial x_1} + D_{22}\frac{\partial\psi_2}{\partial x_2} + D_{24}\left(\frac{\partial\psi_1}{\partial x_2} + \frac{\partial\psi_2}{\partial x_1}\right)\right]\frac{\partial v_5}{\partial x_2} \\
&+ \left[D_{14}\frac{\partial\psi_1}{\partial x_1} + D_{24}\frac{\partial\psi_2}{\partial x_2} + D_{44}\left(\frac{\partial\psi_1}{\partial x_2} + \frac{\partial\psi_2}{\partial x_1}\right)\right]\left(\frac{\partial v_4}{\partial x_2} + \frac{\partial v_5}{\partial x_1}\right).
\end{aligned}$$

For the components of $\mathcal{B}$ is it found that $\mathcal{B}_{ee} = \mathcal{B}_{ep} = \mathcal{B}_{pe} = 0$ whilst,

$$\begin{aligned}
\mathcal{B}_{pp} &= \left[A_{55}\left(\psi_1 + \frac{\partial w}{\partial x_1}\right) + A_{56}\left(\psi_2 + \frac{\partial w}{\partial x_2}\right)\right]\left(v_4 + \frac{\partial v_3}{\partial x_1}\right) \\
&+ \left[A_{56}\left(\psi_1 + \frac{\partial w}{\partial x_1}\right) + A_{66}\left(\psi_2 + \frac{\partial w}{\partial x_2}\right)\right]\left(v_5 + \frac{\partial v_3}{\partial x_2}\right),
\end{aligned}$$

where, in the above, A_{ij}, B_{ij}, D_{ij} for $i,j = 1,2,4$ are as given in Equation (2.50) and A_{ij} for $i,j = 5,6$ are as given in Equation (2.51). It can be seen in the above forms of $\mathcal{A}_{ee}, \mathcal{A}_{ep}, \mathcal{A}_{pe}$ and $\mathcal{A}_{pp}$ that the terms in square brackets together form the stress and bending moment resultants given in Equations (2.52) and (2.53) which shall be expressed here in the forms,

$$\begin{bmatrix} N_1 \\ N_2 \\ N_4 \end{bmatrix} = \begin{bmatrix} N_1^A \\ N_2^A \\ N_4^A \end{bmatrix} + \begin{bmatrix} N_1^B \\ N_2^B \\ N_4^B \end{bmatrix} \quad \text{and} \quad \begin{bmatrix} M_1 \\ M_2 \\ M_4 \end{bmatrix} = \begin{bmatrix} M_1^B \\ M_2^B \\ M_4^B \end{bmatrix} + \begin{bmatrix} M_1^D \\ M_2^D \\ M_4^D \end{bmatrix},$$

where the superscripts A, B and D are used to denote the use of matrices $\mathbf{A}$, $\mathbf{B}$ and $\mathbf{D}$ respectively. In a similar way, the terms in the square brackets of $\mathcal{B}_{pp}$ are in fact the shear force resultants Q_5 and Q_6 as given in Equation (2.54). Substitution of these into the above yields,

$$\begin{aligned}
\mathcal{A}_{ee} &= N_1^A\frac{\partial v_1}{\partial x_1} + N_2^A\frac{\partial v_2}{\partial x_2} + N_4^A\left(\frac{\partial v_1}{\partial x_2} + \frac{\partial v_2}{\partial x_1}\right), \\
\mathcal{A}_{ep} &= N_1^B\frac{\partial v_4}{\partial x_1} + N_2^B\frac{\partial v_5}{\partial x_2} + N_4^B\left(\frac{\partial v_4}{\partial x_2} + \frac{\partial v_5}{\partial x_1}\right), \\
\mathcal{A}_{pe} &= M_1^B\frac{\partial v_1}{\partial x_1} + M_2^B\frac{\partial v_2}{\partial x_2} + M_4^B\left(\frac{\partial v_1}{\partial x_2} + \frac{\partial v_2}{\partial x_1}\right), \\
\mathcal{A}_{pp} &= M_1^D\frac{\partial v_4}{\partial x_1} + M_2^D\frac{\partial v_5}{\partial x_2} + M_4^D\left(\frac{\partial v_4}{\partial x_2} + \frac{\partial v_5}{\partial x_1}\right),
\end{aligned}$$

and

$$\mathcal{B}_{pp} = Q_5\left(v_4 + \frac{\partial v_3}{\partial x_1}\right) + Q_6\left(v_5 + \frac{\partial v_3}{\partial x_2}\right),$$

with the bilinear form expressed now as,

$$a(\mathbf{u},\mathbf{v}) \equiv \int_\Omega \mathcal{A}_{ee} + \mathcal{A}_{ep} + \mathcal{A}_{pe} + \mathcal{A}_{pp}\,d\mathbf{x} + \int_\Omega \mathcal{B}_{pp}\,d\mathbf{x}.$$

As performed for the estimator in Section (4.5) consider the integrals over Ω now as summations of integral contributions taken over each element Ω_k for $k = 1,\ldots,N$. It is then possible to show, via integration by parts and using the notation $\mathbf{v}_{i\blacktriangleright j}$ to denote column vector $[v_i,\ldots,v_j]^T$, that,

$$-a(\mathbf{u},\mathbf{v}) = \sum_{k=1}^{N}\int_{\Omega_k}\left(\operatorname{div}\mathbf{N}^A + \operatorname{div}\mathbf{M}^B\right)\cdot\mathbf{v}_{1\blacktriangleright 2}\,d\mathbf{x} - \sum_{k=1}^{N}\int_{\partial\Omega_k}\left(\mathbf{N}^A + \mathbf{M}^B\right)\cdot\mathbf{n}_k\cdot\mathbf{v}_{1\blacktriangleright 2}\,ds$$

$$
+\sum_{k=1}^{N}\int_{\Omega_k}\left(\operatorname{div}\mathbf{N}^B+\operatorname{div}\mathbf{M}^D\right)\cdot\mathbf{v}_{4\blacktriangleright 5}\,d\mathbf{x}-\sum_{k=1}^{N}\int_{\partial\Omega_k}\left(\mathbf{N}^B+\mathbf{M}^D\right)\cdot\mathbf{n}_k\cdot\mathbf{v}_{4\blacktriangleright 5}\,ds
$$
$$
+\sum_{k=1}^{N}\int_{\Omega_k}\left(\frac{\partial Q_5}{\partial x_1}+\frac{\partial Q_6}{\partial x_2}\right)v_3-\left(Q_5v_4+Q_6v_5\right)\,d\mathbf{x}-\sum_{k=1}^{N}\int_{\partial\Omega_k}\left(Q_5v_3n_1+Q_6v_3n_2\right)\,ds,
$$

with $\mathbf{n}_k$ the unit outward normal to $\partial\Omega_k$ and tensors $\mathbf{N}^A$, $\mathbf{N}^B$, $\mathbf{M}^B$ and $\mathbf{M}^D$ having the form,

$$
\mathbf{N}^A=\begin{bmatrix}N_1^A & N_4^A\\ N_4^A & N_2^A\end{bmatrix},\quad \mathbf{N}^B=\begin{bmatrix}N_1^B & N_4^B\\ N_4^B & N_2^B\end{bmatrix},\quad \mathbf{M}^B=\begin{bmatrix}M_1^B & M_4^B\\ M_4^B & M_2^B\end{bmatrix},\quad \text{and}\quad \mathbf{M}^D=\begin{bmatrix}M_1^D & M_4^D\\ M_4^D & M_2^D\end{bmatrix}.
$$

Using Equation (4.94) it is thus possible to express the error, measured in the energy norm, as,

$$
\begin{aligned}
||\mathbf{e}||^2_{E(\Omega)} = \sum_{k=1}^{N}\int_{\Omega_k} & \left(\operatorname{div}\mathbf{N}_h^A+\operatorname{div}\mathbf{M}_h^B+\mathbf{f}_{1\blacktriangleright 2}\right)\cdot\left(\mathbf{e}_{1\blacktriangleright 2}-\pi_h\mathbf{e}_{1\blacktriangleright 2}\right)\\
& +\left(\operatorname{div}\mathbf{N}_h^B+\operatorname{div}\mathbf{M}_h^D-\mathbf{Q}+\mathbf{f}_{4\blacktriangleright 5}\right)\cdot\left(\mathbf{e}_{4\blacktriangleright 5}-\pi_h\mathbf{e}_{4\blacktriangleright 5}\right)\\
& +\left(\frac{\partial Q_5}{\partial x_1}+\frac{\partial Q_6}{\partial x_2}+f_3\right)\left(e_3-\pi_h e_e\right)\,d\mathbf{x}\\
-\sum_{k=1}^{N}\int_{\partial\Omega_k} & \left(\mathbf{N}_h^A+\mathbf{M}_h^B\right)\cdot\mathbf{n}_k\cdot\left(\mathbf{e}_{1\blacktriangleright 2}-\pi_h\mathbf{e}_{1\blacktriangleright 2}\right)\\
& +\left(\mathbf{N}_h^B+\mathbf{M}_h^D\right)\cdot\mathbf{n}_k\cdot\left(\mathbf{e}_{4\blacktriangleright 5}-\pi_h\mathbf{e}_{4\blacktriangleright 5}\right)+\mathbf{Q}\cdot\mathbf{n}_k\left(e_3-\pi_h e_3\right)\,ds\\
+\int_{\hat\Gamma_1} & N_n(e_1-\pi_h e_1)\,ds+\int_{\hat\Gamma_2}N_s(e_2-\pi_h e_2)\,ds+\int_{\hat\Gamma_3}Q_n(e_3-\pi_h e_3)\,ds\\
+\int_{\hat\Gamma_4} & M_n(e_4-\pi_h e_4)\,ds+\int_{\hat\Gamma_5}M_s(e_5-\pi_h e_5)\,ds.
\end{aligned}
$$

where $\mathbf{Q}=[Q_5,Q_6]^T$ and the h subscript is used to indicate the use of the finite element solution. The above form shows that is is possible to split the error into an in-plane elastic part and terms emanating from the plate degrees of freedom in the model which shall be called the plate elastic part. Unfortunately the presence of material property matrix $\mathbf{B}$ used in $\mathbf{N}_h^B$ and $\mathbf{M}_h^B$ prevents further separation into pure in-plane elastic and plate elastic terms. Upon inspection, however, it is found that for single layer plates and also for the laminated plate modelled in Chapter 7, the matrix $\mathbf{B}$ does equal zero enabling considerable simplifications to be made. In such cases the bilinear form reduces to,

$$
a(\mathbf{u},\mathbf{v})=\int_\Omega\mathcal{A}_{ee}\,d\mathbf{x}+\int_\Omega\mathcal{A}_{pp}\,d\mathbf{x}+\int_\Omega\mathcal{B}_{pp}\,d\mathbf{x},
$$

enabling the creation of in-plane elastic and plate elastic bilinear forms $a_e(\mathbf{u}_e,\mathbf{v}_e)$ and $a_p(\mathbf{u}_p,\mathbf{v}_p)$, expressed as,

$$
a_e(\mathbf{u}_e,\mathbf{v}_e)=\int_\Omega\mathcal{A}_{ee}\,d\mathbf{x}\quad\text{and}\quad a_p(\mathbf{u}_p,\mathbf{v}_p)=\int_\Omega\mathcal{A}_{pp}\,d\mathbf{x}+\int_\Omega\mathcal{B}_{pp}\,d\mathbf{x},
$$

and thus the corresponding energy norms given by,

$$
||\mathbf{u}_e||^2_{E_e(\Omega)}=a_e(\mathbf{u}_e,\mathbf{u}_e)\quad\text{and}\quad||\mathbf{u}_p||^2_{E_p(\Omega)}=a_p(\mathbf{u}_p,\mathbf{u}_p).
$$

The bilinear form may thus be expressed, by integrating by parts over elemental contributions as,

$$
\begin{aligned}
a(\mathbf{u},\mathbf{v}) &= \sum_{k=1}^{N}\int_{\Omega_k}\operatorname{div}\mathbf{T}_e\cdot\mathbf{v}_e\,d\mathbf{x}-\sum_{k=1}^{N}\int_{\partial\Omega_k}\mathbf{T}_e\cdot\mathbf{n}_k\cdot\mathbf{v}_e\,ds\\
&\quad+\sum_{k=1}^{N}\int_{\Omega_k}\operatorname{div}\mathbf{T}_p\cdot\mathbf{v}_p\,d\mathbf{x}-\sum_{k=1}^{N}\int_{\partial\Omega_k}\mathbf{T}_p\cdot\mathbf{n}_k\cdot\mathbf{v}_p\,ds,
\end{aligned}
$$

where $\mathbf{v}_e \equiv \mathbf{v}_{1\blacktriangleright 2}$ and $\mathbf{v}_p \equiv \mathbf{v}_{3\blacktriangleright 5}$ form the partition of $\mathbf{v}$ as introduced earlier into in-plane elastic and plate elastic portions and $\mathbf{T}_e(\mathbf{u}_e) \equiv \mathbf{T}_e$ and $\mathbf{T}_p(\mathbf{u}_p) \equiv \mathbf{T}_p$ form a partition of $\mathbf{T}$, given in Equation (4.96), and which have the form,

$$\mathbf{T}_e = \begin{bmatrix} N_1^A & N_4^A \\ N_4^A & N_2^A \end{bmatrix}, \quad \mathbf{T}_p = \begin{bmatrix} Q_5 & Q_6 \\ M_1^D & M_4^D \\ M_4^D & M_2^D \end{bmatrix} \quad \text{and} \quad \mathbf{q} = \begin{bmatrix} 0 \\ Q_5 \\ Q_6 \end{bmatrix}.$$

By again using Equation (4.94) the error may thus be expressed as,

$$\begin{aligned}
||\mathbf{e}||^2_{E(\Omega)} &= ||\mathbf{e}_e||^2_{E_e(\Omega)} + ||\mathbf{e}_p||^2_{E_p(\Omega)} \\
&= \sum_{k=1}^{N} \int_{\Omega_k} \left(\operatorname{div} \mathbf{T}_e^h + \mathbf{f}_e\right) \cdot (\mathbf{e}_e - \pi_h \mathbf{e}_e)\ d\mathbf{x} - \sum_{s \in S} \int_s \left[\mathbf{T}_e^h \mathbf{n}_s\right] \cdot (\mathbf{e}_e - \pi_h \mathbf{e}_e)\ ds \\
&+ \sum_{k=1}^{N} \int_{\Omega_k} \left(\operatorname{div} \mathbf{T}_p^h - \mathbf{q} + \mathbf{f}_p\right) \cdot (\mathbf{e}_p - \pi_h \mathbf{e}_p)\ d\mathbf{x} - \sum_{s \in S} \int_s \left[\mathbf{T}_p^h \mathbf{n}_s\right] \cdot (\mathbf{e}_p - \pi_h \mathbf{e}_p)\ ds \\
&+ \int_{\hat{\Gamma}_1} \left(N_n - N_n^h\right)(e_1 - \pi_h e_1)\ ds + \int_{\hat{\Gamma}_2} \left(N_s - N_s^h\right)(e_2 - \pi_h e_2)\ ds \\
&+ \int_{\hat{\Gamma}_3} \left(Q_n - Q_n^h\right)(e_3 - \pi_h e_3)\ ds \\
&+ \int_{\hat{\Gamma}_4} \left(M_n - M_n^h\right)(e_4 - \pi_h e_4)\ ds + \int_{\hat{\Gamma}_5} \left(M_s - M_s^h\right)(e_5 - \pi_h e_5)\ ds,
\end{aligned}$$

where use has once again been made of the set S of internal edges introduced in Section (4.4) and where the terms above in square brackets denote jump terms as described in Equation (4.100) measured across each internal edge $s \in S$. It has thus been shown that it is possible to express the error in terms of part concerned solely with the in-plane displacements u and v and which has been termed the in-plane elastic part and a part concerned solely with plate degrees of freedom w, ψ_1 and ψ_2 termed the plate elastic part. Both parts are signified in the above with subscripts e and p respectively as previously described.

Once this has been done it is possible to proceed in a similar way to that in Section (4.5) by working on the components of the above expression. This is firstly done by writing the error as,

$$||\mathbf{e}||^2_{E(\Omega)} = ||\mathbf{e}_e||^2_{E_e(\Omega)} + ||\mathbf{e}_p||^2_{E_p(\Omega)} = E_1^e + E_2^e + E_1^p + E_2^p, \tag{8.1}$$

where,

$$\begin{aligned}
E_1^e &= \sum_{k=1}^{N} \int_{\Omega_k} \mathcal{R}_1^e(\mathbf{u}_h^e) \cdot (\mathbf{e}_e - \pi_h \mathbf{e}_e)\ d\mathbf{x}, \\
E_2^e &= \sum_{k=1}^{N} \int_{\partial\Omega} h_k \mathcal{R}_2^e(\mathbf{u}_h^e) \cdot (\mathbf{e}_e - \pi_h \mathbf{e}_e)\ ds, \\
E_1^p &= \sum_{k=1}^{N} \int_{\Omega_k} \mathcal{R}_1^p(\mathbf{u}_h^p) \cdot (\mathbf{e}_p - \pi_h \mathbf{e}_p)\ d\mathbf{x}, \\
E_2^p &= \sum_{k=1}^{N} \int_{\partial\Omega} h_k \mathcal{R}_2^p(\mathbf{u}_h^p) \cdot (\mathbf{e}_p - \pi_h \mathbf{e}_p)\ ds,
\end{aligned}$$

and where, for the in-plane elastic parts,

$$\mathcal{R}_1^e(\mathbf{u}_h^e) = \operatorname{div}\mathbf{T}_e^h + \mathbf{f}_e \text{ on } \Omega_k,$$

along with,

$$\mathcal{R}_2^e(\mathbf{u}_h^e) = \begin{cases} \frac{1}{2h_k}\left[\mathbf{T}_e\mathbf{n}_s\right], & \text{on } s \in \partial\Omega_k \setminus \partial\Omega \text{ for each } \Omega_k, \\ \frac{1}{h_k}\left[N_n - N_n^h, 0\right]^T, & \text{on } \partial\Omega_k \cap \hat{\Gamma}_1, \\ \frac{1}{h_k}\left[0, N_s - N_s^h\right]^T, & \text{on } \partial\Omega_k \cap \hat{\Gamma}_2. \end{cases}$$

Similarly, for the plate elastic parts,

$$\mathcal{R}_1^p(\mathbf{u}_h^p) = \operatorname{div}\mathbf{T}_p^h - \mathbf{q} + \mathbf{f}_p \text{ on } \Omega_k,$$

along with,

$$\mathcal{R}_2^p(\mathbf{u}_h^p) = \begin{cases} \frac{1}{2h_k}\left[\mathbf{T}_p\mathbf{n}_s\right], & \text{on } s \in \partial\Omega_k \setminus \partial\Omega \text{ for each } \Omega_k, \\ \frac{1}{h_k}\left[Q_n - Q_n^h, 0, 0\right]^T, & \text{on } \partial\Omega_k \cap \hat{\Gamma}_3, \\ \frac{1}{h_k}\left[0, M_n - M_n^h, 0\right], & \text{on } \partial\Omega_k \cap \hat{\Gamma}_4, \\ \frac{1}{h_k}\left[0, 0, M_s - M_s^h\right], & \text{on } \partial\Omega_k \cap \hat{\Gamma}_5. \end{cases}$$

Application of the Cauchy-Schwarz inequality enables the quantities E_1^e, E_2^e, E_1^p and E_2^p to be bounded as,

$$|E_1^e| \leq \left[\sum_{k=1}^N \left[C_{1,k}^{i,e} h_k \|\mathcal{R}_1^e(\mathbf{u}_h^e)\|_{L_2(\Omega_k)}\right]^2\right]^{\frac{1}{2}} \|\mathbf{e}_e\|_{E_e(\Omega)},$$

$$|E_2^e| \leq \left[\sum_{k=1}^N \left[C_{2,k}^{i,e} h_k^{\frac{1}{2}} \|h_k\mathcal{R}_2^e(\mathbf{u}_h^e)\|_{L_2(\partial\Omega_k)}\right]^2\right]^{\frac{1}{2}} \|\mathbf{e}_e\|_{E_e(\Omega)},$$

$$|E_1^p| \leq \left[\sum_{k=1}^N \left[C_{1,k}^{i,p} h_k \|\mathcal{R}_1^p(\mathbf{u}_h^p)\|_{L_2(\Omega_k)}\right]^2\right]^{\frac{1}{2}} \|\mathbf{e}_p\|_{E_p(\Omega)},$$

$$|E_2^p| \leq \left[\sum_{k=1}^N \left[C_{2,k}^{i,p} h_k^{\frac{1}{2}} \|h_k\mathcal{R}_2^p(\mathbf{u}_h^p)\|_{L_2(\partial\Omega_k)}\right]^2\right]^{\frac{1}{2}} \|\mathbf{e}_p\|_{E_p(\Omega)},$$

with suitably defined interplation error constants $C_{1,k}^{i,e}$, $C_{2,k}^{i,e}$, $C_{1,k}^{i,p}$ and $C_{2,k}^{i,p}$ to be given below. The error due to the in-plane elastic part may thus be expressed,

$$\|\mathbf{e}_e\|_{E_e(\Omega)} \leq \left[\sum_{k=1}^N \left[C_{1,k}^{i,e} h_k \|\mathcal{R}_1^e(\mathbf{u}_h^e)\|_{L_2(\Omega_k)}\right]^2\right]^{\frac{1}{2}} + \left[\sum_{k=1}^N \left[C_{2,k}^{i,e} h_k^{\frac{1}{2}} \|h_k\mathcal{R}_2^e(\mathbf{u}_h^e)\|_{L_2(\partial\Omega_k)}\right]^2\right]^{\frac{1}{2}}, \quad (8.2)$$

whilst for the plate elastic part,

$$\|\mathbf{e}_p\|_{E_p(\Omega)} \leq \left[\sum_{k=1}^N \left[C_{1,k}^{i,p} h_k \|\mathcal{R}_1^p(\mathbf{u}_h^p)\|_{L_2(\Omega_k)}\right]^2\right]^{\frac{1}{2}} + \left[\sum_{k=1}^N \left[C_{2,k}^{i,p} h_k^{\frac{1}{2}} \|h_k\mathcal{R}_2^p(\mathbf{u}_h^p)\|_{L_2(\partial\Omega_k)}\right]^2\right]^{\frac{1}{2}}. \quad (8.3)$$

These bounds may then be used in Equation (8.1) to give an alternatively constructed error estimate,

$$\begin{aligned}
||\mathbf{e}||^2_{E(\Omega)} &= ||\mathbf{e}_e||^2_{E_e(\Omega)} + ||\mathbf{e}_p||^2_{E_p(\Omega)} \\
&\leq ||\mathbf{e}_e||^2_{E_e(\Omega)} + ||\mathbf{e}_p||^2_{E_p(\Omega)} + 2||\mathbf{e}_e||_{E_e(\Omega)}||\mathbf{e}_p||_{E_p(\Omega)} \\
&= \left(||\mathbf{e}_e||_{E_e(\Omega)} + ||\mathbf{e}_p||_{E_p(\Omega)}\right)^2,
\end{aligned}$$

This enables the error to be expressed as,

$$||\mathbf{e}||_{E(\Omega)} \leq ||\mathbf{e}_e||_{E_e(\Omega)} + ||\mathbf{e}_p||_{E_p(\Omega)},$$

in which the substitution of the quantities $||\mathbf{e}_e||_{E_e(\Omega)}$ and $||\mathbf{e}_p||_{E_p(\Omega)}$ can be done by employing Equations (8.2) and (8.3) respectively.

One of the main reasons for constructing this alternative formulation is due to the fact that the interpolation error constants can be computed in a similar way to those before but now may be considered for the in-plane elastic part and the plate elastic part separately. These constants may thus be expressed as,

$$C^{i,e}_{1,k} = \sup_{\boldsymbol{\alpha}_e \in V^e_\epsilon} \frac{h_k^{-1}||\boldsymbol{\alpha}_e - \pi_h \boldsymbol{\alpha}_e||_{L_2(\Omega_k)}}{||\boldsymbol{\alpha}_e||_{E_e(\Omega_k)}} \quad \text{and} \quad C^{i,e}_{2,k} = \sup_{\boldsymbol{\alpha}_e \in V^e_\epsilon} \frac{h_k^{-\frac{1}{2}}||\boldsymbol{\alpha}_e - \pi_h \boldsymbol{\alpha}_e||_{L_2(\partial\Omega_k)}}{||\boldsymbol{\alpha}_e||_{E_e(\Omega_k)}}, \qquad (8.4)$$

for the in-plane elastic part whilst for the plate elastic part,

$$C^{i,p}_{1,k} = \sup_{\boldsymbol{\alpha}_p \in V^p_\epsilon} \frac{h_k^{-1}||\boldsymbol{\alpha}_p - \pi_h \boldsymbol{\alpha}_p||_{L_2(\Omega_k)}}{||\boldsymbol{\alpha}_p||_{E_p(\Omega_k)}} \quad \text{and} \quad C^{i,p}_{2,k} = \sup_{\boldsymbol{\alpha}_p \in V^p_\epsilon} \frac{h_k^{-\frac{1}{2}}||\boldsymbol{\alpha}_p - \pi_h \boldsymbol{\alpha}_p||_{L_2(\partial\Omega_k)}}{||\boldsymbol{\alpha}_p||_{E_p(\Omega_k)}}, \qquad (8.5)$$

where there are strong similarities between Equations (8.4) and (8.5) and the original constants given in Equations (5.3) and (5.4) which originate from Johnson and Hansbo, [27]. In the above it can be seen that spaces V^e_ϵ and V^p_ϵ have been used in accordance with Appendix E. As previously, the superscripts e and p again correspond to the in-plane elastic and plate elastic degrees of freedom and thus form the constituents of the two spaces respectively.

The splitting of the estimator enables the denominator for the in-plane elastic interpolation error constants $C^{i,e}_{1,k}$ and $C^{i,e}_{2,k}$ to involve only matrix $\mathbf{A}$ which was introduced in Equation (2.44). The elements of this matrix are as given in Equation (2.33) where it can be seen that they are obtained by integrating the elements of the material constitutive matrix over the plate thickness or alternatively by Equation (2.50) for the laminated plate model where the integration is performed over each laminate. The denominator for the plate elastic interpolation error constants $C^{i,p}_{1,k}$ and $C^{i,p}_{2,k}$ involves matrix $\mathbf{D}$ which was introduced in Equation (2.45) and the terms A_{ij} for $i, j = 5, 6$ as given in Equation (2.47). In a similar way to matrix $\mathbf{A}$ the elements of $\mathbf{D}$ are obtained by using either Equation (2.33) or (2.50) depending upon whether the model is a single layer plate or has laminates. It can be seen that the elements of matrix $\mathbf{D}$ have an additional thickness term squared in the integrand meaning that as the thickness tends to zero the elements of $\mathbf{D}$ will tend to zero at a faster rate than those of $\mathbf{A}$. Since the estimator formulation given in Section (4.5) involves no splitting into in-plane elastic and plate elastic parts the computation of interpolation error constants involves both **A** and **D** and consequently a mixing of thickness powers. It is felt that the new formulation in which the matrices **A** and **D** have been split will be free of this feature and be able to give constants for the in-plane elastic part which have not been 'polluted' by the presence of the plate elastic terms.

Initial investigations into this for the plate test problems quickly show the advantage of the 'split' formulation. For such problems the original interpolation error constant values were found to be,

$$C^i_{1,k} = 94.049218 \quad \text{and} \quad C^i_{2,k} = 183.711731, \tag{8.6}$$

for elements $\Omega_k,\ k = 1, \ldots, N$ on uniform meshes of N quadrilateral elements for example. By computing the new interpolation error constant values, it is found that for the in-plane elastic part,

$$C^{i,e}_{1,k} = 2.714967 \quad \text{and} \quad C^{i,e}_{2,k} = 5.303301, \tag{8.7}$$

whilst for the plate elastic part,

$$C^{i,p}_{1,k} = 94.049218 \quad \text{and} \quad C^{i,p}_{2,k} = 183.711731, \tag{8.8}$$

and where it can be seen that $C^{i,p}_{1,k} = C^i_{1,k}$ and $C^{i,p}_{2,k} = C^i_{2,k}$. The computation of these constants follows the methodology given in Section (6.2) where the problem of finding a supremum of the type given in Equations (8.4) and (8.5) is transformed onto a standard element and the constant values then expressed as,

$$\left(C^i_j\right)^2 = \sup_{\mathbf{x}\in\mathbb{R}^{5n}} \frac{\mathbf{x}^T\mathbf{F}\mathbf{x}}{\mathbf{x}^T\mathbf{E}\mathbf{x}}, \quad \text{for } j = 1 \text{ or } 2,$$

where the element stiffness matrix **E** and matrix **F** which results from the interpolation error are as given in Section (6.2.2). In this original guise the matrices **E** and **F** involve components from both the in-plane elastic and plate elastic parts of the model as previously discussed. Since these parts are uncoupled it is possible, via the interchanging of rows and columns, to express,

$$\mathbf{E} = \begin{bmatrix} \mathbf{E}_e & \mathbf{0} \\ \mathbf{0}^T & \mathbf{E}_p \end{bmatrix} \equiv \mathbf{E}_s \quad \text{and} \quad \mathbf{F} = \begin{bmatrix} \mathbf{F}_e & \mathbf{0} \\ \mathbf{0}^T & \mathbf{F}_p \end{bmatrix} \equiv \mathbf{F}_s,$$

where use has now been made of the subscript s to denote 'split' forms of the original matrices **E** and **F**. It can be seen that the split forms have now been grouped into an in-plane elastic and plate elastic part signified by the now familiar subscripts e and p and which yield $2n \times 2n$ matrices $\mathbf{E}_e$ and $\mathbf{F}_e$ for the in-plane elastic part and $3n \times 3n$ matrices $\mathbf{E}_p$ and $\mathbf{F}_p$ for the plate elastic part along with the $2n \times 3n$ zero matrix $\mathbf{0}$. It follows then that,

$$\sup_{\mathbf{x}\in\mathbb{R}^{5n}} \frac{\mathbf{x}^T\mathbf{F}\mathbf{x}}{\mathbf{x}^T\mathbf{E}\mathbf{x}} = \sup_{\mathbf{x}\in\mathbb{R}^{5n}} \frac{\mathbf{x}^T\mathbf{F}_s\mathbf{x}}{\mathbf{x}^T\mathbf{E}_s\mathbf{x}},$$

since the same row and column interchanges have been carried out for both original matrices **E** and **F**. The procedure of splitting the matrices can now be taken one step further by treating the problem as two smaller ones. This leads to the conjecture that,

$$\sup_{\mathbf{x}\in\mathbb{R}^{5n}} \frac{\mathbf{x}^T\mathbf{F}\mathbf{x}}{\mathbf{x}^T\mathbf{E}\mathbf{x}} = \max\left\{ \sup_{\mathbf{x}\in\mathbb{R}^{2n}} \frac{\mathbf{x}^T\mathbf{F}_e\mathbf{x}}{\mathbf{x}^T\mathbf{E}_e\mathbf{x}}, \sup_{\mathbf{x}\in\mathbb{R}^{3n}} \frac{\mathbf{x}^T\mathbf{F}_p\mathbf{x}}{\mathbf{x}^T\mathbf{E}_p\mathbf{x}} \right\},$$

where it can be seen that the two smaller problems are concerned solely with the in-plane and plate elastic parts of the model and are those which also result from Equations (8.4) and (8.5) respectively. Computed interpolation error constant values for these equations are as given in Equations (8.7) and (8.8) from which it has been observed that $C_{1,k}^{i,p} = C_{1,k}^{i}$ and $C_{2,k}^{i,p} = C_{2,k}^{i}$ in agreement with the above conjecture.

This alternative estimator formulation shows an immediate potential for lowering the global error estimate since the constants for the in-plane elastic part are significantly smaller than those for the plate elastic part. For problems where the in-plane displacements u and v are zero, however, this estimator formulation will offer no advantage since both the residual and jump terms will be zero.

Appendix A

Classical Plate Theory Equilibrium Equations

It is possible for a mechanical system to take many possible configurations in the geometrical sense which do not violate the geometric constraints or essential boundary conditions of the problem. Of these possible configurations one will satisfy Newton's second law which ensures the equilibrium of forces and which we shall call the equilibrium configuration. The other possible configurations can all be considered as variations of this equilibrium configuration and under such variations, in addition to the geometrical constraints not being violated, the forces are fixed at their equilibrium values. In experiencing such displacement configuration variations from the equilibrium configuration due to the action of an actual force the system is said to undergo *virtual displacements* from the equilibrium configuration.

From Reddy, [40], consider the virtual displacement $\delta\mathbf{u}$ of a particle under the action of n concurrent forces $\mathbf{F}_i$ $i = 1, \ldots, n$. It is clear that the work done by a single force $\mathbf{F}_i$ can be expressed as,

$$\delta W_i = \mathbf{F}_i \cdot \delta\mathbf{u}.$$

Consequently the total work done, δW, by all forces is given by,

$$\delta W = \boldsymbol{\mathfrak{F}} \cdot \delta\mathbf{u}, \quad \text{where} \quad \boldsymbol{\mathfrak{F}} = \sum_{i=1}^{n} \mathbf{F}_i,$$

is the vector sum of all the forces acting on the particle. If the particle is in equilibrium then the net force acting on it must be zero meaning that $\boldsymbol{\mathfrak{F}} = \mathbf{0}$ and consequently that $\delta W = 0$. Conversely if $\delta W = 0$ and $\delta\mathbf{u}$ is arbitrary then $\boldsymbol{\mathfrak{F}}$ must be the zero vector. Thus the particle is in equilibrium if and only if,

$$\delta W = 0 \tag{A.1}$$

for any $\delta\mathbf{u}$. As stated in [40], Equation (A.1) is the mathematical statement of the principle of virtual displacements for a particle. For the principle of virtual displacements applied to an elastic body the particles making up the body can move relative to one another and can do work in addition to that by external forces. It thus becomes necessary to consider the work done by internal forces as well as that done by the external forces. From [40] the principal of virtual work states that a continuous body is in equilibrium if the virtual work of all forces acting on the body is zero in a virtual displacement. This results in the requirement that,

$$\delta W_E + \delta W_I = 0,$$

where now δW_E and δW_I are the virtual work portions resulting from external and internal forces respectively. In [40] this quantity is expressed in component form as,

$$-\int_V f_i \delta u_i \, dV - \int_S \hat{t}_i \delta u_i \, ds + \int_V \sigma_{ij} \delta \varepsilon_{ij} \, dV = 0, \tag{A.2}$$

for a plate of volume V under body force $\mathbf{f}$ and where S is the portion of the plate boundary on which the tractions $\hat{t}_i$ are specified. In the above the external work done is given by the first two integrals and the internal work done is given by the third integral. It can be seen in the above that the external work done is given a negative sign to denote that work is performed on the body. In addition it is assumed that elsewhere on the plate boundary the displacements are specified and thus the variation and hence virtual displacement will be zero. As described in Section (2.2.1) the physical dimensions of the plate are such that the volume can be described as,

$$V = \Omega \times \left(-\frac{t}{2}, \frac{t}{2}\right),$$

where t is the thickness of the plate which has top and bottom surfaces at $x_3 = -t/2$ and $x_3 = t/2$ respectively, a midplane Ω at $x_3 = 0$ and an edge $\partial\Omega$. This enables the integral of the surface tractions in Equation (A.2) to be simplified into the integral around the edge plus the integral on both the top and bottom faces. Before doing this we shall express the tractions in a more convenient way. It is clear that the plate the coordinate axes x_1, x_2 and x_3 are orientated as shown in Figure (A.1). This means that it is also possible to express the x_3 components of the tractions $\hat{t}_i$

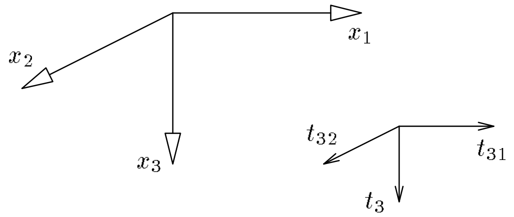

Figure A.1: Plate coordinate axes orientation.

as $\hat{t}_{31}$, $\hat{t}_{32}$ and $\hat{t}_3$ as also shown in Figure (A.1). On the edge, $\partial\Omega$, of the plate however the tractions may be described in a similar way but in terms of the normal $\hat{t}_n$ and tangential components $\hat{t}_{ns}$ and $\hat{t}_{nx_3}$ to the edge along with the displacements δU_n, δU_s and δw. For notational convenience however, the tangential component $\hat{t}_{nx_3}$ shall henceforth be expressed as $\hat{t}_{n3}$. The traction integral may thus be expressed as detailed in [40] as,

$$\int_S \hat{t}_i \delta u_i \, ds = \int_{-\frac{t}{2}}^{\frac{t}{2}} \int_{\partial\Omega} \left(\hat{t}_n \delta U_n + \hat{t}_{ns} \delta U_s + \hat{t}_{n3} \delta w\right) \, ds \, dx_3 + \int_{\Omega} \left(\hat{t}_{31} \delta u + \hat{t}_{32} \delta v + \hat{t}_3 \delta w\right)\Big|_{-\frac{t}{2}}^{\frac{t}{2}} \, dx_1 dx_2. \tag{A.3}$$

This integral may be further simplified by using the fact that the traction components on the upper and lower face of the plate are all zero except on the upper face where $\hat{t}_3 = q(x_1, x_2)$ the distributed transverse load. Thus we obtain,

$$\int_{\Omega} \left[\left(\hat{t}_{31} \delta u + \hat{t}_{32} \delta v + \hat{t}_3 \delta w\right)\right]_{-\frac{t}{2}}^{\frac{t}{2}} \, dx_1 dx_2 = \int_{\Omega} q \delta w \, dx_1 dx_2. \tag{A.4}$$

From [40], by substituting the equations,

$$U_n = u_n - x_3 \frac{\partial w}{\partial n} \quad \text{and} \quad U_s = u_s - x_3 \frac{\partial w}{\partial s},$$

into the first integral of Equation (A.3),

$$\begin{aligned}
&\int_{-\frac{t}{2}}^{\frac{t}{2}} \int_{\partial\Omega} \left(\hat{t}_n \delta U_n + \hat{t}_{ns} \delta U_s + \hat{t}_{n3} \delta w\right) \, ds dx_3 \\
&= \int_{-\frac{t}{2}}^{\frac{t}{2}} \int_{\partial\Omega} \left(\hat{t}_n \left[\delta u_n - x_3 \frac{\partial \delta w}{\partial n}\right] + \hat{t}_{ns} \left[\delta u_s - x_3 \frac{\partial \delta w}{\partial s}\right] + \hat{t}_{n3} \delta w\right) \, ds dx_3 \\
&= \int_{-\frac{t}{2}}^{\frac{t}{2}} \int_{\partial\Omega} \left(\hat{t}_n \delta u_n - x_3 \hat{t}_n \frac{\partial \delta w}{\partial n} + \hat{t}_{ns} \delta u_s - x_3 \hat{t}_{ns} \frac{\partial \delta w}{\partial s} + \hat{t}_{n3} \delta w\right) \, ds dx_3 \\
&= \int_{\partial\Omega} \left[\left(\int_{-\frac{t}{2}}^{\frac{t}{2}} \hat{t}_n \, dx_3\right) \delta u_n - \left(\int_{-\frac{h}{2}}^{\frac{h}{2}} x_3 \hat{t}_n \, dx_3\right) \frac{\partial \delta w}{\partial n} + \left(\int_{-\frac{h}{2}}^{\frac{h}{2}} \hat{t}_{ns} \, dx_3\right) \delta u_s \right. \\
&\qquad \left. - \left(\int_{-\frac{t}{2}}^{\frac{t}{2}} x_3 \hat{t}_{ns} \, dx_3\right) \frac{\partial \delta w}{\partial s} + \left(\int_{-\frac{t}{2}}^{\frac{t}{2}} \hat{t}_{n3} \, dx_3\right) \delta w\right] \, ds \\
&= \int_{\partial\Omega} \left[\hat{N}_n \delta u_n - \hat{M}_n \frac{\partial \delta w}{\partial n} + \hat{N}_s \delta u_s - \hat{M}_s \frac{\partial \delta w}{\partial s} + \hat{Q}_n \delta w\right] \, ds
\end{aligned}$$

where u_n and u_s are the normal and tangential in-plane displacements and,

$$\left(\hat{N}_n, \hat{N}_s, \hat{Q}_n, \hat{M}_n, \hat{M}_s\right) = \int_{-\frac{t}{2}}^{\frac{t}{2}} \left(\hat{t}_n, \hat{t}_{ns}, \hat{t}_{n3}, x_3 \hat{t}_n, x_3 \hat{t}_{ns}\right) \, dx_3. \tag{A.5}$$

Thus Equation (A.2) can now be expressed in the form,

$$\begin{aligned}
0 = &\int_{-\frac{t}{2}}^{\frac{t}{2}} \left[\int_{\Omega} \left(\sigma_{11} \delta \varepsilon_{11} + \sigma_{22} \delta \varepsilon_{22} + \sigma_{12} 2 \delta \varepsilon_{12}\right) \, dx_1 dx_2\right] \, dx_3 - \int_{\Omega} q \delta w \, dx_1 dx_2 \\
&- \int_{\hat{\Gamma}_1} \hat{N}_n \delta u_n \, ds - \int_{\hat{\Gamma}_2} \hat{N}_s \delta u_s \, ds - \int_{\hat{\Gamma}_3} \hat{Q}_n \delta w \, ds + \int_{\hat{\Gamma}_4} \hat{M}_n \frac{\partial \delta w}{\partial n} \, ds + \int_{\hat{\Gamma}_5} \hat{M}_s \frac{\partial \delta w}{\partial s} \, ds,
\end{aligned} \tag{A.6}$$

where $\hat{\Gamma}_i$ for $i = 1, 2, 3, 4, 5$ are the portions of $\partial\Omega$ on which $\hat{N}_n$, $\hat{N}_s$, $\hat{Q}_n$, $\hat{M}_n$ and $\hat{M}_s$ respectively are specified and the contribution from the body force component f_i has been neglected. Generally $\hat{\Gamma}_i$ for $i = 1, 2, 3, 4, 5$ are not the same, they complement respectively the portions Γ_i for $i = 1, 2, 3, 4, 5$ of $\partial\Omega$ on which u_n, u_s, w, $\partial w / \partial n$ and $\partial w / \partial s$ are specified respectively and which themselves constitute the essential boundary conditions.

From Equations (2.6) and (2.27) the strains have the form,

$$\begin{aligned}
\varepsilon_{11} &= \frac{\partial u}{\partial x_1} - x_3\frac{\partial^2 w}{\partial x_1^2} \equiv \varepsilon_1, \\
\varepsilon_{22} &= \frac{\partial v}{\partial x_2} - x_3\frac{\partial^2 w}{\partial x_2^2} \equiv \varepsilon_2, \\
2\varepsilon_{12} &= \frac{\partial u}{\partial x_2} + \frac{\partial v}{\partial x_1} - 2x_3\frac{\partial^2 w}{\partial x_1 \partial x_2} \equiv \varepsilon_4.
\end{aligned}$$

Thus substituting into Equation (A.6) gives,

$$\begin{aligned}
0 = \int_\Omega \Bigg[& \left(\int_{-\frac{t}{2}}^{\frac{t}{2}} \sigma_1 \, dx_3\right) \frac{\partial \delta u}{\partial x_1} - \left(\int_{-\frac{t}{2}}^{\frac{t}{2}} x_3\sigma_1 \, dx_3\right) \frac{\partial^2 \delta w}{\partial x_1^2} + \left(\int_{-\frac{t}{2}}^{\frac{t}{2}} \sigma_2 \, dx_3\right) \frac{\partial \delta v}{\partial x_2} \\
& - \left(\int_{-\frac{t}{2}}^{\frac{t}{2}} x_3\sigma_2 \, dx_3\right) \frac{\partial^2 \delta w}{\partial x_2^2} + \left(\int_{-\frac{t}{2}}^{\frac{t}{2}} \sigma_4 \, dx_3\right) \left(\frac{\partial \delta u}{\partial x_2} + \frac{\partial \delta v}{\partial x_1}\right) \\
& - 2\left(\int_{-\frac{t}{2}}^{\frac{t}{2}} x_3\sigma_4 \, dx_3\right) \frac{\partial^2 \delta w}{\partial x_1 \partial x_2}\Bigg] \, dx_1 dx_2 \\
- \int_\Omega & q\delta w \, dx_1 dx_2 + \text{boundary terms.}
\end{aligned}$$

The quantities integrated over the plate thickness, t, are the in-plane stress and bending moment resultants. These can be expressed in terms of the displacements as given in Equations (2.31) and (2.32). We thus have,

$$\begin{aligned}
0 = \int_\Omega \Bigg[& N_1\frac{\partial \delta u}{\partial x_1} - M_1\frac{\partial^2 \delta w}{\partial x_1^2} + N_2\frac{\partial \delta v}{\partial x_2} - M_2\frac{\partial^2 \delta w}{\partial x_2^2} \\
& + N_4\left(\frac{\partial \delta u}{\partial x_2} + \frac{\partial \delta v}{\partial x_1}\right) - 2M_4\frac{\partial^2 \delta w}{\partial x_1 \partial x_2} - q\delta w\Bigg] \, dx_1 dx_2 + \text{boundary terms.}
\end{aligned}$$

In order to trade differentiation from the virtual displacement terms we now integrate the integral over Ω by parts. Once this is done and terms grouped together it is possible to obtain,

$$\begin{aligned}
0 = \int_\Omega \Bigg[& -\delta u\left(\frac{\partial N_1}{\partial x_1} + \frac{\partial N_4}{\partial x_2}\right) - \delta v\left(\frac{\partial N_4}{\partial x_1} + \frac{\partial N_2}{\partial x_2}\right) \\
& -\delta w\left(\frac{\partial^2 M_1}{\partial x_1^2} + \frac{\partial^2 M_2}{\partial x_2^2} + 2\frac{\partial^2 M_4}{\partial x_1 \partial x_2} + q\right)\Bigg] \, dx_1 dx_2 \\
+ \int_{\partial\Omega} \Bigg[& \delta u\,(N_1 n_1 + N_4 n_2) + \delta v\,(N_4 n_1 + N_2 n_2) - \frac{\partial \delta w}{\partial x_1}(M_1 n_1 + M_4 n_2) - \frac{\partial \delta w}{\partial x_2}(M_4 n_1 + M_2 n_2) \\
& +\delta w\left(\frac{\partial M_1}{\partial x_1}n_1 + \frac{\partial M_4}{\partial x_1}n_2 + \frac{\partial M_2}{\partial x_2}n_2 + \frac{\partial M_4}{\partial x_2}n_1\right)\Bigg] \, ds \\
+ & \text{ initial boundary terms.}
\end{aligned}$$

Using the following relations supplied by Reddy in [40],

$$u_n = un_1 + vn_2, \qquad u_s = -un_2 + vn_1,$$

$$\begin{aligned}
u &= u_n n_1 - u_s n_2, & v &= u_n n_2 + u_s n_1, \\
\frac{\partial}{\partial n} &= n_1\frac{\partial}{\partial x_1} + n_2\frac{\partial}{\partial x_2}, & \frac{\partial}{\partial s} &= n_1\frac{\partial}{\partial x_2} - n_2\frac{\partial}{\partial x_1}, \\
\frac{\partial}{\partial x_1} &= n_1\frac{\partial}{\partial n} - n_2\frac{\partial}{\partial s}, & \frac{\partial}{\partial x_2} &= n_2\frac{\partial}{\partial n} + n_1\frac{\partial}{\partial s},
\end{aligned}$$

and substituting into the above integral over $\partial\Omega$ the integrand $\mathcal{A}$ reduces to,

$$\mathcal{A} = \delta u_n N_n + \delta u_s N_s + \delta w Q_n - \frac{\partial \delta w}{\partial n} M_n - \frac{\partial \delta w}{\partial s} M_s,$$

where,

$$\begin{aligned}
N_n &= N_1 n_1^2 + N_2 n_2^2 + 2 n_1 n_2 N_4, \\
N_s &= (N_2 - N_1)\, n_1 n_2 + N_4 \left(n_1^2 - n_2^2\right), \\
Q_n &= \left(\frac{\partial M_1}{\partial x_1} + \frac{\partial M_4}{\partial x_2}\right) n_1 + \left(\frac{\partial M_2}{\partial x_2} + \frac{\partial M_4}{\partial x_1}\right) n_2, \\
M_n &= M_1 n_1^2 + M_2 n_2^2 + 2 n_1 n_2 M_4, \\
M_s &= (M_2 - M_1)\, n_1 n_2 + M_4 \left(n_1^2 - n_2^2\right).
\end{aligned} \tag{A.7}$$

Substituting back into the integral, this gives,

$$\begin{aligned}
0 = & \int_\Omega \left[-\delta u \left(\frac{\partial N_1}{\partial x_1} + \frac{\partial N_4}{\partial x_2}\right) - \delta v \left(\frac{\partial N_4}{\partial x_1} + \frac{\partial N_2}{\partial x_2}\right) \right. \\
& \left. \qquad -\delta w \left(\frac{\partial^2 M_1}{\partial x_1^2} + 2\frac{\partial^2 M_4}{\partial x_1 \partial x_2} + \frac{\partial^2 M_2}{\partial x_2^2} + q\right)\right] dx_1 dx_2 \\
& + \int_{\partial\Omega} \left[\delta u_n N_n + \delta u_s N_s + \delta w Q_n - \frac{\partial \delta w}{\partial n} M_n - \frac{\partial \delta w}{\partial s} M_s\right] ds \\
& - \int_{\hat{\Gamma}_1} \delta u_n \hat{N}_n \, ds - \int_{\hat{\Gamma}_2} \delta u_s \hat{N}_s \, ds - \int_{\hat{\Gamma}_3} \delta w \hat{Q}_n \, ds \\
& + \int_{\hat{\Gamma}_4} \frac{\partial \delta w}{\partial n} \hat{M}_n \, ds + \int_{\hat{\Gamma}_5} \frac{\partial \delta w}{\partial s} \hat{M}_s \, ds.
\end{aligned} \tag{A.8}$$

As mentioned previously, the boundary portions $\hat{\Gamma}_i$ for $i = 1,2,3,4,5$ complement those portions Γ_i for $i = 1,2,3,4,5$ upon which u_n, u_s, w, $\partial w/\partial n$ and $\partial w/\partial s$ are specified respectively. On the portions Γ_i for $i = 1,2,3,4,5$ the virtual displacements will thus be zero and so Equation (A.8) can be written,

$$\begin{aligned}
0 = & \int_\Omega \left[-\delta u \left(\frac{\partial N_1}{\partial x_1} + \frac{\partial N_4}{\partial x_2}\right) - \delta v \left(\frac{\partial N_4}{\partial x_1} + \frac{\partial N_2}{\partial x_2}\right) \right. \\
& \left. \qquad -\delta w \left(\frac{\partial^2 M_1}{\partial x_1^2} + 2\frac{\partial^2 M_4}{\partial x_1 \partial x_2} + \frac{\partial^2 M_2}{\partial x_2^2} + q\right)\right] dx_1 dx_2 \\
& + \int_{\hat{\Gamma}_1} \left(N_n - \hat{N}_n\right) \delta u_n \, ds + \int_{\hat{\Gamma}_2} \left(N_s - \hat{N}_s\right) \delta u_s \, ds + \int_{\hat{\Gamma}_3} \left(Q_n - \hat{Q}_n\right) \delta w \, ds \\
& + \int_{\hat{\Gamma}_4} \left(\hat{M}_n - M_n\right) \frac{\partial \delta w}{\partial n} \, ds + \int_{\hat{\Gamma}_5} \left(\hat{M}_s - M_s\right) \frac{\partial \delta w}{\partial s} \, ds.
\end{aligned}$$

Since the variations δu, δv and δw are arbitrary in Ω we obtain the equilibrium equations,

$$\begin{aligned}
\frac{\partial N_1}{\partial x_1} + \frac{\partial N_4}{\partial x_2} &= 0, \\
\frac{\partial N_4}{\partial x_1} + \frac{\partial N_2}{\partial x_2} &= 0, \\
\left(\frac{\partial^2 M_1}{\partial x_1^2} + 2\frac{\partial^2 M_4}{\partial x_1 \partial x_2} + \frac{\partial^2 M_2}{\partial x_2^2}\right) + q &= 0.
\end{aligned} \tag{A.9}$$

Similarly, since the variations δu_n, δu_s, δw, $\partial\delta w/\partial n$ and $\partial\delta w/\partial s$ are arbitrary on boundary portions $\hat{\Gamma}_i$ for $i = 1, 2, 3, 4, 5$ we obtain the natural boundary conditions,

$$\begin{aligned} N_n - \hat{N}_n &= 0, \quad \text{on} \quad \hat{\Gamma}_1, \\ N_s - \hat{N}_s &= 0, \quad \text{on} \quad \hat{\Gamma}_2, \\ Q_n - \hat{Q}_n &= 0, \quad \text{on} \quad \hat{\Gamma}_3, \\ M_n - \hat{M}_n &= 0, \quad \text{on} \quad \hat{\Gamma}_4, \\ M_s - \hat{M}_s &= 0, \quad \text{on} \quad \hat{\Gamma}_5, \end{aligned} \tag{A.10}$$

whilst on boundary portions $\Gamma_i = \partial\Omega \setminus \hat{\Gamma}_i$ for $i = 1, 2, 3, 4, 5$ the essential boundary conditions are given by,

$$\begin{aligned} u_n &= \hat{u}_n, \quad \text{on } \Gamma_1, \\ u_s &= \hat{u}_s, \quad \text{on } \Gamma_2, \\ w &= \hat{w}, \quad \text{on } \Gamma_3, \\ \frac{\partial w}{\partial n} &= \hat{\theta}_n, \quad \text{on } \Gamma_4, \\ \frac{\partial w}{\partial s} &= \hat{\theta}_s, \quad \text{on } \Gamma_5. \end{aligned} \tag{A.11}$$

Appendix B

First-Order Shear Deformation Theory Equilibrium Equations

The material in this appendix is concerned with establishing the equilibrium equations for the plate problem modelled using first-order shear deformation theory (FSDT). The preliminary steps for doing this are as described for the classical plate theory in Appendix A. From Equation (A.4) we now proceed by substituting,

$$U_n = u_n + x_3\psi_n \quad \text{and} \quad U_s = u_s + x_3\psi_s,$$

into the first integral of Equation (A.3). This gives,

$$\begin{aligned}
&\int_{-\frac{t}{2}}^{\frac{t}{2}} \int_{\partial\Omega} \left(\hat{t}_n \delta U_n + \hat{t}_{ns}\delta U_s + \hat{t}_{n3}\delta w\right)\, ds dx_3 \\
&\quad = \int_{-\frac{t}{2}}^{\frac{t}{2}} \int_{\partial\Omega} \left(\hat{t}_n \left[\delta u_n + x_3\delta\psi_n\right] + \hat{t}_{ns}\left[\delta u_s + x_3\delta\psi_s\right] + \hat{t}_{n3}\delta w\right)\, ds dx_3 \\
&\quad = \int_{-\frac{t}{2}}^{\frac{t}{2}} \int_{\partial\Omega} \left(\hat{t}_n \delta u_n + x_3\hat{t}_n\delta\psi_n + \hat{t}_{ns}\delta u_s + x_3\hat{t}_{ns}\delta\psi_s + \hat{t}_{n3}\delta w\right)\, ds dx_3 \\
&\quad = \int_{\partial\Omega} \left[\left(\int_{-\frac{t}{2}}^{\frac{t}{2}} \hat{t}_n\, dx_3\right)\delta u_n + \left(\int_{-\frac{t}{2}}^{\frac{t}{2}} x_3\hat{t}_n\, dx_3\right)\delta\psi_n + \left(\int_{-\frac{t}{2}}^{\frac{t}{2}} \hat{t}_{ns}\, dx_3\right)\delta u_s \right. \\
&\qquad\qquad \left. + \left(\int_{-\frac{t}{2}}^{\frac{t}{2}} x_3\hat{t}_{ns}\, dx_3\right)\delta\psi_s + \left(\int_{-\frac{t}{2}}^{\frac{t}{2}} \hat{t}_{n3}\, dx_3\right)\delta w\right] ds \\
&\quad = \int_{\partial\Omega} \left[\hat{N}_n\delta u_n + \hat{M}_n\delta\psi_n + \hat{N}_s\delta u_s + \hat{M}_s\delta\psi_s + \hat{Q}_n\delta w\right]\, ds,
\end{aligned}$$

where, as for the classical case,

$$\left(\hat{N}_n, \hat{N}_s, \hat{Q}_n, \hat{M}_n, \hat{M}_s\right) = \int_{-\frac{t}{2}}^{\frac{t}{2}} \left(\hat{t}_n, \hat{t}_{ns}, \hat{t}_{n3}, x_3\hat{t}_n, x_3\hat{t}_{ns}\right)\, dx_3. \tag{B.1}$$

Thus Equation (A.2) can now be expressed in the form,

$$0 = \int_{-\frac{t}{2}}^{\frac{t}{2}} \left[\int_\Omega (\sigma_{11}\delta\varepsilon_{11} + \sigma_{22}\delta\varepsilon_{22} + \sigma_{12}2\delta\varepsilon_{12} + \sigma_{13}2\delta\varepsilon_{13} + \sigma_{23}2\delta\varepsilon_{23})\, dx_1 dx_2 \right] dx_3 - \int_\Omega q\delta w\, dx_1 dx_2$$

$$- \int_{\hat{\Gamma}_1} \hat{N}_n \delta u_n\, ds - \int_{\hat{\Gamma}_2} \hat{N}_s \delta u_s\, ds - \int_{\hat{\Gamma}_3} \hat{Q}_n \delta w\, ds - \int_{\hat{\Gamma}_4} \hat{M}_n \delta\psi_n\, ds - \int_{\hat{\Gamma}_5} \hat{M}_s \delta\psi_s\, ds, \tag{B.2}$$

where, as in Appendix A, $\hat{\Gamma}_i$ for $i = 1,2,3,4,5$ are the portions of $\partial\Omega$ on which $\hat{N}_n$, $\hat{N}_s$, $\hat{Q}_n$, $\hat{M}_n$ and $\hat{M}_s$ respectively are specified and again the contribution from the body force component f_i has been neglected. Generally $\hat{\Gamma}_i$ for $i = 1,2,3,4,5$ are not the same, they complement respectively the portions Γ_i for $i = 1,2,3,4,5$ of $\partial\Omega$ on which which u_n, u_s, w, ψ_n and ψ_s are specified respectively and which themselves constitute the essential boundary conditions.

From Equations (2.6) and (2.36) the strains have the form,

$$\begin{aligned}
\varepsilon_{11} &= \frac{\partial u}{\partial x_1} + x_3 \frac{\partial \psi_1}{\partial x_1} \equiv \varepsilon_1, \\
\varepsilon_{22} &= \frac{\partial v}{\partial x_2} + x_3 \frac{\partial \psi_2}{\partial x_2} \equiv \varepsilon_2, \\
2\varepsilon_{12} &= \left(\frac{\partial u}{\partial x_2} + \frac{\partial v}{\partial x_1} \right) + x_3 \left(\frac{\partial \psi_1}{\partial x_2} + \frac{\partial \psi_2}{\partial x_1} \right) \equiv \varepsilon_4, \\
2\varepsilon_{13} &= \psi_1 + \frac{\partial w}{\partial x_1} \equiv \varepsilon_5, \\
2\varepsilon_{23} &= \psi_2 + \frac{\partial w}{\partial x_2} \equiv \varepsilon_6.
\end{aligned}$$

Thus substituting into Equation (B.2) gives,

$$\begin{aligned}
0 = \int_\Omega \Bigg[&\left(\int_{-\frac{t}{2}}^{\frac{t}{2}} \sigma_1\, dx_3 \right) \frac{\partial \delta u}{\partial x_1} + \left(\int_{-\frac{t}{2}}^{\frac{t}{2}} x_3 \sigma_1\, dx_3 \right) \frac{\partial \delta\psi_1}{\partial x_1} + \left(\int_{-\frac{t}{2}}^{\frac{t}{2}} \sigma_2\, dx_3 \right) \frac{\partial \delta v}{\partial x_2} \\
&+ \left(\int_{-\frac{t}{2}}^{\frac{t}{2}} x_3 \sigma_2\, dx_3 \right) \frac{\partial \delta\psi_2}{\partial x_2} + \left(\int_{-\frac{t}{2}}^{\frac{t}{2}} \sigma_4\, dx_3 \right) \left(\frac{\partial \delta u}{\partial x_2} + \frac{\partial \delta v}{\partial x_1} \right) \\
&+ \left(\int_{-\frac{t}{2}}^{\frac{t}{2}} x_3 \sigma_4\, dx_3 \right) \left(\frac{\partial \delta\psi_1}{\partial x_2} + \frac{\partial \delta\psi_2}{\partial x_1} \right) + \left(\int_{-\frac{t}{2}}^{\frac{t}{2}} \sigma_5\, dx_3 \right) \left(\delta\psi_1 + \frac{\partial \delta w}{\partial x_1} \right) \\
&+ \left(\int_{-\frac{t}{2}}^{\frac{t}{2}} \sigma_6\, dx_3 \right) \left(\delta\psi_2 + \frac{\partial \delta w}{\partial x_2} \right) \Bigg] dx_1 dx_2 \\
- \int_\Omega & q\delta w\, dx_1 dx_2 + \text{boundary terms.}
\end{aligned}$$

The quantities integrated over the plate thickness, t, are the in-plane stress, bending moment and shear force resultants. These can be expressed in terms of the displacements as given in Equations (2.44), (2.45) and (2.46). We thus have,

$$\begin{aligned}
0 = \int_\Omega \Bigg[& N_1 \frac{\partial \delta u}{\partial x_1} + M_1 \frac{\partial \delta\psi_1}{\partial x_1} + N_2 \frac{\partial \delta v}{\partial x_2} + M_2 \frac{\partial \delta\psi_2}{\partial x_2} + N_4 \left(\frac{\partial \delta u}{\partial x_2} + \frac{\partial \delta v}{\partial x_1} \right) + M_4 \left(\frac{\partial \delta\psi_1}{\partial x_2} + \frac{\partial \delta\psi_2}{\partial x_1} \right) \\
&+ Q_5 \left(\delta\psi_1 + \frac{\partial \delta w}{\partial x_1} \right) + Q_6 \left(\delta\psi_2 + \frac{\partial \delta w}{\partial x_2} \right) - q\delta w \Bigg] dx_1 dx_2 + \text{boundary terms.}
\end{aligned}$$

In order to trade differentiation from the virtual displacement terms we now integrate the integral over Ω by parts. Once this is done and terms grouped together it is possible to obtain,

$$0 = \int_\Omega \left[-\delta u \left(\frac{\partial N_1}{\partial x_1} + \frac{\partial N_4}{\partial x_2} \right) - \delta v \left(\frac{\partial N_4}{\partial x_1} + \frac{\partial N_2}{\partial x_2} \right) - \delta w \left(\frac{\partial Q_5}{\partial x_1} + \frac{\partial Q_6}{\partial x_2} + q \right) \right.$$

$$-\delta\psi_1\left(\frac{\partial M_1}{\partial x_1}+\frac{\partial M_4}{\partial x_2}-Q_5\right)-\delta\psi_2\left(\frac{\partial M_4}{\partial x_1}+\frac{\partial M_2}{\partial x_2}-Q_6\right)\Bigg]\,dx_1dx_2$$
$$+\int_{\partial\Omega}\left[\delta u\left(N_1n_1+N_4n_2\right)+\delta v\left(N_4n_1+N_2n_2\right)+\delta w\left(Q_5n_1+Q_6n_2\right)\right.$$
$$\left.\delta\psi_1\left(M_1n_1+M_4n_2\right)+\delta\psi_2\left(M_4n_1+M_2n_2\right)\right]\,ds$$
$$+\text{ initial boundary terms.}$$

As in Appendix A, the integrand $\mathcal{A}$ of the integral over $\partial\Omega$ can be expressed in terms of normal and tangential components. This is done by using the relations,

$$u_n=un_1+vn_2,\qquad u_s=-un_2+vn_1,$$
$$u=u_nn_1-u_sn_2,\qquad v=u_nn_2+u_sn_1,$$
$$\psi_1=\psi_nn_1-\psi_sn_2,\qquad \psi_2=\psi_nn_2+\psi_sn_1,$$

giving a reduced form of $\mathcal{A}$ expressed as,

$$\mathcal{A}=\delta u_nN_n+\delta u_sN_s+\delta wQ_n+\delta\psi_nM_n+\delta\psi_sM_s.$$

where,

$$\begin{aligned}
N_n &= N_1n_1^2+N_2n_2^2+2n_1n_2N_4,\\
N_s &= \left(N_2-N_1\right)n_1n_2+N_4\left(n_1^2-n_2^2\right),\\
Q_n &= Q_5n_1+Q_6n_2,\\
M_n &= M_1n_1^2+M_2n_2^2+2n_1n_2M_4,\\
M_s &= \left(M_2-M_1\right)n_1n_2+M_4\left(n_1^2-n_2^2\right).
\end{aligned}\tag{B.3}$$

Substituting back into the integral, this gives,

$$\begin{aligned}
0 =& \int_\Omega\Bigg[-\delta u\left(\frac{\partial N_1}{\partial x_1}+\frac{\partial N_4}{\partial x_2}\right)-\delta v\left(\frac{\partial N_4}{\partial x_1}+\frac{\partial N_2}{\partial x_2}\right)-\delta w\left(\frac{\partial Q_5}{\partial x_1}+\frac{\partial Q_6}{\partial x_2}+q\right)\\
&\qquad -\delta\psi_1\left(\frac{\partial M_1}{\partial x_1}+\frac{\partial M_4}{\partial x_2}-Q_5\right)-\delta\psi_2\left(\frac{\partial M_4}{\partial x_1}+\frac{\partial M_2}{\partial x_2}-Q_6\right)\Bigg]\,dx_1dx_2\\
&+\int_{\partial\Omega}\left[\delta u_nN_n+\delta u_sN_s+\delta wQ_n+\delta\psi_nM_n+\delta\psi_sM_s\right]\,ds\\
&-\int_{\hat\Gamma_1}\delta u_n\hat N_n\,ds-\int_{\hat\Gamma_2}\delta u_s\hat N_s\,ds-\int_{\hat\Gamma_3}\delta w\hat Q_n\,ds\\
&-\int_{\hat\Gamma_4}\delta\psi_n\hat M_n\,ds-\int_{\hat\Gamma_5}\delta\psi_s\hat M_s\,ds.
\end{aligned}\tag{B.4}$$

As previously, the boundary portions $\hat\Gamma_i$ for $i=1,2,3,4,5$ complement those portions Γ_i for $i=1,2,3,4,5$ upon which u_n, u_s, w, ψ_n and ψ_s are specified respectively. On the portions Γ_i for $i=1,2,3,4,5$ the virtual displacements will thus be zero and so Equation (B.4) can be written,

$$\begin{aligned}
0 =& \int_\Omega\Bigg[-\delta u\left(\frac{\partial N_1}{\partial x_1}+\frac{\partial N_4}{\partial x_2}\right)-\delta v\left(\frac{\partial N_4}{\partial x_1}+\frac{\partial N_2}{\partial x_2}\right)-\delta w\left(\frac{\partial Q_5}{\partial x_1}+\frac{\partial Q_6}{\partial x_2}+q\right)\\
&\qquad -\delta\psi_1\left(\frac{\partial M_1}{\partial x_1}+\frac{\partial M_4}{\partial x_2}-Q_5\right)-\delta\psi_2\left(\frac{\partial M_4}{\partial x_1}+\frac{\partial M_2}{\partial x_2}-Q_6\right)\Bigg]\,dx_1dx_2
\end{aligned}$$

$$+ \int_{\hat{\Gamma}_1} \left(N_n - \hat{N}_n\right) \delta u_n \, ds + \int_{\hat{\Gamma}_2} \left(N_s - \hat{N}_s\right) \delta u_s \, ds + \int_{\hat{\Gamma}_3} \left(Q_n - \hat{Q}_n\right) \delta w \, ds$$
$$+ \int_{\hat{\Gamma}_4} \left(M_n - \hat{M}_n\right) \delta \psi_n \, ds + \int_{\hat{\Gamma}_5} \left(M_s - \hat{M}_s\right) \delta \psi_s \, ds.$$

Since the variations δu, δv, δw, $\delta \psi_1$ and $\delta \psi_2$ are arbitrary in Ω we obtain the equilibrium equations,

$$\begin{aligned}
\frac{\partial N_1}{\partial x_1} + \frac{\partial N_4}{\partial x_2} &= 0, \\
\frac{\partial N_4}{\partial x_1} + \frac{\partial N_2}{\partial x_2} &= 0, \\
\frac{\partial Q_5}{\partial x_1} + \frac{\partial Q_6}{\partial x_2} + q &= 0, \\
\frac{\partial M_1}{\partial x_1} + \frac{\partial M_4}{\partial x_2} - Q_5 &= 0, \\
\frac{\partial M_4}{\partial x_1} + \frac{\partial M_2}{\partial x_2} - Q_6 &= 0.
\end{aligned} \tag{B.5}$$

Similarly, since the variations δu_n, δu_s, δw, $\delta \psi_n$, $\delta \psi_s$ are arbitrary on boundary portions $\hat{\Gamma}_i$ for $i = 1, 2, 3, 4, 5$ we obtain the natural boundary conditions,

$$\begin{aligned}
N_n - \hat{N}_n &= 0, \quad \text{on } \hat{\Gamma}_1, \\
N_s - \hat{N}_s &= 0, \quad \text{on } \hat{\Gamma}_2, \\
Q_n - \hat{Q}_n &= 0, \quad \text{on } \hat{\Gamma}_3, \\
M_n - \hat{M}_n &= 0, \quad \text{on } \hat{\Gamma}_4, \\
M_s - \hat{M}_s &= 0, \quad \text{on } \hat{\Gamma}_5,
\end{aligned} \tag{B.6}$$

whilst on boundary portions $\hat{\Gamma}_i = \partial\Omega \setminus \Gamma_i$ for $i = 1, 2, 3, 4, 5$ the essential boundary conditions are given by,

$$\begin{aligned}
u_n &= \hat{u}_n, \quad \text{on } \Gamma_1, \\
u_s &= \hat{u}_s, \quad \text{on } \Gamma_2, \\
w &= \hat{w}, \quad \text{on } \Gamma_3, \\
\psi_n &= \hat{\psi}_n, \quad \text{on } \Gamma_4, \\
\psi_s &= \hat{\psi}_s, \quad \text{on } \Gamma_5.
\end{aligned} \tag{B.7}$$

Appendix C

Mathematica Code

This appendix includes Mathematica code, [59], written to solve the ancillary problems encountered in the implementation of the error estimators. The code itself will be split into sections depending upon the task at hand and also split up within each section to include comments and observations.

C.1 Interpolation Error Constant Calculation - Triangles

The code in this section is concerned with the computation of the interpolation error constants for triangular elements and results from the work performed in Chapters 5 and 6. More specifically the following code will detail the process of obtaining the interpolation error constants C_1^i and C_2^i over a triangular element in the context of linear elasticity as discussed in Section (6.1.2). The resulting computed interpolation error constants are subsequently used in the numerical results presented in Section (7.1).

The code begins by defining whether the interpolation error constant is of the type `interior` or `boundary` which corresponds to the constant C_1^i or C_2^i respectively. In the current form the code will take `type = interior` as the `(* *)` denote comment delimiters and so `type = boundary` is ignored. Also defined here are the material properties $E \equiv$ `eval` and $\nu \equiv$ `nu`.

```
type = interior;
(*
type = boundary;
*)
eval = 1;
nu   = 4/10;
```

The node numbering scheme for the triangular element is as shown in Figure (C.1). Nodes for the linear interpolant can be seen on the element vertices numbered one two and three and shown as black bullets ●. The function to be interpolated will be a quadratic and is defined over the element using six nodes, these are those of the interpolant denoted by ● and three further ones at the element midside positions denoted by ●. Next the element shape functions for the interpolant

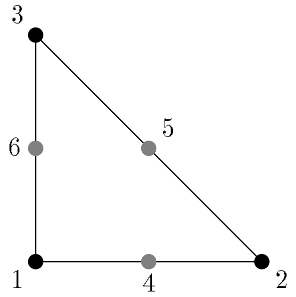

Figure C.1: Nodal configuration on standard triangular element.

are specified at nodes one to three and stored in `Interp`. In addition the shape functions of the higher order function are also specified at nodes one to six and stored in `Func`.

```
Interp = {1-x-y,x,y,0,0,0};
Func   = {(1-2*x-2*y)*(1-x-y),x*(2*x-1),y*(2*y-1),
          4*x*(1-x-y),4*x*y,4*y*(1-x-y)};
```

The sets of shape functions are then subtracted in accordance with Equation (6.16) to give `Phi`. For the computation of the boundary constant C_2^i then on the diagonal edge of the element it is known that $y = 1 - x$ and so this substitution is performed and the resulting formulations stored as `Phil`.

```
Phi = Func - Interp;
If[
   type == boundary,Phil = Phi/.y->1-x
  ];
```

The next step is to define `PreFmx` which is equivalent to that described in Equation (6.19).

```
PreFmx = Table[0,{i,1,2*Length[Phi]},{j,1,2*Length[Phi]}];
If[
   type == boundary,
   PreFmxl = Table[0,{i,1,2*Length[Phil]},{j,1,2*Length[Phil]}];
  ];
Do[
   PreFmx[[2*i-1,2*j-1]] = Phi[[i]]*Phi[[j]];
   PreFmx[[2*i,2*j]]     = Phi[[i]]*Phi[[j]],
   {i,Length[Phi]},{j,Length[Phi]}
  ];
If[
   type == boundary,
   Do[
      PreFmxl[[2*i-1,2*j-1]] = Phil[[i]]*Phil[[j]];
      PreFmxl[[2*i,2*j]]     = Phil[[i]]*Phil[[j]],
      {i,Length[Phil]},{j,Length[Phil]}
     ];
  ];
```

It is now necessary to integrate **PreFmx**. For the case where the boundary constant is required the integration is as detailed in Equation (5.41).

```
If[
   type == interior,
   Print["Integrating element interior."];
   Fmx = Integrate[PreFmx,{x,0,1},{y,0,1-x}];
  ];
If[
   type == boundary,
   Print["Integrating element boundary."];
   Fmx1 = Integrate[PreFmx,{x,0,1}]/.y->0;
   Fmx2 = N[Sqrt[2],16]*Integrate[PreFmx1,{x,0,1}];
   Fmx3 = Integrate[PreFmx,{y,0,1}]/.x->0;
   Fmx = Fmx1 + Fmx2 + Fmx3;
  ];
```

At this point matrix **Fmx** $\equiv \mathbf{F}$ as given in Equation (6.22) has been obtained. The next task is to obtain matrix **Emx** $\equiv \mathbf{E}$ which is defined as in Equation (6.23). Using the material properties, the Lamé coefficients may be computed. These are $\lambda \equiv$ `lambda` and $\mu \equiv$ `mu` and are used to establish the material constitutive matrix `Const`.

```
lambda = nu*eval/((1-2*nu)*(1+nu));
mu     = eval/(2*(1+nu));
Const  = {
          {lambda+2*mu,lambda,0},
          {lambda,lambda+2*mu,0},
          {0,0,mu}
         };
```

In the same way that **PreFmx** was created prior to integration for **Fmx** the same shall now be done for matrix **Emx**.

```
B1 = Table[0,{i,1,2},{j,1,3}];
B2 = Table[0,{i,1,3},{j,1,2}];
PreEmx = Table[0,{i,1,2*Length[Func]},{j,1,2*Length[Func]}];
A[fn_] := Do[B1[[1,1]]=D[fn[[i]],x];B1[[1,3]]=D[fn[[i]],y];
     B1[[2,2]]=D[fn[[i]],y];B1[[2,3]]=D[fn[[i]],x];
     B2[[1,1]]=D[fn[[j]],x];B2[[2,2]]=D[fn[[j]],y];
     B2[[3,1]]=D[fn[[j]],y];B2[[3,2]]=D[fn[[j]],x];
     TempCell = B1.Const.B2;
     PreEmx[[2*i-1,2*j-1]] = TempCell[[1,1]];
     PreEmx[[2*i-1,2*j]] = TempCell[[1,2]];
     PreEmx[[2*i,2*j-1]] = TempCell[[2,1]];
     PreEmx[[2*i,2*j]] = TempCell[[2,2]];,
     {i,1,Length[fn]},{j,1,Length[fn]}
            ]
A[Func];
Emx = Integrate[PreEmx,{x,0,1},{y,0,1-x}];
```

Thus **PreEmx** is obtained by supplying the quadratic shape functions and **Emx** results from the integration of **PreEmx** over the element. The eigenvalues of the generalized eigenvalue problem are then obtained to give the required interpolation error constant as described in Section (5.4).

C.2 Interpolation Error Constant Calculation - Quadrilaterals

The code in this section is concerned with the computation of the interpolation error constants for quadrilateral elements and results from the work performed in Chapters 5 and 6. More specifically the following code will detail the process of obtaining the interpolation error constants C_1^i and C_2^i over a plate element which may be either standard or any of the transition element family in the context of first-order shear deformation theory as discussed in Section (6.2.2). The resulting computed interpolation error constants are subsequently used in the numerical results presented in Section (7.2).

The code will follow the same general structure as that described in Section (C.1). It will be complicated however by the possible presence of irregular nodes and this requires the element to be split into subregions as described in Section (5.7). The code begins by stipulating whether the interpolation error constant is of the `interior` or `boundary` type. These types correspond again to the constants C_1^i and C_2^i respectively as in Section (C.1).

```
type  = interior;
(*
type  = boundary;
*)
north = 0;
east  = 0;
south = 0;
west  = 0;
```

The node numbering on the standard element is as in Figure (C.2). Nodes for the standard bilinear

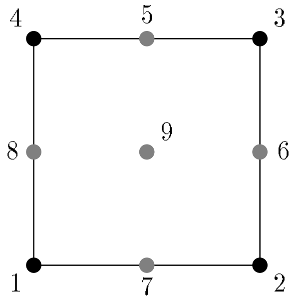

Figure C.2: Nodal configuration on standard square element.

interpolant can be seen on the element vertices numbered one to four and shown as black bullets ●. The above portion of code also has variables `north`, `east`, `south` and `west`. These correspond to the nodes numbered five, six, seven and eight in Figure (C.2) and may be set to unity to invoke the presence of a node in that location. This will in turn modify the interpolant shape functions to that of the corresponding transition element. The function to be interpolated will be a biquadratic and is defined over the element using nine nodes, these are those of the interpolant denoted by ● and five further nodes denoted by ●.

The material properties are as defined in Section (C.1) with Young's modulus $E \equiv$ `eval` $= 1$ and Poisson's ratio $\nu \equiv$ `nu` $= 1/4$. In addition the plate thickness t is also given as `thick` $= 1/10$ and the shear correction factors `AK1` and `AK2`.

```
eval    = 1;
nu      = 1/4;
thick   = 1/10;
AK1     = 5/6;
AK2     = 5/6;
```

The interpolant shape functions, using the values of `north`, `east`, `south` and `west` are then defined and stored in `Interp`.

```
shape9 = 0;
If[north == 1, shape5 = (1/2) (1-Abs[x]) (1+y), shape5 = 0];
If[east == 1,  shape6 = (1/2) (1+x) (1-Abs[y]), shape6 = 0];
If[south == 1, shape7 = (1/2) (1-Abs[x]) (1-y), shape7 = 0];
If[west == 1,  shape8 = (1/2) (1-x) (1-Abs[y]), shape8 = 0];
shape1 = (1/4) (1-x) (1-y) - (1/2) (shape7+shape8);
shape2 = (1/4) (1+x) (1-y) - (1/2) (shape6+shape7);
shape3 = (1/4) (1+x) (1+y) - (1/2) (shape5+shape6);
shape4 = (1/4) (1-x) (1+y) - (1/2) (shape5+shape8);
Interp = {
          shape1,shape2,shape3,
          shape4,shape5,shape6,
          shape7,shape8,shape9,
         };
```

Using the node numbering scheme given in Figure (C.2) the biquadratic shape functions are then stored in `Biquad`. The interpolant shape functions are then subtracted from the biquadratic shape functions as performed in Section (6.2.2) to give `Phi`.

```
Biquad = {
          (1/4) x (x-1) y (y-1), (1/4) x (x+1) y (y-1),
          (1/4) x (x+1) y (y+1), (1/4) x (x-1) y (y+1),
         -(1/2) (x-1) (x+1) y (y+1), -(1/2) x (x+1) (y-1) (y+1),
         -(1/2) (x+1) (x-1) y (y-1), -(1/2) x (x-1) (y+1) (y-1),
          (x+1) (x-1) (y+1) (y-1)
         };
Phi = Biquad - Interp;
```

The next step is to define `PreFmx` which has the form described in Equation (6.37).

```
PreFmx = Table[0,{i,1,5*Length[Phi]},{j,1,5*Length[Phi]}];
Do[
   PreFmx[[5*i-4,5*j-4]] = Phi[[i]]*Phi[[j]];
   PreFmx[[5*i-3,5*j-3]] = Phi[[i]]*Phi[[j]];
   PreFmx[[5*i-2,5*j-2]] = Phi[[i]]*Phi[[j]];
   PreFmx[[5*i-1,5*j-1]] = Phi[[i]]*Phi[[j]];
   PreFmx[[5*i,5*j]]     = Phi[[i]]*Phi[[j]],
   {i,Length[Phi]},{j,Length[Phi]}
  ]
```

It is now necessary to integrate `PreFmx`. This is complicated by the fact that there may be irregular midside nodes. The element is thus split into four subregions over which the integration can be performed.

```
PreFmxA = PreFmx/.{Abs[x]->-x,Abs[y]->y};
PreFmxB = PreFmx/.{Abs[x]->x,Abs[y]->y};
PreFmxC = PreFmx/.{Abs[x]->-x,Abs[y]->-y};
PreFmxD = PreFmx/.{Abs[x]->x,Abs[y]->-y};
```

The subregions are then integrated over. The integration depends on the current value of `type`. If `type = interior` then the integration is as follows.

```
If[
   type == interior,
   Print[Date[]];
   Print["Integrating element interior."];
   Fmx1 = Integrate[PreFmxA,{x,-1,0},{y,0,1}];
   Fmx2 = Integrate[PreFmxB,{x,0,1},{y,0,1}];
   Fmx3 = Integrate[PreFmxC,{x,-1,0},{y,-1,0}];
   Fmx4 = Integrate[PreFmxD,{x,0,1},{y,-1,0}];
   Fmx = Fmx1 + Fmx2 + Fmx3 + Fmx4;
  ];
```

For the case where `type = boundary` the integration is more complicated. Integration is firstly performed around the element perimeter.

```
If[
   type == boundary,
   Fmx1=0;Fmx2=0;Fmx3=0;Fmx4=0;
   Fmx5=0;Fmx6=0;Fmx7=0;Fmx8=0;
   Fmx9=0;Fmx10=0;Fmx11=0;Fmx12=0;
   Fmx13=0;Fmx14=0;Fmx15=0;Fmx16=0;
  ];
If[
   type == boundary,
   Print[Date[]];
   Print["Integrating around perimeter."];
   Fmx1 = Integrate[PreFmxC,{x,-1,0}]/.y->-1;
   Fmx2 = Integrate[PreFmxD,{x,0,1}]/.y->-1;
   Fmx3 = Integrate[PreFmxD,{y,-1,0}]/.x->1;
   Fmx4 = Integrate[PreFmxB,{y,0,1}]/.x->1;
   Fmx5 = Integrate[PreFmxB,{x,1,0}]/.y->1;
   Fmx6 = Integrate[PreFmxA,{x,0,-1}]/.y->1;
   Fmx7 = Integrate[PreFmxA,{y,1,0}]/.x->-1;
   Fmx8 = Integrate[PreFmxC,{y,0,-1}]/.x->-1;
  ];
```

This integration is then followed by integrating along possible lines of slope discontinuity. These lines may possibly occur whenever there is a midside node. For the case where there is either a midside node on the North face or the South face or both North and South faces the following integration is performed.

```
If[
   (type == boundary) && ((north == 1) || (south == 1 )),
   Print[Date[]];
   Print["Integrating North->South line of discontinuity."];
   Fmx9  = Integrate[PreFmxB,{y,1,0}]/.x->0;
   Fmx10 = Integrate[PreFmxD,{y,0,-1}]/.x->0;
   Fmx11 = Integrate[PreFmxC,{y,-1,0}]/.x->0;
   Fmx12 = Integrate[PreFmxA,{y,0,1}]/.x->0;
  ];
```

Similarly, for a node on either the East face or the West face or both we have the following integration.

```
If[
   (type == boundary) && ((east == 1) || (west == 1 )),
   Print[Date[]];
   Print["Integrating East->West line of discontinuity."];
   Fmx13 = Integrate[PreFmxD,{x,1,0}]/.y->0;
   Fmx14 = Integrate[PreFmxC,{x,0,-1}]/.y->0;
   Fmx15 = Integrate[PreFmxA,{x,-1,0}]/.y->0;
   Fmx16 = Integrate[PreFmxB,{x,0,1}]/.y->0;
  ];
```

The integral contributions may now be summed, care must be taken here due to the direction of integration with respect to positive dx and dy.

```
If[
   type == boundary,
   Print[Date[]];
   Print["Summing line contributions."];
   Fmx = Fmx1+Fmx2+Fmx3+Fmx4-Fmx5-Fmx6-Fmx7-Fmx8-
         Fmx9-Fmx10+Fmx11+Fmx12-Fmx13-Fmx14+Fmx15+
         Fmx16;
  ];
```

Thus matrix $\mathbf{F} \equiv$ `Fmx` has now been obtained. The task now is to compute matrix $\mathbf{E} \equiv$ `Emx` as given in Equation (6.42). Firstly though, the material properties are used to evaluate the Lamé coefficients $\lambda \equiv$ `lambda` and $\mu \equiv$ `mu` in the plane stress setting and the plate constitutive matrices `Const` and `Const2`.

```
lambda  = (nu*eval)/(1-(nu^2));
mu      = eval/(2*(1+nu));
Const   = {
           {lambda+2*mu, lambda, 0},
           {lambda, lambda+2*mu, 0},
           {0,0,mu}
          };
Const2  = {
           {mu*AK1, 0},
           {0, mu*AK2}
          };
```

The constitutive matrices are now integrated over the plate thickness as in Equations (6.26), (6.27), (6.28) and (6.29). Once this has been done the results are stored in matrices `Cbend` and `Cshear`.

```
Cbend  = Table[0,{i,1,6},{j,1,6}];
Cshear = Table[0,{i,1,2},{j,1,2}];
Do[
   Cbend[[i,j]] = Integrate[Const[[i,j]],{z,-thick/2,thick/2}]
   {i,1,3},{j,1,3}
  ];
Do[
   tempterm = Integrate[Const[[i,j]]*z,{z,-thick/2,thick/2}];
   Cbend[[i,j+3]] = tempterm;
   Cbend[[i+3,j]] = tempterm,
   {i,1,3},{j,1,3}
  ];
Do[
   Cbend[[i+3,j+3]] = Integrate[
                        Const[[i,j]]*z^2,{z,-thick/2,thick/2}
                               ],
   {i,1,3},{j,1,3}
  ];
Do[
   Cshear[[i,j]] = Integrate[Const2[[i,j]],{z,-thick/2,thick/2}],
   {i,1,2},{j,1,2}
  ];
```

Matrix `Emx` may then be evaluated by firstly evaluating the bending terms and storing them in array `PreEmxb`.

```
Bb1 = Table[0,{i,1,5},{j,1,6}];
Bb2 = Table[0,{i,1,6},{j,1,5}];
Bs1 = Table[0,{i,1,5},{j,1,2}];
Bs2 = Table[0,{i,1,2},{j,1,5}];
PreEmxb = Table[0,{i,1,5*Length[Biquad]},{j,1,5*Length[Biquad]}];
PreEmxs = Table[0,{i,1,5*Length[Biquad]},{j,1,5*Length[Biquad]}];
PreEmx  = Table[0,{i,1,5*Length[Biquad]},{j,1,5*Length[Biquad]}];

Ab[fn_] := Do[
              Bb1[[1,1]]=D[fn[[i]],x];Bb1[[1,3]]=D[fn[[i]],y];
              Bb1[[2,2]]=D[fn[[i]],y];Bb1[[2,3]]=D[fn[[i]],x];
              Bb1[[4,4]]=D[fn[[i]],x];Bb1[[4,6]]=D[fn[[i]],y];
              Bb1[[5,5]]=D[fn[[i]],y];Bb1[[5,6]]=D[fn[[i]],x];
              Bb2[[1,1]]=D[fn[[j]],x];Bb2[[2,2]]=D[fn[[j]],y];
              Bb2[[3,1]]=D[fn[[j]],y];Bb2[[3,2]]=D[fn[[j]],x];
              Bb2[[4,4]]=D[fn[[j]],x];Bb2[[5,5]]=D[fn[[j]],y];
              Bb2[[6,4]]=D[fn[[j]],y];Bb2[[6,5]]=D[fn[[j]],x];
              TempCell = Bb1.Cbend.Bb2;
              PreEmxb[[5*i-4,5*j-4]] = TempCell[[1,1]];
              PreEmxb[[5*i-4,5*j-3]] = TempCell[[1,2]];
              PreEmxb[[5*i-4,5*j-2]] = TempCell[[1,3]];
              PreEmxb[[5*i-4,5*j-1]] = TempCell[[1,4]];
              PreEmxb[[5*i-4,5*j]] = TempCell[[1,5]];
              PreEmxb[[5*i-3,5*j-4]] = TempCell[[2,1]];
              PreEmxb[[5*i-3,5*j-3]] = TempCell[[2,2]];
              PreEmxb[[5*i-3,5*j-2]] = TempCell[[2,3]];
              PreEmxb[[5*i-3,5*j-1]] = TempCell[[2,4]];
              PreEmxb[[5*i-3,5*j]] = TempCell[[2,5]];
              PreEmxb[[5*i-2,5*j-4]] = TempCell[[3,1]];
              PreEmxb[[5*i-2,5*j-3]] = TempCell[[3,2]];
```

```
                PreEmxb[[5*i-2,5*j-2]] = TempCell[[3,3]];
                PreEmxb[[5*i-2,5*j-1]] = TempCell[[3,4]];
                PreEmxb[[5*i-2,5*j]] = TempCell[[3,5]];
                PreEmxb[[5*i-1,5*j-4]] = TempCell[[4,1]];
                PreEmxb[[5*i-1,5*j-3]] = TempCell[[4,2]];
                PreEmxb[[5*i-1,5*j-2]] = TempCell[[4,3]];
                PreEmxb[[5*i-1,5*j-1]] = TempCell[[4,4]];
                PreEmxb[[5*i-1,5*j]] = TempCell[[4,5]];
                PreEmxb[[5*i,5*j-4]] = TempCell[[5,1]];
                PreEmxb[[5*i,5*j-3]] = TempCell[[5,2]];
                PreEmxb[[5*i,5*j-2]] = TempCell[[5,3]];
                PreEmxb[[5*i,5*j-1]] = TempCell[[5,4]];
                PreEmxb[[5*i,5*j]] = TempCell[[5,5]],
                {i,1,Length[fn]},{j,1,Length[fn]}
               ]
 Ab[Biquad];
```

The evaluation of the transverse shear terms is then performed and stored in **PreEmxs**.

```
As[fn_] := Do[
                Bs1[[3,1]]=D[fn[[i]],x];Bs1[[3,2]]=D[fn[[i]],y];
                Bs1[[4,1]]=0*fn[[i]];Bs1[[5,2]]=0*fn[[i]];
                Bs2[[1,3]]=D[fn[[j]],x];Bs2[[1,4]]=0*fn[[j]];
                Bs2[[2,3]]=D[fn[[j]],y];Bs2[[2,5]]=0*fn[[j]];
                TempCell = Bs1.Cshear.Bs2;
                PreEmxs[[5*i-4,5*j-4]] = TempCell[[1,1]];
                PreEmxs[[5*i-4,5*j-3]] = TempCell[[1,2]];
                PreEmxs[[5*i-4,5*j-2]] = TempCell[[1,3]];
                PreEmxs[[5*i-4,5*j-1]] = TempCell[[1,4]];
                PreEmxs[[5*i-4,5*j]] = TempCell[[1,5]];
                PreEmxs[[5*i-3,5*j-4]] = TempCell[[2,1]];
                PreEmxs[[5*i-3,5*j-3]] = TempCell[[2,2]];
                PreEmxs[[5*i-3,5*j-2]] = TempCell[[2,3]];
                PreEmxs[[5*i-3,5*j-1]] = TempCell[[2,4]];
                PreEmxs[[5*i-3,5*j]] = TempCell[[2,5]];
                PreEmxs[[5*i-2,5*j-4]] = TempCell[[3,1]];
                PreEmxs[[5*i-2,5*j-3]] = TempCell[[3,2]];
                PreEmxs[[5*i-2,5*j-2]] = TempCell[[3,3]];
                PreEmxs[[5*i-2,5*j-1]] = TempCell[[3,4]];
                PreEmxs[[5*i-2,5*j]] = TempCell[[3,5]];
                PreEmxs[[5*i-1,5*j-4]] = TempCell[[4,1]];
                PreEmxs[[5*i-1,5*j-3]] = TempCell[[4,2]];
                PreEmxs[[5*i-1,5*j-2]] = TempCell[[4,3]];
                PreEmxs[[5*i-1,5*j-1]] = TempCell[[4,4]];
                PreEmxs[[5*i-1,5*j]] = TempCell[[4,5]];
                PreEmxs[[5*i,5*j-4]] = TempCell[[5,1]];
                PreEmxs[[5*i,5*j-3]] = TempCell[[5,2]];
                PreEmxs[[5*i,5*j-2]] = TempCell[[5,3]];
                PreEmxs[[5*i,5*j-1]] = TempCell[[5,4]];
                PreEmxs[[5*i,5*j]] = TempCell[[5,5]],
                {i,1,Length[fn]},{j,1,Length[fn]}
               ]
As[Biquad];
```

The components of the two arrays **PreEmxb** and **PreEmxs** are then integrated over the element region and the results added to give matrix `Emx`.

```
Emxb = Integrate[PreEmxb,{x,-1,1},{y,-1,1}];
Emxs = Integrate[PreEmxs,{x,-1,1},{y,-1,1}];
Emx = Emxb + Emxs;
```

The eigenvalues of the generalized eigenvalue problem are then obtained to give the required interpolation error constant as described in Section (5.4).

C.3 J-H Estimator Calculation

This appendix includes the Mathematica code, [59], written to verify the computation of the quantity κ in Section (7.1.1) on a uniform mesh. The code has been split up below in order to insert explanations and it is important to note that in order to calculate κ the values for the element diameter $h = h_k =$ `hval` and the interpolation error constant $C_2^i = C_{2,k}^i =$ `c2i` should be set to unity. In the presented guise, the code will calculate the J-H estimator as given in Table (7.5) under the column label 'Mathematica'.

We begin by reading in certain data output from the program. This is stored in the arrays `fenodes`, `fesol`, `xcoors`, `ycoors`, `nside` and `nsid`.

```
fenodes=<</user/mapg/mapgmjl/Elastic/Triangles/fort.1000;
fesol=<</user/mapg/mapgmjl/Elastic/Triangles/fort.1001;
xcoors=<</user/mapg/mapgmjl/Elastic/Triangles/fort.1002;
ycoors=<</user/mapg/mapgmjl/Elastic/Triangles/fort.1003;
nside=<</user/mapg/mapgmjl/Elastic/Triangles/fort.1004;
nsid=<</user/mapg/mapgmjl/Elastic/Triangles/fort.1005;
```

We may then obtain the number of elements `nem` and nodes `nnm`.

```
nem = Dimensions[fenodes][[1]]
nnm = Dimensions[fesol][[1]]
```

Thus the dimensions of the above arrays are `fenodes`(`nem`, $elnods$), `fesol`(`nnm`, ndf),`xcoors`(`nnm`), `ycoors`(`nnm`), `nside`(`nem`, $elsid$) and `nsid`($numsid$, 4). This requires the explanation of further variables $elnods$, ndf, $elsid$ and $numsid$. These are respectively the number of nodes per element, the number of degrees of freedom per node, the number of sides per element and the total number of sides in the mesh. The next task is to specify the material properties. The Young's modulus value E is denoted by `eval` and that or Poisson's ratio ν by `nu`. This enables the Lamé coefficients `lambda` and `mu` to then be calculated and also the constitutive matrix `const`. It can be seen below that `eval=1` and `nu=1/4`, this is merely as an example.

```
eval=1;
nu=1/4;
lambda=(eval*nu)/((1-2*nu)*(1+nu));
mu=eval/(2*(1+nu));
```

```
const={
       {lambda+2*mu,lambda,0},
       {lambda,lambda+2*mu,0},
       {0,0,mu}
      };
```

In accordance with Johnson and Hansbo, [27], we may then compute the interpolation error constants `c1i` and`c2i` using the Lamé coefficients. For this implementation however, `c1i` will not be used in the estimator due to the **f**-dependence having been dropped as discussed in Section (7.1.3).

```
c1i=0.4/Sqrt[lambda+5*mu];
c2i=1.1/Sqrt[lambda+5*mu];
```

Following this the next task is to calculate the element diameter $h = h_k =$ `hval`. As discussed in Section (7.1.1) and in accordance with the authors of [27] this is taken to be,

$$h_k = \sqrt{2A\left(\Omega_k\right)}.$$

This quantity is the same as the discretization parameter d and is equal to the largest edge of the elements divided by $\sqrt{2}$ for the uniform mesh being considered. Since the mesh is uniform, the element diameter will hold for all elements in a given mesh. We thus choose the first element and calculate the diameter.

```
elno=1;
hval=0;
Do[
   side=i;
   sideno=nside[[elno,side]];
   nodea=nsid[[sideno,1]];
   nodeb=nsid[[sideno,2]];
   xa=xcoors[[nodea]];
   ya=ycoors[[nodea]];
   xb=xcoors[[nodeb]];
   yb=ycoors[[nodeb]];
   slength=Sqrt[(xb-xa)^2+(yb-ya)^2];
   If[
      slength>hval,hval=slength
     ],
   {i,1,3}
  ]
hval=hval/Sqrt[2]
```

We next calculate the symmetric stress tensor terms on each element. These are stored in array `stresses(nem,4)` such that, for the tensor components σ_{11}, $\sigma_{12} = \sigma_{21}$ and σ_{22} of a typical element `elno` the storage scheme is,

$$\texttt{stresses(enno},1) = \sigma_{11}, \qquad \texttt{stresses(enno},2) = \sigma_{12},$$

$$\texttt{stresses(enno},3) = \sigma_{21}, \qquad \texttt{stresses(enno},4) = \sigma_{22}.$$

The meshes considered here are uniform and furthermore are of the form illustrated in Figure (7.1). It can be seen therein that two types of element orientations exist in the mesh and these can be found by taking any two elements which share their longest edges with each other. The union of two such elements forms a square region and it is the diagonal of this square region which corresponds to the shared longest edge of the elements. In addition, it can be seen that the whole mesh can be built up by repeating these square regions over the problem domain and consequently we shall call these square regions the mesh repeators. The numbering scheme for the elements in the uniform mesh is such that all elements which lie below the diagonal of their repeator are odd whilst those above are even, this enables the element shape functions to be defined in terms of the global coordinates as in the code below. It should be noted that in the portion of Mathematica code below the nodes of the element are referred to as `nodei`, `nodej` amd `nodek`.

```
stresses=Table[0,{i,1,nem},{j,1,4}];
Do[
   elno=i;
   nodei=fenodes[[elno,1]];
   nodej=fenodes[[elno,2]];
   nodek=fenodes[[elno,3]];
   xi=xcoors[[nodei]];
   yi=ycoors[[nodei]];
   xj=xcoors[[nodej]];
   yj=ycoors[[nodej]];
   xk=xcoors[[nodek]];
   yk=ycoors[[nodek]];
   If[
      OddQ[elno],
      shapei=1-(x-xi)/(xj-xi)-(y-yi)/(yk-yi);
      shapej=(x-xi)/(xj-xi);
      shapek=(y-yi)/(yk-yi);
      xmin=xi;
      xmax=xj;
      ymin=yi;
      ymax=yk
     ];
   If[
      EvenQ[elno],
      shapei=(yj-y)/(yj-yi);
      shapej=1-(xj-x)/(xj-xk)-(yj-y)/(yj-yi);
      shapek=(xj-x)/(xj-xk);
      xmin=xk;
      xmax=xj;
      ymin=yi;
      ymax=yj
     ];
   feu=fesol[[nodei,1]]*shapei+fesol[[nodej,1]]*shapej+
       fesol[[nodek,1]]*shapek;
   fev=fesol[[nodei,2]]*shapei+fesol[[nodej,2]]*shapej+
       fesol[[nodek,2]]*shapek;
   stresses[[elno,1]]=const[[1,1]]*D[feu,x]+const[[1,2]]*D[fev,y];
   stresses[[elno,2]]=const[[3,3]]*(D[feu,y]+D[fev,x]);
   stresses[[elno,3]]=const[[3,3]]*(D[fev,x]+D[feu,y]);
   stresses[[elno,4]]=const[[2,1]]*D[feu,x]+const[[2,2]]*D[fev,y],
   {i,1,nem}
  ]
```

The elemental contributions to the J-H error estimator are now calculated. The first portion of the Mathematica code below computes the unit outward normal to the side `sideno`. This has components `xnorm` and `ynorm`. The jumps in the stress tensor terms between the current element `elno` ant the neighbouring element `adjel` sharing side `sidno` are then obtained and stored as `sts11`, `sts12`, `sts21` and `sts22`. Finally the side contribution for the element is computed and stored in `estim`(`elno`).

```
estim=Table[0,{i,1,nem}];
Do[
   elno=i;
   side=j;
   sidno=nside[[elno,side]];
   If[nsid[[sidno,3]]==elno,adjel=nsid[[sidno,4]],adjel=nsid[[sidno,3]]];
   If[adjel==0,Goto[miss]];
   nodea=nsid[[sidno,1]];
   nodeb=nsid[[sidno,2]];
   xa=xcoors[[nodea]];
   ya=ycoors[[nodea]];
   xb=xcoors[[nodeb]];
   yb=ycoors[[nodeb]];
   slength=Sqrt[(xb-xa)^2+(yb-ya)^2];
   Do[
      If[
         (fenodes[[elno,k]]!=nodea)&&(fenodes[[elno,k]]!=nodeb),
         nodec=fenodes[[elno,k]]
        ];
      {k,1,3}
     ];
   xc=xcoors[[nodec]];
   yc=ycoors[[nodec]];
   xctoa=xa-xc;
   yctoa=ya-yc;
   xctob=xb-xc;
   yctob=yb-yc;
   crossp=xctoa*yctob-xctob*yctoa;
   xatob=xb-xa;
   yatob=yb-ya;
   If[
      crossp>0,
      xnorm=yatob/slength;
      ynorm=-xatob/slength,
      xnorm=-yatob/slength;
      ynorm=xatob/slength
     ];
   sts11=stresses[[elno,1]]-stresses[[adjel,1]];
   sts12=stresses[[elno,2]]-stresses[[adjel,2]];
   sts21=stresses[[elno,3]]-stresses[[adjel,3]];
   sts22=stresses[[elno,4]]-stresses[[adjel,4]];
   intbdy1=((0.5*(xnorm*sts11+ynorm*sts12))^2)*slength;
   intbdy2=((0.5*(xnorm*sts21+ynorm*sts22))^2)*slength;
   estim[[elno]]+=c2i^2*(intbdy1+intbdy2)*hval;
   Label[miss],
   {i,1,nem},{j,1,3}
  ]
```

At this point we have the elemental contributions to the J-H estimator stored in array `estim`. We must now sum over all the elements and take the square root in order to obtain the final global error estimate.

```
estimtot = 0.;
Do[
   estimtot = estimtot + estim[[i]],
   {i,1,nem}
  ]
N[Sqrt[estimtot], 15]
```

Appendix D

Research Correspondence

Included below is an email sent to Professor P.Hansbo, the questions relate to the paper by Johnson and Hansbo, [27].

```
Dear Professor Hansbo,

I am currently a research student at Brunel University in England
under the supervision of Professor J.R.Whiteman who sends his
greetings and best wishes.

I am particularly interested in a posteriori error estimation and
have recently been working on the estimator detailed in the paper
'Adaptive finite element methods in computational mechanics'
(Computer Methods in Applied Mechanics and Engineering, Vol. 101,
pp. 143-181, 1992) produced by yourself and Professor Johnson.

My reason for writing is due to the fact that for the linear
elasticity problem detailed in Section (5.1) of your paper I am
experiencing difficulty in reproducing your efficiency index results
illustrated in Figure (1) of your paper. As with yourselves, I am using
triangular elements of linear type and in addition I am neglecting
the f-dependence and also using your interpolation error constant
bounds supplied in Equation (2.25). Additionally the mesh used is
one consisting of 1089 nodes and 2048 elements with the orientation
of the elements as detailed in Figure (2) (unidirectional). As far
as I am concerned this should reproduce exactly your results in
Figure 1 for the range of log(lambda/mu) and so I cannot see what
is causing the differences. I have already experimented with
differing quadrature rules but none have so far replicated your
results.

Comparing my efficiency index results with yours over the range
of log(lambda/mu) I seem to consistently obtain 4/3 times your
results. Comparing the results we have :
```

Log(lambda/mu)	Your Efficiency index (from Figure 1)	My efficiency index
-4	1.448	1.928
-3	1.448	1.928
-2	1.448	1.931
-1	1.465	1.953
0	1.618	2.155
1	2.165	2.878
2	2.453	3.274
3	2.500	3.331
4	2.506	3.337
5	2.506	3.338
6	2.506	3.338

As can be seen, my numbers are all almost exactly 4/3 times yours. I do not understand why this is but hopefully I may be able to establish why if you would be so kind as to answer a few questions I have.

1) When you use the element 'diameter' h_{k}, what exactly do you mean by this? I am using the longest edge value (i.e. the diagonal on a right angled isosceles triangle). Is this the same as you? This longest edge is also the diameter of the escribing circle in this instance so does that correspond to your use of the word 'diameter'? In addition how do you define the element diameters used in the expressions for the interpolation error constants in Equations (2.9a) and (2.9b)?

2) You say that the results were obtained on a mesh consisting of 1089 nodes and 2048 triangles. Is this a unidirectional mesh (like the one shown in Figure (2) but with 32 horizontal and vertical divisions) or a uniform mesh with different element orientations (eg. the 'union jack' orientation) i.e. with repeators,

```
     ---------      ---------
     |\  |\  |      |\  |  /|
     | \ | \ |      | \ | / |
     |  \|  \|      |  \|/  |
     ---------  or  ---------
     |\  |\  |      |  /|\  |
     | \ | \ |      | / | \ |
     |  \|  \|      |/  |  \|
     ---------      ---------
  unidirectional    union jack
```

I am using a mesh of the above unidirectional type with consists of isosceles right angled triangles.

3) I would be very interested to know of the quadrature schemes you used to compute the results. I appreciate that this may have been a while ago now but this is really the only other area in which differences could stem from.

```
4) Do you have more detailed sets of results for the linear elasticity
   problem? I would find the finite element error measured in the energy
   norm and the global error estimate itself most useful as these are the
   two components of the efficiency index given in Equation (1.9) and
   would enable me to compare the finite element solutions resulting
   from both yours and my computations as well as the computed global
   error estimate value directly.

I would greatly appreciate any help you could give me with regard to
the above questions. I appreciate that the paper was published in
1992 and that it was rather a long time ago but any thoughts you
may have would be of great help.

In addition to the above questions I would appreciate any further
information you may have on the technique you used to establish the
interpolation error constant bounds given in Equation (2.25). I
have attempted to obtain constant values too but unfortunately I
again seem to be unable to obtain values which fall within your
bounds. I would be very interested in reading any further information
on the technique you used to obtain these bounds.

I apologize for the length of this email and I also apologize in advance for
any misinterpretations that I may have made with respect to your paper. I look
forward to reading your reactions to this email and I thank you for taking
the time to read it. Any comments observations and thoughts you have will be
greatly appreciated.

Regards,

Marcus Ludwig.
```

My sincere thanks go to Professor P.Hansbo for his informative and helpful reply which is included below.

```
Dear Dr. Ludwig,

I'll try to answer your questions, but you must realize that I no longer
have the precise code I used in the computations.

> As can be seen, my numbers are all almost exactly 4/3 times yours.
> I do not understand why this is but hopefully I may be able to
> establish why if you would be so kind as to answer a few questions
> I have.
>
> 1) When you use the element 'diameter' h_{k}, what exactly do you
>    mean by this? I am using the longest edge value (i.e. the diagonal
>    on a right angled isosceles triangle). Is this the same as you?
>    This longest edge is also the diameter of the escribing circle
>    in this instance so does that correspond to your use of the word
>    'diameter'? In addition how do you define the element diameters
>    used in the expressions for the interpolation error constants in
>    Equations (2.9a) amd (2.9b)?
>
```

```
I invariably use the square root of twice the area of the triangle, so for the
case in question you should get sqrt(2) times larger "diameter".

> 2) You say that the results were obtained on a mesh consisting of
>    1089 nodes and 2048 triangles. Is this a unidirectional mesh
>    (like the one shown in Figure (2) but with 32 horizontal and
>    vertical divisions) or a uniform mesh with different element
>    orientations (eg. the 'union jack' orientation) i.e. with
>    repeators,
>
>           ---------      ---------
>           |\  |\  |      |\  |  /|
>           | \ | \ |      | \ | / |
>           |  \|  \|      |  \|/  |
>           ---------  or  ---------
>           |\  |\  |      |  /|\  |
>           | \ | \ |      | / | \ |
>           |  \|  \|      |/  |  \|
>           ---------      ---------
>        unidirectional    union jack
>
>    I am using a mesh of the above unidirectional type with consists
>    of isosceles right angled triangles.
>

Unidirectional.

> 3) I would be very interested to know of the quadrature schemes you
>    used to compute the results. I appreciate that this may have been
>    a while ago now but this is really the only other area in which
>    differences could stem from.
>

I used the trick that || u-u_h ||^2 = || u ||^2 - || u_h ||^2  because of
orthogonality.

> 4) Do you have more detailed sets of results for the linear elasticity
>    problem? I would find the finite element error measured in the energy
>    norm and the global error estimate itself most useful as these are the
>    two components of the efficiency index given in Equation (1.9) and
>    would enable me to compare the finite element solutions resulting
>    from both yours and my computations as well as the computed global
>    error estimate value directly.

No, I have not. But I would like to say, however, that there
are some difficulties in the whole concept because
the interpolation estimate is a "worst case scenario": what we
really would like is an estimate of how well we interpolate
the *actual* solution to the problem. Furthermore, in energy norm
for the elasticity problem the interpolation estimate actually
requires the extremum to be taken over a larger set of elements, so
in a sense the whole point is mote. In fact, there is much to be said for
"tuning" the constants by solving over a set of problems with known
exact solution. This then in a sense shows how the involved constants
```

vary over a "nice" or "real" set of solutions.

For an extended discussion you should read
Becker, R.; Rannacher, R. A feed-back approach to error control in finite element methods: basic analysis and examples. East-West J. Numer. Math. 4 (1996), no. 4, 237--264 which is much more careful and precise than we were in our paper (though I don't think they deal with the equations of elasticity).

> In addition to the above questions I would appreciate any further
> information you may have on the technique you used to establish the
> interpolation error constant bounds given in Equation (2.25). I
> have attempted to obtain constant values too but unfortunately I
> again seem to be unable to obtain values which fall within your
> bounds. I would be very interested in reading any further information
> on the technique you used to obtain these bounds.
>

I used trial and error: insert a number of functions and compute the worst possible quotient. You don't say whether you got considerably different results, did you?

Please convey my best regards to Professor J.R.Whiteman.

Sincerely,
Peter Hansbo

Appendix E

Sobolev Imbedding

From Adams, [1], we have the following (Theorem 7.58, p218). Let, $s > 0$, $1 < p \leq q < \infty$ and $1 \leq m \leq n$. Let $\chi = s - (n/p) + (m/q)$. If,

$$\begin{aligned} (i) \quad & \chi \geq 0 \text{ and } p < q, \text{ or} \\ (ii) \quad & \chi > 0 \text{ and } \chi \text{ is not an integer, or} \\ (iii) \quad & \chi \geq 0 \text{ and } 1 < p \leq 2, \end{aligned}$$

then,

$$W_p^s\left(\mathbb{R}^n\right) \hookrightarrow W_q^\chi\left(\mathbb{R}^m\right). \tag{E.1}$$

Consider $\mathbb{R}^n = \mathbb{R}^m = \Omega_k$ with $m = n = 2$ where Ω_k is an element of the general problem domain $\Omega \in \mathbb{R}^2$ and take $s = 1 + \epsilon$, $\chi = 1$, $p = 2$ and $q = 2/(1 - \epsilon) \equiv 2 + \varepsilon$. It follows via condition (i) above that Equation (E.1) takes the form,

$$W_2^{1+\epsilon}\left(\Omega_k\right) \hookrightarrow W_{2+\varepsilon}^1\left(\Omega_k\right). \tag{E.2}$$

This in turn implies that there exists a constant M so that,

$$||u||_{W_{2+\varepsilon}^1(\Omega_k)} \leq M||u||_{W_2^{1+\epsilon}(\Omega_k)}, \tag{E.3}$$

by Adams (Section 1.24, p9) and thus,

$$u \in W_2^{1+\epsilon}(\Omega_k) \Rightarrow u \in W_{2+\varepsilon}^1(\Omega_k). \tag{E.4}$$

It then follows via the Sobolev imbedding theorem,

$$W_p^1(\Omega_k) \subset C(\overline{\Omega}_k), \text{ for } p > 2, \tag{E.5}$$

that,

$$u \in W_2^{1+\epsilon}(\Omega_k) \Rightarrow u \in W_{2+\varepsilon}^1(\Omega_k) \subset C(\overline{\Omega}_k). \tag{E.6}$$

Thus $u \in H^{1+\epsilon}(\Omega_k)$ will be continuous on the boundary of element Ω_k. This result is of great use in the application of the error estimator of Johnson and Hansbo, [27]. Due to the above result an interpolant $\pi_h u$ to u may now be defined at every point over the element Ω_k enabling the following expressions for the interpolation error $\mathbf{e} - \pi_h \mathbf{e}$ where $\mathbf{e} = \mathbf{u} - \mathbf{u}_h$,

$$||\mathbf{e} - \pi_h \mathbf{e}||_{L_2(\Omega_k)} \leq C^i_{1,k} h_k ||\mathbf{e}||_{E(\Omega_k)}, \tag{E.7}$$

and,

$$||\mathbf{e} - \pi_h \mathbf{e}||_{L_2(\partial\Omega_k)} \leq C^i_{2,k} h_k^{\frac{1}{2}} ||\mathbf{e}||_{E(\Omega_k)}, \tag{E.8}$$

to be used. In the above $C^i_{1,k}$ and $C^i_{2,k}$ are the interior and boundary interpolation error constants respectively as first introduced in Section (4.4). Consequently, this enables the required interpolation error constants themselves to be expressed as,

$$C^i_{1,k} = \sup_{\boldsymbol{\tau} \in V_\epsilon} \frac{h_k^{-1} ||\boldsymbol{\tau} - \pi_h \boldsymbol{\tau}||_{L_2(\Omega_k)}}{||\boldsymbol{\tau}||_{E(\Omega_k)}}, \tag{E.9}$$

and,

$$C^i_{2,k} = \sup_{\boldsymbol{\tau} \in V_\epsilon} \frac{h_k^{-\frac{1}{2}} ||\boldsymbol{\tau} - \pi_h \boldsymbol{\tau}||_{L_2(\partial\Omega_k)}}{||\boldsymbol{\tau}||_{E(\Omega_k)}}, \tag{E.10}$$

where, for a general problem in two dimensions the space $V_\epsilon = \left[H^{1+\epsilon}(\Omega_k)\right]^r$ with $r = 2$ or 5 for the linear elasticity or plate models respectively as introduced in Chapter 2 and where $\epsilon \in (0, 1)$ is determined by the regularity of the exact solution of the underlying problem.

References

[1] Adams, R.A., *Sobolev Spaces*, Academic Press, Inc., New York, 1975.

[2] Ainsworth, M. and Oden, J.T.,'A posteriori error estimation in finite element analysis', Report 1995/14, Department of Mathematics and Computer Science, University of Leicester, Leicester, England, 1995.

[3] Ainsworth, M., Zhu, J.Z., Craig, A.W. and Zienkiewicz, O.C., 'Analysis of the Zienkiewicz-Zhu a-posteriori error estimator in the finite element method', *International Journal for Numerical Methods in Engineering*, **28**, pp.2161-2174, 1989.

[4] *ANSYS Workbook, Revision 5.2*, Ansys Inc., 201 Johnson Road, Houston, PA 15342-1300, U.S.A., 1995.

[5] Averill, R.C. and Reddy, J.N., 'Behaviour of plate elements based on the first-order shear deformation theory', *Engineering Computations*, **7**, pp.57-74, 1989.

[6] Babuška, I., and Miller, A.,'A feedback finite element method with a posteriori error estimation: PART I. The finite element method and some basic properties of the a posteriori error estimator', *Computer Methods in Applied Mechanics and Engineering*, **61**, pp.1-40, 1987.

[7] Babuška, I. and Rheinboldt, W.C.,'Error estimates for adaptive finite element computations', *SIAM Journal on Numerical Analysis*, **15**, pp.736-754, 1978.

[8] Babuška, I. and Rodrígues, R., 'The problem of the selection of an a posteriori error indicator based on smoothing techniques', *International Journal for Numerical Methods in Engineering*, **36**, pp.539-567, 1993.

[9] Babuška, I., Strouboulis, T., Upadhyay, C.S. and Gangaraj, S.K., 'η%-superconvergence in the interior of locally refined meshes of quadrilaterals: superconvergence of the gradient in finite element solutions of Laplace's and Poisson's equations',Technical Note BN-1161 and CMC Report No. 93-09, Institute for Physical Science and Technology, University of Maryland, College Park Campus, 1994.

[10] Babuška, I., Strouboulis, T., Upadhyay, C.S. and Gangaraj, S.K., 'Computer-based proof of the existence of superconvergence points in the finite element method; superconvergence of

the derivatives in finite element solutions of Laplace's, Poisson's and the elasticity equations', *Numerical Methods for Partial Differential Equations*, **12**, pp.347-392, 1996.

[11] Babuška, I. and Suri, M.,'The $p-$ and $h-p$ versions of the finite element method, an overview', *Computer Methods in Applied Mechanics and Engineering*, **80**, pp.5-26, 1990.

[12] Bank, R.E., 'The efficient implementation of local mesh refinement algorithms', in *Adaptive Computational Methods For Partial Differential Equations* (ed. Babuška, I., Chandra, J. and Flaherty, J.E.), pp.74-81, Society for Industrial and Applied Mathematics, Philadelphia, 1983.

[13] Bank, R.E. and Weiser, A., 'Some a posteriori error estimators for elliptic partial differential equations', *Mathematics of Computation*, **44**, pp.283-301, 1985.

[14] Barlow, J., 'Optimal stress locations in finite element models', *International Journal for Numerical Methods in Engineering*, **10**, pp.243-251, 1976.

[15] Bodig, J. and Jayne, B.A., *Mechanics of Wood and Wood Composites*, Van Nostrand Reinhold Company Inc., New York, 1982.

[16] Brenner, S.C. and Sung, L.-Y.,'Linear finite element methods for planar linear elasticity', *Mathematics of Computation*, **59**, pp.321-338, 1992.

[17] Choi, C. and Park, Y., 'Transition plate-bending elements for compatible mesh gradation', *Journal of Engineering Mechanics*, **118**, pp.462-480, 1992.

[18] Choi, C. and Park, Y., 'An adaptive h-refinement using transition element for plate bending problems', *International Journal for Numerical Methods in Engineering*, **35**, pp.145-163, 1992.

[19] Ciarlet, P.G., *The Finite Element Method for Elliptic Problems*, North-Holland Publishing Company, New York, U.S.A., 1978.

[20] Datta, B.N., *Numerical Linear Algebra and Applications*, Brooks/Cole Publishing Company, U.S.A., 1995.

[21] Eriksson, K., Estep, D., Hansbo, P. and Johnson, C., *Adaptive finite element methods*, Course notes: VIth SERC Numerical Analysis Summer School, Leicester Uni., England, 18-22 July, 1994.

[22] Gupta, A.K., 'A finite element for transition from a fine to a coarse grid', *International Journal for Numerical Methods in Engineering*, **12**, pp.35-45, 1978.

[23] Handscomb, D.C., 'Error of linear interpolation on a triangle', *Numerical Analysis Technical Report*, Report Number NA95/09, Oxford University Computing Laboratory, 1995.

[24] Houston, P., Mackenzie, J.A., Süli, E. and Warnecke, G., 'A posteriori error analysis for numerical approximations of Friedrichs systems', *Numerische Mathematik* (to appear), 1998.

[25] Jackson, N. and Süli, E., 'Adaptive finite element solution of 1D european option pricing problems', *Numerical Analysis Technical Report*, Report Number NA97/05, Oxford University Computing Laboratory, 1997.

[26] Johnson, C., *Numerical solution of partial differential equations by the finite element method*, Cambridge University Press, 1987.

[27] Johnson, C. and Hansbo, P., 'Adaptive finite element methods in computational mechanics', *Computer Methods in Applied Mechanics and Engineering*, **101**, pp.143-181, 1992.

[28] Labbé, P. and Garon, A.,'A robust implementation of Zienkiewicz and Zhu's local patch recovery method', *Communications in Numerical Methods in Engineering*, **11**, pp.427-434, 1995.

[29] Li, L.-Y., Bettess, P., Bull, J.W., Bond, T. and Applegarth, I., 'Theoretical formulations for adaptive finite element computations', *Communications in Numerical Methods in Engineering*, **11**, pp.857-868, 1995.

[30] Li, X.D. and Wiberg, N.-E., '*A posteriori* error estimate by element patch post-processing, adaptive analysis in energy and L_2 norms', *Computers & Structures*, **53**, pp.907-919, 1994.

[31] Liu, Y.C. and Elmaraghy, H.A., 'Assessment of discretized errors and adaptive refinement with quadrilateral finite elements', *International Journal for Numerical Methods in Engineering*, **33**, pp.781-798, 1992.

[32] Ludwig, M.J., *Adaptive Finite Element Methods with A Posteriori Error Estimates for Elliptic Problems*, M.Sc. Thesis, Department of Mathematics and Statistics, Brunel University, Uxbridge, England, 1994.

[33] Mackinnon, R.J. and Carey, G.F., 'Superconvergent derivatives: a Taylor series analysis', *International Journal for Numerical Methods in Engineering*, **28**, pp.489-509, 1989.

[34] *MATLAB for Sun Workstations, User's Guide*, The MathWorks Inc., South Natick, Massachusetts 01760, January 1989.

[35] Mindlin, R.D., 'Influence of rotary inertia and shear on flexural motions of isotropic, elastic plates', *Journal of Applied Mechanics*, **18**, pp.31-38, 1951.

[36] Mukherjee, S. and Krishnamoorthy, C.S., 'Adaptive FE analysis of plates by shear-flexible quadrilateral Reissner-Mindlin elements', *Finite Elements in Analysis and Design*, **22**, pp.329-366, 1996.

[37] Ochoa, O.O. and Reddy, J.N., *Finite Element Analysis of Composite Laminates*, Kluwer Academic Publishers, Dordrecht, The Netherlands, 1992.

[38] Oden, J.T., Demkowicz, L., Rachowicz, W. and Westermann, T.A., 'Toward a universal $h-p$ adaptive finite element strategy, PART 2. A posteriori error estimation', *Computer Methods in Applied Mechanics and Engineering*, **77**, pp.113-180, 1989.

[39] Oden, J.T. and Reddy, J.N.,*An Introduction to the Mathematical Theory of Finite Elements*, John Wiley & Sons, New York, 1976.

[40] Reddy, J.N., *Energy and Variational Methods in Applied Mechanics*, John Wiley & Sons, New York, 1984.

[41] Reddy, J.N. and Miravete, A., *Practical Analysis of Composite Laminates*, CRC Press, Florida, 1995.

[42] Reissner, E., 'The effect of transverse shear deformation on the bending of elastic plates', *Journal of Applied Mechanics, Trans. ASME*, **67**, A69-A77, 1945.

[43] Rivara, M.C., 'Algorithms for refining triangular grids suitable for adaptive and multigrid techniques', *International Journal for Numerical Methods in Engineering*, **20**, pp.745-756, 1984.

[44] Rivara, M.C., 'Mesh refinement processes based on the generalized bisection of simplices', *SIAM Journal on Numerical Analysis*, **21**, pp.604-613, 1984.

[45] Rodrígues, R., 'Some remarks on the Zienkiewicz-Zhu estimator', *Numerical Methods for Partial Differential Equations*, **10**, pp.625-635, 1994.

[46] Schauman U.K., Stages End House, Gaddesden Row, Hemel Hempstead, Hertfordshire, HP2 6HN, United Kingdom.

[47] Scott, L.R. and Zhang, S., 'Finite element interpolation of nonsmooth functions satisfying boundary conditions', *Mathematics of Computation*, **54**, pp.483-493, 1990.

[48] Shaw, S. and Whiteman, J.R., 'Discontinuous Galerkin method with a posteriori $L_p(0, t_i)$ error estimate for second-kind Volterra problems', *Numerische Mathematik*, **74**, pp.361-383, 1996.

[49] Shaw, S. and Whiteman, J.R. 'Numerical solution of linear quasistatic hereditary viscoelasticity problems II: a posteriori estimates', *BICOM Technical Report*, Report Number 98/3, Brunel University, Uxbridge, England, 1998.

[50] Shaw, S. and Whiteman, J.R. 'Negative norm error control for second-kind convolution Volterra equations', *BICOM Technical Report*, Report Number 98/6, Brunel University, Uxbridge, England, 1998.

[51] Stewart, J.R. and Hughes, T.J.R.,'Explicit residual-based a posteriori error estimation for finite element discretizations of the Helmholtz equation: Computation of the constant and new measures of error estimator quality', *Computer Methods in Applied Mechanics and Engineering*, **131**, pp.335-363, 1996.

[52] Süli, E., 'A posteriori error analysis and adaptivity for finite element approximations of hyperbolic problems', *Numerical Analysis Technical Report*, Report Number NA97/21, Oxford University Computing Laboratory, 1997.

[53] Süli, E. and Houston, P.,'Finite element methods for hyperbolic problems: a posteriori error analysis and adaptivity', *Numerical Analysis Technical Report*, Report Number NA96/09, Oxford University Computing Laboratory, 1996.

[54] Tabbara, M., Blacker, T. and Belytschko, T., 'Finite element derivative recovery by moving least square interpolants', *Computer Methods in Applied Mechanics and Engineering*, **117**, pp.211-223, 1994.

[55] Whiteman, J.R., *Finite Element Course Notes*, Department of Mathematics and Statistics, Brunel University, Uxbridge, England, 1993.

[56] Wiberg, N.-E. and Abdulwahab, F.,'Patch recovery based on superconvergent derivatives and equilibrium', *International Journal for Numerical Methods in Engineering*, **36**, pp.2703-2724, 1993.

[57] Wiberg, N.-E., Abdulwahab, F. and Saulius, Z.,'Enhanced superconvergent patch recovery incorporating equilibrium and boundary conditions', *International Journal for Numerical Methods in Engineering*, **37**, pp.3417-3440, 1994.

[58] Wiberg, N.-E., Abdulwahab, F. and Saulius, Z.,'Improved element stresses for node and element patches using superconvergent patch recovery', *Communications in Numerical Methods in Engineering*, **11**, pp.619-627, 1995.

[59] Wolfram, S., *Mathematica: A System for Doing Mathematics by Computer*, Addison-Wesley Publishing Company, Inc., 1991.

[60] Ženíšek, A. and Vanmaele, M., 'The interpolation theorem for narrow quadrilateral isoparametric finite elements', *Numerische Mathematik*, **72**, pp.123-141, 1995.

[61] Zhang, Z., 'Derivative superconvergence points in finite element solutions of Poisson's equation for the serendipity and intermediate families - a theoretical justification', Department of Mathematics, Texas Tech University, Lubbock, Texas 79409, 1991.

[62] Zhang, Z. and Victory Jr., H.D., 'Mathematical analysis of Zienkiewicz-Zhu's derivative patch recovery technique for quadrilateral finite elements', Department of Mathematics, Texas Tech University, Lubbock, TX 79409, 1994.

[63] Zhang, Z. and Zhang, S., 'Derivative superconvergence of rectangular finite elements for the Reissner-Mindlin plate', *Computer Methods in Applied Mechanics and Engineering*, **134**, pp.1-16, 1996.

[64] Zhu, J.Z. and Zienkiewicz, O.C.,'Superconvergence recovery technique and *a posteriori* error estimators', *International Journal for Numerical Methods in Engineering*, **30**, pp.1321-1339, 1990.

[65] Zienkiewicz, O.C., *The Finite Element Method*, McGraw-Hill Book Company Ltd., 3rd edition, Maidenhead, Berkshire, England, 1977.

[66] Zienkiewicz, O.C. and Zhu, J.Z.,'A simple error estimator and adaptive procedure for practical engineering analysis', *International Journal for Numerical Methods in Engineering*, **24**, pp.337-357, 1987.

[67] Zienkiewicz, O.C. and Zhu, J.Z.,'Error estimates and adaptive refinement for plate bending problems', *International Journal for Numerical Methods in Engineering*, **28**, pp.2839-2853, 1989.

[68] Zienkiewicz, O.C. and Zhu, J.Z.,'The three R's of engineering analysis and error estimation and adaptivity', *Computer Methods in Applied Mechanics and Engineering*, **82**, pp.95-113, 1990.

[69] Zienkiewicz, O.C. and Zhu, J.Z.,'The superconvergent patch recovery and *a posteriori* error estimates. Part 1: The recovery technique', *International Journal for Numerical Methods in Engineering*, **33**, pp.1331-1364, 1992.

[70] Zienkiewicz, O.C. and Zhu, J.Z.,'The superconvergent patch recovery and *a posteriori* error estimates. Part 2: Error estimates and adaptivity', *International Journal for Numerical Methods in Engineering*, **33**, pp.1365-1382, 1992.

[71] Zienkiewicz, O.C. and Zhu, J.Z.,'Superconvergence and the superconvergent patch recovery', *Finite Elements in Analysis and Design*, **19**, pp.11-23, 1995.

[72] Zienkiewicz, O.C., Zhu, J.Z. and Wu, J.,'Superconvergent patch recovery techniques - some further tests', *Communications in Numerical Methods in Engineering*, **9**, pp.251-258, 1993.

[73] Zlámal, M.,'Some superconvergence results in the finite element method', in *Mathematical Aspects of Finite Element Methods*, (ed. de Boor, C.), pp.353-362, Springer-Verlag, Berlin, 1977.